



HAL
open science

Multi-disciplinary study on the hydrogeological behaviour of the Eastern flank of the Merapi Volcano, Central Java, Indonesia

Adrien Selles

► **To cite this version:**

Adrien Selles. Multi-disciplinary study on the hydrogeological behaviour of the Eastern flank of the Merapi Volcano, Central Java, Indonesia . Hydrology. UPMC Université Paris VI, 2014. English. NNT: . tel-01113604

HAL Id: tel-01113604

<https://hal.science/tel-01113604>

Submitted on 6 Feb 2015

HAL is a multi-disciplinary open access archive for the deposit and dissemination of scientific research documents, whether they are published or not. The documents may come from teaching and research institutions in France or abroad, or from public or private research centers.

L'archive ouverte pluridisciplinaire **HAL**, est destinée au dépôt et à la diffusion de documents scientifiques de niveau recherche, publiés ou non, émanant des établissements d'enseignement et de recherche français ou étrangers, des laboratoires publics ou privés.

**THÈSE DE DOCTORAT
DE L'UNIVERSITÉ PIERRE ET MARIE CURIE**

Spécialité: Hydrogéologie

Ecole doctorale Géoscience Ressources Naturelles et Environnement

présentée par

Adrien Selles

pour obtenir le grade de:

Docteur de l'Université Pierre et Marie Curie

**MULTI-DISCIPLINARY STUDY ON THE HYDROGEOLOGICAL
BEHAVIOR OF THE EASTERN FLANK OF
THE MERAPI VOLCANO, CENTRAL JAVA, INDONESIA**

M.	Ghislain de Marsily	Président du Jury
M.	Julio Gonçalves	Rapporteur
M.	Jean-Luc Michelot	Rapporteur
M.	François Beauducel	Examineur
M.	Steve Ingebritsen	Examineur
M.lle	Sophie Violette	Directrice de thèse
M.	Olivier Béon	Invité
M.	Heru Hendrayana	Invité
M.	Wahyu Triraharia	Invité

Soutenue le 26 Juin 2014





Abstract

The current knowledge on the hydrogeological behavior of the volcano-detritic edifices is still sparse and these lacks limit the attempting of water resource management. Since a decade, on the flanks of Merapi volcano, in Central Java, Indonesia, an increasing pressure is done on the water resource with the intensification of the irrigated agriculture practices, the growth of population and the water industrial uses. The lack of knowledge about the water cycle processes by the consumers triggers water use conflicts and the water sharing becomes a central issue. A most accurate understanding of the water cycle in its globality in this kind of context is hence a fundamental point that need to be improved.

This work has been focused on the characterization of groundwater resource through the identification of the extent, the geometry and hydrodynamic properties of the aquifers/aquitards multi-layered system at the experimental catchment scale on the Eastern flank of Merapi volcano. To cover all the processes involved into the groundwater circulation, a multi-disciplinary approach has been chosen.

A new geological and geomorphological approach is performed to characterize the internal structure and the deposit architecture on this zone of the Eastern flank of the Merapi. Based on these results, a geological and geomorphological conceptual model has been built and insists on the channelized detritic formations connected from the upper parts to the low lands through the volcanic edifice and that create preferential groundwater pathways.

The climate characterization with the estimation of the water balance terms and the description of main hydrological processes are described with the monitoring of two hydrological years (2011-2012 and 2012-2013). The tropical climate of this region is characterized by seasonal monsoon (November to May) and dry season (June to October). The global water balance can be distributed as follow: 40% of rainfall are lost by evapotranspiration, 10% runs off and the remaining half infiltrates through the volcano-detritic edifice to recharge the multi-layered aquifers.

The hydrogeological functioning of a complex volcano-detritic environment is explained through the implementation of hydrogeological, hydrochemical and geochemical monitoring on inventoried springs and wells. Two spring belts are described, the first one is characterized by depression spring along a topographic line while a normal fault is probably at the origin of the second one. The identification of a multi-layered aquifer systems has been done based on the determination of the spring water temperature as a relevant tracers of the recharge elevation and the groundwater circulations. The hydraulic properties of these aquifers have been investigated from the analysis of hydraulic tests. Results show a low permeable aquifer close to the surface with a local recharge while a second aquifer system with high permeability and regional recharge is located deeper. The tracer

temperature shows a mixing effect between the first and the second aquifers in the springs at low elevation. This phenomenon is confirmed by the isotope analysis.

The application of a coupled numerical model between flow circulation, first mass transfer and second heat transfer confirms the hydrogeological conceptual model of volcano-sedimentary edifice and allows to quantify the water resource.

Key words: Hydrogeology, volcano-detritic, water balance, Merapi volcano, multi-disciplinary, groundwater modeling

Forewords

This PhD-Thesis has been funded by the ANRT with a CIFRE scholarship and Danone Research. This work takes part of the Klaten project, created in close collaboration with French (CIRAD (Centre de coopération internationale en recherche agronomique pour le développement), UPMC (Université Pierre et Marie Curie)) and Indonesian (IAHRI (Indonesian Agroclimate and Hydrology Research Institute), National NGO BINA SWADAYA, PU (Public Work), BPTP (Institute for Agricultural Technology) and UGM (Universitas Gadjadara)) Institutions with the support of a private partner (DA-CSR DANONE Aqua–Corporate Social Responsibility). Several specialists have been included into the project to supervise a specific thematic. Thus, Benoît Deffontaines (Université Paris East Marne la Vallée, France) has contributed to the understanding of the geological and geomorphological structure of the volcanic edifice, Fayçal Rejiba (UPMC, France) has contributed to the geophysical analysis while Patrick Goblet (Ecole des Mines, France) has provided the numerical code METIS and his knowledge into the numerical modeling part. The chemical analysis have been done by the Laboratory of the BRGM Orléans (France), the Danone laboratory in Evian (France), and the geochemical analysis have been performed by the Laboratoire d’Hydrogéologie d’Avignon (France) and the IDES Interactions et Dynamiques des Environnements de Surface (Orsay, Paris Sud, France).

Contents

Introduction	1
1 Context	6
1.1 Geography and Geology	7
1.1.1 Indonesia and Java geology	7
1.1.1.1 Java Island origin	7
1.1.1.2 Morphology of the study area	11
1.1.2 Merapi volcano, eruptive history	12
1.2 Global climate	17
1.2.1 Atmospheric circulations	17
1.2.2 Monsoon and dry seasons	19
1.2.3 Regional climate network	20
1.3 Hydrology and Hydrogeology	21
1.3.1 Surface stream characteristics	21
1.3.2 Volcano-detritic aquifers	21
1.3.2.1 Aquifer architecture	24
1.3.2.2 Aquifer/Aquitard properties	25
1.3.3 Watershed scale, surface and underground boundaries	26
1.3.3.1 About the rivers' names	26
1.3.3.2 Catchment boundaries	27
1.4 Water as a resource in Klaten and Boyolali Regencies	28
1.4.1 Administrative subdivisions of Indonesia	28
1.4.2 History and demography	29
1.4.3 Land use	31
1.4.4 Water uses	32
1.4.4.1 Agriculture uses	32

1.4.4.2	Domestic uses	33
1.4.4.3	Industrial uses	33
1.4.4.4	Water management group	35
1.4.5	Klaten water conflicts	37
1.4.5.1	Water as a source of myth	37
1.4.5.2	Water as a source of conflict (2003-2004)	38
2	Geological and geomorphological structure	44
2.1	Merapi deposit architecture	46
2.1.1	Sedimentary characteristics of volcanoclastic and reworked epiclastic deposits	46
2.1.1.1	Syn-eruption deposits	47
2.1.1.2	Inter-eruption deposits	53
2.2	Merapi geological history	55
2.2.1	Pre-Merapi	56
2.2.2	Old Merapi	56
2.2.3	Middle Merapi	57
2.2.4	Recent Merapi	58
2.2.5	Modern Merapi	59
2.3	Merapi morphology	61
2.3.1	About the longitudinal and lateral facies variations	62
2.3.2	Top-down dynamic processes: from dismantling to sedimentation	64
2.4	Identification of drainage anomaly	70
2.4.1	River interceptions	70
2.4.2	River incision characteristics	72
2.4.3	Lithological stratigraphical analysis	74
2.4.4	Proposed reconstitution of the recent Merapi volcanic activity from the eastern flank deposits	79
2.4.5	Origin and magnitude of the event	81
2.4.6	Characterize the paleo-river geometry by geophysics methods	82
2.4.6.1	Material and method	82
2.4.6.2	Theory	83
2.4.6.3	Field survey of June and July 2012	85
2.4.6.4	Results of the geophysical survey	86

2.4.6.5	Comparison with available stratigraphic logs	91
2.5	Update of the andesitic volcanic facies conceptual model based on the eastern flank of Merapi	93
2.6	Conclusion	94
3	Climate and hydrological functioning	98
3.1	Methodological approach	99
3.1.1	Surface and ground-water delineations	99
3.1.2	Experimental site and monitoring network	100
3.1.2.1	Existing rain-gauges	100
3.1.2.2	Additional rain-gauges and weather stations	101
3.1.2.3	Thermometers	101
3.1.2.4	River Automatic Water Level Recorders	102
3.1.3	Water balance method	104
3.1.4	Rainfall spatial distribution and intensity	105
3.1.5	PET (ET_0) and RET	106
3.1.5.1	The FAO Penman-Monteith method (PM)	106
3.1.5.2	The effective rainfall	108
3.1.6	Runoff	108
3.2	Study site	108
3.2.1	Site description	108
3.2.2	Land use	110
3.3	Data processing	111
3.3.1	Climate data	111
3.3.1.1	Historical data	111
3.3.1.2	Hydrological years 2011-2013 data	113
3.3.2	Hydrological years 2011-2013 data	113
3.4	Water balance estimation	118
3.4.1	Evapotranspiration	118
3.4.2	Effective rainfall variability	123
3.4.3	River discharge and runoff	125
3.4.4	Water balance estimation	135
3.5	Discussion	136

4	Hydrogeological functioning	140
4.1	Methodology of hydrogeological approach	141
4.1.1	Inventory of the monitoring points	141
4.1.1.1	Spring zone descriptions	142
4.1.1.2	Deep and shallow well description	151
4.1.1.3	Geochemical analysis	167
4.2	Results	169
4.2.1	Shallow aquifer	169
4.2.2	Deep aquifer	178
4.2.2.1	Aquifer hydraulic gradients	183
4.2.2.2	Pumping test measures	184
4.2.3	Spring monitoring	190
4.2.3.1	Temporal evolution	190
4.2.3.2	Physico-chemical variable spatial distribution	198
4.2.4	Hydrogeochemical approach	207
4.3	Hydrogeological functioning synthesis	215
4.3.1	Aquifer system description	215
4.3.1.1	Shallow aquifer system	215
4.3.1.2	Deep aquifer system	215
4.3.1.3	Recharge areas and outlet zones	216
4.3.2	Water transit time estimation	217
4.3.3	Hydrogeological conceptual model	223
4.3.3.1	A complex multi-layered system	224
4.3.3.2	Upper part	225
4.3.3.3	SB1 zone	225
4.3.3.4	SB2 zone	225
5	Groundwater modeling	228
5.1	Flow and heat transfer modeling in hydrogeology	230
5.1.1	Temperature as groundwater tracer	230
5.1.2	Application in volcanic areas	233
5.2	METIS code: a groundwater, mass and heat transfers code	233
5.2.1	Mathematical formulation	234
5.2.1.1	Flow circulation	234

5.2.1.2	Mass transport	235
5.2.1.3	Heat transfer	235
5.3	Numerical model configuration	236
5.3.1	From observations to modeling	236
5.3.2	Model geometry	239
5.3.3	Flow simulation	239
5.3.3.1	Flow parameters	239
5.3.3.2	Flow boundary conditions	241
5.3.4	Mass transfer simulation	244
5.3.4.1	Mass transfer parameters	244
5.3.4.2	Mass transport boundary conditions	245
5.3.5	Thermal simulation	245
5.3.5.1	Thermal parameters	245
5.3.5.2	Thermal boundary conditions	245
5.3.6	Modelling strategy	246
5.4	Simulation results	246
5.4.1	Flow calibration	246
5.4.2	Flow calibration constrained by mass transport simulation	250
5.4.3	Model geometry sensitivity tests	253
5.4.4	Sensitivity test on thermal parameters	257
5.4.5	Transfer time estimation	261
5.5	Synthesis	263
6	Hydrochemical approach	268
6.1	Hydrochemical and geochemical analysis	269
6.1.1	Major and Minor elements	269
6.1.2	Emerging contaminant analysis	270
6.2	Results	271
6.2.1	Groundwater hydrochemical properties	271
6.2.1.1	Water quality	271
	Conclusion	285
	Bibliography	319

A Geology and geomorphology	321
A.1 Pyroclastic rocks classification	322
A.2 Merapi volcano evolution	324
B Geophysics	325
B.1 Profiles	325
B.2 Lines	330
B.3 Soundings	332
C Hydrogeology	335
C.1 Hydraulic test protocol	335
C.2 Spring physico-chemical variables measures	339
C.2.1 Spring monthly flow rate	339
C.2.2 Spring monthly temperature	342
D Pictures	344

Acknowledgment

J'ai souvent trouvé qu'il y avait une analogie entre faire une thèse et réaliser un film: une pré-production hasardeuse, un tournage intense et une post-production pressée par une date de sortie en salle... Et comme dans les films, une thèse doit avoir son générique où les gens de l'ombre sont mis en valeur.

Je voudrais remercier ceux qui reliront ce travail avec un peu plus d'attention que la moyenne et qui me font l'honneur d'en être rapporteurs: merci donc à Julio Gonçalves et Jean-Luc Michelot. Je remercie également François Beauducel, Steve Ingebristen et Ghislain de Marsily pour avoir accepté le rôle d'examineur.

Un grand merci à Sophie Violette pour sa confiance, sa patience et surtout tous ses conseils en tant que directrice de thèse. Merci d'avoir su me pousser à "sauter à l'eau"...

Dans la foulée, je voudrais bien sur remercier Véronique Léonardi qui après m'avoir supporté en stage de Master à Montpellier, a eu l'idée saugrenue de me faire parvenir fin 2010 une offre de thèse "qui pouvais m'intéresser"... Merci Véro pour ton soutien!

I would like to say "Terima Kasih banyak" to Pak Heru Hendrayana for all his support in Indonesia. We can not imagine a better "manager" to go to the field.

Dans le rôle des producteurs exécutifs, je voudrais remercier toute l'équipe de Danone Research qui ont financé cette thèse. Tout d'abord un grand merci à Olivier Béon pour ses bons conseils, ses critiques et son aide qui m'ont permis d'entrevoir le monde de l'entreprise "à grande échelle".

Je me souviendrais toujours d'une ascension particulière du Merapi, ainsi que des nombreux jours sur le terrain avec ce dessinateur hors-pair. Sa pédagogie et son sens de l'humour en ont guidé déjà beaucoup et je suis fier de faire parmi de ceux là. Merci énormément Benoît Deffontaines, un géologue pas comme les autres.

Première équipe

I would like to thank all the indonesians colleagues that have supported me during nearly two years...

First, my dear Bimo, he was my first "contact" with this huge and complex Indonesian culture. I am still impress of his knowledge and his clear view on this "crazy" country. Makasih masbro.

On the field, I could not work completely alone. That is why Heri and Uzy were more than helpful to find several springs and also to tell me when it was useless to climb up there... I hope we will meet again in front of exotic geological outcrops! Mater nuwun!

Thanks to Eric, Narulita and Marco. It is not easy to have a french advisor, who climb everywhere, who draw more than he talks and who ask to speak english all the time... Sorry guys to have been so annoying but you were a great team, the “dream team” and it was only because I was beginner in “advisor stuff” that I was asking you “how are you?” all the time! You did a very good job and I really hope to see you again!

A big thanks to Idah, who share with me the big question mark of Merapi in term of water resource. Ida is this kind of person that you want to cross at least one time. Positive, funny and workoholic. Thanks for your bahasa class mbak!

It will be impossible to thank you as you deserve masbro. Mas Asta, officially my “driver” but a very good friend at first. Driver (pilot?), cooker, GPS, news collector, karaoke singer, pool professional, action movies fan, pigeon trainer... he can do everything, and he did anything to help me. Your company will miss me masbro. Sampai ketemu di Perancis!

Another masbro was very helpful on the field. Mas Eko, thanks for your kindness. Your eternal smile whatever was the situation (no keys? no gazoline? nobody? no problem!) is like an engraved stamp! Good job mas, I’m waiting for you in Europe...

I would like to thank all the AQUA factory in Klaten. Pak Atik, Pak Raden and so many others. Thanks for your “javanese” welcome and your support.

Mbak Fainta was here since the beginning and it was definitely more than a collaboration. I will never forget our long discussions along a rice field. Terima Kasih mbak. Good luck for the future...

Saya pikir orang-orang berikut tidak akan pernah membaca baris ini tapi saya ingin berterima kasih atas bantuan mereka dalam setiap jenis. Terima kasih Mbak Marni untuk rumah Anda "siap dalam dua minggu"! Semua orang dari PU klaten dan Boyolali untuk data berharga Anda dan dukungan Anda. Terima kasih kepada orang-orang Gumuk yang melihat "bule" datang dan pergi setiap minggu! terima kasih kepada semua orang yang saya telah bertemu di lereng Merapi!

Terima kasih Rita, Wulan, Sam and Yono. Terima kasih atas diskusi panjang sekitar tempe goreng. Terima kasih Wulan untuk iklan radio! Seperti pengalaman! Saya berharap untuk melihat kalian lagi guys!

Je pense à tous ces gens sur les chemins de source, près des villages qui voyaient un “bule” passer et repasser parfois plusieurs fois par semaine avec des bidons ou des appareils de mesure. A tous ces gens qui m’ont parfois ouvert leur puits, leur porte, offert leur repas ou juste un “teh panas” mais qui m’ont toujours regardé avec des grands yeux avant

d'échanger des sourires qu'on ne voit pas sous toutes les latitudes, à tous ces "Merapiens" je voulais dire un immense merci. Au fond, vous m'avez donné la motivation pour continuer quand ce n'étais pas la joie.

J'ai une pensée pour Yann Brault, initiateur du projet Klaten et qui nous a quitté en 2012, sans pouvoir voir les avancées de son ambitieuse idée. Merci pour ta bonne humeur et tes appels riches en quiproquos Yann. Tu nous manques tous.

When you are abroad, each encounter seems to play a role. Here, I want to thank all these globetrotters and Indonesians who help me to live my condition of free electron. Thanks to Katya and Sarah for the "paper wars" and the long discussions about the world. Thanks to Mike and Ken for the American karaoke ("I love this bar"), the beach parties and the food festivals! Thanks to Alex, Ella and Briony for the Australian accent and the artistic sharing! Thanks to Ellert for the Dutch jokes!

My Polish is still bad but now I know that anyplace is good to see the stars. Dziękuję Gocha. It was a wonderful adventure and you are the best roommate that I could have.

Sweet Charlotte. I do not have word to express how much I liked to share your road for a while. A perfect bulan madu illuminated by your smile and your positive point of view of everything. Even if it is not easy to find someone to travel with, Charlotte is one of them. But I will never challenge you again to make another "head-head" game, you have definitely won!

And finally I want to thank my sweet indonesian sister. Titik was always here. Ready for everything even if sometimes, it was hard (high mountain right?). You were the best support sister. Thanks and keep swimming!!!

I will forget a lot but I want to thanks all the people that I meet/cross during these two years: Andrian, Kate, Rully, Ichan, Winanto, Ana, Zita, Ryanto, Icha, Kartini, Olivia, Kristina, Sinta, Mada, Dara, Bimo, Sheng, T4, Mewa, Maryadi, Iwan, Wahyu, Amy, Elmer, Samras, Krishna... Terima kasih!

Seconde équipe

Revenons en France...

Je tenais à remercier Pierre Ribstein et Jean-Marie Mouchel pour m'avoir accueilli dans leur laboratoire qui a maintenant un nouveau nom, Sysiphe devient Metis. Merci à ces gardiens du temple qui à eux deux font l'ouverture et la fermeture du labo.

Continuons dans le laboratoire Parisien avec ceux sans qui la recherche serait purement impossible. Merci Nora Roger pour son sourire, sa disponibilité et son extraordinaire faculté à transmettre le sentiment que "tout va bien se passer" et "qu'il n'y a pas que le boulot dans la vie". Merci à Valérie Girard qui doit supporter les modifications et les petites erreurs de dernière minute de nous autre, petits thésard, qui partons en mission parfois à l'autre bout du planisphère. Toujours un soutien, merci pour tout Valérie.

Merci aussi à Dominique Daloz pour tout ces ordres de mission qui se sont accumulés dans son bureau.

Merci aux mystérieux 3ème étage et ses occupants qui malgré la distance énorme (1 étage, pensez donc...) étaient toujours sympathiques lors des pauses repas ou pause café de 15h15. Merci donc à Quentin qui a été le premier du trio à soutenir, Sylvain, Julien, Ludovic, Jamel et Fayçal.

Les laborantins ont aussi été d'une aide précieuse. Merci à Jacques Thiberioz pour les brefs rappels d'analyse de lames minces! Je remercie Benjamin bien sur, pour les longs débats cinématographiques. Un partenaire de cinoche comme on n'en fait plus depuis Ed Wood! Merci mec (promis je te rends ton dvd de Devil Story la semaine prochaine...). J'en profite pour remercier Simona, la plus française des Roumaine qui m'a toujours impressionné avec sa faculté à apprendre! Je remercie aussi Olivier qui était un vrai boute-en-train qui rafraichissait nos pause déjeuner. Merci à Sarah pour ses crises de fou rire, ses blagues Serbes et les gâteaux qui n'ont pas été assez nombreux. Luis, merci pour ta bonne humeur et les cervezas!

Venons en maintenant au fameux couloir. Le 56-55 du 4ème. Celui où l'on peut travailler en étant sur que l'on trouvera quelqu'un à qui parler de tout et de rien, de deviner le nom d'un fleuve, parfois de discuter boulot et même de croiser des tomates ou des golfeurs.

Merci à Daniele pour les footings au jardin des plantes et les escalopes de veau! Un immense merci au bureau SIG en commençant par Julie qui avec son accent belge était toujours un sourire agréable à croiser. Merci à Marie pour sa patience en ArcGis mais aussi un grand merci pour son dévouement et ses talents de photoshopeuse afin de faire des carnets ou des pochettes de fin de thèse drôle et toujours très fins. Merci à Gaby, pour ton crane toujours brillant et tes conseils Feng Shui. Merci Matthieu pour les long débats cinéma et les bons restos Viennois, j'espère qu'on te reverras aux soirées! Ludo, merci pour tes conseils de grand maître à la force tranquille. Super logo by the way...

Merci à Aurélien Baro, grande star du labo qui a donné plus de surnoms et d'aller simple au piquet que je n'en avais jamais entendu. Merci pour tes blagues même si elles sont souvent redondantes, merci aussi pour tes discussions volcaniques et pardonne nous nos blagues potaches.

Merci aux doctorants qui sont encore en train de vivre leur thèse à plein temps, Bahar pour son incroyable faculté à apprendre le français! Une iranienne pas comme les autres ça c'est sur! Bon courage pour la suite Bahar, et merci encore pour les repas livrés aux thésards en stade terminal et les longues discussions à Vienne! Tes glissades matinales vont me manquer!; Stephanie pour sa collection de cannettes et sa franchise toujours agréable; Marie B. pour ses discussions, sa prestation de Tomb Raider et son eau gazeuse; Pierre-Stephane pour son flegme à la Bob Dylan et son style à la Gaston Lagaffe et surtout pour ses bons conseils musicaux; Thibault pour arriver presque aussi tôt que moi; Sarah,

on se retrouve sous le ciel parisien, ce n'est plus la MSE mais merci d'avoir été là. Merci à Vincent pour son "check" matinal et ses mystérieuses plantations dans son bureau. Un éternel thésard qui a la sagesse d'un ancien chercheur. Bref, un grand monsieur ce papy Vincent.

Un grand merci à François membre central du thème CFP, ainsi nommé par Aulérien et qui m'a transmis ce rare plaisir d'être le premier arrivé au labo pour pouvoir faire une pause d'1h30 à 15h. Merci pour tes conseils d'hydrogéologue, de photographe et surtout de baisers fougueux. Je voudrais remercier un duo de comique qui se complète: Monsieur P. Brigode et Monsieur U. Oudet. Pierre, merci pour tant de conseils durant cette dernière année parisienne. Merci pour t'être arrêté pour prendre ses auto-stoppeuses à Hawaï. Ah ouais? De grands moments en mémoire (l'AGU, le Nash, un prêt de vélib à très long terme...). Monsieur, chapeau bas, barbe et désormais moustache haute! Mon cher Ugo maintenant, ton rire restera dans les annales, ainsi que tes blagues qui tournaient d'ailleurs autour principalement de ces dernières. Un personnage inoubliable, toujours là pour discuter, lancer les pauses et la cantine et boire une bonne bière le mardi soir. Merci pour tout ça Ugo.

Un grand merci à l'équipe d'hydrologie sociale avec Vazken, Charles, Nicolas, Thibault, Anne, Emma, Pierre Nicole, Florent, Laurent... et plein d'autres Anthoniens fan de freezbee et de chouffe mamanaise...

Une attention particulière au bureau 410 dans lequel j'ai pu faire l'intérim et poser mes bagages lors de mes brefs retours en France. C'est un bureau encombré d'histoires et d'objets parfaitement inutiles où il fait bon vivre. Et pour y avoir vécu une semaine non-stop, j'espère que la boîte de quenelles de veau côtoiera encore longtemps un microscope et un taille crayon de 1921. Merci Amadou, ta présence rassurante; Wilfried pour tes blagues, une coupe de cheveux mémorable et nos longues discussions; Nejla pour ta bonne humeur contagieuse et tes petits gâteaux toujours bienvenus, bonne chance pour la fin et à un de ces quatre à Vienne! Juliette, cachée derrière ton immense écran et posée sur Ginger, ta bouillotte poule (cela ne s'invente pas), je te dis merci pour les conseils sur R, les discussions sur l'avenir de l'agriculture mais aussi juste pour les bavardages toujours plus agréables les uns que les autres. Ne lâche rien, on se retrouve de l'autre côté. Ma très chère Claire, une pensée très particulière pour toi, grande sœur de thèse qui a l'étrange faculté de redonner du peps à n'importe qui en racontant ses aventures burlesques. J'ai eu la chance de partager cette drôle d'aventure avec toi du 410 à la bibliothèque de l'Hotel de ville, sachant que la mention "drôle" je te la dois particulièrement. Raphaël, petit dernier du 410 qui par sa haute cuisine (des gâteaux d'environ 30 cm) et sa sympathie a su tout de suite imposer sa marque. Bon courage pour la suite Raph, force et robustesse! Merci à Jacques et Christian, petits frères de thèse qui sont un exemple de travail intensif et passionné avec ce qu'il faut de timidité et de déconnade pour toujours passer un bon

moment.

Il était dans le 410 pour sa thèse mais j'avais déjà croisé ses tentacules au fin fond du bush Brésilien, Poulpy Paul, je te dois une fier chandelle. Merci pour ton flegme, ta drôlerie toujours bien calibrée et bien placée. Merci pour tout tes conseils, tes critiques et tes "Courrier international" qui trainaient partout. J'espère te recroiser en sortant des toilettes à Singapour ou ailleurs...

Un merci aux anciens qui m'ont vu arriver mais qui sont partis avant ma fin. Merci à Celestine pour ton appartement certes petit mais qui te ressemblait tellement. Merci au cornichon Fares, cornichon Guillaume (ça boom à Berlin?), Alex, Sandro, Pilar, Aurélien, Agnes, David, Chen et bien d'autres.

Merci au bureau des Emérites, où la routine n'a pas sa place. Au milieu de plusieurs strates de bibliographie, Michel tient le cap comme personne lorsqu'il est là (sinon, c'est Mélanie et moi qui répondions au téléphone...). Merci pour tes conseils éclairés Michel et pour tes anecdotes que seul un aventurier de la recherche comme toi peut avoir. Merci à mon autre co-bureau, la douce Mélanie qui a toujours le sourire, même de bon matin sous la douche.

Je ne pouvais pas remercier ma colloc de thèse. Pour avoir partagé bien plus qu'un emploi du temps de thèse collé-serré, je voudrais te remercier pour tout Cyrielle. Le labo fut notre unique lieu de vie pendant cette douce période de rédaction et je suis heureux de l'avoir partagé avec toi. Remplir les colonnes sèches qu'étaient nos manuscrits n'auraient pas été aussi plaisant sans toi. Tes blagues, nos longues discussions et ta franchise ont été salvateurs. On l'a fait!

Troisième équipe

Celle avec qui tout commença. Car avant Paris et l'Indonésie, il y a eu Avignon et Montpellier... Même si je n'ai pas souvent été présent ces derniers temps, j'ai beaucoup pensé à vous.

Merci au groupe de cocos d'Avignon: Nicolas, ami de toujours; Juliette partenaire de voyage; Aurélie pile comique; Aurélien, dandy dopé aux voyages; Vicky, pour ta vivacité; Tim, merci pour ce fameux pull à qui je dédis cette thèse!!! ; Bym, vieux grigou, pour nos échanges de passionnés passionnants; Mug, pour ces bons vieux fous rires; Psou, pour être toujours là et avoir pensé à moi pour Clotilde; Roro, pour ta bonne humeur indestructible.

Merci aux géologues de Montpellier, Dimitri, Greg, Théo, Rémi, et bien sur Clément pour ses délires et sa capacité folle de pouvoir faire des blagues aussi bonnes que sa musique, Eglantine pour ses chocolats chaud et sa franchise, j'espère vite regrimper avec toi! Merci Vivien pour tes conseils d'hydrogéologue et ton flegme à tout épreuves. Merci Amélie, Marie (ou Marie Chantal?), Benjammin (Ben ou Benji pour son nom de scène), Mylène, Laure & Virgile et un grand merci à Marine pour m'avoir laissé partir, ça a été douloureux

mais je suis content du chemin que l'on a fait. Merci aussi à Elise pour les discussions critiques ciné (mais qui a aimé "le Prophète"!?). Merci à Loïc pour son dévouement et son amitié sans faille, quelque soit le continent. Merci à Estelle et Niels pour les pic nic sous la pluie!

Un grand merci bien sur à ma famille: Papa, nous n'avons jamais été aussi proche que lors des skype hebdomadaires finalement, merci pour tout tes petits défauts qui au finalement tellement apportés; Maman, merci pour tout, il y aurait de quoi faire une thèse sur tout ce que je te dois, et même si la discipline de cette thèse est difficile à définir (philo?, histoire?, sport?, littérature?...), j'en connais le titre: Carpe Diem ; merci à mes grand parents qui m'ont toujours soutenu même quand je parlais sur un endroit que l'on ne savait pas mettre sur la carte; Sophie pour tes conseils et ta bienveillance, Emeline, pour tes dessins, ta sensibilité et juste toi; Marcelyne, je te conseille de ne pas faire une thèse quand tu seras grande; Annie, Vincent, Camille, Noémie et Sarah, voyez, maintenant c'est moi qui part loin; Jean-Loup pour m'avoir montré que le terrain c'était la base de la recherche.

Je ne sais pas comment remercier celle qui a bien voulu partager un bout de chemin avec moi. Un immense merci à Marceline ou Marcel pour les intimes qui maintenant me supporte au quotidien. Ce n'est pas simple de supporter un thésard mutique qui mange des nouilles avec des escalopes de poulets au petit déjeuner. Tu m'as tellement apporté. Et puis, tu m'as permis d'assouvir mon plus vieux fantasme (de sortir avec la maitresse...). Depuis ce retour en vélib, tu étais là quand ça n'allait pas et quand ça allait bien, tu y étais souvent (toujours?) pour quelque chose. Les petits bonheurs de tous les jours étaient doubles parce que je les vivais avec toi. Merci pour tout ma parisienne. Ce bout de chemin restera précieux. Tu es ma Kate Capshaw en mieux (et en brune!) et j'ai hâte de partir pour de nouvelles aventures avec toi...

Je voudrais aussi remercier ceux qui ne liront jamais ceci: le cyber-café Genesis à Yogyakarta, le Nasi Goreng d'en face, la boulangerie de jussieu, John Williams, Radio Nova, Steven Spielberg ("Call him Dr Jones"), Don Rosa (je suis sur tes pas Balt), Hans Zimmer et tant d'autres...

Pour finir ce générique interminable, merci au lecteur assidu où procrastinateur acharné qui aura lu toutes ces lignes. Un conseil de docteur: n'arrête jamais de te poser des questions.

à tous ceux qui se sont déjà demandés d'où venait l'eau du robinet...

Introduction

Water resource in tropical environment are usually considered to be in sufficient quantity because of their large amount of rainfall and it is easy to think that water issues are rare in these regions. Nevertheless, the tropical rainfall distribution is highly heterogeneous both in space and in time which triggers water use conflicts between water consumers such as the farmers or industrial companies. These conflicts come from the low knowledge of the water cycle by the users. They could be avoid with better knowledge about the climate pattern, in order to anticipate its negative effect on water resources during the extreme hydrological year (i.e. flood or drought event).

The tropical climate is characterized by seasonal monsoons with high amount of rainfall during several month and dry season with almost no precipitation. On a hydrological point of view, the surface water is nearly not available during the dry season since the streams are ephemeral. Therefore, climate is not the only responsible of the unequal water resource distribution. During the dry season or in locations where the rain is barely distributed, groundwater represents the main and sometimes the unique water resource. This resource depends of the climate through the recharge but also of the geological structure, the aquifer hydraulic properties and the extraction rate by the users. Indeed, the increase of the demography, the intensification of the irrigated agriculture practices and the trade of private drinking water companies in these regions increase the pressure on the water resources.

In locations with complex geological structure, the challenge is to identify the aquifer structures, to understand the groundwater circulations and to quantify the groundwater resource in view to improve its management.

Indonesia is a country among others that combines these two specifics issues: it is located in tropical humid zone and is mainly constituted by recent volcano-sedimentary edifices, which are considered as heterogeneous hydrogeological formations because of their large range of permeability and complex deposit architecture. The current knowledge about the hydrogeological behavior of the volcano-detritic edifices is still sparse even in the scientific literature, hence, these lacks limit the attempting of water resource management. A most accurate understanding of the water cycle in its globality in this kind of context is thus a fundamental point to improve the water management.

The Merapi volcano is one of these volcano-sedimentary edifice, located in Central Java, near the cultural city of Yogyakarta. Its activity is characterized by explosive eruptions occurring every 4-5 years (Melchior, 2011; Gertisser et al., 2011). The last major eruption occurred in 2010 where more than 300 people died and several villages were burned during the dome collapse and the pyroclastic flow events (Charbonnier et al., 2013). Therefore, most of the geological studies are focused on the characterization of the eruptive activity of the Merapi rather than the groundwater circulations. Some studies mentioned the groundwater/magma interaction and questioned the role of the water into the eruption cycle of even their explosive power but the authors are barely talking about the groundwater resource as crucial value (Commer et al., 2006). However, the issue of water resources is essential, even in crisis time. Indeed, during the eruptions of 2006 and 2010, several assistance projects have been created to build emergency deep wells to supply drinking water to refugees. The efficiency of these wells have been criticized in particularly due to a lack of knowledge about the groundwater circulation (MacRae & Hodgkin, 2011).

Because of the flank collapse events of the last eruptions, the crater is now opened to the South and West sides of Merapi, giving a horseshoe shape to the summit (Van Bemmelen, 1949; Gertisser et al., 2012b). This geomorphological particularity creates a preferential pathway for the pyroclastic flows and lahars (Charbonnier et al., 2013). Thus, the geological, geomorphological and hazard studies are mainly focused on these flanks. In contrast, the North and East flanks are spared by the recent major eruptions but have a complex geological evolution.

Despite the deadly volcanic activity, the population surrounding the Merapi is close to one million in a half of inhabitants with a growing demography which is increasing the pressure on the water resource. In addition, Central Java and especially Klaten and Boyolali Regencies are considered as “Java island rice granary” with a high productive rice cropping which need more water every year (Bourgeois et al., 2008). The governmental institutions and several bottled water companies are settled up in Klaten/Boyolaly Regencies and provide drinking water to the population. Since a decade, the cost to make a deep bore well in view to extract groundwater for irrigation or direct consumption is affordable for most of local farmers. Therefore, the number of private bore wells in this region sharply increases without any control or sustainability management. The cooperation between the agriculture practices, needing large amount of water, and the private company is fragile and conflicts appear since the beginning of the 2000’s. The lack of informations about the water cycle processes and resource quantification intensifies the tensions. Therefore, there is an urgent need to better understand the water cycle in its globality through a methodological approach at watershed scale for this type of environnement in view to quantify and protect the groundwater resource.

This PhD program is included as part of the “Klaten project” which has been developed

with the objective to better understand the water cycle on the Eastern flank of Merapi and to identify the extent, the geometry and the hydrodynamic properties of the potential aquifers. The final goal is to provide an estimation of the recharge rate, the recharge area and the water balance on the main aquifer bodies.

The Merapi volcano is a representative example of volcano-sedimentary edifice and this project is an opportunity to filled the lack of knowledge and propose a hydrogeological conceptual model for this kind of volcano-detritic environment.

To carry out this mission, a multi-disciplinary approach has been undergo. This approach appears as the best way to understand the water cycle in its globality, from atmosphere compartment to underground one through the surface one. Thus, this study is focused on several objectives:

1. To improve the knowledge on the hydrogeological functioning of volcano-sedimentary edifice in equatorial climates where literature is scarce regarding to complex systems with a rainfall distribution very heterogeneous both in space and in time.
2. To suggest a quantification of the water balance and water resources through a multi-disciplinary approach developed throughout an experimental site based on:
 - (a) the characterization of the deposits and their hydrodynamic properties (geology, geomorphology, geophysics) leading to the establishment of a geological 3D model
 - (b) the implementation of a monitoring network of climatic, hydrological, hydrogeological and geochemical variables on two hydrological years (2011-2012 and 2012-2013), identifying recharge areas, preferential flow paths, relevant tracers to characterize flows and finally to propose a conceptual model of flow
 - (c) using a coupled numerical model with flow circulation, first with mass transfer, second with heat transfer to validate or not the assumptions and in view to propose a quantification of the water resource.
3. To provide scientific bases and keys of concrete actions to clear a recurring problem of conflicts to users and managers of water resources.

This work is divided in six chapters that provide the necessary keys to the overall understanding of the system:

- Chapter 1: *What? Where? Why?* This first chapter introduces the global context of this project and defines the boundaries of the study area. An assessment on current knowledge about geology, climate, hydrology and hydrogeology in this case of environment is drawn up.

- Chapter 2: *How is the deposit architecture of a volcano-sedimentary edifice?* Combining the Merapi's history details found into the literature, field observations of facies deposits and GIS analysis, the geological and geomorphological structure of a volcano-detritic edifice is detailed. Based on new field observations, the aquifer and aquitard formations have been identified. The geometry of the aquifer layers has been confirmed by geophysics (geo-electric) methods. A 3D conceptual model of the deposit architecture of the Eastern flank of Merapi is hence proposed.
- Chapter 3: *What is the climate pattern? How is the hydrological behavior of an andesitic volcano in tropical environment? What is the hydrologic balance at watershed scale?* As the historical climatic data were no available, the implementation of climate and hydrological monitoring network, allows us to obtain, over two hydrological years (2011-2012 and 2012-2013), a new data set of climatic variables such as rainfall, air temperature, solar radiation, humidity etc. and hydrological data such as river flow rate. Using a water balance estimation, the recharge of the groundwater system is hence calculated.
- Chapter 4: *How the groundwater circulations work in volcano-sedimentary edifices?* As a pilote effort, we have implemented a thorough hydrogeological monitoring network. This monitoring allows to identify the groundwater flows dynamics with low cost, simply-measured but relevant tracers. Finally, the data interpretation lead us to built a hydrogeological conceptual model for groundwater circulations into this volcano-detritic edifice.
- Chapter 5: *Is it possible to validate the conceptual model?* In this synthetic chapter, combining all the previous interpretation into a coupled flow first with mass transfert, second with heat transfer numerical model (METIS model ([Goblet, 1981](#))) the validation (or not...) of the hydrological conceptual model assumptions is realized.
- Chapter 6: *How is the water quality?* In this final chapter, we will be focused on the hydrochemical and hydro-geochemical pattern of the groundwater resource based on the monitoring and several analyses performed in 2012 and 2013.

1 Context

Introduction

This chapter describes the global framework of this research project to better understand the stakes related to the groundwater knowledge. The study of groundwater resource is subject to several factors such as the choice of the study area, the population and its water uses, the climate variables and the geology. In the first part of this chapter, the morphology of Central Java and the geological context will be presented with a brief introduction to Merapi volcano history which will be detailed in the Chapter 2. The second part is dedicated to the climate situation in Java. The third part is a short review of the hydrogeological properties of the volcano-sedimentary aquifers. The fourth part is focused on the anthropic occupation, the water users and their conflicts on the Eastern flank of Merapi volcano.

1.1 Geography and Geology

1.1.1 Indonesia and Java geology

1.1.1.1 Java Island origin

Indonesia is a large archipelago of more than 18 000 islands stretched over 5000 km from east to west between 95° and 141° E, and across the equator from 6°N to 11°S (Fig. 1.1). Indonesia is situated at the boundaries of three major tectonic plates: Eurasia, India–Australia and Philippine Sea-Pacific. The India-Australian plate was moved northward and subducted under the Eurasian plate. The subduction zone can be traced from northern tip of Sumatra until the Lesser Islands that create deep submarine trench. Most of the earthquakes also concentrate in this subduction zone. This subduction also triggers the formation of volcanic range that extends from Sumatra, Java to Lesser Islands ([Van Bemmelen, 1949](#)).

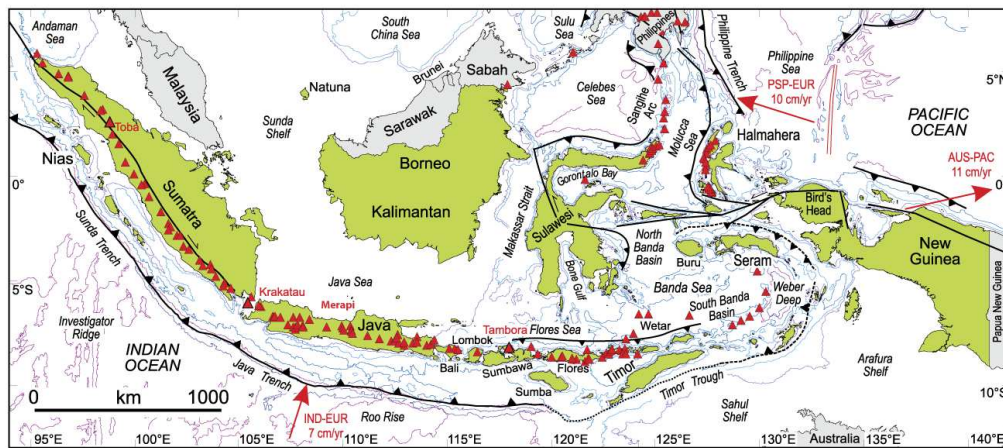


Figure 1.1: Geography of Indonesia, tectonic boundaries and volcanic activity. Indonesia is in green, and neighbouring countries are in grey. Bathymetric contours are at 200 m, 1000 m, 3000 m, 5000 m, and 6000 m. The location of the three most famous explosive eruptions known of the Indonesian volcanoes are shown in red text. Red arrows show plate convergence vectors for the Indian plate (IND-EUR) and the Philippine Sea plate (PSP-EUR) relative to Eurasia, and for the Australian plate relative to the Pacific plate (AUS-PAC). There is little thrusting at the Timor trough. The Seram trough and Flores-Wetar thrusts are the sites of active thrusting. Modified after [Hall \(2008\)](#).

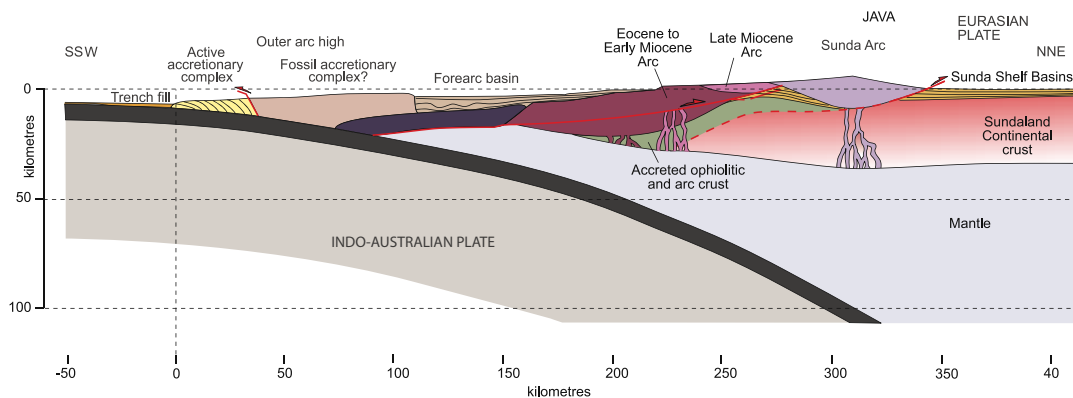


Figure 1.2: Regional cross-section of Java margin (Modified after [Clements et al. 2009](#)).

The subduction zones are well defined by seismicity extending to depths of about 600 km and by volcanoes. There are at least 95 volcanoes in Indonesia that have erupted since 1500, and most are situated between 100 and 120 km above descending lithospheric slabs ([Hamilton, 1988](#)).

Java is one of the many islands at the Eurasian margin. Its area is 127 000 km². This island is the result of orthogonal subduction. The volcanic island appears to have a relatively simple structure ([Van Bemmelen, 1949](#); [Clements et al., 2009](#)).

After Cretaceous collision of an Australian micro-continental fragment with the Java–Meratus subduction system, subduction ceased and there was a passive margin south of Java until

the Eocene (Hall, 2002a; Katili, 1975). Several studies (Smyth et al., 2005; Clements et al., 2009) consider there is Gondwana crust beneath parts of East Java and that there is a continental crust beneath the Southern Mountain that extends west almost to Yogyakarta. Clements et al. (2009) suggest that the Southern Mountains arc was originally present in this area but was subsequently thrust northwards and removed by erosion (Fig. 1.2).

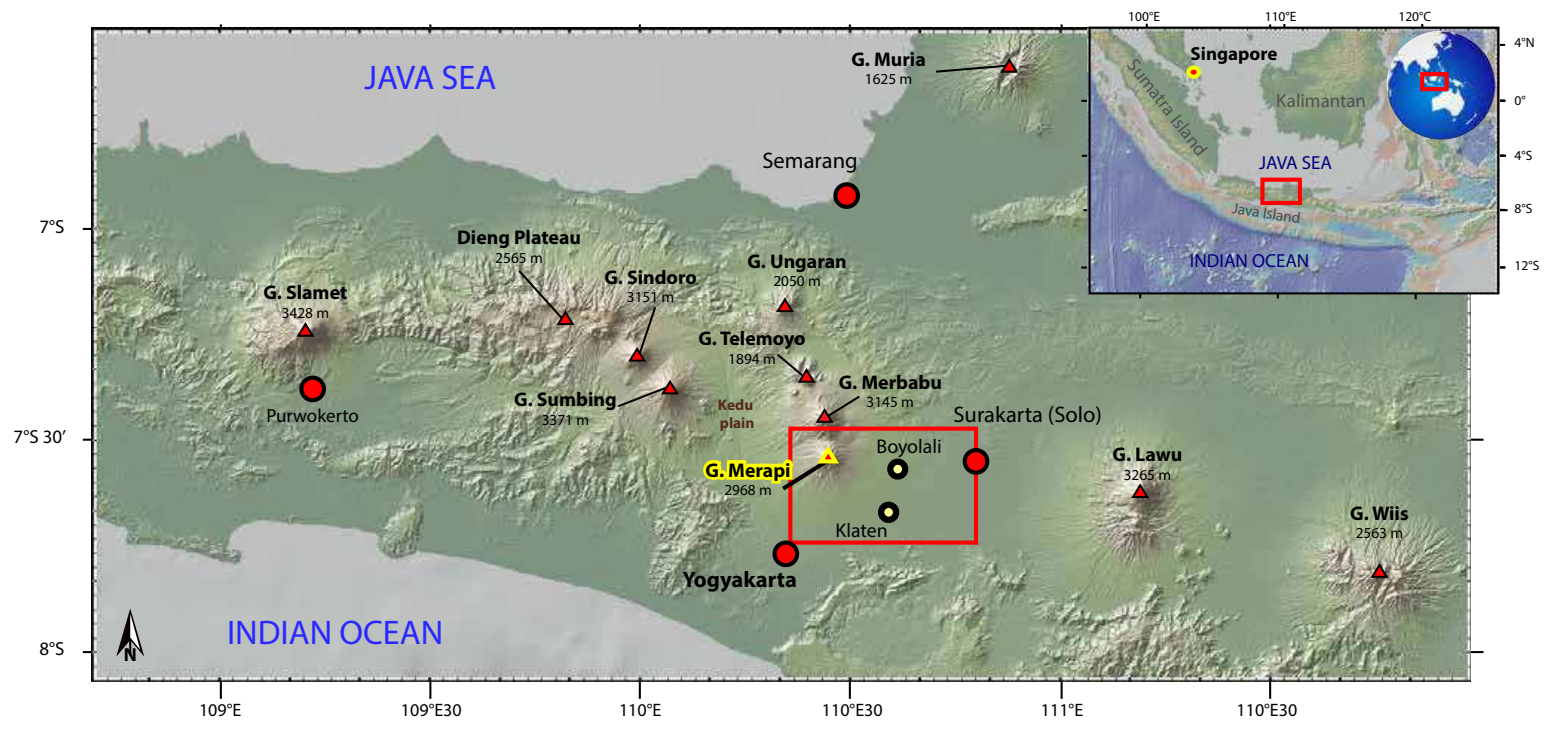


Figure 1.3: Index map of the study area. Maps obtained by GeoMapApp (Ryan et al., 2009).

1.1.1.2 Morphology of the study area

Central Java Province is located between 108°30' - 111°30' east longitude and 5°40' - 8°30' south latitude (Fig. 1.3). The area is approximately 32.5 km². The geography of Central Java is regular with small strips of lowlands near the northern and southern coasts with mountain ranges in the region center. To the west lies the Java's second highest and active stratovolcano, the Mount Slamet (3428 m). Further east is the Dieng Volcanic Complex on Dieng Plateau (2565 m). Southeast of Dieng lies the Kedu Plain, which is bordered to the east side by the twin volcanoes of Mount Merapi (2965 m) and Mount Merbabu (3145 m). South of Semarang, lies Mount Ungaran (2050 m), and to the north-east lies Mount Muria (1602 m). To the east near the border with East Java lies Mount Lawu (3265 m), where its eastern slopes are in the East Java province. Central Java exposes a deeper structural level than either East or West Java; the upper thrust sheet of the volcanic arc has been removed and now exposes the rocks of the deep-marine trough, and the underlying basement is exposed. The unconformity separates Upper Cretaceous basement rocks and the Cenozoic succession, suggesting about 30 M.y. during which uplift and erosion occurred. [Smyth et al. \(2005\)](#) proposed three units, each representing a different period of arc activity. East Java can be subdivided into three parts, broadly parallel to the elongation of the island, representing: (1) the early Cenozoic Southern Mountains Arc, (2) the Kendeng basin, and (3) a marine shelf north of the basin.

1. The Southern Mountain Arc is constituted by an arc and ophiolitic rocks of Cretaceous age. A volcanic arc was built upon basement rocks from the middle Eocene to the Miocene in southern Java ([Smyth et al., 2005](#)).
2. The Kendeng Basin lies directly behind and to the north of the Southern Mountain Arc. The basin infillings were dated from middle Eocene to Miocene, similar to the Southern Mountains Arc. Gravity calculations indicate that the basin may contain as much as 10 km of sediments ([Smyth et al., 2008](#)).
3. The early Cenozoic Sunda Shelf is constituted by pre-Cenozoic basement rocks (ophiolitic and arc rocks), which include chert and basic volcanic and meta sedimentary rocks. Basin development began in the Eocene. There are between 2000 and 6000 m of Eocene to Pliocene shallow marine clastic and extensive carbonate sedimentary rocks within fault-controlled basins ([Hamilton, 1988](#)).

[Smyth et al. \(2008\)](#); [Clements et al. \(2009\)](#); [Karnawati et al. \(2006\)](#) showed a NE–SW fault, named Opak River fault, aligned with the Muria–Progo lineament, that is one of a conjugate pair of strike-slip faults that bound Central Java. A component of this fault was the epicenter of the Yogyakarta earthquake in 2006 ([Walter et al., 2008](#)). There is no surface evidence of strike-slip movement on either of the faults near Merapi volcano, but

they have a similar orientation to the cross-arc normal faults in East Java, and could be extensional faults covered by young deposits. Normal faulting on these faults would be consistent with the deeper structural levels exposed in Central Java. The length of the Opak River fault is not well defined and could be more important to the North (Fig.1.4). As we will see in Chapter 2, we showed that even though there is no surface evidence of fault, the hydrogeological features may confirm this structure at depth.

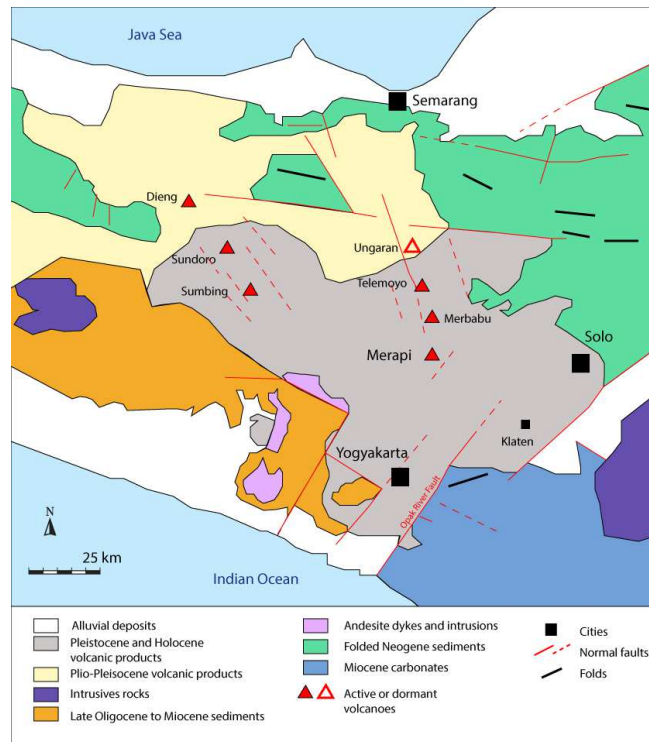


Figure 1.4: Geological map of Merapi and Yogyakarta basin showing the Opak River fault. Modified after [Karnawati et al. \(2006\)](#); [Walter et al. \(2008\)](#).

1.1.2 Merapi volcano, eruptive history

Merapi is an andesitic composite volcano located in Central Java, Indonesia (Lat: $7^{\circ}32'29,51''$ S; Long: $110^{\circ}26'55,77''$ E) (Fig. 1.6). It belongs to a chain of volcanoes (Ungaran, Telemoyo, Merbabu and Merapi) oriented $N65^{\circ}$ in an area of Java where the subduction is oriented along a north-south direction. Merapi volcano is one of the most active volcanoes of Indonesia, some of its eruptions being very violent ([Boudon et al., 1993](#); [Gertisser et al., 2011](#)). Its recent volcanic activity is characterized by the extrusion of viscous lavas forming lava domes in the summit area. The gravitational instability and collapse of these lava domes form small-volume pyroclastic density current (PDC) at regular intervals of a few years.

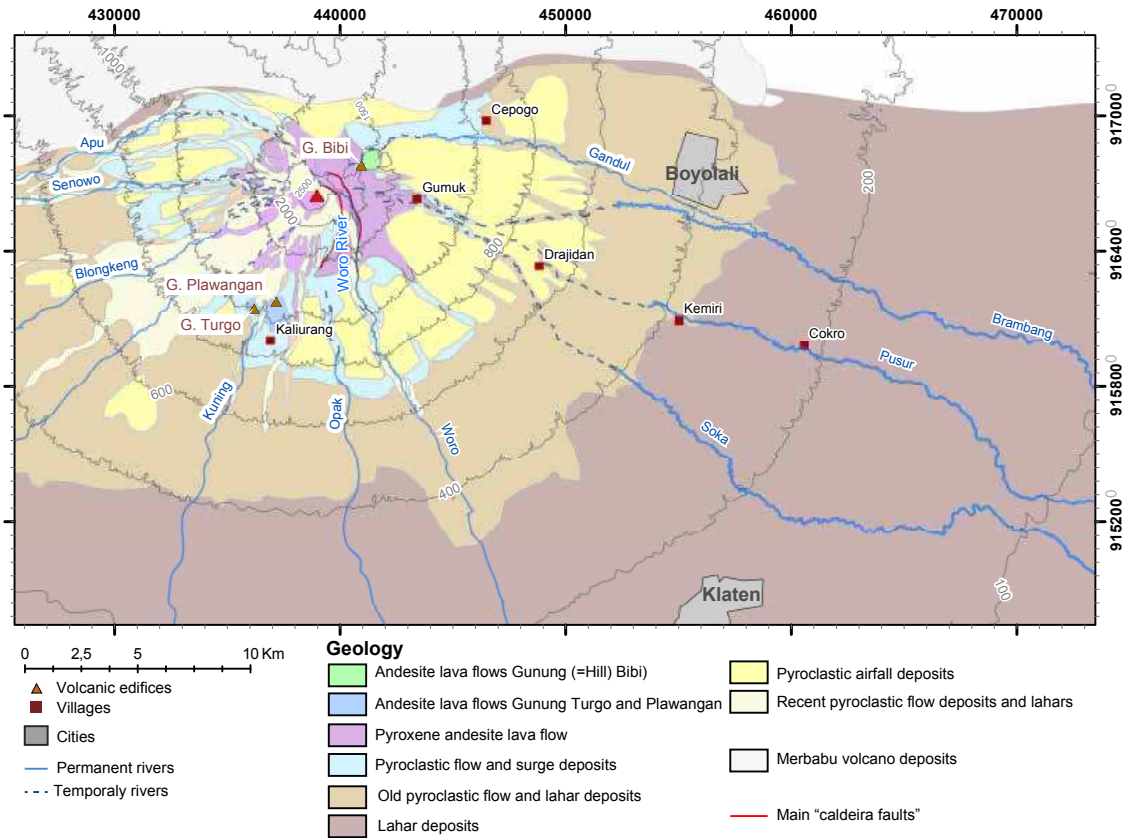


Figure 1.5: Simplified version of the 1:50000 geological map of Merapi volcano published in 1989 (Wirakusumah et al., 1989). UTM coordinates.

The topography of the volcano is conical-shaped with a mean dip angle of 5° up to 1300 m, 15° up to 1700 m and 40° up to the summit (Berthommier, 1990) (Fig. 1.6). The summit structure of Merapi itself is characterized by a crater which has moved westwards in recent years and is occupied by an unstable lava dome that is composed of very viscous lava. This area is essentially formed by unconsolidated rock as well as fractured lava blocks and ash matrix breccia (Beauducel, 1998).

The geologic map shown on Fig. 1.5, illustrates the extent of Merapi's volcanic deposits. The youngest deposits are primarily pyroclastic flow, lahar, and avalanche deposits. Recently erupted lavas extend no further than 5 km from the summit. Volcanic products of Young Merapi are largely confined to the SW flank of the volcano. The geological history of Merapi volcano will be explained further in the Chapter 2.



Figure 1.6: Sunrise on Merapi volcano, view from the Merbabu volcano (North).

The most recent eruption cycle started in 1992 after few years of calm. Since the eruption started in 1992, lava dome had been continuously extruded growing almost half a meter per day. In 1994, the entire collapse of lava dome generated pyroclastic flows which traveled several kilometers from the summit and killed 43 people. After the 1994 eruption, lava avalanches and pyroclastic flow had continued forming a new lava dome in the crater until the eruption activity calmed down in the late 2002. After five years of repose, volcanic activity at Merapi restarted in July 2005 with an increase in the number of volcanic earthquakes and deformation of the summit area. This renewed episode of unrest ended with the extrusion of a new lava dome on April 28th 2006 (Charbonnier & Gertisser, 2011). After a tectonic earthquake on May 27th, located 35 km south of Merapi, the largest pyroclastic density current descended 7 km down the south flank and killed two persons, who took refuge in a tunnel that had been built for their protection. Due to the particular location of the active lava dome, and the presence of a topographic barrier to the south of the new dome, the rockfalls of May 2006 were directed mainly towards the south-western flank of Merapi with runout distances of typically less than 4 km. Over a period of about two months, the 2006 dome collapsed repeatedly. The activity of Merapi dropped to background levels in early July 2006 (Walter et al., 2008).

The November 4–5th eruption was considered as a 100-year return period event by Surono et al. (2012). It was approximately ten times larger and more explosive than eruptions of the past several decades (Pallister et al., 2013). Recognizing the magnitude of this eruption and the potential threat of additional ones, the President of Indonesia requested assistance from the international community. On the morning of November 6th BNPB (Indonesian: Badan Nasional Penanggulangan Bencana, National Disaster Management Agency) provided a victim report. At that time there were 198 488 refugees, 218 people

were injured, and 353 people died. The 2010 VEI 4 (i.e. Volcanic Explosivity Index from [Newhall & Self \(1982\)](#)) explosive eruption of Merapi volcano reached a magnitude and intensity larger than the frequent eruptions of the 20th century. About 0.03 to 0.06 km³ of pyroclastic materials from pyroclastic density currents (PDCs) and tephra fallout were ejected during the eruption ([Suroño et al., 2012](#); [Komorowski et al., 2013](#); [Charbonnier et al., 2013](#)). This is ten times higher than other Merapi dome-collapse block-and-ash deposits produced in the 20th century ([Andreastuti et al., 2000](#); [Newhall et al., 2000](#); [Schwarzkopf et al., 2005](#)). Since 2010, several “small eruptions” have been inventoried. Most of them were gas plume with ash fall until 2 km above the summit and debris avalanche collapse. The most significant ones occurred in July 2013, November 2013 and recently in March 2014 with an ash plume that rose 9.8 km asl (above sea level). (BBTTK, Volcanic Observatory of Yogyakarta).



Figure 1.7: Morphology of the summit area. Before the October–November eruption (left) and after the eruption (right). Depth of the new crater is about 200m ([Suroño et al., 2012](#)).

According to [Thouret et al. \(2000\)](#), more than 1.1 million of people are at risk by Merapi eruption impacts with more than 400 000 people into the direct hazard zone (less than 30 km from the summit). Nevertheless, the local communities on the volcano have developed a system for living on its slopes and conceptualizing its hazards, which is based on naturalizing, familiarizing, and ‘domesticating’ the threat from the volcano. The villagers themselves say that eruptions favor grasslands as opposed to forests on Merapi’s upper slopes. They also say that periodic ash falls help to keep these grasslands unusually productive.



Figure 1.8: Panorama of Merapi crater in March 2013. The andesitic dome is clearly visible (center).

Eruptions are not the only danger on Merapi flanks. The young eruptive material can be remobilized during an intense rainfall event and generate a lahar. The Indonesian word “lahar” is applied as a general term for rapidly flowing, highly concentrated and poorly-sorted sediment-laden mixtures of water and rock debris from a volcano, not including normal streamflow (Smith & Lowe, 1991). Generally, lahars at Merapi volcano are brief events, related to rainstorms which commonly last 1 or 2 h (Lavigne et al., 2000). To reduce the damages and the casualties, several dam structures have been built since the late 1970’s but these dams were not calibrated for a high volume of material as the 2010 eruption produced (De Belizal et al., 2011).

Every watershed located under the active cone of the volcano was covered by the 2010 pyroclastic deposits, which raises the issue of the volcanoclastic remobilization of those deposits by rainfalls (de Bélizal et al., 2013). The lahars can be produced during a decade after a major eruption as at Mount Pinatubo (Philippines) after the 1991 eruption (Bautista, 1996). The major hazard zones regarding the lahars are located on the South and West sides of Merapi volcano and especially along the rivers (Fig. 1.9) (Lavigne & Thouret, 2003). Following the major eruption in November 2010, from December 2010 to April 2011, the area of mount Merapi recorded an exceptionally high frequency of lahars (several episodes per week) on the southern slopes of the volcano.

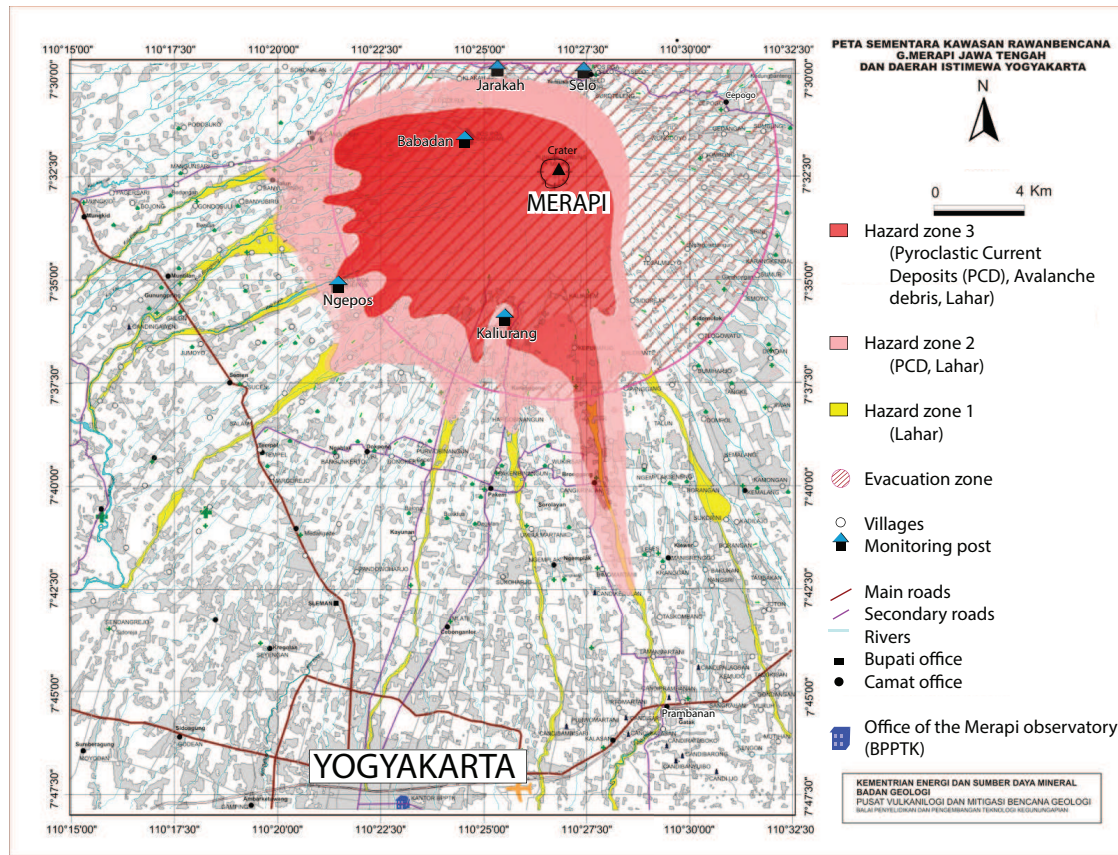


Figure 1.9: Hazard map of Merapi area modified after Merapi Volcano Observatory of Yogyakarta (Balai Penyelidikan dan Pengembangan Teknologi Kegunungpian (BPPTK)) after the eruption of November 2010.

The lahars can occur during the eruptive activity or during the quiescent periods. Lahars initiation generally requires an adequate water supply to remobilized the unconsolidated pyroclastic sediment. This flowing water is chiefly due to rainfall runoff (Neall, 1996). Since these processes are unpredictable, rapid and highly hazardous, direct observation and measurements are difficult to achieve (Vázquez et al., 2014). It is therefore necessary to characterize the hydroclimatic pattern such as the rainfall distribution and intensity not only to improve our knowledge on the groundwater resources but also to better anticipate the lahar formation to reduce the casualties.

1.2 Global climate

1.2.1 Atmospheric circulations

Central Java is included into the Indo-Pacific Warm Pool (IPWP) which is the warmest body of open-ocean water on Earth. Defined as the region where mean sea surface temperature (SST) is greater than 28 °C, the IPWP spans from the western tropical Pacific

Ocean, through the Indonesian archipelago, and across the eastern tropical Indian Ocean (Abram et al., 2009). The vigorous atmospheric convection that occurs over the warm pool influences the global distribution of heat and water vapour. Because of this, changes in the temperature, size and position of the IPWP have a profound effect on global climate (Pierrehumbert, 2000). Climate variability in the IPWP region is influenced by three major climate systems: the El Niño–Southern Oscillation (ENSO) (Rasmusson & Wallace, 1983) including its component the Walker circulation (Julian & Chervin, 1978), the Asian–Australian monsoon (Webster et al., 1998) and the Indian Ocean Dipole (IOD) (Saji et al., 1999). These three systems influence rainfall variability throughout the tropics and subtropics.

ENSO is a recurring pattern of climate variability in the eastern equatorial Pacific that is characterized by anomalies in both SST (referred to as El Niño and La Niña for warming and cooling periods, respectively) and sea-level pressure (Southern Oscillation). These anomalies appear every two to five years and last for several months or even a few years. Sea surface pressure fluctuations are most pronounced over Indonesia and in nearby tropical Pacific areas (Fig. 1.10). During El Niño events, deep atmospheric convection associated with the Indonesian low shifts eastward, induces drought over the Indonesian archipelago (Trenberth & Hoar, 1996).

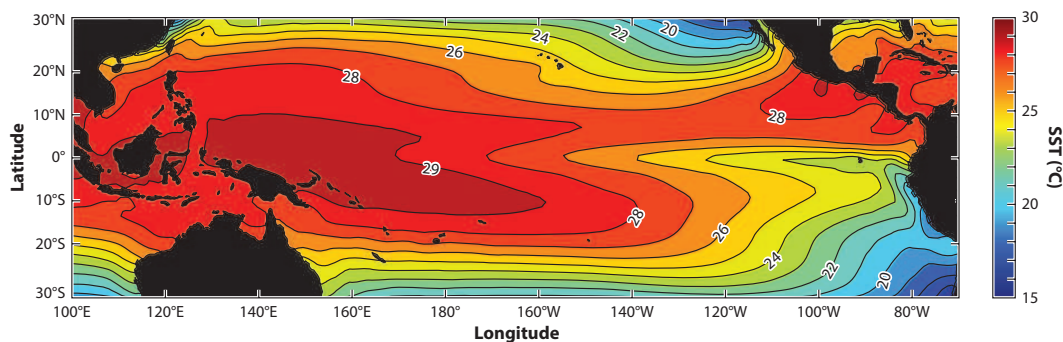


Figure 1.10: Mean sea-surface temperature (SST) in the tropical Pacific Ocean for the period January 1982–December 2012 (Clarke, 2014).

The Indian Ocean Dipole (IOD) is a coupled ocean and atmosphere phenomenon in the equatorial Indian Ocean that affects the climate of Australia and other countries that surround the Indian Ocean basin (Saji et al., 1999). A positive IOD period is characterized by cooler than normal SST in the tropical eastern Indian Ocean and warmer than normal SST in the tropical western Indian Ocean. Conversely, a negative IOD period is characterized by warmer than normal SST in the tropical eastern Indian Ocean and cooler than normal SST in the tropical western Indian Ocean. Thus, Indonesian climate is strongly affected by the inter-annual variation of the tropical sea surface temperature (SST) in the Pacific and Indian Oceans (Aldrian & Dwi Susanto, 2003).

Inter-annual variations in rainfall are influenced by the strength of the monsoons and the phase of ENSO, where anomalous cold SSTs, weaker Walker Circulation, and decreased vertical convection over the Indo-Pacific Warm Pool (IPWP) during El Niño events extent southeasterly flow over Java, lengthening the dry season and causing drought (Hendon, 2003).

Indonesian rainfall is highly coherent with local and remote SSTs during the dry half of the year (June–October) but uncorrelated with SST during the peak of the wet season (January–March). Drought conditions during the dry season occur in conjunction with the development of El Niño in the Pacific, when anomalous cold SSTs typically surround Indonesia while warm anomalies develop in the eastern Pacific and western Indian Oceans (Hendon, 2003). Conversely, enhanced Indonesian rainfall during the dry season occurs during the development of La Niña, with SST anomalies opposite to those of El Niño. The accompanying circulation anomalies during the dry season are consistent with these SST anomalies: diminished rainfall is accompanied locally by anomalous surface southeasterlies and the large-scale sinking motion, indicative of a weakened Walker circulation. Using the stable isotopes analysis of coral and lake sediments, several authors were able to compile a detailed reconstruction of SST variability and thus the monsoon regimes, spanning most of the last two millennia (Oppo et al., 2009; Konecky et al., 2013; Rodysill et al., 2013; Tierney et al., 2010). An abrupt and prolonged weakening of the northern hemisphere monsoons that began at 4400 years BP has been identified by Fleitmann et al. (2007) and is consistent with the warming of SSTs (i.e. warm pool expansion) in the northern part of Indonesia after 4300 years BP. This episode of monsoon weakening was part of a wide-scale change in tropical climate throughout Asia, the middle-east and eastern Africa and has been implicated in the collapse of a number of civilizations (Ha et al., 2012).

Rodysill et al. (2013) suggest that severe multidecadal drought occurred in East Java throughout the turn of the 19th century and was driven by locally reduced convection resulting from a combination of heightened El Niño activity and volcanic eruptions. Volcanic eruptions are indeed an important natural cause of climate change on many time scale (Robock, 2000; Hansen & Lacis, 1992). That is why the geological pattern has to be studied in the framework of any hydroclimatic and hydrogeological approach.

1.2.2 Monsoon and dry seasons

The Asian–Australian monsoon refers to the subtropical seasonal reversals in the atmospheric circulation and associated precipitation, leading to two distinct phases, “wet” and “dry” (Webster et al., 1998). In Java, one rainy season occurs when the cross equatorial flow turns westerly, bringing heavy precipitation from the northwest (October to May)

(Hamada et al., 2002). The corresponding trade wind south-easterlies are dry and characterized by a low-level inversion which caps deep convection (June to September) (Rodysill et al., 2013) (Fig. 1.11). In Central Java, the mean annual rainfall varying from 1700 mm up to 4200 mm per year (Hadi & Shrestha, 2011). The rainfall spatial distribution is strongly dependent on the reliefs (Aldrian & Dwi Susanto, 2003). Mean temperature in Central Java ranges between 14 and 28°C (Naylor et al., 2007).

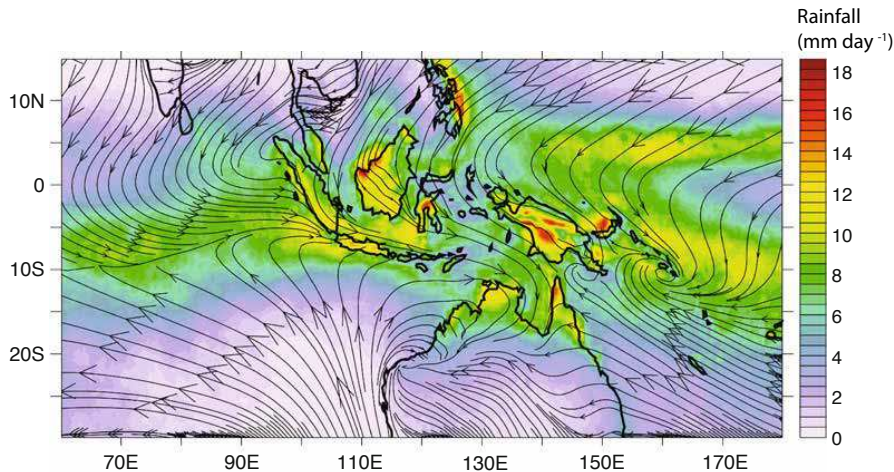


Figure 1.11: Observed rainfall (mm/day) on the period December to March averaged over 2001–2010, from the satellite based data TRMM-3B43. The stream lines show the surface wind from the atmospheric reanalysis ERAinterim averaged over the same period (Jourdain et al., 2013).

Onset date is defined to be the first wet day of the first 5-day sequence receiving at least 40 mm that is not followed by a dry 10-day sequence receiving less than 5 mm within the following 30 days from the onset date (Moron et al., 2008). The date of onset of the rainy season is of particular importance for the agriculture sector over Indonesia (Naylor et al., 2007). It determines the suitable time for planting crops, while delayed onset during El Niño years (Hamada et al., 2002) can lead to crop failure. For irrigated rice farmers in Java, information on onset timing is also important for developing strategies to avoid exposure of the second rice crop to higher drought risk at dry season planting (May–August), particularly for farmers located at the tail end of the irrigation system. Farmers in Indonesia often suffer from “false rains” in which isolated rainfall events around the expected onset date do not signal the sustained onset of the monsoon (Naylor et al., 2001).

1.2.3 Regional climate network

Because of this “storm” pattern with isolated rainfall events, the climate monitoring is difficult. With the encouragement from the international community since the end of the 80’s, the government of Indonesia is drafting a decree requiring all local authorities to

provide the policies needed to conduct scientific research on climate (World Bank, 2013). Nevertheless, the network is not yet well developed and the maintain of the existing rainfall stations is clearly lacking, especially in rural areas.

1.3 Hydrology and Hydrogeology

1.3.1 Surface stream characteristics

Java is almost entirely from volcanic origin, and contains numerous volcanoes and forty five are considered active (Katili, 1975). These Quaternary volcanoes are relatively high (ranging from 1100 to 3600 m asl). Rivers flowing from the Javanese volcanoes tend to flow radially from the summit and have very steep profiles (Mizutani, 1990).

We saw that in Central Java, the climate is defined by an alternation between dry season and wet season with local, brief and intense rainfall events. Thus, the runoff in high altitudes is intermitent, depending on the rain pattern. During the dry season, most of the upper part of the stream do not have flow. The alluvial sediments into the river beds are non consolidated, highly permeable and allow the water to seep into the loose detritic formations (Oguchi et al., 2001). In contrast, during the wet season, the non-cohesive material is remobilized into torrential rivers or sometimes hyperconcentrated flow (also called lahar). Thus, in rainy period, the rivers in volcano-detritic environment are characterized by an important hydro-sedimentary transport able to change the stream structure such as the destruction of temporary dams, and the river bed deformation.

In the low lands, the processes are different. In one hand, during the dry season, the rivers are perennial thanks to the groundwater contribution. On the other hand, during the wet season, the remobilized products and the debris flows from upstream are accrued in plains.

1.3.2 Volcano-detritic aquifers

The literature dedicated to volcanic rocks hydrogeology is scarce, although the topic is explicitly considered in some widely used textbooks. Detailed chapters on volcanic rock hydrogeology can be found in Custodio (2004); Fetter (1994); Hudak (1996) and several studies are focused on that thematic (Custodio et al., 1983; Falkland, 1999; Hurwitz et al., 2003; Jalludin & Razack, 2004; Lloyd et al., 1985).

Volcanic rocks are formed by the solidification of molten rock at or near the ground surface. Volcanic rocks cover a wide range of chemical and mineralogical compositions. Generally, volcanic rocks are basic, with a low silica content (basalt and basalt-like rocks), some are rich in plagioclase (tholeiites) and others may be rich in olivine (alkaline basalts). High

silica content is found in acidic rocks, such as rhyolites, and andesites and phonolites have an intermediate silica content (Waples & Waples, 2004). A variety of landforms develop in volcanic rock terrains which are linked to the composition of the eruptive products and the type of eruption.

Near the volcanoes, the ratio of lavas to pyroclasts is highly variable, from high in some basaltic shield volcanoes, such as those in Hawaii (Whittier et al., 2009), to very low in explosive eruptions, mainly of the acidic type, but also of the basic eruptions when groundwater increased the gas content of up-flowing magma (phreato-volcanoes) (White & Schmincke, 1999). Explosions not only form large quantities of pyroclasts but also take broken parts (xenoliths) of deep volcanic or non volcanic formations to the surface.

Most of the studies about the hydrogeology of the volcanic rocks are focused on basaltic rocks (Custodio et al., 1983; Macdonald et al., 1983; Violette et al., 1997; Kiernan et al., 2003; D'Ozouville et al., 2008; Singhal & Gupta, 2010; Pryet et al., 2012; Violette et al., 2013; Vittecoq et al., 2014). The volcano-sedimentary environments are barely represented and few studies are only focused on these environments (Cruz et al., 2007; Ayenew et al., 2008; Hurwitz et al., 2003) especially in tropical conditions (Charlier et al., 2011). The main reason is that the generalization of the volcano-detritic aquifer characteristics is more complicated to make than for the basaltic aquifers. Even if the volcano-detritic aquifers could be assimilated to porous media, they show a high variability of deposit processes, geometries, nature of rock and hydrodynamic properties.

Most of the papers about the volcano-detritic aquifers are focused on hydrothermal resources (Giggenbach & Soto, 1992; Cruz, 2003; Cruz et al., 2007; Carvalho et al., 2007) and scarcely on the “cold” water (Manga, 1998; Manga & Kirchner, 2004). The fact is that each case of volcano-detritic aquifers has its own properties. Indeed, volcano-sedimentary rocks are highly susceptible to weathering and the degree of welding due to the weathering or the eruption conditions affects the porosity (the porosity ranges from 5% to 50% depending on the welded portion (Smith, 1960)). The rare information about the hydrodynamic properties of this type of aquifer comes from the petroleum research (Sruoga & Rubinstein, 2007).

Despite this lack of studies and data about the hydrogeological properties of the detritic stratovolcanoes, the water resources of this kind of environment affect millions of people (Norini et al., 2004; Zernack et al., 2009). More than 700 volcanoes inventoried in the world are stratovolcano type (Fig. 1.12) and just in South-Asia, more than 110 million people live within 100 km of a stratovolcano.

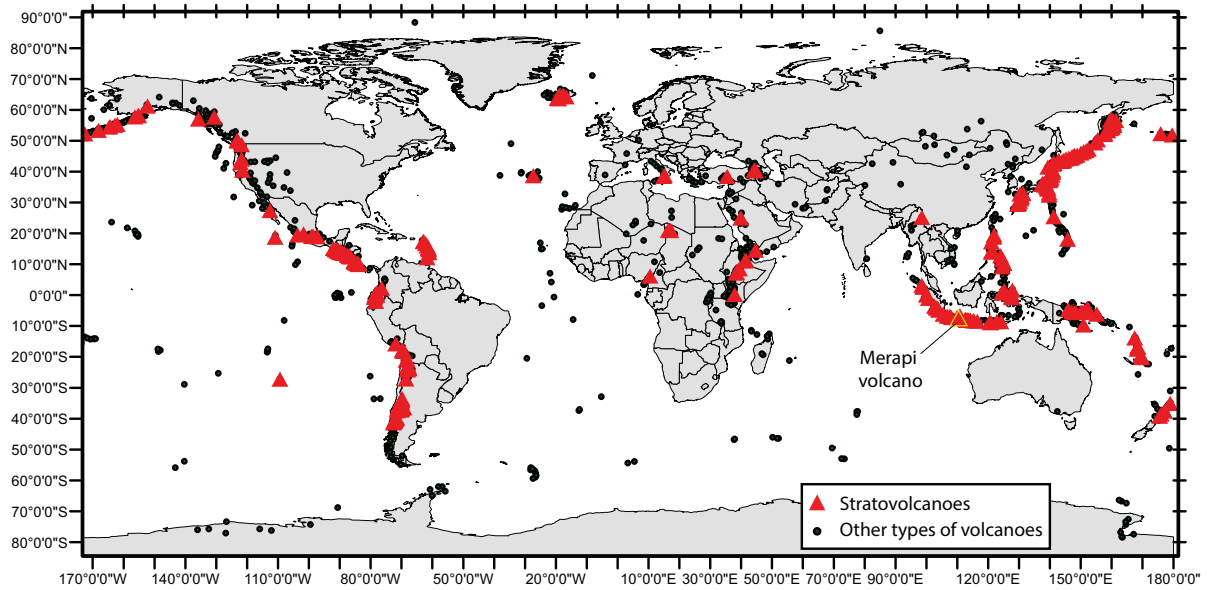


Figure 1.12: Map showing volcanoes that have been active in the last 10 000 years. Red triangles indicate the stratovolcanoes, the black points indicate the other types of volcanoes (calderas, shield volcanoes etc.). Data from the Smithsonian Institution, Global Volcanism Program.

Lloyd et al. (1985) proposed a conceptual model for the hydrogeological system in Indonesia (Fig. 1.13). According to him, recharge occurs on the upper parts, close to the volcanic vent. From the upper slopes to the intermediate slopes, unconfined conditions prevail. At the junction between the intermediate and lower slopes, the aquifers became multilayered and confined with the accumulation of clays and tuffs. On the lower slopes, major springs occur due to incisions marked by topographical variations and lithological differences.

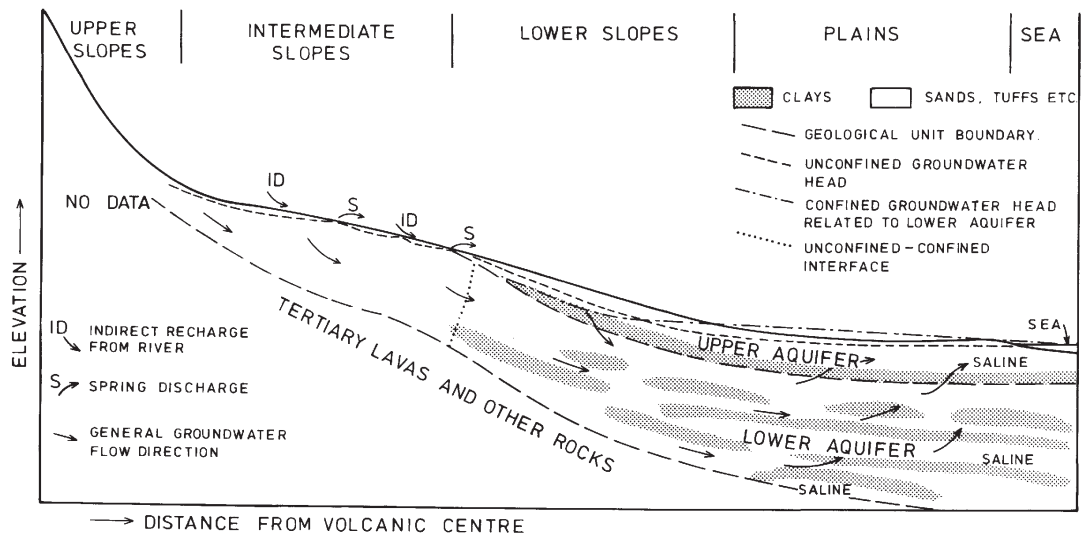


Figure 1.13: Conceptual diagram of the hydrogeology of the volcanic-sedimentary sequence (Lloyd et al., 1985).

1.3.2.1 Aquifer architecture

From a sedimentological point of view, andesitic volcanism has different components: 1) this type of volcanism is a negative factor in the upper part of the edifice with the explosive event and the gravitary destruction of the eruptive cone composed by lava flow and PDCs (Pyroclastic Density Current) deposits; 2) the andesitic volcanism is also a constructive agent with the remobilization of the upper part formations whose are easily erodible because most of them are non-cohesive and accumulate in the low land. The valleys and depressions of old landscapes carved into relatively poorly permeable volcanics may later be fully or partly covered by new outpourings, fallouts and remobilized sediments. Hence, rock hydraulic properties change in both vertical and horizontal directions (Sruoga & Rubinstein, 2007; Mueller et al., 2011). Moreover, some formations and structures with a local extension can produce contrasting hydraulic properties, including the interbedding of sediments and palaeosoils. They have to be taken into account when dealing with groundwater occurrence and flow.

From the hydrogeological point of view, the most important volcanic formations are lavas, pyroclastics, ignimbrites and dykes. Properties of volcanic rocks vary with their position relative to the emission point. In volcano-detritic environment, the distal formations tend to be free of lava flows and are dominated by pyroclastic, airfall and remobilized material. Close to the volcanic vent, the structure is complex, with the abundance of pyroclastic formation mixed with massive and sometimes fractured lava flows (Custodio, 2004).

The formation of perched saturated zones is not rare when recharge rate is high, and some very poorly permeable layers are found (Cabrera & Custodio, 2004). In sloping ar-

eas, springs appear when such a layer intersects the land surface. The outflow is generally only a fraction of local recharge, the rest following more or less vertical path toward the water table. Part of the flow of the perched springs and seeps may be locally evaporated or transpired by the vegetation growing at the site. The remaining flow often re-infiltrates downstream if permeable formations are found, but in other situation ravines with perennial flow can be found (Charlier et al., 2011).

The thickness of the unsaturated zone may vary from shallow (high rainfall rate, flat areas, poorly permeable materials, or a combination of them) to very deep, sometimes several hundred metres (low rainfall, sloping areas, highly permeable materials or a combination of them) e. g. in hydrothermal systems of Cascade Range (Hurwitz et al., 2003).

1.3.2.2 Aquifer/Aquitard properties

Volcanic formations are highly variable and so are their hydrogeological properties, which cover the full range of possible values found in natural formations. Total porosity of volcanic formations is generally high, due to voids created by ex-solved gases and to the frequent scoriaceous and brecciated parts, as well as to their often clastic nature. Pyroclastic deposits include ash, cinder, lapilli and blocks. The porosity and permeability of these deposits are essentially from granular type. The porosity of lapilli and pumice can exceed 40% (Flint & Selker, 2003). Recent coarse pyroclastic deposits are generally less consolidated and very permeable (50%) (Mueller et al., 2011), while ashes and cinders have a relative good porosity but as the material is very fine-grained, the permeability is relatively low. In contrast the massive andesitic lava flows have generally less than 5% total porosity when they are not fractured (Custodio, 2004).

In andesite-type volcanism, the pyroclastic formations exhibit very contrasted hydraulic conductivities, ranging in between 10^{-7} and 10^{-3} m.s⁻¹ (Foster et al., 1985). Welded tuffs, formed at high temperatures by the fusion of rock fragments, have very low hydraulic conductivity and can be considered as aquitard formations (Wood & Fernandez, 1988). In contrast, the pyroclastic flow and block and ash deposits have a high hydraulic conductivity. The Table 1.1 shows a synthesis of the physical and hydrodynamic parameters for the main rock types on the andesitic volcano-detritic edifices present in the literature.

Rock types	Porosity %		Effective porosity %		Hydraulic conductivity m/s		Reference
	Range	Arithmetic mean	Range	Arithmetic mean	Range	Arithmetic mean	
Tephra and tuffs	-	-	2 to 47	21	10^{-12} to 10^{-5}	10^{-9}	Smyth and Sharp, 2006 Flint and Selker, 2003
Breccia (lahar)	30 to 45	39	5 to 33	12	10^{-6} to 10^{-3}	10^{-4}	McWorter and Sunada, 1977 Singhal and Gupta, 2010
Pyroclastic flow deposits	15 to 70	45	10 to 50	33	10^{-7} to 10^{-3}	10^{-5}	Mueller et al., 2011 Hahn et al., 1997 McWorter and Sunada, 1977
Andesitic lava	3 to 30	17	-	-	10^{-11} to 10^{-8}	-	Entwisle et al, 2005

Table 1.1: Representative values of porosity, effective porosity and hydraulic conductivity for the main rock types on andesitic volcano-detritic edifices.

1.3.3 Watershed scale, surface and underground boundaries

1.3.3.1 About the rivers' names

The rivers and streams of Indonesia could have several names. It may be related to the fact that the same river has several names according to different languages. There is more than 700 regional languages in Indonesia including the Javanese language spoken by more than 75 Millions of people (Riza, 2008). Central Java represents the center of the Javanese culture and the places, mountains (i.e. in Javanese *Gunung*) and rivers (i.e. *Kali*) have commonly a double name: in Javanese and in national language (*Bahasa Indonesia*). The other reason of this multiple names is the administrative structure. Indeed, the notion of watershed is not taken into account by the administration in charge of water management and the rivers are not always considered as a upstream-downstream continuity. Thus, as our study area is divided between Klaten and Boyolali regencies, some rivers have different names on each district area.

The Fig. 1.14 shows the names of the main rivers used in this study. In order to clarify the reading, names have been chosen for each river studied. The river with the following names Kali (K) Mogol, K. Logerit, K. Gandul, K. Brambang and K. Jebol will be called Brambang River. The K. Brongkol and K. Pusur will be notified as Pusur River. The K. Sabrang, K. Soka, K. Gawe and K. Babadan will be grouped under the name of Soka River.

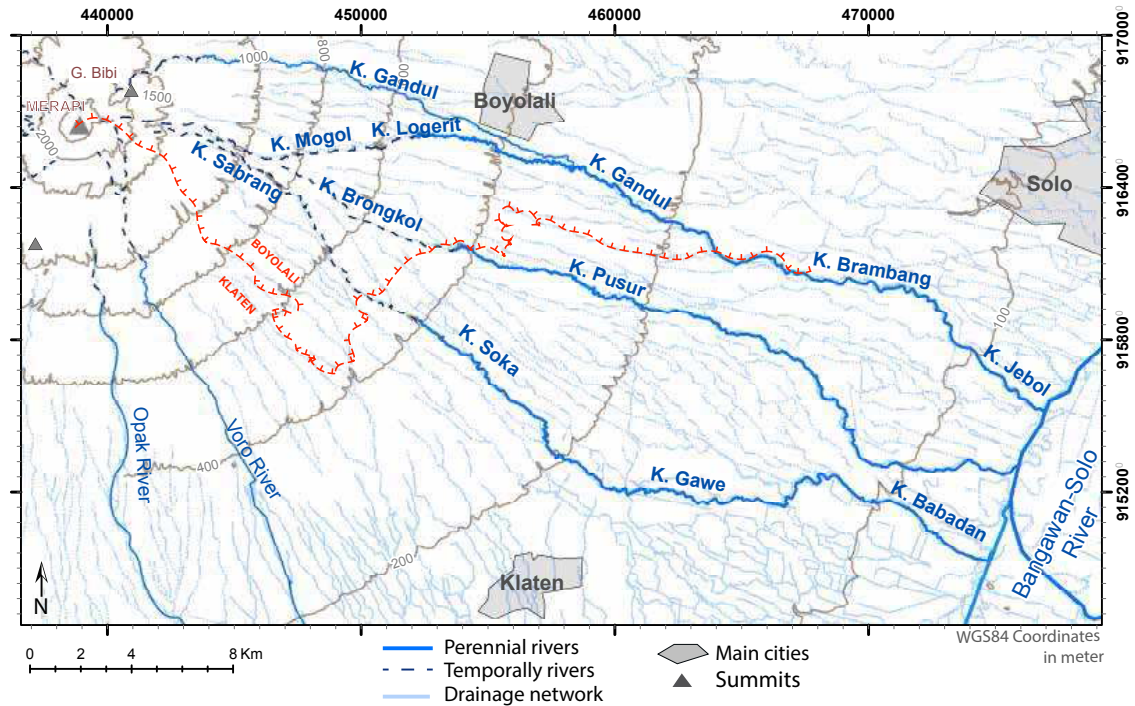


Figure 1.14: Study area map with the complete names of the rivers (K. means *Kali*, i.e. river in Javanese). The red line separates the Boyolali and the Klaten districts.

1.3.3.2 Catchment boundaries

The delimitation of the watershed boundaries is crucial in volcano-sedimentary environment. We saw that the hydrological behavior of a volcano-detritic edifice under tropical climate is characterized by brief and intense flood in answer to local storm rainfall events. The rivers are radially channelized along the volcano profile and the hydrological watersheds possess an elongated shape with a relative constant width. For instance, the Fig. 1.15 shows the hydrological watersheds of three main rivers on the Eastern flank of Merapi volcano. In red on the Figure, the Pusur river hydrological watershed is less than 2 km wide for 32 km long. This watershed is “closed” upstream by two others watersheds, the Brambang river watershed to the North and the Soka river watershed to the South. These surrounded watersheds reach the altitude 1500 m in contrast to the Pusur watershed which stopped at 800 m.

Considering the hydrogeological properties of the volcano-sedimentary formations, we saw that the upstream parts are suitable to the water infiltration while the downstream land are defined as discharge zone. Moreover, the heterogeneity of the aquifer architecture and hydraulic properties make it difficult to define the hydrosystem geometry. Therefore, the hydrological and hydrogeological watershed will have different extension and one major

objective of this research project is to define the hydrogeological watershed boundaries.

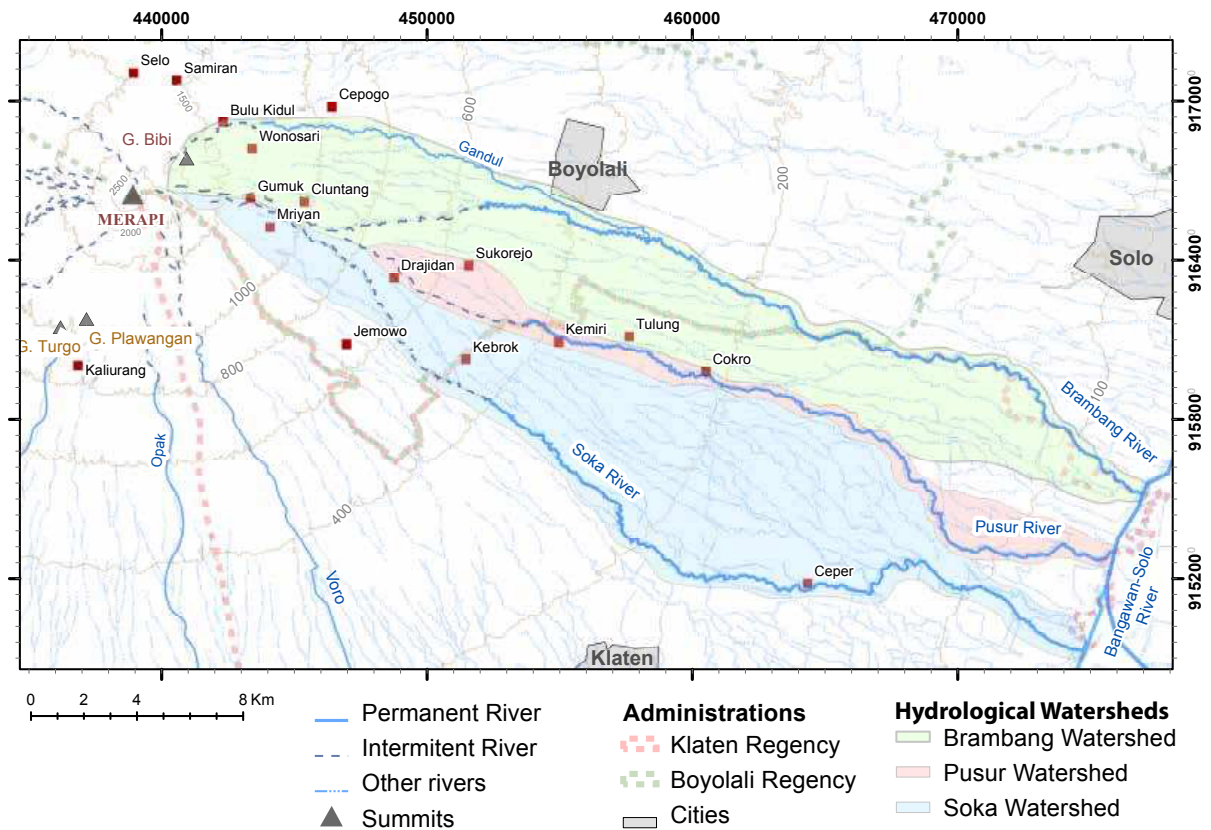


Figure 1.15: Map of the three hydrological watershed locations studied in this research project on the Eastern flank of Merapi volcano. UTM projection.

1.4 Water as a resource in Klaten and Boyolali Regencies

1.4.1 Administrative subdivisions of Indonesia

Indonesia is divided into provinces which are made up of regencies and cities. Provinces, regencies and cities have their own local governments and parliamentary bodies. A province is headed by a governor. Each province has its own legislative body, called *Dewan Perwakilan Rakyat Daerah* (translated as "Regional People's Representatives Assembly").

Regency (Indonesian: *Kabupaten*) and city (Indonesian: *Kota*), are local levels of government beneath the province. Both regency and city are at the same level, having their own local government and legislative body. The difference between a regency and a city lies in differing demographics, size and economics. Generally the regency has larger area than city, and city has a non-agricultural economic activities. A regency is headed by a regent (Indonesian: *Bupati*), and a city is headed by a mayor (Indonesian: *Walikota*).

Each regency or city is divided into districts (*Kecamatan*).

The head of a district is known as a "*Camat*", who is a civil servant, responsible to the regent (for regency) or to the mayor (for city). Each district is divided into *desa* (village) or *kelurahan*.

In Indonesian, as in English, village (*desa*) has rural connotations. In the context of Indonesian Government Administration, a *Desa* can be defined as a body which has authority over the local people in accordance with acknowledged local traditions of the area. *Desa* is headed by "Head of *Desa*" (Indonesian: *Kepala Desa*). In contrast, a *Kelurahan* has less power than a *Desa* and is headed by a "*Lurah*". *Lurahs* are civil servants, directly responsible to their *Camat*.

1.4.2 History and demography

In this region, a famous pre-historic heritage, fossils of "Pithecanthropus Erectus Javanicus" (called "Java man") were discovered ([Theunissen et al., 1990](#); [Zaim et al., 2011](#)) and proved that the ancient human being lived here since 1.5 million years B.P.. The temple of Borobudur (the 8th and 9th centuries) is a heritage of glorious period of Buddhism and cultural glory of Central Java. In contrast, during the period from 928 A.D. until the 15th century, the civilisation moved to the East and the reasons for this shift have puzzled archaeologists and historians for many decades ([Miksic, 1990](#)). This period is characterized by the decline of the agro-hydraulic Indo-Javanese kingdoms ([Maurer, 1990](#)).

Before the colonization by the Dutch in 1596, the sultan of Yogyakarta took over the traditional agro-hydraulic irrigation system with the creation of cultivated terraces around the fertile volcanoes. The colonization by the Dutch lasted for about 350 years and stopped in March 1942. During this period they brought along the modern infrastructure to increase the irrigation and their left driving. The agriculture became more diversified, combining rice, sugar cane and tobacco. The Japanese occupation forces landed in Indonesia for three years and half during the Second World War. The August 17th 1945 the Indonesian people proclaimed their independence. The complex irrigation infrastructures introduced by the Dutch were difficult to maintain and the rehabilitation was relatively limited since 1960. The situation will not be improved with the military government of Suharto. The rehabilitation of the large irrigation system occurred in 1974 until 1984 during the Green Revolution Technology ([Kyuma et al., 2006](#)).

Central Java benefits from a strategic position. Besides bordering two other provinces, it is framed by Java Sea in north and Indonesia Ocean in south. The coast is stretching along 656.1 km, provides a high opportunity to develop fisheries, coastal fishpond and commercial exchanges. The governmental administration is divided into 29 regencies and 6 cities.

Merapi volcano is located at the junction of 4 regencies: Magelang Regency (1130 km²) to the West, Boyolali Regency (1015 km²) to the North, Klaten Regency (665 km²) to the East and Sleman Regency (574 km²) to the South (Fig. 1.16). Sleman Regency is included within the Special Yogyakarta province (3133 km²) while the other belong to Central Java Province.

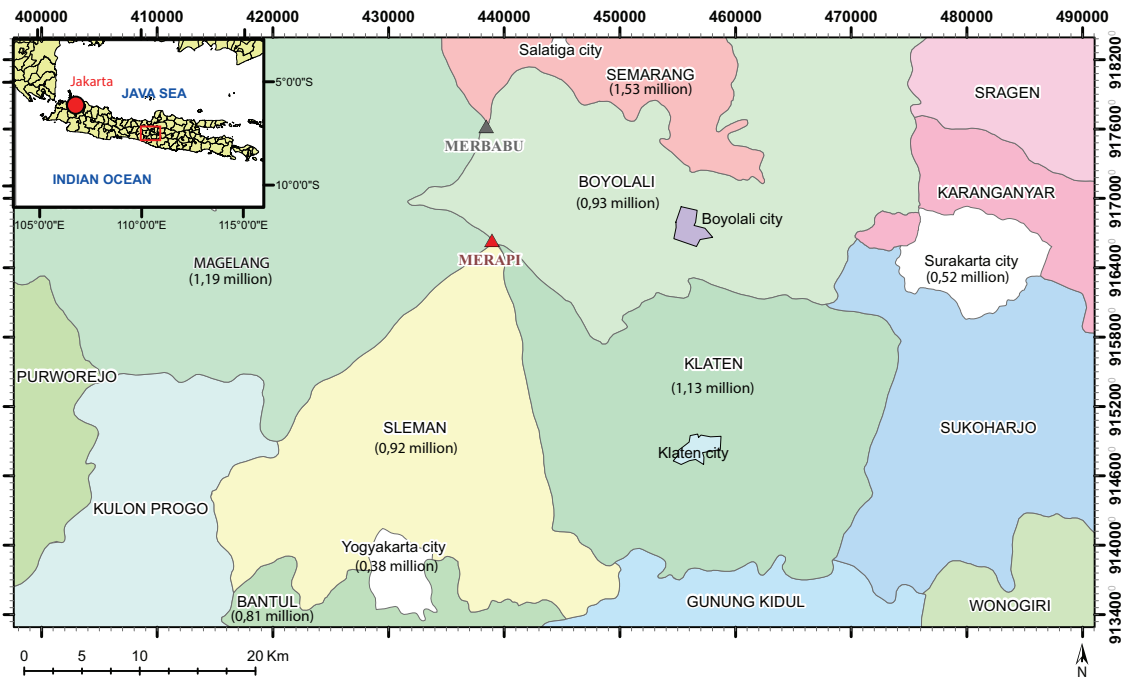


Figure 1.16: Main regencies and cities surrounding Mount Merapi. Numbers in brackets are estimated populations from World Bank, 2013

Despite a century of near-continuous eruptions, the local population continues to increase but with a relative decreasing growth rate since 20 years (Tab. 1.2). Today, more than 3 million people live within 40 km of Merapi. The special district of Yogyakarta (with a total of 3.5 million inhabitants) is included in the middle of south zone of Central Java province. The city of Yogyakarta, with a population of about 380 000, lies 28 km from the summit. This province is framed by the Progo River, and the Opak River in the east, which sourced from top of Merapi and ends in the Java Sea in its south side. Yogyakarta Province is the second smallest province in Indonesia and has the highest population density of Java (more than 1 700 person/km²). The Sleman regency, which sits 0-40 km from the summit and has a population of 0.9 million, lies in the path of Merapi's frequent lahars and pyroclastic flows.

Central Java demography		
Year	Pop.	$\pm\%$
1971	21 877 136	-
1980	25 372 889	+16.0%
1990	28 520 643	+12.4%
1995	29 653 266	+4.0%
2000	31 228 940	+5.3%
2010	32 382 657	+3.7%

Table 1.2: Demography evolution in Central Java from 1971 to 2010 (Statistik, 2010)

1.4.3 Land use

Due to its active volcanic history, volcanic ash makes Central Java an highly fertile agriculture land. The slopes of the East flank of Merapi can be divided in four land occupation zones related to the elevation (Fig. 1.17). In high elevations, above 1400 m asl, the steep slopes are covered by secondary forest, part of the National Park of Merapi volcano. This forest is regularly used by the farmer for supply in wood and grass. From 1300 to 800 m asl, the first villages are settled on the top of ridges, on the sides of deep gullies. On flat areas and sometimes on the slopes of more than 40° , the villagers crop vegetables and roses during the beginning of the rainy season (October-March) and tobacco during the end of the rainy season and all the dry season (March- September). From 800 to 400 m asl, the gullies are less deep and agro-forestry terraces are dominant from Drajidan to Kemiri villages.

Below 400 m asl, the main rivers are permanent and the low slopes allow the irrigation of paddy-fields. Farmers grow two rice crops in the wet season: a direct-seeded crop called “*Gogorancah*” in the early wet season (November–February), with yields varying between 3.5 and 6.8 $\text{ton}\cdot\text{ha}^{-1}$ and a transplanted crop called “*Walik Jerami*” in the late wet season (March–June), with yields between 1.2 and 4.5 $\text{tons}\cdot\text{ha}^{-1}$ (Setyanto et al., 2000; Wihardjaka et al., 1999). In irrigated areas of Klaten, farmers grow rice 2-3 times per year with average yields of 5-6 $\text{tons}\cdot\text{ha}^{-1}$, that is means 0,25 to 1 $\text{m}^3\cdot\text{m}^{-2}\cdot\text{year}^{-1}$ is needed in the irrigation area (Tuong, 2000). In some areas where the water is less available, the corn is used as a substitute to rice.

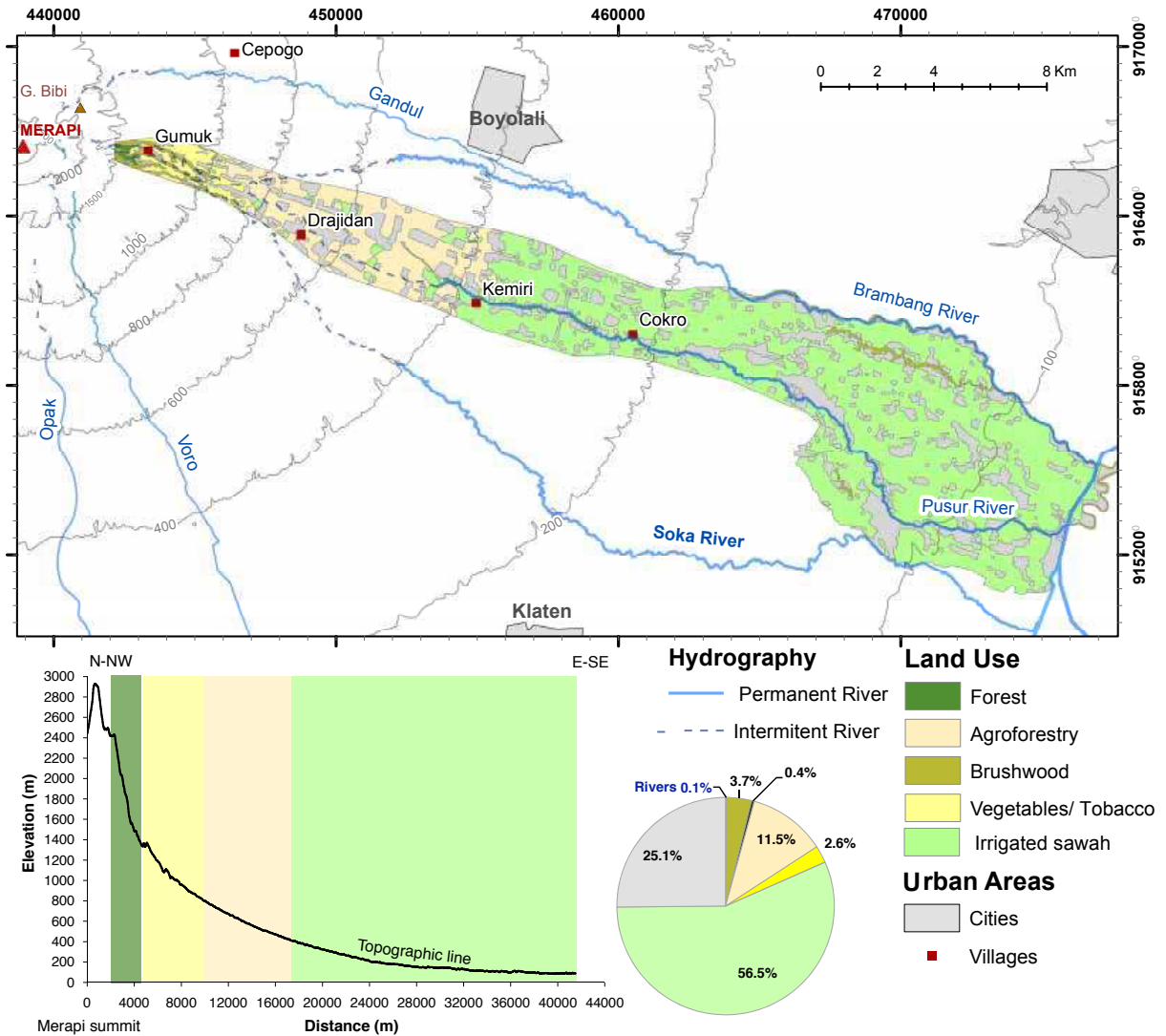


Figure 1.17: Land use map on the East flank of Merapi resulting from the field and satellite image analysis by the CIRAD and IAHRI (Lidon, 2012).

1.4.4 Water uses

1.4.4.1 Agriculture uses

The neighbouring regencies of Klaten, Boyolali and Sukoharjo in Central Java are among the most productive rice-growing areas of Indonesia. Over a harvested area of more than 150 000 ha, these regencies produce close to a million tons of rice per year (Winarto & Stigter, 2013).

Most of the water used for the agriculture benefits to the irrigated sawah. The term sawah refers to a levelled and bounded rice field with an inlet and outlet for irrigation and drainage (Wakatsuki et al., 2013). The water input in sawah depends on the rates of

the outflow processes, on the duration of land preparation, crop growth, the hydrological conditions and soil characteristics. For a typical 100 days season of modern high-yielding rice, the total water input varies from 700 to 5300 mm with 1000 - 2000 mm as a common value for many lowland areas (Tuong & Bouman, 2003). Tuong (2000) have estimated the amount of water “used” to produce 1 kg of rice in the range of 500–2000 Liters if only evapotranspiration is taken into account. Rainwater and irrigation water are necessary for rice growth in two ways: to maintain soil moisture and – in wet irrigation – to maintain the standing layer of water over the paddy field. That is why the crop is grown during the wet season, which reduces the irrigation demand by effectively using rainwater.

The water used for irrigation has three main origins. One part of the water is coming from the river: several dams were built across the permanent rivers and channel system deviates part of the river flow. For the lowland, another part of the water comes from many natural and permanent springs which feed the irrigated areas with a consequent flow rate. The last part of the water is coming from private shallow borewells. Most of them do not exceed a depth of 20 m. The pumps are activated during the dry season in addition of the river and spring water. Most irrigation wells are pumped several hours each day. The pumping rates range from 2 to 10 L.s⁻¹.

1.4.4.2 Domestic uses

Most households obtain water for domestic needs from the shallow aquifer, the rest is from rivers and rain collectors. The oldest wells have a large diameter (1-2.5 m) to accommodate a rope with a bucket through a pulley. These house wells can be deep (more than 40 m) but the average depth is around 20 m. Some wells have been deepened during the last decade because they were above the water table. Several houses have pumping machine and pump several hours each day. Pumping rates are highly variable and depends on the lithology, the well depth and the pump strength. Most of the houses do not pump more than 3 L.s⁻¹. The water is used for domestic purpose as washing clothes, bath, cooking and drinking. The groundwater is also use to feed the livestock as many houses have one or several cows and are specialized in milk production (around Boyolali city in particular) (Murti, 2012).

1.4.4.3 Industrial uses

Industries mostly use the groundwater to fullfill the industrial water quality requirement. In Klaten Regency, there are at least two companies specialized in drinking bottles production: 1) Club company and 2) Danone AQUA company.

Club belongs to the PT.Tirta Bahagia Group and has 17 plants of bottled mineral water spread over Indonesia. On Merapi volcano, Club have several wells around 200 m asl near

Cokro village. The date of drilling, depth, flow rate of these wells are unknown. The transportation from the factory to the stores is taken over by trucks.

AQUA is one the Indonesian biggest bottled water manufacturer company since 1973. It controls 80 percent of the sale of drinking water in gallon containers. In 1998, the French food company Danone announced the unification of both companies and in 2000, the products labeled Danone-AQUA are launched under PT. Tirta Investama name (Kusuma, 2008). In Klaten, the first well (production well) was drilled in early year 2002 at 20 m from Sigedang and Kapilaler springs (Fig. 1.18), in Delanggu village (Sriyana, 2011). These springs are used for irrigation and domestic purpose and have a high flow rate (over $0.2 \text{ m}^3 \cdot \text{s}^{-1}$). The total production well depth is 100 m but the aquifer layer has been identified from 30 to 55 m under the soil surface (Kartadinata, 2002). Two other wells have been drilled in 2003 and 2005. The particularity of these wells is their artesian properties. A glass tube has been implemented on the monitoring well 1 in order to read directly the water level of the confined aquifer. It is at 7 m above the soil surface and no fluctuation is recorded. The detailed logs are described into the Chapter 4.

Just after the drilling, the artesian flow rate has been measured at $64 \text{ L} \cdot \text{s}^{-1}$ but $48 \text{ L} \cdot \text{s}^{-1}$ are used for drinking water production, the overflow is going to the irrigation system (Fig. 4.9).



Figure 1.18: Sigedang spring. Its flow rate provides water to the downstream irrigated areas and is daily used by the people for laundry and cleaning activities but also for relaxing bath.

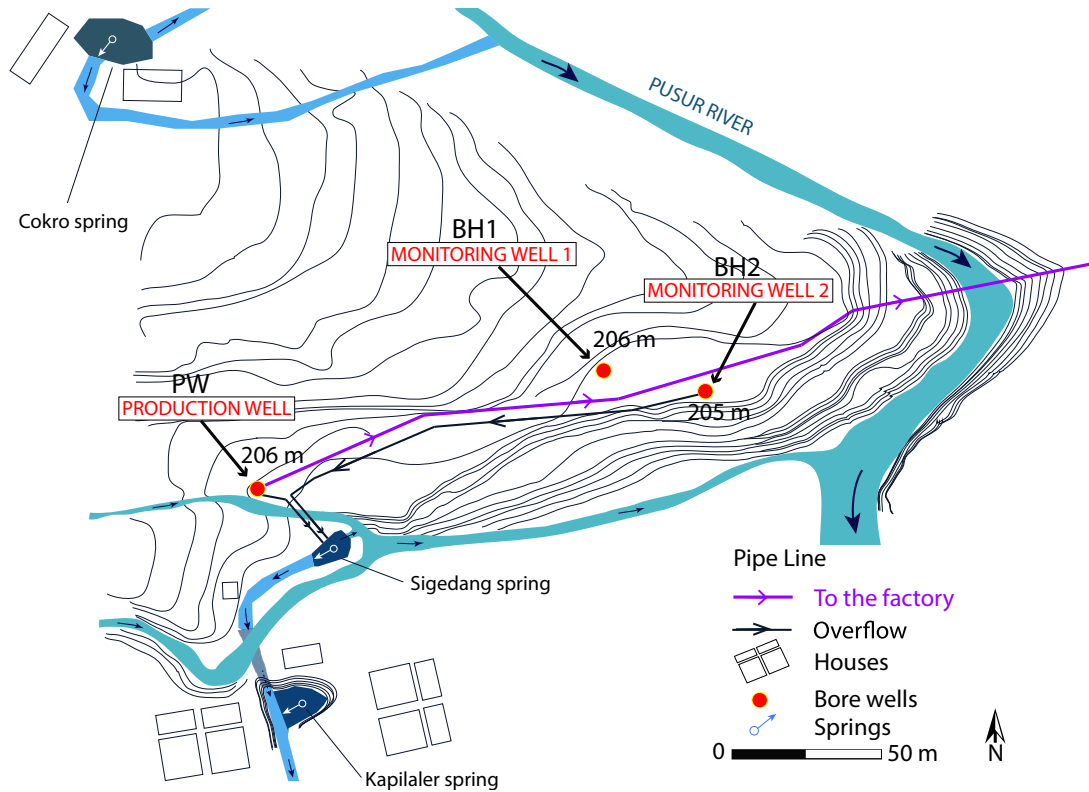


Figure 1.19: Danone-AQUA production and monitoring wells location map.

In addition to the official companies, several borewells have been drilled by private land owners in view to sell the groundwater to villages where it is not available. More than five “water operators” have been inventoried on the East flank of Merapi volcano and the wells will be described later. These wells are often very deep (200 m) and located upstream any permanent rivers or major springs. During the dry season, 6000 L trucks are filled with water and brought to the customers.

1.4.4.4 Water management group

1.4.4.4.1 National policy and regulation

Policy and regulatory responsibilities for the water and sanitation sector are shared among several ministries. While the Ministry of Health is responsible for water quality-related aspects, and to a certain extent rural services, responsibility for the urban sector is shared between the Ministry of Home Affairs and the Ministry of Public Works. The National Development Planning Agency (Bappenas) has a role in planning investments. The Ministry of Industry and Trade also has some responsibilities for the regulation of bottled water. A National Water Supply and Environmental Sanitation Working Group (Pokja AMPL) coordinates between departments and with donors and other stakeholders. The

working group does not have a legal basis, nor secure funding. The provision of water services to the urban areas is the responsibility of PDAMs (Perusahaan Daerah Air Minum), Local Government Owned Water Utilities.

In Indonesia, the expansion of cities and industries is a challenge for the sustainability of irrigated areas, agricultural granaries of the country with more than 1000 inhabitants per km². Faced with a growing urban and industrial demand, the sustainable management of water resources becomes a major challenge for every inhabitant. This issue is reflected by the current Indonesian institutional context governed by the Law on Irrigation (UU77/2001) and the recent National Water Act (UU7/2004), currently considered by the Constitutional Court, providing for the decentralized management and participatory water resources and abolishing the monopoly of public bodies over the exploitation and distribution of water ([Anonymous, 2004](#)).

1.4.4.4.2 Rural areas

The rural areas of Indonesia such as Klaten and Boyolali Regencies, have a long history of community-managed water supply services using naturally occurring springs, rainwater and groundwater resources. However, community capacities to sustain such water systems over long periods have tended to be limited (Fig. 1.20). Past rural water supply and sanitation projects have often not invested sufficiently in building community capacity to plan, implement, operate and maintain services in ways that benefit and satisfy all sections of rural societies, conditions necessary for service sustainability. Rural consumers have not consistently been offered voice and choice in decisions related to establishing and managing services. Services have often been provided in a top-down manner by agencies external to the community, using public sector or funds providers and contractors answerable to government agencies rather than to the users of services. This has led to mismatches between what the users want and get, a lack of community ownership of rural water supply and sanitation facilities and unclear responsibilities for maintenance.



Figure 1.20: Water tank in rural area used for rain water storage during the rainy season and distribution during the dry season.

1.4.5 Klaten water conflicts

1.4.5.1 Water as a source of myth

Besides its economic and daily life value, the water and especially the groundwater from the springs has an important place within the religious life in Central Java. In the Javanese mystical life, mountains and the water coming from them, are mostly mentioned as gods' places or the centres of supernatural powers. This myth is a cultural heritage of Javanese original animism religion of the 7th century. It is common knowledge that well-intended spirits of ancestors or nature-spirits often take residence at the places with water (Vanhoebrouck, 2004). Any modification around a spring or a drilling program will be done with several ceremonies and under very strict calendar (Fig. 1.21). Moreover, the Islam religion, which is the main religion in Indonesia, requires water and sanitation access in every mosque, adding a spiritual value to the water resource. Hence, all the discussions or issues about water are considered as crucial and sensitive topic by the population.



Figure 1.21: Offering near the Slembi spring. The offering can be made for special occasions or to invoke the “spring spirit” with request on the spring flow rate.

1.4.5.2 Water as a source of conflict (2003-2004)

The confrontation of different demands of water users generates conflicts exacerbated both by the lack of information on available water resources and knowledge on water cycle. Moreover the real needs but also the lack of rules and the resource allocation process enhance the discord .

There is an unequal distribution of the water in the Klaten area, the villages located in the upper parts of the volcano do not have continuous access to the water resources. During the dry season (June to October), the rivers do not flow and the springs have low flow rates thus they need to buy the water transported by tanker on bumpy roads from the villages located in the lower parts where the spring flow rates are high. In the lower parts, the irrigation water comes mainly from water intakes constructed over the rivers and natural springs. The collected water is sent in perimeters through a very dense network of small open canals (Bourgeois et al., 2008).

Since the middle of the 90’s, the rural populations of Klaten experience an increased degradation of the water access (Bourgeois et al., 2008). The increased water demand for potable and irrigation supply cannot be met totally by the existing systems. These systems utilize the most easily accessible surface water which are now almost completely allocated. Where second and third crops are already grown, the supply comes from groundwater exploitations. The utilization of additional water resources depends upon

developing surface storage and exploiting groundwater at the regional scale (Lloyd et al., 1985). Many users are concerned, including the fish farmers and the private and public companies such as the water supply of the Solo city managed by the PDAM or Danone-AQUA society.

In 2003 and 2004, a group of farmers and head of villages have protested against the decreasing flow rate observed in the irrigation canals. The local NGO and the medias have accused the PDAM and Danone-AQUA to be responsible of this lack of water. In 2005, the government and Danone-AQUA found an agreement and a new borewell was drilled on the society site and was dedicated to supply the irrigation network. Nevertheless, conscious of its sensitive position in this area, the Danone-AQUA society decided to start a “research and development” project to inform the water users, to calm the tensions, to improve the sustainable use of groundwater and to improve the scientific background on water cycle in the Eastern flank of Merapi volcano.

In 2006, the Indonesian Agroclimate and Hydrology Research Institute (IAHRI, Bogor, Indonesia), the International Center of Agricultural Research for Development (CIRAD, Montpellier, France) and a local NGO, Bina Swadaya have been solicited to characterized the climate and surface water pattern with the collaboration of the local institutions as the Research and Assessment Institute for Agricultural Technology (BPTP, Klaten, Indonesia). Bina Swadaya programs are focused on the local community development through various activities such as micro finance, educational training or farm production marketing.

For the groundwater resource characterization, the collaboration between the local university, UGM (Yogyakarta, Indonesia) and Paris 6 University (France) promotes, since 2011, an investigation to conduct a multidisciplinary study (geology, geomorphology, hydrochemistry, hydrogeology, hydrology...). The expected results of this survey were to give important knowledge of hydrogeology conditions, especially the delineation of the hydrogeological watershed (recharge and discharge areas), the information about the groundwater circulations (transfer time, aquifer properties) and the quantification of the fluxes (recharge, discharge...).

Synthesis

In this part, we saw that Merapi volcano, Central Java, Indonesia has an activity conditioned by the subduction zone which gives it andesitic lava flow and explosive eruption types. Many studies are focused on the West side of volcano but barely to the Eastern flank. However, the population density in this area is high and is located in hazard zones. The dangers of Merapi volcano come not only from its explosive and massive eruptions but also from the remobilized material as lahar or debris avalanche which can occur during quietness periods. These phenomenons are linked to the rock properties but especially to the climate and the hydrology pattern of the area.

Merapi volcano is located under tropical humid conditions characterized by a monsoon regime divided in wet and dry seasons (October to May and June to September, respectively). During the wet seasons, the climate is distinguished by localized high rainfall rate. This special climate behaviour requires a well documented monitoring network. However, the monitoring of the climate pattern at the watershed scale is still scarce in Central Java and it is not really well maintained. The hierarchy of the Indonesian administration can appears complicated but the decisions are taken at the local scale and can be very efficient. The main issue seems to be the national politic priority controlled by economics pressure. Nonetheless, the recent laws and directives show an interest to the environmental thematics and suggest an improvement.

In the literature only a few volcano-detritic hydrogeological conceptual model can be found. We saw that the volcanoclastic sediments are considered as porous media. Nevertheless, their hydraulic properties are highly heterogenous and the variation depends of many factors as the distance from the source point, the deposit conditions, the time or the alteration of the formation. On hydrogeological point of view, the aquifer formations are the pyroclastic deposits, the ignimbrite, the debris avalanche deposits and the lava flow when they are fractured. The aquitard formations are the indurated tuffs, the ashes, the lapilli and the massive andesitic lava flow among others. The better understanding of the geometry of the structure and the composition of the volcanoclastic deposits are crucial to developp a hydrogeological conceptual model.

Around Merapi volcano, the water resource utilization has a long history. The agriculture is particularly well developed with a staged system of crop varieties depending on the elevation and the water availability. The anthropic pressure on the groundwater resource is increasing with the demography growing. Moreover, the water exploitation are not well monitored yet.

This kind of behaviour shows that even if the East flank of Merapi is located in tropical humid environment with apparent no water resource issues, the repartition of its resource is unequal and can trigger conflicts. That confirms the need to better understand the

groundwater circulations and to quantify them in order to settle a sustainable management of the groundwater resource at the watershed scale.

That is why the collaboration between the universities Paris 6 & UGM on the one hand and the CIRAD & IAHR on the other hand, had the objective to develop a multidisciplinary study about the surface water and groundwater circulations on the Eastern flank of Merapi volcano.

2

Geological and geomorphological
structure

Introduction

Volcanic terrains show a high heterogeneity and the diversity of processes and dynamism linked to the tropical environment complicate the understanding of the deposit nature and their geometry. The stratovolcanoes evolves rapidly in one hand because a huge volume of material can be produced in few hours at local or regional scale and in the other hand because the erosional and transport processes can remobilized an important part of the non-consolidated material especially on edifices subjected to heavy rainfalls in tropical climates.

Many studies have been settled on volcano-detritic deposits (Blyth, 1970; Cioni et al., 1999; Wright et al., 1980; Cole et al., 1992; Walker, 1971) but finally the global overview of the structure and geometry of edifices subjected to tropical climates are still poorly known. The aims of this chapter are to characterize the volcano-detritic deposit dynamics through the geological and geomorphological processes based on Merapi volcano.

Merapi Mount is 2989 m high and results from the subduction of the Indo-Australian plate below the Eurasian plate. Merapi volcano has been the main topic of many articles (Van Bemmelen, 1949; Gertisser et al., 2012b; Melchior, 2011; De Belizal et al., 2011; Dove, 2007; Simoen, 2001; Berthommier, 1990; Gomez et al., 2010; Newhall et al., 2000; Camus et al., 2000) but little description of the East flank geological and geomorphological evolution has been done. Indeed, most of the publications are focused on the active part: the West and South sides. Different steps of the “building-dismantling cycle” of a stratovolcano can be observed simultaneously on Merapi. Indeed, several parts of the edifice have been spared by the last eruption, allowing to analyze the ancient transport and material remobilization processes.

Hence, in order to reconstruct the eruptive and the geomorphological history of a stratovolcano in more detail and to recognize the hazard potential in an “inactive” part, it is important to understand the depositional processes that contributed to the construction and dismantling of the volcano.

In this chapter, a multi-disciplinary analysis of the East flank of Merapi volcano is proposed, including geology, geophysics and geomorphology, to better understand the mechanisms which progressively built the edifice by deposition of syn- and post-eruptive volcaniclastics, as well as reworked deposits. This approach allows the reconstruction of volcanic and other landscape-forming events operating over the life-span of this stratovolcano, based on the sedimentological classification.

2.1 Merapi deposit architecture

Based on the description of the volcanoclastic deposits from the literature, the field surveys helped to characterize the geological structure of the East flank of Merapi. Several field surveys have been performed between June 2011 and June 2013. During the campaign along the main rivers, more than 100 points and outcrops have been identified. The first step was to identify the facies of the deposits. As the volcanoclastic sediments display systematic changes in composition, texture, geometry and distribution, the identification and the geological mapping is difficult. The dense vegetation and the extreme climatic condition during the rainy season in the upper part and the important urbanization in the lower parts do not facilitate the observations. The second steps was to use the facies description to confirm the geological history of Merapi found in the literature. Finally, to complete the context description, the geophysics and the GIS analysis allowed to describe the geomorphological characteristics and to identify a drainage network anomaly on the East flank of Merapi volcano.

2.1.1 Sedimentary characteristics of volcanoclastic and reworked epiclastic deposits

Merapi mount is an andesitic stratovolcano with a high frequency of explosive eruptions (Voight et al., 2000). These types of explosions commonly generate a large diversity of juvenile lithic elements. The accumulation of material from these flows can produce thick and widespread deposits able to cover areas up to 20 000 km² for a single eruptive event (Carey, 1991; Criswell, 1987). Moreover, these units are loosely consolidated and emplaced as thick, landscape-covering layers or valley fills that are susceptible to rapid erosion by fluvial processes. The measured denudation rates for volcano-sedimentary material in humid to tropical climates range from 25 to 105 mm/year (Rijsdijk, 2005; Hildenbrand et al., 2008). These values are three to four times greater than the estimated erosion rates for the relief in non-volcanic areas (El-Swaify et al., 1982). Before listing the different types of deposits observed on Merapi volcano and its geological history, it is necessary to introduce the notions of *direct eruptive deposits* and *indirect eruptive deposits* (Fig. 2.6). The direct eruptive products are characterized by high-volume sedimentation in a short time and with a volcanic activity origin, whereas the indirect eruptive products are the remobilized material with no direct effect from the volcanism but only from the erosional processes. Contrary to the terms and concepts of syn-eruption and inter-eruption deposits (Lirer et al., 2001; Smith, 1991), these new definitions consider the potential simultaneity of volcanic activity and material remobilization.

2.1.1.1 Syn-eruption deposits

We divided the direct eruptive deposits into the following two categories: the volcanoclastic deposits and the lava flow deposits. Merapi activity is characterized by the alternation of a small volume of effusive products and explosive eruptions with high volcanic sediment production. The term volcanoclastic as defined by Fisher (1966) refers to all clastic sediments and rocks, regardless of depositional processes, whose particles are predominantly of volcanic origin. The term “sediments” is interpreted in this study in the broadest possible sense to include all fragmentary volcanics, ranging from those emplaced by magmatic processes to the products of “normal” sedimentary processes.

2.1.1.1.1 Pyroclastic deposits

The pyroclastic deposits are created by explosive fragmentation of magma during volcanic eruptions and can occur via two primary mechanisms (Blyth, 1970). The first mechanism involves the rapid ex-solution of dissolved magmatic gases during rapid decompression events (magmatic eruptions), and the second mechanism results from the interaction of hot magma with external water sources (phreatomagmatic eruptions) (Brown & Calder, 2005). Pyroclastic deposits typically comprise a mixture of juvenile components (Criswell, 1987). Due to the large differences in the physical properties of these components and the sorting and sedimentation processes operating during pyroclast dispersal, the lateral and vertical distributions of these components may vary significantly within a deposit (Carey, 1991). The pyroclastic deposits produced during the magmatic eruption on Merapi can be divided into the following three major facies: fall, flow and surge (Wright et al., 1980). These facies can be both graded and inversely sorted along their longitudinal profile (Fisher, 1979; Legros & Marti, 2001). Regarding the longitudinal variation (upstream-downstream), the pyroclastic deposits are often cross-stratified (Fig.2.6, longitudinal variation section).

2.1.1.1.1.1 Pyroclastic falls

The pyroclastic fallout deposits can be thick over 20 km away from Merapi vent (Fig.2.6, 1). This unit is characterized by a uniform composition, good sorting, a mantle bedding and widespread distribution (Stinton & Sheridan, 2008). Transport of pyroclastic fallout material is by ballistic trajectory and turbulent suspension (Kelfoun et al., 2000). Energy is supplied initially to the fragments by the eruption and later by wind. Composed of fine ash and grain with a variable proportion of lapilli, these deposits are defined as tephras, ash cloud or tuff units (Fig.2.1) (Carey, 1991).



Figure 2.1: Pyroclastic fall deposits

2.1.1.1.1.2 Pyroclastic surges

Three modes of origin for pyroclastic surges have been differentiated herein: (1) from collapsing eruption columns, (2) from the tops of moving pyroclastic flows, and (3) directly from a crater (Dellino & Volpe, 2000). The stratigraphic position of the pyroclastic surge deposits relative to the pyroclastic flow deposits has significant implications with respect to eruption and flow mechanics (Vazquez & Ort, 2006). Many surge deposits are poorly exposed or discontinuous (Fujinawa et al., 2008). The following types of pyroclastic surge deposits have been identified: (1) Ground surge deposit: occurs immediately below a pyroclastic flow deposit and may originate from a collapsing eruption column or directly from a crater. (2) Base surge deposit: originates from a collapsing phreatomagmatic eruption column and is not associated with hot pyroclastic flows. (3) Ash cloud deposit: deposit from an ash cloud that mechanically segregates from the top of a pyroclastic flow and occurs above it or may become detached and flow independently (Fisher, 1979). The indurated base surge from the phreatomagmatic eruption during the Recent Merapi period is visible in the river incision of the Brambang and Soka Rivers over 10 km from the summit. The base surge deposits are concentrated into the valley sides and can reach the interfluves (Fig.2.6, 3). The alteration profile depends on the outcrop surface (Fig. 2.2).



Figure 2.2: Pyroclastic surge deposits incised by temporarily river.

2.1.1.1.1.3 Pyroclastic flows

Pyroclastic flow (awan panas in Indonesian) deposits are the result of gravity-driven mass flows from explosive eruptions (Takahashi & Tsujimoto, 2000). The unit formed by several flow units is called “ignimbrite” (Mathisen & McPherson, 1991). The ignimbrite is a combination of the pyroclastic fall, surge and flow. Sparks (1975) identified an idealized vertical sequence of ignimbrite deposit (Fig. 2.3) which comprises a reversely graded fine grained basal ash layer (layer 2a on the Fig. 2.3) below the massive main flow unit (layer 2b) in which pumice clasts are reversely graded and enriched toward the bottom (layer 2 b.1). Various types of layer 1 deposits have been recognized. These layers may represent independent precursory event with variable texture and composition usually placed by frontal portions of the pyroclastic flow (Walker, 1971). The layer 3 is composed by fallout, surge, flow and ash cloud deposits accompanying the pyroclastic flow. The range of texture can be highly variable. The overall geometry of flow deposits can be quite variable depending on the topography surrounding the source and the volume discharged during the event. Small-volume flows tend to fill the valleys (Carey, 1991). Large-volume flows are thick enough to cover the interflaves of the existing topography. Based on their depositional processes, the facies presents vertical variations but also lateral variations (Fig. 2.5, 2)(Wohletz & Sheridan, 1979). Indeed, the clasts of the pyroclastic flow deposit trend to be finer and more compact with the distance from Merapi vent (Fig. 2.4).

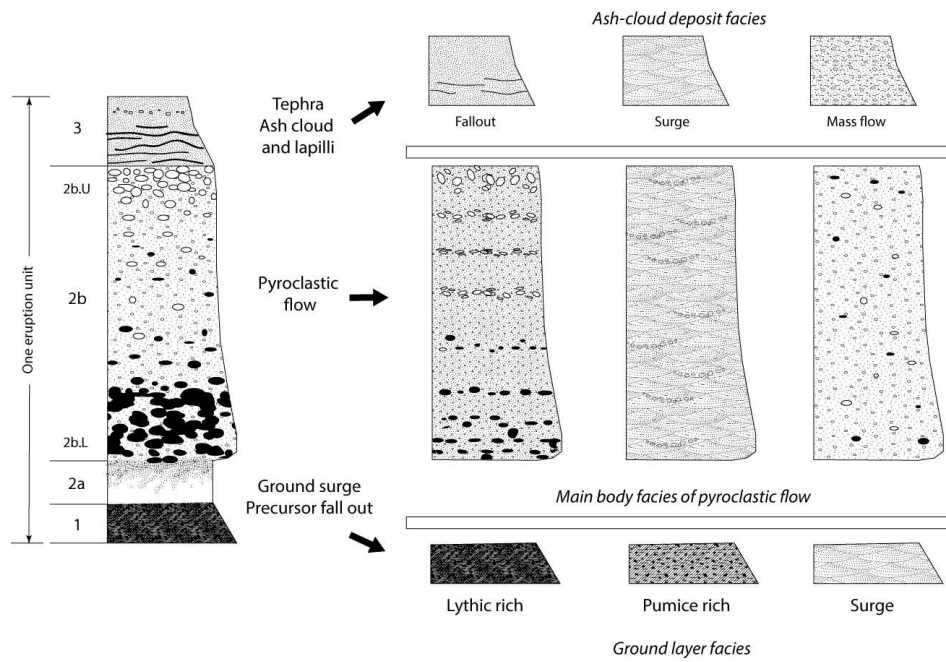


Figure 2.3: Schematic profile of an ignimbrite flow unit and the illustration of the wide ranges of facies of layers 1, 2 and 3. Modified after Sparks (1976).



Figure 2.4: Pyroclastic flow deposits with fine brown cemented matrix and coarse decimetric lava rocks included.

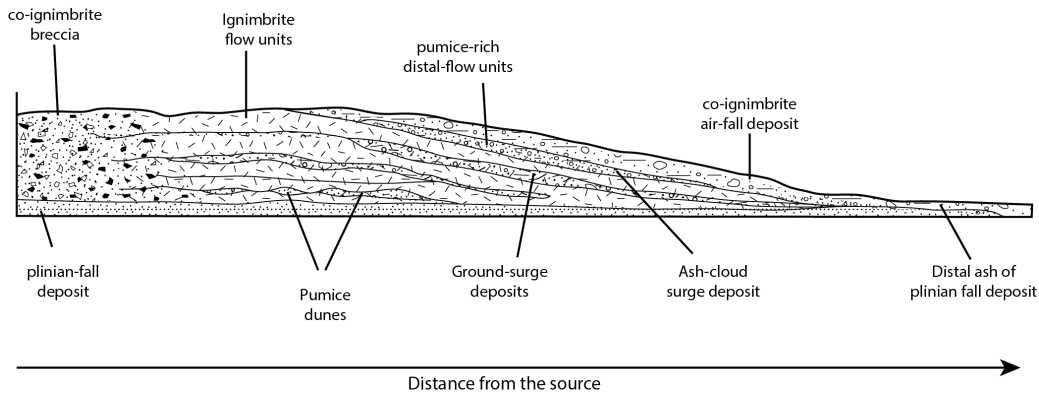


Figure 2.5: Lateral facies variation of the pyroclastic flow deposits. Modified after [Wright et al. \(1980\)](#).

2.1.1.1.2 *Lava flow deposit*

The lava flow deposits of Merapi are porphyric, massive, thick (> 15 m) and typically are not found beyond 4 to 5 km from the summit ([Walker et al., 1973](#)). A large volume of lava flow deposits can fill the valleys (Fig.2.6, 4). Small silicic lava domes are formed, and a process of building and destruction of this dome produces pyroclastic flow and block and ash deposits defined as a “Merapi type eruption” ([Charbonnier & Gertisser, 2011](#)). A portion of the old relief around Merapi is more basaltic (Gunung (G.) Bibi, G. Turgo and G. Plawangan; “gunung” means mount in Indonesian) and reflects a change in the magmatic composition of the lava flow units ([Newhall et al., 2000](#)). The lava flow deposits are fractured in the proximal zone. Upstream, the successive inflation and deflation of the volcanic axis during the eruptions weakens the lava formation, whereas downstream, the lava is massive and unfractured.

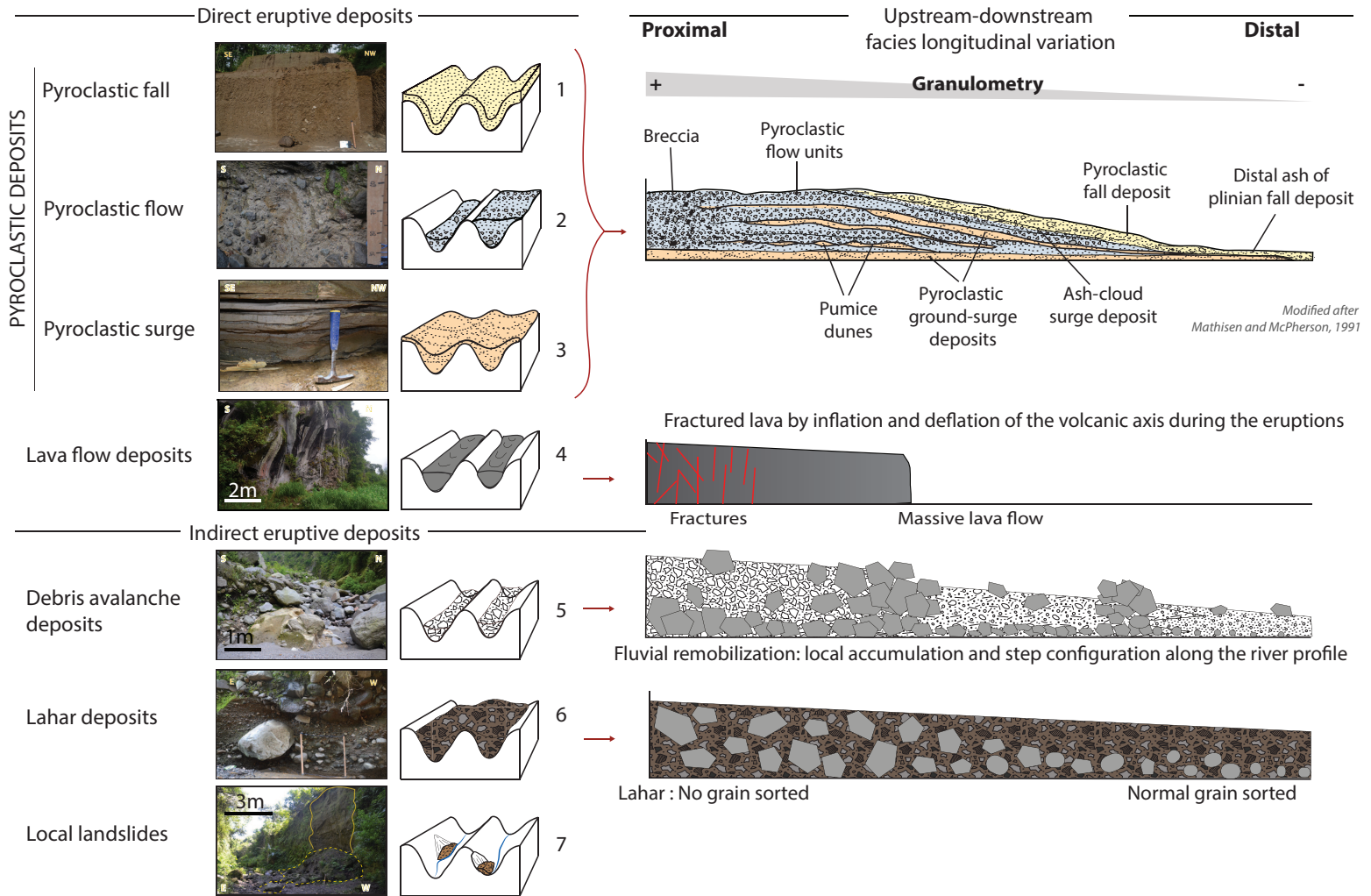


Figure 2.6: Lithofacies of the volcanoclastic and reworked epiclastic deposits on the East flank of Merapi volcano and their depositional conditions into the valleys and interfluvies. Note that the deposits can be cross-stratified and accumulated.

2.1.1.2 Inter-eruption deposits

The indirect eruptive deposits have no direct link with the volcanic eruptions and are primarily dominated by normal streamflow facies with a lateral extent governed by the migration of the channel during their remobilization. An important exception to this description is the debris-flow and lahar units caused by a heavy and long rainfall event or the crater failure due to the earthquake phenomenon (Lavigne & Thouret, 2003; Capra et al., 2002). These deposits are particularly difficult to distinguish from direct eruptive facies, primarily because the indirect eruptive deposits can be formed even during the eruption stage and quickly remobilize the direct eruptive deposits. Considering that the eastern flank of Merapi has been relatively spared from the recent eruptions, the indirect deposits are the most common on the shallow outcrops.

2.1.1.2.1 Debris avalanche

Repetitive eruptions at a single location frequently construct a volcanic edifice in the form of an accumulation of unconsolidated material (Fig.2.6, 5). These piles are frequently unstable and can experience massive slope failures, termed sector collapses, in which a large portion of the edifice collapses to form a debris avalanche or block and ash flow (Siebert, 1984; Capra et al., 2002; Schwarzkopf et al., 2005). A sector collapse typically produces a horseshoe-shape with a headwall scarp. The detached mass typically slides, initially, as large coherent blocks that progressively fragment distally (Belousov et al., 1999). The debris avalanche often forms the cores of small conical hills or hummocks characteristic of many proximal and axial debris avalanche deposits with a “step-configuration” (Palmer & Neall, 1991; Procter et al., 2009).

The term “lahar” is an Indonesian word defined by Smith & Lowe (1991) as a “rapidly flowing mixture of rock debris and water, other than normal streamflow, from a volcano”. A lahar is a rapidly flowing, poorly sorted sediment mixture of rock debris and water with a sediment concentration from 40% to 60% volume or from 40% to 80% weight (Lavigne et al., 2000; Smith, 1991) (Fig.2.6, 6). Recent historical lahar deposits are difficult to distinguish from older lahar deposits (and occasionally even from pyroclastic flow deposits). The solid discharge of the lahar can be enormous. Lavigne & Thouret (2003) have estimated the solid volume remobilized on Merapi near the Batang River (south flank) as 10^6m^3 during one event (Surjono & Yufianto, 2011). Typically, the lahar deposits are poorly sorted upstream and contain particles that range in grain size from clay-size to boulder-size, whereas downstream, the proportion of the boulders decreases. The textures are typically sandy gravel or gravely sand because the source material is coarse block-and-ash debris. However, in certain sectors, the source material can be composed of fine ash-cloud tephra. Thus, the percentage of each size fraction can vary for a given section from deposit to deposit and within a single deposit (Lavigne et al., 2000).

The lahars can be “hot” or “cold”; hot lahars are generated by rainfall during or relatively soon after an eruption episode and cold lahars are generated during interruption periods. The frequency and the extent of the lahar deposits depend on the rainfall intensity and duration (Rodolfo & Arguden, 1991).

2.1.1.2.2 *Landslide*

On sloping surfaces, most remobilization events are initiated by the significant rainfall after deposition of the tephra and pyroclastic layers (Fig.2.6, 7). Several landslide deposits are visible into the tephra layers, especially during the rainy season. Even if with this process the volcanoclastic material returns to the river, the volume of the landslide deposits is lower than the debris flow or the debris avalanche phenomenon.

Based on the relationship between the distance from the vent and the volcanoclastic types, Smith (1988); Vessel & Davis (1981); Manville et al. (2009a); Bogie & Mackenzie (1998) have proposed a conceptual model for the andesitic volcano edifices (Fig.2.7). Smith (1988) has defined central-proximal-medial-distal facies changes for the volcano-sedimentary units. The central zone, or summit zone, is characterized by the most recent caldera with the lava dome and the massive andesitic lava flow surrounded by a detritic breccia. The andesitic lava flow deposits continue until the proximal zone, primarily composed of an alternation of poorly sorted pyroclastic flow and tephra deposits (Karatson et al., 2010). The medial zone is situated between 5 km to 10 km from the volcanic axis. On several stratovolcanoes, a break in slope is often observed in this area. The medial zone is constituted by an abundance of remobilized deposits as lahar and block layers and a certain amount of tuff deposits. Farther than 10 km from the vent, into the distal zone, the direct eruptive formations are rare, and the remobilization of the volcanic products will fill the sediment basin downstream from the volcano. This configuration is too simple and does not consider the lateral variations of the facies and the continuity of some of the formations through the different zones.

Although Merapi is a stratovolcano, its geological history and its geomorphological dynamic do not fit well with this conceptual model. We update the geometry of the volcano-detritic deposits using the observations on Merapi volcano, especially on the eastern flank where the facies have been well preserved.

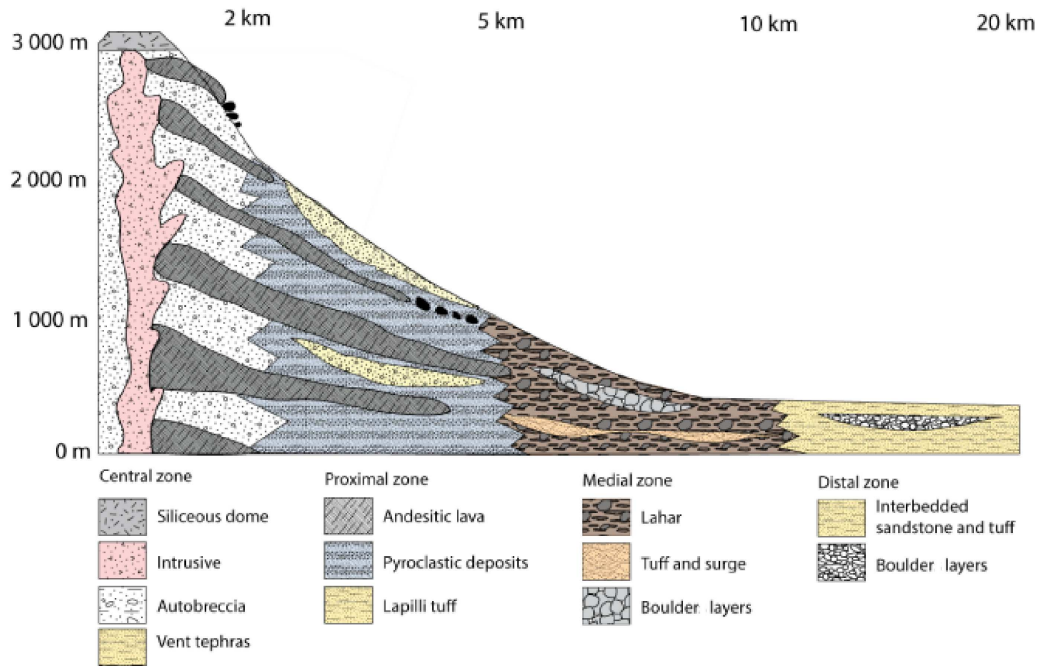


Figure 2.7: Volcaniclastic facies trends illustrates central-proximal-medial-distal facies variations in an andesitic system. Modified after [Vessel & Davis \(1981\)](#); [Smith \(1988\)](#); [Bogie & Mackenzie \(1998\)](#); [Riggs & J. \(1991\)](#).

2.2 Merapi geological history

Although Merapi has been the subject of several studies, its geological history remains controversial ([Berthommier et al., 1990](#); [Camus et al., 2000](#); [Newhall et al., 2000](#); [Gertisser et al., 2012b](#)). Based on this literature, we choose to divide Merapi history into the following five periods: Pre-Merapi, Old Merapi, Middle Merapi, Recent Merapi and Modern Merapi. This division was chosen because each period change corresponds to a major eruptive activity of Merapi and is primarily accompanied by a change in the eruption type or chemical composition of the eruptive products.

The field surveys have allowed the correlation of the deposits described in the literature with the outcrop observations.



Figure 2.8: Picture of Gunung Merapi and Gunung Bibi (to the right) from Klaten

2.2.1 Pre-Merapi

The estimated age of Pre-Merapi by the Ar/Ar method is more than 200 000 years BP to 30 000 years BP (Gertisser et al., 2012b).

From the north, a relief anomaly named Gunung Bibi is visible (Fig.2.8); a hill shape protrudes at 250 m above Merapi material (Fig. 2.9). The G. Bibi is interpreted as a residual hill of an old volcanic structure (Camus et al., 2000) or as an alternative vent (Newhall et al., 2000). The weathered formation is composed of basalt and basaltic andesite lava dated with the K–Ar method at 0.67 ± 0.25 Ma (Berthommier, 1990) however, the recent age estimation with the Ar-Ar method resulted in an age of $109\,000 \pm 60\,000$ years BP, and the value of this new age is relatively limited due to the large analytical uncertainty (Gertisser et al., 2012b). In this study, we considered the G. Bibi to be older than 200 000 years BP. This Pre-Merapi structure could have a complex history with several major eruptions and destructions.

Considering that the more recent Merapi material rests on the G. Bibi, it is clear that the eastern flank has been maintained and protected by this internal structure.

2.2.2 Old Merapi

The estimated age of the Old Merapi period by the U/Th method is 30000 years BP to 4800 years BP (Gertisser et al., 2012b).

The literature describes major volcanic deposits dated approximately 31,000 years BP. This age dates its antecedent to any major eruption or flank-collapse event at Merapi, as proposed by [Newhall et al. \(2000\)](#) and [Camus et al. \(2000\)](#). At this stage, the slopes of Merapi were relatively low. During this period, the activity was divided into the following two main formations:

1. Local basalt emission, visible on the lateral southern relief of G. Plawangan and G. Turgo (Fig. 2.9). Even if no outcrop of the basaltic series has been found on the eastern flank (except the G. Bibi), a lateral emission could be possible.
2. Breccia deposit origins:
 - Dismantling blocks of old lava formation
 - St Vincent's type of pyroclastic flow characterized by a grey sand matrix and angular black lava clasts (diameter < 50 cm). The St Vincent eruption type was defined after the eruption of Soufriere, St. Vincent in 1979, in which nuées ardentes were observed to form simultaneously with a strong vertical eruption column that attained an altitude of approximately 20 000 m.

The breccia deposits have been immediately remobilized into the lahar with the rainfall. Thus, the valleys have been incised by a top-down erosion process. The product of these lahars filled the flat area surrounding Merapi.

The final stage of the Old Merapi is characterized by an alternation of massive andesitic lava flow (the Batulawang series) that filled the valley up to an 1100-m elevation (more than 20-m thick) and a significant St Vincent-type pyroclastic flow named the Holocene Pyroclastic Series ([Gertisser & Keller, 2003](#)) dated between 11000 and 6700 years BP ([Berthommier, 1990](#)).

The filling of the valley by the lava and the accumulation of pyroclastic flow deposits has changed the drainage system. The rivers incised the pyroclastic flow, avoiding passing through the filled paleo-valley. Relief inversion occurred, and the erosion process accelerated with the lahar phenomenon ([Pain & Ollier, 1995](#); [Cundari & Ollier, 1970](#)). The river incision increased, and more remobilized material covered the downstream portion of the volcano ([Lavigne et al., 2000](#)). The Old Merapi stage ended with a flank collapse approximately 4800 years BP ([Gertisser et al., 2012a](#)), which is detailed later.

2.2.3 Middle Merapi

The estimated age of the Middle Merapi period by the U/Th method is 4800 years BP to 2200 years BP ([Bahar, 1984](#))

At this stage, the active crater was at the Pasarbubar location (Berthommier, 1990). The Middle Merapi period began with a major eruption of the “Saint Helens’ type” (Newhall et al., 2000). This catastrophic eruption provided Merapi with its “horse feet” shape.

The “St Helens’ type” eruption date on Merapi has been estimated at approximately 5000 to 2200 years BP (Camus et al., 2000). The youngest age of 4.8 ± 1.5 ka is interpreted to provide an upper age limit for the latest inferred flank collapse of the older Merapi edifice (Gertisser et al., 2012b). This eruption destroyed the West side of the volcano at the level of the hyperbolic Kukusan fault (Van Bemmelen, 1949). A blast series can be observed on the eastern flank, which formed the “print rock” (Batu padas) composed of bamboo mold and a vegetation sheet cemented into an orange-reddish fine matrix. This blast deposit is visible until 1200 m asl near the Musuk village, and its extension was most likely larger, but erosion destroyed the potential outcrops.

Associated with this catastrophic event that was focused on the west side is a significant remobilization of material that could be possible to the east.

After the “St. Helens type” caldera avalanche, the activity was characterized by a new andesitic lava flow deposit (Gadjah Mungkur series dated at 1.7 ± 1.7 ka by Gertisser et al. (2012b) and was located at the western part of the Kukusan fault (Fig. 2.9). This lava formation extension is less significant than the Batulawang series. The alternation with the St. Vincent-type pyroclastic flow deposits continued until 2200 years BP (Berthommier, 1990). The flank collapse eruption changed the configuration of Merapi, and since this event, the eastern flank of Merapi, except certain tephra units (i.e. Gumuk series (Andreastuti et al., 2000)), has been spared from significant eruptions.

2.2.4 Recent Merapi

The estimated age of the Recent Merapi period by the U/Th and ^{14}C method is 2,200 years BP to 300 years BP (Andreastuti et al., 2000; Newhall et al., 2000)

The activity of this period was divided into the following 3 parts:

1. Andesite lava flow deposits, which reach 1300 m asl to the east and 1700 m asl to the west.
2. St. Vincent-type pyroclastic flow deposit (dated at 2000 years BP) with angular clast into a sand matrix. These series are visible until 400 to 300 m asl into the rivers, where the fine material reaches these elevations. One pyroclastic event combined with a hot lahar extended to Yogyakarta City and covered the Prambanan temple at approximately 600 years BP (Voight et al., 2000).
3. Sub-plinian and phreato-sub-plinian activity, characterized by thick ashes and lapilli deposits (named the Gumuk series). This formation can be found far from the

summit (20 km from the vent), and the rice fields of the downstream area are made in this series.

The alternation of all of these formations involved relief formation (a valley filled by the lava and river incision into the pyroclastic and ash deposits) and several lahar phenomena, which cover the old formation from 300 to 100 m asl (Smith & Lowe, 1991). The youngest dome collapse pyroclastic flow deposit on the Eastern flank of Merapi was dated at approximately 1700 years BP (Gertisser et al., 2012b).

2.2.5 Modern Merapi

The estimated age of the Modern Merapi period is 300 years BP to the present.

This period has been monitored and observed with precision and has been described by many authors (Voight & Davis, 2000; Andreastuti et al., 2000; Siebert, 1984). The main eruptions have been concentrated on the west and south sides of Merapi. The volcanic activity is characterized by effusive episodes with construction of an andesite lava dome and explosive periods with destruction of this dome (determined as Merapi eruption type). The collapse of the dome creates a pyroclastic flow canalized into the rivers and able to reach 17 km away from the summit (the Kali Gendol area in 2010 (Komorowski et al., 2013; Jousset et al., 2013)). The hot material of this pyroclastic flow can be remobilized during an intense rainfall event and can produce hot lahar, which is often more destructive and with an extension that is more significant than the eruption itself (Surjono & Yufianto, 2011).

The eruption stage initiates the widespread direct eruptive aggradation of thick deposits. Because these materials are poorly consolidated, the hydrological channel incises the direct eruptive deposits and delivers the sediments to a more distal zone. After a short transition period, the degradation of the direct eruptive deposits decreases, and a “normal” stream flow transports the polygenic elements and constructs the gravel bedload deposits. Smith (1991) has described an aggradation-degradation cycle controlled by volcano-sedimentary input. These processes influence the geomorphology of the volcano with filling and incising the valley, depending on the volume of the direct eruptive deposits and the rainfall intensity (Sisavath, 2011).

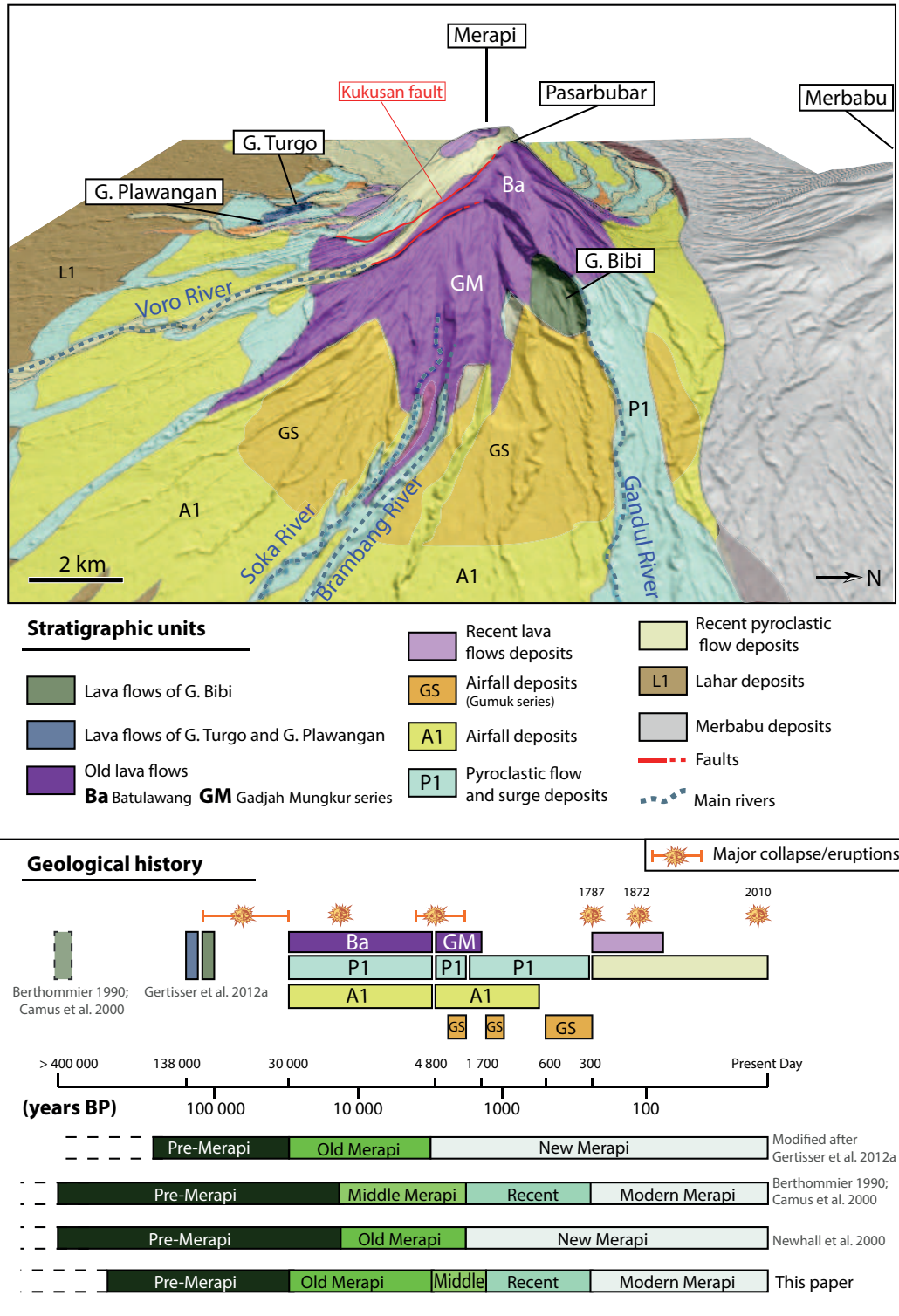


Figure 2.9: East 3D views of the upstream Merapi flank and the major geological features. The geological history of Merapi volcano is detailed. Its geological history is complex and therefore controversial (Berthommier et al., 1990; Camus et al., 2000; Newhall et al., 2000; Voight et al., 2000; Gertisser et al., 2012b). In this study, we propose a combination of periods described in the literature: Proto-Merapi: >200 ka to 30 ka BP; Old Merapi: 30 ka to 4.8 ka BP; Middle Merapi: 4.8 ka to 2.2 ka BP; Recent Merapi: 2.2 ka to 0.3 ka BP and Modern Merapi: 0.3 ka BP to the present. Modified after the geological map by Wirakusumah et al. (1989) and Merapi DEM (ground resolution 15 m, courtesy of C. Gerstenecker, Technische Universität Darmstadt, Germany (Gerstenecker et al., 2005).

2.3 Merapi morphology

The stratovolcanoes have been repeatedly referred to as “stratocones”, implying a conical shape (Grosse et al., 2012; Karatson et al., 2010). The eastern flank of Merapi volcano is elongated in a northwest to southeast direction, measuring approximately 40 km in length between Merapi summit and the Bengawan-Solo River. The studied zone included the surface between the Voro River to the south and the Gandul/Brambang River to the north. This area ranges from 4 km upstream to 27 km downstream in width. The maximum and minimum altitudes are 2990 m (Merapi summit) and 100 m asl, respectively (amplitude 2890 m). The average elevation is 1545 m asl, and 60% of the flank is lower than the average elevation.

The eastern Merapi flank can be divided into 4 parts, reflecting the 4 facies zones described by Bogie & Mackenzie (1998) (Fig. 2.7). The Central zone (above 2000 m asl) shows high slopes (ranging from 40° to 80°) covered by the recent deposits of Merapi and the forest. The Proximal zone is steeples (slopes ranging from 20 to 30°). The river incisions are deep (more than 80-m deep) and close to each other; the limited area between them is cultivated with tobacco and vegetables. Downstream from the proximal zone, the lava flow deposits are not visible, and a break in slope is observed (2.10). The slope of the Medial zone decreases progressively from 20 to 10°. This zone is primarily used for agroforestry with high urbanization. The slopes in the distal zone are relatively low (less than 10°), and rice cropping is the primary activity.

Based on the longitudinal profile of the rivers, we can note that the Soka River profile elevation is slightly lower than the other rivers, most likely reflecting an advanced state of erosion or a slope with a N-S orientation of Merapi deposits (Fig. 2.10). This N-S orientation of the volcanoclastic products can be explained by the presence of the G. Merbabu. To the north, Merapi merges with Merbabu Volcano (3145 m asl) at 1000 m asl.

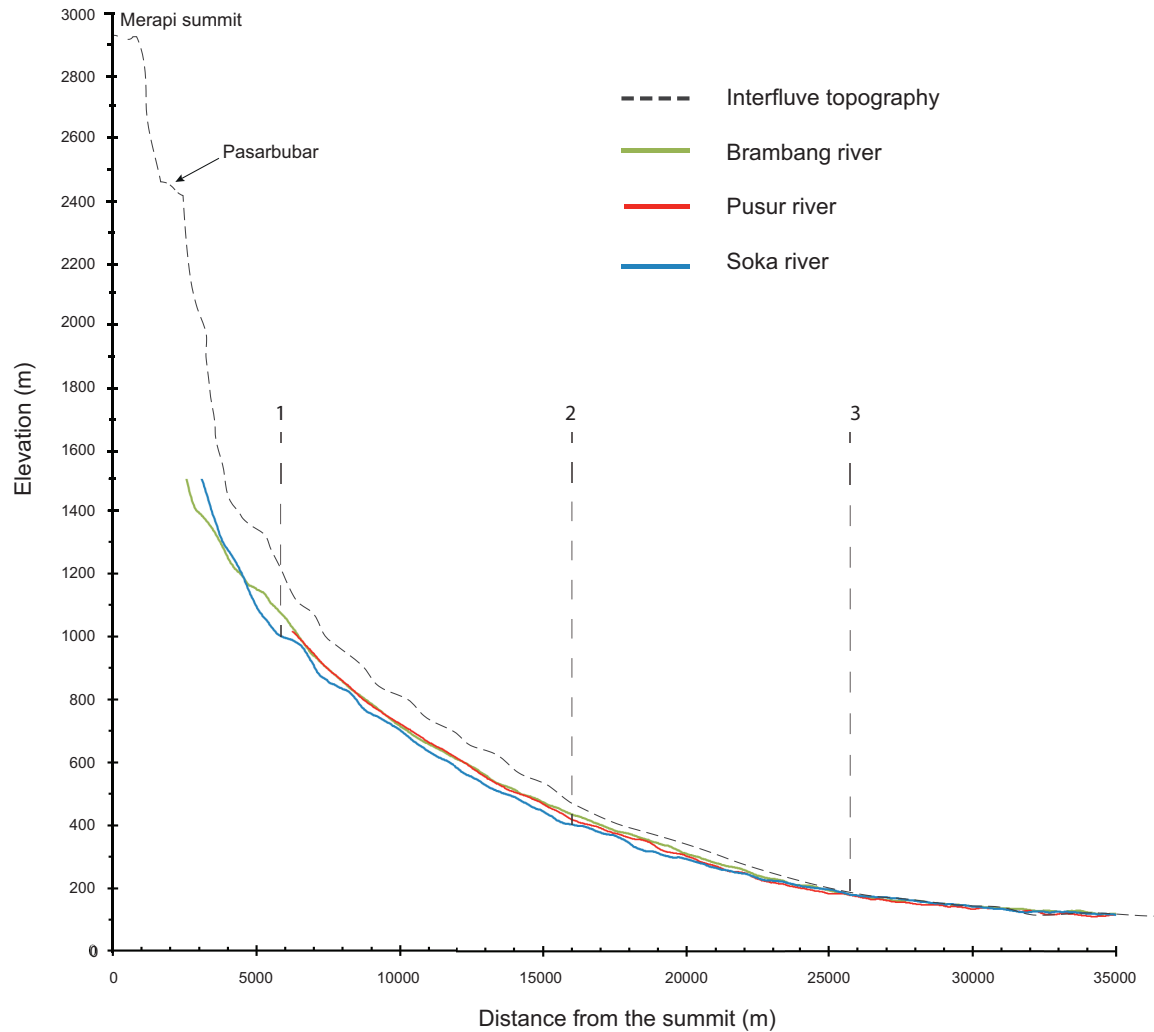


Figure 2.10: Longitudinal profiles of the three main rivers on the eastern flank of Merapi: the Brambang (green), Pusur (red) and Soka (blue) Rivers and the interfluvial topography (dot line) based on the DEM ASTER GDEM V2 data. The Soka River profile elevation is lower than the other rivers, reflecting an advanced state of erosion. The presence of the Merbabu volcano to the north could also explain a N-S orientation of Merapi deposits. In the north, Merapi deposits rest on Merbabu volcano but not in the south. Note three breaks in slope at 1000 m asl, 400 m asl and 200 m asl.

2.3.1 About the longitudinal and lateral facies variations

During Merapi's evolution, the deposit types show an important heterogeneity. Based on the literature [Andreastuti et al. \(2000\)](#); [Camus et al. \(2000\)](#), a geological survey along the three main rivers Pusur, Soka and Brambang rivers, allowed to establish a classification and a spatial repartition of the deposits on the eastern flank of Merapi (Tab. 2.1). The main aspect of volcano-clastic sediments is that they are principally composed of fragments generated by volcanic processes rather than weathering. Moreover, these debris are loosely consolidated and emplaced as thick, dismantling layer or valley fills that are susceptible to rapid erosion.

Because of the complex nature of the volcano-clastics deposit, Merapi formations have highly variable primary porosity. During the eruptions, the circulation of such hot and fast materials as the pyroclastic flow or surge burn the soil and modify the composition of the paleo-topography. This facies is composed by brown to red coloration indurated rocks with sometimes burned vegetation elements (mainly bamboo). Its lateral extent can be important (more than 1 km). In some outcrops, a charcoal layer can be find under the cooked paleo-soil. As this layer is hardly indurated, the cooked-paleo-soil surface could play the role of an impervious layer for the water flow circulation.

Litho facies code	Grain size	Size graded	Stratification	Clast orientation	Interpretation	Hydrodynamic properties
P	Actual pedogenic features: red, brown coloration, finer grained, root clasts.					-
Ps	Cooked paleosoil, dark to red coloration, charcoal					Aquitard
T	Tephra, volcanic ashes, fine to medium	Normal	Cross-beds	None	Fallout tuff	Aquitard
Tp	Tephra, yellow to red coloration, volcanic ashes, fine to medium	Normal	Cross-beds	None	Base surge to phreatomagmatic eruption deposits	Aquitard
M	Mud, silt, fine grain	Massive	Laminated	None	Weathered tuffs	Aquitard
SL	Breccia, sand, from fine to coarse with conglomerate	Reverse to normal	Planar	None	Hyperconcentrated flood flow (lahar)	Aquifer
PF	Gravel to boulders, sand consolidated matrix	Normal or reverse	Planar cross-beds	None	Pyroclastic flow	Aquifer/ Aquitard
Gb	Gravel, pebble matrix	Reverse to normal	Normal	Long-axis elongation	Channel fills	Aquifer
BL	Boulders layers (> 1m)	Normal to reverse	None	None	Debris-flow deposits	Good aquifer
ALF	Massive andesitic lava flow deposits					Aquitard

Table 2.1: Litho-facies determination of the volcano-sedimentary deposits and hydrogeological type of formations of the East flank of Merapi volcano.

It is important to notice that our study area has been spared by most of the recent major eruptions since at least 1786. Indeed, the recent pyroclastic flows and lava flow deposits have been concentrated on the North, South and West sides. The East flank is in an inter-eruption stage, where the most recent sediments come from the remobilization of the old volcanic materials by hyper-concentrated flow (lahar), gravitational collapse of the massive lava and the local landslides [Selles et al. \(2012\)](#).

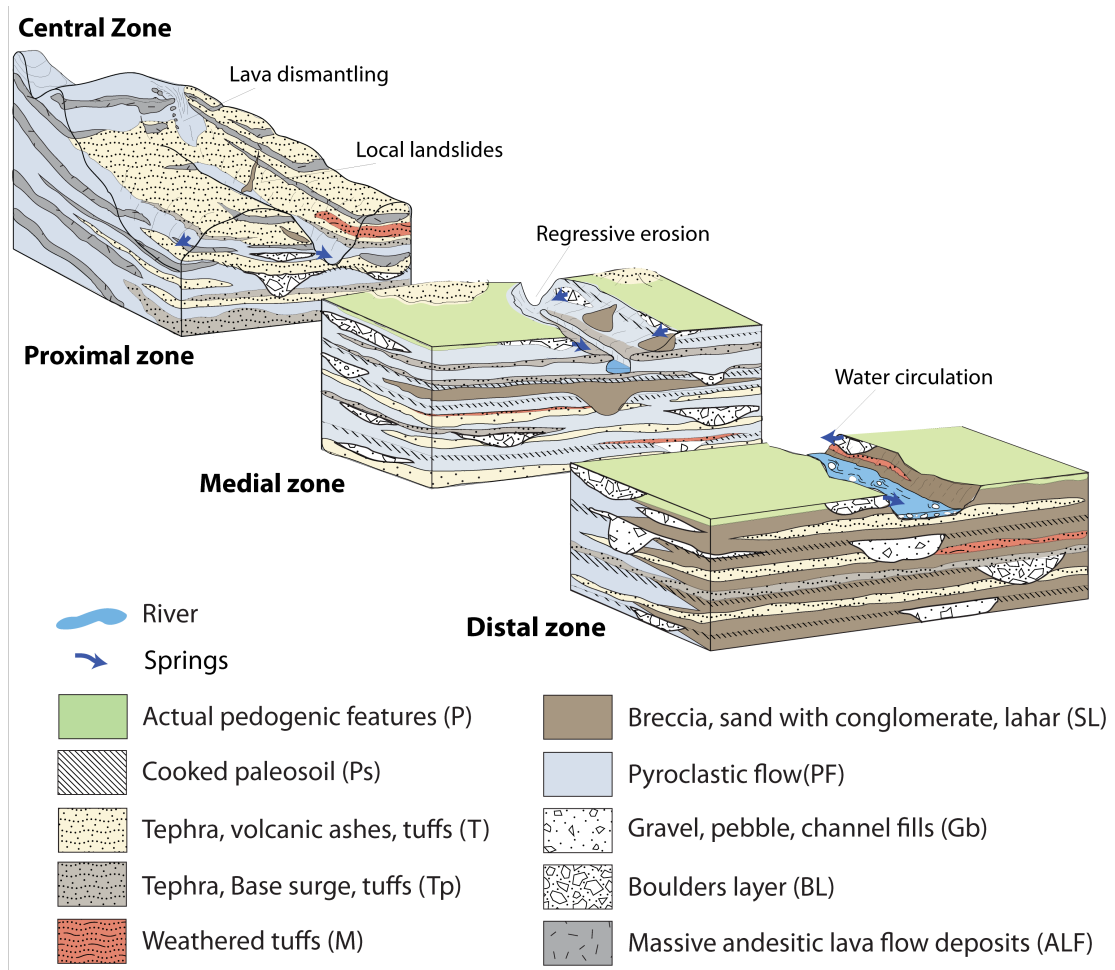


Figure 2.11: Conceptual model of the geometrical repartition of the volcano-clastic deposits along the eastern flank of Merapi volcano.

2.3.2 Top-down dynamic processes: from dismantling to sedimentation

As in mountainous area, stratovolcanoes are lead by top-down sedimentary processes (Hooke, 2003). Thus, based on field observation, the characteristics of the depositional environment along Merapi profile have been described for each facies zone and summarized in Tab. 2.2.

Characteristics	Central (2962-2400m asl)	Proximal (2400-800m asl)	Medial (800-400m asl)	Distal (400-200m asl)
Geomorphology				
Slope angle	20-45°	15-20°	≤ 4°	≤ 2°
Distance from the vent	0-2 km	2-10 km	10-15 km	15-25 km
Deposits				
<i>Lithofacies</i>				
Abundant	ALF, PF	ALF, BL, SL, Tp, T, PF	PF, Gb, Tp, T, Ps, SL	T, Tp, P, SL, Ps
Minor	T, BL	M, Gb	P, BL	PF, Gb, M
Rare		P, Ps	M	BL
<i>Geometry</i>				
Thickness	ALF ≥ 20m PF ≥ 30m BL ≥ 5m T ≥ 5m	ALF ≥ 10m; T, PF ≥ 15m BL, SL ≥ 5m; Tp ≥ 2m M ≤ 2m; Gb ≥ 5m P, Ps ≤ 0.5m	Gb ≥ 10m; SL ≥ 4m; T ≥ 15m P, Ps ≤ 1m; BL ≥ 2m; Tp ≥ 2m; PF ≥ 5m; M ≥ 1m	T ≥ 15m; Tp ≥ 2m SL ≥ 5m; Gb ≥ 3m; PF ≥ 2m; P, M, Ps ≤ 1m; BL ≤ 1m
Shape	Massive (ALF), instable and well cemented deposits (PF),	Mostly channel form, debris flow deposits, some tabular deposit (ALF, T)	Channel form, tabular deposits (PF) local landslides	Tabular deposits (T, Tp, Ps) some channel form (Gb) hyper-concentrated flood flow (lahar)

Table 2.2: Characteristics of the volcano-sedimentary deposits environment along the East flank of Merapi volcano.



Figure 2.12: The last step to the top of Merapi. In foreground, a lava block fractured under the combined action of rain and temperature (night/day). September 2012.

In the central zone the lava deposits thicknesses are variable and range from 10 to 30 m. The covered surfaces are important in the upper part and more local along the slopes. In the downstream zones, the rivers are filled by huge andesitic blocs coming from the dismantling of the lava flow deposits in the upper parts (Fig. 2.14). This process creates channels of blocks can be transported far from the source (more than 10 km). These layers can be covered by the airfall or pyroclastic flow deposits during the eruptions (formation with a large recovering influence). The tuffs and the lava play the role of impervious barriers (Fig. 2.13).

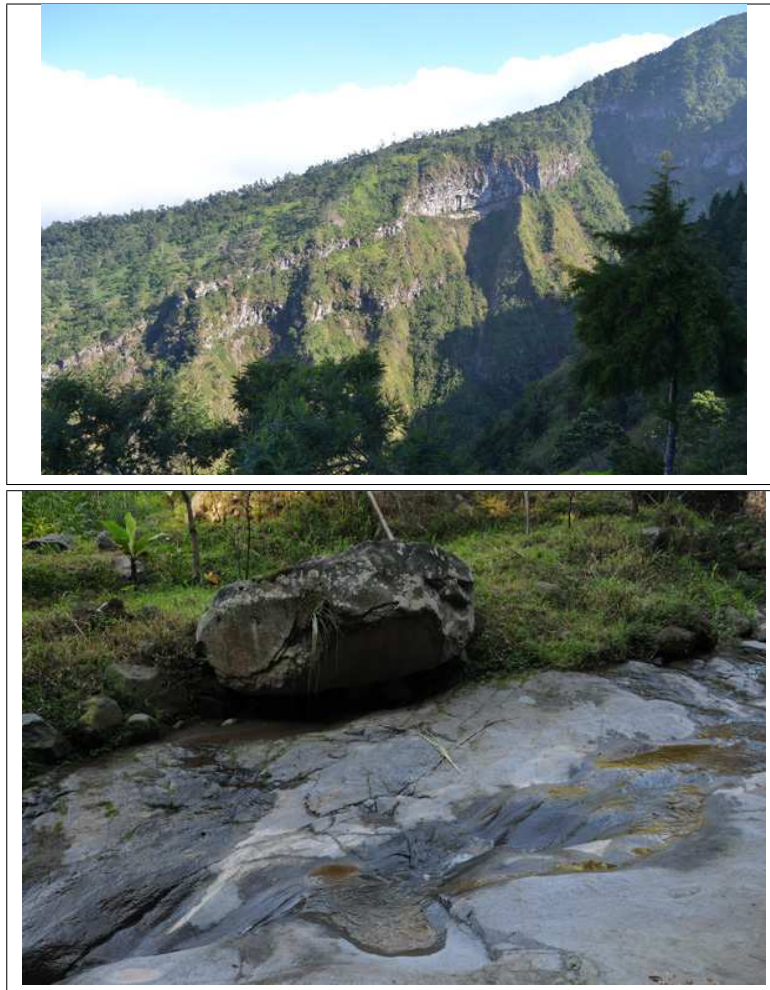


Figure 2.13: Massive andesitic lava flow deposit incised by the river (up). These massive and thick layers (more than 20 m) constituted a long aquitard formation and the water flow over is (down).

Downstream, the slopes are less steep and the river profile is in stair steps, with several natural dams composed by metric to decametric blocks of grey andesite. From 1250 to 970 m of elevation and over 3.5 km, 7 major dam blocks were identified. These dams have a low proportion of sand matrix. The blocks can be angular to sub-angular with a maximal diameter of 8 m.

Only the Brambang river shows a perennial flow around 958 m asl. Upstream of this point, the Brambang River shows seepage due to the occasional rain but no permanent flow during the dry season. Two phenomenons control the hydrodynamic and the hydrogeological condition:

- The dam blocks play the role of infiltration zones where the water disappears (upstream of the dam). Then, after the natural dam, the base flow comes from the bottom of the gullies, filled by the blocks. We suppose that the real hydraulic gradient of the river does not follow the “stair steps” of the actual river bed, but a more linear one on the bottom of the ancient (paleo) valley, now filled with the blocks.
- The surge and especially the indurated paleo-soil facies form an impervious boundary. At the boundary between the pyroclast density current deposits with a sandy matrix and the indurated paleo-soil, several seepage zones are visible.

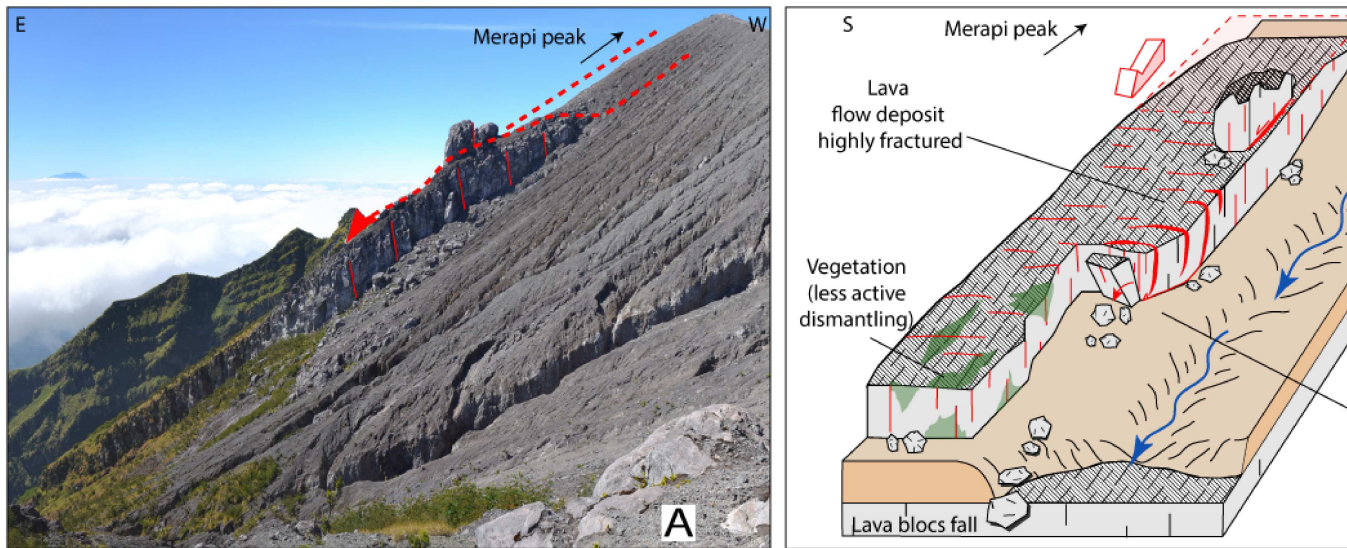


Figure 2.14: Dismantling process of the lava flow deposits in the upper slopes of Merapi. The andesitic lava flow deposits are fractured and collapse by blocks or by full “lava plate”. After drawing of Benoit Deffontaines.

The dam blocks occur on average every 600 m along the Soka and Brambang rivers; there are no dam blocks on the Pusur river. The paleo-soils are visible from 6.1 km of the summit (1050 m asl). This distribution reflects the type of eruption and dismantling processes of Merapi. The andesitic lava flow deposits are altered and lay down fine and less consolidated material. The huge blocks of andesite fall near the source and are remobilized during the next flood (Fig. 2.17). The paleo-soils result from the surge and air fall deposits during the phreatomagmatic stage of Merapi (Camus et al., 2000), during the early stage of construction. Thus, the deposits are visible in the lower layers of the volcano-clastic series. We suppose that surge and paleo-soil deposits exist even at the higher elevation but have been covered by the new air fall and lapilli deposits.

The conceptual model Fig. 2.16, proposed a 3D view of the deposits observed and the hydrodynamics of the upper Brambang River and Soka river.



Figure 2.15: Andesitic lava block into the Brambang river bed remobilized during flood events. The stick length is one meter.

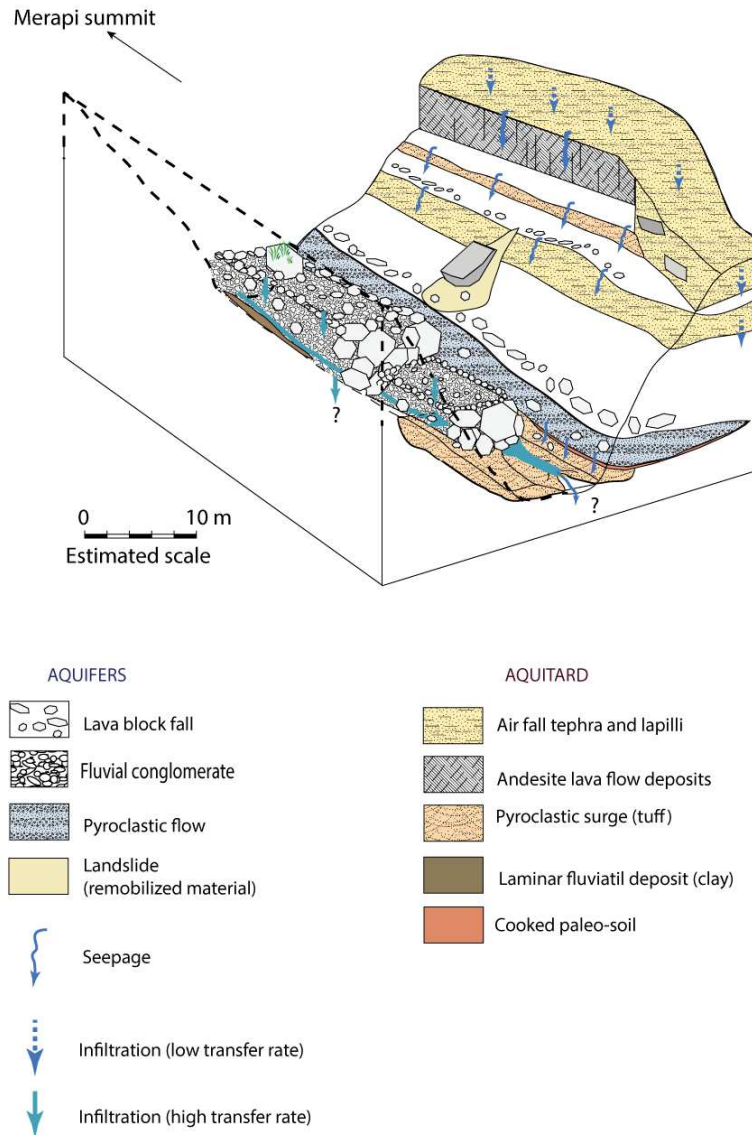


Figure 2.16: Conceptual block diagram of the upper Brambang and Soka Rivers (900 to 1200 m asl). All the major features have been concentrated in one portion of the river.

The hydrodynamic functioning can be divided into low and fast transfers. The air fall and lapilli deposits are rapidly saturated and the transfer through these formations will be slow. When the water reaches an impervious layer (i.e. massive lava flow deposits, pyroclastic surge deposits, base surge with indurated paleo-soil), the water will runoff on the slopes of the valley to the block accumulation. The absence of matrix and the fact that the blocks are not well agglomerated facilitates rapid water transfer. The clay deposits resulting from the low energy fluvial environments can play the role of impervious layers in the blocks channel. The water can infiltrate directly and follow the bottom of the paleo-valley along an impervious layer. At the end of the block accumulation (dam

blocks (Fig. 2.17), water is visible and flows along the impervious layer (welded tuff or massive lava flow) until an altered part, where it infiltrates to the lower formations.



Figure 2.17: Andesitic lava block laying on welded tuff deposits on the Soka river. The blocks are accumulated in “natural dams” within the river meander, until the next flood which will remobilize most of them.

2.4 Identification of drainage anomaly

We saw that the deposits have a channelized organization resulting from the buried paleo-rivers. Therefore, a link can be made between the internal structure and the present surface drainage organization. The objective is to improve the geological and geomorphological conceptual model of the eastern flank of Merapi sub-surface through the analysis of its surface drainage pattern.

2.4.1 River interceptions

To describe the drainage network of Merapi, a GIS analysis was conducted, and the data acquired were processed using a digital elevation model (DEM) with a 15-m ground resolution (courtesy of C. Gerstenecker, ([Gerstenecker et al., 2005](#))) and the Advanced Spaceborne Thermal Emission and Reflection Radiometer (ASTER), Global Digital Elevation Model Version 2 (GDEM V2) from the National Aeronautics and Space Administration (NASA) with a 30-m ground resolution and 1 x 1 degree tiles ([Tachikawa et al., 2011](#)). The drainage network has been extracted from the DEM and validated by satellite images (ALOS 2010 images with a 10-m ground resolution).

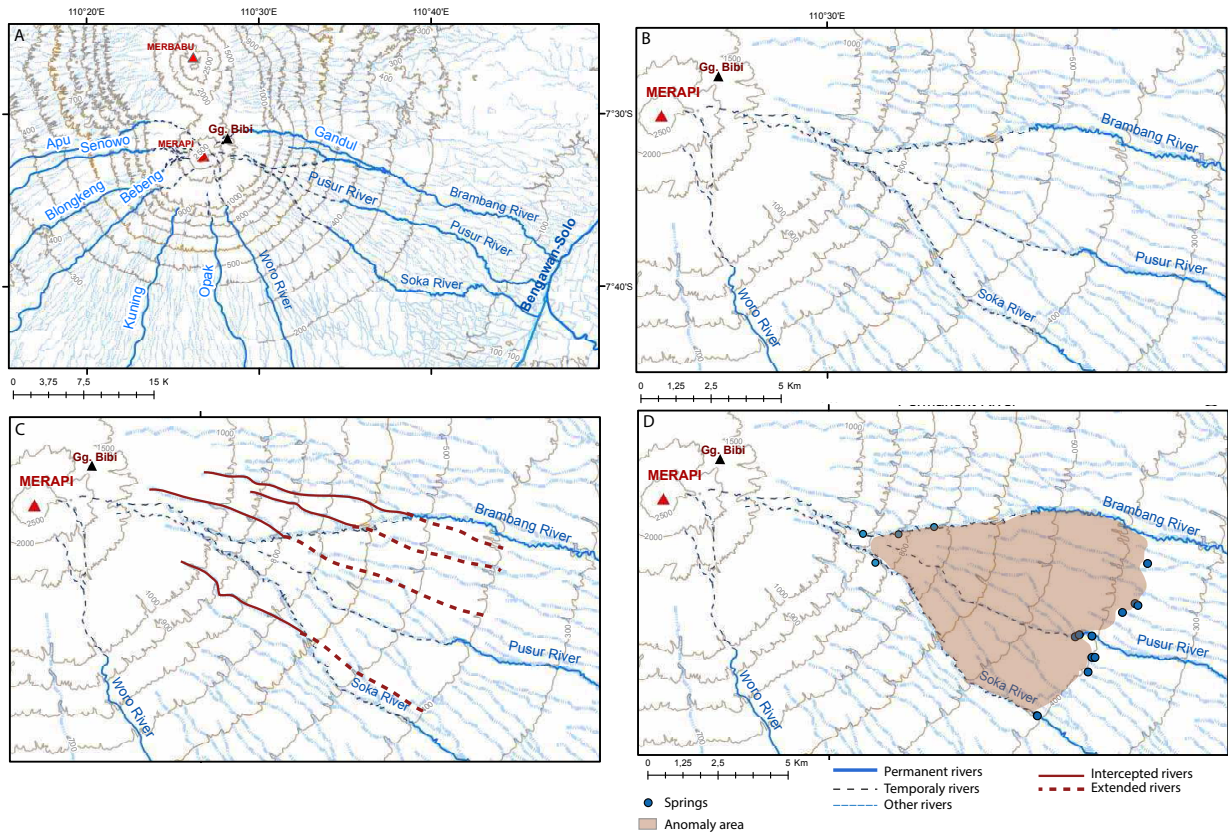


Figure 2.18: Map of the drainage network on Merapi volcano. A) Global view of the main rivers around the eastern flank of Merapi, B) identification of the drainage system anomaly with intercepted drainages by the Soka and Brambang Rivers, C) upstream (700 to 400 m asl) theoretical geometry of the drainage network, D) the map of the anomaly area characterized by a triangular shape and the springs occurrence at the downward limit of the anomaly.

The global plan view shows radial centrifugal organization of the drainage network (Fig. 2.18, part A). On the northern flank, the presence of the Merbabu volcano curves the pathway of the rivers to the south. The drainage network of Merapi is distributed to the west, the south and east only. On the eastern part, the radial outward organization of the drainage network is not well developed, and the upper portion of the Soka and Brambang Rivers are parallel from 1500 to 700 m of elevation with a NW-SE direction (Fig. 2.18, part B).

From 1000 to 600 m asl, the valleys of ephemeral rivers with radial organization are intercepted by the Soka and the Brambang Rivers, which diverge symmetrically 30° to the southeast for the Soka River and 25° to the northwest for the Brambang River (W-E direction) (Fig. 2.18, part B). Downstream (at 400 m asl), in the extension of the interrupted valleys, several rivers appear to be connected to the Soka and Brambang Rivers (Fig. 2.18, part C). Moreover, several natural springs have been inventoried along the topographic line 400 m asl (Fig. 2.18, part D).

2.4.2 River incision characteristics

River interception causes the drainage network anomaly. Two hypotheses can explain the divergence of the Soka and the Brambang Rivers: 1) a residual cone from the previous building stage of Merapi (as the G. Bibi) could form a relief from 700 to 400 m asl and stop river incision, 2) the accumulation of a detrital fan linked to an extreme catastrophic event. These phenomena can affect regional drainage patterns by shifting the watershed and diverting major rivers (Manville et al., 2009b; Manville & Hodgson, 2011; Rodolfo & Arguden, 1991). Paleo-relief will favor a volcanic chevron shape (Torres et al., 2004) and the triangular shape observed on the eastern flank of Merapi supports the theory of detrital fan accumulation during a flank collapse event.

To better characterize the drainage network anomaly, the DEM ASTER GDEM V2 model has been used to extract 9 transverse topographic profiles at different elevations on the eastern flank of Merapi from 1550 m asl to 400 m asl (Fig. 2.19). The positions of the Brambang, Pusur and Soka Rivers are indicated by the colored arrows. The incision of the rivers is indicated in their respective valleys.

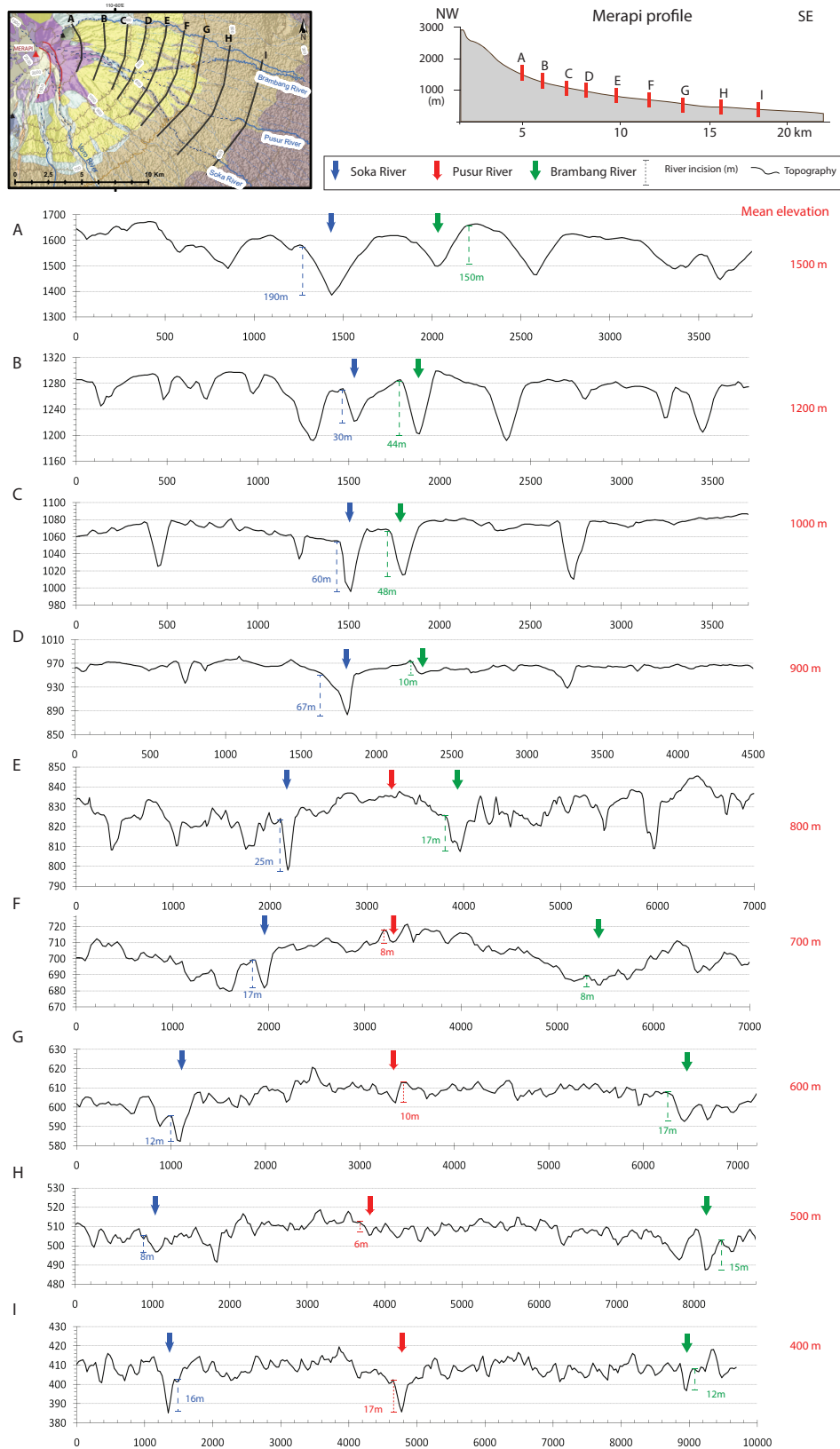


Figure 2.19: Transversal topographic profiles at 9 different elevations showing the variation in river incision depths estimated from the DEM (15-m resolution) (courtesy of C. Gerstenecker, Technische Universität Darmstadt, Germany) for profiles A to G and from the DEM ASTER GDEM V2 model (30 m of ground resolution) for profiles H and I. The vertical and the horizontal scales are not the same on each profile. Note the incision difference between the two rivers, Soka and Brambang, and the Pusur River in the central position. This difference disappears below 400 m asl, highlighting the downstream end of the drainage anomaly.

From 1500 to 900 m asl, the Brambang and Soka Rivers have a deep valley incision ranging from 10 to 190 m. At 800 m asl (Profile E), the Pusur River valley appears between the Soka and the Brambang Rivers. The incision is relatively small compared with the other rivers (less than 10 m), reflecting more recent development. At 400 m asl, the Pusur valley shows an incision similar to and even deeper than that of the Brambang and the Soka Rivers (17 m for the Pusur, 16 m for the Soka and 12 m for the Brambang). The relatively small incision of the Pusur River between 800 and 400 m asl compared with the Soka and Brambang Rivers reflects the presence of a deposit burying the initial valley of the Pusur River. That finding is highlighted by the fact that, below 400 m asl, the Pusur River has an equivalent incision with the surrounding rivers, and several springs are aligned along the topographic line at 400 m asl.

These transversal topographic profiles allow mapping of the drainage network anomaly. The area concerned is located between the Soka and the Brambang Rivers where they split, and stops near 400 m asl; hence, the triangular shape is confirmed. This anomaly occurs from 700 to 400 m asl. Based on the DEM ASTER GDEM V2 model, the longitudinal profiles of the Brambang, Pusur and Soka Rivers show three break in slope at 1000 m asl, 400 m asl and 200 m asl, respectively (Fig. 2.10). The drainage network anomaly occurs between two breaks in slope (i.e., 1000 and 400 m asl) in which the slope is decreasing.

2.4.3 Lithological stratigraphical analysis

To identify the lithological facies of the triangular anomaly, field surveys have been focused along the 3 main rivers. Several lithostratigraphic logs have been collected along the Brambang, the Soka and the Pusur Rivers to define the lateral continuity of the geological formations. The study area has been divided in four zones depending on the formation occurrence and their elevations (Fig. 2.20). Note that this stratigraphy represents the shallow units of the edifice, and an interpolation of the old (buried) deposits must be performed carefully.

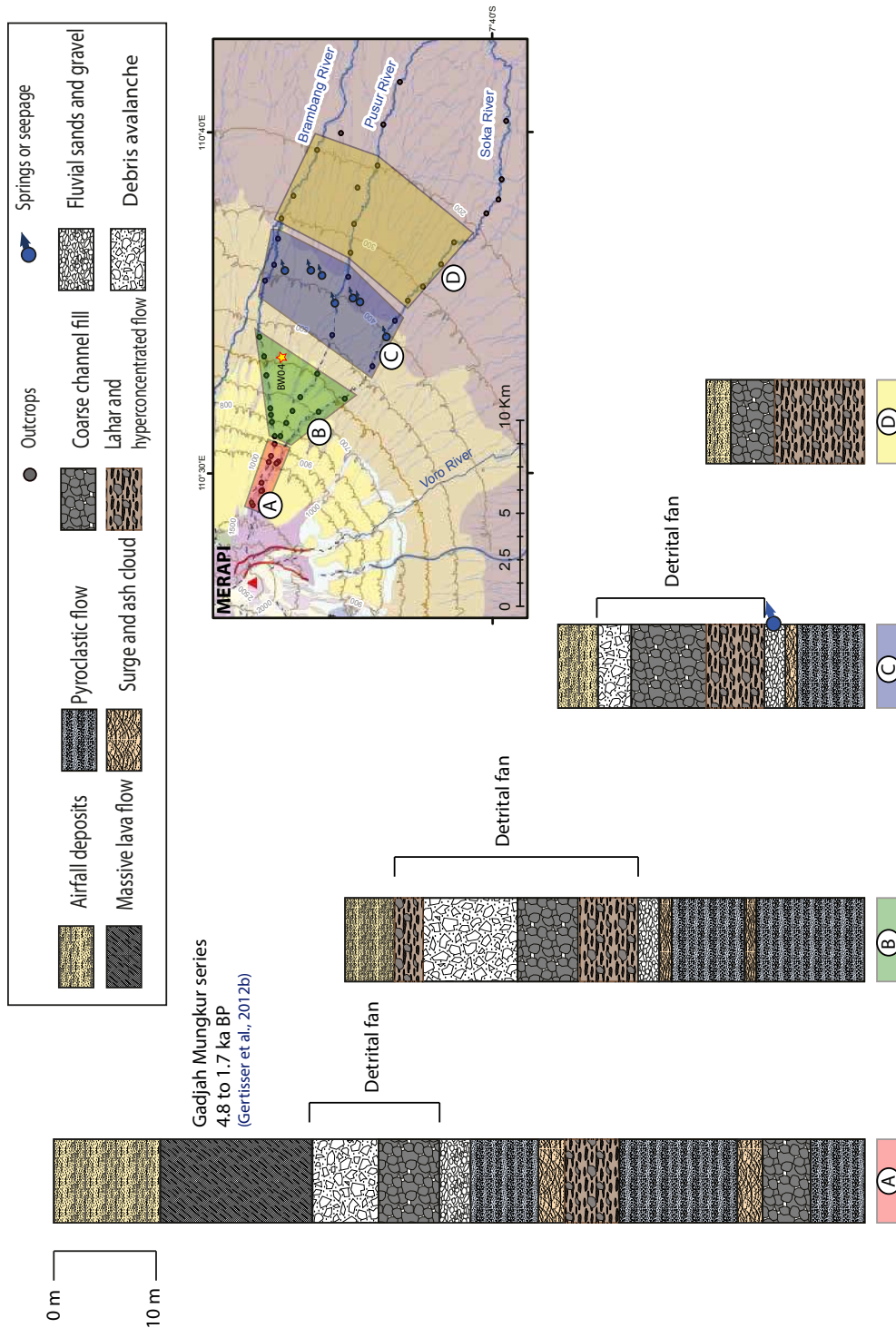


Figure 2.20: Correlation of simplified lithostratigraphic sections of Merapi Volcano along the Brambang, Pusur and Soka rivers upstream (left) to downstream (right). The logs represent the synthesis of 4 zones depending on the elevation: zone A: from 1500 to 900 m asl, zone B: from 900 to 600 m asl, zone C: from 500 to 350 m asl and zone D: from 350 to 200 m asl. Note that the thickness of the formation is decreasing with the elevation.

In the zone A (from 1500 to 900 m asl) the Brambang and the Soka valleys are framed by massive andesite lava deposits above 1000 m asl. The andesite lavas are covered by a thick layer of tephra (primarily composed of ashes and lapilli) (Fig. 2.21 H). This tephra layer covers the eastern flank until 40 m from the summit and represents activity at Merapi over the last 2000 years. The deposits are characterized by mantle bedding of tephras and lapilli, normal and inverse graded beds, and the absence of through cross-stratification and ripple cross-lamination (5 to 20 m thick).

The thick lava flows (more than 20 m thick) overlie a formation of angular andesite clasts interpreted as debris avalanche layer formed by the erosion of the upper lava flow deposits (Fig. 2.21 A and B). This formation is poorly sorted, non-stratified with poly lithologic elements; Up to 75% of the deposits is composed by small volcanic fragments and some andesite clasts are up to 2 m in diameter. This formation shows a relatively constant thickness of 10 m.

Below the debris avalanche layer, the formation is composed by large rounded boulder with sandy hyperconcentrated flow deposits. This unit is poorly sorted with erosive basal contacts (Fig. 2.21 C and D). This layer has been identified as channelized debris-flow deposits.

This sequence can be found also on the log of the zone B and C (Fig. 2.20) with an alternation with lahar and hyperconcentrated flow (Fig. 2.21 E and F).

Under this sequence, a thin layer of gravel to pebble sized clasts (up to 1 m of diameter) is visible. It shows clay and interbedded features. This formation has been noted as fluvial deposits.

Below the fluvial formation, valley sides are composed of a build-up of pyroclastic flow deposits and remobilized material. The remobilized deposits display sedimentary structures, including trough cross-stratification, horizontal stratification, ripple cross-lamination, and parallel thin lamination. Several coarse block and ash deposits are visible near the bottom of the river (block diameter: max. 2 m).

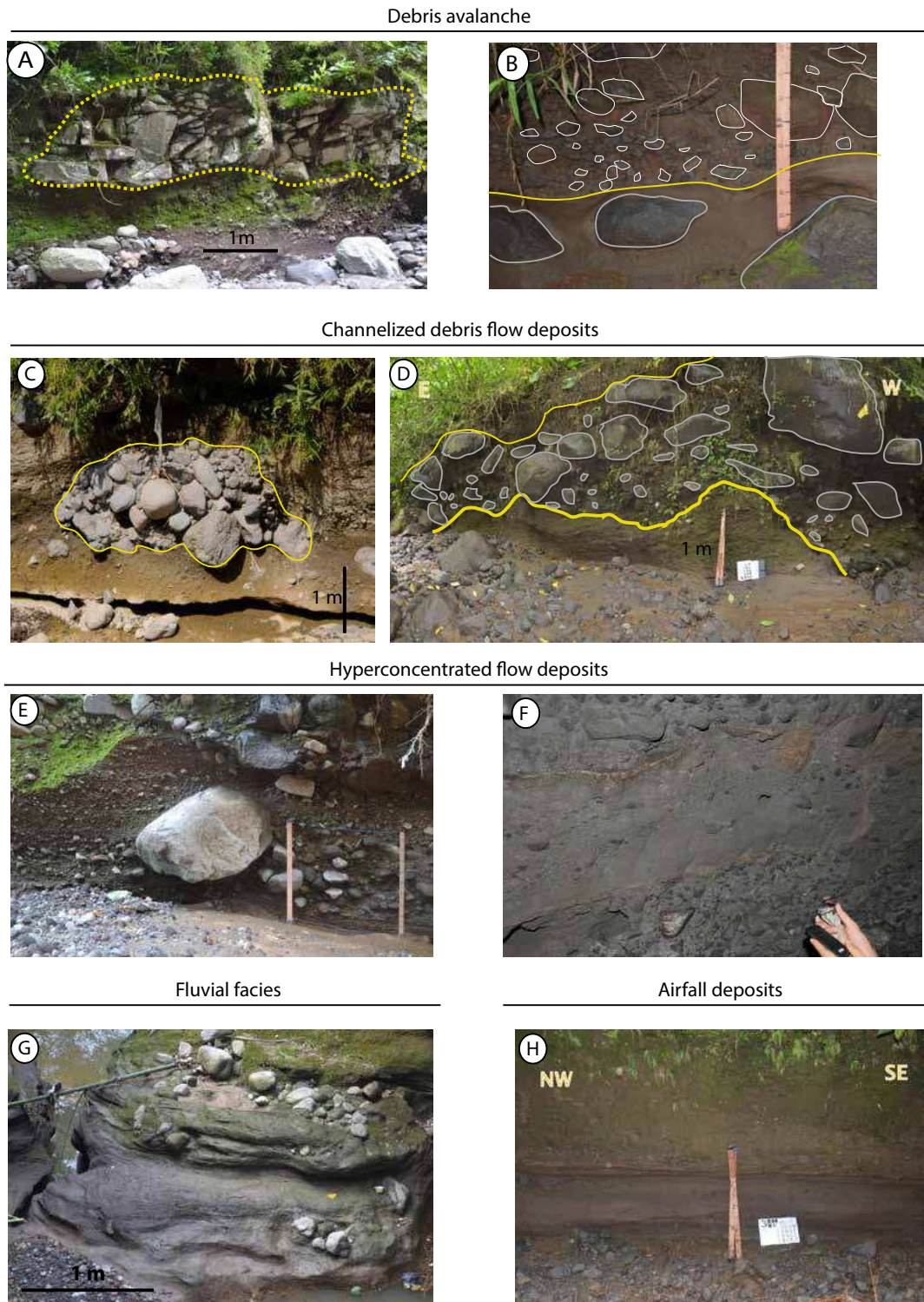


Figure 2.21: *Debris avalanche deposits*: A) Large fractured megaclast of andesite, B) Basal layer with poly lithologic gravel and boulders, *Channelized debris flow deposits*: C) Channel axial profile filled by a coarse debris flow deposit, D) Longitudinal profile of channel filled by boulder and sandy matrix; *Hyperconcentrated debris flow*: E) Moderately normal graded pebble and large andesite boulder, F) Poly lithologic hyperconcentrated flow; *Fluvial deposits*: G) Sedimentary figures of bedding deposits with mature gravels; *Aeolian deposits*: H) Fine-grained cross-bedded sand.

The anomaly is primarily composed of indirect deposits as a debris avalanche formation. No proof of a massive residual cone, such as the G. Bibi, has been found. Thus, the anomaly observed on the drainage network on the eastern flank of Merapi results from detrital fan accumulation. The detrital fan rests on the break in slope from 700 to 400 m asl. Below 400 m asl, the older formations are visible, reflecting a complex history. [Rodolfo & Arguden \(1991\)](#) have observed the same phenomenon in Philippines but at a local scale (4 km²).

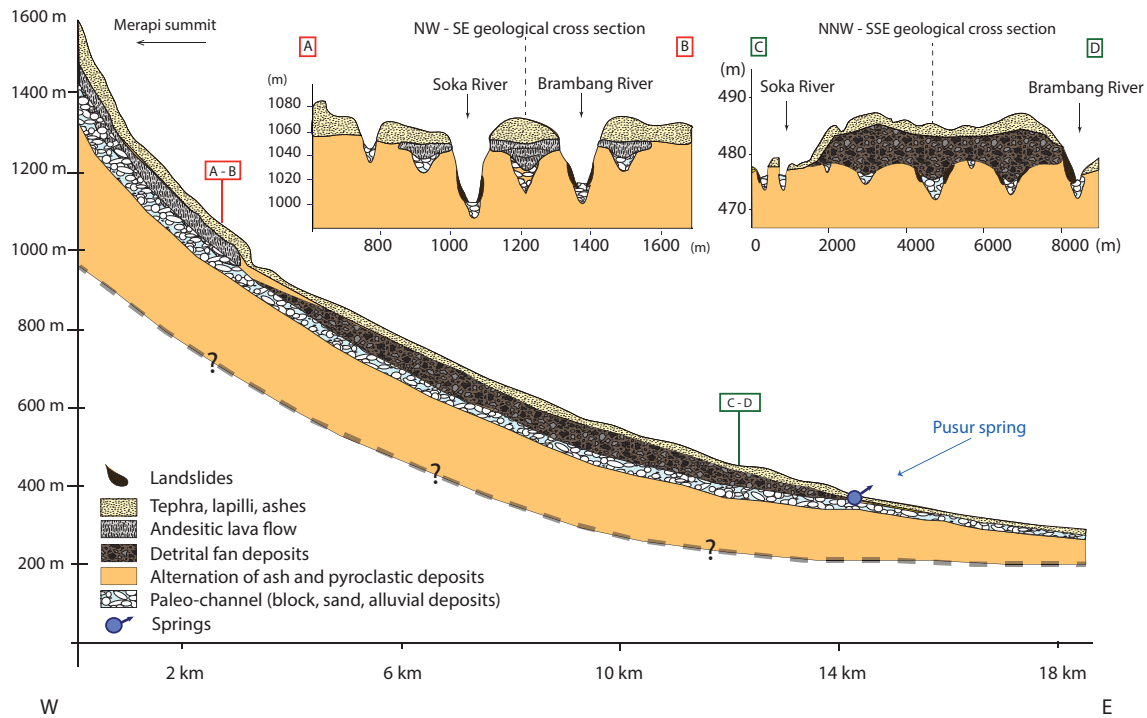


Figure 2.22: Topographical and geological longitudinal cross-section of the detrital fan along the Pusur River axis (NW-SE) with 2 additional transversal cross-sections along the isohypses at 1000 and 500 m asl. The lithological facies have been simplified into 5 units. The local landslide formations are represented on the valley sides. Note that the paleo-Pusur River (represented by the central paleo-channel) is covered by an andesitic lava flow in the upstream parts and by the detrital fan downstream. The spring alignment at 400 m asl occurs at the termination of the detritic system where the paleo-channel outcrops.

Based on interpretation of the elevation profiles and the stratigraphic logs, a cross section along the Pusur river axis of the detritic alluvial fan can be constructed (Fig. 2.22). The lithological facies have been simplified in 5 units: i) tephra layers, ii) andesitic lava flow, iii) detrital fan, iv) pyroclastic deposits and v) block and alluvial deposits. Two cross sections have been made at 1000 m and 500 m asl to better visualize the architecture of the detrital fan.

At 1000 m asl, the valleys are filled with alluvial and block deposits from the dismantling of the andesitic lava flow deposits. Below the lava flow, the paleo-rivers are also composed of alluvial deposits. At the termination of the lava flow deposits near 800 m asl, the detrital

fan covers the paleo-topography until 400 m asl. The paleo-formation outcrops at 400 m asl near the spring belt.

Based on the geological history described earlier, it is possible to link this detrital fan formation to a major flank collapse followed by the upstream valley fill with lava flow deposits. Figure 2.23 proposes a reconstruction of the superficial recent geomorphological history of the eastern flank of Merapi volcano in 4 synthetic steps.

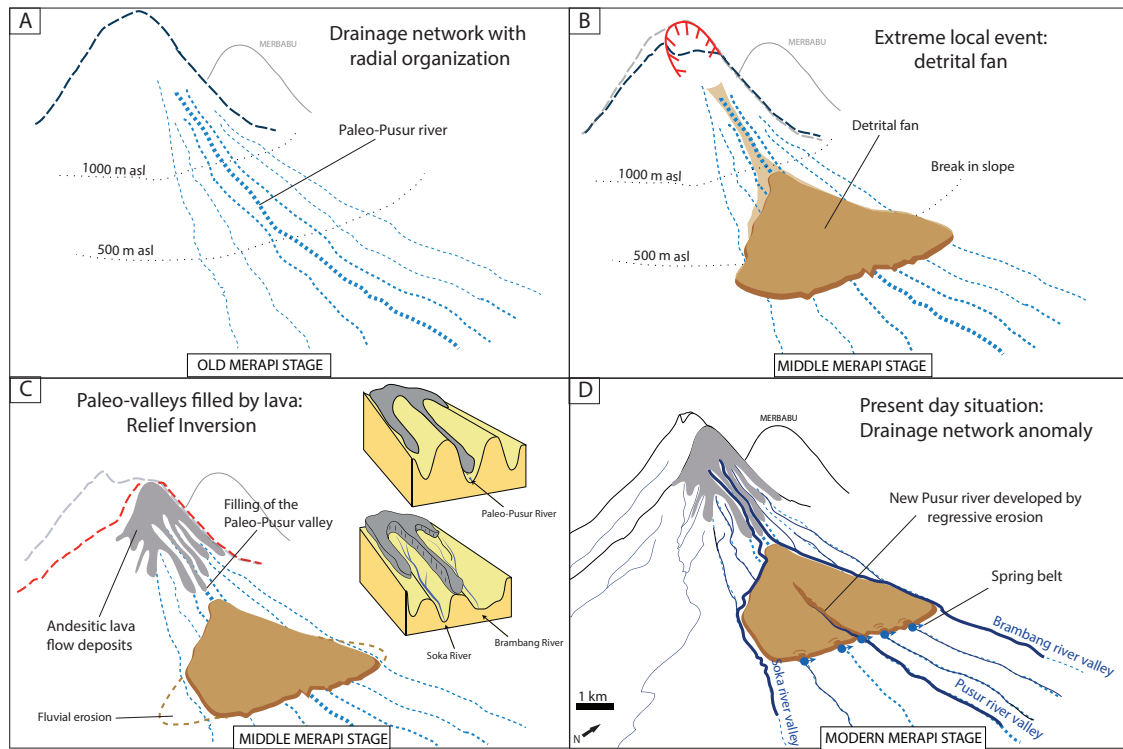


Figure 2.23: Synthetic reconstitution of the recent superficial geomorphological history of the eastern flank of Merapi volcano. A: During the Old Merapi period, the rivers were organized radially. B: An extreme event occurred at the beginning of the Middle Merapi stage (approximately 5 ka BP). A detrital fan of debris avalanche deposits lay on the breaking slope near 500 m asl. C: After the extreme event at the end of the Middle Merapi stage (from 4 ka to 1.7 ka BP), the production of andesitic lava filled the paleo-valleys and closed the paleo-Pusur River. The high rate of erosion caused a relief inversion. D: Present day situation: the rivers flow in the paleo-interfluves, channelized by the lava flow deposits. The Brambang and Soka Rivers are divergent around the detrital fan and catch the surrounding radial rivers. The present day Pusur River incises the detrital fan by regressive erosion. At the end of the fan, an alignment of springs (spring belt) shows a change of lithology between the fan and the paleo-topography. Drawing on Merapi DEM (15-m resolution) (courtesy of C. Gerstenecker, Technische Universität Darmstadt, Germany, [Gerstenecker et al. \(2005\)](#)).

2.4.4 Proposed reconstitution of the recent Merapi volcanic activity from the eastern flank deposits

In the first step, during the Middle Merapi stage, rivers were radially oriented from the summit. The paleo-Pusur valley reached more than 1000 m asl.

After an extreme event that most likely combined a landslide resulting from an intense eruption activity combined with probably high precipitation, an enormous debris avalanche and debris flow accumulation was created at the first break in slope, between 1000 and 400 m asl.

[Camus et al. \(2000\)](#) have described an intense eruption estimated between 5000 and 2200 years BP. Moreover, [Griffiths et al. \(2010\)](#); [Dubois et al. \(2014\)](#) have shown an abrupt shift to warm temperature near 4 ka which coincides with periods of stronger Australian-Indonesian Summer Monsoon. We suggest that a combination of intense eruption with high precipitation inferred a detrital fan of debris avalanche deposits.

The debris avalanche and debris flow deposits formed a fan with a triangular shape covering approximately 45 km² and a volume estimated at 2.2 to 3.1 km³. The fan filled the paleo-Pusur valley and the surrounding rivers above 400 m asl. At this time, the active crater was located in the Pasarbubar area, thus the crater rim was lower than the present one and culminated around 2000 m asl. Therefore, the total collapse height of the debris avalanche was lower than 2000 m. Considering the hyperconcentrated debris flow deposits on the Soka and Brambang sides, a part of the fan was remobilized during rainstorms event and was channelized on the downstream rivers. [Rodolfo & Arguden \(1991\)](#) have observed the same phenomenon in Philippines but at a local scale (4 km²).

At the end of the Middle Merapi stage, the production of massive andesitic lava flow (the Gadjah Mungkur series), dated from 4.8 to 1.7 ka BP ([Camus et al., 2000](#); [Gertisser et al., 2012b](#)) filled the “collapse amphitheatre” left by the debris avalanche and the paleo-valleys above 1000 m asl. The upper portions of the valleys, including the paleo-Pusur River, were clogged by the lava flow deposits. Hence, we infer that the creation of the detrital fan occurred before the Gadjah Mungkur series and was associated with the major eruption/cone avalanche described by [Gertisser et al. \(2012b\)](#) thus, estimated at approximately 4.8 ka BP.

Afterward, rainfall-induced erosion inverted the relief. By comparison with rapid erosion of the 2010 eruption deposits on the southern side of Merapi volcano (nearly 100 m of incision in less than 3 years), we can suppose that the total inversion occurred rapidly. The massive lava flow, which was significantly harder, could not be incised and is now the interfluvium, whereas the paleo-interfluviums of the non-consolidated material have been eroded and are now the valleys. Upstream, the Soka and Brambang Rivers developed on the older interfluviums between the Pusur River and its neighboring rivers, Soka and Brambang. The fan diverted the Soka and Brambang Rivers above 400 m asl where they captured the nearby rivers at the downstream tip of the detrital fan deposit. A similar drainage network anomaly is visible on the South-East flank of Semeru volcano (East Java) between the Kobohan and Kembar rivers ([Thouret et al., 2007](#)).

Regressive erosion headwards along the Pusur River then incised the detrital fan, enabling

evaluation of the erosion balance. Considering that the date of the detrital fan event is linked to the 4.8 ka eruption, regressive erosion has progressed by 9 km since. Stream incision reveals the paleo-Pusur channel and creates a natural spring. Therefore, this process can explain the alignment of the springs at 400 m asl and their occurrence where buried paleo-channels meets the end of the fan deposit.

2.4.5 Origin and magnitude of the event

The highest point of the origin of the avalanche on the volcanic edifice is usually difficult to assign with precision, because of the failure of volcanic edifice. On the East flank of Merapi, based on the geological history, the highest point of crater rim Pasarbubar was substituted (i.e. 2000 m asl) to the present crater. The maximum runout (L) ranges from 1.6 to 14 km, and the maximum collapse height (H) ranges from 0.16 to 2.1 km. The ratio ranges from 0.15 to 0.11. The apparent friction coefficient for the East flank of Merapi and other volcanic avalanches, is graphically represented in Fig. 2.24.

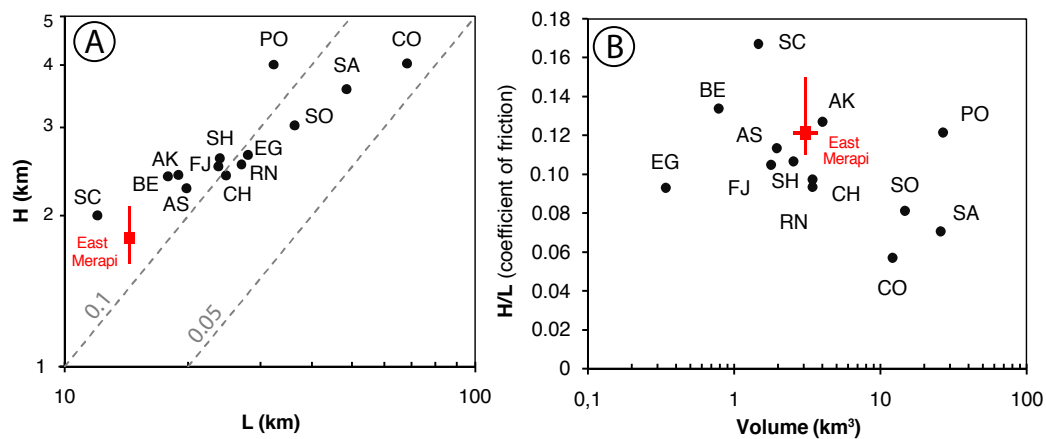


Figure 2.24: (A) Apparent coefficient of friction (H/L) versus volume of the deposit, and (B) relation between the maximum collapse height (H) and maximum travel distance (L) of the East flank of Merapi avalanche compared to other avalanches on stratovolcanoes. (RN=Roque Nublo (Canary Islands); EG= Egmont (New Zealand); FJ=Fuji (Japan); AS=Asama (Japan); AK=Akagi (Japan); CH=Chokai (Japan); BE=Bezymianny (Russia); SC=Schiveluch (Russia); SH=St.Helens (USA); CO=Colima (Mexico); PO=Popocatepetl (Mexico); SO=Socompa (Argentina/Chile); SA=Shasta (USA); the red shape shows the range of values for the East flank of Merapi avalanche). The data are taken from Siebert (1984); Ui et al. (1986) and Garcia Cacho et al. (1994). The dashed lines in (B) represent the H/L constant ratios.

The graph A presents the relation between the maximum collapse height of debris avalanche (H) and its maximum runout distance (L) for well-known stratovolcanoes such as Colima or St.Helens (Siebert, 1984; Ui et al., 1986; Garcia Cacho et al., 1994). The East Merapi ratio is slightly smaller than the other stratovolcanoes but follow the main trend. That show that this event was not as intense as the St.Helens eruption type described on the

West flank by Camus et al. (2000) but we saw that the impact on the morphology of the East flank and its surface water and groundwater resource was important.

The graph B shows the relationship between the coefficient of friction noted H/L (Siebert, 1984) and the volume of the debris avalanche deposits. All these data are very similar and comparable with those calculated for other volcanoes and enable the East flank of Merapi to be placed in the same group as other important volcanic avalanches in term of volume.

2.4.6 Characterize the paleo-river geometry by geophysics methods

In the lower parts of Merapi flank, geological outcrops are scarce, thus, direct observations are difficult. In order to identify the geological and geomorphological structures in this zone, a geophysical survey using electrical method, was done between June and July 2012, with the collaboration of the geophysical department of UPN.

This campaign had dual objectives: i) better understand the deposit architecture in the distal zone of the Eastern flank of Merapi volcano and ii) to determine a location for two monitoring wells. These deep wells will allow study of hydraulics properties and hydraulic gradient of aquifers in the low-lands. The drilling program will be detailed in Chapter 4.

2.4.6.1 Material and method

2.4.6.1.1 Study site The geophysical survey was conducted around 250 m asl near the AQUA production well (X: 0460835; Y: 9159270; Z: 206 m), described in Chapter 4. 10 profiles (dipole-dipole) and 17 soundings (Schlumberger method) were performed.

The main difficulty was to find an area large enough to make the geo-electrical profiles. The space between the rivers and the villages limited the exploration locations. In order to not create conflict with the local people, an agreement was concluded between UGM and the BAPPEDA institution (Badan Perencanaan Pembangunan Daerah = Territory and land management office). This agreement allowed the geophysical survey on the village land.

2.4.6.1.2 Equipment During the geophysical survey of June and July 2012, a resistivity meter SYSCAL R1 Plus has been used. This resistivity meter is provided by IRIS instrument. It has been used both for the resistivity sounding and resistivity profiling. The maximum output voltage is 600 Volt and the maximum output current is 2500 mA. The resolution is 1 μ V after stacking. Four electrodes were connected to the resistivity meter. This method was used near the spring area at 200 m asl to better understand the aquifer geometry near their discharge point.

2.4.6.2 Theory

2.4.6.2.1 Basic principles Electrical resistivity studies are based on the circulation of current flow through a subsurface medium consisting of layers of materials with different individual resistivities. For simplicity, all layers are considered to be horizontal. For measuring the ground resistivity, a current has to be transmitted with two electrodes, while the potential created on the surface by the circulation of this current into the ground is measured with two other electrodes.

Progressively increasing the distance between the transmitting and the receiving electrodes increases the depth of investigation (sounding array for aquifer depth and thickness determination); translating the four electrodes together permits detecting lateral change of resistivity (profiling array).

Resistivities vary from one material to another. For example, the resistivity of a good conductor such as clay is on the order of $10 \Omega\text{m}$, the resistivity of an intermediate conductor such as saturated sand is around $100 \Omega\text{m}$, and the resistivity of poor conductors such as dry sandstone is $2000 \Omega\text{m}$ (Kirsch, 2006). Due to this great variation, measuring the resistivity of an unknown material has the potential to identify that material. In field studies, the resistivity of a material may be combined with reasoning along geologic lines to identify the materials that constitute the various underground layers.

Groundwater, through the various dissolved salts it contains, is ionically conductive and enables electric currents to flow into the ground. Consequently, measuring the ground resistivity can also identify the presence of water, taking in consideration the following properties:

- a hard rock without pore or fracture and a dry sand without water or clay are very resistive: $500\text{-}2000 \Omega\text{m}$
- a porous or fractured rock saturated by water has a resistivity which depends on the resistivity of the water and on the porosity of the rock (see below): $60\text{-}200 \Omega\text{m}$
- an impermeable clayey material is characterized by low electrical resistivity in the range of $5 - 60 \Omega\text{m}$ and is often a target in electrical or electromagnetic surveys.

2.4.6.2.2 Device and experiment To calculate the ground resistivity there are two earth electrodes (A and B) and 2 electrodes measure the potential difference (M and N) (Fig. 2.25).

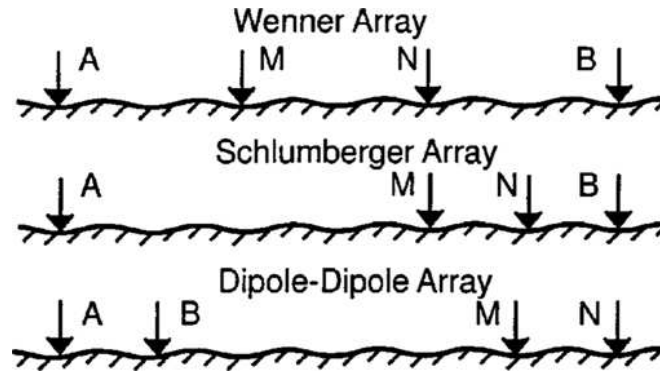


Figure 2.25: Some common electrode configurations for resistivity studies [Herman \(2001\)](#)

There are two measurement techniques: electrical sounding and electrical resistivity profile. Sounding provides vertical information on the depth of the layers (1D) while the electrical profile will give information on the lateral resistivity heterogeneities (2D).

For the sounding point, the Schlumberger device was used, while the dipole-dipole device was used for the electrical resistivity profiles. The maximum cable length was 200 m. In order to have a maximum depth of investigation of 100 m, the profile length had to be 600 m. Each profile was done in 3 parts with 4 electrodes and a electrode spacing of 25 m. With this configuration, the maximal resolution of the profile is 10 m. This resolution is low to describe the high heterogeneity of the material. But this configuration need more than 1 day to be proceed. With a higher resolution, the manipulation time would have been too long.

2.4.6.2.3 Softwares For inversion of the profiles, the software RES2DINVx64 was used. This computer program will automatically determine a two-dimensional (2-D) resistivity model of the subsurface for the data obtained from electrical field surveys. The 2-D model used by the inversion program consists of a large number of rectangular blocks. The distribution and size of the blocks are automatically generated by the program using the distribution of the data points. The depth of the two bottom rows of blocks is set to be approximately equal to the median depth of investigation of the data points with the largest electrode spacing. A finite-difference modelling routine is used to calculate the apparent resistivity values, and a non-linear smoothness-constrained least-squares optimization technique calculates the resistivity of the model blocks ([deGroot Hedlin & Constable, 1990](#)).

The inversion routine used by the program is based on the smoothness-constrained least-squares method ([Loke et al., 2003](#); [deGroot Hedlin & Constable, 1990](#)). The smoothness-constrained least-squares method is based on the following equation:

$$(J^T J + \lambda F) \Delta q_k = J^T g - \lambda F q_k \quad (2.1)$$

where $\mathbf{F} = \alpha_x \mathbf{C}_x^T \mathbf{C}_x + \alpha_z \mathbf{C}_z^T \mathbf{C}_z$

\mathbf{C}_x = horizontal roughness filters

\mathbf{C}_z = vertical roughness filter

\mathbf{J} = Jacobian matrix of partial derivatives

\mathbf{J}^T = transpose of \mathbf{J}

λ = damping factor

\mathbf{q} = model change vector

\mathbf{g} = data misfit vector

The optimization method tries to reduce the difference between the calculated and measured apparent resistivity values by adjusting the resistivity of the model blocks subject to the smoothness constraints used. A measure of this difference is given by the root-mean-squared (RMS) error.

The raw data were cleaned according to the homogeneity of the resistivity values along the profile. Indeed, some isolated high values of resistivity could be observed on the borders of the profiles. These values have been deleted and a new inversion done. The difficulty was to not delete too much data in order to keep a vertical and horizontal resolution high enough (here, 10 m).

2.4.6.3 Field survey of June and July 2012

The geo-electrical survey was done June 4th July 20th 2012, with an interruption between the 13th of June and the 2nd of July. The team was supervised by Pk. Agus Sentiento (UPN) and myself. 17 soundings (Schlumberger method) and 10 profile lines (dipole-dipole method) were done. Nine profiles were made following the highest slope in upstream and downstream the AQUA production well and one profile was done perpendicularly to the slope (profile n°2). Seven profiles are located on the North side of the Pusur river (Fig. 2.26).

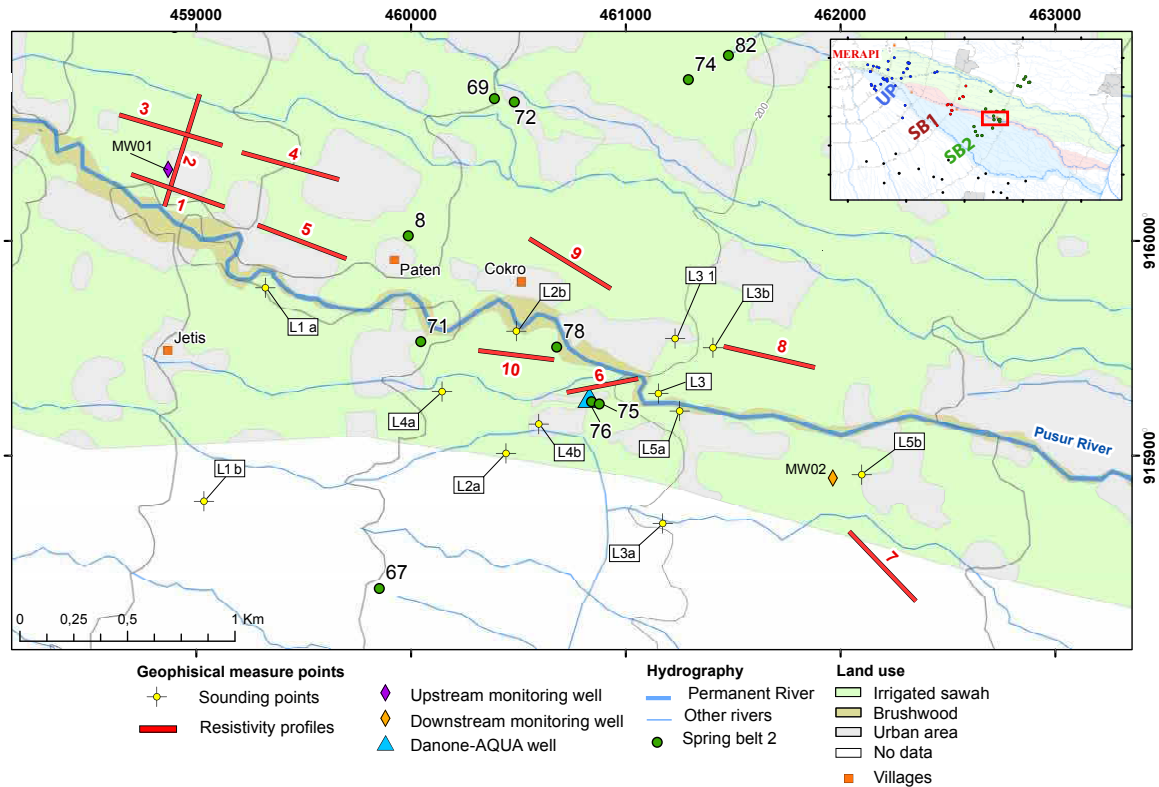


Figure 2.26: Geophysical profiles and resistivity sounding points around the Pusur River near the springs (SB2) and Danone-AQUA wells.

There is a relation between the maximal distance between the electrodes and the maximum depth measurement point; therefore, to reach the maximum depth of 100 m, the profile has to be 600 m long (maximal distance allowed by the equipment) with electrodes spaced at 25 m. All the resistivity profiles and soundings are available in B.

2.4.6.4 Results of the geophysical survey

To identify the presence of groundwater from resistivity measurements, the absolute value of ground resistivity can give information: for a practical range of fresh water resistivity of 10 to 80 Ωm , and the usual target for aquifer resistivity is between 50 and 100 Ωm . Most of the time it is the relative value of the ground resistivity which is considered for detecting groundwater; in a hard rock (resistant) environment, a low resistivity anomaly will be the groundwater target.

On several profiles, the projections of the wells and springs near the profile section are shown. It is important to notice that the profiles with a RMS error value above 10% have to be considered because the electrode spacing is too large compared to the resistivity variability. Indeed, this factor indicates that the precision of the profile representation is not optimal. But considering the vertical and horizontal resolution of the profile it is the

most accurate version that can be made.

2.4.6.4.1 Electrical resistivity profiles The electrical resistivity profiles are shown in annexes. The resolution of each profile depends upon the distance between the electrodes during the acquisition. For the 10 profiles, the distance between the electrodes is 25 m, allowing a resolution of 10 m on the resistivity profile on x and z axis.

The profiles 3, 4, 9 and 8 can be assimilated to one line, as can profiles 1, 5, 10 and 6. The distances between several profiles are important (up to 900m) but simple interpolation can be used to identify the geometrical structure. These two assimilated lines show a high lateral and vertical heterogeneity of the resistivity values (Appendix B.2)

Lines-1-5-10-6: On profiles 1 and 5, the cross section is vertically divided in 4 discontinuous horizons but not continuous: i) a shallow zone (~ 10 meters deep) with a low resistivity (less than $80 \Omega\text{m}$), ii) around 12 to 30 m deep, a zone of higher resistivity (over $100 \Omega\text{m}$), iii) between 30 and 60 m deep, the resistivity values decrease (less than $70 \Omega\text{m}$), and iv) from 70 m to 100 m deep, a high resistivity zone is visible (until $300 \Omega\text{m}$). The profile 1 shows one anomaly of low resistivity at 100 m deep at $x=200$ m.

This configuration is not visible on profiles 10 and 6. The sub-surface is characterized by a low resistivity zone (less than $60 \Omega\text{m}$). From the sub-surface until 50 m deep on the profile 10, the resistivity values are relatively high (more than $80 \Omega\text{m}$) with some anomalous zones at $x=300$ m (values under $50 \Omega\text{m}$). On the profile 6, the resistivity values increase at $x=300\text{m}$ (until $750 \Omega\text{m}$). These extreme values can be explained by a very resistant material (massive lava flow deposit for example).

Lines-3-4-9-8: On profile n°3 we can see vertical alternation between high resistivity zones (0 to 20 m deep respectively and 90 to 100 m with a resistivity range in between 80 to $170 \Omega\text{m}$) and low resistivity zone (30 to 80 m deep with a resistivity range in between 25 to $70 \Omega\text{m}$). The aquifer layer could be located between 40 to 80 m deep.

Profile n°4 shows an alternation of a high resistivity values ($150 \Omega\text{m}$ between 0 and 20 m deep; more than $240 \Omega\text{m}$ between 80 and 100m deep) and low values (between 30 and $70 \Omega\text{m}$ at 30 to 70 m deep). This low resistivity zone can be interpreted as the potential aquifer zone. The high resistivity zone around 100m deep seems to have a local extension.

On profile n°9, three main horizons can be described: a shallow zone with low values of resistivity (less than $30 \Omega\text{m}$ between 0 to 20 m deep), then a high resistivity zone (more than $100 \Omega\text{m}$ between 25 and 50 m deep) and, from 60 until 100 m deep, low resistivity values (less than $50 \Omega\text{m}$). This configuration shows a potential shallow

aquifer zone and a deep aquifer around 70 m deep. However, the vertical resolution of the profile is 10 m and it is difficult to really identify the shallow aquifer with this resolution.

Profile 8 shows a large low resistivity zone from the surface to 70 m deep. Then, resistivity increases until 340 Ωm . Profile 8 is located after the springs belt in the irrigation area.

Perpendicular-lines: Profiles 2 and 7 are perpendicular to the main slope of Merapi (Fig. 4 and 5). Profile 7 is not truly perpendicular because of the issues on site to find the ideal location.

Profile 2 (Fig. 2.27) presents a high resistivity zone near the surface (until ~ 30 m deep with more than 80 Ωm) with some shallow low resistivity anomalies. Between 40 and 80 m deep at $x=300\text{m}$, the resistivity values are low (less than 50 Ωm). This zone disappears on the borders of the section. This shape suggests a paleo-channel configuration. Indeed, based on field observations along the Pusur river, the aquifer layers are composed by lava boulders and bloc layers with a relatively low proportion of matrix. These layers follow the paleo-valley. The perpendicular profile n°2 allows visualization of a one paleo-channel that can be interpreted as a aquifer layer. The dimension of this paleo-channel is around 40 m height and 150 m wide and it is buried 30 m deep.

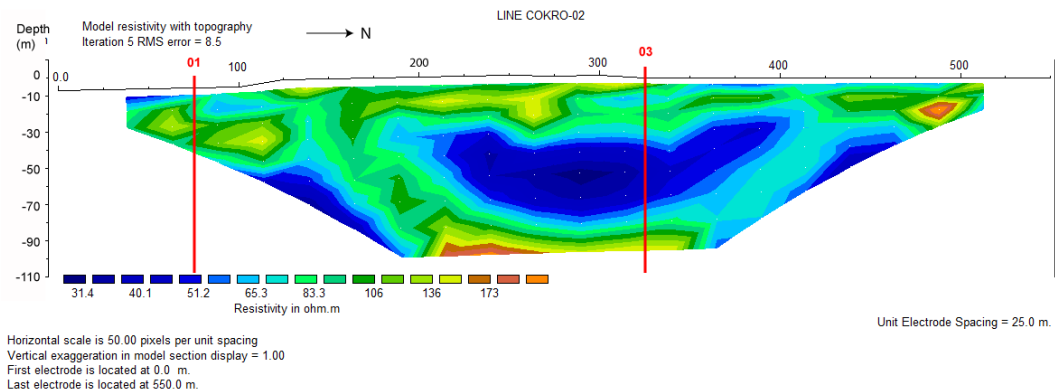


Figure 2.27: Electrical resistivity of the profile 2.

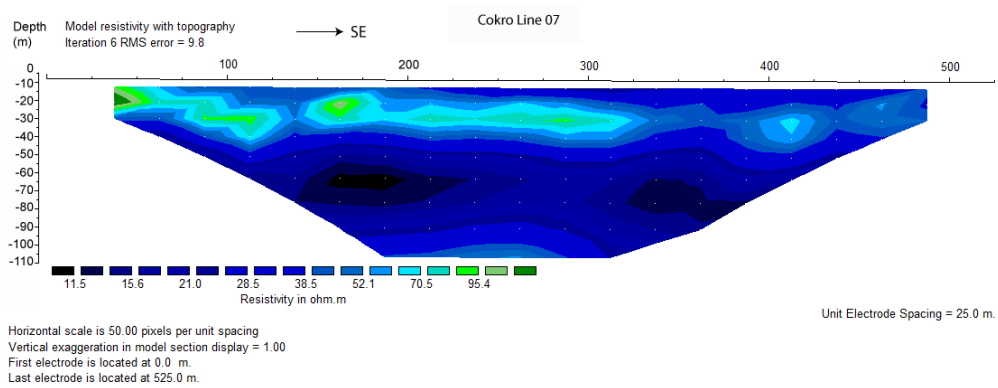


Figure 2.28: Electrical resistivity of the profile 7.

According to the geological surveys, we know that the lithological facies in this area are mainly composed of breccia, sand and boulders of andesitic lava. We can consider that the low resistivity zones correspond to zones with a high proportion of water. The paleo-valley could also play a main role in the groundwater flow circulation. In order to choose the location for the implementation of 2 monitoring wells, these zones will be the target of the prospection.

Profile number 7 (Fig. 2.28) presents a very low resistivity range (between 10 to 100 Ωm). Located below the discharge area (spring belt), we can consider that the lithological facies is probably different. Based on the lithological log in AQUA well and the geological map of Wirakusumah et al. (1989), the lithological facies below the discharge area is composed of clay and silt material, from the fluvial deposits. After the circulation into the paleo-channel, water flow circulation could be slowed by the clay material in this zone. The “accumulation” of water resulting from restricted groundwater flow circulation can explained the low value of resistivity on this profile.

2.4.6.4.2 Vertical electrical sounding points (VES) The 17 vertical electrical sounding (VES) points show a resistivity range between 2 Ωm to 600 Ωm . The results of the VES curves obtained from the partial curve matching were used to constrain the interpretation using iteration software (RES2DINVx64). This invariably reduces overestimation of depths.

VES are used to verify the results of the profile inversion (Fig. 2.31, 2.29 and 2.30) and to interpolate the thickness of the layers in the area where the profiles were done. The electrical sounding investigation maximal depth is around 50 m.

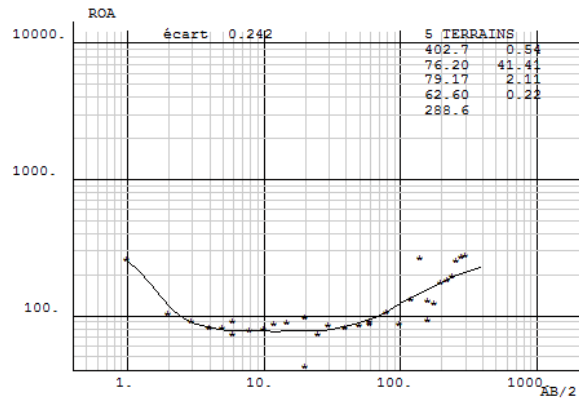


Figure 2.29: Electrical sounding n°10 with inversion model of the thickness of the layers (m).

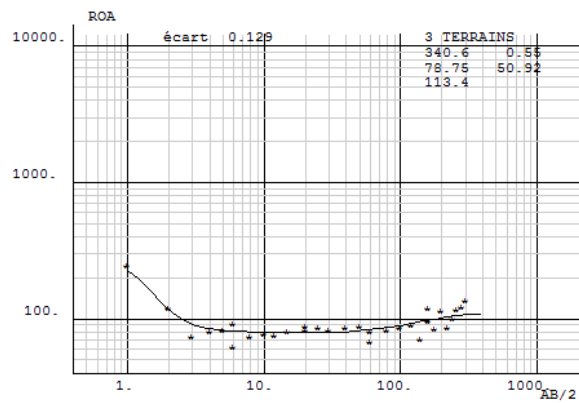


Figure 2.30: Electrical sounding n°13 with inversion model of the thickness of the layers (m).

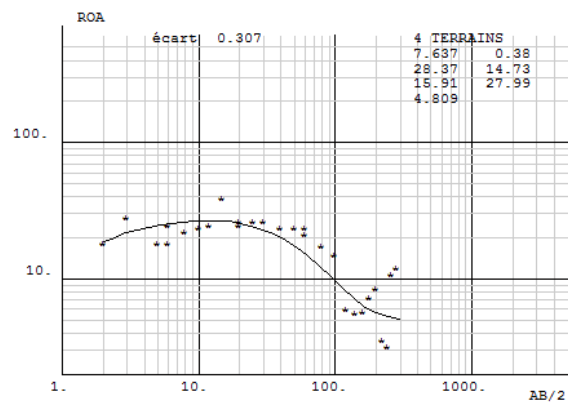
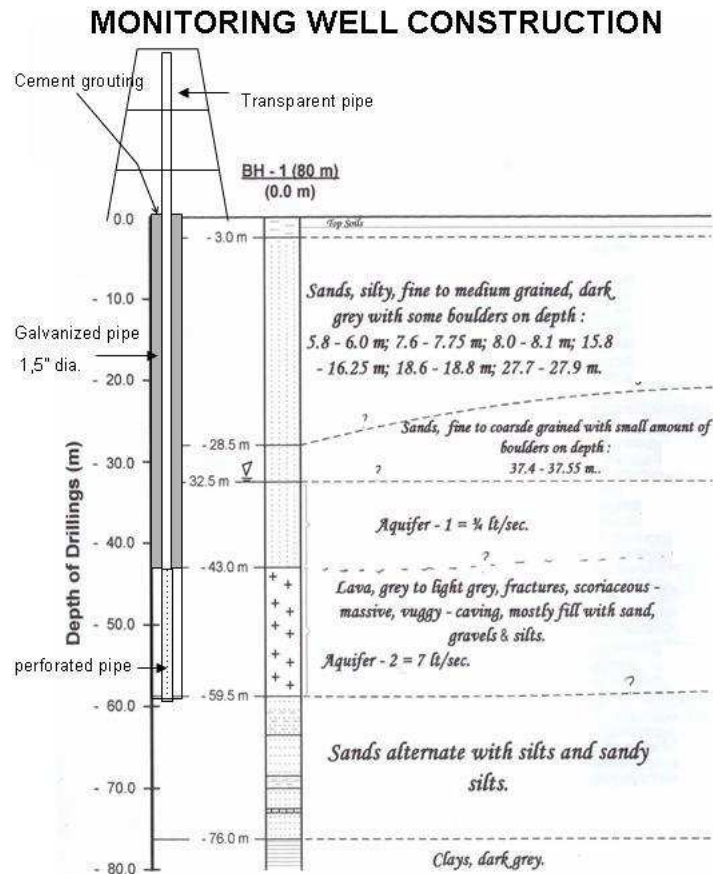


Figure 2.31: Electrical sounding n°1 with inversion model of the thickness of the layers (m).

2.4.6.5 Comparison with available stratigraphic logs

In order to confirm the interpretations made with the geophysical soundings and profiles, comparison of the geo-electrical results with a stratigraphic log is essential. Unfortunately at the time of data processing, we only had one litho-stratigraphic log available in this area, at Danone AQUA monitoring well. There are a lot of “illegal” bore wells in this spring zone, but most of them do not go deeper than 10 meters. They tap the shallow unconfined aquifer. Indeed, we saw that the shallow layers are often low resistivity zones, indicating a zone with a high proportion of water; therefore, the farmers use the shallow aquifer and do not need to go further. Moreover, no stratigraphic log is made during the drilling of this kind of well.

The Fig. 2.32 depicts the logs of the production and monitoring wells of AQUA. The wells can be projected of 20 m on profile n°6 (Fig.2.33). The spring of Sigedang is very close to the AQUA well: the spring is at 60 m to the south of profile n° 6.



TIV. KLATEN, CENTRAL JAVA

Figure 2.32: Litho-stratigraphic logs of the AQUA monitoring wells

On profile n°6, interpretation and correlation with the litho-stratigraphic log is delicate. Several horizons show a high resistivity values heterogeneity. Moreover, all the elements (spring and wells) have been projected, and the profile does not really cross these benchmarks. In view of the complexity of the lithological material, it is not surprising to be able to perfectly correlate the litho-stratigraphic logs with profile n°6.

On the profile n°6, 32 m, the low resistivity zone may correspond to the layer termed “sand, silty, fine to medium grained, dark, grey with some boulders” on the stratigraphic log. The shallow zone of high resistivity can be interpreted as the sand and boulder layer.

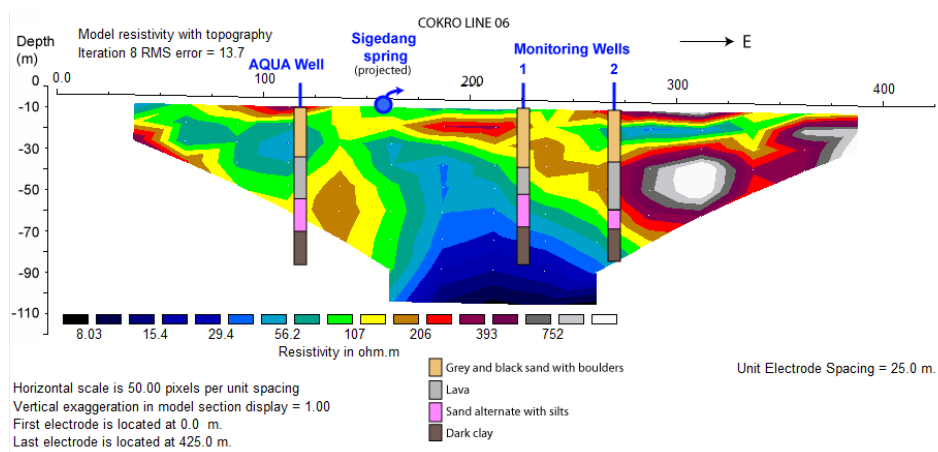


Figure 2.33: Electrical profile n°6 and the location of the AQUA wells projected 20 m to the north and Sigedang spring projected 60 m to the north.

Layers identified as “lava, massive, fractures and scoriaceous” are shown on the 2 logs (described in Chapter 4) but no major structure is visible at the well locations. It is possible that the “massive lava” is in reality only a boulder layer with huge size (several meters). In fact, a lava flow deposit at 23 km from the summit does not seem possible according to the historical eruptive behavior of Merapi volcano. Nevertheless, the possibility of a basaltic episode with an effusive eruption during the building of pre-Merapi has to be considered [Camus et al. \(2000\)](#); [Berthommier \(1990\)](#). The aquifer layer can be identified as a zone with a resistivity range between 50 and 80 Ωm (at 40 to 70 m deep). The layers with a very low resistivity (less than 20 Ωm) on the profile are probably the layers named “clays, dark grey” on the logs.

Comparison between the litho-stratigraphic logs and the geo-electrical results allows us to confirm the interpretations of a paleo-channel organization composed by massive block and sand.

2.5 Update of the andesitic volcanic facies conceptual model based on the eastern flank of Merapi

Based on the geomorphological history of the eastern flank of Merapi, a new analysis of the conceptual model of deposit architecture for an andesitic stratovolcano is proposed (Fig. 2.34). The partition follows the facies variation from the summit (upstream) to the volcano base (downstream) but also depends on drainage network location and the 3D architecture.

Lava flow deposits and block and ash formations are primarily located close to the vent. The relief inversion induced by the lava channelizes the rivers into the pyroclastic flow units. In the valley incisions, the dominant facies are the pyroclastic flow and the surge deposits in alternation with local lahar units. The accumulation of debris avalanche and debris flow deposits has a triangular shape that can disturb the drainage network. At the end of the medial zone, the slopes are low, and the lahar formations accumulate in a fan around the main rivers. Downstream, the slopes are lower, and fine sediments are dominant. In the upper part of this profile, the lava flows erode, and the blocks accumulate along the main rivers. The same process occurred during the building of the volcano and created paleo-channels along the profile. This conceptual model considers the eruptive and non-eruptive activities. The valley zones have more indirect sediments with a detrital fan shape, whereas the interfluvial zones are dominated by direct eruptive formations.

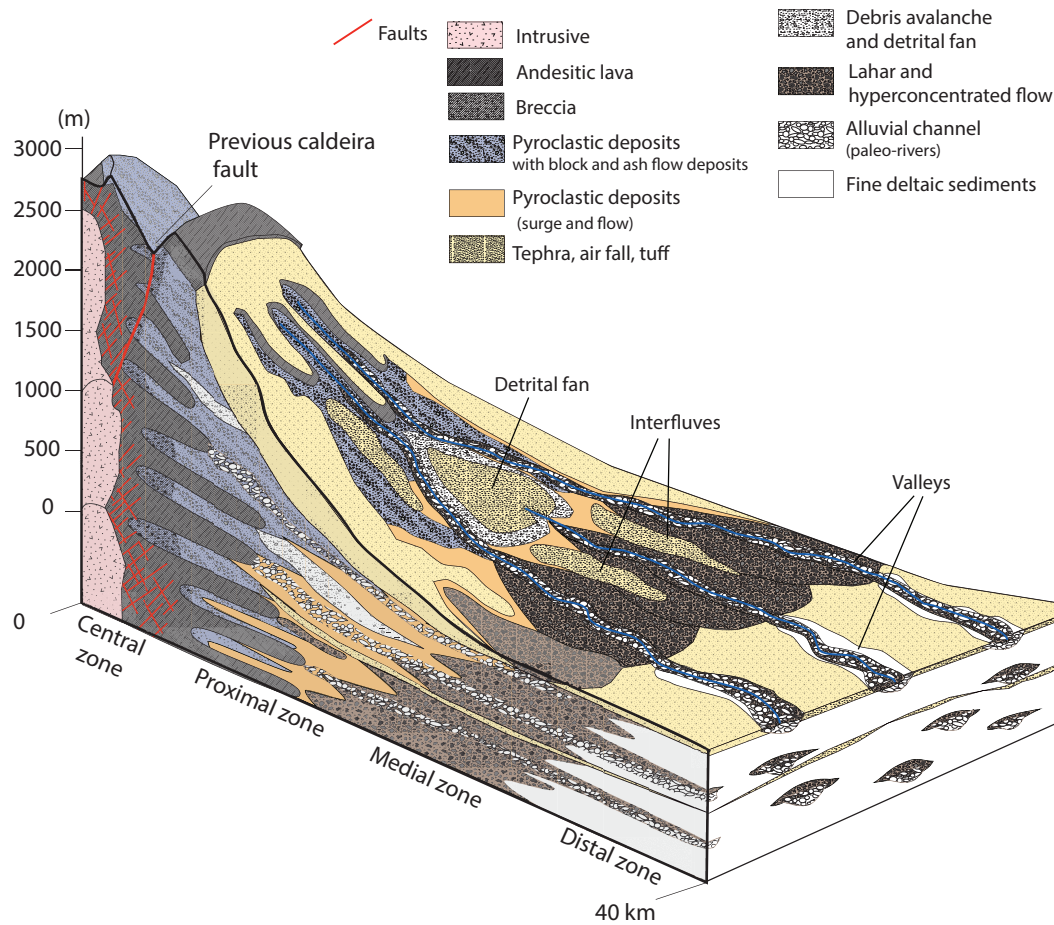


Figure 2.34: Schematic conceptual model of the volcanoclastic distribution of facies associated with andesitic stratovolcanoes adapted for the eastern flank of Merapi volcano. The facies illustrate the proximal to distal variation and the lateral distribution, depending on the valley and the interfluve dynamic.

2.6 Conclusion

The facies architecture of a stratovolcano depends on a complex interaction between direct eruptive, indirect eruptive deposits, gravitational instability and erosion processes. In this study, we propose a new definition of the volcanoclastic product facies considering lateral variation. Eruption products overlay the paleo-topography at the regional scale such as tephra layers while pyroclastic flows and debris avalanche or the lava flow deposits are primarily concentrated in valleys. Indirect eruptive products are more complicated to define because they have both landscape eroding and landscape covering properties. In the upper portion of the strato-cone, the erosion processes are dominant with the remobilization of pyroclastic and volcanoclastic deposits, the incision of the valleys and the removal of lava flow deposits. However, in the lower portions, the indirect eruptive products are concentrated and accumulated around the valley areas.

Merapi volcano has a complex history, and we observed that the definition of the active period remains controversial. In the case of the eastern flank of Merapi, this area has not been impacted by major eruptions for nearly 2000 years; thus, it is a preferential zone that can be used to study geomorphological evolution. Erosional processes are more clearly identified on this part than on the other flanks of Merapi. However, distinguishing original deposits from the remobilized material is a delicate issue in this context.

Analysis of the geometry of the deposits enabled the identification of a drainage network anomaly. We interpret this anomaly as an accumulation most likely of both detrital material and eruption products on the paleo-Pusur valley. Based on several studies with age estimation data, we propose a new geo-morphological chronology of the shallow eastern flank. We associate fan formation with a major flank collapse during the Middle Merapi stage (from 4800 to 1700 years BP). The drainage anomaly arises from the combination of the detrital fan formation and the filling of the valley in the upper portion by the lava flow units that channelized surface water flow. The incision of the surrounding rivers, the Brambang and Soka Rivers, originate in the alternative pathways used by the surface water.

In this study, by combining a literature review and observation data, we propose an update to the conceptual model of the architecture of stratovolcano volcanoclastic products. This new conceptual model is a synopsis of research to better understand the internal structure of a complex stratovolcano and can be used for multiple purposes such as hazard prediction, hydrogeology, geomorphological or geological studies.

Finally, we outline a general erosional history for the shallow formation of the eastern flank of Merapi volcano for which geomorphological studies are rare. The remobilization and re-sedimentation of the volcanic products may result in catastrophic events, such as burial of the valleys, which would ultimately cause damage, even in distant areas. Severe volcanic hazards caused by re-sedimentation of volcanoclastic debris will spread extensively, and their effects will persist for a longer duration than those by primary eruptive processes. These results highlight the significant and rapid transformations that the surface water network may experience and opens up several research opportunities on the effect of a local event on the population or the groundwater resources in andesitic volcanic areas.

3

Climate and hydrological functioning

Introduction

Hydrological processes in humid tropical areas have been substantially documented (Elsenbeer, 2001; Legesse et al., 2003), but there is a lack of knowledge with regard to volcanic regions where the framework generates a high spatial variability of flow paths. In the humid tropical climate, characterization of the main hydrological processes may be complicated by large seasonal variations in all aspects of the water balance (Cook et al., 1998). Moreover, in volcanic regions, deposits are characterized by polygenetic materials with high contrasts in permeability (Sruoga & Rubinstein, 2007).

In collaboration with the CIRAD and the IAHR, this present study aims to establish the hydrological behavior of a tropical watershed through a water balance method. The approach combined the treatment of the historical data and the recent data processing on two hydrological years, 2011-2012 and 2012-2013 (i.e.: the period from October 2011 to November 2013). This section is structured in three parts: i) the presentation of the study site at the extended Pusur watershed scale on the Eastern flank of Merapi volcano, ii) the hydro-meteorological data treatment analysis, iii) the quantification of the terms of the water balance during a hydrological year 2011-2012 at watershed scales.

3.1 Methodological approach

3.1.1 Surface and ground-water delineations

This study is focused on the Pusur River watershed, on the south-eastern flank of Merapi volcano. For this study, this watershed is extended until the two lateral watersheds to better take account of the hydrogeological boundary. The hydrological borders are the Soka river to the South, the Brambang river to the North, the Dengkeng and Bengawan Solo rivers to the East and the scarp of the Woro river to the West which is a major geological feature of Merapi. The total area is around 390 km² and the distance between Merapi peak and the Dengkeng river is 37 km. The elevation range is between 100 and 1500 m. (Fig.3.1)

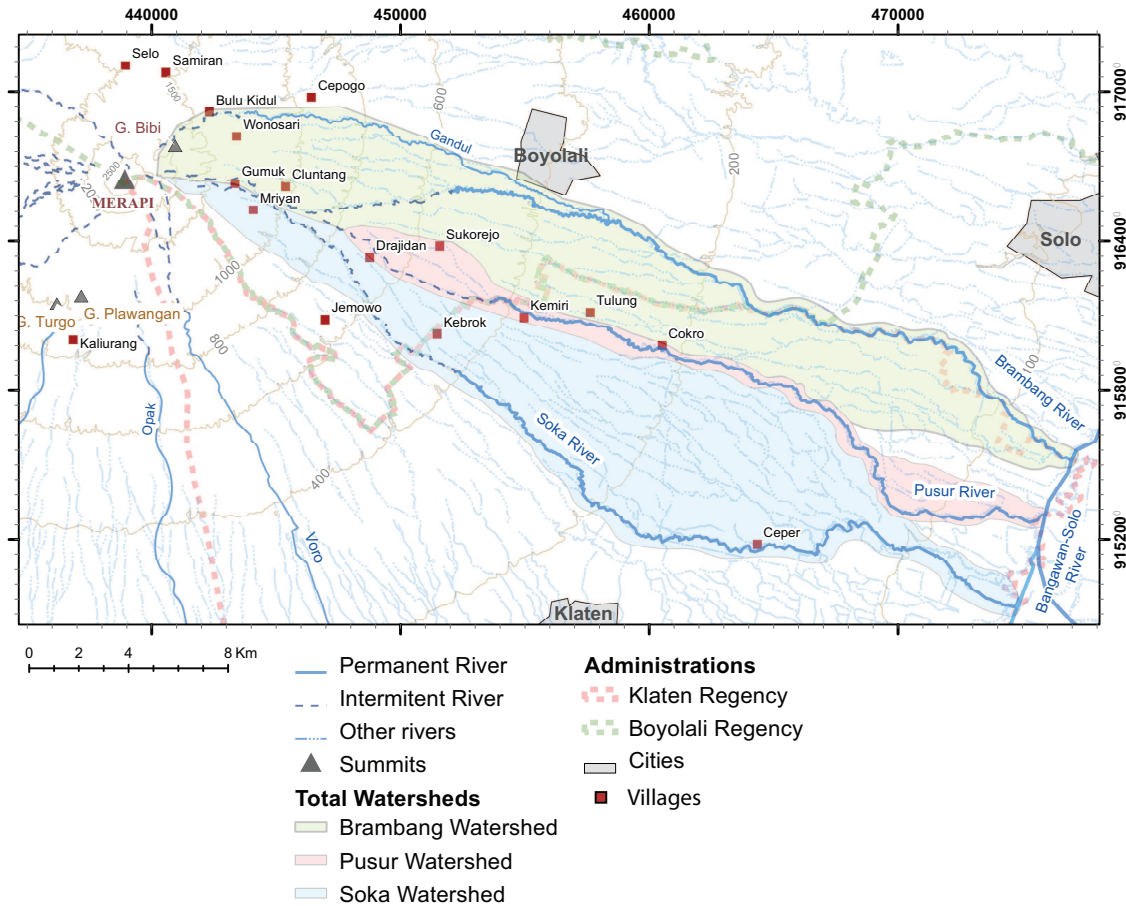


Figure 3.1: Study area and the hydrological watersheds of Pusur, Soka and Brambang Rivers.

3.1.2 Experimental site and monitoring network

3.1.2.1 Existing rain-gauges

The climatic network managed by the local administrations of the Department of Public Utilities (DPU Klaten and DPU Boyolali) is poorly maintain and constantly damaged (Fig. 3.2). Since 1989, beginning of the climate daily monitoring in this area, no complete hydrological years are available on the 15 stations covering the East flank of Merapi. Our project partners from the IARHI and CIRAD used a method to insure homogeneity of data series in view to complete missing data (Lidon, 2012). Nevertheless, the first action was to identify the reason of the low quality of this monitoring and to improve the data acquisition since October 2011. After discussions with the DPU Klaten and Boyolali, and several field surveys to make the inventory of the rain-gauge quality, the improvement of the rain-gauge stations on the East flank of Merapi has been done since December 2011.



Figure 3.2: Deficient raingauge at Gedaren village.

3.1.2.2 Additional rain-gauges and weather stations

In view to quantify the groundwater recharge, three automatic rain gauges and one weather station have been installed in October 2011 in the upper part of the study area. The equipment is the HOBO RG3 data logger (resolution of 0.2mm and accuracy of $\pm 1\%$) with a temperature sensor were installed in Boyolali (448m asl), Sukorejo (629m asl) and Jemowo (665m asl). A weather station has been installed in Gumuk village (1456m asl), this village is the highest accessible place on the East flank of Merapi and this location has been considered as representative of the recharge area of the hydrogeological system (surface: 60 km²). The Wireless Vantage Pro2 Plus Weather Station (Davis) is recording the following parameters: air temperature, rainfall, air humidity, wind speed and direction, solar radiation, heat index and the air pressure with a sampling time set at 1 min since November 11st 2011. The interval time was extended to 15 min from November 2011 to October 2013. To complete the new climatic network, the manual rain-gauge of the AQUA production well location (221m asl) has been partially repair in December 2011. Nevertheless, the data quality collected at the AQUA location is not optimal.

3.1.2.3 Thermometers

The thermometer measured the air temperature every 15 min (range -20°C to 70°C and accuracy $\pm 0.47^\circ\text{C}$) from September 2012 to October 2013. Before this date, the temperature was measured every morning by a local operator. Therefore, the air temperature before September 2012 was not representative of the daily air temperature but of the maximal temperature (Fig. 3.3).



Figure 3.3: Manual temperature monitoring.

3.1.2.4 River Automatic Water Level Recorders

The runoff at the outlet of a micro-catchment in the upper part of the watershed at Gumuk village (1400 m asl) has been measured by a stream gaging station composed by an automatic water level recorder (AWLR) located in a specially designed section of the stream. This AWLR has been installed in collaboration with the BPTP Klaten under the supervision of the IARHI and CIRAD (Fig. 3.5).

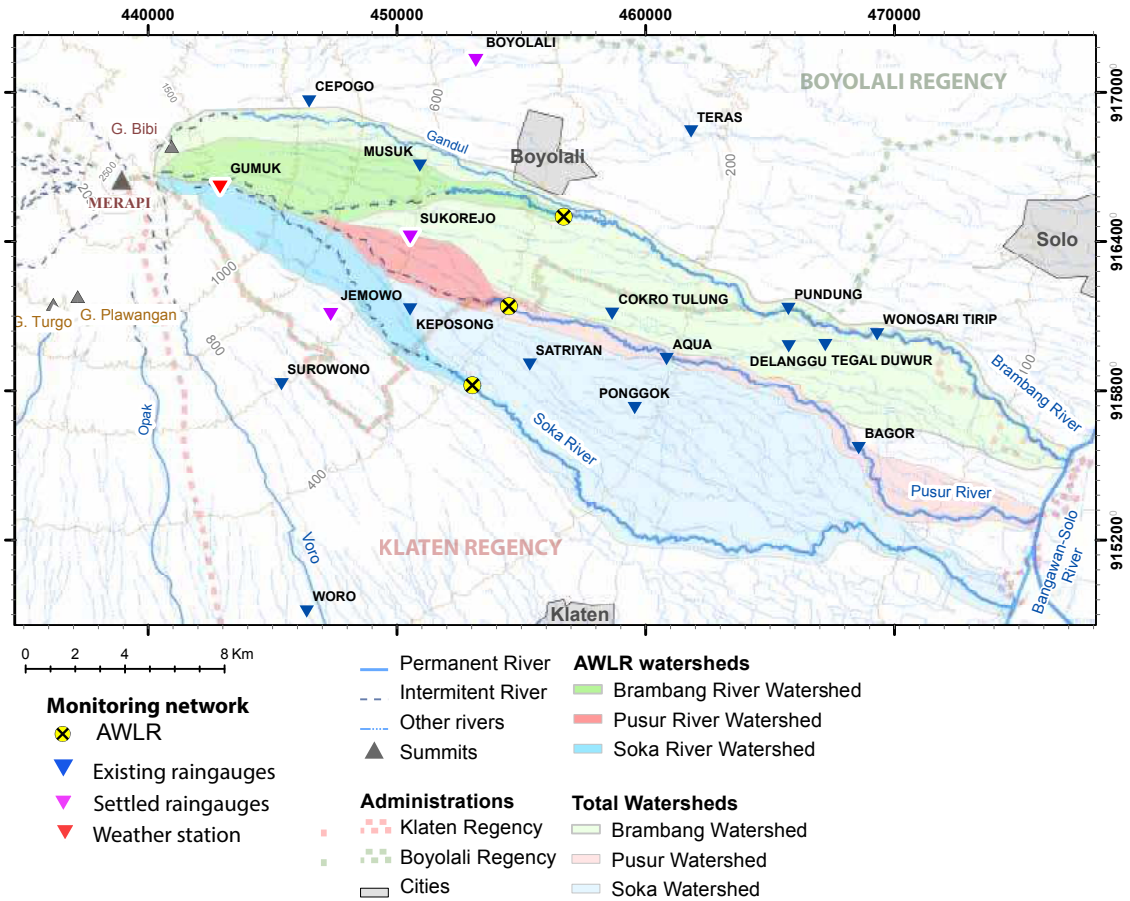


Figure 3.4: Hydroclimatic network map. Existing rain-gauges managed by the Klaten and Boyolali regencies (blue), the new rain-gauges installed in Jemowo, Sukurejo and Boyolali village (purple), weather station in gumuk village (red) and the Automatic Water Level Recorders (AWLR) settled on the main rivers.



Figure 3.5: Automatic Water level recorder (AWLR) on the Pusur river at Kemiri dam (400 m asl). The floating system is protected from the solid discharge by a PVC tube (in white) and fixed on the dam's wall.

3.1.3 Water balance method

Water balance models were developed in the 1940s by [Thornthwaite \(1948\)](#) and revised by [Thornthwaite & Mather \(1955\)](#). The method is essentially a book-keeping procedure which estimates the balance between the inflow and outflow of water. In a standard soil water balance calculation, the volume of water required to saturate the soil is expressed as an equivalent depth of water and is called the soil water deficit. The soil water balance can be represented by:

$$G_R = P - RET + \Delta S - R_o \quad (3.1)$$

where,

G_R : Groundwater recharge

P : Precipitation

RET : Real evapotranspiration

ΔS : change in Soil Mixture Storage (SMS)

R_o : runoff

The water balance is an accounting of the inputs and outputs of water (Fig.3.6). The water balance of a watershed can be determined by calculating the input, output, and storage changes of water at the ground. The major input of water is from precipitation, the output can be decomposed by evapotranspiration, runoff and groundwater storage.

Precipitation (P) in the form of rain makes up the primarily supply of water to the surface. The evapotranspiration is decomposed in two parts:

1) the potential evapotranspiration (PET) as the amount of water that would be evaporated under climatic conditions but with an unlimited supply of water. However, the main formulas, like Penman-Thornthwaite formulas have been established for grassland a critical attention have to be taken on the PET estimation.

One of the most important factors that determines water demand is solar radiation. As energy input increases the demand for water, especially from plants increases.

2) The real evapotranspiration (RET) is the effective evapotranspiration depending on the PET and the water availability. The RET is defined as the sum of water evaporated from the soil and the plants when the soil is at its current specific humidity and plants at a stage of real physiological development and health ([Musy & Higy, 2004](#)). The soil moisture storage (SMS) refers to the amount of water held in the soil at any particular time. The amount of water in the soil depends of soil properties like soil texture and organic matter content. First the rainfall supply the PET, then if the PET is satisfied

and the soil moisture is full, then additional water input is considered surplus also called effective rainfall. This effective rainfall could pool at the surface, flow over the surface as runoff and in streams, or percolate through the soil and participate to the groundwater recharge.

The effective rainfall (P_{eff}) is defined as the difference between the precipitation and the evapotranspiration. The effective rainfall is the amount of rainfall available to contribute to the runoff and the infiltration (groundwater recharge).

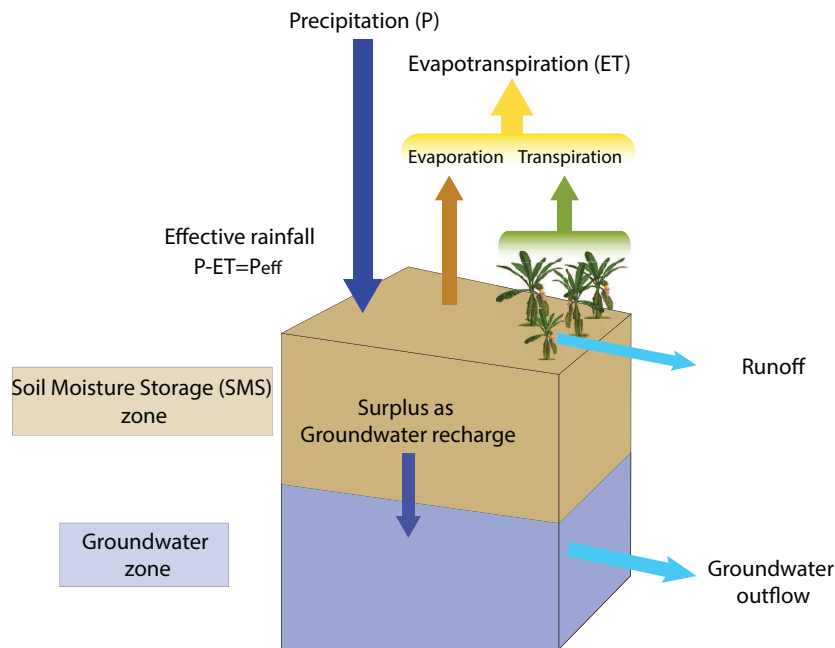


Figure 3.6: Water balance processes illustration.

3.1.4 Rainfall spatial distribution and intensity

The spatialization of rainfall takes into account daily rainfall data gauged on 14 monitoring sites located within and around the survey area from October 2011 to November 2013. Given the topography that limits the adequacy of Thiessen method and the limited number of stations that make difficult to use kriging method, the estimation of rainfall amount at ungauged location has been done according to isohyet method. This is a graphical technique which involves drawing estimated lines of equal rainfall over an area based on point measurements. The magnitude and extent of the resultant rainfall areas of coverage are then considered versus the area in question in order to estimate the precipitation value (Jain & Singh, 2005).

3.1.5 PET (ET_0) and RET

In order to estimate the monthly effective rainfall, the potential evapotranspiration (PET) has been estimated after a method detailed by [Kartiwa et al. \(2013\)](#) based on the FAO Penman-Monteith method ([Allen et al., 1998](#)).

3.1.5.1 The FAO Penman-Monteith method (PM)

Apart from the site location, the FAO Penman-Monteith (PM) ([Allen et al., 1998](#)) equation requires air temperature, humidity, radiation and wind speed data for daily, weekly, ten-day or monthly calculations according to the following equation :

$$PET = \frac{0.408\Delta (R_n - G) + \gamma \frac{900}{T+273} u_2 (e_s - e_a)}{\Delta + \gamma (1 + 0.34 u_2)} \quad (3.2)$$

where

PET reference evapotranspiration (potential evapotranspiration) [mm day⁻¹]

R_n net radiation at the crop surface [MJ m⁻² day⁻¹]

G soil heat flux density [MJ m⁻² day⁻¹]

T mean daily air temperature at 2 m height [°C]

u_2 wind speed at 2 m height [m s⁻¹]

e_s saturation vapour pressure [kPa]

e_a actual vapour pressure [kPa]

$e_s - e_a$ saturation vapour pressure deficit [kPa]

Δ slope vapour pressure curve [kPa °C⁻¹]

γ psychrometric constant [kPa °C⁻¹]

As the PM equation is taking into account the climate variables, within the survey area. The only complete data set is for Gumuk site (2 hydrological years data: 2011-2012 and 2012-2013). To take into account the effect of elevation on PET, the data of the agroclimate station located in Borobudur (300 m) were taken into account although it's located on the other side of Merapi.

On these two sites the comparison between daily evapotranspiration values calculated on a monthly basis and the fraction of the measured extraterrestrial radiation that actually passes through the clouds R_s shows a significant linear relationship between these 2 parameters. It illustrates that the fraction of the extraterrestrial radiation that actually

passes through the clouds and reaches the earth's surface is the main energy source for PET.

According to the analysis made by [Kartiwa et al. \(2013\)](#), the computing process of PET involves four steps:

1. Computing of T_{Max} according to the site elevation and the month:

$$TMax_{month j} = a_{month i} \times (Elevation)^{k_{month i}} \quad (3.3)$$

where

$Tmax$ Daily maximum temperature [°C]

Elevation Local elevation [m a.s.l.]

2. Estimating ΔT (Tmax-Tmin) according to Tmax value previously calculated and to the site elevation

$$\Delta T = -28.296 + 1.150 \times T_{Max} + 5.519.10^{-3} \times Elevation \quad (3.4)$$

where

ΔT Difference between T_{Max} and T_{Min} [°C]

T_{Max} Daily maximum temperature [°C]

Elevation Local elevation [m a.s.l.]

3. Estimation of R_s according to the value of ΔT previously calculated and to R_a extraterrestrial radiation of the month relative to the site following this equation:

$$R_S = K \sqrt{T_{max} - T_{min} R_a} \quad (3.5)$$

where

R_S Solar radiation

R_a Extraterrestrial radiation [MJ m⁻² day⁻¹]

T_{max} Maximum air temperature [°C]

T_{min} Minimum air temperature [°C]

K adjustment coefficient

4. Estimation of PET according to the value of R_s previously calculated.

$$PET = 0.222 R_s - 0.557$$

3.1.5.2 The effective rainfall

P_{eff} has been calculated considering the RET from the Thornthwaite water balance method (Thornthwaite, 1948) and defined as $P_{eff} = P - RET$, where P is the rainfall measured by the stations.

3.1.6 Runoff

With the support of the Department of Public Utilities, four Automatic Water Level Recorders (AWLR) have been installed on the Soka River, two on the Pusur River and one on the Brambang River around 400 m of elevation. The AWLR system is a float-operated OTT Thalimedes Shaft Encoder with integral data logger that allows to record water level every 6 minutes. The locations have been defined to allow the record of the low flow rate during dry season and the high levels during the rainy season. The section will be measured and two rating curves will be used to calculate the discharge. The four AWLR were set up according to the delineation of Pusur catchment and of its recharge area. This delineation was carried out combining secondary data developed from previous survey, available maps, remote sensing images (Google earth images and ALOS images) and site investigation. It led to delineate the survey area as the area combining the Pusur River catchment area (drainage basin). The complete description of the AWLR installation is detailed by Lidon (2012).

3.2 Study site

3.2.1 Site description

Based on the location where the “water conflicts” appears in 2004, the previous hydrogeological investigation made in 2007 by the Indonesian university, UGM (Universitas Gadjah Mada at Yogyakarta, Indonesia), has defined the Pusur River as the central zone of the study area. This river direction is NW-SE from Merapi volcano to the West and flows into the Bengawan-Solo River, considered as the East boundary of the system and flowing afterwards to the North. To complete this preliminary study, the area has been extended

to the two main rivers bordering the Pusur river, the Brambang river to the North, and the Soka river to the South (Fig. 3.7) in view to integrate groundwater processes.

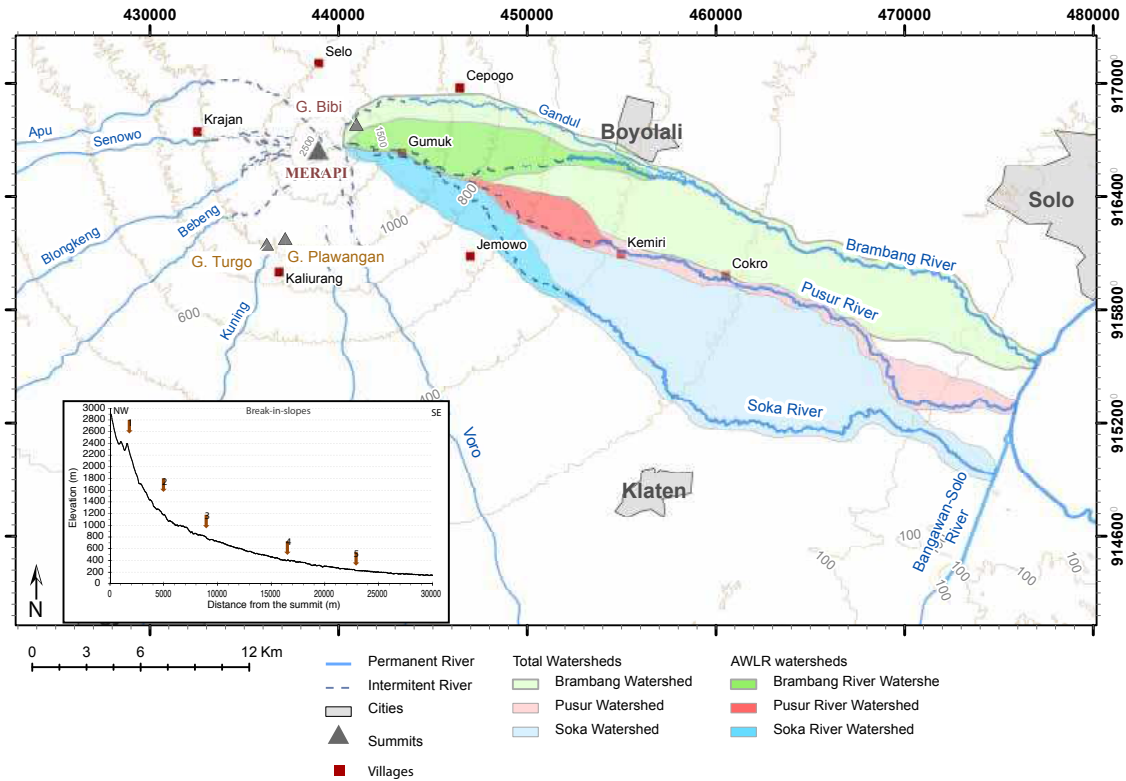


Figure 3.7: Map of the hydrological watershed locations on the Eastern flank of Merapi volcano. For each river, the hydrological watersheds monitored by the automatic water level recorder (AWLR) at 400 m asl is separated from the total watersheds extended from 2500 to 85m asl. In thumbnail, the elevation profile of the Eastern flank of Merapi volcano with the identification of 5 main break-in-slopes (2400m asl, 1200m asl, 800m asl, 400m asl and 220m asl). After the data from the Advanced Spaceborne Thermal Emission and Reflection Radiometer (ASTER), Global Digital Elevation Model Version 2 (GDEM V2) from the National Aeronautics and Space Administration (NASA) with 30 meters of resolution and 1 x 1 degree tiles.

As the geomorphology of the watersheds is complex with high variation of slopes and an important range of elevation (from 2500m asl to 85m asl), the hydrological analysis need to be done at different scales of watersheds. In a first hand, in order to evaluate the hydrological water balance in the upper parts, considered as the main recharge area, the automatic water level recorders (AWLR) were set up at 400 m asl on the main rivers, Brambang river, Pusur river and Soka river. These locations has been chosen considering the break in slope observed on Merapi elevation profile at 400m asl (Fig. 3.7). In the other hand, the total watersheds of the three rivers have been considered. The Tab. 3.1 shows the surface of the AWLR and the total watersheds. The AWLR catchments

represent 16%, 20% and 26% of the Soka, Pusur and Brambang watershed total surface respectively.

AWLR catchments	Upper Soka	Upper Pusur	Upper Brambang	
	X (m)	453430	454130	457510
AWLR coordinates	Y (m)	9157786	9161710	9165010
	Z (m)	362	412	350
River	Soka	Pusur	Brambang	
District	Jatinom	Tulung	Mojosongo	
Regency	Klaten	Klaten	Boyolali	
Length km	10.0	4.6	11.4	
Catchment surface km ²	21.8	10.8	30.3	

Total catchments	Soka	Pusur	Brambang	
	X (m)	474870	475930	476962
Outlet coordinates	Y (m)	9149660	9153010	9155164
	Z (m)	91	82	84
Length km	40.3	33.2	40.5	
Catchment surface km ²	142.6	41.8	150.9	

Table 3.1: Location of the automatic water level recorders (AWLR) used to monitor surface water fluxes within the 3 catchments and details of the total catchments located within the experimental site. The coordinates are expressed in meters within WGS84 referential (UTM).

3.2.2 Land use

All the watersheds are covered by the same 3 main types of land use: cropping system based on vegetable and tobacco (located above 800m asl, Fig. D.7), agroforestry (between 400 and 800m asl) and rice field and corn (below 400m asl, Fig.). The most important village density is located below 400m asl. Above 400 m of elevation, surface water is not available during the dry season (June to September), while the water amount coming from the rainfall is high during the wet season. In low lands, the rice fields cover 54% of the total experimental site (176 km²). In irrigated areas, farmers grow rice 2-3 times per year with average yields of 5-6 t/ha. More details about the land use are describe in the Chapter 1.



Figure 3.8: Rice field on the low land, near Klaten city.

3.3 Data processing

In order to characterize the climate conditions and estimate a water balance on the two hydrological years 2011-2012 and 2012-2013, a brief description of the historical data has been done then the terms of the water balance have been defined. For each terms, their variability along the study area has been assessed.

3.3.1 Climate data

3.3.1.1 Historical data

The historical rainfall data records have been collected from the DPU Klaten and DPU Boyolali. The chronicles begin in 1989 for the 16 stations in Klaten Regency and 2005 for the 7 stations in Boyolali Regency. Afterwards a first treatment to sort the low quality data, it appears that the historical rainfall data cannot be really used. The monitoring was not continuous for all the stations and several overestimation of the rainfall rate have been identified. Nevertheless, the station of Cokro-Tulung (Klaten Regency) (X:458651; Y:9161092; Z: 301m asl) shows 24 years of daily monthly data (1989-2013) with only 4 years of lack (1990-1994) (Fig. 3.9). The Cokro-Tulung chronicle allows to better understand the hydrological context of the study zone. The annual rainfall ranges from 917 (in 1996-1997) to 2415 mm/year (2007-2008) with a mean at 1715 mm/year. We could note the low rainfall value of the end of the 90s and the decreasing trend of the precipitation from the years 2001 to 2004.

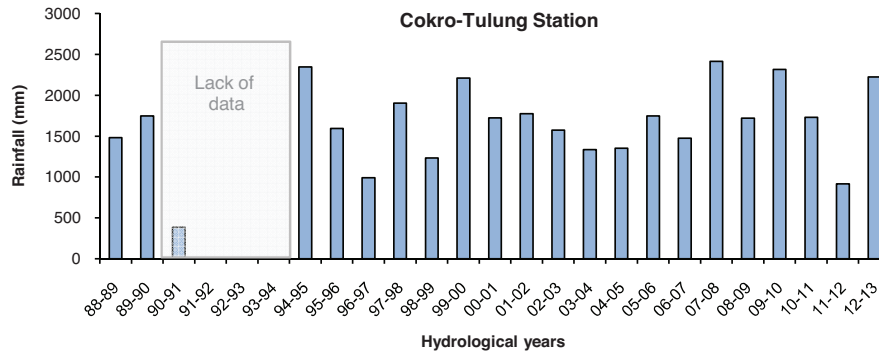


Figure 3.9: Long series of annual rainfall registered in Cokro Tulung (hydrological years Nov. 1989- Oct. 2013)

The chart Fig. 3.10 shows the annual variation of the monthly rainfall at Cokro-Tulung station since 1989. Even if the range of data is important (in January, the monthly rainfall ranges from 39 to 571 mm), the main part of the data confirm the seasonal behavior of the climate with a “rainy” and “dry” seasons. The rainy season starts in November and ends in June while the relatively short dry season begins in July and ends in October. This seasonality will define our hydrological year which starts in November to ends in October. The peak of the rainy season is in January with an average rainfall of 329 mm. For this study, we have monitored two hydrological years: Nov. 2011-Oct. 2012 and Nov. 2012-Oct. 2013. These years are compared to the historical data at Cokro-Tulung station. It appears that the year 2011-2012 is a relatively medium year with mean monthly rainfall below or close to the median value expect for December 2011. In contrast, the year 2012-2013 have six months above the median value and can be considered as a year with very high rainfall.

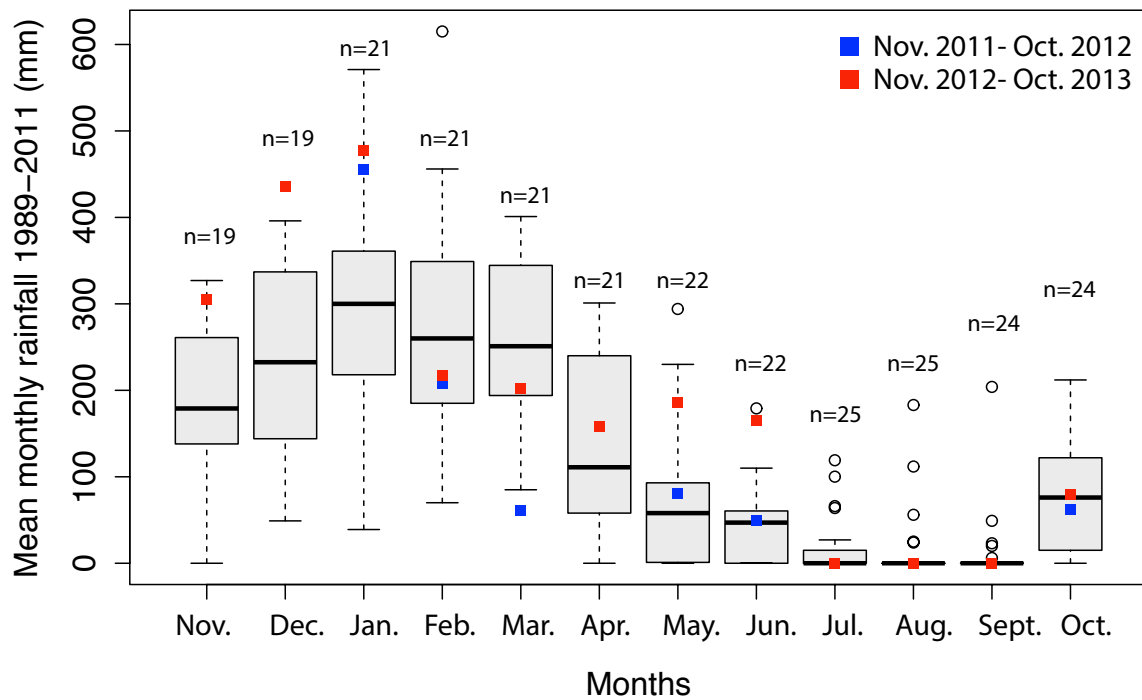


Figure 3.10: Monthly rainfall distribution through 24 years in Cokro-Tulung station (1989-2013). The monitored years 2011-2012 and 2012-2013 are isolated to define the trend of these years compare to the historical chronicle. The blank dots are the extreme events values, the dot line represent less than 25% of the data, the black line is the average monthly value, n=number of hydrological years.

3.3.1.2 Hydrological years 2011-2013 data

The chart Fig. 3.11 shows the monthly rainfall for the period November 2011 to October 2013 at three stations with different elevations: Gumuk, 1436 m asl, Musuk, 631 m asl and the station located near the bore-well of Danone AQUA at 244 m asl. The annual rainfall for the period Nov. 2011 to Oct. 2012 is 1570 mm for Gumuk, 2820 mm for Musuk and 1880 mm for AQUA.

The highest value is not located near Merapi summit as we could expected with a common orographic rainfall gradient (Roe, 2005) but near mid-elevation (600 m asl), in the North-East of Merapi volcano, near Musuk village. The seasonality effect is still clear for all the station regardless the elevation (80% of the annual precipitation happen between November and June).

From Nov. 2012 to Oct. 2013, the total rainfall is 1510 mm for Gumuk, 3650 mm for Musuk and 1480 mm for AQUA. We note the low decrease for Gumuk and AQUA (-3% and -20% respectively) between the two years but the important increasing rate of rain for Musuk station (+30%). At the monthly scale, the variation can be important for all the stations. For instance, in February for Gumuk (+90% of rain in 2012-2013), in December for Musuk (+300%) and in January for AQUA (-105%). This high monthly

variation characterizes the local and extreme events in this area. Likewise, the Fig. 3.12 shows the low influence of elevation on patterns of precipitation with the annual rainfall for the 18 stations on the two monitored years. By contrast, the annual rainfall is more important for the period 2012-2013 for 16 stations. That shows an increasing trend of the rainfall rate between the two years.

This increasing trend appears also on the isohyets maps Fig. 3.13 and Fig. 3.14 showing the spacial distribution of the rainfall on the watersheds for the period 2011-2012 and 2012-2013 respectively. The isohyet map highlights the local extreme rainfall rate on this kind of region. This pattern reveals a local storm effect is relatively common on the tropical zones (Griffiths et al., 2003; Aldrian & Dwi Susanto, 2003). Two rainfall gradients are combined on the Eastern flank of Merapi: the first one is a South-North gradient with a maximum rainfall rate on the North; the second one is East-West with the maximum on the West. The second gradient could describe the low orographic gradient. Combining these two gradients, regardless the year, the maximum of rainfall is located at Musuk (around 600m asl).

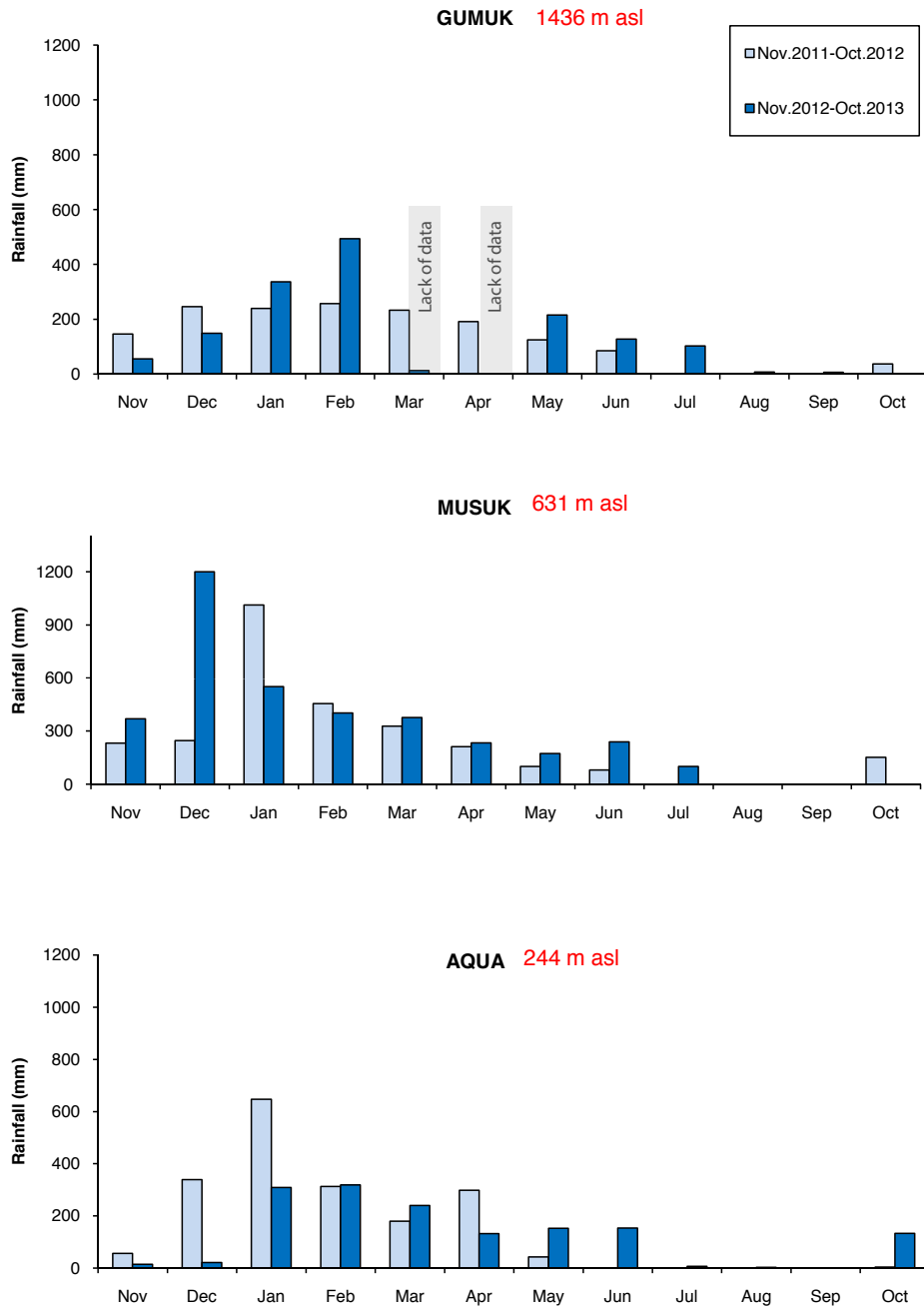


Figure 3.11: Monthly rainfall at three elevations: 1436, 631 and 244 m asl, Gumuk, Musuk and AQUA respectively, for the hydrological year 2011-2012 and 2012-2013.

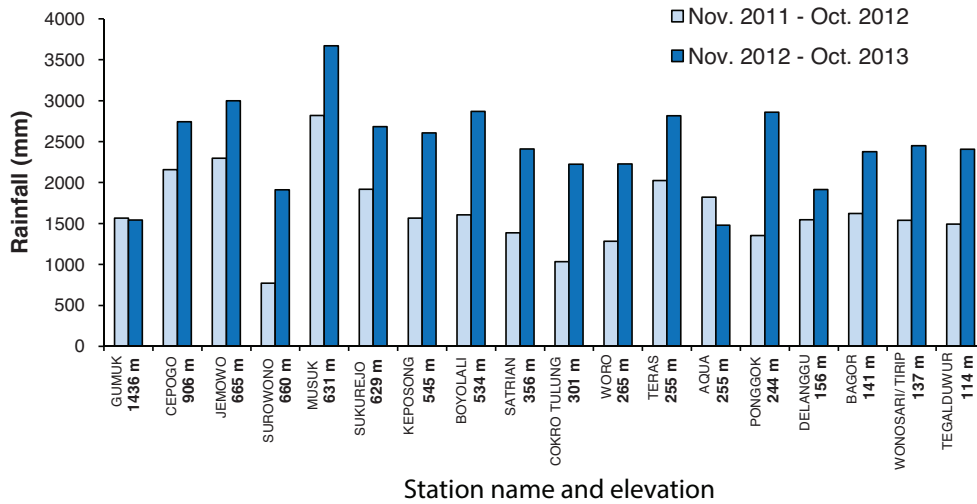


Figure 3.12: Annual rainfall for all stations of the research area sort by elevation for the period Nov. 2011 to Oct. 2012 (light blue) and Nov. 2012 to Oct. 2013 (deep blue).

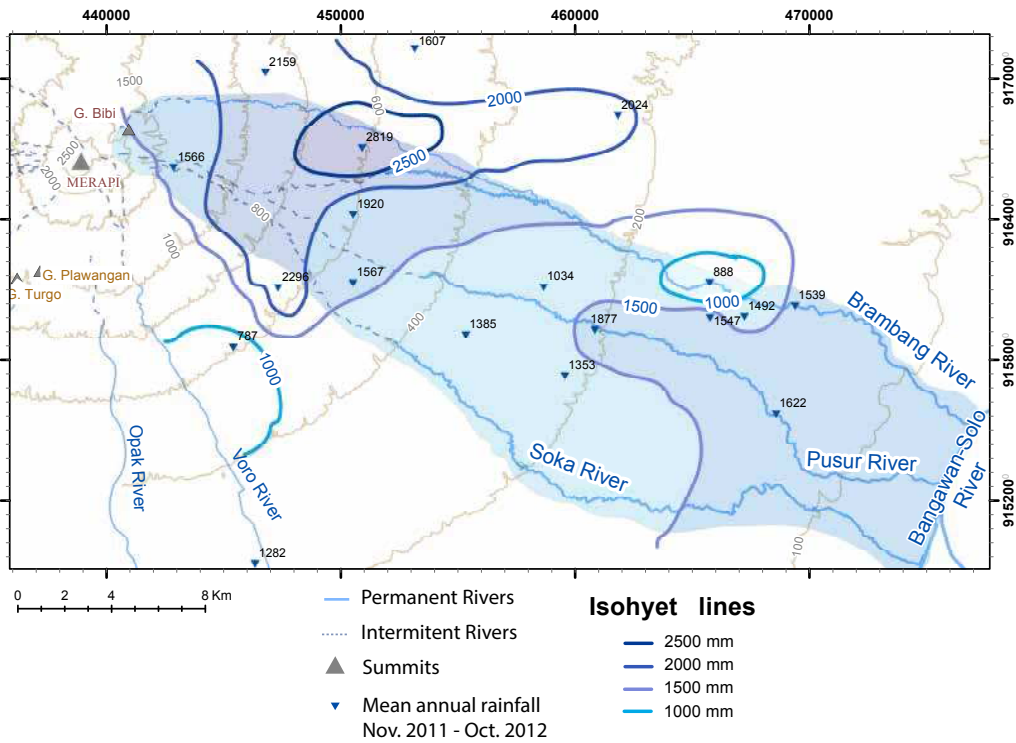


Figure 3.13: Isohyet map for the hydrological year 2011-2012.

We saw in the Chapter 1 that the rainfall amount during the monsoons is linked to the SST anomalies and El Niño or La Niña phenomenon. The high rainfall amount of 2012-2013 could be linked with a development of La Niña which enhanced Indonesian rainfall (Hendon, 2003).

3.4 Water balance estimation

3.4.1 Evapotranspiration

In order to estimate the water balance on the Upper Pusur, Upper Soka and Upper Brambang watersheds, an estimation of the potential evapotranspiration (PET) is required. In Gumuk (village on the highest accessible point of the study area at 1456 m asl) the climatic variables (temperatures, humidity, solar radiation, wind direction and speed) have been recorded every 15 min and averaged at the monthly scale (Fig. 3.15). These variables will be used to calculate the PET by the Penman- Monteith equation.

During the hydrological year 2011-2012, the monthly air temperature is relatively constant (near 19°C) with a slight decreasing trend during the dry season (July-August 2012). During the year 2012-2013, the monthly temperature is higher and shows more variations ($20^{\circ}\text{C} \pm 1^{\circ}\text{C}$).

The monthly air humidity is close to the 90% during the rainy season of the 2011-2012 year and as expected, decreases to 70% at the end of the dry season. In 2012-2013, the humidity increases again to 90% and seems decrease during the next dry season but later than during the first year (June in 2011-2012 and August in 2012-2013).

The wind speed varies between 1 to 1.5 $\text{m}\cdot\text{s}^{-1}$ during the year 2011-2012 and shows high variation during the year 2012-2013 ($1 \pm 1 \text{ m}\cdot\text{s}^{-1}$). The solar radiation increases from 0- 2.0 $\times 10^5 \text{ W}\cdot\text{m}^{-2}$ to 6.5 $\times 10^5 \text{ W}\cdot\text{m}^{-2}$ during the year 2011-2012 and decreases in 2012-2013. The low values in 2012-2013 mean that the cloudiness was probably higher in 2012-2013 than in 2011-2012. That can explain the delay to the decrease of air humidity and the high temperature. Thus, we could expect that the hydrological year 2012-2013 presents more rainfall amount than 2011-2012.

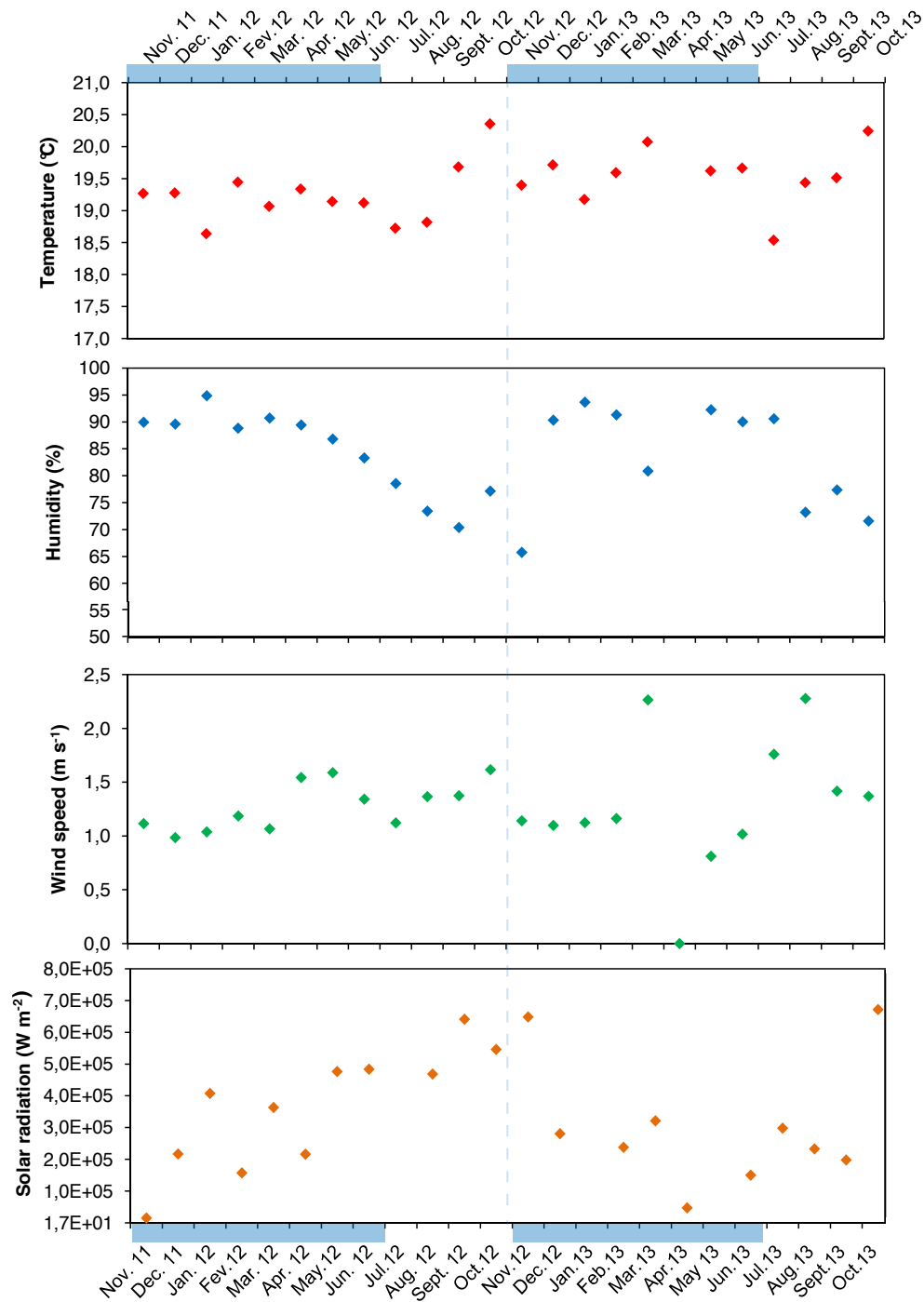


Figure 3.15: Monthly average of climatic variables measured at Gumuk Weather Station (1456 m asl) over the two hydrological years 2011-2012 and 2012-2013. The blue marks demarcate the rainy season.

To complete this climate data base, 14 thermometers have been installed on the rain gauge stations within the survey area at different elevations. The daily temperature is manually measured by the local operators. This temperature is considered as representative of the maximal temperature of the day (Tmax). Using a methodology described earlier, the

mean monthly PET is calculated on the study area for the period from November 2011 to October 2012. Nevertheless, the quality of these values have to be considered carefully. Indeed, it appears that the operators did not measure the temperature at fixed time and the error on the temperature can be higher than 5°C.

The climatic data for the 2012-2013 year are still not fully available, thus, in order to estimate the PET for the second hydrological year, we used the daily temperature data and the solar radiation of the Gumuk weather station over the year 2012-2013 to characterize the correlation between the PET variation along the elevation profile. Hence, using the same methodology linking the Tmax and the solar radiation, the PET for the period 2012-2013 can be calculated.

The Fig. 3.16 represents the annual PET value according to stations sorted by decreasing elevation and compare the PET of the two hydrological years 2011-2012 and 2012-2013. This chart shows an inverse correlation between the elevation and the annual PET values for the two hydrological years. The annual PET values are slightly lower in 2012-2013 than 2011-2012 due to the link with the solar radiation.

The high PET values in low elevations are linked to the solar radiation amount, which is more important in the low land where the clouds are rarer than in the highlands. The monthly PET ranges from 21 to 177 mm.month⁻¹ over the years 2011-2012 and 2012-2013. At the watershed scale, over the two years, the PET ranges around 900 mm.year⁻¹ (Fig. 3.3) for the AWLR catchments, it means in between 400 to 1500 m asl and 1330 mm.year⁻¹ for the complete study area in between 100 to 1500 m of elevation.

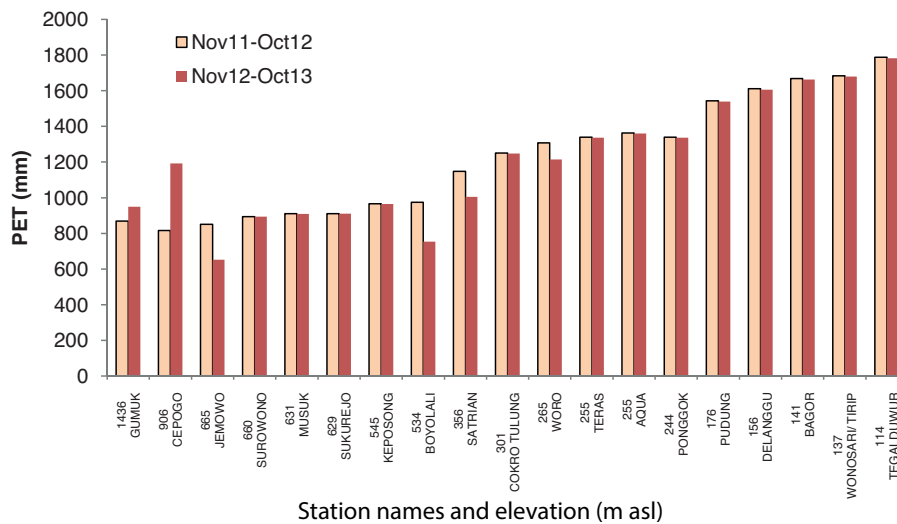


Figure 3.16: Annual potential Evapotranspiration (PET) by Thornthwaite method in millimeters for all the stations and their elevation (m asl) for the period of November 2011 to October 2013.

Period	Catchment	Surface (km ²)	PET (mm)	Volume (m ³)
2011-2012	Upper Soka	21.5	888.9	19.6 E+6
	Upper Pusur	11.2	957.3	10.5 E+6
	Upper Brambang	32.6	884.3	25.1 E+6
	Total	65.3	2730.5	73.1 E+6
	Total watersheds	333.0	1331.1	440 E+6
2012-2013	Upper Soka	21.5	883.6	19.3 E+6
	Upper Pusur	11.2	931.6	10.1 E+6
	Upper Brambang	32.6	1027.4	29.1 E+6
	Total	65.3	2842.6	73.7 E+6
	Total watersheds	333.0	2337.1	447.0 E+6

Table 3.3: Average annual potential evapotranspiration estimation (PET) by Thornthwaite method and its volume calculation at the watershed scale. The “Upper” watersheds define the catchment monitored upstream the AWLR. The “Total Watershed” is defined as the complete study area combining the 3 main watersheds (Soka, Pusur and Brambang watersheds).

The PET is defined as maximum amount of water liable to be evaporated on a continuous theoretical covered soil but in order to quantify the real amount of water evacuate of the system, the real evapotranspiration (RET) has to be estimated.

A Thornthwaite water balance method is used to calculate the real evapotranspiration (RET) (Thornthwaite, 1948). The soil moisture storage (SMS) has been estimated to 20% of the soil volume. This percentage has been measured by the BPTP (Institute for Agricultural Technology) in laboratory after soil analysis (the complete results of these analyses are not available and have to be discussed). That is meant that for 1 m³ of soil, 0.200 m³ will constitute the SMS, i.e. 200 mm.

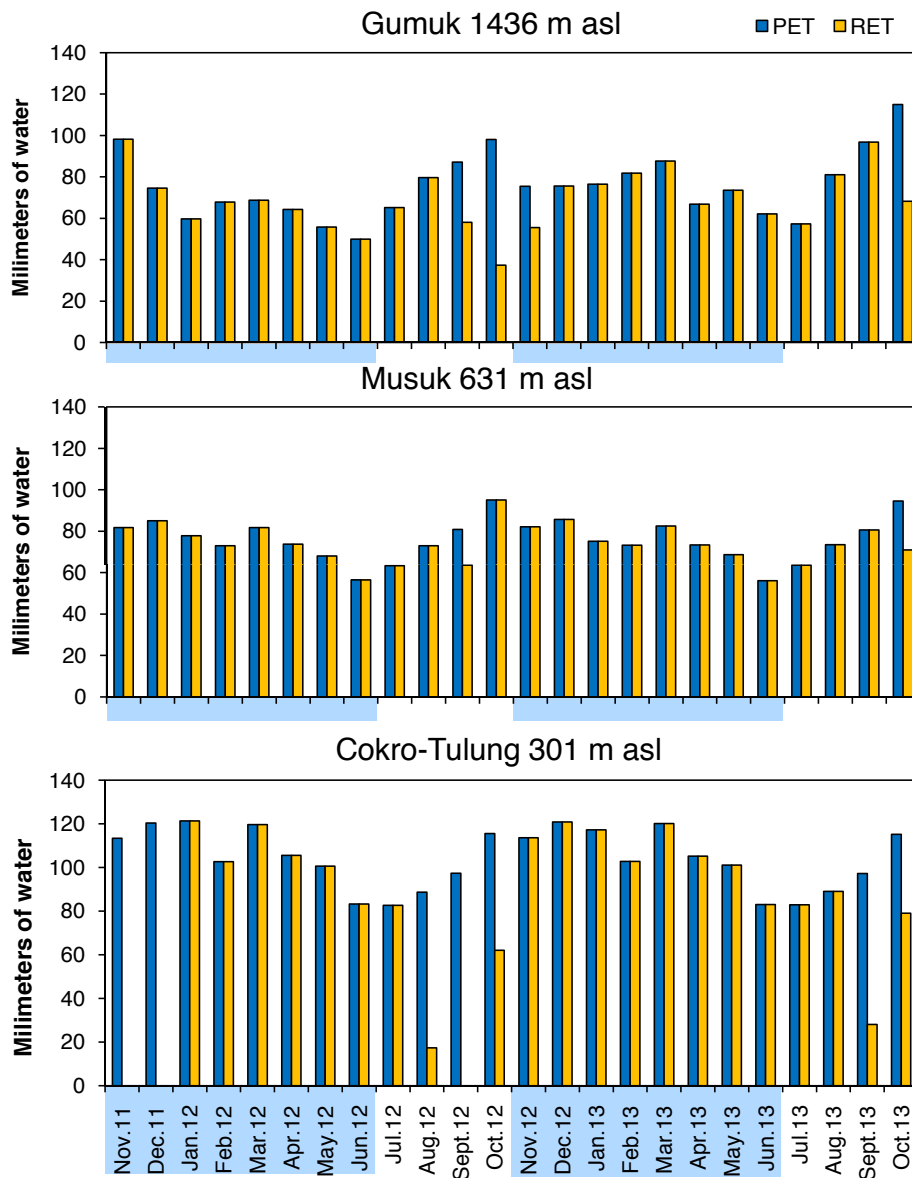


Figure 3.17: Comparison between the monthly average Potential Evapotranspiration (PET, blue bars) and the Real evapotranspiration (RET, yellow bars) at three elevations, 1436 m asl (Gumuk), 631 m asl (Musuk) and 301 m asl (Cokro-Tulung) over the period Nov.2011- Oct. 2013. The blue marks show the rainy seasons.

The Fig. 3.17 shows the comparison between the monthly cumulated PET and RET for three elevations, 1436, 631 and 301 m asl (Station of Gumuk, Musuk and Cokro-Tulung respectively). The RET follows the trend of the PET with a slight decreasing trend at the end of the rainy season (April to June) and an increase at the end of the dry season (August to November).

The average annual RET for Gumuk is estimated at 779 mm in 2011-2012 and 883 mm in 2012-2013; for Musuk at 893 mm 2011-2012 and 885 mm in 2012-2013; and for Cokro-

Tulung 795 mm in 2011-2012 and 1143 mm in 2012-2013.

For all the elevations, the PET is satisfied at least seven months per year with a maximum of 11 months (at Musuk station). The PET is not satisfied during the dry season and especially at low elevations. The low precipitation amount combined with the high PET demand create this gap between PET and RET during the dry season in the lowlands.

We are now able to calculate the difference between the rainfall and the RET, defined as the effective rainfall.

3.4.2 Effective rainfall variability

The spatial variability of the annual effective rainfall within the survey area is illustrated by the following Fig. 3.18 and Fig. 3.19. As the rainfall, the effective rainfall isoline maps show the high variability of distribution. It range from 79 to 1879 mm year⁻¹ in 2011-2012 year and 410 to 2844 mm year⁻¹ in 2012-2013. The patterns show the combined effect of North East - South West gradients with the maximum value on Musuk station (600 m asl). The spatial and temporal variability of the effective rainfall is directly linked to the rainfall spatial variability with the same gradient influence and the same increasing trend between the years 2011-2012 and 2012-2013.

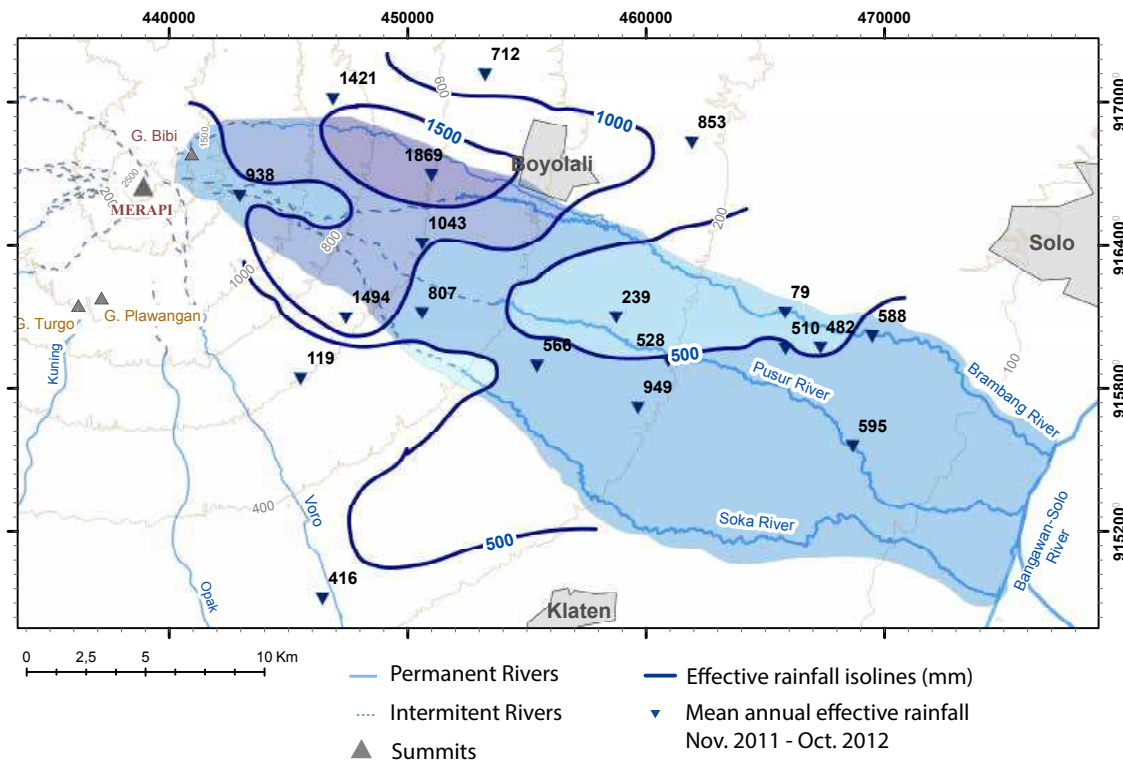


Figure 3.18: Estimation of the annual effective rainfall (mm) over the study area from November 2011 to October 2012.

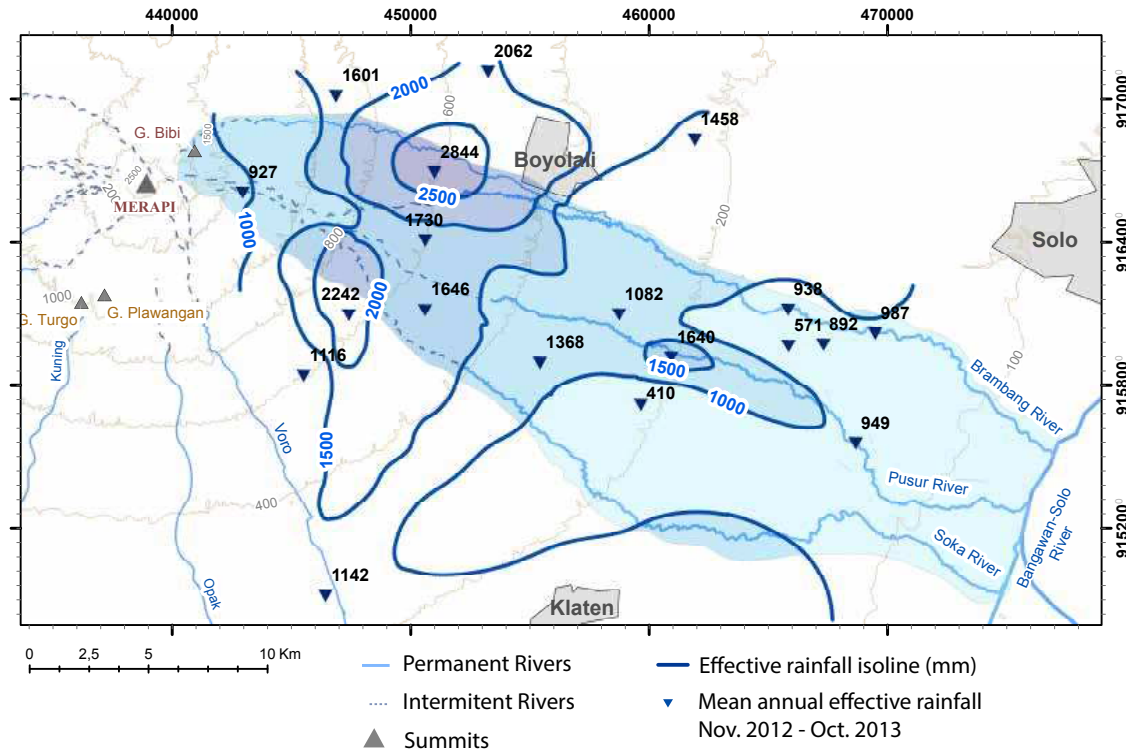


Figure 3.19: Estimation of the annual effective rainfall (mm) over the study area from November 2012 to October 2013.

The Table 3.4 shows the annual effective rainfall and the volume associated for each AWLR catchment and for the total survey area for the period 2011-2012 and 2012-2013. Taking into account all catchments, the comparison of monthly values of weighted rainfalls and effective rainfall shows a strong correlation (R^2 0.95) between the two data sets; the effective rainfall represents on average 80% of the total rainfall. Because rainfall allows to explain 95% of effective rainfall variability, there is every reason for assuming that the uncertainty over the PET values will only have a limited impact on the terms of the water balance as far as the order of magnitude of PET values are consistent [Kartiwa et al. \(2013\)](#).

On the total watershed, the effective rainfall shows a high increase between 2011-2012 and 2012-2013 (658 mm in 2011-2012 to 1142 mm in 2012-2013). This gap can be explained by the increasing trend of the rainfall over the watershed in 2012-2013. We saw that the cumulated rainfall in 2011-2012 is 1639 mm compare to 2337 mm in 2012-2013. Moreover, the PET did not increase in 2012-2013, enhancing the gap between the two hydrological years.

Period	Catchment	Surface (km ²)	Effective rainfall (mm)	Volume (m ³)
2011-2012	Upper Soka	21.5	1000.6	21.5 E+6
	Upper Pusur	11.2	924.6	10.3 E+6
	Upper Brambang	32.6	1263.2	37.9 E+6
	Total	65.3	3188.4	69.7 E+6
	Total watersheds	333.0	658.4	440.1 E+6
2012-2013	Upper Soka	21.5	1694.6	37.1 E+6
	Upper Pusur	11.2	1668.4	18.4 E+6
	Upper Brambang	32.6	1726.7	54.4 E+6
	Total	65.3	5089.7	219.8 E+6
	Total watersheds	333.0	1142.8	447.0 E+6

Table 3.4: The effective rainfall and its volume calculation at the watershed scale. The “Upper” watersheds define the catchment monitored upstream the AWLR. The “Total Watershed” is defined as the complete study area combining the 3 mains watersheds (Soka, Pusur and Brambang watersheds).

3.4.3 River discharge and runoff

Based on the work of our partners from the CIRAD and IAHR, the hydrological pattern of the three main rivers (Upper Soka, Upper Pusur and Upper Brambang rivers) has been described (Lidon, 2012).

The hydrographs of the three AWLR show a pattern of violent stream during the raining season. Punctual events of flood occur rapidly (less than one hour) and some of them can be powerful (more than $2 \text{ m}^3 \cdot \text{s}^{-1}$ during less than 12 hours). The Fig. 3.20 shows the monthly discharge volumes of the three rivers from December 2011 to December 2012. The Upper Soka and Upper Pusur rivers follow a similar pattern with a relatively stable discharge volume along the year ranging from $200 \times 10^3 \text{ m}^3 \cdot \text{month}^{-1}$ to $790 \times 10^3 \text{ m}^3 \cdot \text{month}^{-1}$ respectively. Their peaks occur in January-February, 3-4 months after the beginning of the rainy season. The Upper Pusur discharge is lower than the Upper Soka river, linked to the catchment surface. At the same way, the Upper Brambang volume discharge is higher than the two others, because its catchment surface is more important. However, the Upper Brambang, peak occurs in January and discharge decreases from March to October while the Upper Soka and Upper Pusur volumes stay relatively stables. This decreasing trend indicates an influence of the climate seasonality on the Upper Brambang catchment and not on the other ones.

This seasonality is clearly visible on the mean daily hydrographs with the main flood events occurring between November and June (Fig. 3.21, Fig. 3.22 and Fig. 3.23). Nevertheless, the river is never dry, there is still a base flow during the dry season, showing a contribution of the groundwater.

The hydrographs are compared to the cumulated monthly effective rainfall over the upper watershed and the daily effective rainfall of the the most representative station on the upper watershed. The flood occur few hours and sometimes less after the rainfall event

which are usually strong and highly localized. For instance, the flood event on the Brambang river of the 01/01/2012 started at 19:12, reached the flow rate peak at 19:40 with $17 \text{ m}^3 \cdot \text{s}^{-1}$ and the recession curves attained the base flow rate of $0.3 \text{ m}^3 \cdot \text{s}^{-1}$ the 02/02/12 at 07:20 (i.e. = 12 hours after the peak). Thus, the flow rate recession is also very fast and occurs in few hours, which is representative of a system hydrologically highly reactive. Nevertheless, some specificity can be noticed: on the Soka river (Fig. 3.21), the peak of effective rainfall in January ($60 \text{ mm} \cdot \text{day}^{-1}$) produces a high flow rate nearly instantaneously (more than $1 \text{ m}^3 \cdot \text{s}^{-1}$) but in contrast, the event in May with similar amount of rain ($62 \text{ mm} \cdot \text{day}^{-1}$) was not followed by an increase of flow rate. The difference between these events is the amount of water accumulated before the event itself. Indeed, in January, the rainfall events are more frequent and the soil is already saturated when the high storm rainfall event occurred. In May, we can see that the effective rainfall events are scarce and the soil is probably not saturated. Then, during the high precipitation event, most of the effective rainfall will infiltrate and contribute to the soil and the groundwater recharge. That means, that the upper part of the total watershed is subjected to a runoff-threshold effect depending on the soil saturation.

This threshold has been studied by the CIRAD through the implementation of an experimental site at micro-catchment scale at Gumuk, nearby on the weather station location. This micro-catchment has an area of 5.4 ha between 1471 and 1081 m of elevation. The work of the Master student Brice Auvet on this area allows to quantify the infiltration threshold at $30 \text{ mm} \cdot \text{h}^{-1}$ (Auvet, 2013). We can suggest that this order of magnitude can be applied over the upper part of the watershed since this type of young andic-type volcanic soils, are also characterized in many studies, by substantial infiltration and saturated hydraulic conductivity of over $60 \text{ mm} \cdot \text{h}^{-1}$ and low runoff rates (Poulenard et al., 2001; Zehetner & Miller, 2006; Cattani et al., 2009). In these conditions, runoff requires high-intensity rainfall and the infiltration (i.e.: the groundwater recharge) is the predominant process in this area.

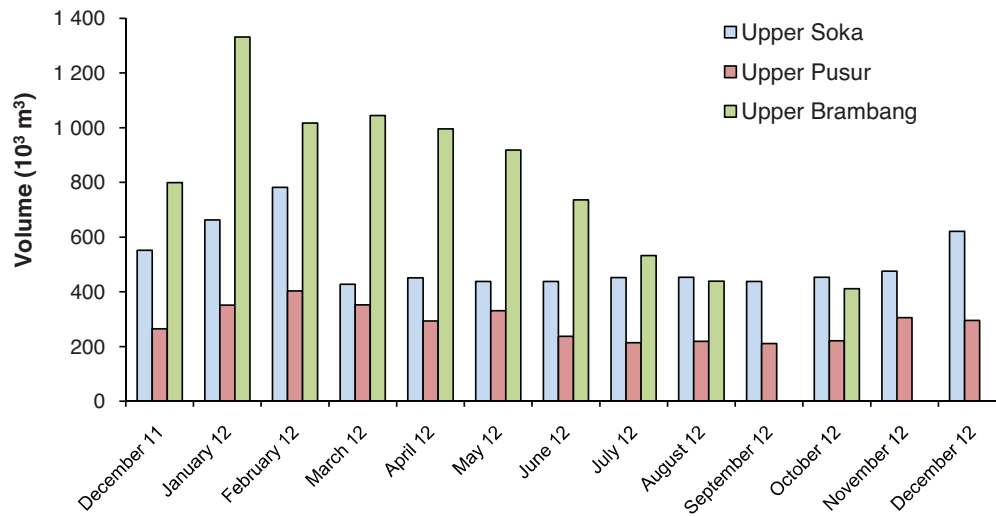


Figure 3.20: Monthly volumes of water registered by the AWLR on the Upper Brambang, Upper Pusur and Upper Soka rivers from December 2011 to December 2012.

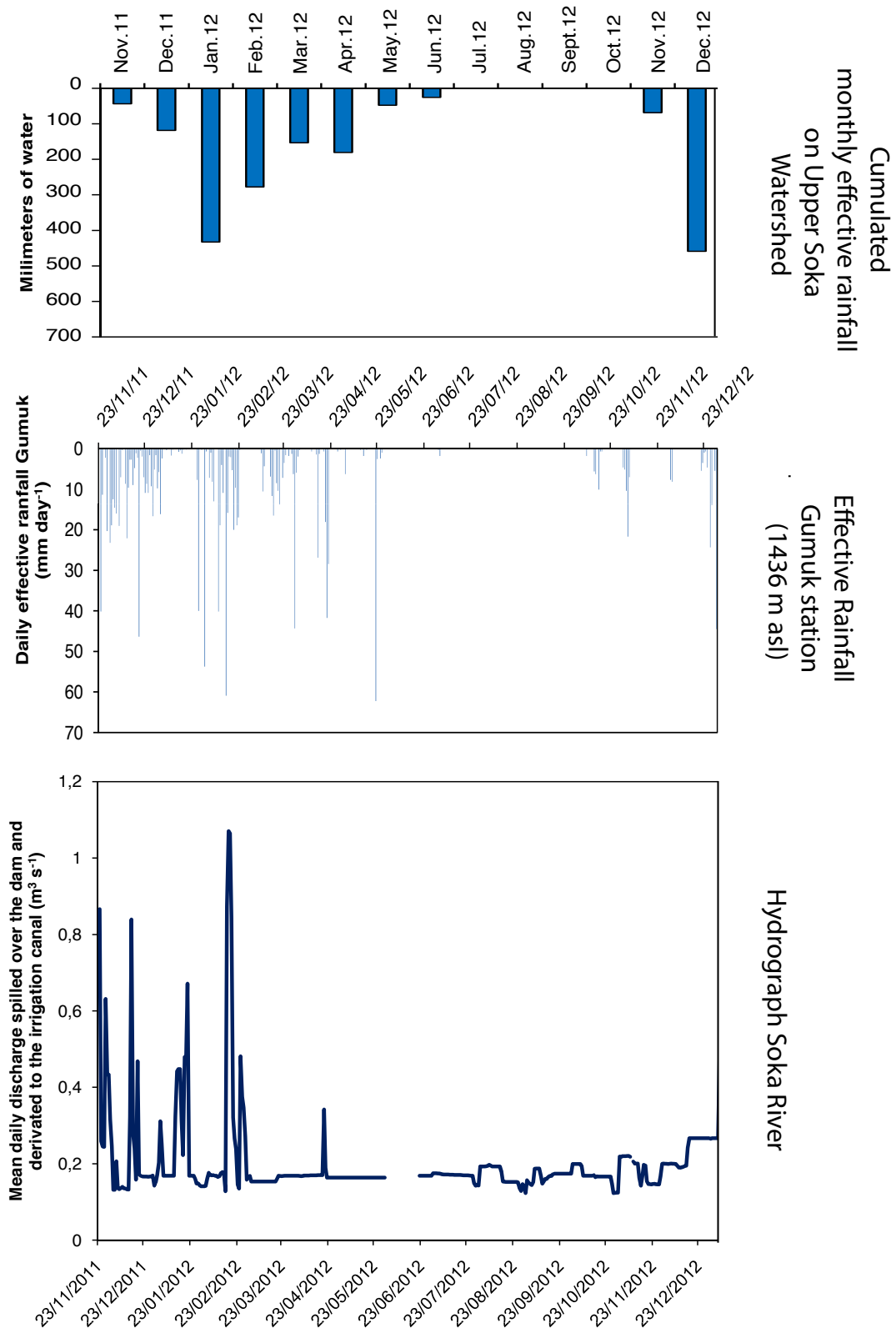


Figure 3.21: Estimated mean daily discharge ($\text{m}^3 \cdot \text{s}^{-1}$) spilled over the dam where the AWLR (15 min recorder) is settled and derived to the intake on Upper Soka AWLR site, compare to the daily effective rainfall at Gumuk station and the monthly cumulated effective rainfall calculated over the upper Soka watershed from November 2011 to December 2012

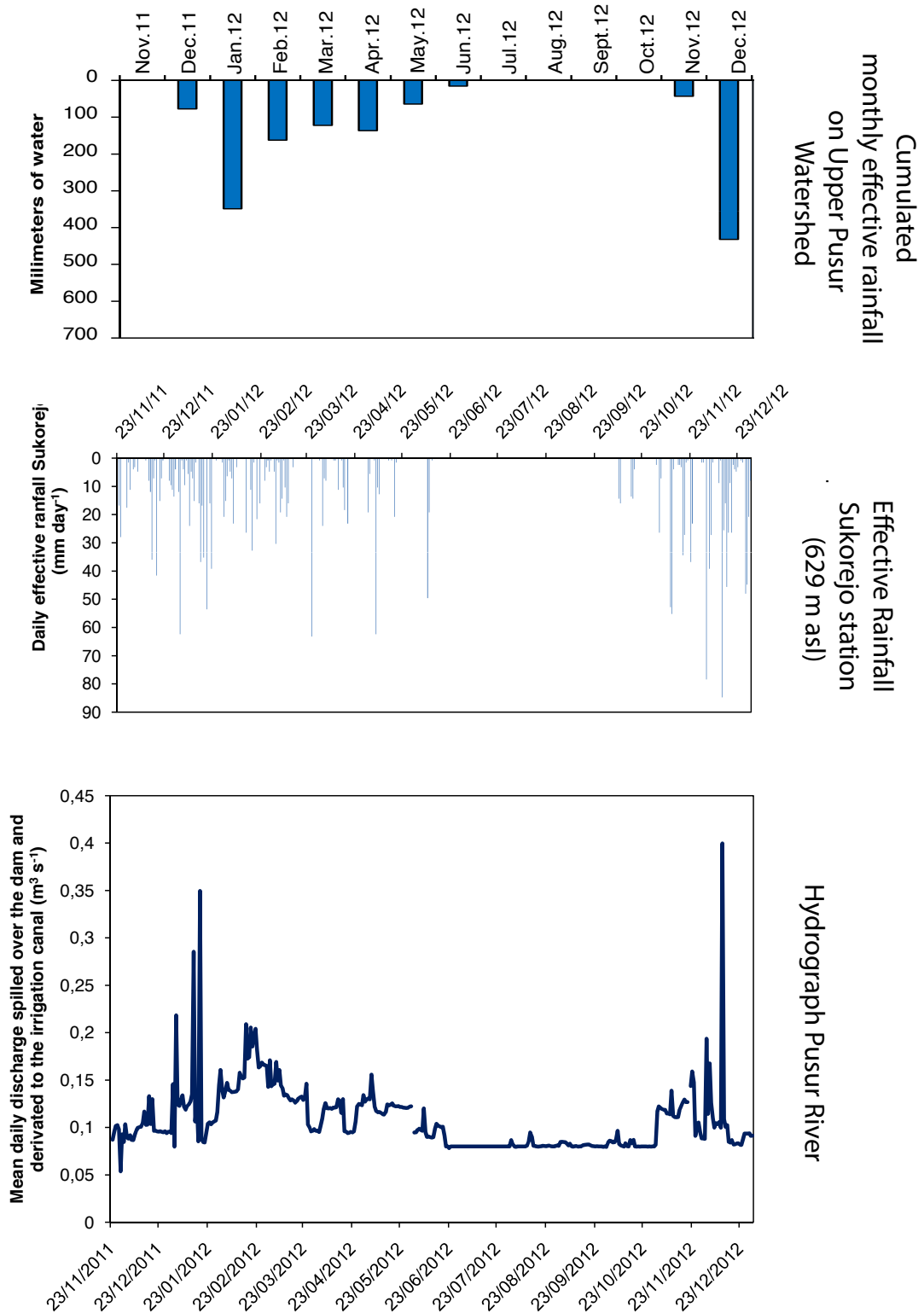


Figure 3.22: Estimated mean daily discharge ($\text{m}^3 \cdot \text{s}^{-1}$) spilled over the dam and derived to the intake on Upper Pusur AWLR site (15 min recorder), compare to the daily effective rainfall at Sukorejo station and the monthly cumulated effective rainfall calculated over the upper Pusur watershed from November 2011 to December 2012

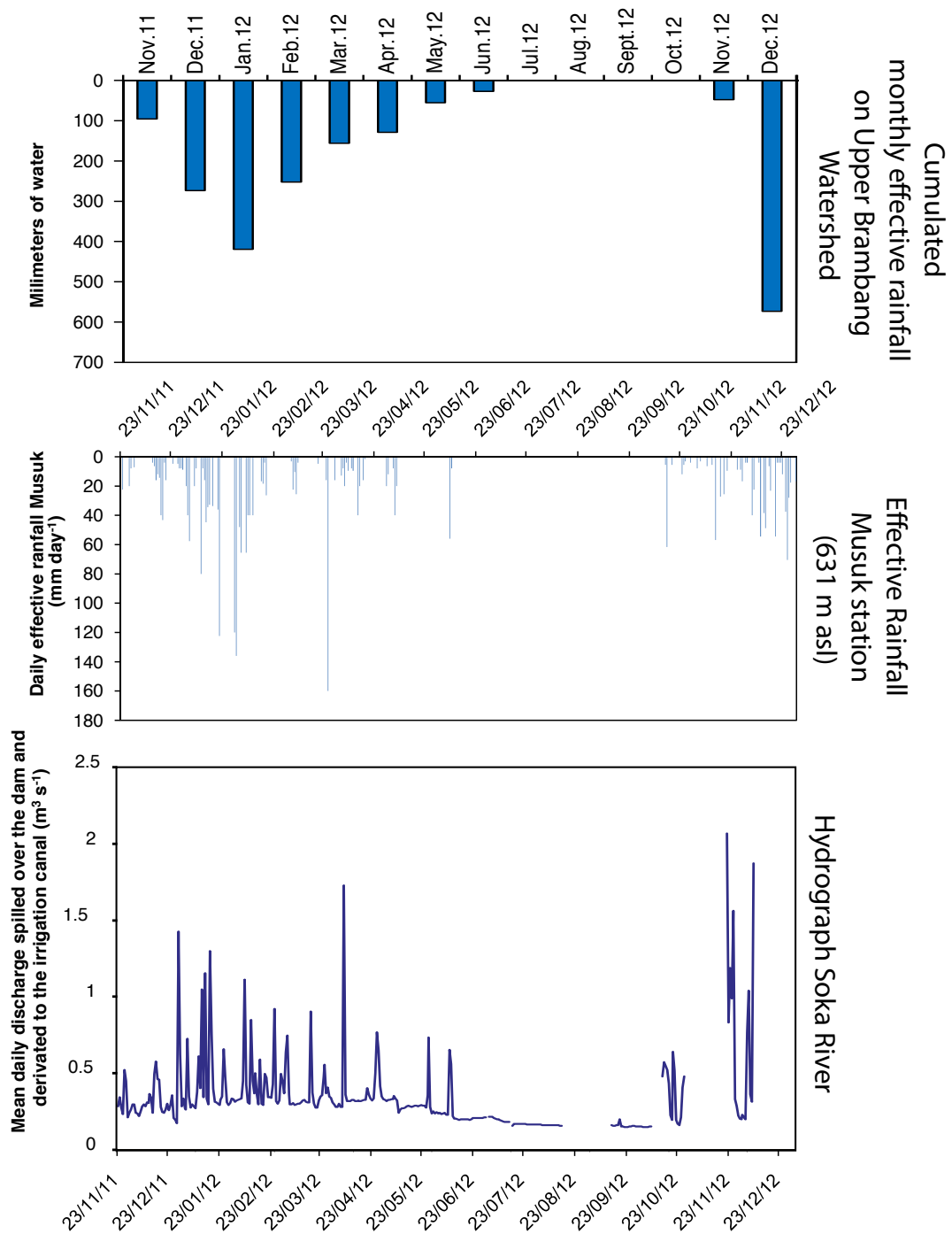


Figure 3.23: Estimated mean daily discharge ($\text{m}^3 \cdot \text{s}^{-1}$) spilled over the dam and derived to the intake on Upper Brambang AWLR site (15 min recorder), compare to the daily effective rainfall at Musuk station and the monthly cumulated effective rainfall calculated over the upper Brambang watershed from November 2011 to December 2012

Based on the semi-automated analysis method developed under Excel by the CIRAD team (Kartiwa et al., 2013), the hydrographs obtained on the upper Pusur, upper Soka and the upper Brambang have been divided in separate flows. The analysis assumes that the surface flow includes three components; runoff, base flow and spring flow. The runoff is defined as the quantity of water discharged in surface streams, the base flow is the portion of flow that comes from subsurface and the spring flow represents the groundwater contribution.

Spring flow has been identified as a specific component in so far as it is the only source of surface water during dry season while the stream bed is dry upstream the spring zone (Fig. 3.24).

For each flooding event, the hydrograph analysis consists in:

- i) Deducting the term “base flow” as the cumulate component of the spring flow rate and the real base flow which is unknown and regarding to the short recession time could be relatively low.
- ii) Categorizing the 3 specific points that characterize the hydrograph: (i) time of the pick discharge (T2) (ii) rising time of surface runoff (T1) and (iii) inflection point of the recession limb of the hydrograph (T3) assuming that beyond that point base flow is prevailing. iii) Establishing the equation of the base flow depletion over time before the flood event (RC1) as well as after the inflection point (RC2); the recession trends are fitted to currently used simple exponential equation:

$$Q_t = Q_0 e^{-kt} \quad (3.6)$$

where

Q_t is the flow at time t ,

Q_0 is the flow at $t=0$,

k is a constant

- iv) Estimating base flow assuming that:

- the depletion process persists until the pick of the flood: it leads to estimate the base flow between T1 and T2 according to equation RC1 which is extended in time to time T2.
- the depletion curve after time T3 fits equation RC2. It leads to extend the equation RC2 backward to time T3.
- the increase of the base flow between T2 and T3 is linear

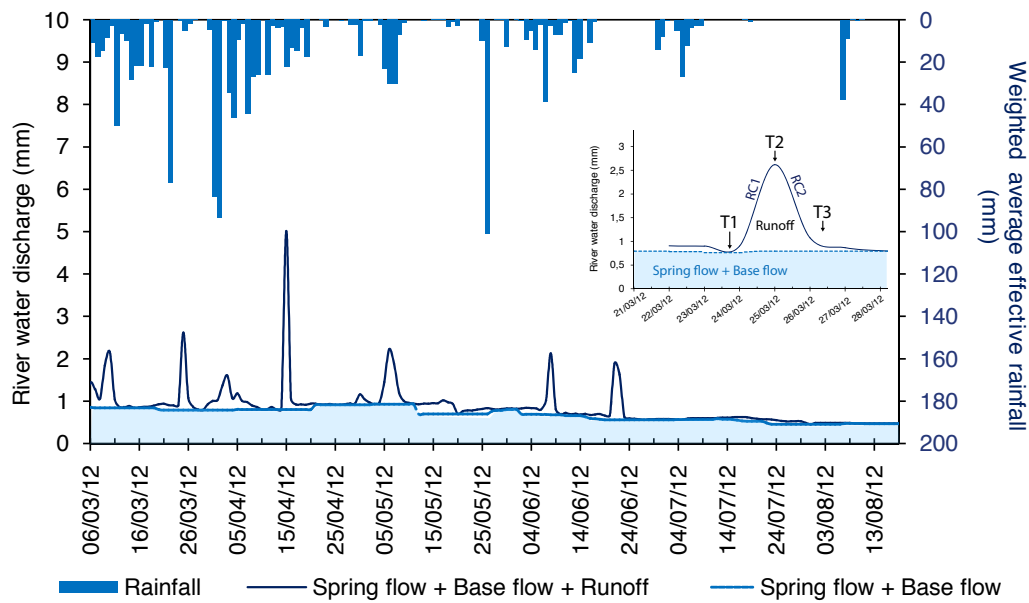


Figure 3.24: Example of hydrograph analysis with the separated flows on the Brambang hydrograph. The hydrograph is decomposed in two parts: i) the direct runoff of the rainfall and ii) the flow coming from subsurface and groundwater contribution (base flow).

Based on this analysis, the Fig. 3.25, Fig. 3.26 and Fig. 3.27 show the distribution of the river discharge volume divided between the runoff and the base flow (simplified as groundwater flow contributions) over the 2011-2012 hydrological year. The Upper Soka and Upper Pusur rivers have a similar behavior: the base flow is relatively stable during the year (around $430 \times 10^3 \text{m}^3 \cdot \text{month}^{-1}$ and $210 \times 10^3 \text{m}^3 \cdot \text{month}^{-1}$ for the Upper Soka and Upper Pusur respectively). In average, the base flow represents 86% (min: 63%; max: 100%) of the Pusur river discharge and 76% (min: 29%; max: 100%) of the Soka river discharge. The total discharge variations are coming from the runoff changes, in other words, the groundwater contribution is relatively constant through the hydrological year and only the climate has an influence on the water discharge variations on the Pusur and the Soka rivers during this period.

The base flow represents 80% (min: 31%; max: 100%) of the water discharge of the Brambang river. Unlike the upper Pusur and upper Soka rivers, upper Brambang river shows an important variation of the monthly volumes of the base flow (ranging from $300 \times 10^3 \text{m}^3 \cdot \text{month}^{-1}$ in November to $790 \times 10^3 \text{m}^3 \cdot \text{month}^{-1}$ in January) (Fig. 3.27). That is meant a decreasing trend from the groundwater contribution to the river discharge during the dry season. The hydrogeological system in the upstream part of the Brambang river plays a major role into the river discharge at 400 m of elevation.

The Soka and the Pusur rivers do not flow before 400 m asl. The base flow measured at the AWLR is due to two springs located less than 1 km from the AWLR. Above

these springs, the rivers are dry, excepted during the high rain events. In contrast, the Brambang river flows all year long with low base flow from 900 m of elevation, where are located the closest springs from the AWLR (6 km upstream them). Thus, the relative base flow stability of the Pusur and Soka rivers can be explained by the proximity to the groundwater contribution which is relatively constant along the year. However, on the Brambang river base flow can be influenced by two phenomenon: 1) the distance from the spring submits the base flow to possible re-infiltration into the non-consolidated material in the river bed which can contribute to the deep groundwater recharge and do not reach the AWLR location, 2) the springs at the origin of the base flow at 900 m of elevation are temporary and their flow rate reflect the seasonal variations.

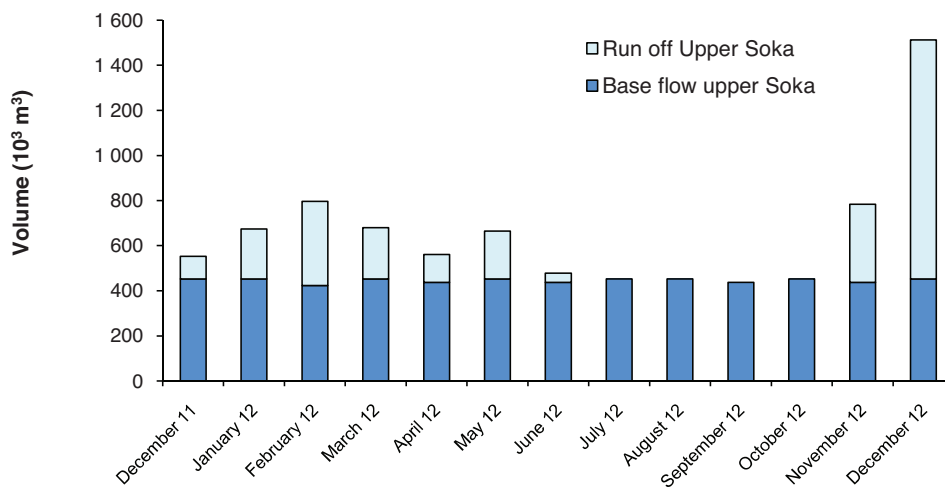


Figure 3.25: Monthly volumes of water registered by the AWLR on the upper Soka river from December 2011 to December 2012. Runoff (surface-hypodermic flow) and base flow (flow passing through an aquifer) contribution are separated.

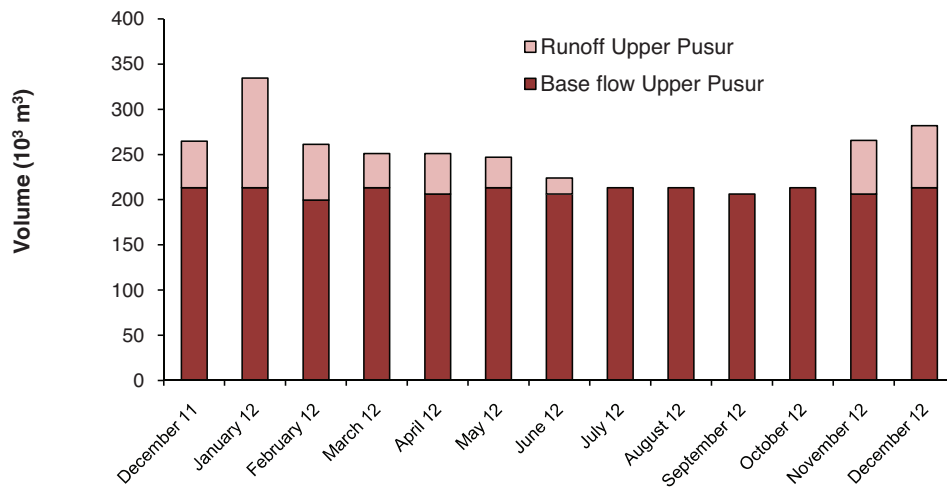


Figure 3.26: Monthly volumes of water registered by the AWLR on the upper Pusur river from December 2011 to December 2012. Runoff (surface-hypodermic flow) and base flow (flow passing through an aquifer) contribution are separated.

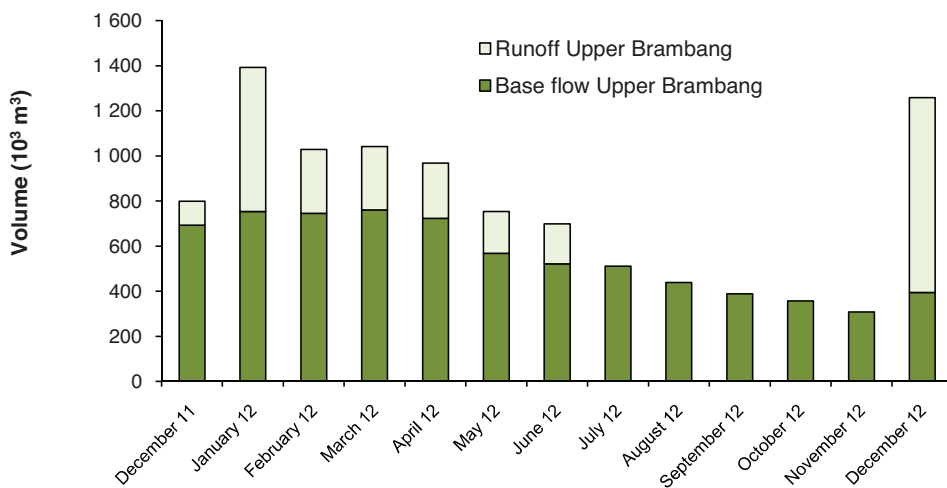


Figure 3.27: Monthly volumes of water registered by the AWLR on the upper Brambang river from December 2011 to December 2012. Runoff (surface-hypodermic flow) and base flow (flow passing through an aquifer) contribution are separated.

The hydrograph analysis to separate the flows, has been only made on the hydrological year 2011-2012 because the AWLR data of 2012-2013 are not yet fully available. We hope that this analysis can be completed as soon as possible but in view to establish a complete water balance over the two hydrological years, a strong assumption has been made to estimate the runoff for the second year. We have considered that the proportion of effective rainfall contributing to the runoff was the same over the two monitored years. During the next section the percentage of effective rainfall that contributes to the runoff is calculated over the period November 2011 to October 2012. This percentage is then

reported to the effective rainfall of 2012-2013.

3.4.4 Water balance estimation

Based on the Thornthwaite method (Thornthwaite, 1948), the water balance is calculated at the annual scale on the period of November 2011 to October 2012. The results are expressed in millimeters, in volume according to the hydrological watershed (Millions of m^3) and in percentage of the annual rainfall (Table 3.6). The runoff and the groundwater recharge are expressed in percentage of effective rainfall.

The coefficient of runoff is low and ranges from 4.4 to 11.9% ($0.5 \times 10^6.m^3$ to $2.6 \times 10^6.m^3$ respectively) of the effective rainfall (Table 3.5). We assume that the annual coefficient of runoff for the period 2012-2013 can be assimilated as similar as the runoff coefficient for the period 2011-2012. Thus, for the total watershed, we consider the same percentage of effective rainfall contribute to the runoff rate.

The annual groundwater recharge is relatively high and ranges from 33% to 45% of the effective rainfall in 2011-2012 and from 43% to 45% of the effective rainfall in 2012-2013. Over the period 2011-2012 and considering the three watersheds, 45.5 millions of m^3 contributes to the groundwater recharge and 64.2 millions of m^3 in 2012-2013. The groundwater recharge is closely correlated with annual precipitation rate and during the second year the precipitation rate was higher than the first one.

	2011-2012			2012-2013		
	$10^6 m^3$			$10^6 m^3$		
	Peff	Runoff	%	Peff	Runoff	%
Soka	21.5	2.6	11.9%	36.4	4.3	11.9%
Pusur	10.3	0.5	4.4%	18.4	0.8	4.4%
Brambang	37.9	2.7	7.1%	39.4	2.8	7.1%

	2011-2012			2012-2013		
	$10^6 m^3$			$10^6 m^3$		
	Peff	Base flow	%	Peff	Base flow	%
Soka	21.5	5.8	26.9%	36.4	9.8	26.9%
Pusur	10.3	2.7	26.4%	18.4	4.9	26.4%
Brambang	37.9	7.2	18.9%	39.4	7.4	18.9%

Table 3.5: Runoff and base flow volume estimation for the hydrological year 2012-2013 deduced from the portion of the effective rainfall of the year 2011-2012. The runoff values are expressed in milion of m^3 and in percentage of effective rainfall.

Nov 2011- Oct 2012

Surface (km ²)	Upper Soka			Upper Pusur			Upper Brambang			Total WS		
	mm	10 ⁶ m ³	%	mm	10 ⁶ m ³	%	mm	10 ⁶ m ³	%	mm	10 ⁶ m ³	%
	21.50			11.19			30.20			333		
Rainfall	1879	40.4	100%	1773	19.8	100%	2337	62.2	100%	1639	546.0	100%
PET	889	19.1	47%	957	10.7	55%	1027	25.0	40%	1331	443.4	81%
RET	824	17.7	44%	848	9.5	48%	945	24.3	39%	913	304.1	56%
Eff Rainfall	1055	22.7	56%	925	10.3	53%	1392	37.9	61%	658	219.3	40%
Runoff	119	2.6	6%	40	0.5	2%	95	2.7	4%			
Base flow	269	5.8	14%	244	2.7	14%	237	7.2	12%			
Deep groundwater recharge	613	13.2	33%	640	7.2	36%	930	28.1	45%			
Soil Moisture Storage	55	1.2	4%	0	0.3	1%	0	0.0	0%			

Nov 2012- Oct 2013

Surface (km ²)	Upper Soka			Upper Pusur			Upper Brambang			Total WS		
	mm	10 ⁶ m ³	%	mm	10 ⁶ m ³	%	mm	10 ⁶ m ³	%	mm	10 ⁶ m ³	%
	21.50			11.19			30.20			333		
Rainfall	2298	49.4	100%	2703	29.9	100%	2337	66.1	100%	2337	778.3	100%
PET	884	19.0	47%	932	10.3	34%	1027	29.1	44%	1342	447.0	57%
RET	840	18.1	44%	917	10.1	34%	945	26.7	40%	1187	394.9	51%
Eff Rainfall	1458	31.3	56%	1786	19.8	66%	1392	39.4	60%	1143	380.6	49%
Runoff	201	4.3	6%	72	0.8	2%	93	2.8	4%	58	40.4	5%
Base flow	456	9.8	20%	434	4.9	16%	246	7.4	11%	1084	340.2	44%
Deep groundwater recharge	1037	22.3	45%	1139	12.7	43%	966	29.2	44%			
Soil Moisture Storage	0	0.0	0%	117.8	1.4	5%	0.0	0.0	0%			

Table 3.6: Water balance estimation on the AWLR watersheds and the total watersheds (WS) for the period from Nov.2011 to Oct. 2013. The results are expressed in millimeters (mm), millions of cube meters (10⁶m³) and percentage of rainfall.

3.5 Discussion

The first uncertainty concerns the data collection. The absence of climatic and hydrological data during periods of several days can lead to an underestimation or overestimation of water balance terms. The local storm pattern of the rainfall induced a very reactive hydrological system. Thus, lacks of data on the rainfall or on the river discharge measures, even for short period (less than an hour) can lead to miss the record of these phenomenon.

We found a significant sediment transport during large events that can impair the measurement as it may change the section (river bed). Thus, continuous calibration of the height relationship of water and flow is required.

It would be preferable to perform more regular measures on the long period to calibrate the observations. Moreover, the management of the equipment is important over this kind of climate.

The PET calculation process has been developed according to linear relationships that

reflect physics processes. Its weakest point concerns the relationship between ΔT and T_{\max} . The statistical determination of each relationship involves a level of uncertainty that leads to their accumulation in the PET determination.

The method is based on the air temperature measures to be automated, because the manual measurements showed their gaps (time measuring irregular and sometimes late).

The use of the Penman method over tropical humid region and the estimation of the SMS based on the soil analysis can be questioned. The andesitic soils are still poorly known.

The PET or runoff estimation for the 2012-2013 hydrological year have to be validated by the observations. It is truly possible that the runoff has been underestimated regarding the high increasing trend of the rainfall during this period.

In order to validate this water balance interpretation and characterize the inter-annual variation of the hydrological functioning of the Eastern flank of Merapi volcano, a long term and continuous hydro-climatic data acquisition is required for the next years.

Synthesis

This part has led to characterize the rainfall and PET variability within three watersheds in the upper part of Merapi volcano (Upper Soka, Upper Pusur and Upper Brambang rivers) and within the complete study area (330 km²). The hydrological year in this region is divided in two units: a wet season, which starts in November and ends in June and a dry season from July to October.

Rainfall pattern significantly differs both in space and time, according to the historical rainfall chronicles. The hydrological year 2011-2012 has a medium rainfall rate while the year 2012-2013 has high precipitation (more than 25% than the average). On the hydrological year 2011-2012, the annual rainfall on different catchments in the upper parts ranges from 1773 mm for the Upper Pusur watershed to 2337 mm for the Upper Brambang watershed. The following year (2012-2013) shows an increasing trend of the rainfall rate, ranging from 2298 mm to 2703 mm.year⁻¹.

The PET estimation is based on Penman method with the climatic data from Gumuk and Borobudur stations. The interpretation results finds that the annual value of PET decreases according to the elevation; 1700 mm year⁻¹ at 114 m asl to 900 mm year⁻¹ at 1436 m asl. The PET annual variation is relatively low (less than 10%).

Using Thornthwaite water balance model, the RET has been estimated. The average annual RET over the three catchments is estimated at 872 mm.year⁻¹ in 2011-2012 and 900 mm.year⁻¹ in 2012-2013. The rainfall and the RET have been combined to calculate the effective rainfall for each watershed. The effective rainfall represents in average 55% of the rainfall in 2011-2012 and 60% in 2012-2013. The effective rainfall has a strong

correlation coefficient with the rainfall data, showing that the uncertainty on the PET values have a limited impact on the water balance results.

The hydrograph data have been analyzed to describe the river discharge pattern on each watershed. It led to identify two components of the discharge flow: the runoff (surface water) and the base flow (groundwater contribution). The latter shows a strong impact on the river discharge with a constant contribution for the Pusur and the Soka rivers all year long while on the Brambang river, the groundwater contribution is decreasing at the end of the dry season. The constant contribution is linked to the short distance (less than 1 km) between the water discharge measures and two perennial springs on the Soka and Pusur rivers whereas on the Brambang river, the springs are furthest upstream (6 km) and the springs are temporary.

Water balance interpretation highlights an important infiltration capacity of the upper catchments (33% to 45% of the rainfall depending on the year and the watershed). Based on the estimation of the water flow that recharges groundwater, the volume related to the zone above 400 m of elevation is estimated at approximately 48.5 million m³ during the hydrological year 2011-2012 and 64.2 million m³ in 2012-2013. These figures have to be regarded in relation with 2011-2012 rainfall pattern that seems representative of median rainfall conditions and 2012-2013 rainfall that seems representative of high rainfall condition (referring to long series rainfall data registered in Cokro-Tulung).

The water cycle on the Eastern flank of Merapi volcano combined several extreme processes which make this area very complex. The tropical location of this area brings a high rainfall rate (more than 2000 mm. year⁻¹) with an important spatial variability. Even if this kind of climate pattern have been studied before ([Cook et al., 1998](#); [Charlier, 2007](#)), the specificity of the geomorphology, geology and the contribution of the groundwater make this study area as an important piece to better understand the water cycle on the andesitic strato-volcanoes.

Hydrogeological functioning **4**

Introduction

The integrated characterization of the structure and functioning of the hydrogeological systems is essential at the watershed scale, especially in view to manage and protect the water resources. These problematics for groundwater are crucial in the specific context of humid tropical condition where water resources are generally not equitably distributed, temporally and spatially. Indeed, seasonal climate controlled by monsoon phenomenon does not make the water resources available all year long and some parts of the watershed can be a hindrance to the water storage. The issue of groundwater knowledge and its management is particularly essential in volcano-detritic andesitic context (Charlier, 2007; Foster et al., 1985). Moreover, the hydrogeological conceptual models of groundwater circulation are scarce in volcano-sedimentary environment and need update.

We saw that Merapi volcano is characterized by a large variety of facies rocks (Chapter 2). Each formation coming from several processes as sedimentation, remobilization and alteration, which can even change the morphological, hydrodynamical and chemical rock properties itself. This diversity of facies results in significant variability of the occurrence, circulation and chemistry of the groundwater. Furthermore, the hydrogeological variability can be caused not only by different geodynamic, geomorphological, climatical, geological or socio-economical processes but also by differences in hydrological factors such as rainfall, evaporation, recharge, land use and human population.

In this kind of context, we used a multidisciplinary approach to identify and better understand the hydrogeological processes at the watershed scale. After the characterization of the climatic conditions and the development of a 3D conceptual model of the geological architecture, we are able now to make the inventory of the hydrogeological features on the Eastern flank of Merapi and to develop a groundwater monitoring through them in view to propose a hydrogeological conceptual model. As the groundwater monitoring in this region is scarcely developed, the aim was to settle a long term, systematic measurements providing essential new data needed to evaluate changes in the resource over time.

The chapter is divided in two parts, the first part describes the methodology of each discipline, then in a second part, the results of these disciplines will be discussed and combined to built a hydrogeological conceptual model of the groundwater circulation.

4.1 Methodology of hydrogeological approach

4.1.1 Inventory of the monitoring points

To establish an experimental site, first the inventory of the existing hydrogeological element is necessary in order to monitor the groundwater systems along at least two hy-

drological years (2011-2012 and 2012-2013). Second, we have built a monitoring network to measure regularly (monthly or bi-weekly or continuously) physico-chemical variables, water levels, water discharges of points as springs, shallow dug wells and deep bore wells that can be used as “access” to the groundwater systems. Finally, the collected data have been gathered in GIS data base.

4.1.1.1 Spring zone descriptions

Between May 2011 and March 2013, several field surveys were done with the objective to inventory the springs around the East flank of Merapi. Over this period, several small springs stopped or do not flow at the time we made the inventory. Main of the springs have been found after (long) discussions with the local people. This inventory gathers the main perennial springs and several temporary springs with measurable flow rate (minimal $0.01 \text{ liter second}^{-1}$) but can certainly be improved in the upper parts of Merapi flank. Nevertheless, this inventory can be considered as representative of the different spring types and flow rate ranges.

There was no existing accurate and complete data base of springs in this area. The DPU of Klaten and Boyolali have a list of the major springs used for irrigation but neither coordinates or precise description of the hydrogeological properties of the springs can be found. Because the springs are the natural direct access to the aquifer systems, they are a crucial source of information to the hydrodynamic and hydrochemical properties of these systems. Thus, an inventory of springs and their detailed description is needed in our study.

More than 100 springs have been inventoried (Fig. 4.1). At high altitudes, the springs are randomly distributed and are mainly located on the side of the gullies. Lower, the springs are line up along the topographic curve 400 m elevation. We speak about *spring belt* distribution. At 200 m asl, the springs are line up but not on a topographic curve but on a NE-SW orientation. Nevertheless, as the spring alignment form a curve or a line, we speak about spring belt distribution as well. Hence, the springs of Merapi volcano can be divided in 3 zones depending on their distribution and their elevation as follows: upper springs, spring belt 1 (400 m asl) and spring belt 2 (ranging from 221 to 283 m elevation) (Fig. 4.2). Some other springs can be found near Klaten city but are outside our study area and will not be detailed here. The springs were also classified following the typology defined by Fetter (1994) into *contact springs*, *depression springs* and *fault springs*.

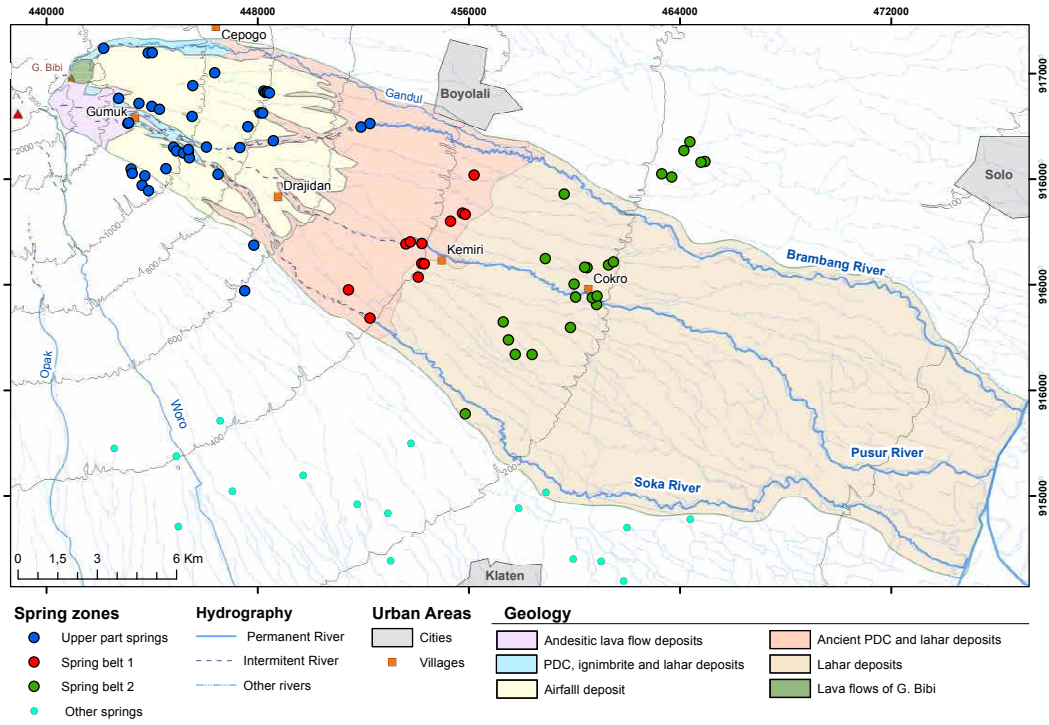


Figure 4.1: Spatial distribution of the inventoried springs. On the study area including the watersheds of the Soka, Brambang and Pusur rivers, 3 springs zones have been identified depending on their elevations.

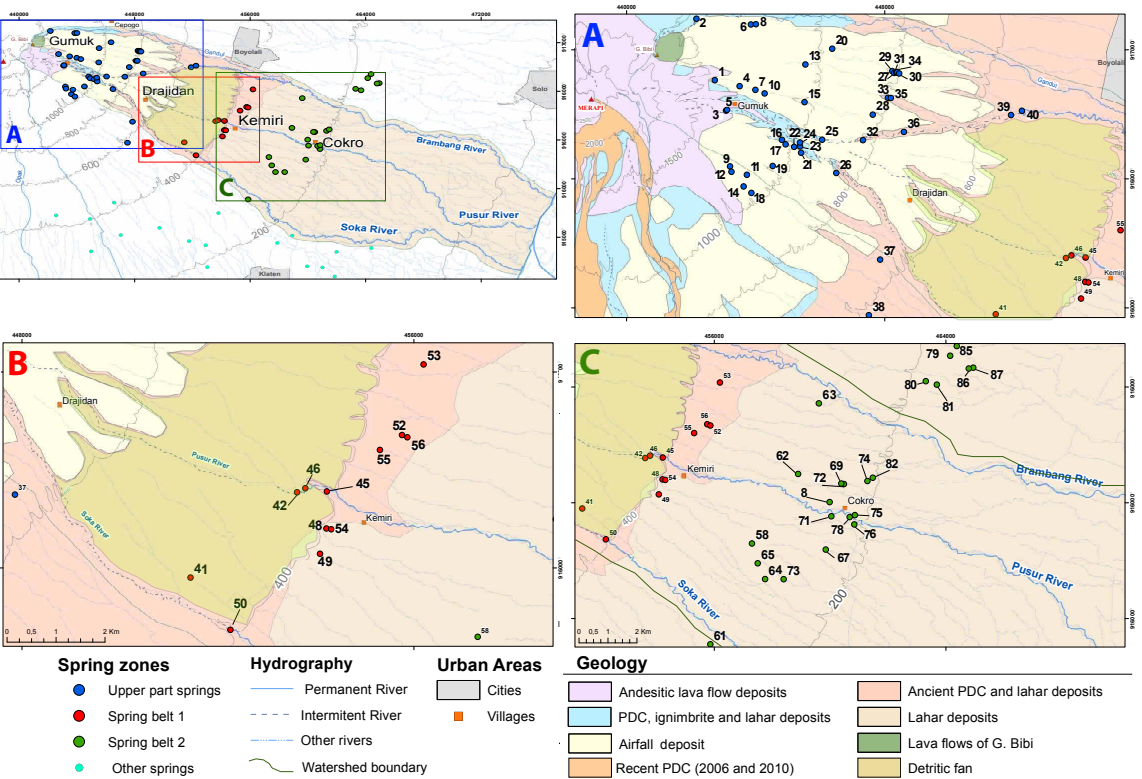


Figure 4.2: Spring zones defined depending on the spring elevations with the geological map modified after Wirakusumah et al. (1989). (A) the upper spring zone with lithological contact springs on the gully sides at the boundary between an aquifer and aquitard formation. (B) Spring belt 1, depression springs located along the topographic curve 400 m asl and covered by the detritic fan. (C) Spring belt 2, probably contact fault springs line up around 220 m asl.

The upper springs are mainly lithological contact spring type (Fig. 4.6, A), marking the limit between pyroclastic and block and ash deposits (BAF) considered as aquifer formations and indurated tuff, cook paleosol and massive andesitic lava flow, assimilated to aquitard layers. These springs located from 1500 to 600 m asl, are mainly no permanent during the dry season and have a low flow rate ($< 0.0001 \text{ m}^3 \cdot \text{s}^{-1}$) (Fig. 4.3).

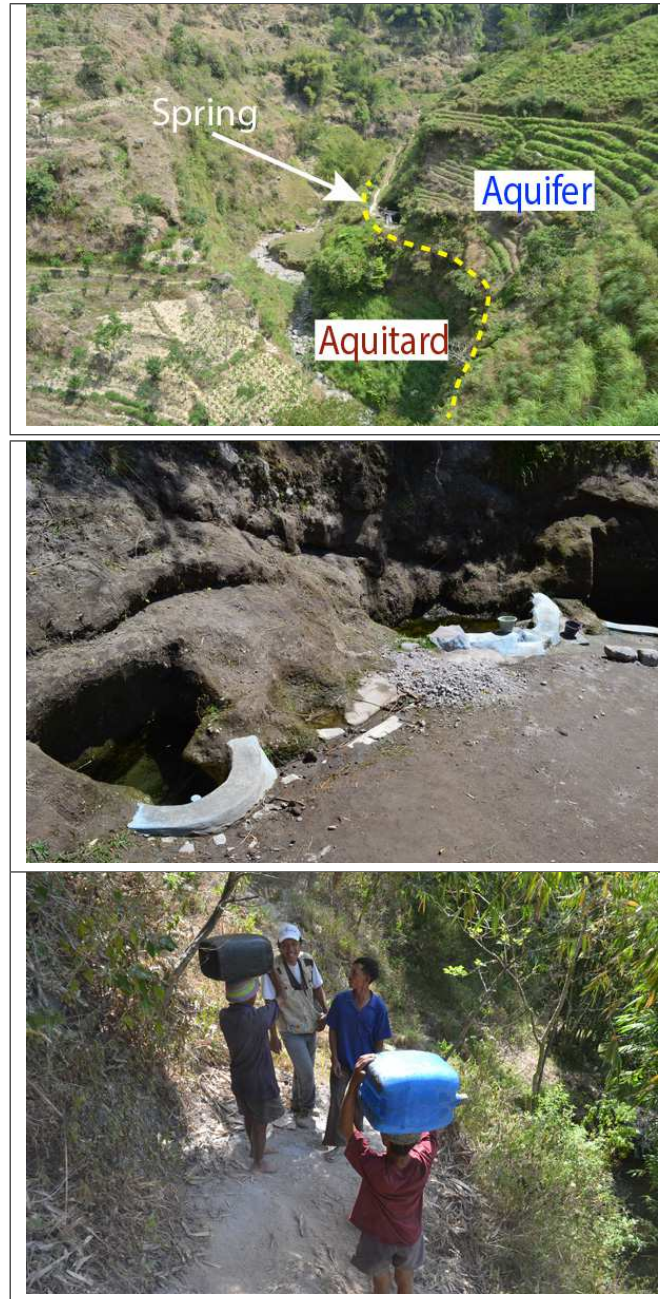


Figure 4.3: Upper part springs. UP: River incision reveals the perched aquifer layer and spring conditions are observed. MIDDLE: Small temporary springs into tuff and lapilli deposits. BOTTOM: The “Water bearers” carry the water from the springs, mainly close to the rivers to the village located on the ridge.

The spring belt 1 (SB1) is located at 400 m asl and these springs are characterized by depression springs. The regressive erosion incised into the topography until the aquifer top formations. Moreover, these springs are lined up at the boundary between the detritic fan described earlier in Chapter 2, composed by remobilized material which lays up the aquifer formed by the paleo-channels. This cover formation can give local confined properties to the aquifers. These springs flow all along the year with a relative constant flow rate (\sim

0,01 m³.s⁻¹) (Fig. 4.4).

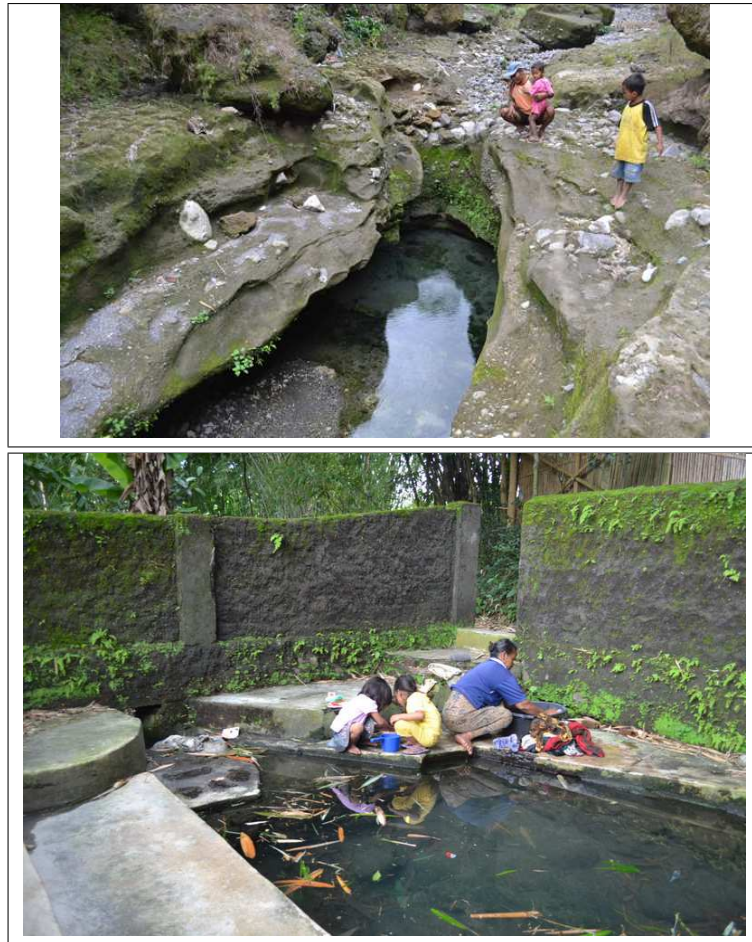


Figure 4.4: Springs on the spring belt 1 location (SB1). Pusur and Tambak springs respectively. The Pusur river is perennial with a important flow rate while the other have high seasonal variations. Tambak spring is daily used for domestic cleaning activities.

The spring belt 2 (SB2) is more complicated to explain as no lithological limit has been noticed on the field and a first interpretation could class these springs as depression springs as the contact in between aquifer and aquitard formations is not visible at the outlet and even downstream. So only the top of the water table is reached by the incision. Nonetheless, the highest flow rates observed at this SB2 ($> 1 \text{ m}^3.\text{s}^{-1}$), indicate that these springs are controlled by an important and local geological feature (Fig. 4.5). Based on the geological map presented in the first part, Chapter 1, we suppose that the continuity of the Opak fault, observed in the South-East part of the Yogyakarta basin, could play a role in the springs belt 2 distribution in Klaten area. Indeed, a major fault within the deep Tertiary formation could have an impact on the Quaternary volcanic formation and creates a discontinuity which can be combined with the slope change to explain the vertical ascent of the groundwater to the surface. Thus, the SB2 springs could

either be depression springs or fault springs. A detailed geological and geophysical survey could validate the “fault” proposition, nevertheless, as developed in the further text, the hydrodynamical data, the physico-chemical variables and the isotope analysis will allow to select an assumption. A conceptual model of the SB2 geometry will be proposed at the end of this part.



Figure 4.5: Selected springs on the spring belt 2 (SB2) location. UP: Gedong spring, with an averaged flow rate of 500 L.s^{-1} , is mainly used for village water supply (pumping foreground). MIDDLE: Sunsang spring with a is mainly used as fish farming and BOTTOM: Cokro spring with averaged flow rate above 1000 L.s^{-1} is used ofr different purposes as cities drinking supply, irrigation supply and aquatic park supply.

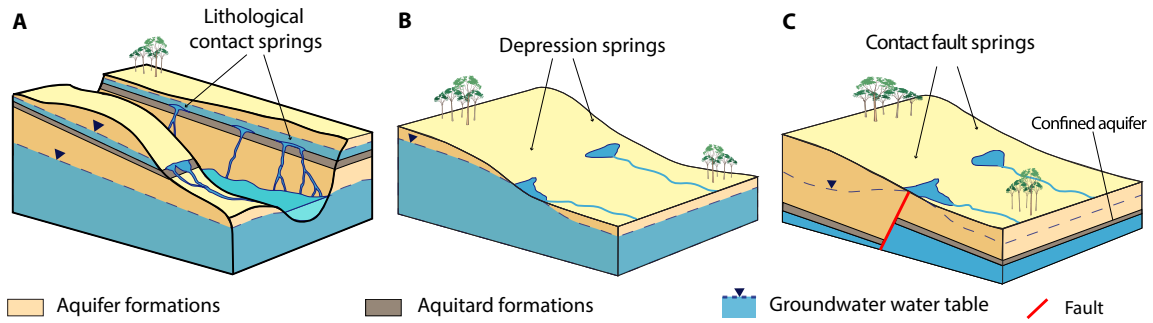


Figure 4.6: Types of springs identified on Eastern flank of Merapi volcano, terminology after [Fetter \(1994\)](#). (A) Lithological contact Springs occur where the erosion reveals the boundary between aquifer layers overlying less permeable rock or aquitards. (B) Depression springs are formed when the groundwater table intersects surface topography. (C) Contact fault springs lie along fault lines where the lithological formations have shifted from each other along the fault plan forming a barrier or a drain to groundwater movement.

In view to characterize the physico-chemical temporal variations of each spring zones, a regularly hydrochemical monitoring has been implemented in October 2011 until now (bi-monthly until August 2012 and monthly after this date). After 3 months (July to September 2011) of field surveys over all the springs, 20 springs have been selected and considered as representative to their respective spring zones (Tab. 4.1). These springs have been evaluated according to their physico-chemical criteria as the flow rate, the water temperature and their electric conductivity. The springs were selected when their values were close to the average value for all the springs of their zone.

Num.	Spring name	UTM (WGS84)		Elevation (m asl)	Spring type	Spring zone	Village	District	Regency
		X (m)	Y (m)				Desa	Kecamatan	Kabupaten
1	Jelok	442735	9167059	1396	Lithological contact	Upper	Wonolelo	Musuk	Boyolali
2	Bulu Kidul	442167	9168961	1358	Depression	Upper	Suroteleng	Selo	Boyolali
6	Wonoganggu	443853	9168783	1210	Lithological contact	Upper	Wonodoyo	Cepogo	Boyolali
7	Tutup	443993	9166758	1206	Lithological contact	Upper	Wonolelo	Musuk	Boyolali
20	Candirejo	446373	9168033	986	Lithological contact	Upper	Gedangan	Cepogo	Boyolali
26	Lanjaran	446500	9164181	875	Lithological contact	Upper	Lanjaran	Musuk	Boyolali
30	Sokorejo	448360	9167300	830	Lithological contact	Upper	Musuk	Musuk	Boyolali
38	Kali Suden	447510	9159772	591	Lithological contact	Upper	Jemowo	Musuk	Boyolali
42	Pusur	453617	9161544	446	Depression	SB1	Kemiri	Tulung	Boyolali
44	Soka	452252	9158755	435	Depression	SB1	Kayumas	Jatinom	Klaten
49	Karangduren	454085	9160288	414	Depression	SB1	Sudimoro	Tulung	Klaten
53	Slembi	456198	9164154	392	Depression	SB1	Jurug	Mojosongo	Boyolali
55	Gandol	455307	9162408	389	Depression	SB1	Tambak	Mojosongo	Boyolali
61	Jolotundo	455867	9155110	283	Fault Contact	SB2	Jambeyan	Karang Anom	Klaten
67	Ponggok	459853	9158381	259	Fault Contact	SB2	Ponggok	Polanharjo	Klaten
72	Nilo	460481	9160647	244	Fault Contact	SB2	Daleman	Tulung	Klaten
74	Pelem	461292	9160751	236	Fault Contact	SB2	Wunut	Tulung	Klaten
75	Sigedang	460828	9159296	226	Fault Contact	SB2	Ponggok	Polanharjo	Klaten
76	Kapilaler	460841	9159251	225	Fault Contact	SB2	Ponggok	Polanharjo	Klaten
78	Cokro	460678	9159505	221	Fault Contact	SB2	ꦗꦺꦝꦺꦤ꧀	Tulung	Klaten

Table 4.1: Spring monitored since October 2011 until now. The altitudes have been measured with a Differential Global Positioning System (DGPS) with an accuracy of 0.01 m.

From October 2011 to August 2012, the electric conductivity, temperature, total alkalinity, total dissolved solids (TDS) and pH have been measured on site with a field pack every 15 days on the 20 springs. As we will see in section 4.2.3, the temporal variations of the

physico-chemical variables are relatively low then in order to improve the time on the field, from September 2012 to now (beginning of 2014), the springs are monitored every month. The flow rate was difficult to measure on the upper springs regarding their very low flow rate and thus it was estimated with a bucket and a chronometer, in contrast, the flow rate on SB1 and SB2 has been measured with a current meter.

4.1.1.2 Deep and shallow well description

After the natural access to the groundwater systems, the objective was to find several points to measure the groundwater level over the time to monitor the aquifer dynamic. Two accesses were available, the shallow dug wells identified into the villages and the bore wells, used by the industrial or by private owner. The help of the NGO Bina Swadaya village facilitators allowed to access to these wells. As these wells are misinformed in terms of geology and equipment and not always available on the long term, two monitoring wells have been drilled upward and downward the second spring belt for this groundwater research study only.

4.1.1.2.1 Dug wells

Almost every house has a dug well in their backyard or sometimes inside the house itself. In view to record the water level evolution of the shallow aquifer system (less than 50 m), 15 dug wells have been selected (Tab. 4.2). The selection has been made with the collaboration of the village facilitators from the local NGO, Bina Swadaya. These village facilitators helped us to take contact with the dug wells' owners whom allowed us to perform measurements every week in their wells. The total depth of the dug wells ranges from 5 to 43 m. Most of the wells are located near the SB1 (11 wells, with depth ranging from 6 to 43 m) (Fig. 4.8). Two wells are located above 800 m asl (DW01 and DW02) with depth of 25 and 22 m. The well DW04 is located on the detritic fan zone with a total depth of 37 m. The DW03 is an ancient well, dug by the Japanese during the second world war and is the shallower monitored well with a depth of 5 m. This selection distribution is not surprising regarding the fact that the well owners allowed us to monitor their wells in the area where the access to the water is not a issue. Indeed, near the SB1, the water is relatively easily available (i.e. because of the springs, the river flow is permanent) and the owners are more prone to approve measures. In contrast at the high elevations, the water is a scarce commodity and it is more complicated to have their permission to access to their dug wells (Fig. 4.7).



Figure 4.7: Dug well near 450 m elevation (23 m deep).

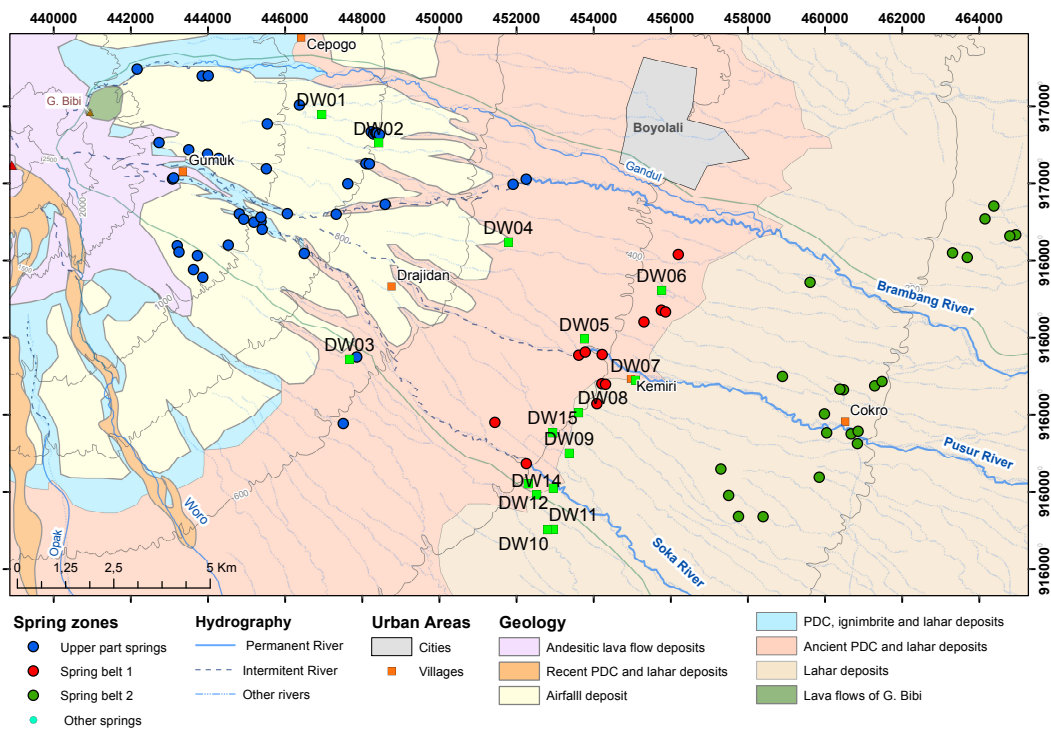


Figure 4.8: Monitored dug well locations on geological map modified after Wirakusumah et al. (1989).

In order to minimize the error on the water level records, each well elevation has been measured during a leveling campaign made in June 2012 by the Geodesic team of UGM University with a Differential Global Positioning System (DGPS). The lithology crossed by the well is unknown. The water level monitoring was carried every week with a roll meter or a electric water level probe in the morning by the village facilitators from October 2011 to January 2013 and by UGM technician after that date.

Code	Dug well name	UTM WGS84 Coord.			Total depth (m)	Pump system	Village	District	Regency
		X (m)	Y (m)	Z (m)			Desa	Kecamatan	Kabupaten
DW01	Sendengrejo	446952	9167789	953	25	No	Sumbung	Cepogo	Boyolali
DW02	Candiyoso	448427	9167052	808	22	No	Musuk	Musuk	Boyolali
DW03	Sumur Kulon	447674	9161444	646	5	No	Jemowo	Musuk	Boyolali
DW04	Giling	451795	9164479	555	37	No	Sukorejo	Musuk	Boyolali
DW05	Singosari	453762	9161971	438	30	Yes	Singosari	Mojosongo	Boyolali
DW06	Tambak	455764	9163232	378	6	No	Tambak	Mojosongo	Boyolali
DW07	Kemiri	455087	9160903	380	10	No	Sudimoro	Tulung	Klaten
DW08	Sidomulyo	453610	9160057	405	10	Yes	Mundu	Tulung	Klaten
DW09	Pomah	453368	9159009	387	13	Yes	Pomah	Tulung	Klaten
DW10	Karangsalam	452954	9157035	355	30	Yes	Glagah	Jatinom	Klaten
DW11	Karangsalam	452801	9157026	358	35	Yes	Glagah	Jatinom	Klaten
DW12	Randurejo	452951	9158104	377	30	Yes	Baru	Jatinom	Klaten
DW13	Saren	452301	9158215	400	43	Yes	Socokansi	Jatinom	Klaten
DW14	Socokansi	452526	9157929	386	35	No	Socokansi	Jatinom	Klaten
DW15	Markoasri	452939	9159538	410	17	Yes	Mundu	Mundu	Klaten

Table 4.2: Dug well monitored since October 2011 until now. The elevation of the dug wells has been measured with Differential Global Positioning System (DGPS) with an accuracy of 0.01 m.

4.1.1.2.2 Danone-AQUA bore wells

The first well (production well) was drilled in early year 2002 at 20 m from Sigedang and Kapilaler springs, in Delanggu village. A small stream flows between the Kapilaler and Sigedang spring and between Sigedang spring and BH1 as well (Fig. 4.9). This stream empties into the Pusur rivers which flows from the West and forms a meander at 90 m to the East of the monitoring well 2. This zone has been highly modified by the human activity. At 145 m to the North of the production well, the Cokro spring is used as water leisure park. This spring has the highest flow rate of Merapi flank with more than $1.3 \text{ m}^3 \cdot \text{s}^{-1}$.

Two other wells have been drilled in 2003 and 2005. The monitoring well 1 is located at 100 m from the production well and 23 m from the monitoring well 2. All these wells are artesian. A glass tube has been implemented on the monitoring well 1 in order to read directly the water level of the confined aquifer. It is at 7 m above the soil surface and no fluctuations are recorded.

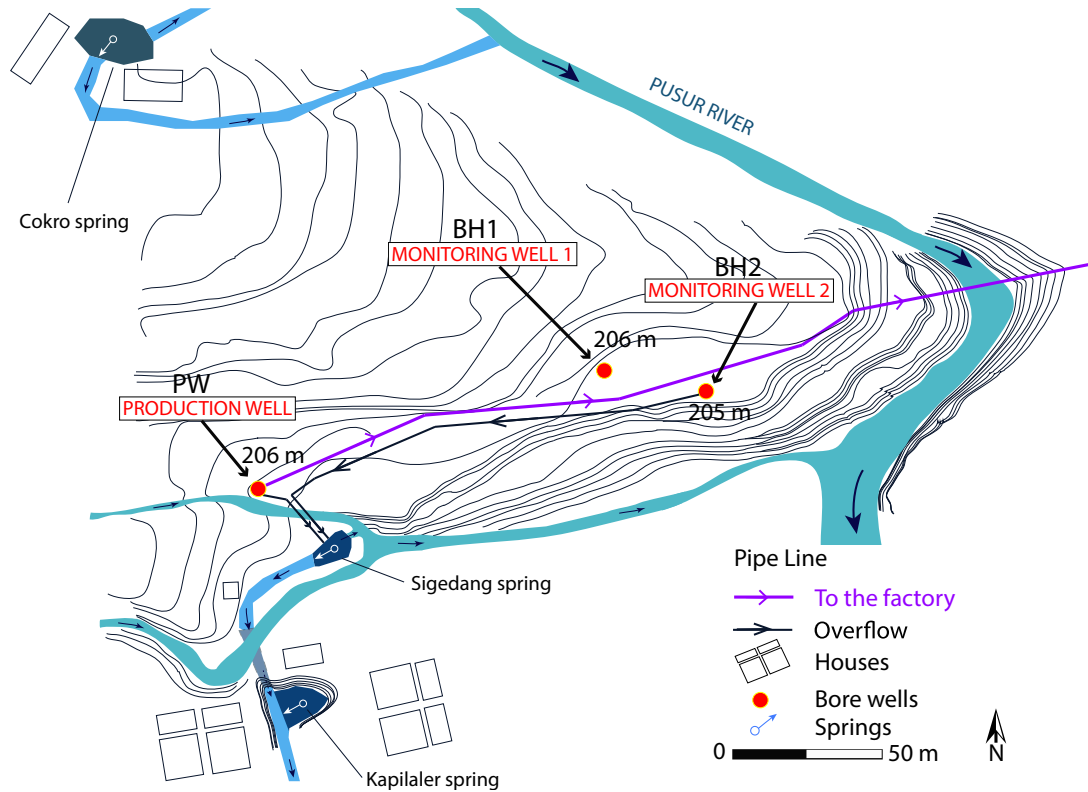


Figure 4.9: Danone-AQUA production and monitoring well location map.

4.1.1.2.2.1 *Physico-chemical variable monitoring*

Unfortunately, no hydrodynamic data are available between the well drilling and 2009. Full chronicles of hourly physico-chemical variables averaged in daily data base are only available for the period from August 2009 until now. At Danone AQUA production well, the artesian flow is measured continuously (every 5 seconds) with a automatic flow meter, as well as the discharge going to the factory used for the production, the water temperature, the electric conductivity (EC) and the pH.

As the wells are artesian, a resourceful system has been settled on BH1. A glass column has been installed on the well in order to read visually the water level above the soil surface. This installation has been done to reassure the local people about the constant level and allowing them to check the water level directly without any “machine” intermediary. At this well, only the water level is therefore measured manually every day, nevertheless, the data quality has to be discussed since a tap is connected to the tube and the gardener regularly uses this water. At BH2, the artesian flow, the temperature, the pH and the EC are measured continuously at hourly scale averaged at daily time scale.

4.1.1.2.2.2 *Stratigraphic log*

During the drilling of the Danone-AQUA wells, lithological stratigraphic logs have been established and detailed into a internal report (Kartadinata, 2002). The logs detail the lithology but also the depth of the aquifer layers. These aquifer layers have been identified during the drilling and also with a diagraphy of resistivity and spontaneous potential (data not available). For the production well, two aquifer systems have been identified (Fig. 4.10). The first formation composed of multi-aquifer layers is located between the depth 2.5 and 35 m with an impervious layer of clay from the depth 26 to 30 m which represent the first aquitard (Fig. 4.10, A and B). The aquifer lithology is composed by grey sands with gravels and few small boulders (2 - 7 cm of diameter) of andesite lava flow fragments characteristic of lahar deposits which can be assimilated to pyroclastic and remobilized deposits. The second aquifer system is situated at the depth 42 to 71 m within an alternation of sandy gravel, metric andesitic lava flow fragments and grey sands (Fig. 4.10, C). The artesian pattern of the Danone-AQUA well has been observed when the drilling reached the depth 43 m. During drilling in April 2002, the initial water level depth was measured at 2.7 m below the ground surface but the final water level is measured at 7.9 m above the ground (artesian behavior). The screen has been settled between the depth 18 and 28 m but the casing is open at 45 m deep, allowing to take water from both systems. That means that the water level is representative of the combination of two aquifer systems. The elevation of the water level are 203 m asl during the drilling and 213 m asl after the end.

In 2001, the first interpretation of the lithological stratigraphic log proposed that the aquifer was contained into a fractured lava flow deposits. We saw that according to the geological literature and our geological field survey, the fact that Merapi produced in the past lava flow deposits able to reach this distance from the summit (more than 20 km from the summit) has a low probability. Regarding the data collected during this research project, another theory is proposed and will be detailed later (cf. section 4.2.3).

For the two other wells located near the production well, two aquifer systems have also been found (Fig. 4.11). For BH1, the aquifer system 1 is located from the depth 11 to 20 m and 28 to 42 m within grey sands and andesitic boulders. The second aquifer system is between the depth 45 and 59 m with lithology composed by lava flow fragments. The aquitard formation has been identified from 26 to 30 m deep by silt and clay layers. The initial water level of this well is unknown but the final one can be “visualized” with the glass column at 7.9 m above the ground surface (i.e. 213 m asl). On BH2, the two aquifer systems are between the depth 15 and 41 m (aquifer system 1) and 47 and 62 m (aquifer 2). The main aquifer lithology is still grey sands with small boulders for the first one and andesitic lava flow fragments and sands for the second one. These aquifers are separated by 2 m of compacted fine grey sand and clay between 40 and 42 m deep. The screens have been settled between 41 and 56 m for BH1 and 43 and 59 m for BH2. Regarding to

the artesian behavior of the second aquifer system, we can suppose that if the screen was located deeper, in order to isolate the shallow and deep aquifers, the water level could be higher (i.e.: the flow rate could be more important).

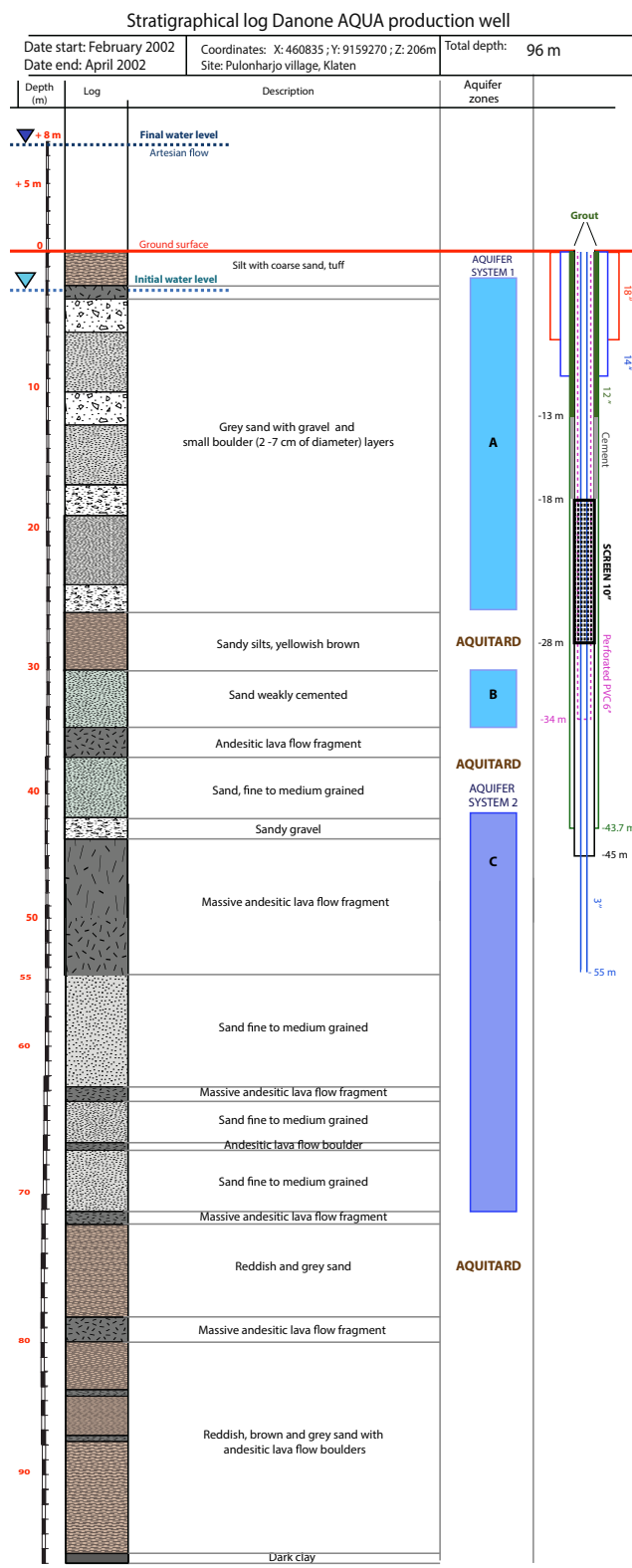


Figure 4.10: Lithological stratigraphic log of Danone-AQUA production well (PW) and the identified aquifer layers, modified after Kartadinata (2002). The elevation of the dug wells have been measured with Differential Global Positioning System (DGPS) with an accuracy of 0.01 m. On the left, on the scale, the light blue arrow represents the water level of the first aquifer while the deep blue represents the second aquifer system.

Chapter 1). These bore wells are an opportunity to monitor the deep groundwater. An inventory of the existing bore wells on our study area has been done in view to implement a monitoring network of the deep groundwater evolution. In total, more than 100 bore wells have been found on the Eastern flank, in both regencies, Klaten and Boyolali but only 30 are into our study area (Fig. 4.12). These bore wells have a depth ranging from 33 to 185 m. 17 wells are located on the detritic fan deposits (i.e. from 400 to 800 m asl). The others are concentrated on the south part of the Soka river watershed, near Klaten city. These last wells have been drilled in the Kapilaler irrigated area, major rice production place due to its close distance to Klaten city and the main transport axes. Unfortunately, the owners of the inventoried bore wells did not allow us to install any equipment in their wells. Furthermore, most of the well caps are welded, preventing any opening tentative. Nevertheless, we were able to gather informations about the wells as their total depth, the screen depth or the initial water level before pumping.

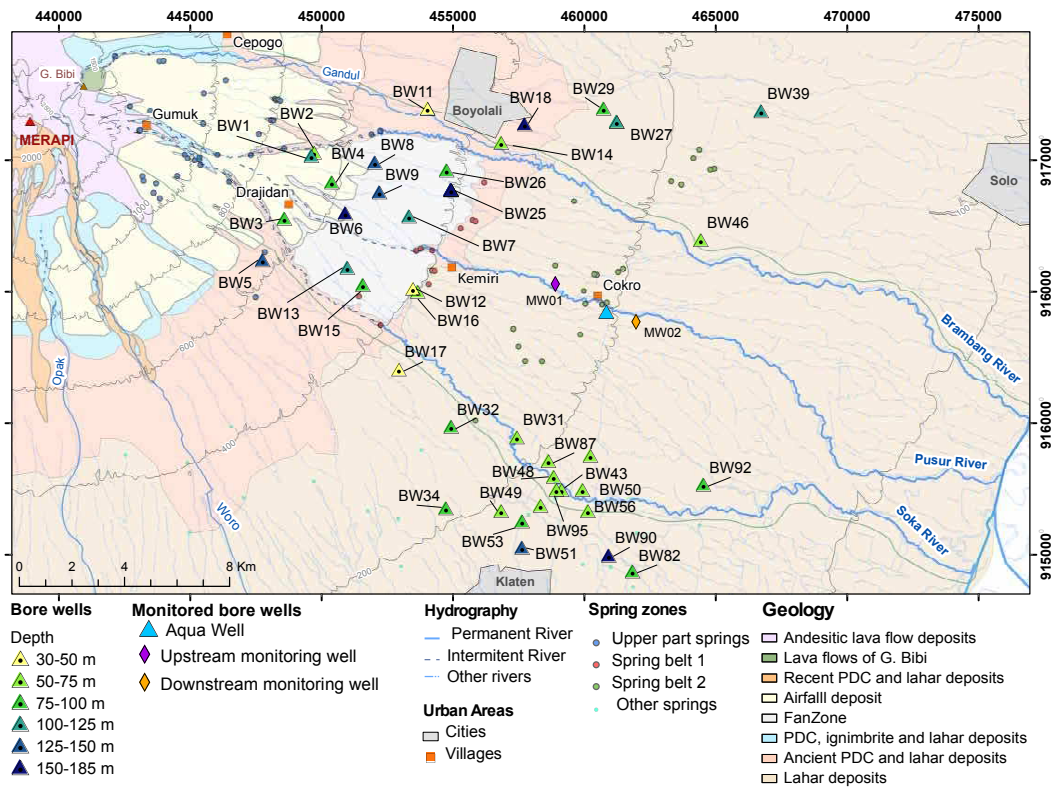


Figure 4.12: Bore wells inventoried on the Eastern flank of Merapi volcano. The color chart of the wells indicates the total depth.

4.1.1.2.4 New research bore wells

As the existing deep wells monitoring was not possible except for the Danone-AQUA wells, a drilling program has been made in view to better understand the deep groundwater dynamic. A geophysical survey has been carry out in collaboration with UPN University

(Yogyakarta, Indonesia) to determine the exact drilling location. The geological survey method is detailed in Chapter 2.

Two bore wells have been drilled upstream and downstream the SB2 between October 2012 and April 2013, near the Pusur river (Fig. 4.13). The drilling locations have been decided in collaboration with the concerned local head of villages (For MW2: *Bapak* Yudi Kusnandar, head of Karanglo village; and for MW1: *Bapak* Sunardi, head of village Pucang Miliran) and with the authorization of the Agriculture Department of Klaten Regency.

The objectives of these bore wells are: i) to better identify the lithological facies around the SB2; ii) to study the hydraulic properties and hydraulic gradient of each aquifer system around the spring belt, iii) to start a long term continuous monitoring of the deepest aquifer water level. Like on the Danone-AQUA wells, two aquifer systems have been found: a shallow and a deep one. The depth of each aquifer systems is detailed in section 4.1.1.2.4.2.

The location for the upstream well MW01 is 2.2 km to the North-West from the Danone-AQUA production well (WGS84: X: 458887; Y: 9160283; Z: 267 m asl), near Ngaldas village. The drilling start the 17th February 2013 and ended the 4th April 2013 with a total depth of 98 m. The water level depth has been measured at 11.5 m deep (255 m asl) during the drilling (19th February) and at 10.5 m (i.e. 256 m asl) at the end of the drilling operation. The increase of 1 m shows that the system is confined, but no artesian behavior has been identified.

The downstream well MW02 is located 1.2 km to the South-East of the Danone-AQUA production well (Location WGS84: X: 461978; Y: 9158983 ; Z: 191 m asl), near Karanglo village. The drilling start the 30th October 2012 and ended the 4th January 2013 with a total depth of 91 m. The water level depth has been measured at 4.5 m deep the 5th November and at 5.5 m (i.e. 185 m asl) at the end of the drilling operation. The aquifer system is hence unconfined. Since January 2013, the MW2 is monitored with a Levelogger Edge by Solinst (model 3001). The water level, the temperature and the barometric pressure is recorded every hour.

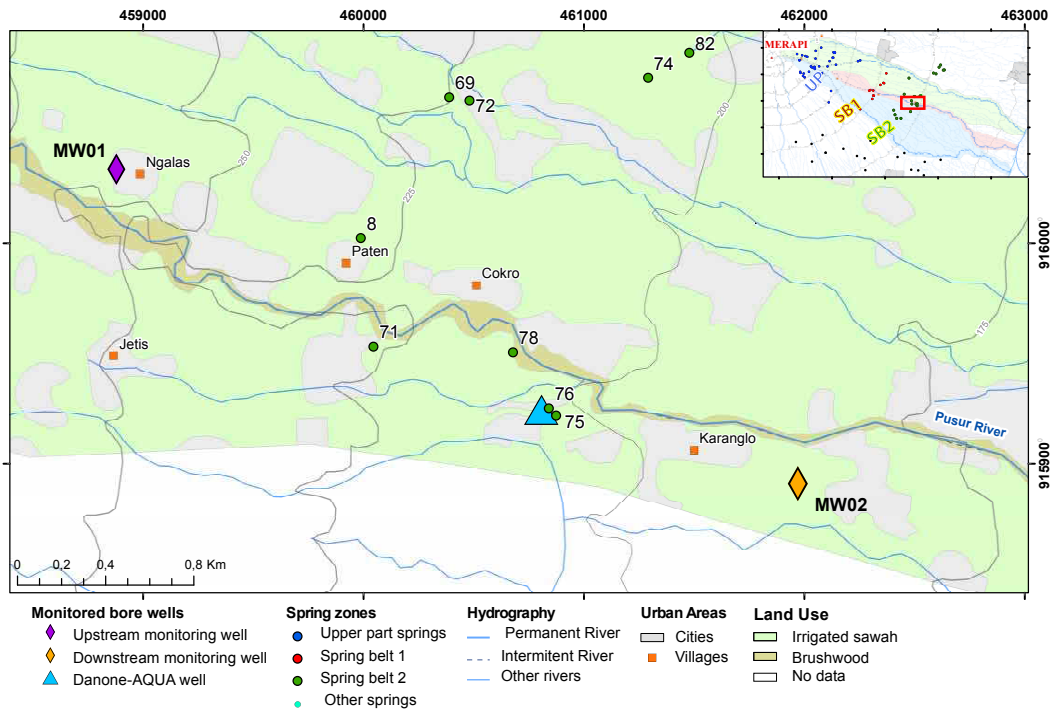


Figure 4.13: Monitored bore wells MW01 upstream the SB2, Danone-AQUA well and MW02 downstream the SB2 near the Pusur River.

4.1.1.2.4.1 *Drilling protocol*

The wells have been drilled using coring method in view to analyze the rock samples and built a stratigraphical log along the wells.

Each well was built in several steps:

1. Drilling in 6 inches (") using coring method without mud until the end of the first aquifer (Fig. 4.14, B). Implementation of two screens of 3 m. For MW1, the screens were located from 21 to 24 m and 34 to 37 m deep. For MW2 the screens were located from 9 to 12 m and 19 to 21 m deep.
2. Long pumping test (72 h) with a constant flow rate ($2 \text{ L}\cdot\text{s}^{-1}$) of the first aquifer system with a water level and discharge monitoring on the springs and the wells around.
3. Enlargement of the hole, drilling in 8" with destructive method until the end of the first aquifer (Fig. 4.14, B).
4. Grouting the 2" space between the pipe and the ground hole. To avoid any contamination between the aquifer systems.
5. Drilling in 6" with the coring method.

6. Drilling until the impermeable layer below the second aquifer (Fig. 4.14, E).
7. A final pipe 4" with a screen in front of the second aquifer level was settled (Fig. 4.14, D to E).
8. Gravel pack implementation from the bottom of the well until the grouting (Fig. 4.14, B to E).
9. Long pumping test with a constant flow rate (2 L s^{-1}) in the second aquifer with water level and discharge monitoring on the springs and the wells around. The screens were installed from 64 to 67 m and 72 to 75 m deep for MW1. They were installed from 42 to 45 m and 65 to 68 m deep for MW2.
10. Installation of the pressure and barometric probe with a direct cable inside the casing to monitor the second aquifer water level.

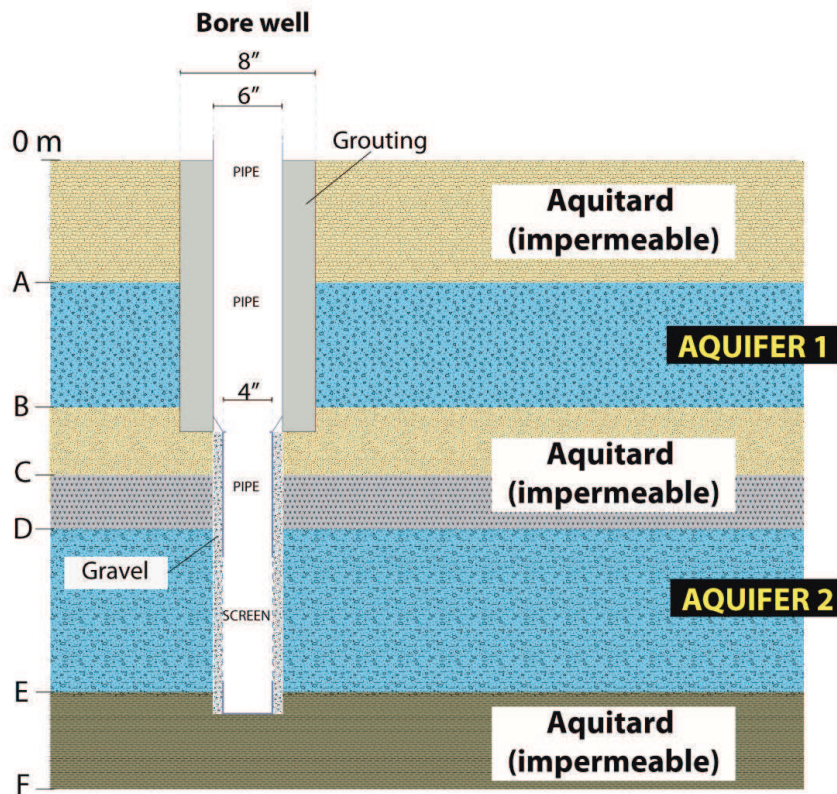


Figure 4.14: Schematic diagram of the monitoring wells (MW01 and MW02) configuration.

4.1.1.2.4.2 Stratigraphic log

As the MW01 and MW02 wells have been drilled using coring method, we were able to establish the detailed lithological stratigraphic log of these strategic locations for the understanding of the deep groundwater circulations. Upstream the second spring belt,

the log of MW01 reveals two aquifer systems. The first one is composed by an alternation of grey sands, andesitic boulders, gravels for the permeable formations (1 to 6 m thick), with clay, tuff and silt for the aquitard layers (0.5 to 2 m thick) (Fig. 4.15, A, B and C). This multilayered system has been identified from the depth 11 m to 42 m. This accumulation of permeable and impervious layers translates distinct deposit conditions with several episodes of air fall deposits (clay, tuff), eruption events (grey sands and boulders from the pyroclastic deposits) and fluvial processes (sands, gravels and blocs).

The second aquifer system is deeper, from the depth 63 to 76 m through fine grey sand and massive boulders of andesite lava flow deposits. As the initial water level depth measured at 11.5 m changed to 10.5 m (1 m higher) when the drilling tool reached this zone, this aquifer is confined which can be explained by the presence of clay at 50 m deep (Fig. 4.15, D). During the drilling, when we reached this clay layer, a pumping test of the first aquifer system has been done (See section 4.1.1.2.4.3). Then, as described earlier, the first system was isolated by cement before to drill until the aquifer system 2. Then, another pumping test was performed. In view to monitor the evolution of this second aquifer system, two screens of 3 m long have been implemented at 64-67 m and 72 -75 m to record the water level fluctuation of the second aquifer only.

Downstream the SB2, at MW02, the aquifer systems are divided in 4.5 to 33 m deep for the shallow one and the deep one is in two parts, 43 m to 51 m deep and 62 to 70 m deep. The same configuration is observed as at MW01: i) Aquifer system 1 is a multilayered system with sand, clay and gravel characteristic of several deposit processes (Fig. 4.16, A and B), ii) the second aquifer system is located into sandy layers with andesitic lava flow boulders which can come from a lahar formation without the clay matrix (Fig. 4.16, C and D). Like for MW01, a first pumping test was performed on the aquifer system 1 and the aquifer system 2. At the end, the final screens have been settled at 42-45 m and 65-68 m deep to record the water level fluctuation of the second aquifer only.

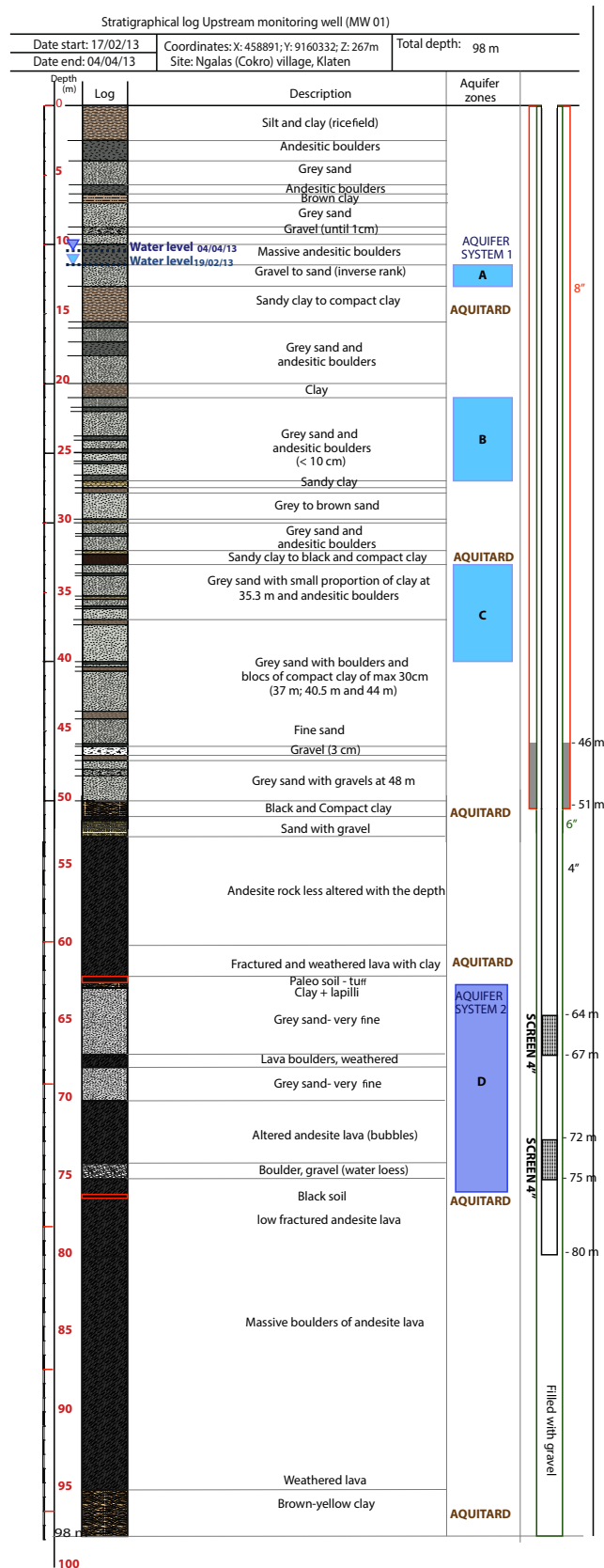


Figure 4.15: Lithological stratigraphic log of the monitoring well (MW01) located upstream the spring belt 2 and the identified aquifer layers. The elevation of the dug wells have been measured with Differential Global Positioning System (DGPS) with an accuracy of 0.01 m. The water level has been measured for the first aquifer system the 19/02/2013 (clear blue) and for the second one the 04/04/2013 (deep blue). As the water level of the deep aquifer is above the first one, the second aquifer system is confined.

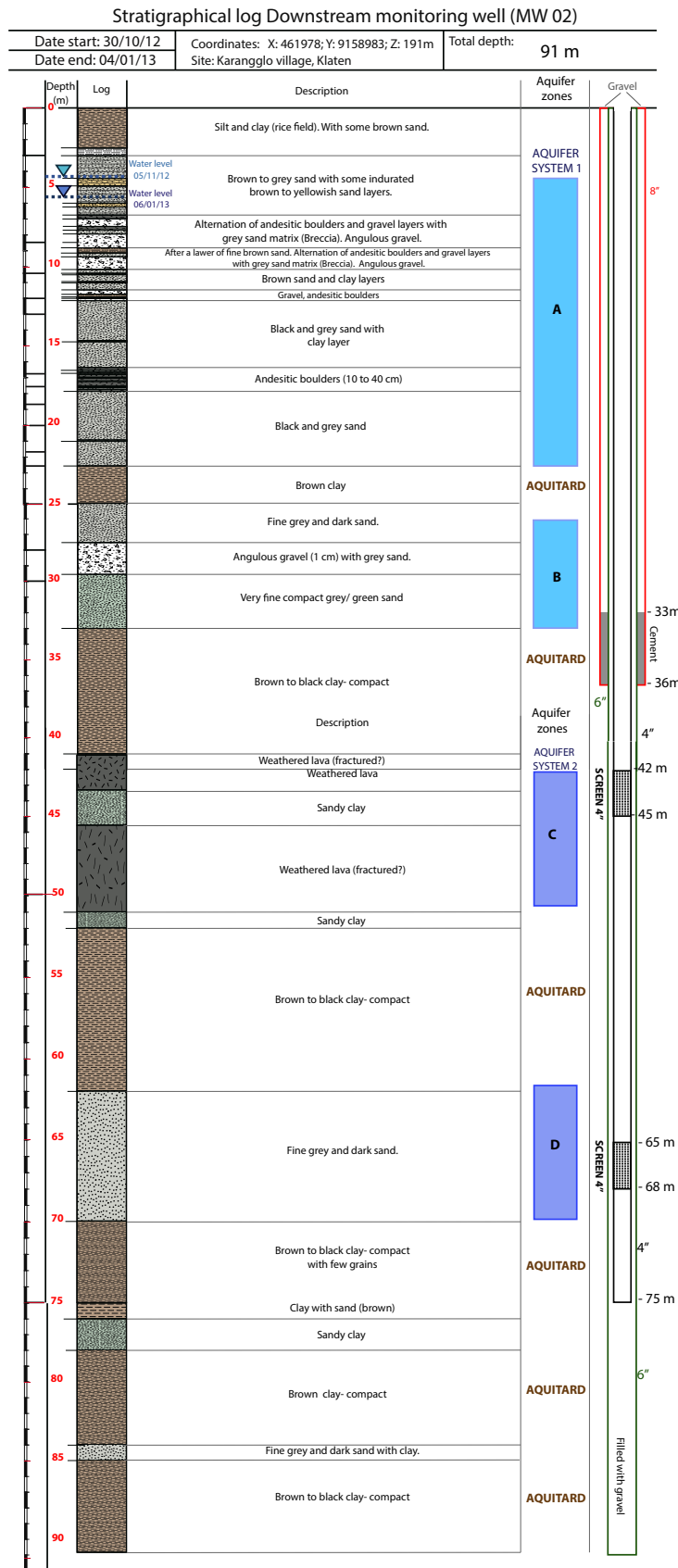


Figure 4.16: Lithological stratigraphic log of the monitoring well (MW02) located downstream the spring belt 2 and the identified aquifer layers. The elevation of the dug wells have been measured with Differential Global Positioning System (DGPS) with an accuracy of 0.01 m. The water level has been measured for the first aquifer system the 05/11/2012 (clear blue) and for the second one the 06/01/2013 (deep blue). As the water level of the deep aquifer is below the first one, the second aquifer system is unconfined.

4.1.1.2.4.3 Hydraulic test protocol

The principle of a hydraulic test and especially here, long duration pumping test, involves applying a hydrodynamic stress to an aquifer by extracting groundwater from a pumping well. Response data from pumping tests are used to estimate the hydraulic properties of aquifers. The long duration pumping test is performed at a constant flow rate for a period of time. The drawdown is measured as a function of time into the pumping well. These measurements are then incorporated into an appropriate well-flow equation to calculate the hydraulic parameters of the aquifer such as hydraulic conductivity and transmissivity. In view to estimate the storativity of the aquifer, an observation well is required at less than 100 m from the pumping well. In our case, there was no observation well, thus the storativity could not be estimated.

Because Merapi is a volcano-sedimentary edifice, the majority of the deposits can be assimilated to a porous media. Thus, for the hydraulic test, the methods used are not those used in fractured basaltic volcanic environments but the method developed in porous sedimentary media. The method is detailed in Appedix C.

In total, four hydraulic tests have been performed on both MW01 and MW02. But only three are valid. The pumping test data on the deep aquifer of MW1 are not continuous and several major equipment troubles on site do not allow to proceed at one relevant interpretation. No piezometric well were available during the pumping thus S_y estimation was not possible.

On each monitoring well, one pumping test on steady flow was done on the shallow aquifer system considered as unconfined (during 42h the 07/12/2012 for MW02 and 44 hours the 05/04/2013 for MW01) and one pumping test with constant flow rate on the second aquifer system, considered as confined at the MW1 (during 41 hours the 31/01/2013 for MW02 and 30/08/2013 for MW01 which is the non-valid test). All the tests were done with a constant flow rate of $0.002 \text{ m}^3 \cdot \text{s}^{-1}$ (i.e. $2 \text{ L} \cdot \text{s}^{-1}$) with a single pump disposed between the two screens (i.e. not directly in front of the screen to avoid well compaction on the side of the casing). The results and interpretation of the pumping tests are described in section 4.2.2.2.

The pumping tests of the shallow aquifer for MW1 and MW2 in December 2012 and January 2013 have been complicated by several rain events and several tests have been done. The results present here are the most complete data.

Water level observations are susceptible to distortion due to the influence of fluctuations in barometric pressure. These distortions can be significant in aquifer test cases or water level monitoring where interference due to pumping effects or water level variations are small, because barometric pressure effects can make up a large proportion of the total observed water level fluctuations. It is therefore important to consider, and correct for, effects of barometric pressure changes when analyzing aquifer test water level data. The

pressure measurement recorded by a pressure DIVER probe into the well is the total pressure, (i.e. sum of standing head of water above the probe plus the pressure induced by the atmosphere). In order to represent only the water level changes (i.e. the actual water level record), the barometric pressure must be subtracted (Clark, 1967; Furbish, 1991; Quilty & Roeloffs, 1991; Rasmussen & Crawford, 1997). That is why we have installed a barometric probe near the cap of the well MW2 to measure at the hourly scale the atmospheric pressure. The record is then subtracted to the pressure measured into the well, in order to only keep the water pressure variation.

4.1.1.3 Geochemical analysis

Isotopic information can be used to interpret the origin and mode of groundwater recharge, refine estimates of time scales of recharge and groundwater flow, decipher reactive processes, provide paleohydrological information, and calibrate groundwater flow models. Each groundwater system in an area is known to have a unique chemistry, which is acquired as a result of chemical alteration of the meteoric water recharging the system. Hence, hydrochemistry can be interpreted to understand the key processes that have occurred during the movement of water through aquifers and to obtain information about the recharge, the rate and direction of movement, the nature of the aquifer through which it has circulated and anthropogenic activities influencing it (Glynn & Plummer, 2005).

Isotope hydrology is a key to understand fundamental physical, chemical, biological, and climate forcing processes occurring in a watershed. Isotopes can help address, among other hydrological aspects, areas of recharge and discharge as well as cross-boundary groundwater flow and river-aquifer interactions. Water molecules carry unique fingerprints, based in part on differing proportions of the oxygen and hydrogen isotopes that constitute all water. Studies of groundwater within volcanic areas using isotopic tracers have previously shown their efficiency (Scholl et al., 1996; Mulligan, 2006; Demlie et al., 2007; Asai et al., 2009; Yitbarek Baye, 2009; Bertrand, 2009; Bertrand et al., 2010; Mandal et al., 2011).

In the present work, an attempt is made to sample water in the Eastern flank of Merapi giving emphasis to the aquifer systems. Sampling campaigns have been performed both in dry and wet seasons to define the temporal variability of the groundwater, the isotopic pattern and their datation. The samples were analyzed for their stable isotopes, tritium and carbon 13 and 14.

4.1.1.3.1 Isotope analysis

4.1.1.3.1.1 Stable hydrogen and oxygen isotopes

The ocean is the ultimate source of groundwaters and its hydrogen and oxygen stable isotope composition is quite constant (Gat, 1996). Evaporation processes are more effective

for the light water molecules, thus, clouds are relatively depleted in heavy isotopes. Over the lands, clouds start to condense and the first rains are enriched in the more condensable heavy isotopes. The rest of the clouds becomes weakened in heavy isotopes, therefore, rain is progressively lighter as the raining out of cloud proceeds. As a result, rain tends to be lighter the further inland it is or the higher clouds rise up a relief. [Gonfiantini et al. \(2001\)](#) have shown that in tropical regions, the slope of the isotopic composition of precipitation versus altitude and the initial isotopic composition of atmospheric vapor change seasonally and appear to be related to the amount of precipitation: in wet months the isotopic gradient vs. altitude is larger than in dry months.

Groundwater have an isotopic composition primarily related to the composition of the recharging rains. During the passage through the aquifers, the isotope composition of water is essentially a conservative property at ambient temperatures. The isotope composition of groundwaters are thus useful tools for identifying recharge sites (utilizing geographic effects on the isotopic composition of rain, such as the altitude effect), tracing mixing patterns ([Bertrand, 2009](#)).

During the sampling survey of March and November 2012 (end and beginning of the wet season respectively), 10 samples were destined for isotopic analysis (Oxygen ^{18}O , Deuterium ^2H and tritium ^3H). They were conserved into brown glass bottles at ambient temperature (25°C). The isotopic composition of rainwater and groundwater were measured by mass spectrometry at the Laboratoire d'Hydrogéologie d'Avignon (France). The results are expressed in ‰ versus VSMOW (Vienna Standard Mean Ocean Water). The uncertainties are respectively of $\pm 0.15\text{‰}$ for $\delta^{18}\text{O}$, $\pm 1\text{‰}$ for $\delta^2\text{H}$ and $< 0,4$ Tritium Unit (TU) for ^3H .

4.1.1.3.1.2 Tritium

Tritium is produced naturally in the upper atmosphere by interaction of nitrogen, and, to a lesser extent, oxygen with cosmic rays (solar radiation), although much greater production accompanied the atmospheric testing of thermonuclear bombs between 1951 and 1980. Tritium's short half-life and recent anthropogenic production make it an excellent indicator of modern groundwater recharge.

The average natural pre-atomic bomb tritium content in rain was 5 to 10 TU ([Carlston et al., 1961](#)). After the nuclear tests, the values rose in 1963 to about 800 TU in the northern hemisphere and up to 60 TU in the southern hemisphere ([Happell et al., 2004](#)). With the reduction of the nuclear tests since the 90's, atmospheric tritium values gradually decreased to the global present value of a few tens of TU ([Mazor, 1975](#)). This man-made introduction of tritium enables us to determine the age of groundwater in terms of being recharged prior or post atomic bomb tests. Considering the half-life of tritium (12.3 years), water with a high concentration of Tritium can be considered as "recent" water

(after 1951). The figure 4.17 shows the temporal evolution of Tritium in the precipitation at Jakarta (Indonesia, 445 km from Merapi, over the period 1959-1997) and Quezon city (Philippines, 2715 km from Merapi, for the period 1999-2007) (IAEA-WMO, 2001). The decreasing trend of the tritium concentration has been extrapolated for the Jakarta station in view to determine the value in 2012.

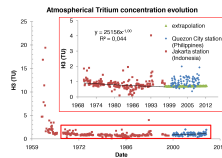


Figure 4.17: Atmospheric Tritium concentration time evolution at Jakarta (Indonesia) between 1959 and 1997 completed by the data from Quezon city (Philippines) between 1999 and 2007 and the data extrapolation until 2012 based on the trend line equation. IAEA-WMO (2001)

4.2 Results

In order to establish a conceptual model of the groundwater circulations, all the results from the pluri- disciplinary approach described above are assembled in this section. First, the aquifer systems will be detailed in two parts: i) the shallow aquifer system will be described through the water level monitoring into the dug wells located above 400 m of elevation, ii) the deep aquifer system will be characterized by the water level monitoring and the new pumping tests performed on the monitoring wells (MW1 and MW2). Second, the springs physico-chemical variables temporal and spatial evolution will be outlined with the identification of the potential groundwater tracers. Third, the results of the hydrogeochemical approach will be presented with the input of the stable isotope analysis on the understanding of the groundwater circulation.

4.2.1 Shallow aquifer

This section presents the shallow aquifer unit located between 900 to 200 m asl. Above 600 m asl, the groundwater occurrence is represented by several small perched aquifers drained by temporary small lithological contact springs. The relief of the landscape is highly rugged and most of the slopes are steep (until 45°). The settlements are scarce on this sharp topography and are mainly establish on the ridges formed by the accumulation of ashes and airfall deposits accumulated on massive lava flow formations. The extend of the perched aquifer is relatively limited and the thickness of the unsaturated zone can be important. Moreover, we saw that the upper part of the volcano has a role of recharge area. Therefore, the monitoring of the monitoring of the shallow aquifer was focused on the dug wells between 400 to 900 m asl.

The dug wells are usually shallow (less than 30 m deep) and incise the first aquifer system composed by an alternation of aquifer (brown to grey sand, gravel decimetric coarse lava blocks) and aquitard (welded tuff, burnt paleo-soil and fine compacted ash). Most of the wells have a pumping system mainly used during the dry season (June to October) at the flow rate of at least three hours per day. The wells DW02 located above 600 m asl has been drilled in several steps because of the decrease of the water table since a decade. However this decrease was not observed at DW01 well, which is shallower.

The Fig. 4.18 and Fig. 4.19 show the average monthly water level on the 15 monitored dug wells located from 355 to 953 m elevation) compared with the monthly effective rainfall at 1456 m asl (Gumuk station) and 631 m asl (Musuk station). These stations represent two different recharge areas: Gumuk station is located at the upper boundary of the watershed and quite far from the dug wells whereas Musuk station is relatively close to wells and can bring informations on the direct and local recharge to the shallow aquifer.

Three trends can be noticed:

- 1) (red titles on the Fig. 4.18 and Fig. 4.19) On 5 wells (DW10, DW11, DW12, DW13 and DW14), the water levels presents a low decreasing trend from October 2011 to October 2012 (0.5 to 1 m of decrease) then a relative rapide increase (more than one meter up) after a maximum in August 2013 (ranging from 329 to 352 m asl).
- 2) (green titles on the Fig. 4.18 and Fig. 4.19) On 8 wells (DW01, DW02, DW03, DW06, DW07, DW08, DW09 and DW15), the water level presents seasonal oscillation with an increase from February to April and a minimum in October and November. The water level oscillation ranges from 0.6 to 1 m).
- 3) (blue titles on the Fig. 4.18 and Fig. 4.19) The last trend is observed on 2 wells (DW04 and DW05) with a water level relatively stable through the year 2011-2012 and a significant decrease (1meter for DW05 and 3 meters at DW04) at the end of 2013.

It appears that even if the wells are relatively close to each other (less than 200 m for the wells DW13 and DW14) their water levels have a large range (12 m of difference for these same wells). This important difference shows that the dug well water level measurements are probably not representative of one unique aquifer.

These measures demonstrate the strong impact of the precipitation on the shallow aquifer systems. The peak in the middle year 2013 identified in the trend 1 is consistent with the high rainfall during the year 2012-2013 that occurred in December-February 2013. The water level decrease (trend 1 and 2) into the wells following the second trend can be explained by the rainfall distribution which was relatively low in this area during the year 2011-2012. The last trend (3) shows that the water level is not impacted by the recharge in 2011-2012 but the increase of rainfall produced an increase in 2012-2013. It seems that the water level growth into the shallow aquifer systems is subject to a threshold effect for

this zone (located on the detritic fan).

The shallow aquifer seems reactive to the climatic seasonal variations with a delay ranging from three months (e.g. DW01 or DW07) to six months (e.g. DW04). This time probably corresponds to the water transit time through the unsaturated zone composed by low permeable material (welded tuff, air-fall deposit). The water level variations of the shallow aquifer system stay relatively low: less than three meters and for the wells majority, the variations range on less than one meter. This behavior is representative of porous aquifer with thick unsaturated zone.

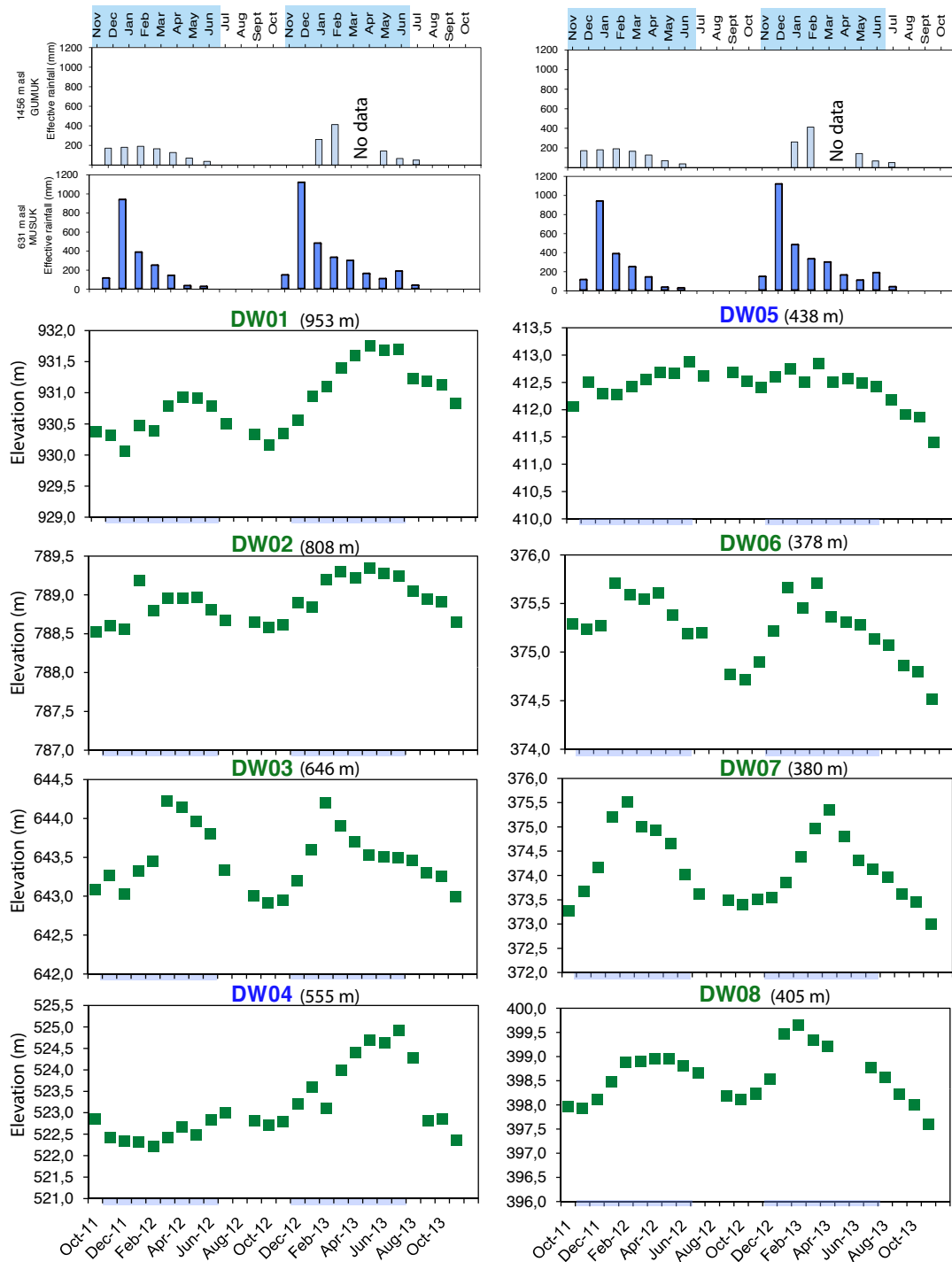


Figure 4.18: Monthly average water level (bi-monthly measurement) elevation of the 15 monitored dug wells (first part) compared with the monthly rainfall at two elevations (Gumuk, 1456 m asl and Musuk, 631 m asl). The rainy season period is highlighted in blue. The error on the water level measurement is 0.1 m. Three variation trends can be observed (cf Text): dug wells with Red titles= trend 1; Green titles= trend 2; Purple titles= trend 3.

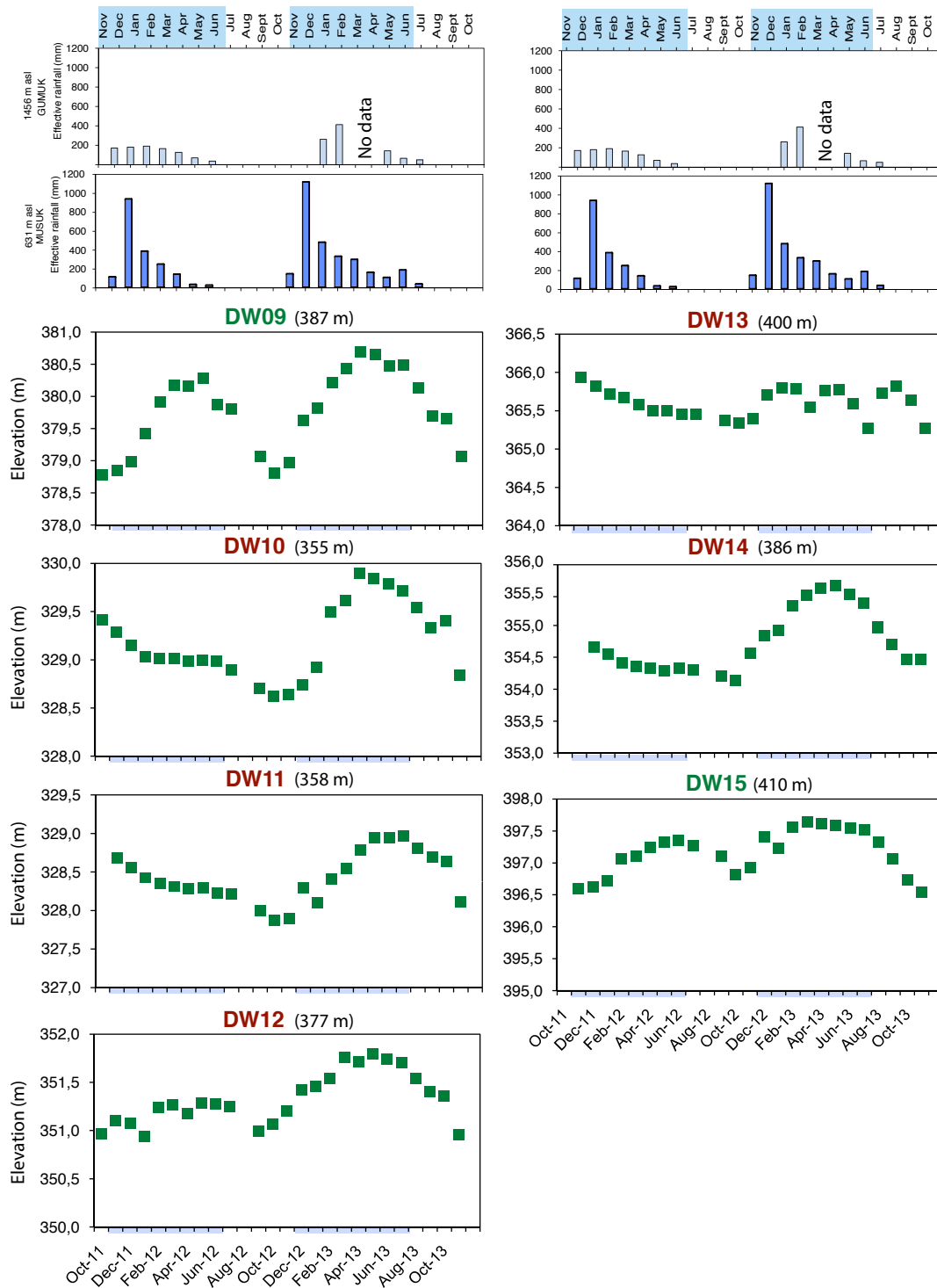


Figure 4.19: Monthly average water level (bi-monthly measurement) elevation of the 15 monitored dug wells (second part) compared with the monthly rainfall at two elevations (Gumuk, 1456 m asl and Musuk, 631 m asl). The rainy season period is highlighted in blue. The error on the water level measurement is 0.1 m. Three variation trends can be observed (cf Text): dug wells with Red titles= trend 1; Green titles= trend 2; Purple titles= trend 3.

The water level monitoring allows us to draw the piezometric map of the shallow aquifer at specific date (Fig. 4.22). We choose to use the end of the dry season (September 2012) considering the low variations during the years (less than three meters). The spring elevations and the water level measurements into the dug wells have been taken as reference for the piezometric lines. The shallow aquifer is a multi-layered system (Fig. 4.20) and the hydraulic gradient between the water level measurements have to be taken carefully. Regarding the high incision of the rivers, the river bed elevations have not been used to draw that map as the aquifers are mainly perched and probably disconnected each others. The springs occur along the river incisions showing that the rivers drain the shallow aquifer. Nevertheless, the river flow disappears along the river bed, showing that the temporary river beds are a preferential infiltration zone.



Figure 4.20: Multi-layered configuration with alternation of pervious (grey andesitic boulders and gravels) and impervious layers (brown tuff and compacted ash) assimilated similar at the shallow aquifer (Brambang river).

The dug well water level monitoring leads to a better understanding of the shallow aquifer system that can be summarized in a simple conceptual model (Fig. 4.23). The shallow aquifer system observed through the dug wells (at least the first 30 m below the ground surface) is composed by an alternation of aquitard (welded tuffs, air-fall deposits) and aquifer (sand, ignimbrite, decimetric lava blocks) formations. During the dry season, several disconnected perched aquifer formations provide a constant but low water level into the dug wells. As the perched aquifers are disconnected, the measured piezometric head is not representative of a regional and unique aquifer, thus important variation of water table elevations can be observed. When the river incision crosses the perched aquifer, several perennial springs flow into the dry river bed, which is a preferential zone for the deep infiltration and groundwater recharge. Indeed, the remobilized material (metric

lava blocks, coarse and gravel material) is highly permeable and allows an important infiltration (Fig. 4.21).



Figure 4.21: Dry river bed composed by remobilized and unconsolidated boulder and lava block which create a preferential zone for water infiltration compared to the river edges composed by thick ash airfall and tuff deposits.

During the wet season, the water level increases while the water infiltrates into the unsaturated zone and reaches the different aquifer layers. The temporary springs flow when the soil saturation threshold is attained. The water transit time through the unsaturated zone ranges between few days to 3 months according to the water level measurements. The run-off is accumulated into the river bed which is rapidly saturated and creates a river flow. At the end of the rainfall event, the river flow will seep and supply the groundwater recharge.

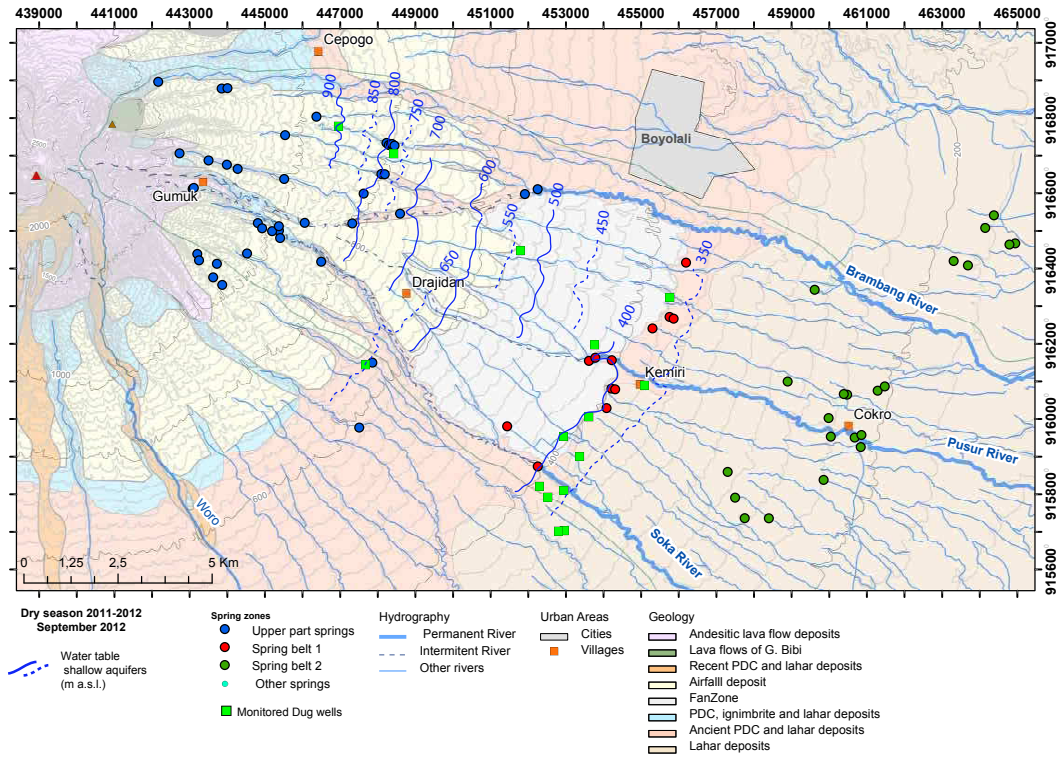


Figure 4.22: Piezometric map of the shallow aquifer at the end of the dry season 2011-2012 (September 2012) based on the water level monitoring of 15 dug wells.

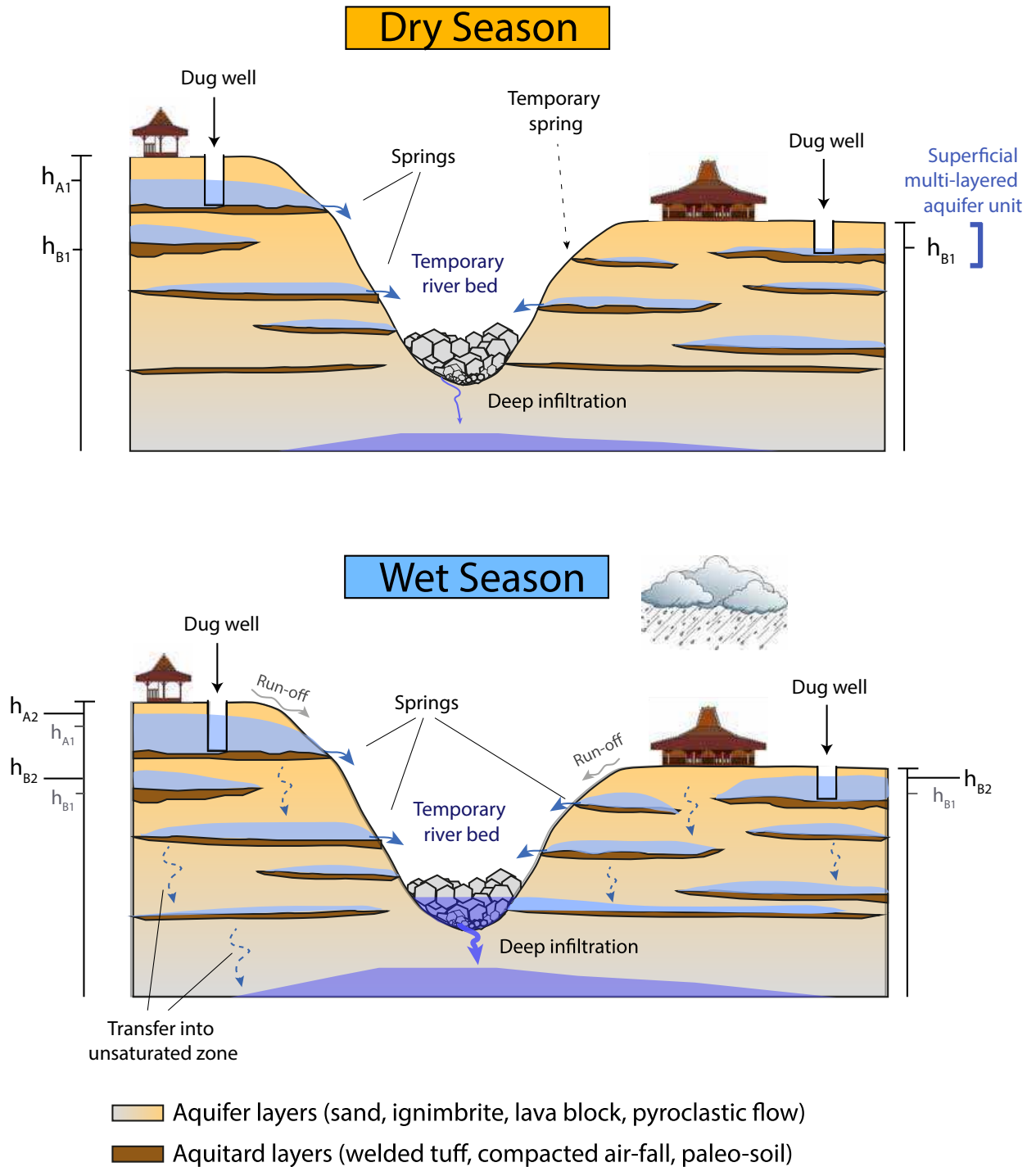


Figure 4.23: Illustration of the seasonal water level variations of the upper part of the shallow multi-layered aquifer system measured into the dug wells. The shallow aquifer system (at least until 30 m below the ground surface) is composed by an alternation of aquitard (welded tuffs, air-fall deposits) and aquifer (sand, ignimbrite, decimetric lava blocks) formations. During the dry season, several disconnected perched aquifer formations provide a constant water level into the dug wells. Where the river incises the perched aquifer several perennial springs flow into the dry river bed, which is a preferential zone for the deep infiltration and groundwater recharge. During the wet season, the water level increases while the water infiltrates into the unsaturated zone and reaches the different aquifer layers.

4.2.2 Deep aquifer

As the same way the dug wells brought information about the hydrodynamic behaviour of the shallow perched aquifer in the upper parts, the water level recorded in bore wells near the spring belt 2 are keys to understand the groundwater dynamic near a main discharge area.

The artesian flow rate of the Danone AQUA production well is crucial in the understanding of the spring zone. If we compare the chronicle data of rainfall with this evolution, considering that the effective rainfall contributes to the recharge of this aquifer system, we can identify the reactivity of the aquifer to the seasonal variation and estimate the transfer time.

The Fig. 4.24, shows the daily evolution of the artesian flow rate at the bore well exploited by Danone AQUA on the period October 2009 to December 2013. It is compared with the evolution of the daily rainfall in Musuk station, located at 631 m asl. As we do not have an evaluation of the PET over the historical data, we were not able to compare the water level fluctuations with the effective rainfall.

The flat signal of flow rate from October 2009 to June 2009 is due to bad calibration of the flow rate recorder. The artesian flow rate follow an increasing trend from 5200 m³.day⁻¹ and reaches a peak at 5780 m³.day⁻¹ in November 2011. The flow rate slightly decreases after November 2011 to stabilize at 5400 m³.day⁻¹. The increase occurs after the hydrological year 2009-2010, which had the maximum annual cumulated rainfall over the observed period (3153 mm for Musuk station). It is clearly visible that during the dry season 2009-2010, the monthly rainfall rate is strangely high with more than 200 mm in August, usually the driest month of the year.

The National Oceanic and Atmospheric Administration (NOAA) reported that El Niño conditions spotted in 2009. El Niño events are characterized by dry conditions over West Pacific. Nevertheless, [Clarke \(2014\)](#) have noticed high rainfall rate in Philippines few months before the El Niño of 2009. According to them, this El Niño event was preceded by La Niña. Conventionally in these regions, La Niña events are generally wet. This has been explained by the presence and greater chances of formation of vertical shear winds during La Niña events which is not present during El Niño events. Thus, the 2009 events are consistent with the empirical observation that in Indonesia, such as in the Philippines, wet conditions precede an El Niño event.

Supposing that the water infiltrated near Musuk station during the 2009-2010 hydrological year, could explain the peak of the artesian flow rate recorded in AQUA well in 2011, that suggests a transfer time longer than the hydrological year.

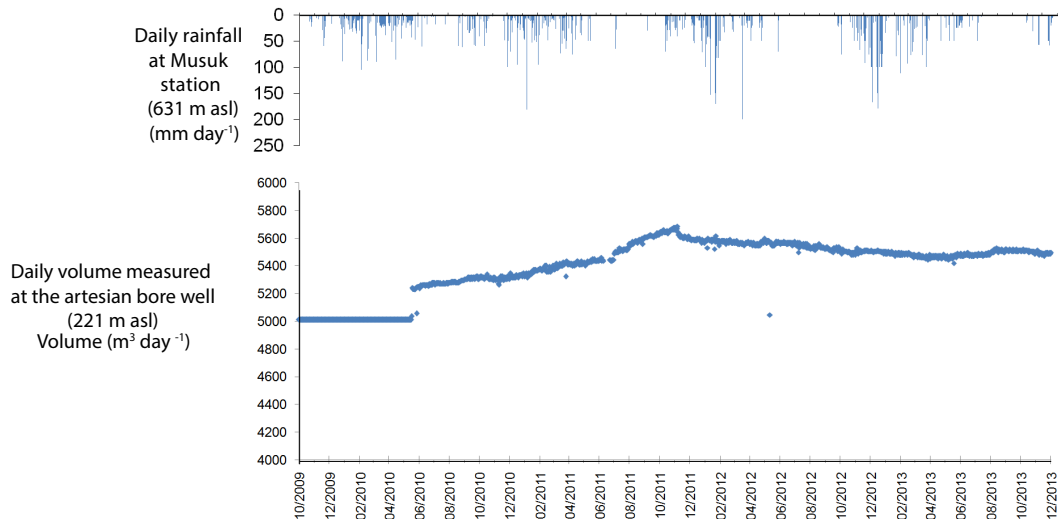


Figure 4.24: Comparison of the monthly rainfall of Musuk (631 m asl) and Cokro (301 m asl) stations with the monthly average production artesian flow rate within the Danone AQUA well October 2009 to December 2013 for Musuk and AQUA well and from August 2008 to December 2013 for Cokro station.

Regarding the temporal variation of the other physico-chemical variables on the production well of AQUA, no fluctuations are clearly visible except a slightly decrease trend of water temperature ($-0.5\text{ }^{\circ}\text{C}$ over the period August 2009 to July 2013). This trend could suggests an input of cold groundwater which confirms the flow rate increase.

The water level measures are made on the barometric glass tube on Danone-AQUA site. Unfortunately, these values are not usable because the manual observations can be distorted by the random flush of the tube made by the gardener to use the water for the grass irrigation. That situation has been mentioned and we can hope that the water level will become a valuable chronicle in the future.

The electric conductivity is stable at $230\text{ }\mu\text{S cm}^{-1}$ except from July 2012 where the calibration of the equipment has been done and a gap appears.

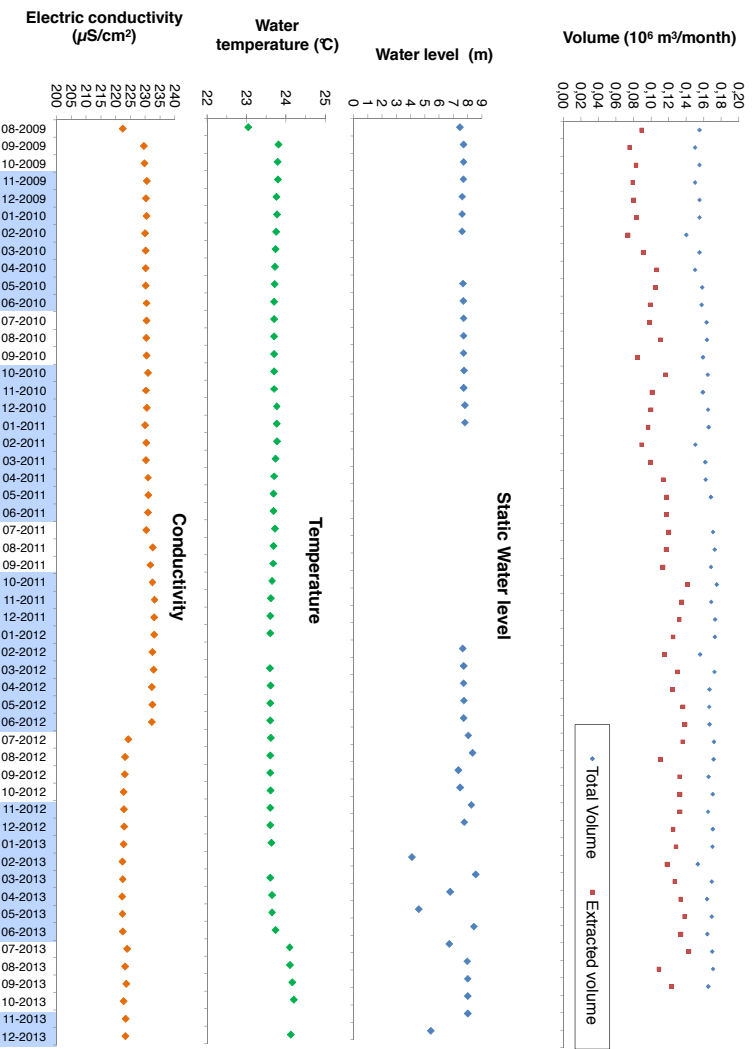


Figure 4.25: Comparison of the monthly average artesian and production flow rate within the Danone AQUA well with the water level, temperature and Electric conductivity over the period October 2009 to December 2013 for Musuk and AQUA well and from August 2008 to December 2013 for Cokro station. The first chart shows the total volume flowing out the artesian well and the extracted volume used by Danone-AQUA for the drinking bottle production. The difference is released and considered as overflow to the Sigedang spring and then used for irrigation purpose.

With the two new monitoring wells drilled upstream and downstream the SB2, we have two references for the water level variation. Therefore, we can compare them with the precipitation to verify the reactivity of the aquifer to the recharge process.

The Fig. 4.26 shows the daily effective rainfall at three elevations (Gumnuk, 1456 m asl; Musuk, 631 m asl and Cokro, 221 m asl) in parallel to the daily water level elevation on the monitoring wells (MW1 and MW2) and as the water level at Danone AQUA (BH1) is not valid, we use the daily flow rate in $\text{m}^3 \cdot \text{day}^{-1}$ over a period from January 2013 to March 2014. It appears that the MW1 and MW2 have fluctuations on less than 0.5 m. The daily flow rate of Danone-AQUA production well (PW) have low variation as well, reflecting the relative stability of the aquifer during the year.

However, a similar trend can be observed on the three wells. At the end of the wet season 2012-2013, in July-August 2013, the water level of MW2 and the flow rate of PW are slowly but steadily increasing and reach a maximum value in September 2013 and decrease slowly to recover the initial value at the beginning of the wet season 2013-2014.

The increase and decrease cycle could represent the climate seasonality but here it is clearly delayed compared to the rainfall data. The delay is even more important at PW than on the other wells. This decoupling between the rainfall and the water level variations indicates that the water transfer through thick unsaturated zone and the deep aquifer system is probably longer than the hydrological year.

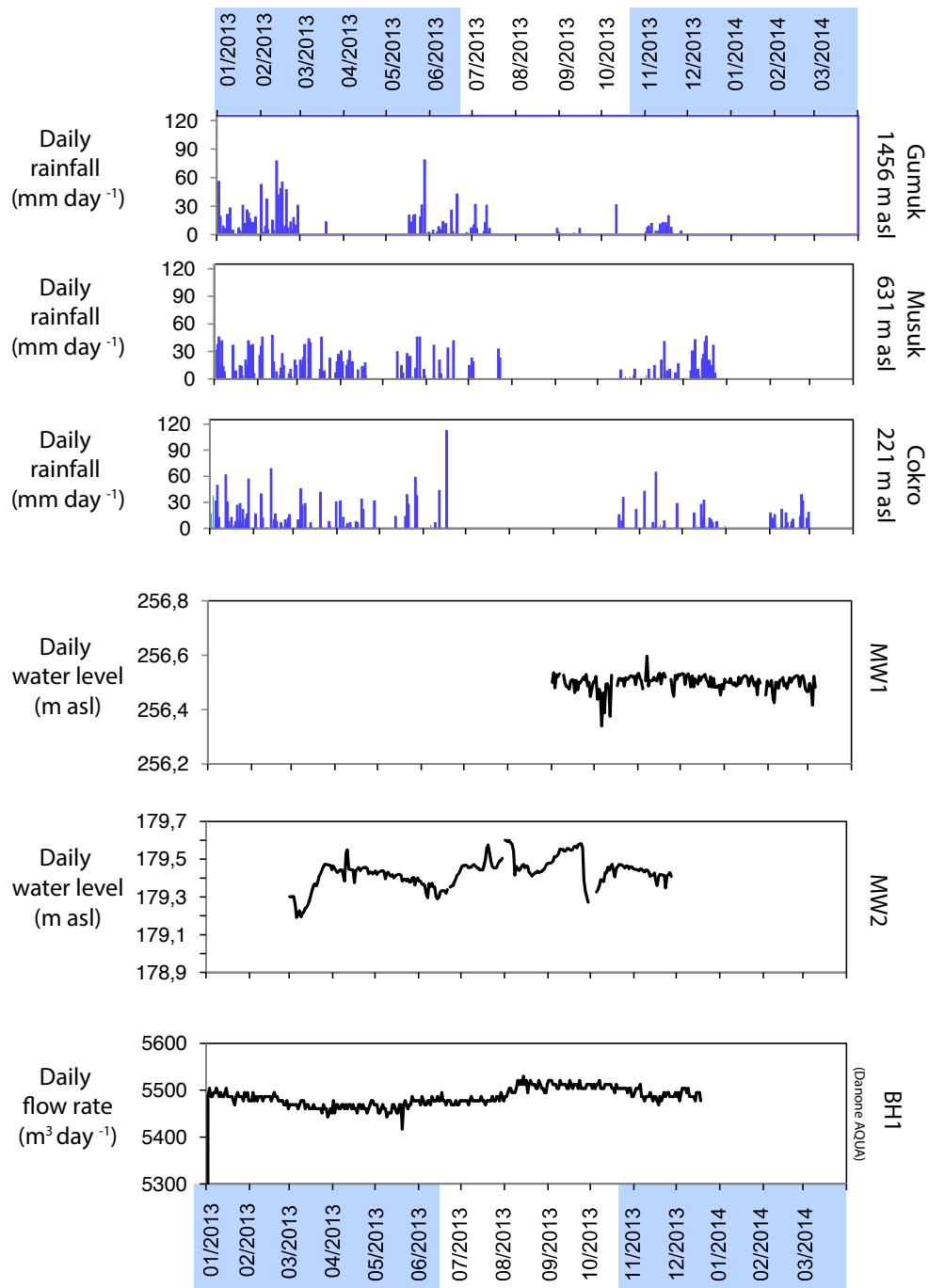
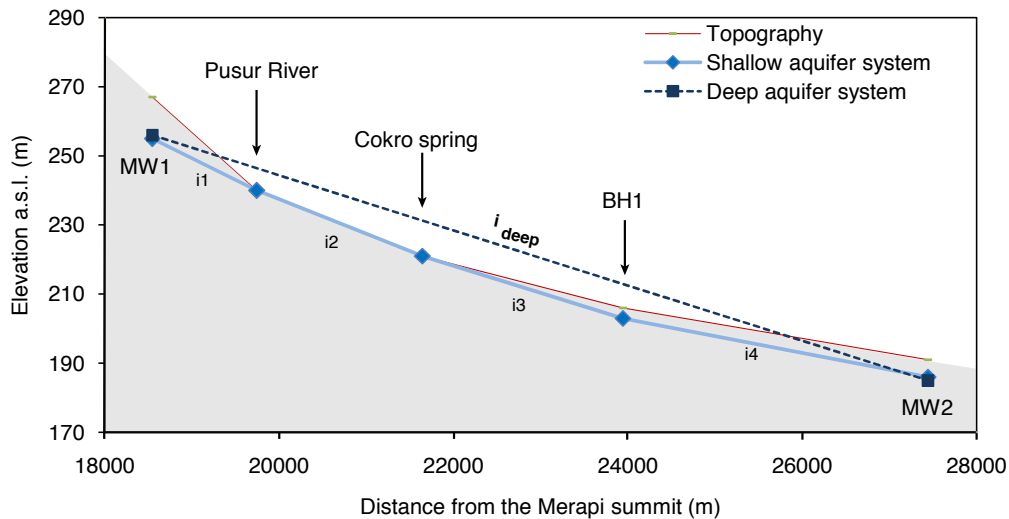


Figure 4.26: Comparison of the daily rainfall of Gumuk, Musuk and Cokro stations with the daily average water level elevation within the monitoring well 1 (MW1) the monitoring well 2 (MW2) and with the daily flow rate at the Danone-AQUA well (PW) for the period January 2013 to March 2014. The date in blue represents the wet season.

4.2.2.1 Aquifer hydraulic gradients

The hydraulic heads of MW1, BH1 (AQUA well) and MW2 can be linked together and thus obtained the hydraulic gradient for each aquifer system. The Fig. 4.27 shows the water level elevation on each aquifer system depending on the distance from Merapi summit. The topography is represented in red line and passes by the leveled points. Based on the stratigraphic log (section 4.1.1.2.4.2) and the dug well water table analysis (Fig. 4.22), the shallow aquifer is close to the topography. At 20 km from the summit, as the river incision crosses the aquifer formation, the Pusur river drained the shallow aquifer. On the field, direct observations show the increase of river flow rate along its profile. The hydraulic gradient between MW1 and the Pusur river (i_1) is 12.5×10^{-3} (i.e.: lower than the topography slope 22×10^{-3}). From the Pusur to Cokro spring, the hydraulic gradient of the shallow aquifer follows the topography (the slope and i_2 have the same value: 10×10^{-3}). After Cokro spring, the hydraulic gradient is higher than the topographic slope ($i_3=7.83 \times 10^{-3}$ whereas topographic slope = 6.52×10^{-3}). This characteristic is maintained with the last hydraulic gradient between BH1 and MW2 still higher than the topography ($i_4=4.86 \times 10^{-3}$ versus 4.29×10^{-3}).

The deep aquifer is confined at MW1 (i.e. the water level into the well is higher than at the beginning of the drilling). This assumption can be confirmed by the chemical analysis in the section 4.2.3. At BH1 well, the combined deep and shallow aquifer water level is 8 m above the ground surface, that is meant, the deep aquifer is still confined and artesian. Nonetheless, the deep aquifer is not confined anymore at MW2 location because the water level of both aquifers is not higher than the water level of the shallow aquifer only. As we do not have more than two points representing the deep aquifer only BH1 and Cokro show the shallow and the deep aquifer water level), the gradient of the deep aquifer is calculated at 7.98×10^{-3} . This representation and the hydraulic calculation show that the SB2 area is an important discharge zone for both aquifers.



Shallow Aquifer		
Measured point	Elevation (m asl)	Distance (m)
MW1	255	18543
Pusur	240	19743
Cokro	221	21643
BH1	203	23943
MW2	186	27443

H= Elevation of the points (m)
 L= distance between the points (m)
 i= hydraulic gradient (-)

i_1		
MW1-Pusur river	dH	15
	dL	1200
	i	12.50E-03

i_2		
Pusur River-Cokro	dH	19
	dL	1900
	i	10.01E-03

Deep aquifer		
Measured point	Elevation (m asl)	Distance (m)
MW1	256	18543
MW2	185	27443

i_{deep}		
MW1-MW2	dH	71
	dL	8900
	i	7.98E-03

i_3		
Cokro-BH1	dH	18
	dL	2300
	i	7.83E-03

i_4		
BH1-MW2	dH	17
	dL	3500
	i	4.86E-03

Figure 4.27: Piezometric head representation between the three monitored wells, the Cokro spring (spring n°78) and the Pusur river. The elevations have been measured with a differential GPS and the hydraulic gradients of the shallow and deep aquifer system can be calculated.

4.2.2.2 Pumping test measures

Using the methods described in section 4.1.1.2.4.3, the hydraulic parameters have been determined for each aquifer system through long duration pumping tests.

4.2.2.2.1 Upstream SB2 monitoring well (MW1)

During the pumping test of April 2013 on the shallow aquifer (from 11 to 13 m, 22 to 27

m and 33 to 40 m below the ground surface), the maximal drawdown has been recorded at 1.2 m after 44 hours, which is relatively low (Fig. 4.28). The low pumping flow rate ($0.002 \text{ m}^3 \text{ s}^{-1}$) could explain the brief decrease and the slight variations observed after 13 hours (i.e. 50 000 seconds) following the beginning of the pumping. After 44 hours of pumping (160 000 sec.), technical issues on site forced us to stop the water extraction. Then, the recovery has been almost instantaneous (8 hours), but the initial water level has not been recovered and a low decrease has been observed after more than 82 hours of observation.

The interpretation of this hydraulic test has to be done cautiously. Indeed, the low drawdown induced by the low extracted water flow rate has been reached rapidly (less than 6 hours after the beginning of the pumping). The low variations cannot be considered as significant since the error produces by the measure conditions are more important than them. As a matter of fact, the bad quality of electricity supply could slightly change the flow rate and provoke these variations.

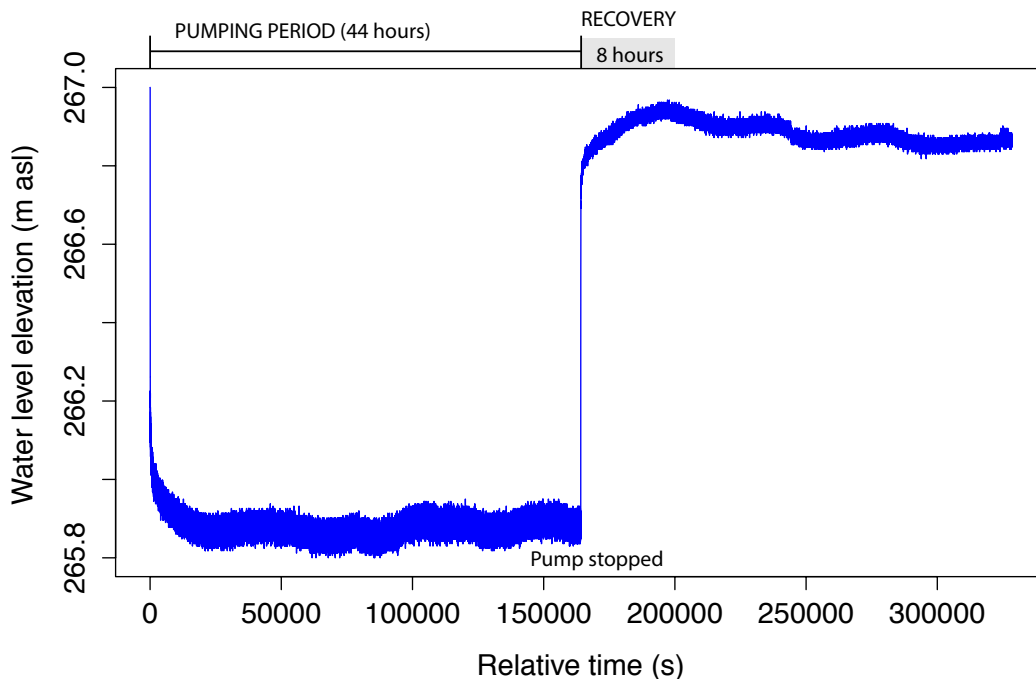


Figure 4.28: Water level elevation corrected with atmospheric pressure during the pumping well in April 2013 at MW1 well.

The Fig. 4.29 shows the log/log plot of the drawdown (in meter) versus the relative time (in second) since the beginning of pumping on the shallow aquifer. It appears that the curve follow the Theis-type curve. We suggest two reasons: 1) the pumping test did not last enough time and the unconfined characteristic “tail” curves is not visible, 2) the flow

rate during the pumping test was not sufficient to induce a significant drawdown. Indeed, the maximal drawdown is 1.2 m which is weak.

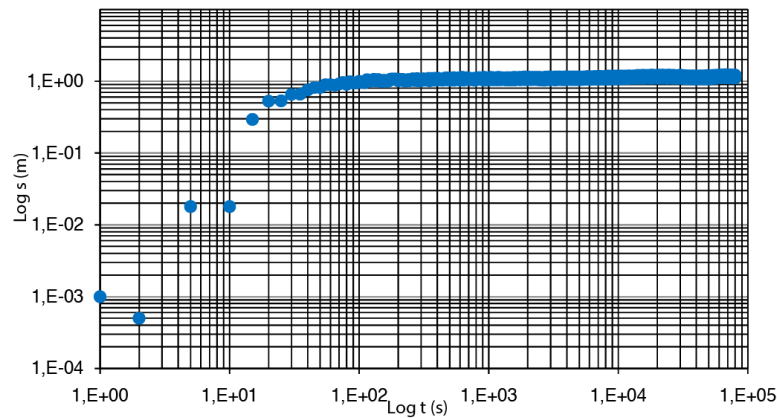


Figure 4.29: Log/log plot of the drawdown (m) versus time (s) of the pumping test at MW1 on the shallow aquifer. $Q=0.002 \text{ m}^3 \text{ s}^{-1}$ with maximal drawdown of 1 m.

Using the equation C.4 with the parameters obtained by graphical method with the Fig. 4.29, the transmissivity is estimated at $3.66 \times 10^{-4} \text{ m}^2 \cdot \text{s}^{-1}$. Based on the stratigraphical lithological log and the electric diagraphy, the shallow aquifer thickness is estimated at 25 m and thus, the hydraulic conductivity of the shallow aquifer is calculated at $1.46 \times 10^{-5} \text{ m} \cdot \text{s}^{-1}$.

4.2.2.2.2 Downstream SB2 monitoring well (MW2)

Upstream the SB2, the pumping test of the shallow aquifer (from 4.5 to 33 m below the ground surface), made a maximal drawdown of 0.98 m after 42 h. After the end of the pumping, the recovery has been brief but the initial water level has not been recovered. We intentionally let the error of water level record at the end of the recovery curve (up, right of the diagram 4.30) in order to highlight the crucial need to have good data quality. This error has been produced by the collapse of the probe cable support which result a change to the probe position into the well.

Using the equation C.4 with the parameters obtained on the curve Fig. 4.31 and estimating the aquifer thickness to 30 meters, the transmissivity has been estimated at $1.22 \times 10^{-3} \text{ m}^2 \cdot \text{s}^{-1}$ and the hydraulic conductivity at $4.07 \times 10^{-5} \text{ m} \cdot \text{s}^{-1}$.

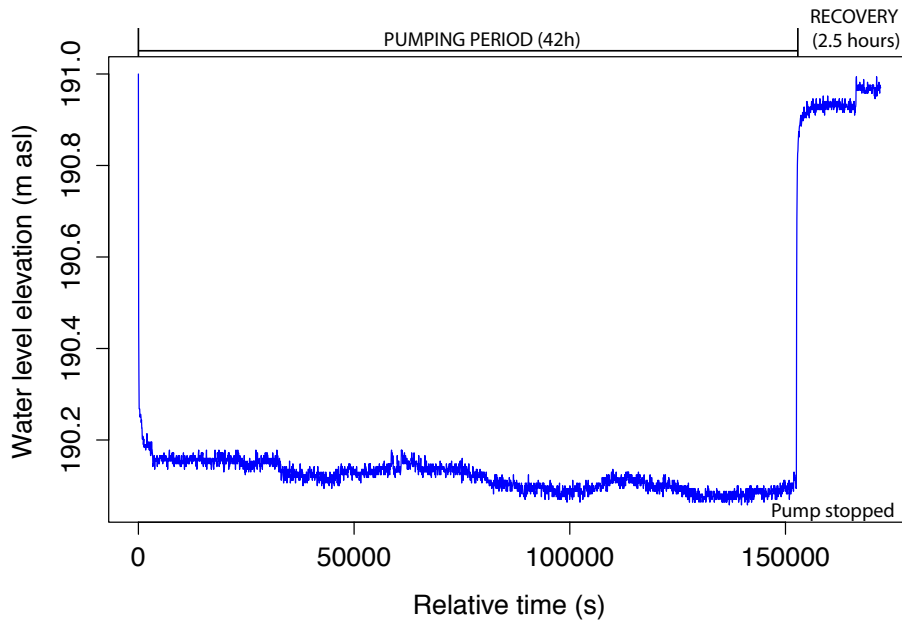


Figure 4.30: Drawdown and recovery (m) versus relative time (s) of the pumping test at MW2 on the shallow aquifer. $Q=0.002 \text{ m}^3 \text{ s}^{-1}$ with maximal drawdown of less than 1 m.

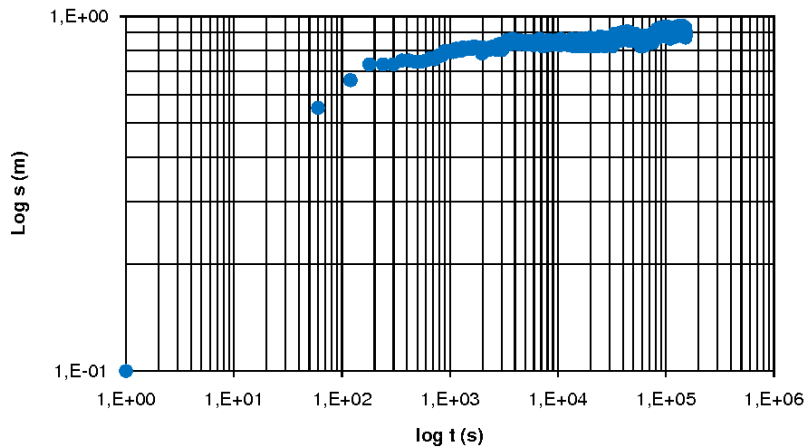


Figure 4.31: Log/log plot of the drawdown (m) versus time (s) of the pumping test at MW2 on the shallow aquifer. $Q=0.002 \text{ m}^3 \text{ s}^{-1}$ with maximal drawdown of less than 1 m.

The pumping test of the deep aquifer (41 to 51 m and 62 to 70 m below the ground surface) creates a drawdown of 17.3 m (Fig. 4.32) after just 3 hours (11 000 sec) with a constant flow rate of $2 \text{ L} \cdot \text{s}^{-1}$. This drawdown is much higher than for the shallow aquifer system, it is an indication that the hydraulic conductivity is lower. The equilibrium has been reached after 30 hours of pumping (110 000 sec). The recovery lasted less than 2 h and reached the initial water level. That indicates a low permeable material but in fact, regarding to the stratigraphical log and the low flow rate, the hydraulic conductivity is

not representative of the aquifer layer only but the gravel pack instead.

Nevertheless, using the Theis method for confined aquifer with the curve of the log of drawdown plot versus the log of relative time since the pumping started, the transmissivity has been calculated at $5.41 \times 10^{-3} \text{ m}^2 \text{ s}^{-1}$, therefore, for deep aquifer thickness of 20 m, the hydraulic conductivity is estimated at $2.7 \times 10^{-4} \text{ m s}^{-1}$.

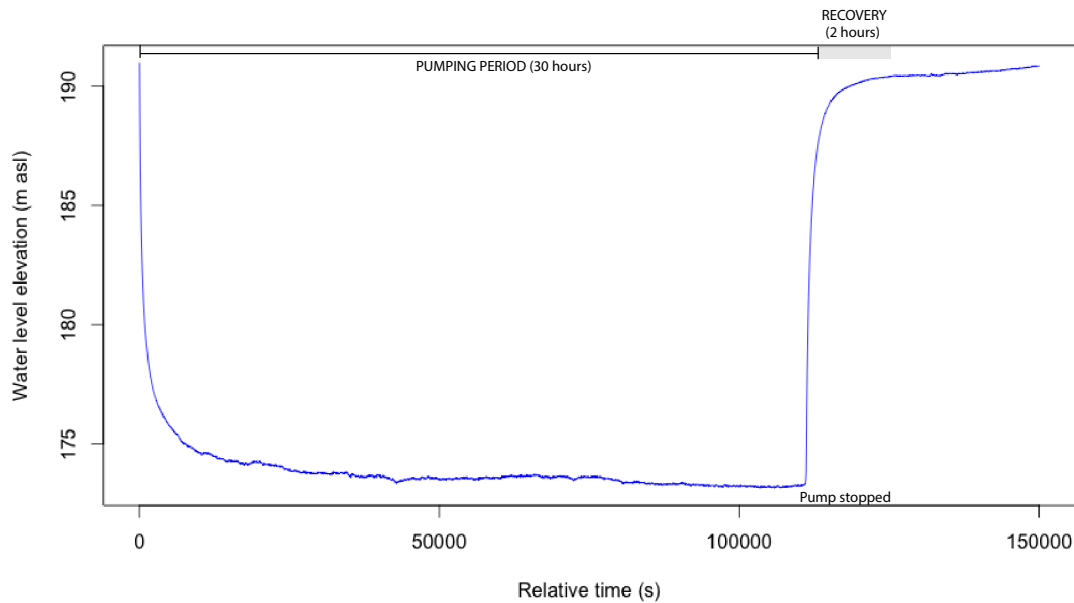


Figure 4.32: Drawdown and recovery (m) versus relative time (s) of the pumping test at MW2 on the shallow aquifer. $Q=0.002 \text{ m}^3 \text{ s}^{-1}$ with maximal drawdown of 17.3 m.

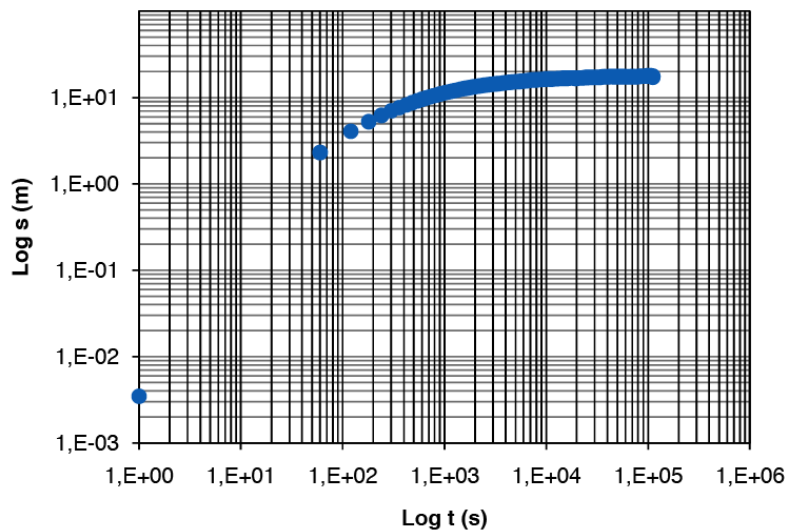


Figure 4.33: Log/log plot of the drawdown (m) versus time (s) of the pumping test at MW2 on the deep aquifer. $Q=0.002 \text{ m}^3 \text{ s}^{-1}$ with maximal drawdown of 17.3 m.

The Tab. 4.3 summarizes the hydraulic parameters obtained through these pumping

tests. We see that the shallow aquifer system has low hydraulic conductivity (10^{-5} m.s^{-1}) compared to the deep one (10^{-4} m.s^{-1} , one order of magnitude between both).

Location	Thickness (m)	T ($\text{m}^2.\text{s}^{-1}$)	K (m.s^{-1})
MW1 Shallow	25	3.66×10^{-4}	1.46×10^{-5}
MW2 Shallow	30	1.22×10^{-3}	4.07×10^{-5}
MW2 Deep	20	5.41×10^{-3}	2.70×10^{-4}

Table 4.3: Hydraulic parameters of the shallow and deep multi-layered aquifer systems at MW1 and MW2 locations.

Based on the results of the pumping tests, it appears that the deep aquifer system has good water circulation conditions. The stratigraphic lithological log shows that the lava boulders and the gravel formed the main part of this aquifer system. Regarding the thickness of the aquifer layers and their lithology, we can make an analogy between the material constituting the deep aquifer system and the remobilized products into the modern river beds.

These beds are an accumulation of massive block of lava flows, coarse and gravel layers, all of them are non-consolidated and highly permeable. Indeed, the water balance calculated in Chapter 3 shows that the main recharge occurs in the upper part of the river bed by intense infiltration through the alluvial detritic products.

Moreover, the geological observations shown in the Chapter 2, the presence of channelized formations with low resistivity value near the SB2 at the same depth than the aquifer layers identified on the monitoring wells. These channelized, highly permeable and non-consolidated, structures can be interpreted as paleo-rivers buried by the accumulation of new volcanic sediments with the eruptions, the extreme climatic and flank collapse events (Fig. 4.34). These cover layers have a low permeability and formed the shallow aquifer system. Surrounded by low permeability formation, the channelized paleo-rivers formed a preferential path way for groundwater circulation.

Now that we better understand the hydrodynamic of these two systems, the next section will be focused on their temporal evolution and the spatial distribution of the groundwater physico-chemical variables.



Figure 4.34: Picture of small buried paleo-channel on the Soka river side. The andesitic boulders are unsorted and buried into a fine matrix of ash and tuff.

4.2.3 Spring monitoring

4.2.3.1 Temporal evolution

The temporal chronicles of spring flow rate over the period November 2011 to October 2013 have been divided according to the three spring zones. The Fig. 4.35 shows the monthly average flow rates by spring zone. For each spring zone, the average flow rate of the zone is framed by the minimal/maximal range value of individual spring. This representation allows to see the mean trend of spring zone flow rate variation while keeping down the extreme values of flow rates.

For the eight upper springs, the mean monthly flow rate is low and stable all hydrological year long ($0.012 \text{ m}^3 \cdot \text{s}^{-1}$). During the dry season, the minimal flow rate is null, showing that several springs do not flow. The maximal value reach $0.1 \text{ m}^3 \cdot \text{s}^{-1}$ during the maximum of the wet season (February).

At SB1 zone, the average monthly flow rate is higher (near $0.04 \text{ m}^3 \cdot \text{s}^{-1}$) with seasonal variations linked to the rainfall. The maximal and minimal values are 0.14 and $0.006 \text{ m}^3 \cdot \text{s}^{-1}$ respectively.

The average monthly flow rate of the SB2 is similar to the SB1 zone but no major variations are recorded. The Min/Max range is more important with maximal values at $1.16 \text{ m}^3 \cdot \text{s}^{-1}$ and minimum flow rate at $0.005 \text{ m}^3 \cdot \text{s}^{-1}$. The value is remarkably stable through the alternation of dry and wet seasons.

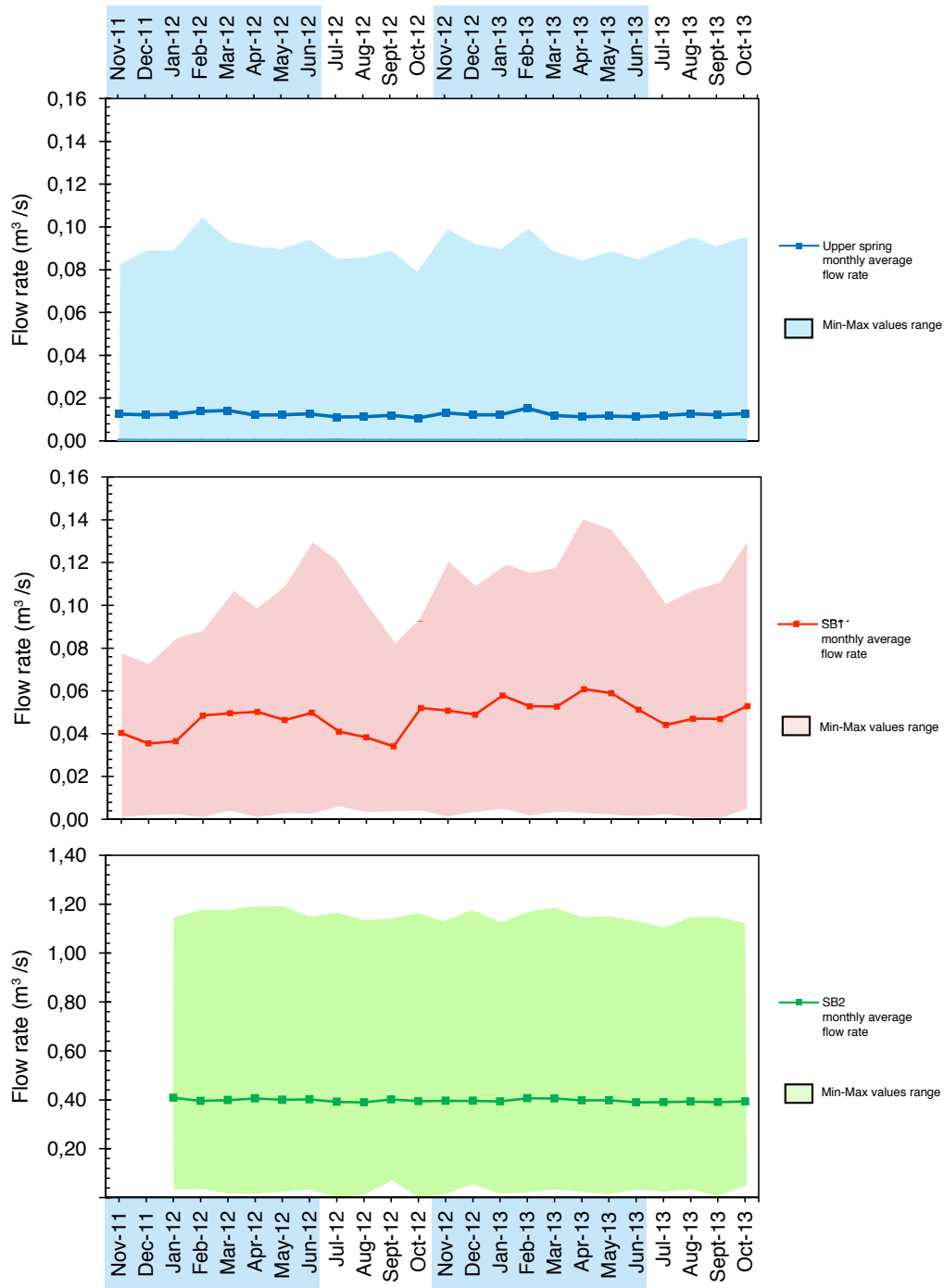


Figure 4.35: Monthly average values and minimal and maximal values of flow rate on the 20 monitored springs from November 2011 to October 2013. The results have been divided in 3 spring zones (upper, SB1 and SB2). The wet seasons are indicated in blue.

This representation brings information on the global characteristics of the three spring zones (upper, SB1 and SB2). Considering the high geological complexity of Merapi sys-

tem, a precise description of each spring zone is needed. The Fig. 4.36 shows the temporal evolution of the mean monthly flow rate for each monitored spring with a parallel with the effective rainfall at Gumuk, Musuk and AQUA stations. The error on each measure depends of the spring zone. For the Upper springs, the mean monthly flow rate are given with an error of $0.0005 \text{ m}^3.\text{s}^{-1}$ while at SB1, the error is $0.001 \text{ m}^3.\text{s}^{-1}$ and for SB2, the error on flow rate is at $0.01 \text{ m}^3.\text{s}^{-1}$.

The two first diagrams depict the flow rate evolution of the upper springs, the second diagram is a zoom of the first one. Whereas on the Fig. 4.35, the upper spring flow rate appeared as stable, these diagrams revealed that the flow rate of each spring highly varies depending on the rainfall. During the dry season, four springs do not have water flow (the springs 6, 7, 26 and 30). However, the spring n°2 is not sensitive to the seasonal rainfall variation and has a flow rate ten times higher than the seven other springs. That indicates a different groundwater circulation. The particularity of this spring will be described later.

The springs of the SB1 have several flow rate patterns. While majority of flow rates are below $0.05 \text{ m}^3.\text{s}^{-1}$, the spring 42 and 44 have perennial flow rates with increasing trend from $0.07 \text{ m}^3.\text{s}^{-1}$ to $0.1 \text{ m}^3.\text{s}^{-1}$. We saw that these springs have chemical compositions close to the SB2.

The SB2 flow rates are stable for all the springs over the hydrological years 2011-2012 and 2012-2013. Nevertheless, several spring groups can be defined depending to their flow rate value. The spring 78 (called Cokro spring) has the highest mean monthly flow rate with $1.2 \text{ m}^3.\text{s}^{-1}$. The lowest flow rate is observed at the spring 74 (called Pelem spring) with $0.005 \text{ m}^3.\text{s}^{-1}$.

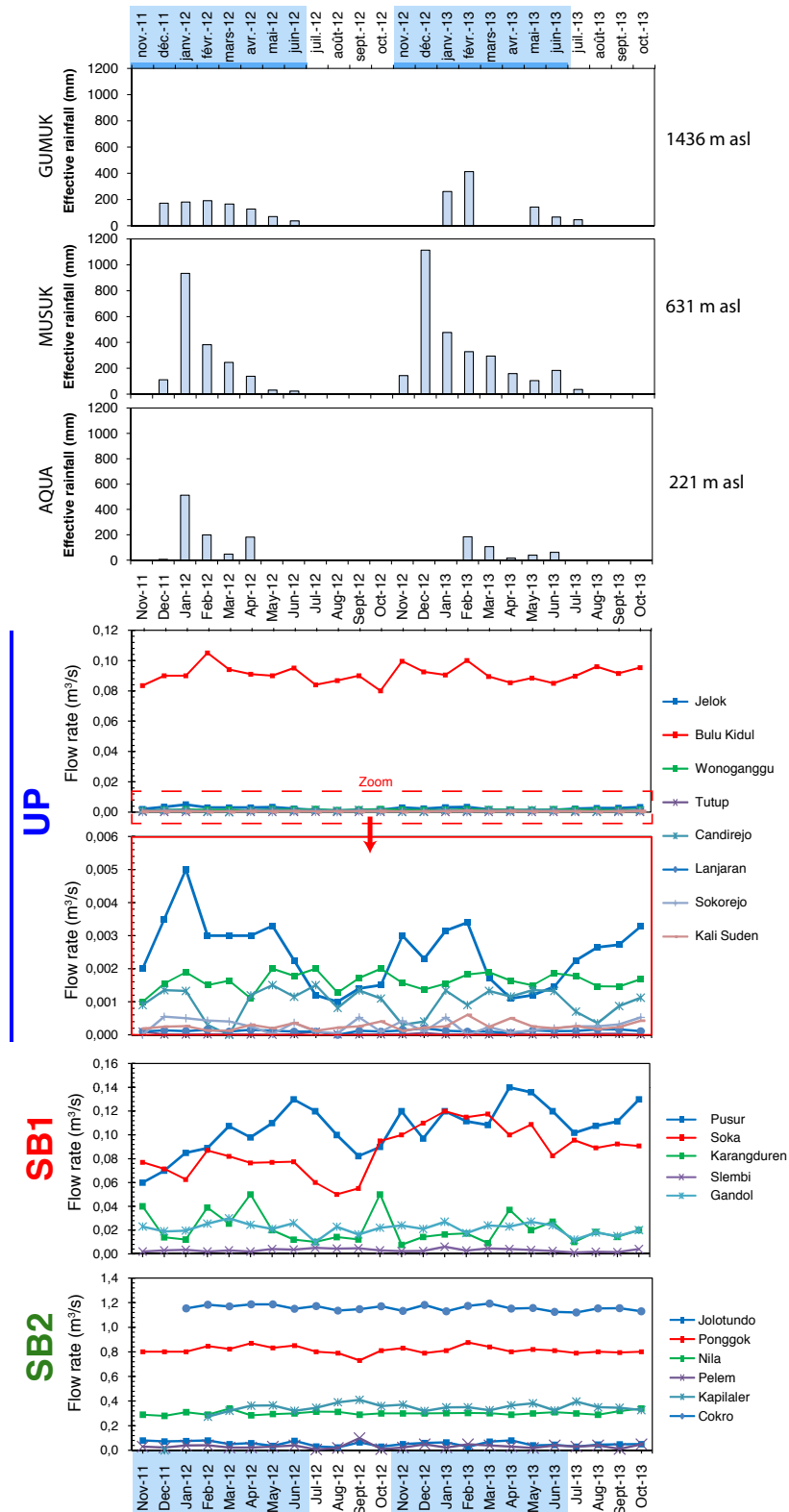


Figure 4.36: Monthly average values and minimal and maximal values of flow rate on the 20 monitored springs from November 2011 to October 2013 compared with the monthly rainfall at three elevations (Gumuk, 1456 m asl; Musuk, 631 m asl; and AQUA, 221 m asl). The results have been divided in three spring zones (upper, SB1, SB2). The wet seasons are indicated in blue. The error on each measured depends of the spring zone. For the Upper springs, the mean monthly flow rate are given with an error of $0.0005 \text{ m}^3 \cdot \text{s}^{-1}$; at SB1 the error is $0.001 \text{ m}^3 \cdot \text{s}^{-1}$ and for SB2, the error on flow rate is at $0.01 \text{ m}^3 \cdot \text{s}^{-1}$.

The Fig. 4.37 shows the temporal evolution of monthly average of electric conductivity (EC) on the twenty monitored springs over two hydrological years (2011-2012 and 2012-2013). The values are presented with an error of $10 \mu S \text{ cm}^{-1}$. The upper springs are divided in two groups, a group with low EC values ($100 \mu S \text{ cm}^{-1}$) and another group at $290 \mu S \text{ cm}^{-1}$. These two groups are relatively stable with a slight increasing trend over the two years. The springs 20, 30 and 38 belong to the second group.

The SB1 zone has scattered values with wide fluctuations (almost $100 \mu S \text{ cm}^{-1}$ of variation depending on the spring). The EC values are higher than for the upper springs but the springs 42 and 44 have the lowest values, marking again the specificity of these springs.

At SB2, the springs have stable values with slight and punctual decrease of EC (in April 2012 for instance). These gaps could be induced by the remobilization of dust and detergent into the springs by the local population.

Thus, except for SB1 zone, the EC signal is constant through the hydrological years.

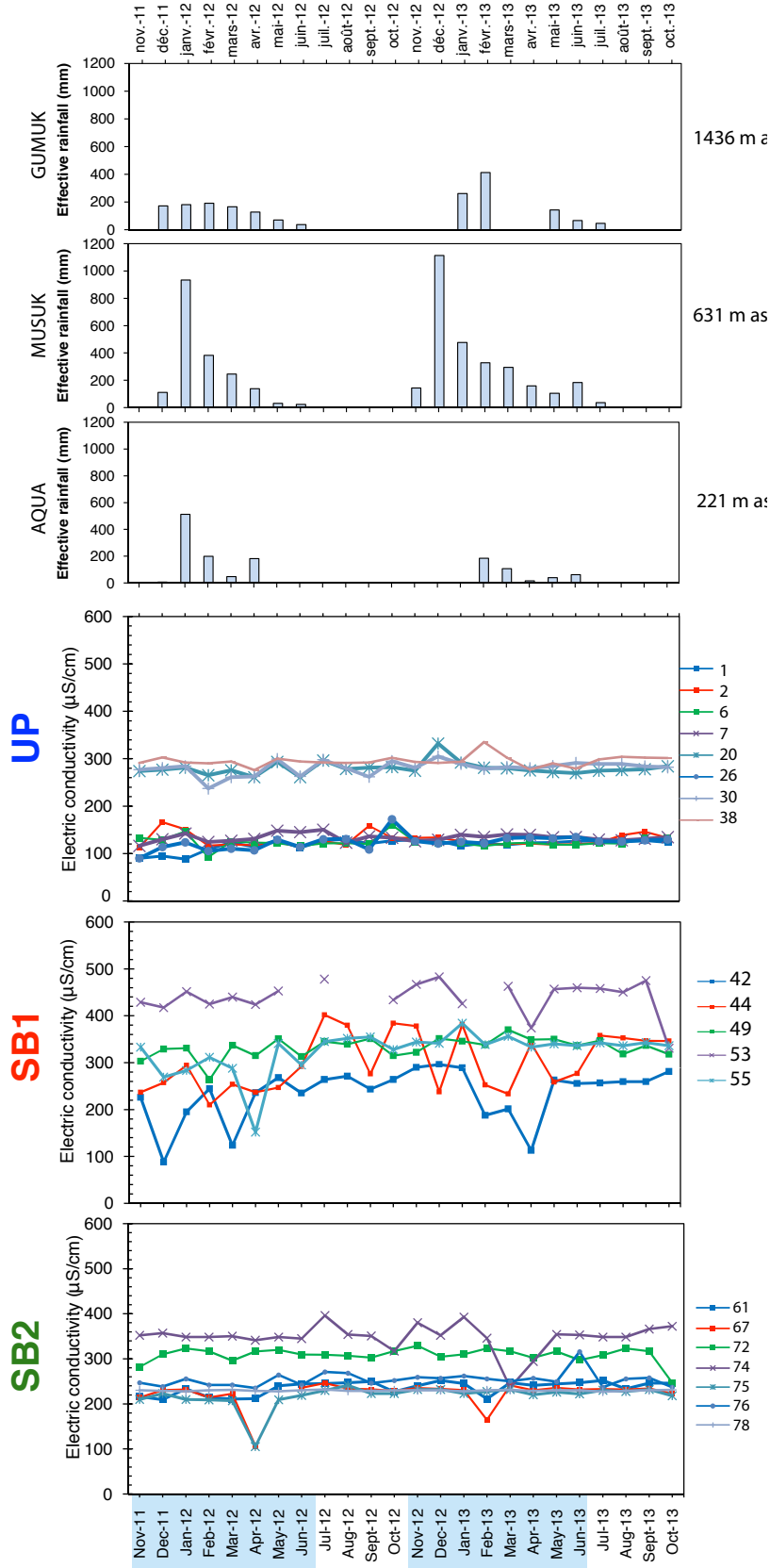


Figure 4.37: Monthly average values of electric conductivity on the 20 monitored springs from November 2011 to October 2013 compared with the monthly rainfall at three elevations (Gumuk, 1456 m asl; Musuk, 631 m asl; and AQUA, 221 m asl). The results have been divided in three spring zones (upper, SB1, SB2). The wet seasons are indicated in blue. The values are presented with an error of $10 \mu S \text{ cm}^{-1}$.

The temperature temporal evolution is presented on the Fig. 4.38 with an error of 0.5°C on the mean monthly temperature. The upper springs have temperatures ranging between 19.5°C and 25°C (amplitude 5.5°C , average 22.25°C). The lowest temperature belongs to the spring with the highest flow rate (spring n°2). The fluctuations are important (-3°C in August 2012 for the spring n°26) and could be imputed to the local rainfall variations. The SB1 also has a high temperatures ranging from 24°C to 28.4°C (amplitude 4.4°C , average 26.2°C) and the values are more assembled. The springs 42 and 44 have lowest temperature and highest water flow rate respectively. The monthly temperature is relatively stable with no seasonality markers.

The SB2 temperature range is 22°C to 25.5°C (amplitude 3.5°C , average 23.75°C). The temperature are stables for all the springs over the two hydrological years stating that the aquifer drained by the springs is not reactive to the seasonal variations of air temperature.

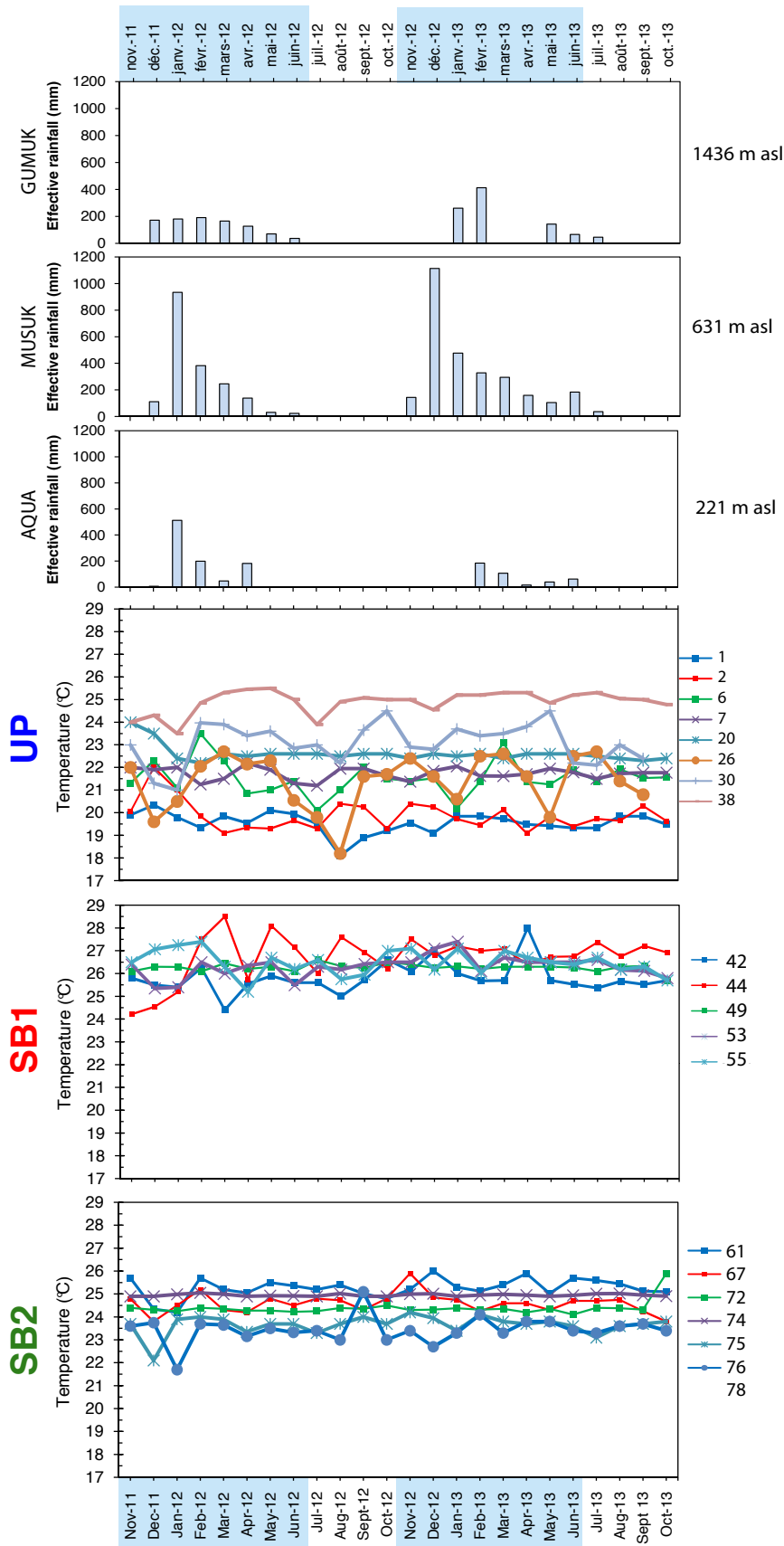


Figure 4.38: Monthly average values of water temperature on the 20 monitored springs from November 2011 to October 2013 compared with the monthly rainfall at three elevations (Gumuk, 1456 m asl; Musuk, 631 m asl; and AQUA, 221 m asl). The results have been divided in three spring zones (upper, SB1 and SB2). The wet season are indicated in blue.

The pH and the Total Alkalinity follow exactly the same trend of the EC variation on the three spring zones (upper, SB1 and SB2). The temporal evolution of the physico-chemical variables has shown that the spring zones are not homogeneous. There are springs with special behavior such as higher flow rate, electric conductivity and temperature or seasonality variation which do not follow the trend of the majority of springs of the zone. These “special” springs confirm the geological interpretation with heterogeneous aquifer architecture and multi-layered aquifer system. We saw that globally, the upper springs and the SB1 are reactive to the rainfall intensity and seasonal variability whereas SB2 seems not sensitive to these variations. That suggests different transfer time through the hydrosystem and we can suppose that the transfer time is brief for the upper spring (i.e. faster than the hydrological year) and relatively longer for SB2 (i.e. longer than the hydrological year). The SB1 has an intermediate transfer time with some springs with brief response to the rainfall and some springs with SB2 pattern.

4.2.3.2 Physico-chemical variable spatial distribution

As for the temporal evolution of the spring water physico-chemical variables, the relation between these variables and the elevation allows to identify the spring zones. The Fig. 4.39 shows the mean flow rate of the twenty monitored springs depending their elevation during the wet season 2012-2013 (i.e. January 2013) and during the dry season of the same year (August 2013). As the flow rate range between the spring zones is wide, the flow rate axis is expressed in logarithmic scale. Above all, the difference between the two periods (dry and wet seasons) is minimal, showing a relative stationarity of the system. Then, we can notice an increasing trend of the flow rate with the decrease of elevation. It makes sense that the upper part of the volcano is considered as recharge area while the low land is the discharge zone. Nevertheless, we can note that the spring n°2 has a high flow rate compared to the other springs of the upper parts. Placing the average monthly flow rate of January 2013 on the map (Fig. 4.40), the spring n°2 is located on the East side of the G. Bibi, volcanic relief which is constituted of basaltic lava flow deposits and culminated at 2000 m. The specific characteristic of the spring n°2 can be explain by the fact that this spring drain an aquifer constituted of massive fractured lava flow. The meteoric water infiltrated through fractured lava and recharge a basaltic aquifer type with high hydraulic conductivity. The other springs are draining perched aquifers formed by ash, tuff and cinder formations, characterized by low hydraulic conductivity. We can note also that the spring n° 42 and 44 are located into the river bed of the Pusur and Soka rivers respectively. We saw with the geological study that the river bed are channelized and constituted by an accumulation of blocs and gravel coming from the dismantling part of the summit. We suggest that the paleo-channels of the previous rivers have been

buried by the recent eruption and flank collapses and then incised by the river thanks to the regressive erosion. Composed by gravel, sand and boulders these paleo-channels have a high hydraulic conductivity and constitute a preferential way to the groundwater as the surrounding material is finer and more impermeable. The spring n°42 and 44 have different physico-chemical variables because of good aquifer properties compared to the other springs located at this altitude.

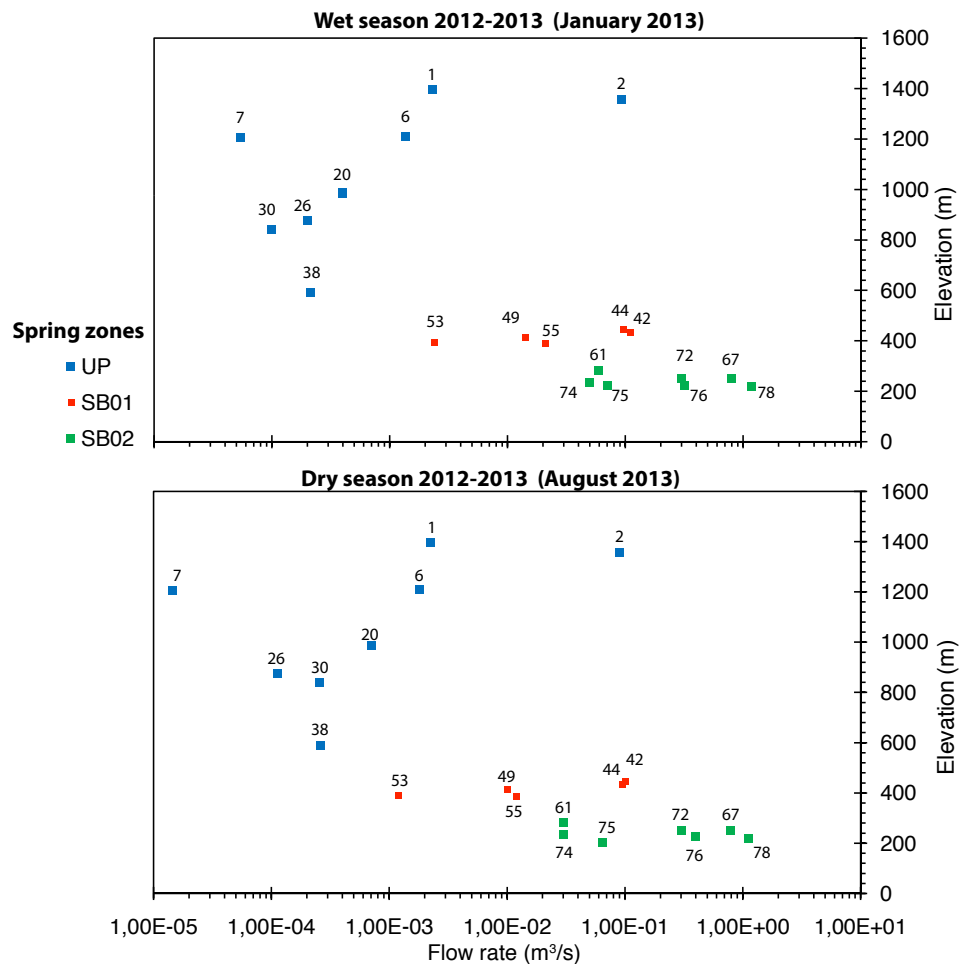


Figure 4.39: Average water flow rate of the monitored springs during the wet season 2012-2013 (January 2013) and during the end of the dry season (August 2013). The results have been divided in three spring zones (upper, SB1, SB2).

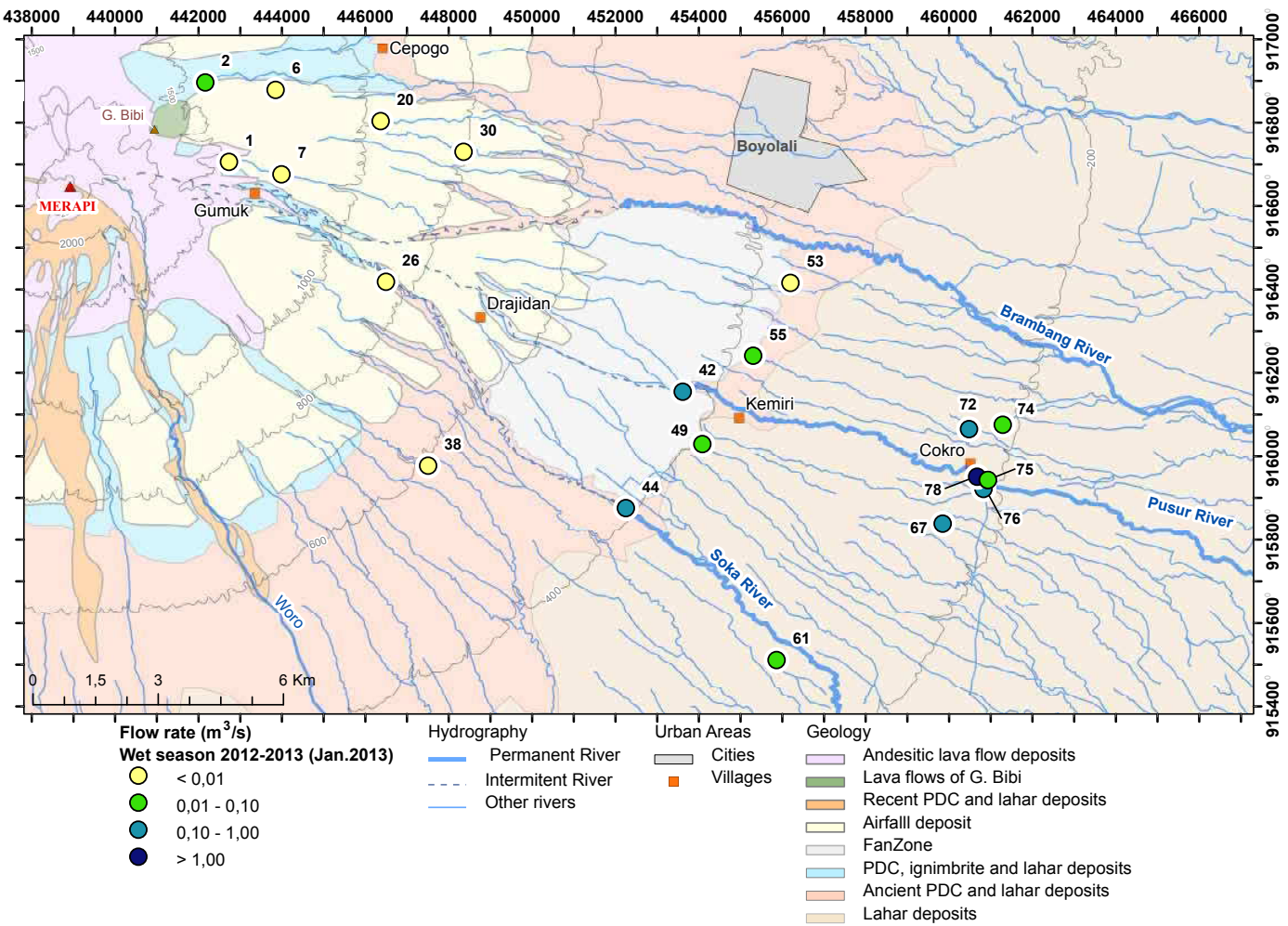


Figure 4.40: Average water flow rate of the monitored springs during the wet season 2012-2013 (January 213) reported on the geological map.

The distribution of the electrical conductivity (EC) along the elevation profile (Fig. 4.41) shows also an increasing trend with the decrease of altitudes (100 $\mu S\ cm^{-1}$ to 460 μS

cm⁻¹). The springs from SB2, have low values of EC (the spring n°76 with 240 μS cm⁻¹ for instance). The springs 72 and 74 have high electrical conductivity values, compared to the other springs of SB2. These springs have a low flow rate and thus are more sensitive to the local pollution.

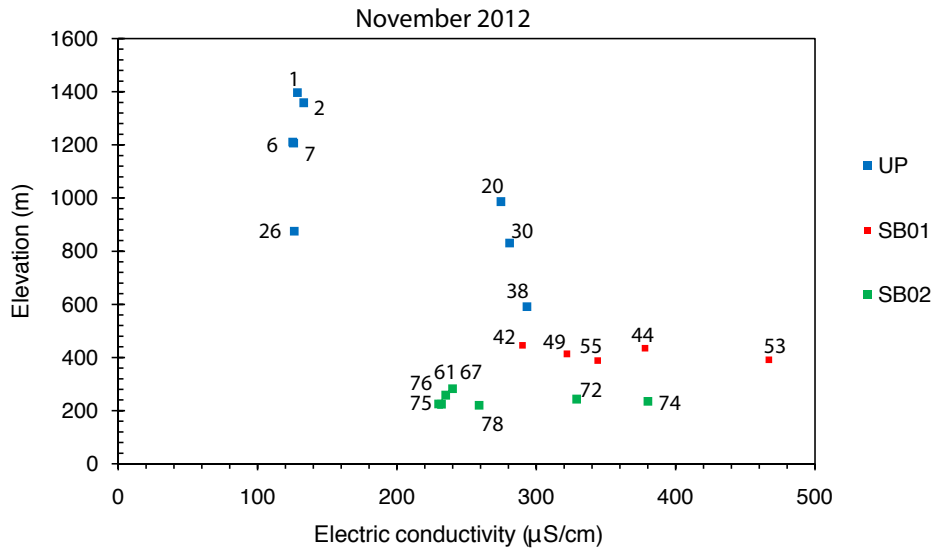


Figure 4.41: Monthly average electrical conductivity values on the 20 monitored springs in November 2012.

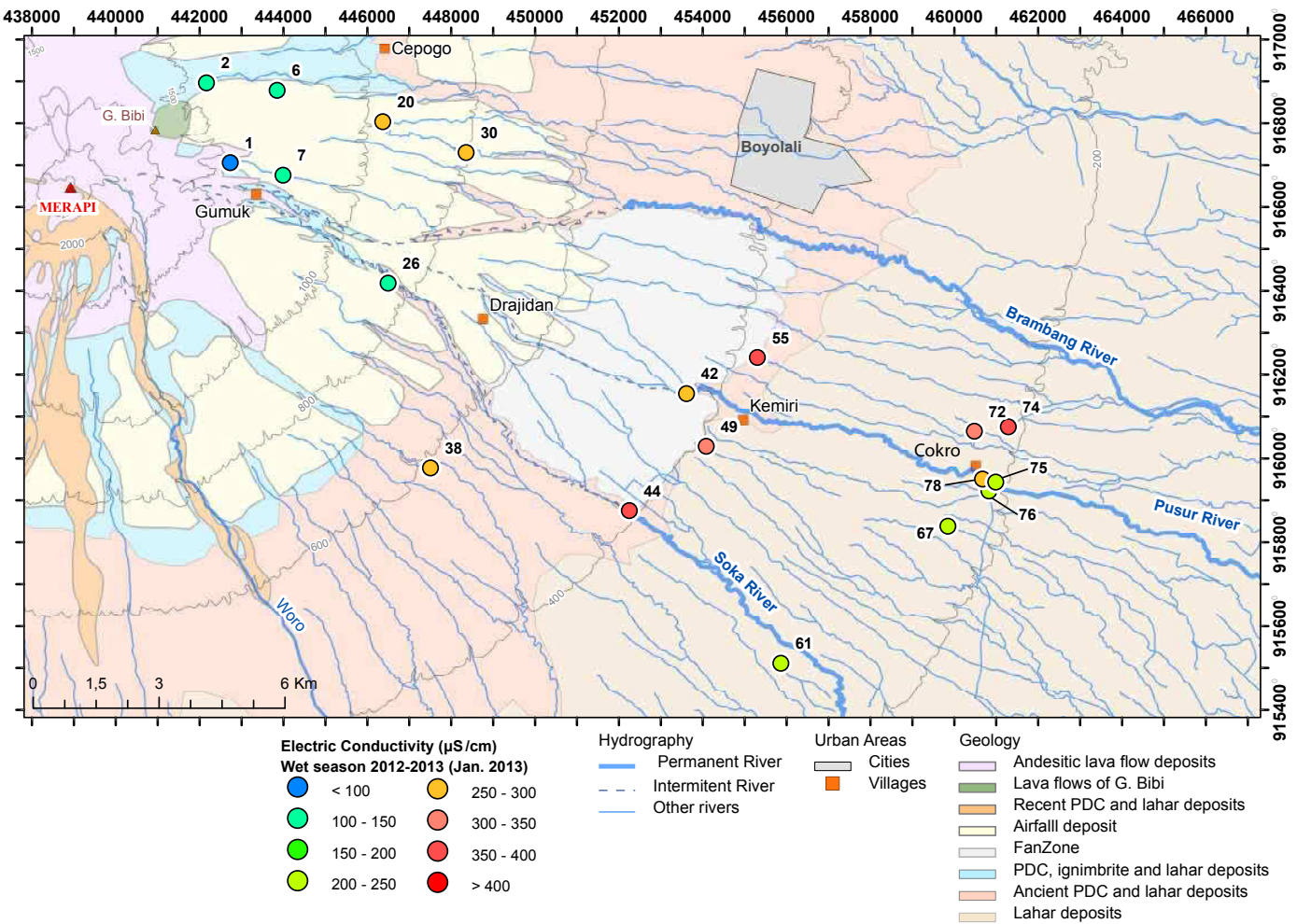


Figure 4.42: Monthly average electrical conductivity values on the 20 monitored springs in January 2013.

The Fig. 4.43 shows the annual mean spring water temperature depending on the altitude for the two hydrological year 2011-2012 and 2012-2013. As we explain earlier, the temporal variation of springs physico-chemical variables is relatively constant throughout

the year thus the trend of the spring zone temperature is similar over the two years. The dashed line in Figure shows the relationship between the mean annual surface temperature and elevation inferred from climate stations at Gumuk (1436m asl) and the manual thermometers settled at different elevation describes in Chapter 3. As expected in tropical region, the linear relation between temperature and elevation observed during the two years of monitoring (2011-2012 and 2012-2013) reflects minimal climatic variations. The spring water temperature follows the orographic gradient calculated in Chapter 3, -0.8°C per 100 m of elevation (19°C at 1436 m asl to 28.5°C at 250 m asl). However, we can notice that the SB2 groundwater temperature is lower than the expected air temperature at these altitudes. The latter means that unlike other springs, the water at SB2 does not have a temperature similar to the one at the outlet elevation. The SB2 shows temperature ranging from 23 to 25°C . This temperature anomaly is also clearly visible on the map Fig. 4.44.

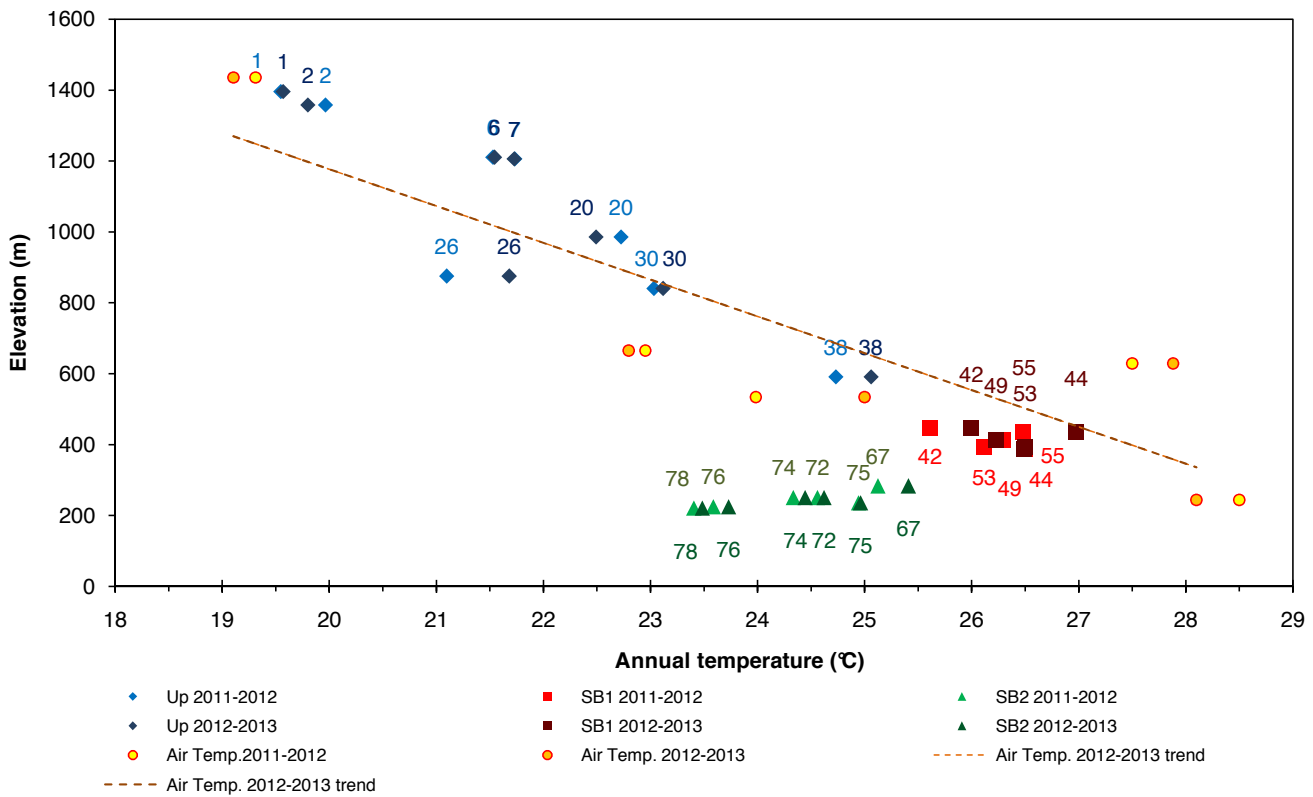


Figure 4.43: Annual average values of water and air temperatures on the 20 monitored springs for two hydrological years Nov. 2011 - Oct. 2012 and Nov.2012 - Oct. 2013. The dashed line represents the orographic air temperature gradient. The temperature is noted with an error of 0.1°C for the springs and 0.2°C for the air.

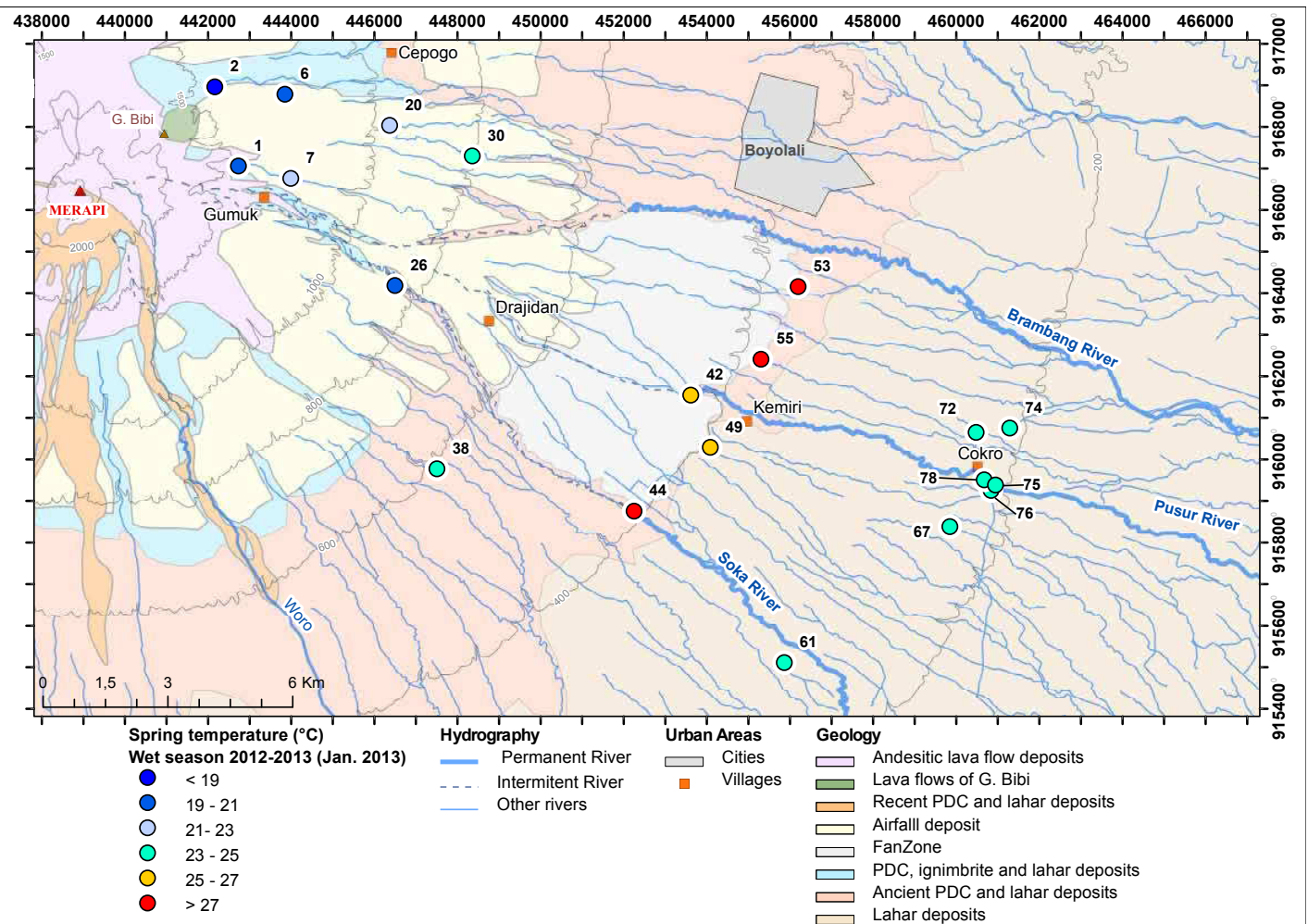


Figure 4.44: Monthly average values of water temperature on the 20 monitored springs in January 2013.

It is well known that water moving through a groundwater system transports heat and thus changes the subsurface temperature distribution. Temperature can therefore be used as a tracer of hydrologic processes such as recharge elevation or for testing conceptual

hydrogeologic models (Andrews et al., 1982). Temperature offers several advantages as a tracer of recharge elevation because it is easy, quick, and inexpensive to measure accurately in the field (Manga & Kirchner, 2004).

For a given aquifer, as the groundwater velocity increases, the heat added by geothermal warming is diluted into larger volumes of water, and consequently, spring temperatures become colder. In fact, spring temperatures can be colder than the mean annual surface air temperature at the discharge elevation if the water is recharged at much higher elevations while air temperature decrease with increase of elevation, as first noted by Alexander von Humboldt in 1844 (Davis, 1999). In contrast, for very low velocities (typically a result of low permeabilities), the subsurface temperature gradient is nearly undisturbed by groundwater flow and the temperature of spring water will be close to the mean annual surface temperature at the discharge elevation. The water flows through the aquifer along the x direction, and we assume that at any given position x, the temperature of the aquifer is uniform across its thickness and thus it is thermally well mixed (Langseth & Herman, 1981).

Considering the water temperature as tracer of the recharge elevation on Merapi volcano two possibilities are envisaged:

- i) Without mixing effect: the entire water comes from the upstream zone where the water temperature is close to the air temperature at this elevation, in our case, between 800 to 600 m asl.
- ii) With mixing effect: the spring water temperature results from a mix between the water at the same temperature as the air near the outlet (400 to 200 m asl) and a part of the water coming from the highest elevation (1200 m asl), where the water temperature is similar to the air temperature at the recharge elevation.

In case of a mixing effect, we are able to calculate the mixing ratio for each spring of the SB2. The hypothesis is made that the water observed at the spring belt 02 results of a mixing effect between the water infiltrated in the recharge area and the water infiltrated at the elevation with a similar water temperature, according to the graph B, it is around 800 m asl. The results of the mixing ratio are shown in the tab.4.5. The mixing ratio ranges from 24% to 57% for the water coming from 1200 m asl and 43 to 76% for the water coming from 400 m asl.

Spring code	Spring Name	Elevation (m)	Annual mean water temperature (°C) (2011-2013)	Mixing proportion (%)	
				1200 m asl	400 m asl
61	Jolotundo	283	25.3	20	80
67	Ponggok	251	24.6	33	67
74	Pelem	236	25.0	25	75
76	Kapilaler	233	23.7	51	49
75	Sigedang	225	23.7	51	49
78	Cokro	221	23.4	57	43

Table 4.4: Water mixing ratios on six springs of SB2 zone considering recharge areas located at 1200 m asl and 400 m asl. The ratios are established based on the comparison of the annual mean spring temperature (over the period 2012-2013) and the orographic air temperature gradient (-0.8°C per 100 m elevation).

4.2.4 Hydrogeochemical approach

4.2.4.0.1 Input of the isotope analysis On the basis of these data, this section will be focused on: (1) isotope variations in precipitation and groundwater within a stratovolcano located in a temperate humid climate region based on $^{18}\text{O}/^2\text{H}$ ratio ; (2) identification of recharge elevation with the relationship between $\delta^{18}\text{O}$ values and the elevation and (3) using the tritium analyses to estimate the age of the groundwater recharge within the andesitic stratovolcano.

4.2.4.0.2 $^{18}\text{O}/^2\text{H}$

On Fig. 4.45 and Fig. 4.46 are plotted the mean isotopic composition of each sampled points ($\delta^2\text{H}$ versus $\delta^{18}\text{O}$) for the end of the wet season (April 2012) and the end of the dry season (October 2012). Based on the data from the GNIP Station (IEA) Jakarta, the local meteoric line (LMWL) has been built (equation: $\delta^2H = 8.1\delta^{18}O + 12.7$). This line has been compare to the World Meteoric Water Line (WMWL) (equation: $\delta^2H = 8\delta^{18}O + 17$, (Craig, 1961)).

All the groundwater samples fall between the WMWL and the LMWL (Fig. 4.45 and Fig. 4.46). This feature, firstly, confirms the meteoric origin of groundwater. Secondly, positions of groundwater samples are consistent with the inter-annual and spatial variability of isotopic signatures trend in precipitations, especially in mountainous areas. In any region, the $\delta^{18}\text{O}$ values of rainfall at higher altitude generally are more negative and the magnitude of this altitude effect depends on local climate and topography Yurstever & Gat (1981). Indeed, above these terrains, topographic reliefs strongly influence precipitation by lifting atmospheric moisture and by facilitating precipitation at the windward slope (mainly North and East zone of Merapi). No main differences of the isotopic sig-

nature are visible between the samples taken at end of the wet season and the end of the dry season.

The relationship between the $\delta^{18}\text{O}$ and the elevation of the sampling site at the end of the rainy season (April 2012) and the end of the dry season (October 2012) is shown in the second diagrams on Fig. 4.45 and Fig. 4.46. No major change can be noticed between the two series. The BH1 sample comes from the isotopic survey from UGM in 2007 with only $\delta^{18}\text{O}$ value.

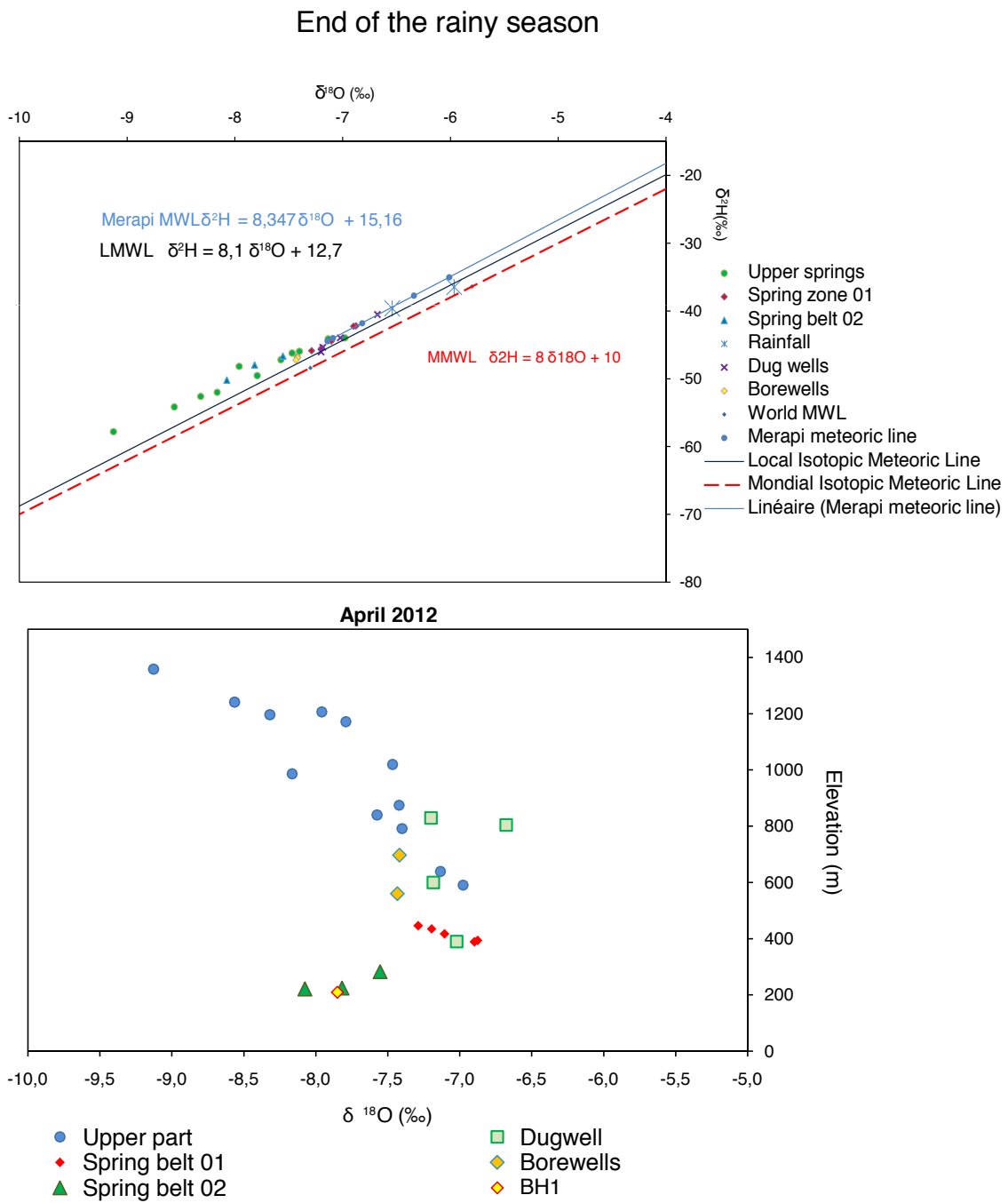


Figure 4.45: Relationship between the $\delta^{18}\text{O}$ values from the 3 spring zones (upper, SB1 and SB2), the dug wells, bore wells (data from the isotopic survey of April 2012) and the AQUA production well (data from the UGM isotopic survey in November 2007) according to the elevation

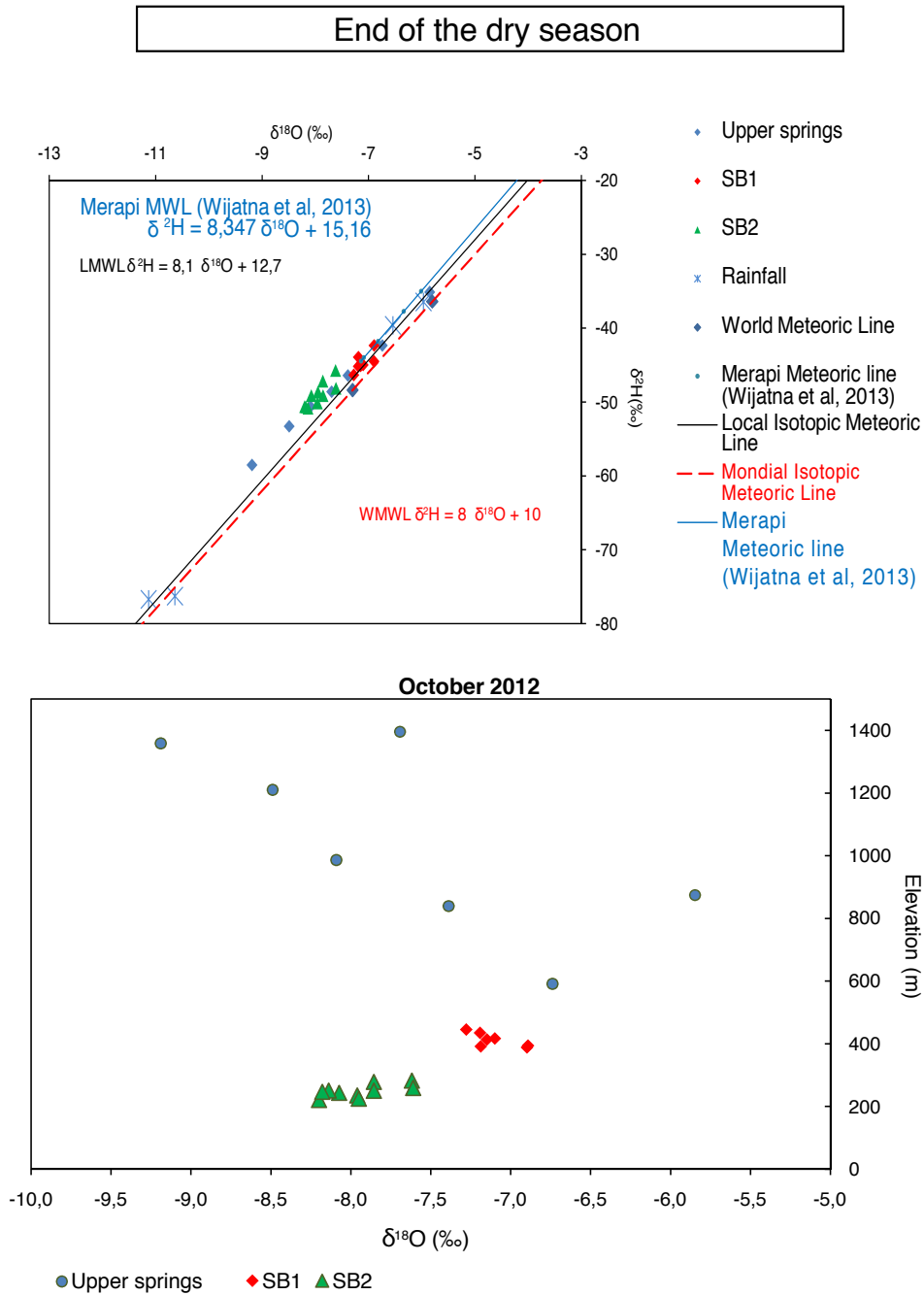


Figure 4.46: Relationship between the $\delta^{18}\text{O}$ values from the three spring zones (upper, SB1 and SB2) (data from the isotopic survey of October 2012) according to the elevation

The spatial distribution of $\delta^{18}\text{O}$ values for springs is shown in Fig. 4.47. Low $\delta^{18}\text{O}$ values (below -7.4 ‰) occur in the upper part of the East flank of Merapi volcano whereas the

high values (above -7.3‰) are observed downstream. This pattern is in good agreement with the spatial distribution of precipitation, suggesting that the spatial distribution of $\delta^{18}\text{O}$ values in groundwater primarily reflect the altitude effect of precipitation.

Nevertheless, an anomaly with low values (-7.4 to -8.3‰) is visible for the spring waters of the second spring belt (200 m asl). This anomaly indicates that the recharge area for the groundwater observed at the second spring belt is located to the upper part area of the Eastern flank of Merapi. At the opposite, the spring belt 01 (400 m asl) shows high values of $\delta^{18}\text{O}$ and may confirm the occurrence of a “local” hydrosystem with a recharge area close to the elevation of the spring outlets.

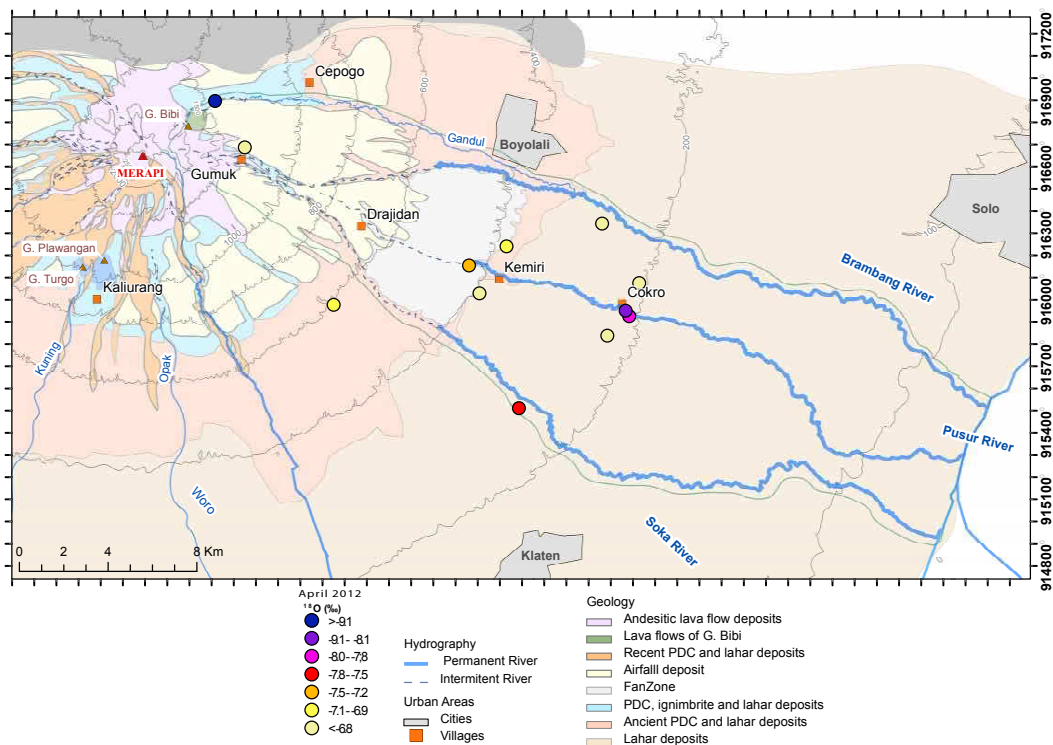


Figure 4.47: $\delta^{18}\text{O}$ spatial distribution into the groundwater in April 2012.

It is clear that $\delta^{18}\text{O}$ decreases with the increasing elevation (altitude effect) with a gradient of 0.29‰ per 100 m. This trend is also observed for $\delta^2\text{H}$. The decreasing trend of $\delta^{18}\text{O}$ with the increasing elevation is different for each spring zone. The AQUA well shows an isotopic signature close to the SB2. Depending upon the elevation effect on the isotopic composition of the rainfall, groundwater isotopic composition-altitude relationship can therefore be used to identify potential zones of recharge. The springs in the upper part drain local perched aquifers with limited watersheds and the $\delta^{18}\text{O}$ of groundwater in this area is an approximate indicator of the $\delta^{18}\text{O}$ of rainfall in that region, this range of gradient is likely to be reflected in the signature of the groundwater system also, which

is recharged from different elevation. Considering that the values of $\delta^{18}\text{O}$ to the springs in the SB2 represent the $\delta^{18}\text{O}$ value during the recharge, the recharge elevation can be estimated between 1200 to 800 m asl. But like the temperature tracer, two hypothesis are then possible:

- i) Groundwater of the SB2 comes entirely from the elevation with the same rainfall $\delta^{18}\text{O}$ value (near 800 m asl).
- ii) Groundwater of the SB2 results from a mix between a deep confined aquifer and a shallow unconfined aquifer with different elevation recharge area. The rain water infiltrated comes from two different elevations: one on the recharge area above 1200 m asl for the deep aquifer and the second from the recharge area of the shallow aquifer around 400 m asl.

In case of a mixing effect, we are able to calculate the mixing ratio of the springs for the second spring belt. The hypothesis is made that the water observed at the spring belt 02 results of a mixing effect between the water infiltrated in the recharge area and the water infiltrated around 400 m asl (Tab. 4.5).

Considering a recharge area located above 1200 m asl, the average value for the $\delta^{18}\text{O}$ concentration in the spring water at this elevation is -8.55‰ . At 400 m asl, the average value of $\delta^{18}\text{O}$ is -7.07‰ . The average of $\delta^{18}\text{O}$ concentration at the spring belt 02 (200 m asl) is -7.92‰ . Therefore, the proportions of the origin of the water of the second spring belt are:

1. 57% from the recharge area (1200m asl) with a range of values between 33% to 68% according to the springs.
2. 43% from 400 m asl with a range of values between 32% to 67% according to the springs.

This stable isotope analysis confirms the interpretation made with the spring water temperature: the SB2 belongs to a hydrosystem with deep water path (regional aquifer system) whereas the SB1 is the discharge zone of a “local” aquifer system.

Spring code	Spring Name	Elevation (m)	$\delta^{18}\text{O}$ (‰)	Mixing proportion (%)	
				1200 m as	400 m asl
61	Jolotundo	283	-7.55	33	67
67	Ponggok	251			
74	Pelem	236			
76	Kapilaler	233			
75	Sigedang	225	-7.82	50	50
78	Cokro	221	-8.08	68	32

Table 4.5: Mixing ratios deduced from the spring’s $\delta^{18}\text{O}$ concentrations , considering recharge areas at 1200 m and 400 m asl for six springs of the SB2 zone.

There is a good correlation between the mixing ratios obtained with the isotope and the ratio deduced with the water temperature ($R^2= 0.85$) (Tab. 4.4). The latter means that we have here two independent tracers showing the same mix proportions of shallow and deep groundwater circulation at the SB2 zone.

4.2.4.0.3 Tritium

In April 2012, five sites have been sampled for tritium analysis according to their elevation and spatial location. Three perennial upper springs have been selected (springs n°2, 7 and 33), the Pusur spring has been chosen for the SB1 zone (spring 42) and the spring n°75 for the SB2 area. In October 2012, in order to complete the tritium variability overview of Merapi groundwater, eleven samples have been selected over the three spring zones (3 upper springs, 3 SB1 samples and 6 SB2 samples).

The figure 4.48 shows the spatial distribution of the tritium concentration on the East flank of Merapi. The samples are limited but we can see that the low values are concentrated below 400 m asl (range 0.4 to 0.7 TU).

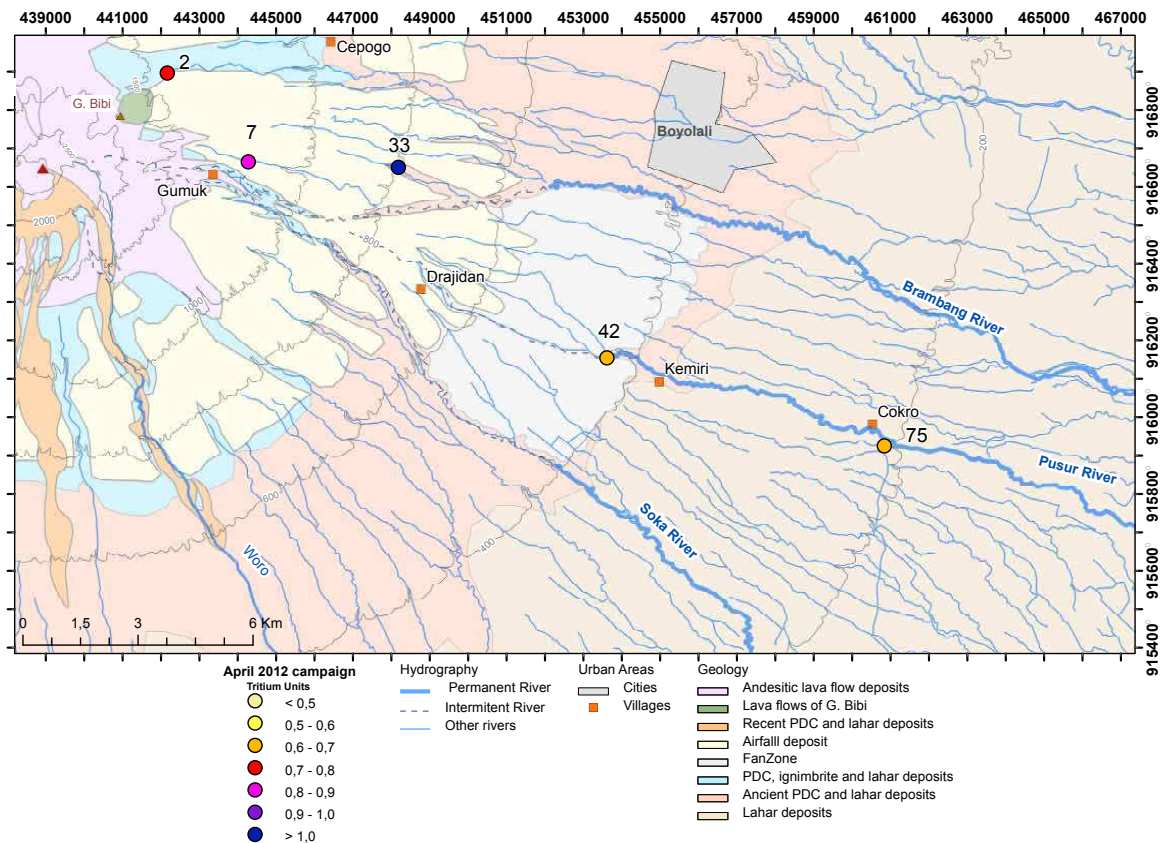


Figure 4.48: Spatial distribution of ^3H values in spring water (sampling survey of March 2012)

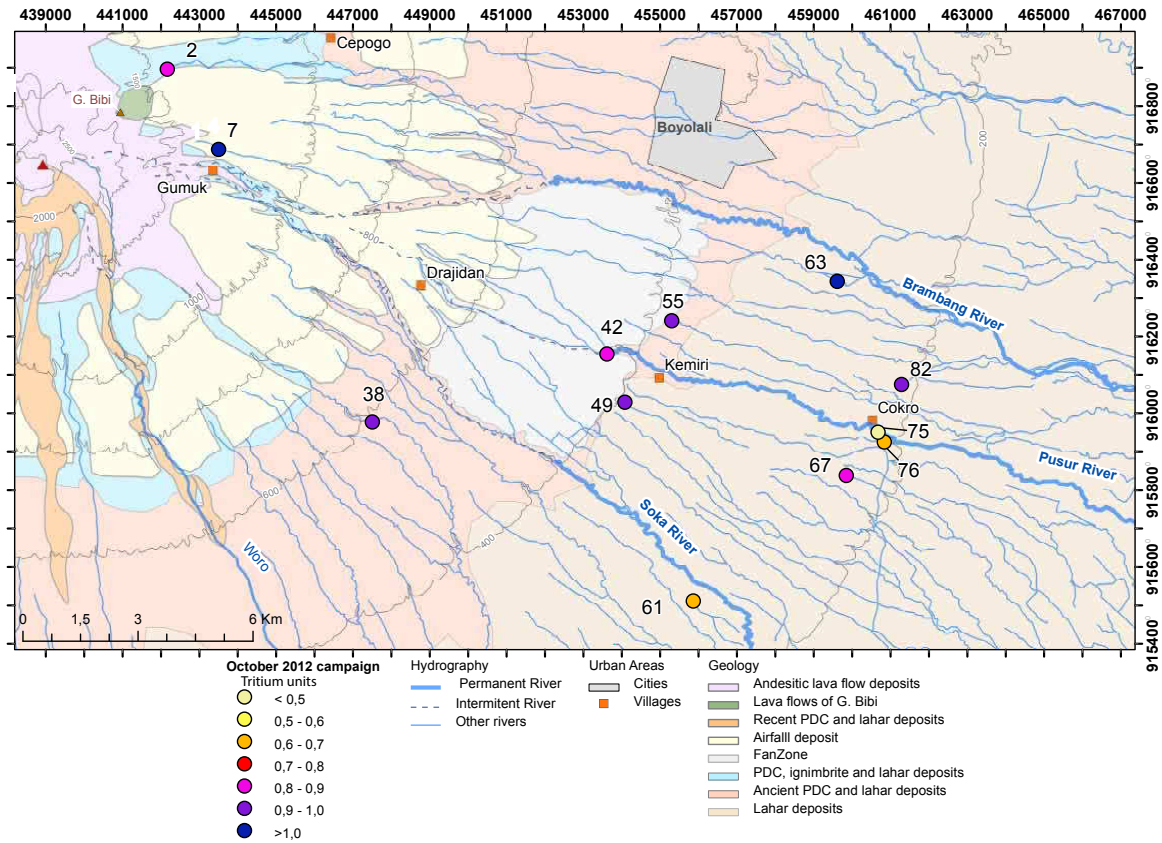


Figure 4.49: Spatial distribution of ^3H values in spring water (sampling survey of October 2012)

The average concentration in tritium for April 2012 campaign is 0.68 TU with a maximal value at spring 33 and 7 (1 TU) and a minimal value at spring 75 (0.4 TU). For the October 2012 campaign, the average concentration in tritium is 0.92 TU and the maximal value at spring 7 (1.2 TU) and minimal value at spring 75 again (< 0.5 TU). Figure.4.17 shows that the atmospheric value of tritium has been below 1 TU since 1968. Therefore, two solutions can be considered:

1. Groundwater on the East flank of Merapi show a tritium value ranging from 0.4 to 1.0 TU thus, their infiltration date was before the atomic test (1951).
2. Groundwater on the East flank of Merapi have a short transit time through the volcano-sedimentary system and their infiltration date is 1968 maximum.

To determine the real “age” of the groundwater, a preliminary estimation of the transit time of the water through the system can be made based on the hydrodynamics. We have shown that SB2 is a mixture of groundwater from two contrasted altitudes. We know that the water from the highest altitude takes the longest way, but it retained its infiltration

temperature. So, we can suggest that the circulations in the second aquifer are relatively rapid.

The highest value is in the spring 33 and 7 which have a very low flow rate. We can suppose that these springs drain a local and limited (“shallow”) hydrosystem or drain the unsaturated zone.

4.3 Hydrogeological functioning synthesis

Before discussing the quantitative aspects of the hydrogeological functioning of the eastern flank of Merapi, a brief summary of the state of knowledge about the aquifer systems is presented in the first part.

4.3.1 Aquifer system description

At this state we are able to describe two kinds of aquifer systems: a shallow one and a deep one. The multilayered systems have distinct hydrodynamical behavior and thus, hydrogeological characteristics.

4.3.1.1 Shallow aquifer system

The shallow aquifer system is composed by an alternation of i) welded tuffs, cooked paleo-soils layers and fine and compacted air-fall deposits, considered as aquitard formations and ii) sand, gravel, decimetric lava boulders and coarse products from ignimbrite deposits, considered as aquifer layers. The thickness of these layers ranging from centimetric to metric scale but the total shallow aquifer thickness can reaches 30 m. In the upper part of the Eastern Merapi flank, the aquitard layers incised by the river valleys allow the creation of disconnected perched aquifers. When the steep slopes intercept these perched aquifers, perennial or temporary springs occur. This aquifer system has a wide lateral and longitudinal extend and can be found from 1400 m asl to 200 m asl over more than 22 km long and 10 km wide. The high heterogeneity of lithological facies give a low hydraulic conductivity to this shallow aquifer system (average value determined by the pumping tests in low land areas: $2.73 \times 10^{-5} \text{ m.s}^{-1}$).

4.3.1.2 Deep aquifer system

The deep aquifer formation is built by the accumulation of detritic and alluvial material into the river beds. With their torrential behavior, the streams transport sand, boulders, gravel and metric to decametric andesitic lava blocks collapsed near the summit and are

carried to the low elevation. The phenomenon is still observable on site and decametric blocks have been found into the river beds until 20 km from Merapi summit.

During the several eruptional steps of the volcanic edifice building, these river beds have been covered and buried by fine air-fall, welded tuff and compacted pyroclastics deposits. These systems of paleo-riverbeds are channelized from the high altitudes (1000 m asl) to the low lands (200-100 m asl). Because their channelized geometry, the lateral extend of these systems is weak (20 to 30 m wide) and their thickness is also limited and do not exceed 35-40 m. Because of the coarse and high permeable material of their composition, these paleo-channel deep aquifer systems present a high hydraulic conductivity ($2.7 \times 10^{-4} \text{ m.s}^{-1}$).

4.3.1.3 Recharge areas and outlet zones

Despite distinct configurations, the shallow and deep aquifer systems are linked by their recharge and discharge zones. According to the spring water temperature monitoring and the isotopic analyses, the shallow aquifer is characterized by a local recharge whereas the deep aquifer system has a regional recharge. The recharge area of the shallow aquifer is located on the detritic fan (c.f. Chapter 2 Description of the Detritic fan) near the discharge zone defined as spring belt zone at 400 m asl, at 15 km from the Pasar bubar ridge. We have identified 21 springs on this spring belt 1 (SB1) and most of them are depression spring type and drain the shallow multi-layered aquifer. Nevertheless, two springs drain the shallow river beds of the Soka and Pusur rivers. These springs (n°42 for the Pusur spring and 44 for the Soka spring) have high and constant flow rate along the year and have a recharge area located on the detritic fan. The SB1 occurrence can be explained by the termination of the detritic fan at 400 m asl creating a slight break slope which induces an incision of the shallow aquifer system by the topography. We suggest that the SB1 represents only the intersection between the topography and the top of the aquifer. Thus, downstream the SB1, the rivers drain the aquifer along several kilometers. The discharge zone of the deep aquifer is located between 200 to 283 m elevation and is represented by a second spring belt (SB2) with important and perennial springs. The spring occurrence is probably caused by a regional fault observed on the South-East shore of the Yogyakarta basin. This fault creates a preferential vertical groundwater circulation near 200 m asl on Merapi Eastern flank.

Still according to the physico-chemical monitoring and the isotope analyses, the recharge location of the deep aquifer is at this point, still controversial. Two assumptions can be made: first, the water infiltration occurred in medium elevation (near 600 m asl) through the temporary river beds, filled by unconsolidated material and contributes to the groundwater recharge on the paleo-channel system; Second, the recharge occurred at two elevations: at high elevation (above 1200 m asl) through a large unsaturated zone (until

100 m thick) and reaches the outset of the paleo-channel near 1000 m elevation. Thus, the water flowing at SB2 could result of a mix between shallow and deep groundwater circulations. We will see in the following part that this assumption appears as more probable.

The remain question involves the groundwater residence time into the aquifer systems. The next section is focused on the estimation of the water transit time based on hydrodynamics and considering several assumptions.

4.3.2 Water transit time estimation

In order to calculate the groundwater transit time, we calculate the cinematic velocity (or the average linear groundwater velocity). Based on the Darcy's law, the cinematic velocity of water flowing through the pore of the rock matrix is expressed as:

$$u^* = -\frac{Kdh}{n_e dL} \quad (4.1)$$

with:

u^* = cinematic velocity (m.s^{-1})

K = hydraulic conductivity (m.s^{-1})

dh = Difference of water level elevation along a flow line (m)

dL = Linear distance along a flow line (m)

n_e = the effective porosity

Then, the time needed by the water to transit into the system from the recharge area to the spring is calculated:

$$t = \frac{L}{u^*} \quad (4.2)$$

with

u^* = the water cinematic velocity (m.s^{-1})

t = the water transit time (s)

L = the distance of the flow path (m)

The groundwater flow transit time could be decomposed in two components: the first component taking into account a vertical transit through the fine material with a low conductivity located in the upper part (recharge area) then, a second component, taking

into account a horizontal flow into preferential water flow path. The first transfer is mainly occurred in unsaturated zone and through low permeable formations. As we noticed, the main infiltration occurs into the temporary river beds and the unsaturated zone thickness from the river bed to the water table is not well know and can probably varies from 100 to 1000 m. Thus, for our transit time estimation, the unsaturated zone will not be taken into account and the residence time will be underestimated. Nevertheless, this preliminary estimation can be validated or not by the isotope tracer and later by the numerical modeling approach.

The horizontal transfer occurs in saturated zone, where the aquifer systems are following the very pervious formation of paleo-channel of the buried rivers and the streams. A calculation of the paleo-channel of the buried rivers length has been made taking into account of the present-day river sinuosity. This estimation has been reported on the average distance between the beginning of the paleo-channel and the springs of the SB2.

As the hydraulic gradient driving the flow in saturated conditions in high elevations of the deep aquifer is unknown, we tried to assess it considering that the gradient observed between MW1 and MW2 could be extended in upstream parts (noted " i_{deep} (extended)" on Fig. 4.50) . This theoretical gradient allows to estimate the probable water level in the recharge zone. The highest point of the recharge area is fixed at 1500m asl, before the morphological fault at 3 km from the summit (Pasar Bubar ridge (PBR)). The piezometric surface at this point is estimated at 400 m asl (Fig. 4.50).

Based on the piezometric map from the dug wells monitoring, the water table of the shallow aquifer can be plotted on Merapi Eastern profile (Blue line in Fig. 4.50). We saw that this water table is theoretical as the upper part is constituted by disconnected perched aquifer.

We have considered four circulation cases noted "A", "B", "C" and "D". The saturated cross-sections considered for each case are detailed on Fig. 4.51. The cases "A" and "B" concern the shallow aquifer circulation and its pathway to the upper springs and the SB1. The recharge elevation has been fixed at 4 km (L1) from the PBR, which corresponds to a piezometric head of 950 m (h_1) on the saturated cross-section (Fig. 4.51, A). The average elevation of the upper springs is estimated at 800 m asl (h_1) at 5 km (L1) from the PBR. Thus, the difference of head between the recharge and the outlet is 150 m (dh) and the distance is 2000 m (dL). B) For the SB1, the configuration considers a recharge area lower than the upper springs ($h_1= 700$ m, $L_1= 7$ km). Therefore the vertical distance (dh) is 300 m and the horizontal distance is 8 km (dL).

For the SB2, two configurations are described: "C" considers one unique recharge area while "D" supposes that the SB2 water comes from a combination of high and low elevations. The "C" configuration considers that the groundwater of SB2 has one unique recharge area at 7 km from the PBR. This location has been chosen according to the

air temperature gradient. Indeed, near 800 m elevation (i.e. 7 km from the PBR), the air temperature is 23.5°C which is the average spring temperature of SB2. Considering that the temperature is a tracer of the recharge elevation, we suggest that the infiltration occurred at 800 m asl. Based on the extended hydraulic gradient of the deep aquifer, the water table at this topographic elevation is fixed at 390 m. The horizontal distance from the recharge and SB2 is 15 km (dL) while the piezometric head difference is 190 ml (dh). The case “D” is divided in two parts: i) following the same method, the recharge is located at 2 km from PBR which corresponds to the piezometric head 400 m (Fig. 4.51, D, left side), ii) and a low zone of recharge is fixed at 18 km from the PBR (Fig. 4.51, D, right side).

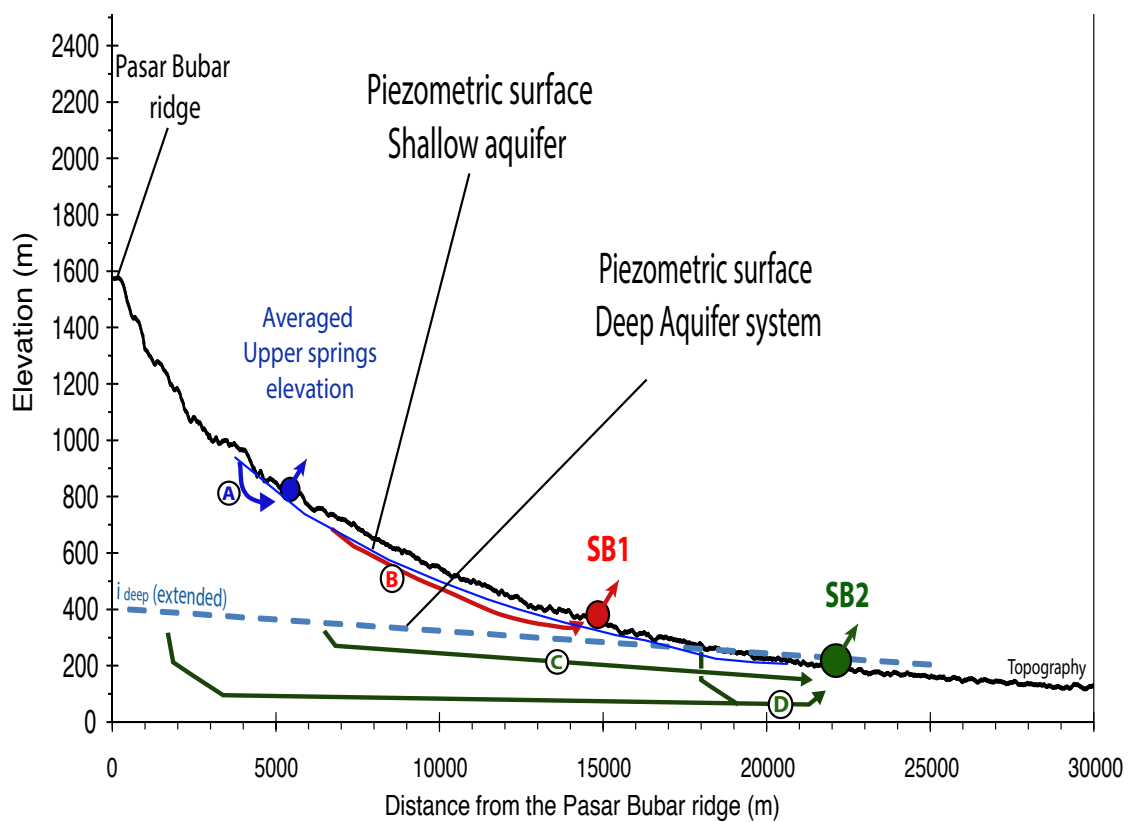


Figure 4.50: Distances and elevations chosen to calculate the groundwater transit time from the recharge areas to the spring zones (upper, SB1, SB2) through four pathways reported on the East flank of Merapi cross-section (from DEM ASTER GDEM V2 with 30 m ground resolution). (cf Fig. 4.51).

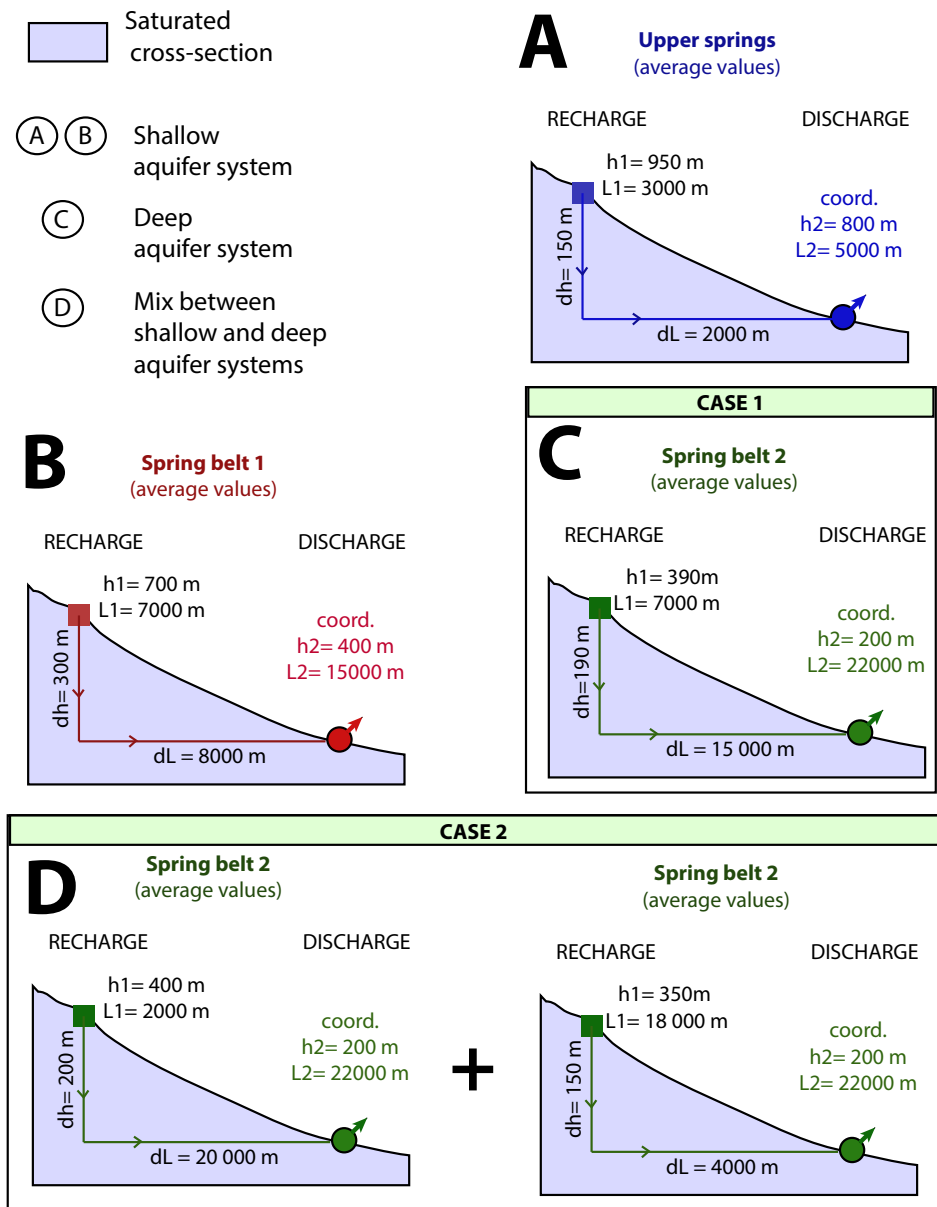


Figure 4.51: Saturated cross-sections considered to calculate the groundwater transit time associated to each spring zone: (A) upper springs, (B) spring belt 1 (SB1), and two configurations possible for the second spring belt (SB2) where (C) suggests one unique recharge area whereas (D) considers a mix between shallow and deep groundwater circulations.

In the upper part (above 800 m asl), the air fall, tephra and tuff deposits are the main representative lithological facies. Considering the hydraulic parameters calculated with the pumping tests, we are able to appraise the water velocity for each spring zones with the equation 4.1. After that, we can calculate the transit time with the equation 4.2 with $L = dL$.

The estimation of the hydraulic conductivity in the upper part has been estimated at $1 \times 10^{-8} \text{m.s}^{-1}$ after the literature (Flint & Selker, 2003; Singhal & Gupta, 2010).

The effective porosity values have been estimated based on the literature values (Wingard, 1971; Flint & Selker, 2003; Entwisle et al., 2005; Mueller et al., 2011). We consider that the effective porosity ranging from 20 % for the pathways to the upper springs, 30% for the SB1 and 40% for SB2 pathways.

The results of the transit time estimation are summarized into the Tab. 4.6.

			A	B	C	D	
			Unique recharge zone	Unique recharge zone	Unique recharge zone	Case 2	
			UP	SB01	SB02	High elevation recharge area	Low elevation recharge area
			UP	SB01	SB02	SB02	SB02
Units			UP	SB01	SB02	SB02	SB02
Piezometric head upstream	h1	(m)	950	700	390	400	350
Piezometric head downstream	h2	(m)	800	400	200	200	200
Distance from P.B.ridge upstream point	L1	(m)	4000	7000	7000	2000	18000
Distance from P.B.ridge downstream point	L2	(m)	5000	15000	22000	22000	22000
	dh	(m)	150	300	190	200	150
	dL	m	1000	8000	15000	20000	4000
Porosity	n_e	(-)	0.2	0.3	0.4	0.4	0.4
Hydraulic conductivity	K	($m.s^{-1}$)	1.00E-08	1.00E-05	2.00E-04	2.00E-04	2.00E-04
Hydraulic gradient	dh/dl	(-)	0.150	0.038	0.013	0.010	0.038
Darcy velocity	u^*	($m.s^{-1}$)	7.50E-09	1.25E-06	6.33E-06	5.00E-06	1.88E-05
Horizontal distance	Lh	(m)	1000	8000	15000	20000	4000
Transit time	t	(s)	1.33E+11	6.40E+09	2.37E+09	4.00E+09	2.13E+08
Transit time	t	(year)	4225.1	202.8	75.1	126.8	6.8
						Total transit time (year)	
						133.5	

Table 4.6: Calculation of the cinematic velocity and the water transit time for each spring zone after the Darcy's law based on the hydraulic parameters estimated with the pumping test.

As expected, the lowest Darcy velocity is obtained on the upper springs water pathway ($7.5 \times 10^{-9} m.s^{-1}$). The alternation of low permeable formation does not favour the groundwater circulation. Considering an averaged distance of 1 km between the recharge and the outlet, we find a water residence time of 4225 years. This long transit time has

to be interpreted carefully. The strong assumption of a continuous shallow aquifer in the upper parts is probably not realistic and the distance from the recharge and the many outlets, caused by the interception of the topography and the perched aquifer, is less than 1 km. Thus, this result mainly shows that even if the upper parts is favourable to the infiltration (cf. Chapter 3-Water balance estimation), the lithological facies and the deposit architecture create a weak water circulation.

The SB1 circulation has a Darcy velocity of $1.25 \times 10^{-6} \text{ m.s}^{-1}$ and a transit time of 202 years. Here again, the transit time represents the longest possibility by the water. The transit time is more realistic but still high.

The SB2 circulation of the “C” case has a Darcy velocity of $6.33 \times 10^{-6} \text{ m.s}^{-1}$ and a transit time of 75 years. The high hydraulic conductivity of the paleo-channel and their unconsolidated material allows a relatively high water velocity. Nevertheless, if we consider the case “D” with two recharge zones, the water velocity ranges from $1.8 \times 10^{-5} \text{ m.s}^{-1}$ to $5.0 \times 10^{-6} \text{ m.s}^{-1}$ with an associated water travel time of 6.8 and 126 years. Thus, a total transit time of 133 years.

All the estimated transit time are above 50 years and thus valid one of the assumption deduced from the observation of the tritium analyses. The water on the East flank of Merapi has an infiltration date anterior to the first atomic atmospheric test (1951). Moreover, this estimation does not take into account the water transfer through the unsaturated zone that decreases the Darcy velocity.

A numerical approach based on a hydrogeological conceptual model can help to validate this transit time estimation.

4.3.3 Hydrogeological conceptual model

As a conclusion of the hydrogeological functioning interpretation, we propose a hydrogeological conceptual model of the Eastern flank of Merapi volcano.

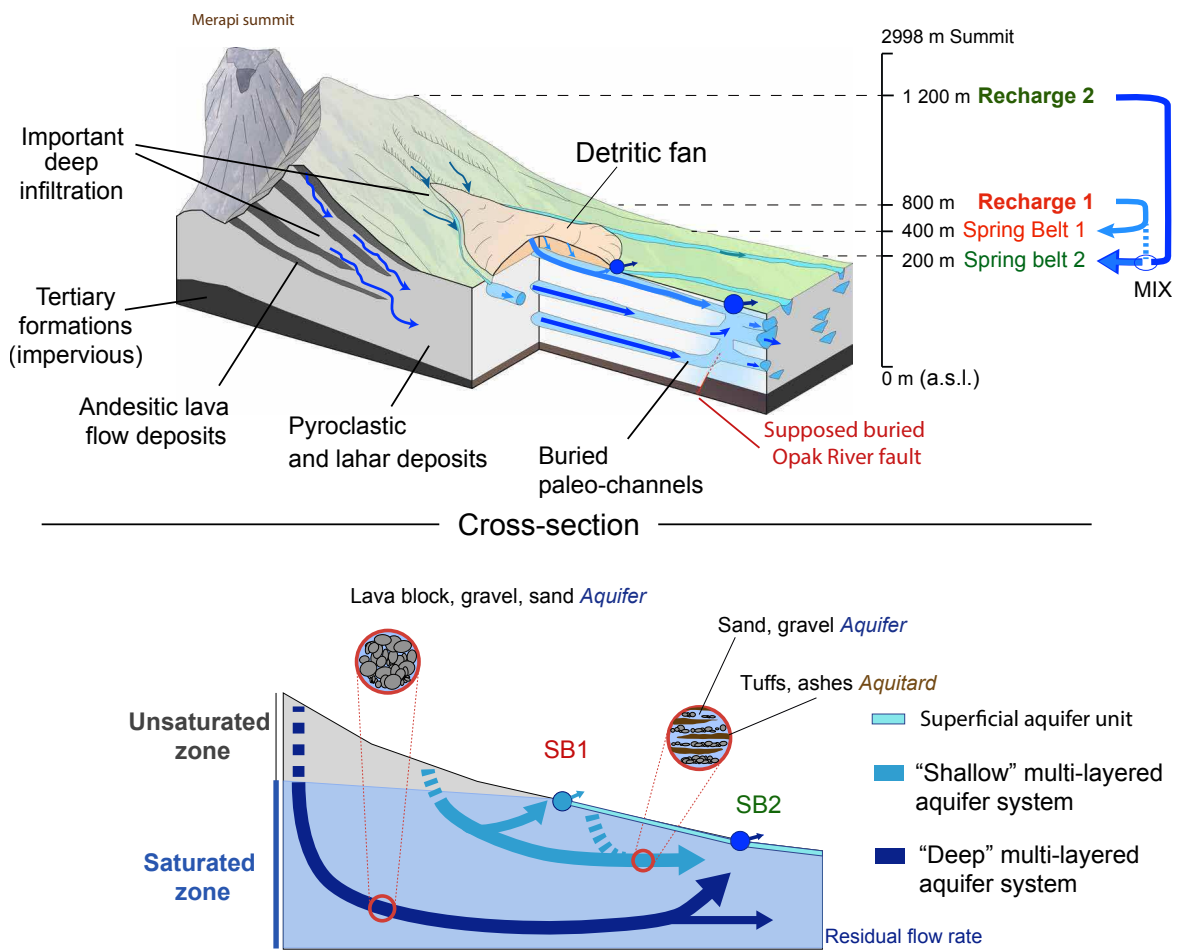


Figure 4.52: Hydrogeological conceptual model of the Eastern flank of Merapi volcano. Identifying two groundwater circulations through a shallow aquifer system composed by an alternation of aquifers and aquitards, and with a deep aquifer system formed by preferential path flow whose are the buried paleo-rivers.

4.3.3.1 A complex multi-layered system

At regional scale, the East flank of Merapi volcano can be described as heterogeneous multi-layered system. The detritic deposits architecture described in Chapter 2 is composed by an alternation of aquitard and aquifer formations with large range of geometry and hydrodynamic properties. The flank can be divided in three hydrogeological units: 1) the upper part, located above 800 m elevation, 2) the spring belt 1 zone, ranging from 400 m asl to 800 m asl and 3) the spring belt 2 zone, below 400 m asl. These zones represent the main discharge zones and possess distinct hydrodynamic behaviors.

4.3.3.2 Upper part

Above 800 m asl, the river incisions reveals an alternation between massive andesitic lava flow deposits which are fractured near Merapi summit, and explosive material composed by air fall, pyroclastic and welded tuff deposits. The massive non-fractured lava and the welded tuff formation formed the aquitard formations on which several disconnected perched aquifer layers can be found. These unconfined aquifer formations are composed of coarse pyroclastic flow and ignimbrite deposits. These aquifers have a large range of thickness and lateral extent depending on the topography and the underlying aquitard formation size (Fig. 4.23).

The water table of these aquifers is relatively close to the topographic surface (less than 30 m deep) and the hydraulic conductivity is estimated at $1.0 \times 10^{-8} \text{ m.s}^{-1}$ according to the literature. Even if the recharge is the main process over the area, the hydrodynamic properties of the lithology do not favour a fast water transfer and the cinematic velocity has been calculated at $7.5 \times 10^{-9} \text{ m.s}^{-1}$.

The unconsolidated material is easily erodible and remobilized by the temporary stream during the rainy season, thus, the slopes of the gullies are steep and cross the aquifer layers, creating small lithological contact springs. Some spring flows depend of threshold and stop during the dry season. On the perennial springs, the flow goes into the temporary river beds which constitute a preferential zone for the infiltration and thus the groundwater recharge.

4.3.3.3 SB1 zone

We saw that between 800 m and 400 m asl, near 5000 years BP, an extreme flank collapse event created a detritic fan with triangular shape that disturbed the drainage network. At the termination of this fan, a spring alignment along the topographic curve forms the spring belt 1 (SB1). These springs are perennial and have a medium flow rate range ($\sim 0,01 \text{ m}^3 \cdot \text{s}^{-1}$).

The fan zone creates a large recharge area and covers the paleo-rivers. The unconsolidated accumulation of lava boulders, sand and coarse material forms the aquifer layers of at least two springs (e.g. Pusur and Soka springs, n°42 and 44 respectively). The springs drain a semi-confined shallow aquifer composed by pyroclastic and detritic material. The hydraulic conductivity has been estimated at $1.0 \times 10^{-5} \text{ m} \cdot \text{s}^{-1}$ and the cinematic velocity of the porous media has been calculated at $1.26 \times 10^{-6} \text{ m} \cdot \text{s}^{-1}$.

4.3.3.4 SB2 zone

The main discharge zone of the Eastern flank of Merapi system is located between 200 to 283 m elevation and is represented by a second spring belt (SB2) with important and

perennial springs. The spring occurrence is probably caused by a regional fault observed on the South-East shore of the Yogyakarta basin. This fault creates a preferential vertical groundwater circulation near 200 m asl on Merapi Eastern flank.

These important springs drain deep aquifer layers composed by paleo-channel buried into the air-fall, tuff and lahar formations. These paleo-channels are in average less than 30 m thick and near 50 m wide. Their hydraulic conductivity has been estimated at $2.0 \times 10^{-4} \text{m.s}^{-1}$ with a cinematic velocity of $5.0 \times 10^{-6} \text{m.s}^{-1}$.

We have shown that the flow rate and the high permeability of the paleo-channel preserve the recharge air temperature signature temperature through the system. The latter means we can use the water temperature as tracer of the recharge elevation validated. The stable isotope analyses have validated this assumption and are defined as independent tracer from the temperature.

These aquifers become confined as they extend from the upper part to the low lands. The hydraulic gradient measured between two monitoring wells upstream and downstream has been determined at 7×10^{-3} . We have suggested several mix possibilities between shallow and deep circulation observed at SB2, we propose that the main recharge area is located upstream the detritic fan, between 600 to 1200 m asl. The average mixing ratio of the shallow and deep aquifers ranging from 37 to 50% of water coming from 1200 m asl and the rest coming from 600 to 400 m asl.

To summarize: the climatic, hydrological, hydrogeological and geochemical variables monitoring on two hydrological years, allow to identify recharge areas, preferential flow paths, relevant tracers to characterize flows and to propose a conceptual model of flow of complex volcano-detritic environment (Fig. 4.52).

The next step will be the validation of this conceptual model using coupled flow circulation, mass transport or heat transfers numerical modeling (METIS code ([Goblet, 1981](#))).

5

Groundwater modeling

Introduction

Understanding groundwater circulation through a complex geological formation is hard to complete with field observation only. Indeed, the field observations and measurements are hindered by the time scale and the distances over which groundwater flow operate within watersheds. Within zones where the data are limited, the lacks in the groundwater knowledge is a real issue and recent studies need to make simple assumptions to fill these gaps (Bethke, 1989).

Mathematical modelling of groundwater flow, heat transfer and chemical mass transport at the watershed scale has been increasingly used during the last decade to studying a large range of hydrogeological processes (Person et al., 1996). These models provided important insights to the understanding of the groundwater pathways, infiltration rates and transport processes within aquifer formations (Garven, 1995). A wide range of models is now available but while they differ by their complexity and the processes represented, they are all based on the similar set of assumptions of the basic flow laws. Even if the mathematical models can represent processes operating at geologic time scale, they need field investigations and laboratory data to be representative of the real phenomenons.

In the preceding chapters, the combination of multi-disciplinary study allowed us to built a conceptual model of the groundwater circulations of an andesitic volcano-sedimentary edifice represented by the Eastern flank of the Merapi volcano. In order to confirm this conceptual model and better quantify the groundwater circulations, the data acquired between 2011 and 2013 have been used as calibration data for a hydrogeological modelling approach. The objectives of this chapter are: i) to valid the conceptual model through a simple model, flow and mass transport or heat transfer and ii) to better quantify the groundwater circulation and confirm the water balance. To reach these goals the approach is performed in a 2D vertical cross section with the METIS code (Goblet, 1981) and has been done in two steps:

- 1) The groundwater flow combined to mass transfer will be simulated in steady state using the recharge isotopic gradient as a constraint and trying to reproduce the spring isotopic concentration ($\delta^{18}O$) as calibration data. During this procedure, the hydrodynamic parameters have been fitted by trial and error method. The mass transfert parameters are those propose in the litterature.
- 2) The thermal properties will be integrated into the model and the groundwater flow combined to the heat transfert will be simulated using air temperature gradient as a constraint and trying to reproduce the spring temperature.

The first part of this chapter briefly reminds the use of the temperature as tracer of groundwater circulation in hydrogeology. Then, the flow and heat transfer model code METIS (Goblet, 1981) is presented. After that, the model configuration chosen for the

Eastern flank of the Merapi application is detailed. The final part presents the results of the simulations and their discussion.

5.1 Flow and heat transfer modeling in hydrogeology

5.1.1 Temperature as groundwater tracer

Heat transfer is discussed into many topics in hydrogeology. It is recognized that water moving through a groundwater system transports heat and thus changes the subsurface temperature distribution. Temperature can therefore be used as a tracer of hydrological processes and for testing conceptual hydrogeological models ([Andrews et al., 1982](#)). Temperature offers several advantages as a tracer because it is easy, quick, and inexpensive to measure accurately in the field. The temperature of groundwater also provides insight into the subsurface geological processes that generate heat.

Most of the studies are approaching the problem from the field of geothermics regards perturbations in the thermal profile as anomalies, which might be explained by interaction between the geothermal system and groundwater flow influenced by superficial conditions which might be seasonal. During the system recharge, the infiltration of meteoric water creates a negative gradient induced by the circulation of cold water. A positive gradient stronger than the geothermic gradient is induced by a regional groundwater flow from the depths and evacuating them to the limits of the system (from a fault or a dyke) ([Anderson, 2005](#)).

Without groundwater flow, subsurface temperature in the geothermal zone (around 10 m deep) follows the geothermal gradient, usually represented by an increase of 1°C per 20 to 40 m of depth. Within the geothermal zone, the temperature profile is not subjected to seasonal variations and is expected to be approximately linear except when perturbed by groundwater flow, although changes in thermal conductivity also curve the thermal profile (Fig. 5.1).

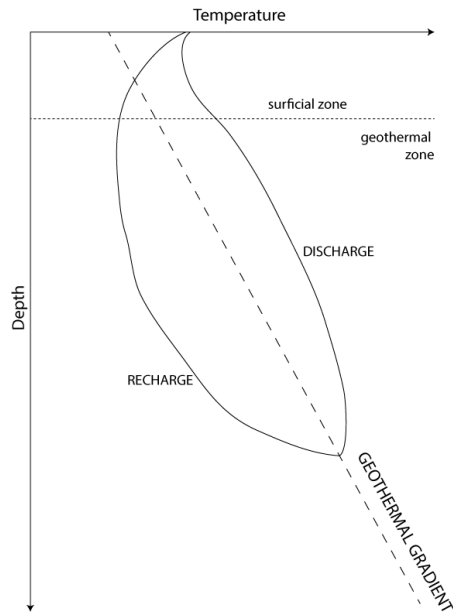


Figure 5.1: Schematic temperature profiles showing deviations from the geothermal gradient caused by surface warming in the surficial zone and convection in the geothermal zone. The ground water recharge results in concave upward profiles, whereas groundwater discharge results in convex upward profiles (modified after [Taniguchi et al. 1999](#)).

Hence, groundwater flow perturbs the geothermal gradient by infiltration of relatively cool water in recharge areas and upward flow of relatively warm water in discharge areas, causing concave upward profiles in recharge areas and convex upward profiles in discharge areas respectively (Fig.5.2). Within the surficial zone, temperature is influenced by seasonal heating and cooling of the land surface. Shallow groundwater temperature is $\sim 1^{\circ}\text{C}$ to 2°C higher than the mean annual surface temperature ([Parsons, 1970](#)). The amplitude of temperature fluctuations decreases with depth; below ~ 1.5 m temperatures are not significantly influenced by diurnal fluctuations at the land surface ([Beck et al., 1990](#)). Temperature profiles in the superficial zone potentially provide information about seasonal recharge/discharge events from precipitation and exchanges with surface water ([Forster & Smith, 1989](#)).

The perturbation of the thermal gradient is more marked in mountainous terrains. Greater relief found in mountainous terrain causes an enhanced vertical component of groundwater flow that may enhance advective disturbance of the thermal regime. Furthermore closely spaced ridges and valleys in high-relief terrain cause an advective disturbance that has a restricted lateral extent when compared to the long-wavelength disturbances typical of low-relief terrain. As a consequence groundwater flow within a mountain massif can cause large-amplitude, short-wavelength perturbations of the thermal regime that may distort the view of broad regional-scale variations in heat flow ([Forster & Smith, 1989](#)).

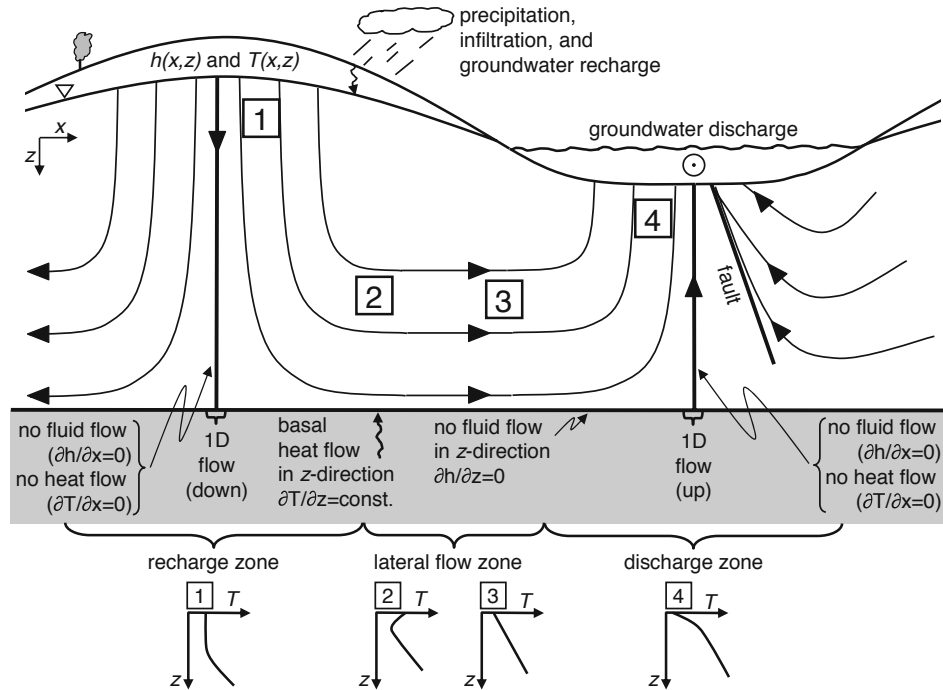


Figure 5.2: Illustration of a typical (forced-convection) groundwater flow field caused by topographic relief (at any scale) that repeats horizontally and results in the indicated boundary conditions. The bold flow lines indicate the edges of unit flow cells where boundary conditions apply. The boundary conditions are zero groundwater and constant heat flow at the base, no heat and no groundwater flow at the sides (usually due to model symmetry representing repeated ridge-valley combinations), and constant hydraulic head and mean annual surface temperature (possibly following the adiabatic lapse rate of the atmosphere) at the top, representing the water table. A fault is included as a reminder that an advective heat discharge boundary condition may be required. Numbers indicate typical steady-state geotherm profiles expected in the respective groundwater flow field regions: (1) isothermal (cold) near-surface profile in a recharge region, (2) low-temperature horizontal flow at some depth that has not completely thermally equilibrated at the given position, (3) linear profile as thermally equilibrated flow is perpendicular to the geothermal heat flow vector, and (4) elevated near-surface geothermal gradients in discharge zones (Saar, 2011).

Several articles are focused on analytical and numerical solutions to study basin-scale transport in two and three dimensions (Stallman, 1963; Sass et al., 1994; Hayba & Ingebritsen, 1994; Raymond et al., 2011). Sass et al. (1994) and Deming (1993) showed that the effect of ground water flow on the thermal regime depends on the magnitude of the seepage velocity and the depth of circulation. Therefore, the general conclusion of most of the model results using the groundwater temperature as a tracer is that the predicted temperature of spring water depends on the groundwater volumetric flux of water. For a given aquifer, as the groundwater velocity increases, the heat added by geothermal warming is diluted into a larger volume of water, and consequently, spring temperatures become colder (Manga, 1998). In fact, spring temperatures can be colder than the mean annual surface temperature at the discharge elevation if the water is recharged at much higher elevations where the air temperature is cooler, as first noted by Alexander von Humboldt (cited in Davis, 1999).

5.1.2 Application in volcanic areas

The volcanic areas are preferential zones to study the heat and flow circulations (Ingebritsen et al., 1992; Nagao & Uyeda, 1995; Violette et al., 1997; Manga, 1998; James et al., 2000; Hurwitz et al., 2003; Manga & Kirchner, 2004). The studies are mainly focused on hydrothermal systems. Indeed, hydrothermal behavior allows to quantify relatively easily the heat transfer into an aquifer (Saar, 2011). The results of Hurwitz et al. (2003) suggest that the permeability structure of a volcanic edifice and underlying material is the dominant control on water table elevation and the distribution of pressures, temperatures, and fluid phases at depth. When permeabilities are isotropic, water table elevation decreases with increasing heat flux and increases with increasing recharge, but when permeabilities are anisotropic, these effects can be much less pronounced. Several authors combined different methods with the heat transfer, as the isotopes (oxygen, hydrogen, carbon), to determine the groundwater flow pattern (Andrews et al., 1982; James et al., 2000).

Heat discharge at springs is a valuable metric to constrain groundwater circulation depths and large-scale flow patterns, despite the difficulties in estimating background heat flow rates and associated geothermal gradients, issues with preservation of the heat signal despite water mixing and (partial) thermal equilibration during water ascent. The method is attractive because spring temperatures and discharge rates can be easily measured, groundwater recharge temperatures can be relatively easily inferred from $\delta^{18}\text{O}$ and δD measurements in the same spring water, and springs integrate processes over relatively large subsurface regions.

5.2 METIS code: a groundwater, mass and heat transfers code

The code METIS (Modélisation des Ecoulements et des Transferts avec Interactions en milieu Saturé) developed at the Ecole Nationale Supérieure des Mines de Paris (Goblet, 1981), simulates flow circulation, mass transport and heat transfers in two or three dimensions. Finite element numerical methods are used for spatial and temporal discretization of the differential equations. METIS allows three types of spatial discretization : the base mesh represents one, two or three dimensions, a principal medium, considered as a porous medium, which can represent either a medium granular structure, a finely fractured media and structures of higher permeability (scaled fractured areas) can explicitly be introduced into the mesh. These structures are represented by elements of reduced dimension (one-dimensional elements in a two-dimensional meshes or two-dimensional elements in a three-dimensional mesh). Finally, it is possible to represent a dispersion including diffusion and advection phenomenon from each node along a "virtual" direction. This code has been used within the volcanic edifice of the Piton de la Fournaise, Reunion

island, France, to determine the internal structure of the hot-spot volcano and the role of the groundwater circulation (Violette et al., 1997).

5.2.1 Mathematical formulation

The METIS code uses the fundamental equations of flow and heat transfers. METIS assimilates the system as a combination of impermeable matrix and empty spaces where the water circulates. This set is considered as a continuous medium with mean hydraulic properties (porosity and permeability).

5.2.1.1 Flow circulation

The flow is supposed non-turbulent state. The subsurface distribution of heat in saturated porous media can be described by two differential equations, one describing the fluid potential and the other the temperature. All symbols and values used in this study are defined in Tab. 5.1. We use as fluid potential an equivalent freshwater head given by the simplification of the Darcy law :

$$h = \frac{p}{\rho_0 g} + z \quad (5.1)$$

where p is the fluid pressure, ρ_0 an arbitrary reference density, g the gravitational constant, and z the elevation above sea level. The groundwater flow in response to pressure gradients is described by:

$$\nabla \cdot \left(\frac{\rho_0 g \bar{k}}{\mu(\theta)} \nabla h \right) = S_S \frac{\partial h}{\partial t} \quad (5.2)$$

Symbol	Description	Values	Units
h	Hydraulic head	Computed	m
p	Fluid pressure		kg m ⁻¹ s ⁻²
z	Elevation above sea level	Measured	m
ρ_0	Reference water density	1000	kg m ⁻³
g	Gravitational constant	9.81	m s ⁻²
\bar{k}	Permeability tensor		m ²
K	Hydraulic conductivity	Calculated from hydraulic tests	m s ⁻¹
θ	Temperature	Computed	°C
θ_0	Recharge temperature	Measured	°C
μ	Dynamic viscosity	Computed	Pa s
S_S	Specific storage coefficient		m ⁻¹
$\bar{\alpha}$	Dispersivity tensor composed of α_L and α_T		m
α_L	Longitudinal dispersivity	12	m
α_T	Transversal dispersivity	5	m
U	Darcy velocity	Computed	m s ⁻¹
ω	Total porosity		%
$\omega_{aquifer}$	Cinematic porosity Aquifer	40	%
$\omega_{aquitard}$	Cinematic porosity Aquitard	20	%
γ_W	Water specific heat	4.18 x 10 ⁶	J m ⁻³ K ⁻¹
γ_R	Rock specific heat	2.50 x 10 ⁶	J m ⁻³ K ⁻¹
γ	Specific heat of the medium		J m ⁻³ K ⁻¹
λ_W	Water thermal conductivity	0.6	W m ⁻¹ K ⁻¹
λ_R	Rock thermal conductivity	2.2	W m ⁻¹ K ⁻¹
q_{heat}	Source term of heat		W m ⁻³
C	Concentration		%

Table 5.1: Parameters used in groundwater flow, heat transfer and mass transport simulations.

5.2.1.2 Mass transport

To account for advection, kinematic dispersion, and molecular diffusion the mass transport equation is expressed as:

$$\nabla \cdot ((\bar{\alpha}U + \omega d)\nabla C - CU) = \omega \frac{\partial C}{\partial t} + q_m \quad (5.3)$$

with α is the dispersivity, ω is the total porosity, U is the Darcy velocity, d is the diffusion coefficient in porous media (diffusion coefficient in pure water multiplied by the tortuosity coefficient), C is the mass concentration and q_m is a source term corresponding to the added or withdrawn mass of tracer per unit volume per unit of time.

5.2.1.3 Heat transfer

Density variations are not accounted for our simulations as we consider that the maximum effect of temperature on density is negligible in shallow continental context (Castro et al., 2005). Indeed, the system is only composed by fresh water and we consider that there is

no saline intrusion because the sea shore is located at more than 30 km from the Merapi with complex geological setting in between and the conceivable high water mineralization due to the magmatic chamber is occurring at large depth (at least 1.5 km deep) and therefore out of our model scale (Müller & Haak, 2004; Commer et al., 2006).

The heat transfer equation accounting kinematic dispersion and conduction is given by (Houpeurt et al. (1965) in de Marsily (1986)) :

$$\nabla \cdot ((\bar{\alpha}\gamma_W U + \lambda)\nabla\theta - \gamma_W \vec{U}\theta) = \gamma \frac{\partial\theta}{\partial t} + q_{heat} \quad (5.4)$$

with

$$\lambda = \omega\lambda_W + (1 - \omega)\lambda_R \quad (5.5)$$

$$\gamma = \omega\gamma_W + (1 - \omega)\gamma_R \quad (5.6)$$

where $\bar{\alpha}$: dispersivity tensor composed by α_L the longitudinal dispersivity (m) and α_T the transversal dispersivity, λ is the thermal conductivity of the medium, λ_W and λ_R are the thermal conductivities of water and the rock, respectively; γ is the specific heat of the medium, γ_W and γ_R are the specific heat of the water and rock, respectively; ω is the porosity, and q_{heat} is a source term corresponding to the added (or withdrawn) heat per unit volume per unit of time.

5.3 Numerical model configuration

For this study, all the simulations are in 2D-vertical cross section and were conducted in steady state flow situation solved with the finite element method. We saw that there were no significant seasonal variation within temperature or water flow rate in the Eastern Merapi spring belts, hence, it is consistent to simulate a steady flow situation.

When the flow and the mass or the heat transfer are combined, i) the code solves the flow equation first, based on the values of water viscosity and density, and calculates the pressures, ii) the transport equation is then solved using the velocity field created from the pressure calculated in the first step, iii) the code calculates a new field of volumic mass. As input of the simulations, the code will need spatial distribution of the physical parameters and the initial and boundary conditions.

5.3.1 From observations to modeling

To build a flow circulation and thermal model of such a complex system, we needed to know the geometry of the internal structure of the volcano, the saturated part, the rate

of the recharge and its spatial distribution. We also needed the orographic gradient of air temperature, the ^{18}O concentration, the nature of heat transfer processes (conduction versus advection) and the spatial distribution of the physical properties. The model configuration is based on:

- 1) The results of the geological and geomorphological study for the internal structure and the identification of the aquifer and aquitard formations;
- 2) The hydroclimatic observations to define the boundary conditions (flow: groundwater recharge, mass: $\delta^{18}\text{O}$ concentration, heat: air temperature...);
- 3) The hydrogeological measurements and literature review to estimate the spatial distribution of the hydraulic and physical parameters to validate our simulations;
- 4) The physico-chemical variables (Groundwater discharge Q and $\delta^{18}\text{O}$ concentration and temperature) at the outlet of the spring belts as validating data.

The geological analysis has allowed to choose a representative cross-section of the complex 3D system (Fig. 5.3, A). The West boundary is characterized by the Pasarbubar ridge (in red dot line on Fig. 5.3, A) culminated at 1500 m asl. The cross-section profile passes by the thin interfluvium between the Soka and the Brambang rivers at 1000 m asl and continues through the middle of the detritic fan to reach the SB1 at 400 m asl and then the SB2 near 200 m asl. The profile is assimilated to 1 m wide with 200 m depth and a total length of 22 km and it is supposed to represent the saturated part of the system.

The conceptual model defined two groundwater circulations, i) a shallow aquifer system (5-40 m deep) with recharge areas located on the detritic fan (800 to 400 m asl) and between the two spring belts (400 to 200 m asl); ii) a deep aquifer system (50-75 m deep) with regional recharge located in high elevations (1500-800 m asl). The first aquifer system provides groundwater flow to the SB1 and SB2 while the second aquifer provides water to the SB2 only and the rest continues to the East and is noted as residual flow rate (Fig. 5.3, B). This multilayered system suggests it might be repeated at depth, with other aquifer layers.

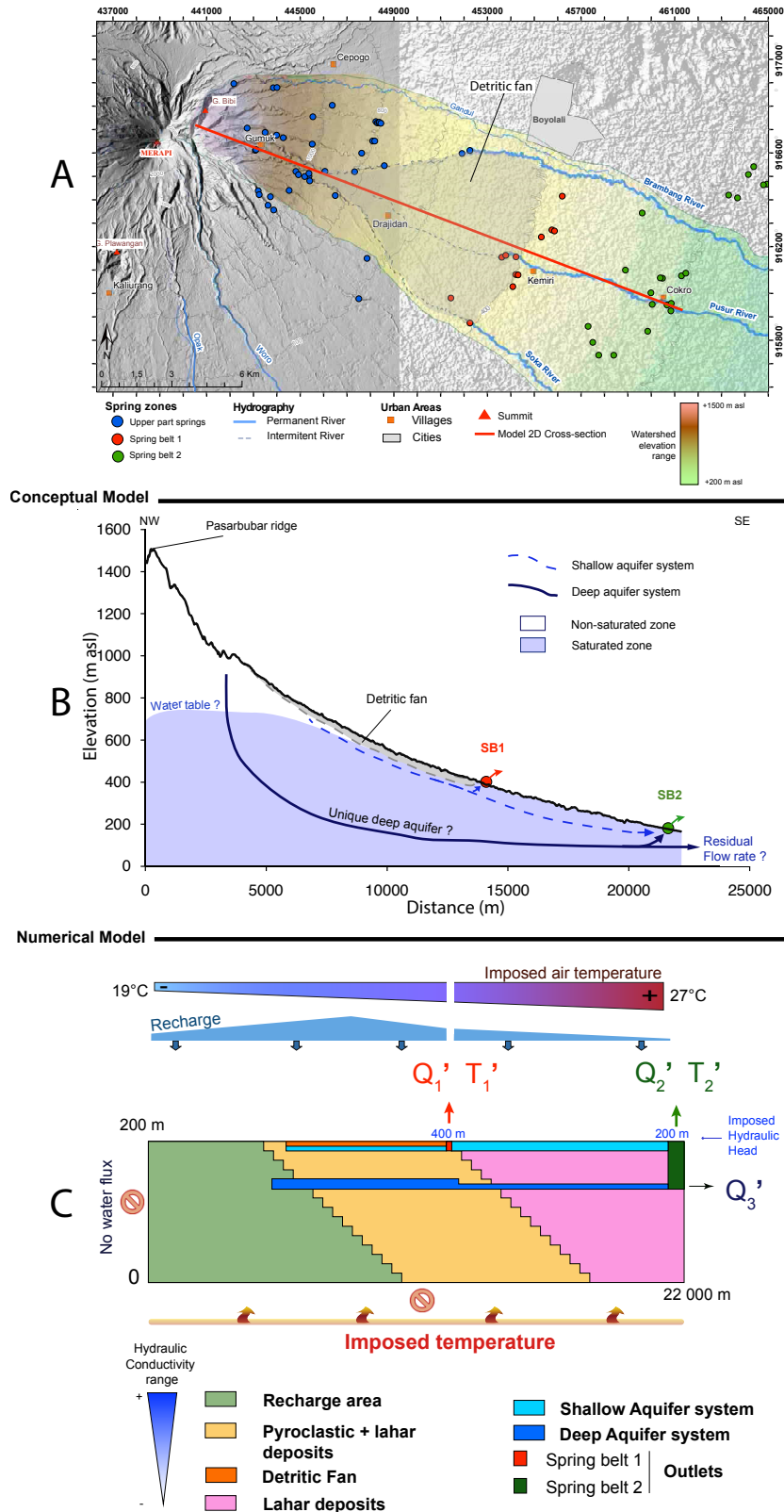


Figure 5.3: From observations to modeling: A) Eastern flank of Merapi map with the experimental catchment boundaries, the spring zones and the cross-section chosen for the modeling. On the left, the precise DEM (ground resolution 15 m, courtesy of C. Gerstenecker, Gerstenecker et al. (2005)) shows the ancient caldera which culminates at 1500 m asl (red dot line) as west boundary of the watershed. On the right, the DEM ASTER GDEM V2 with 30 m ground resolution. B) Schematic illustration of the conceptual model of the groundwater circulation through the saturated zone on the Eastern flank of the Merapi. The spring belt 1 (SB1) at 400 m asl drains a shallow aquifer with local recharge area covered by detritic fan. This shallow aquifer reaches also the spring belt 2 (SB2) near 200 m asl. The remaining questions concern the water table position in the high elevations and the number of deep aquifer systems. C) hydraulic conductivity grid configuration employed in numerical simulations with the METIS model and the flow and heat boundary conditions.

5.3.2 Model geometry

The remaining questions and thus, the main targets of the modeling, are the water table elevation in the upper parts, the number of deep aquifer systems linked to the SB2 and the portion of groundwater flow rate which continues to the East. To achieve those targets in addition to the validation of the geometrical structure and the hydraulic parameters, the conceptual model has been reduced to the saturated portion of the NW-SE cross-section of the Eastern flank of the Merapi volcano. The mesh in finite elements has been built with the automatic mesh generator linked to METIS code named COMET (Goblet, 1981). As the saturated zone only is considered, the mesh grid is assimilated to a simple box and the topography is not taken into account although known hydraulic heads are imposed at the spring belt elevations (400 m for SB1 and 200 m for SB2).

The spring belts are reported on 2D cross-section and the spring positions have been averaged at one unique elevation. Therefore, in reality the spring elevations at SB2 ranging from 221 to 283 m asl and have been reported at 200 m on the model cross-section. The mesh grid is discretized on a grid of 441 x 21 cells of 10 m high and 50 m large with a finer discretization near the surface and at the outlets with cells of 5 m large. In total, the mesh grid has 10465 elements and 10944 nodes (Fig. 5.3, C).

The thickness of the aquifer layers is initially estimated to 10 m after the geophysics measures and the field observations of the visible paleo-channels. This value will be discussed with the simulations.

We saw that the deep aquifer layers were composed by buried paleo-river channel. We can suggest that several similar processes could happened and create n number of paleo-channel structures. Thus, simulations with more than one deep aquifer system will be tested.

The boundary conditions are applied over the external nodes of the grid. Some of the boundary conditions will not be changed during the simulations while the others will be tested.

5.3.3 Flow simulation

5.3.3.1 Flow parameters

Physical parameters are attributed to the mesh elements. They characterize the internal structure of the volcanic edifice and could be change during the different simulations in order to test the system sensibility to these parameters. The structure has been highly simplified and can be divided in eight units (Fig. 5.3, C):

1. **Recharge area**: defined as high permeability zone, representing the alternation of non consolidated material that facilitates the infiltration and thus, the deep ground-

water recharge. This zone extends from the Pasarbubar ridge (1500 m asl), considered as initial point of the 2D cross section, to 7000 m downstream (1000 m asl). In depth, the geometry has been drawn with “stair step shape” to take into account the different building stages of the edifice.

2. **Pyroclastic and lahar unit**: characterized as volcanic matrix with relatively low permeability properties composed by pyroclastic flow, air fall and remobilized material (lahars) formations. This unit covers the zone from 7000 to 15000 m from the Pasarbubar ridge. In depth, the geometry has been drawn with the same “stair step shape” than the recharge zone.
3. **Lahar unit**: zone with low permeability composed by lahar and air-fall deposits (impervious). This unit fills the section from 15000 to 22000 m from the ridge. In depth, the geometry has been drawn with the same “stair step shape”.
4. **Detritic fan**: this unit is composed by remobilized materials, tephra, pyroclastic formations and is relatively low permeable. The fan forms a shallow unit from 7500 m to 14950 m from the ridge;
5. **Shallow aquifer unit**: based on the hydraulic tests and the lithological stratigraphic log, this zone is an alternation of aquitard (tuff and air fall) and aquifer (gravel, lava blocks, sand) layers with relatively high permeability.
6. **Deep aquifer unit**: defined as buried paleo-channel with massive lava block, coarse and sandy material characterized by high permeability zone.
7. **SB1**: the spring belt 1 has been defined as high permeability zone and reduced to 50 m of discharge zone at 15000 m from the ridge and 50 m deep.
8. **SB2**: the spring belt 2 has been reduced at 100 m of discharge zone and 80 m deep.

The hydraulic parameters of the aquifers have been defined based on the pumping test analysis, however, the modeling is a consistent way to assess the validity of these data. Thus, the hydraulic conductivity of the aquifer layers but also of the aquitard layers will be tested.

The initial hydraulic conductivities for each unit are summarized in the Tab. 5.2. The other values have been taken after the literature of volcano-sedimentary edifice (Hurwitz et al., 2003; Flint & Selker, 2003; Custodio, 2004; Cattoni et al., 2007; Singhal & Gupta, 2010).

Units	Hydraulic Conductivity (m s^{-1})
Recharge area	5.0×10^{-4}
Pyroclastic + lahar formations	1.0×10^{-9}
Detritic fan	1.0×10^{-6}
Lahar formations	1.0×10^{-12}
Shallow aquifer	1.0×10^{-5}
Deep aquifer	2.7×10^{-4}
SB1	3.0×10^{-4}
SB2	3.0×10^{-4}

Table 5.2: Initial hydraulic conductivity values of the model units. The values of the shallow and deep aquifer are based on the hydraulic tests while the others are based on the literature for the corresponding lithology [Hurwitz et al. \(2003\)](#); [Flint & Selker \(2003\)](#); [Custodio \(2004\)](#); [Cattoni et al. \(2007\)](#); [Singhal & Gupta \(2010\)](#).

5.3.3.2 Flow boundary conditions

The flow boundary conditions are represented by:

- No-flow condition on the West and at the base of the grid.
- The East boundary is in free flow.
- Two hydraulic heads are imposed at the spring belt locations: 400 m asl for the SB1 and 200 m asl for the SB2.
- The spatial distribution of the recharge at the top of the grid with the values estimated from the hydrological analysis (cf. Chapter 3) for the hydrological year 2011-2012. To better represent the steady state of the system, the hydrological year 2011-2012, considered as medium year has been taken as reference for the recharge amount.

The recharge, expressed in meter has been reported to the unit surface of the model cross-section. We suggest that the infiltrated flux calculated by the hydrological balance was reasonably accurate. We have calculated the recharge at different scale: the upper part (zone above 800 m asl, 52 km^2), on the detritic fan zone (800 to 400 m asl, 51 km^2) and between the two spring belts (400 to 200 m asl, 57.4 km^2). The recharge for each zone over the period of 2011-2012 has been calculated at 1 m (upper part), 1 m (fan zone) and 0.8 m (SB1 to SB2 zone). When we multiply the recharge by the length of the model cross-section unit line, we obtain the recharge that will be used as input in our model (Fig. 5.4). The values are detailed in the Tab. 5.3. The total mean annual recharge is $149 \times 10^6 \text{ m}^3 \cdot \text{y}^{-1}$.

The flow rates measured every month on each spring have been averaged over the hydrological year and reported on the unitary surface in order to take into account the total flow rate of the spring belt on the model's cross-section. For SB1, the mean annual flow rate over 2011-2012 is $8.92 \times 10^6 \text{ m}^3 \cdot \text{y}^{-1}$ (i.e. $0.3 \text{ m}^3 \cdot \text{s}^{-1}$). Considering the spring belt width

equals to 8.7 km, we find that the reference measured annual flow rate of the Aquifer 1 (Q1) is $3.25 \times 10^{-5} \text{ m}^3 \cdot \text{s}^{-1}$.

The annual flow rate of SB2 over 2011-2012 is $118 \times 10^6 \text{ m}^3 \cdot \text{y}^{-1}$ (i.e. $3.7 \text{ m}^3 \cdot \text{s}^{-1}$) and for a spring belt width of 10.4 km. Reported on the unitary surface, the mean annual flow rate becomes $3.57 \times 10^{-4} \text{ m}^3 \cdot \text{s}^{-1}$. The reference measured annual flow rates is $3.57 \times 10^{-4} \text{ m}^3 \cdot \text{s}^{-1}$ for the Aquifer 2 (Q2).

Considering these annual flow rate estimation, 85% of the recharge is flowing out by the spring zones (i.e. $127 \times 10^6 \text{ m}^3 \cdot \text{y}^{-1}$ with 5% at SB1 and 80% at SB2). The residual flow rate continues through the Merapi flank and reaches the eastern hydraulic boundary considered as Bengawan-Solo river. This residual flow rate will be calculated by METIS but the order of magnitude of this flow rate is near 15% of the recharge.

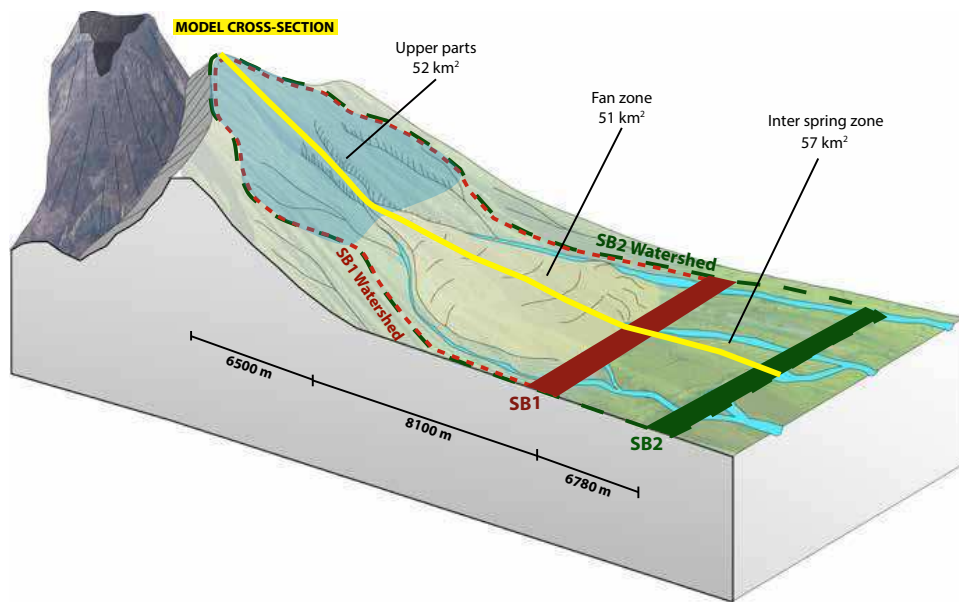


Figure 5.4: Simplified diagram of the different zones used for the numerical model. The recharge is calculated for 3 zones (upper parts, the fan zone and the area between the two spring belts) along the model cross-section line.

Zones	Surface m ²	Length m	Annual recharge m.y ⁻¹	Recharge m.s ⁻¹	Annual recharge volume m ³ .y ⁻¹	Recharge volume m ³ .s ⁻¹	Number of cells on model grid
Upper Part	5.20E+07	6500	1	3.17E-08	5.20E+07	1.65	139
Fan Zone	5.10E+07	8100	1	3.17E-08	5.10E+07	1.62	158
Inter spring zone	5.70E+07	6780	0.8	2.54E-08	4.56E+07	1.44	137
Total	1.60E+08	21700	2.8	8.87E-08	1.49E+08	4.71	434

Volume calculation for each spring zone reported to 1 m cross-section (volume/ spring zone width). The discharges model (noted Q1 obs and Q2 obs) will be used as simulation references. The values are annual average.

Discharge	Annual discharge volume m ³ .y ⁻¹	Discharge volume m ³ .s ⁻¹	Spring zone width m	Discharge model m ³ .s ⁻¹
SB1	8.92E+06	0.28	8700	3.25E-05
SB2	1.18E+08	3.74	10450	3.58E-04
Total	1.27E+08	4.02		

Q1 Obs
Q2 Obs

One part of the groundwater does not flow out by the spring zones and continues downstream to the eastern hydraulic boundary (Bengawan-Solo river). This residual discharge, noted Q3, can be estimated to the difference between the recharge and the discharge. It will be calculated by METIS

Recharge-discharge	Annual discharge m ³ .y ⁻¹	Discharge m ³ .s ⁻¹	Spring zone width m	Discharge model m ³ .s ⁻¹
Residual flow	2.17E+07	0.69	10450	6.57E-05

Q3

Table 5.3: Recharge and discharge values calculated from the observations to the METIS model. The mean annual recharge is expressed in m.s⁻¹ and m³.y⁻¹. The model discharge is calculated from the average annual discharge of the springs and reported on the model cross-section unit line.

Regarding the flow circulation, the observation data for the calibration procedure are the spring flow rate annual average reported on the unitary section of the model for SB1 and SB2, the water table elevation measures of the deep aquifer at BH1 and MW1 bore well, the hydraulic gradient deduced from these values. For the shallow aquifer, the piezometric map based on the shallow wells monitoring is also considered as reference.

5.3.4 Mass transfer simulation

5.3.4.1 Mass transfer parameters

In view to constrain the flow simulations, they are combined with mass transfer. The objectives of these tests are to approach the $\delta^{18}O$ isotope concentrations observed on SB1 and SB2 and to constrain the flow simulations by the $d^{18}O$ concentration. Therefore, in view to simplify the concentration simulations, the isotope concentration has been re-scaled (Fig. 5.5). According to the new normalized concentrations, the SB1 isotope concentration ranges from 3 to 3.6 while the SB2 ranges from 2.2 to 3.

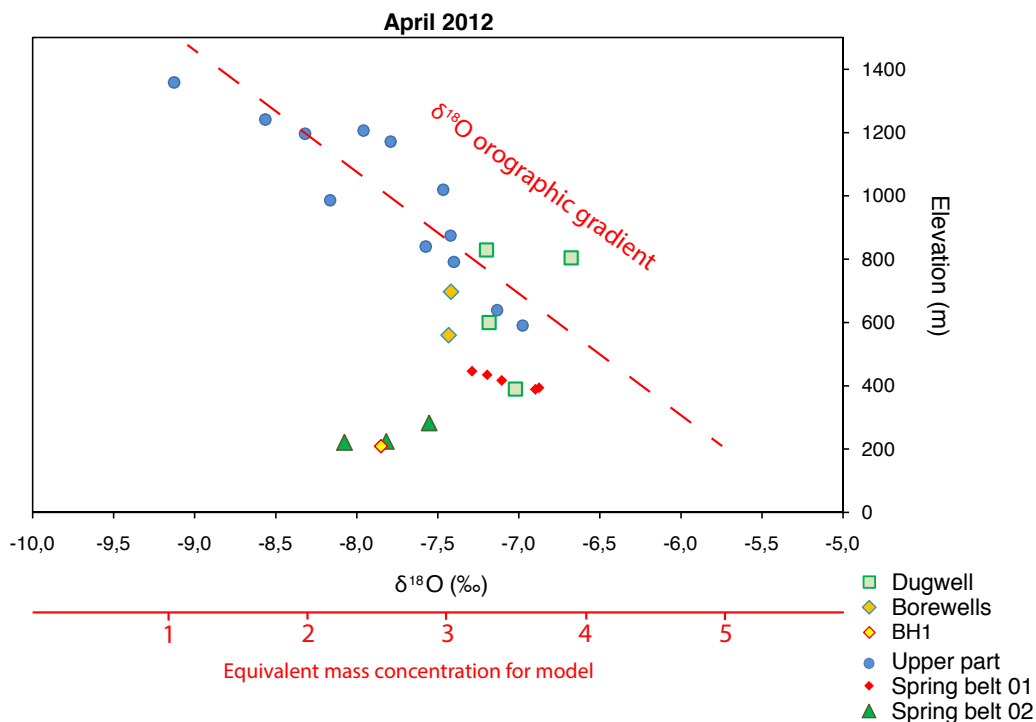


Figure 5.5: Calculation of the mass equivalent to the $\delta^{18}O$ concentration along the model profile based on the isotope orographic gradient observed in April 2012. The concentration has been normalized to simplify the mass transfer input parameter.

5.3.4.2 Mass transport boundary conditions

The isotope circulation is conditioned by the rainfall isotopic signature, thus, the orographic isotopic gradient identified in Chapter 3 of -0.29% per 100 m is reproduced with the normalized concentration (Fig. 5.5). Thus, the normalized concentration is located on the surface boundary and linked to the recharge and thus applied on the same nodes except the nodes with free condition to represent the outlet at SB1 and SB2.

5.3.5 Thermal simulation

5.3.5.1 Thermal parameters

For the thermal circulation, the input parameters are deduced from the literature and summarized in the Tab. 5.4. The aquifer and aquitard layers' specific heat γ are calculated with the equation 5.5 while the thermal conductivity of the aquifer and the aquitard formations λ are calculated with the equation 5.6.

Medium	Porosity	Specific heat			Thermal conductivity		
	(%)	(J m ⁻³ K ⁻¹)			(W m ⁻¹ K ⁻¹)		
	ω	γ_W	γ_R	γ	λ_W	λ_R	λ
Water	-	4.18×10^6	-	-	0.6	-	-
Pyroclastic rocks	26	-	2.50×10^6	-	-	2.2	-
Aquifer (paleo-channel)	57	-	-	3.44×10^6	-	-	1.28
Aquitard (wedded tuff, massive lava flow)	13	-	-	2.72×10^6	-	-	1.99

Table 5.4: Thermal transfer parameters depending on the lithological formation (Mueller et al., 2011; Winograd, 1971)

5.3.5.2 Thermal boundary conditions

The thermal boundary conditions concern the top and the bottom of the model grid:

- The imposed air temperature at the surface of the grid except on the spring belt nodes. We saw that the inter-annual air temperature variation were negligible. In case of climate change, this condition could be tested but this aspect will not be developed here. For our study, the imposed air temperature follows the gradient previously calculated (cf Chapter 3) of -0.8°C per 100 m. Hence, the air temperature is ranging from 19°C in the upper parts and 27°C in the lower lands.
- imposed temperature at the bottom of the grid is estimated after the global geothermal gradient of $+3.3^\circ\text{C}$ per 100 m depth for 200 m deep. This gradient is into the range of the Indonesian geothermal gradient calculated at the global scale ($+3$ to $+6^\circ\text{C}$ per 100 m) (Lubis et al., 2008; Hall, 2002b; Nagao & Uyeda, 1995). The initial

imposed temperature is thus 22°C all along the section. This temperature condition will be discussed through several simulations.

The thermal simulations are calibrated with the annual mean spring temperatures at SB1 and SB2 (noted T1 and T2 respectively). Hence, for the hydrological year 2011-2012, we have a range of temperature from 25.5 to 27 °C for SB1 and from 22.5 to 25.0°C for SB2.

5.3.6 Modelling strategy

The first step is to calibrate the flow circulation into the model structure, then to constrain this circulation with mass transfer calibration and at the end, to apply thermal conditions to reproduce the spring temperatures. For each simulation the following simulated variables have been verified with the observed ones:

- The spring flow rate (SB1 and SB2)
- The piezometric level of the shallow and deep aquifers
- The water velocity through the shallow and deep aquifers
- The mix ratio between Aquifer 1 and Aquifer 2 with the isotope concentration at SB1 and SB2
- The “residual” amount of water (Q3 on the Fig. 5.3, C) continuing to the East without flowing to the monitored springs
- The spring $d^{18}O$ at SB1 and SB2
- The spring temperature at SB1 and SB2

5.4 Simulation results

5.4.1 Flow calibration

The simulation of the groundwater flow is performed in steady state. For the flow calibration, the initial structure presented in Fig. 5.6 with eight distinct zones has been used.

The objective was to compare the simulated and observed flow rates at SB1 and SB2, and the water table profile of each aquifer along the cross-section. We needed especially to represent the confined properties of the deep aquifer as it is observed in Danone AQUA well and MW1. Nevertheless, the Danone-AQUA well is a mix of the shallow and the deep aquifer contributions, thus, only MW1 will be taken as a reference of the deep aquifer water table elevation.

The first step was to confirm the hydraulic conductivity of each aquifer layers represented by a buried paleo-channel in particular. Remember that by pumping test we obtained $1.0 \times 10^{-5} \text{ m.s}^{-1}$ for the hydraulic conductivity of Aquifer 1 (K1), and $2.7 \times 10^{-4} \text{ m.s}^{-1}$ for the hydraulic conductivity of Aquifer 2 (K2). We then test the influence of the variation of K1 while K2 remains fix and vice versa.

The Fig. 5.6 shows the result obtained with the initial conditions based on the conceptual model. In the one hand, it appears that the simulated flow rates are not fitting with the observed one (overestimation of Q1 and underestimation of Q2). On the other hand, the piezometric heads are widely overestimated with more than 2000 m in the upper part. Remember that at 7km from the Pasar Bubar ridge, the topography is at 780 m elevation, thus, these hydraulic heads are out of range. For all these reasons, a flow calibration have to be done.

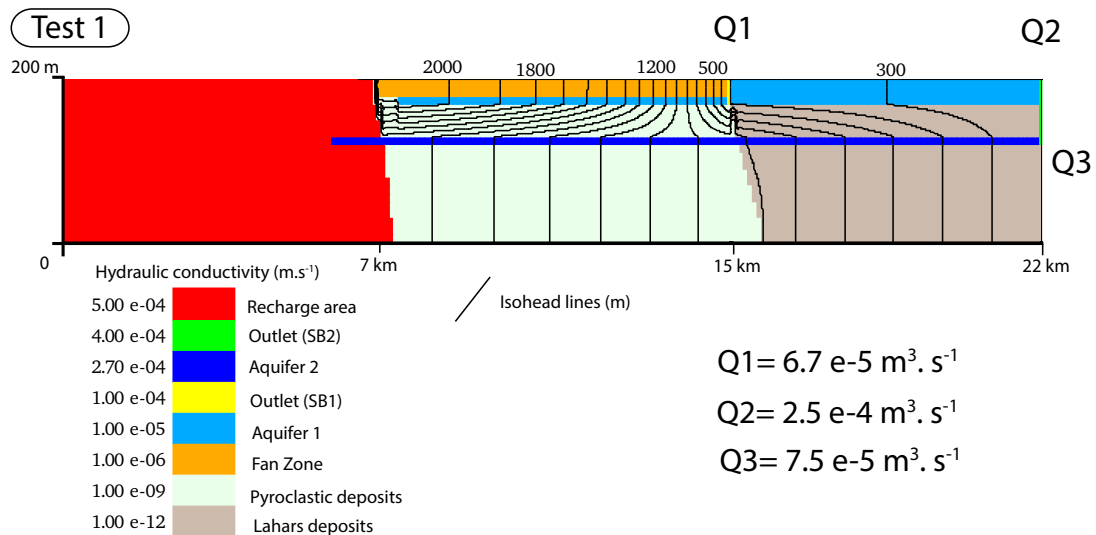


Figure 5.6: Test 1: Flow simulation with initial configuration after the conceptual model. The simulated flow rate (Q1 and Q2) are compared to the observed ones ($Q1_{obs}: 3.25 \times 10^{-5} \text{ m}^3 \cdot \text{s}^{-1}$ and $Q2_{obs}: 3.57 \times 10^{-4} \text{ m}^3 \cdot \text{s}^{-1}$). Simulation in 2D cross-section calculated in steady flow with METIS.

25 runs have been done with several tests on the hydraulic conductivity values for the aquifer units and the fan zone. The results are described in Tab.5.5. The best calibration is obtained with the test 20: $Q1 = 5.7 \times 10^{-5} \text{ m}^3 \cdot \text{s}^{-1}$ and $Q2 = 3.1 \times 10^{-4} \text{ m}^3 \cdot \text{s}^{-1}$ and a maximal piezometric head for the Aquifer 2 at 774 m (Fig. 5.7). In this test (n°20), we divided the deep aquifer in two parts: upstream SB1 and downstream SB2. As we could see on the field, the SB1 is located at break in slope level. At 400 m asl, the river incisions are less important and the river beds are less deep. Therefore, we suggest that the paleo-channel follows the same particularity with relatively high thickness in high elevation (20 m) and becomes narrow thickness with the decrease of the elevation (10 m).

The flow rate at SB1 is still overestimated and the piezometric head is still high considering that on the field, people who tried to drill a bore well did not find water before at least 100 m deep. Even if these information were not confirmed by direct measurement, we suggest that in the upper part, the water table is relatively far from the ground surface. Thus, the simulation still need to be improved.

Test	Aquifer 1 K1	Hydraulic conductivity K (m.s ⁻¹)		Fan Zone Kfan	Q1 obs	Q2 obs	Calculated Residual flow rate Q3(m ³ .s ⁻¹)	Calculated Maximal piezometric head h (m)
		Aquifer 2 upstream K2a	Aquifer 2 downstream K2b		3.25E-005 Calculated Flow rate SB1	3.57E-004 Calculated Flow rate SB2		
					Q1 (m ³ .s ⁻¹)	Q2 (m ³ .s ⁻¹)		
<i>Tests on Aquifer 1</i>								
1	1.00E-005	2.70E-004	2.70E-004	1.00E-006	6.70E-005	2.50E-004	7.50E-005	2000
2	1.00E-004	2.70E-004	2.70E-004	1.00E-005	8.20E-005	3.27E-004	7.34E-005	1640
3	2.00E-004	2.70E-004	2.70E-004	1.00E-005	3.25E-005	3.60E-004	7.40E-005	981
4	5.00E-004	2.70E-004	2.70E-004	1.00E-005	7.60E-005	5.00E-004	7.60E-005	911
5	4.00E-004	2.70E-004	2.70E-004	1.00E-005	7.40E-005	4.60E-004	7.60E-005	924
<i>Tests on Aquifer 2 (complete)</i>								
6	2.00E-004	1.00E-004	1.00E-004	1.00E-005	1.10E-004	3.20E-004	7.18E-005	1567
7	2.00E-004	4.00E-004	4.00E-004	1.00E-005	5.50E-005	3.80E-004	7.50E-005	794
8	2.00E-004	6.00E-004	6.00E-004	1.00E-005	3.90E-005	4.01E-004	7.80E-005	671
9	2.00E-004	8.00E-004	8.00E-004	1.00E-005	3.10E-005	4.10E-004	7.66E-005	644
10	2.00E-004	2.70E-004	1.00E-004	1.00E-005	9.90E-005	3.38E-004	7.20E-005	1210
<i>Tests on Aquifer 2 (downstream)</i>								
11	2.00E-004	2.70E-004	1.00E-005	1.00E-005	1.50E-004	2.10E-004	6.90E-005	1620
12	2.00E-004	2.70E-004	4.00E-005	1.00E-005	1.20E-004	3.00E-004	7.08E-005	1430
13	2.00E-004	2.70E-004	2.00E-004	1.00E-005	7.70E-005	3.60E-004	7.30E-005	1050
14	2.00E-004	2.70E-004	4.00E-004	1.00E-005	5.90E-005	3.80E-004	7.40E-005	909
15	2.00E-004	2.70E-004	8.00E-004	2.00E-006	4.70E-005	3.90E-004	7.56E-005	818
<i>Tests on Fan Zone</i>								
16	2.00E-004	2.70E-004	2.70E-004	4.00E-006	6.75E-005	3.70E-004	7.40E-005	989
17	2.00E-004	2.70E-004	2.70E-004	8.00E-006	6.80E-005	3.70E-004	7.40E-005	983
18	2.00E-004	2.70E-004	2.70E-004	1.50E-004	7.70E-005	3.60E-004	7.30E-005	925
19	2.00E-004	2.70E-004	2.70E-004	2.00E-004	6.31E-005	3.57E-004	7.36E-005	901
<i>Tests on Aquifer 2 (upstream)</i>								
20	1.00E-004	5.00E-004	2.70E-004	1.00E-004	5.70E-005	3.10E-004	7.20E-005	774
21	1.00E-004	4.00E-004	2.70E-004	1.00E-004	7.60E-005	3.07E-004	7.20E-005	816
22	1.00E-004	3.00E-004	2.70E-004	1.00E-004	5.50E-005	3.50E-004	7.30E-005	815
23	1.00E-004	1.00E-004	2.70E-004	1.00E-004	1.10E-004	3.20E-004	7.10E+005	1050
24	1.00E-004	6.00E-004	2.70E-004	1.00E-004	7.30E-005	3.60E-004	7.40E-005	719
25	1.00E-004	2.00E-004	2.70E-004	1.00E-004	9.22E-005	3.40E-004	7.29E-005	894

Table 5.5: Hydraulic conductivity sensitivity test and results on flow rates at SB1 and SB2 (Q1 and Q2 respectively), residual flow rate (Q3) and maximal piezometric head (h) for selected flow simulations.

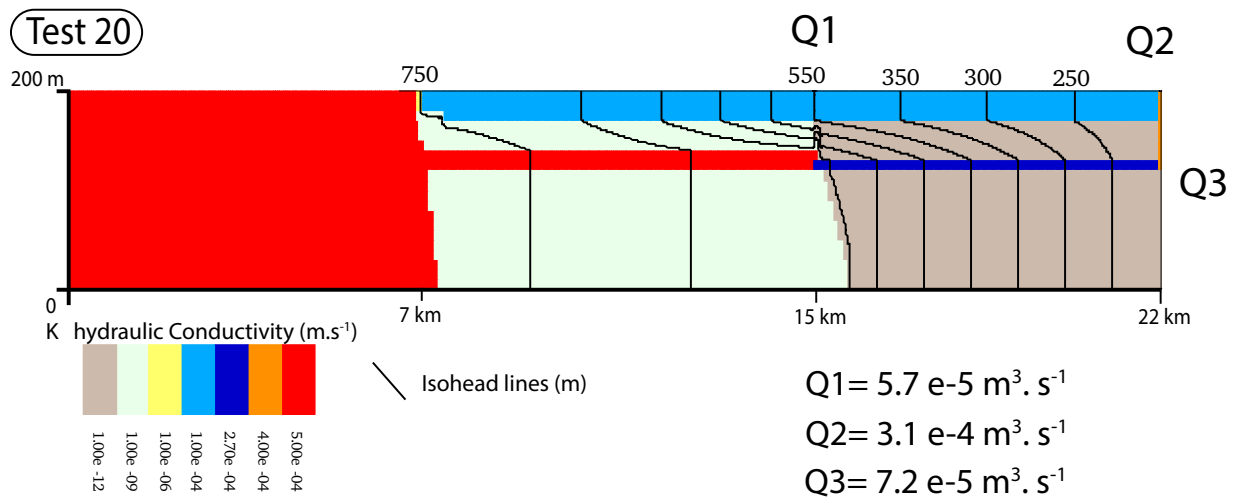


Figure 5.7: Test 20: Flow simulation n°20 with best results. The simulated flow rates (Q1 and Q2) are compared to the observed ones (Q1obs: $3.25 \times 10^{-5} \text{m}^3 \cdot \text{s}^{-1}$ and Q2obs: $3.57 \times 10^{-4} \text{m}^3 \cdot \text{s}^{-1}$). Simulation in 2D cross-section calculated in steady flow with METIS.

5.4.2 Flow calibration constrained by mass transport simulation

To improve the numerical model results, the flow simulations are constrained by mass transport calibration. In order to reproduce the mass concentration observed with the isotope analyses at SB1 and SB2, 18 tests have been performed. The tests were focused on the hydraulic conductivities of each units but in contrast with the previous test serie, we divided here the 2D cross-section in nine units and not eight. We have considered that the Aquifer 1 and the detritic fan could be divided in two parts each. This division is an assumption to take into account the lateral facies variation describes earlier (cf. Chapter 2).

The results of the flow calibration and mass transport are summarize in the Tab.5.6. Several configurations can be considered but the best simulated values were obtained with the test 40. The Fig. 5.8 represents the mass concentration distribution along the cross-section modelized. The distinct shallow and deep circulations are here clearly visible. The high permeability of the upper part allows a massive transfer of low concentrated mass to the low lands while the shallow circulation see its concentration increases with the decrease of elevation. The concentrations obtained at SB1 and SB2 are still relatively high.

Test	Aquifer 1up K1up	Aquifer 1up K1up	Hydraulic conductivity K (m.s-1)				Fan zone down Kfan down	Pyroclaste	Lahar	Recharge	C1 Obs		C2 Obs		Q1 obs		Q2 obs		Calculated Residual flow rate Q3(m3.s-1)	Calculated Maximal piezometric head h (m)		
			2.5 to 3.5		1.5 to 2.5						3.25E-005		3.57E-004		Calculated Concentration		Calculated Flow rate SB1				Calculated Flow rate SB2	
			C1	C2	Q1 (m3.s-1)	Q2 (m3.s-1)					Q1	Q2	Q1	Q2								
Test on Fan zone downstream																						
26	1.00E-004	1.00E-004	5.00E-004	2.70E-004	1.00E-004	1.00E-004	1.00E-009	1.00E-012	5.00E-004	3.6	2.9	5.70E-005	3.10E-004	7.40E-005	769							
27	1.00E-004	1.00E-004	5.00E-004	2.70E-004	1.00E-004	8.00E-005	1.00E-009	1.00E-012	5.00E-004	3.5	2.7	5.69E-005	3.10E-004	7.40E-005	771							
28	1.00E-004	1.00E-004	5.00E-004	2.70E-004	1.00E-004	5.00E-005	1.00E-009	1.00E-012	5.00E-004	3.5	2.7	7.20E-005	3.10E-004	7.40E-005	777							
Test on Fan zone upstream																						
29	1.00E-004	1.00E-004	5.00E-004	2.70E-004	1.00E-005	8.00E-005	1.00E-009	1.00E-012	5.00E-004	3.5	2.6	5.39E-005	3.90E-004	7.50E-005	887							
30	1.00E-004	1.00E-004	5.00E-004	2.70E-004	5.00E-005	5.00E-005	1.00E-009	1.00E-012	5.00E-004	3.5	2.6	6.50E-005	3.70E-004	7.48E-005	819							
31	1.00E-004	1.00E-004	5.00E-004	2.70E-004	8.00E-005	5.00E-005	1.00E-009	1.00E-012	5.00E-004	3.5	2.7	7.00E-005	3.70E-004	7.40E-005	791							
Test on lahar zone																						
32	1.00E-004	1.00E-004	5.00E-004	2.70E-004	8.00E-005	5.00E-005	1.00E-009	1.00E-009	5.00E-004	3.5	2.7	6.30E-005	3.70E-004	7.40E-005	802							
33	1.00E-004	1.00E-004	5.00E-004	2.70E-004	8.00E-005	5.00E-005	1.00E-009	1.00E-006	5.00E-004	3.5	3.2	4.30E-005	3.30E-004	7.20E-005	687							
34	1.00E-004	1.00E-004	5.00E-004	2.70E-004	8.00E-005	5.00E-005	1.00E-009	1.00E-014	5.00E-004	3.5	2.7	6.57E-005	3.70E-004	7.47E-005	815							
35	1.00E-004	1.00E-004	5.00E-004	2.70E-004	8.00E-005	5.00E-005	1.00E-009	1.00E-011	5.00E-004	3.5	2.7	5.00E-005	3.70E-004	7.47E-005	815							
Test on pyroclastic zone																						
36	1.00E-004	1.00E-004	5.00E-004	2.70E-004	8.00E-005	5.00E-005	1.00E-012	1.00E-012	5.00E-004	3.5	2.6	6.50E-005	3.80E-004	7.50E-005	834							
37	1.00E-004	1.00E-004	5.00E-004	2.70E-004	8.00E-005	5.00E-005	1.00E-006	1.00E-012	5.00E-004	3.1	3.2	1.00E-004	3.30E-004	7.20E-005	686							
38	1.00E-004	1.00E-004	5.00E-004	2.70E-004	8.00E-005	5.00E-005	1.00E-006	1.00E-006	5.00E-004	3.2	3.4	5.40E-005	3.30E-004	7.20E-005	677							
39	1.00E-004	1.00E-004	5.00E-004	2.70E-004	8.00E-005	5.00E-005	1.00E-009	1.00E-011	5.00E-004	3.3	2.9	7.40E-005	3.20E-004	7.10E-005	815							
40	1.00E-004	1.00E-004	5.00E-004	2.70E-004	8.00E-005	5.00E-005	1.00E-007	1.00E-012	5.00E-004	3.5	2.6	5.09E-005	3.70E-004	7.40E-005	687							
Test on Recharge area																						
41	1.00E-004	1.00E-004	5.00E-004	2.70E-004	8.00E-005	5.00E-005	1.00E-009	1.00E-011	1.00E-003	3.5	2.6	6.30E-005	3.70E-004	7.47E-005	811							
42	1.00E-004	1.00E-004	5.00E-004	2.70E-004	8.00E-005	5.00E-005	1.00E-009	1.00E-011	1.00E-004	3.5	2.4	7.10E-005	3.80E-004	7.40E-005	813							
Test on Aquifer 1 downstream																						
43	1.00E-004	1.00E-005	5.00E-004	2.70E-004	8.00E-005	5.00E-005	1.00E-009	1.00E-011	5.00E-004	3.5	2.5	6.50E-005	3.80E-004	7.47E-005	815							
44	1.00E-004	1.00E-006	5.00E-004	2.70E-004	8.00E-005	5.00E-005	1.00E-009	1.00E-011	5.00E-004	3.5	2.4	7.09E-005	3.80E-004	7.40E-005	815							

Table 5.6: Tests on the hydraulic conductivity of the model units and the impact on the simulated mass concentration at SBland SB2 (C1 and C2 respectively), the simulated flow rates of SB1 and SB2 (Q1 and Q2), on the simulated residual flow rates and the simulated maximal piezometric head.

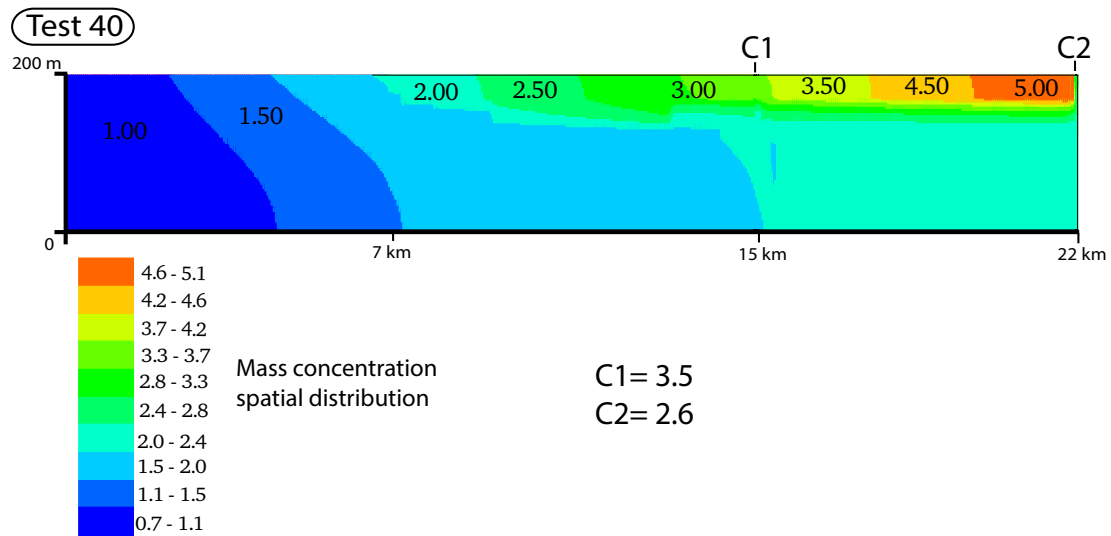


Figure 5.8: Test 40: Mass concentration spatial distribution within 2D cross-section. The simulated concentrations C1 and C2 values have to be compared to the observed ones: C1obs. ranges from 2.5 to 3.5 and C2 obs. from 1.5 to 2.5. All the simulations have been calculated in steady flow with METIS.

The configuration n°40 leads to a modification of the hydraulic properties of the model. The Fig.5.9 shows the hydraulic conductivity units deduced from the best simulations. The simulated flow rate is still overestimated for SB1 (more 56%) while the flow rate of SB2 is well simulated (only 3% of overestimation). The hydraulic head of the aquifer 2 in the upper parts is estimated at 687 m which is consistent with the field observations (Fig. 5.10).

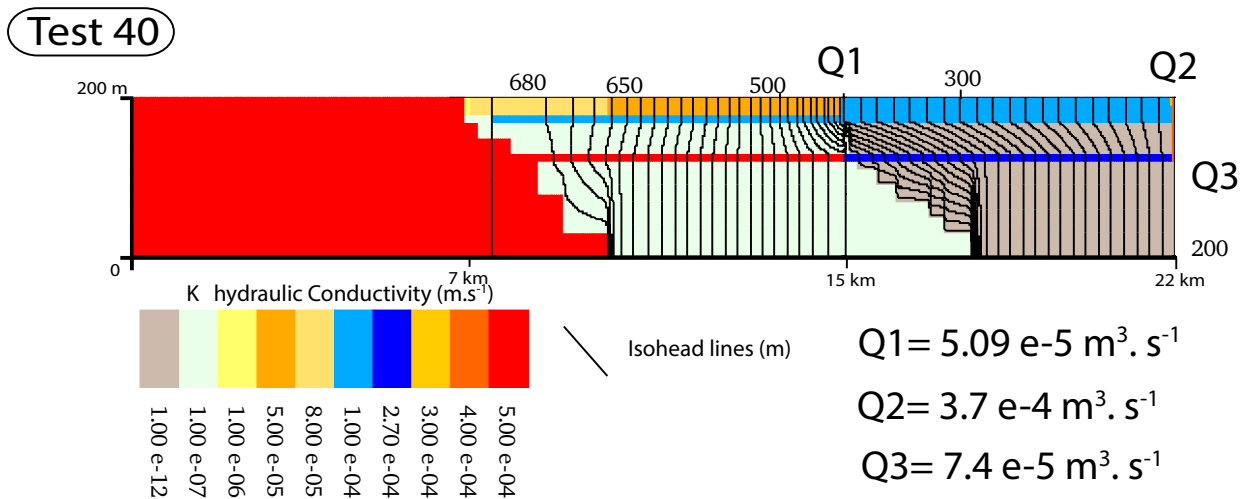


Figure 5.9: Test 40: Hydraulic head along the model profile. The simulated flow rate (Q1 and Q2) are compared to the observed ones (Q1obs: $3.25 \times 10^{-5} \text{m}^3 \cdot \text{s}^{-1}$ and Q2obs: $3.57 \times 10^{-4} \text{m}^3 \cdot \text{s}^{-1}$). Simulation in 2D cross-section calculated in steady flow with METIS.

Even if the mass transport has allowed to improve the simulation results, the geometry of the model has to be re-considered in order to better estimate the flow rate and the mass concentration at SB1 and SB2.

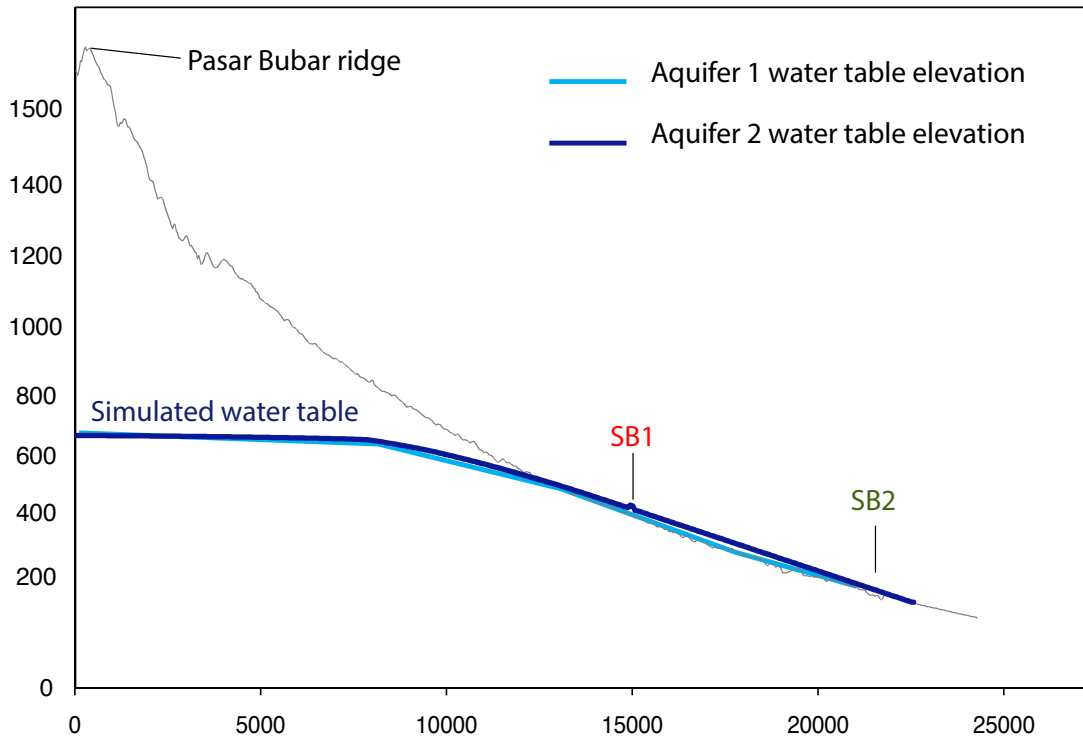


Figure 5.10: Water table simulation for the aquifer 1 and Aquifer 2 with the test 40. The topographic profile has been drawn after the DEM ASTER GDEM V2 with 30 m ground resolution.

5.4.3 Model geometry sensitivity tests

Still with the flow and mass transport simulations, we have performed a sensitivity test on the model geometry as the aquifer layers or the detritic fan thickness and the number of deep aquifers. Taking the test 40 as reference, 8 runs have been performed. The results are listed in the Tab. 5.7.

The presence or not of a third aquifer system has been tested (test 50) and it appears that the flow rate simulations are better with, than without another deep aquifer system. This result is consistent with the theory of multi-levels of buried paleo-channels and the stratigraphical log interpretation. We saw that several aquifer layers have been found near 80 m depth during the drilling upstream the SB2.

The thickness of the deep aquifer systems have been tested (from 10 to 20 m on tests 45 and 46). The best results are those with paleo-channels of 10 m thick. This result confirms the field observations made on the present day rivers.

The detritic fan thickness has been tested with the test 47 (10 to 20 m). The mass concentration is not sensitive to the fan thickness contrary to the flow rates. The best results are obtained with a detritic fan of 20 m. It appears that the best configuration is composed by three aquifer systems of 10 m thick.

The test 50 reaches to well simulate the concentration and to not over estimate the flow rate at SB1 (Fig. 5.11 and Fig.). Moreover, with this test, we are able to estimate the water table at 583m asl at 5 km from the ridge (Fig. 5.12). This estimation is consistent with the field survey where the village at 600 m asl explained they need to drill almost 150 to 200 m deep to find the water. The descriptions of the wells' owners were rarely precise but the simulation confirms the order of magnitude of the water table elevation in the upper parts. Nevertheless, the aquifer systems in the upper parts are more complex than an unique "basal" aquifer system. The temporally contact springs inventoried at high elevations show in reality that the upper part of the edifice is constituted by many probably disconnected perched aquifers laying on aquitard formations (wedded tuffs, air fall or massive lava flow deposits). A precise 3D modeling approach considering the non-saturated zone with more calibration data as precise geophysics could be an improvement to better characterize this zone.

In the low land, the confined properties of the aquifer 2 (deep aquifer) is verified with a water table elevation at 202 m (2 meters above the spring hydraulic head), namely relatively close to the hydraulic head observed at MW1.

The residual flow rate, noted Q_3 , is estimated at $7.50 \times 10^{-5} \text{m}^3 \cdot \text{s}^{-1}$ and if we reported this value in real volume with multiplying this flow rate with the length of the watershed after the SB2, we obtain $2.47 \times 10^7 \text{m}^3 \cdot \text{y}^{-1}$ which is "flowing out" the eastern border of the model", feeds the irrigated downslope area and reaches the Bengawan Solo river to the East part of the watershed.

Test	Aquifer 1 upstream	Aquifer 2 upstream	Aquifer 2 downstream	Fan Zone upstream	Fan Zone downstream	Aquifer 3	Aquifer 3	Calculated Conc. SB1	Calculated Conc. SB2	Calculated Flow rate SB1	Calculated Flow rate SB2	Calculated Residual flow rate	Calculated Maximal piezometric head
	K1a	K2a	K2b	Kfana	Kfanb	K3a	K3b	C1	C2	Q1 (m ³ .s ⁻¹)	Q2 (m ³ .s ⁻¹)	Q3(m ³ .s ⁻¹)	h (m)
40	10	10	10	20	20			3.5	2.6	5.09E-005	3.70E-004	7.40E-005	687
45	10	20	10	20	20			3.5	2.6	5.90E-005	3.80E-005	7.51E-005	726
46	10	20	20	20	20			3.5	2.5	3.45E-005	4.00E-004	7.60E-005	638
47	10	10	20	10	10			3.5	2.6	4.50E-005	3.90E-004	7.59E-005	694
48	10	20	10	20	20			3.5	2.4	4.60E-005	3.65E-004	7.40E-005	711
49	10	20	10	20	20			3.5	2.4	4.80E-005	3.65E-004	7.42E-005	711
50	10	10	10	20	20	10	10	3.4	2.4	3.60E-005	3.10E-004	5.80E-005	593
51	10	10	10	20	20	20	10	3.4	2.4	1.80E-005	3.30E-004	5.90E-005	535
52	10	10	10	20	20	10	20	3.4	2.4	1.36E-005	3.40E-004	6.04E-005	579

Table 5.7: Sensitivity tests of the geometry of the different units in calculated flow and mass simulations and their impact on the mass concentration at SB1 and SB2, the SB1 and SB2 flow rates, the calculated residual flow rate and the calculated maximal piezometric head.

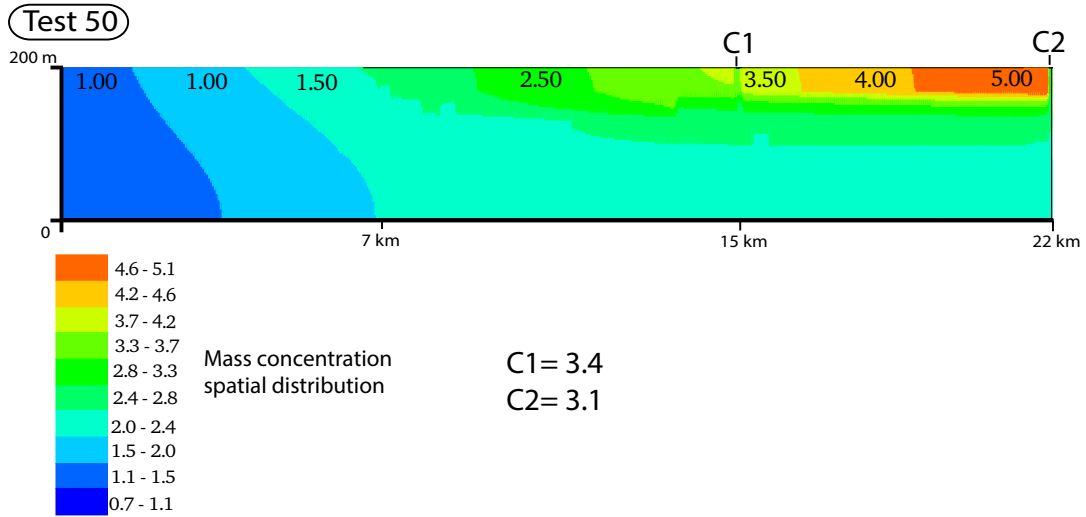


Figure 5.11: Test 50: Calculated mass concentration spatial distribution within 2D cross-section after the model geometry sensitivity test n°50. The calculated concentrations C1 and C2 values have to be compared to the observed ones: C1obs. ranges from 2.5 to 3.5 and C2 obs. from 1.5 to 2.5. All the simulations have been calculated in steady flow with METIS.

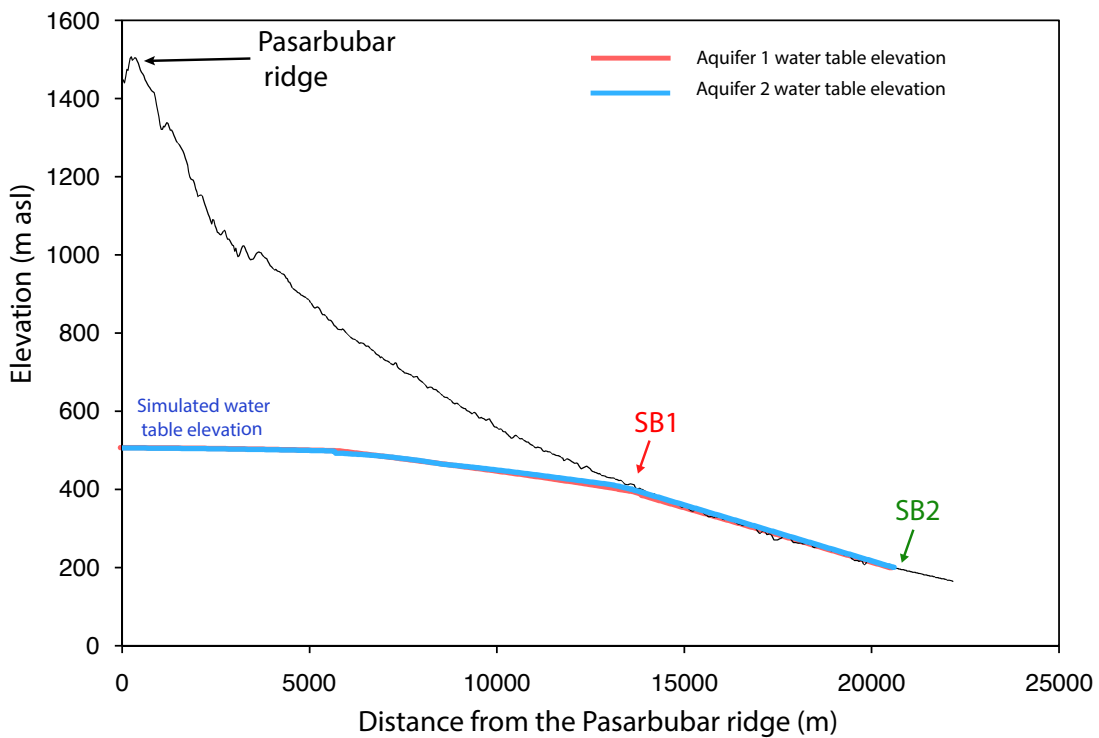


Figure 5.12: Water table simulation for the aquifer 1 and Aquifer 2 with the test 50. The topographic profile has been drawn after the DEM ASTER GDEM V2 with 30 m ground resolution.

5.4.4 Sensivity test on thermal parameters

From the flow circulation calibration then the flow and mass transfer calibration, we have determined a correct internal structure of the volcanic edifice (the test 50). Now, we are able to calibrate the thermal conditions in order to simulate the spring temperatures.

The effect of the geothermal flux coming from inside of the Earth is assimilated to a constant imposed temperature at the bottom of the model (200 m deep from the surface). Considering an average surface temperature of 15°C for all the cross-sections (averaged temperature between night and day temperature and high and low elevation values) and a mean geothermal gradient of +3.3°C per 100 m depth, a temperature of 22°C has to be imposed as the thermal boundary condition.

14 runs have been performed to calculate the impact of the variation of the thermal parameters on the spring temperatures (Fig. 5.8).

The test 50 has been taken as reference case (geometry and flow parameter distribution) of flow circulation and thermal simulations have been performed on this configuration.

Test	Imposed temperature (°C)	Geothermal gradient	Longitudinal dispersivity	Transversal dispersivity	Porosity Aquitard	Porosity Aquifer	Aquitard volumetric heat capacity	Aquifer volumetric heat capacity	Thermal conductivity Aquitard	Thermal Conductivity aquifer	T1	T2
		°C per 100m	α_L	α_T	ω	ω	γ	γ	λ	λ		
			(m)	(m)	(-)	(-)	(J.m ⁻³ .K ⁻¹)	(J.m ⁻³ .K ⁻¹)	(W.m ⁻¹ .K ⁻¹)	(W.m ⁻¹ .K ⁻¹)	Observations	
											25.5-27	22.5-25
											Simulations	
50	22	+3.3	25	5	0.13	0.57	2718400	3457600	1.992	1.288	25.7	24.9
53	22	+3.3	25	25	0.13	0.57	2718400	3457600	1.992	1.288	25.8	26
54	22	+3.3	25	10	0.13	0.57	2718400	3457600	1.992	1.288	25.8	25.4
55	22	+3.3	10	5	0.13	0.57	2718400	3457600	1.992	1.288	25.7	24.9
56	22	+3.3	15	5	0.13	0.57	2718400	3457600	1.992	1.288	25.7	24.8
57	33	+9.0	15	5	0.13	0.57	2718400	3457600	1.992	1.288	26.1	28.7
58	30	+7.5	15	5	0.13	0.57	2718400	3457600	1.992	1.288	26	27.7
59	27	+6.0	15	5	0.13	0.57	2718400	3457600	1.992	1.288	26.06	26.7
60	24	+4.5	15	5	0.13	0.57	2718400	3457600	1.992	1.288	25.8	25.6
61	21	+3.0	15	5	0.13	0.57	2718400	3457600	1.992	1.288	25.7	24.6
62	18	+1.5	15	5	0.13	0.57	2718400	3457600	1.992	1.288	25.6	23.6
63	15	+0.5	15	5	0.13	0.57	2718400	3457600	1.992	1.288	25.5	22.6
64	0	-	15	5	0.13	0.57	2718400	3457600	1.992	1.288	25.1	17.7
65	22	+3.3	15	5	0.13	0.2	2718400	2836000	1.992	1.88	25.7	24.9
70	22	+3.3	15	5	0.02	0.57	2533600	3457600	2.168	1.288	25.7	25

Table 5.8: Thermal parameter sensitivity test with the impact on the spring temperatures (T1 and T2 at SBI and SB2 respectively)

The results are summarized into the chart Fig. 5.13. On the profile, the imposed temperature at the bottom is fixed at 22°C. The spring temperatures are into the range of the observed data (T1=25.9°C, Obs= 25.5 to 27 and T2=24.2°C, Obs.=22.5 to 25°C). The deformation of the thermal gradient by the groundwater circulation through the buried paleo-channel is clearly visible on the profile. The chart Fig. 5.13 shows the simulated spring temperatures at SB1 and SB2 depending on the imposed temperature variations. The range of observed annual mean spring temperatures is noted with colored zones. The simulated temperatures of the SB1 are relatively stable for an imposed temperature ranging from 15 to 33 °C. In contrast, the SB2 temperatures increase with the bottom imposed temperature resulting of the geothermal gradient increase (from 22.5 to 29°C). Considering the range of the observed temperatures (green zone, between 22.5 and 25°C), the simulated temperature of SB2 are acceptable for an imposed geothermal temperature ranging from 15 to 24°C. The chosen geothermal gradient (+3.3°C per 100 m) induces an imposed temperature of 22°C remains in the range of the valid temperature. One test has been performed with removing any effect of the geothermal gradient on the system. In this case, the simulated temperatures reach 25.7°C for SB1 and 24.7°C for SB2. These values are still included into the observed temperature range. This shows that in this range of depth (0-200m) the geothermal gradient has a low impact on the annual mean spring belt temperatures. Indeed, the water transit time is probably fast enough to limit the warming effect of the groundwater and the amount of water is certainly large enough to evacuate the heat discharge of the geothermal gradient as shown by [Manga & Kirchner \(2004\)](#) in the Cascades volcanic arc.

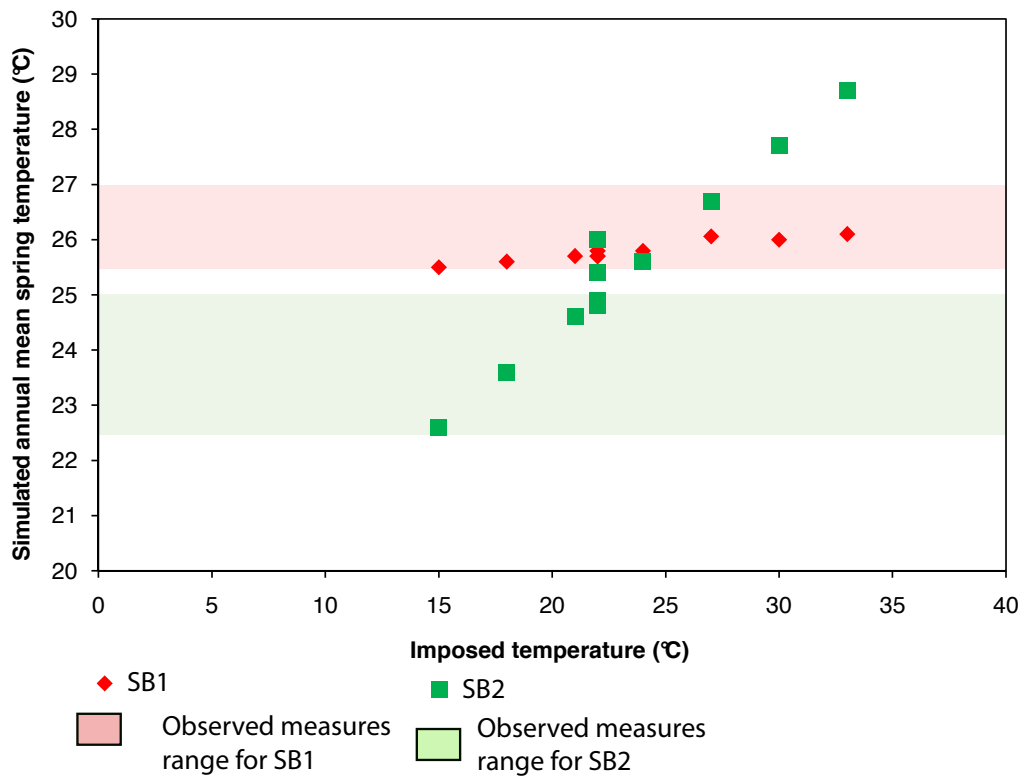


Figure 5.13: Impact of the variation of the imposed temperature considered as geothermal gradient on the mean annual spring temperature (T1 and T2 at SB1 and SB2 respectively). The range of observed spring temperature range is noted by reddish and green zones.

Using the same structure configuration, we calibrate the thermal longitudinal and transversal dispersivity parameters (α_L and α_T). The test results are presented in the Table 5.8. The calculated SB1 temperature is less sensitive to the dispersivity variation than SB2 (less than 1°C of variation). The best calibration is obtained with the test D4 ($\alpha_L = 15$ m and $\alpha_T = 5$ m).

The calculated spring temperatures is relatively weakly impacted by the variation of thermal conductivity and volumetric specific heat. This is because heat transport by advection outweighs transport by conduction. At the end, it is the hydraulic properties that are predominant. The best simulation results are obtained with the test 56. The Fig. 5.14 shows the calculated temperature profile for this test. The flow perturbation on the temperature gradient is clearly visible near the SB2 location (Fig. 5.15).

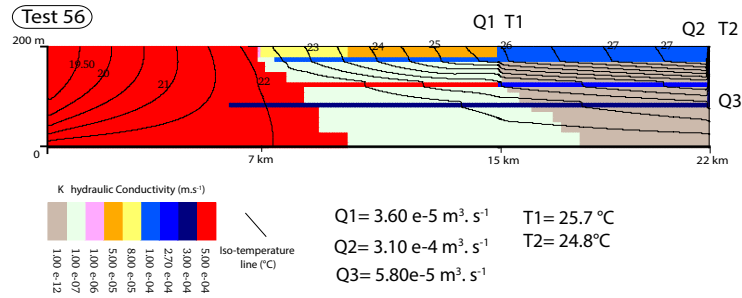


Figure 5.14: Calculated temperature spatial distribution for the test 56 with the bottom imposed temperature at 22°C.

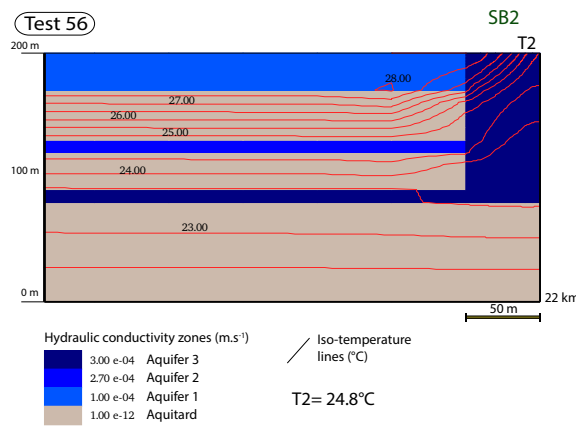


Figure 5.15: Zoom of the SB2 zone on the calculated temperature profile for the test 56 with imposed temperature 22°C.

5.4.5 Transfer time estimation

Based on the flow parameters, METIS code determines the Darcy velocity for each elements of the grid. The visualizer COMET allows to draw the velocity with vector forms and color code (Fig. 5.16). We extract the Darcy velocity profile for the Aquifer 1, Aquifer 2 and Aquifer 3 from the best simulation result (test 56) in view to estimate the water transfer time from the recharge area to the SB1, from the recharge to SB2 and between the spring belts. The average Darcy velocity is then calculated for the aquifer layers. The recharge area extends from 0 km to 7 km from the ridge and we consider two water path ways, a maximal and a minimal one. The maximal pathway takes account of the total distance from the ridge to the final point considered (SB1 or SB2). The minimal pathway origin is defined as the paleo-channel occurrence (near 7 km from the PB ridge).

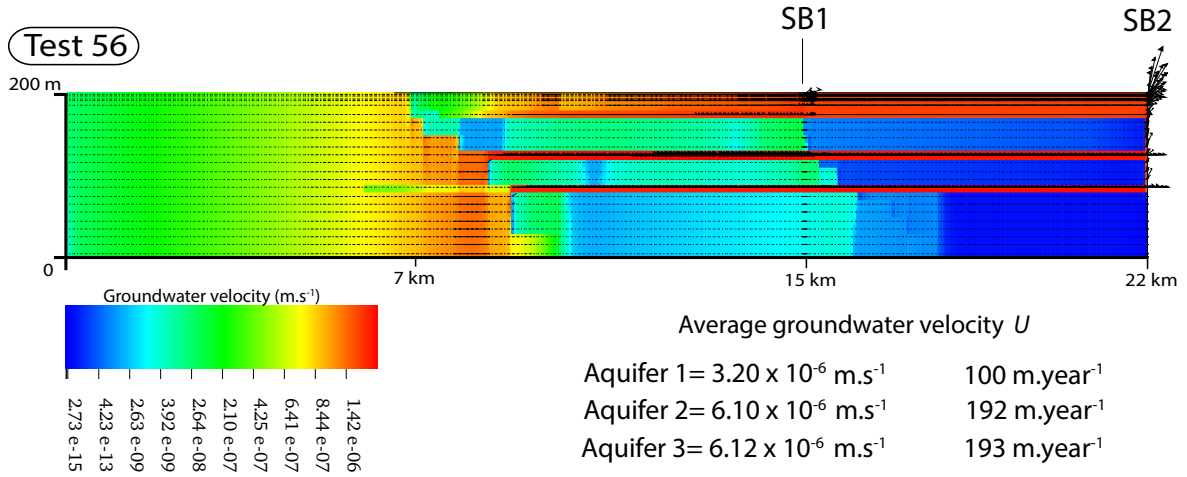


Figure 5.16: Groundwater Darcy velocity calculated by the model METIS for flow, mass and heat transfer and visualized with COMET and the distances used to calculate the water transfer time. The vector representing the velocity ranging from $2.3 \times 10^{-15} \text{ m.s}^{-1}$ to $2.5 \times 10^{-5} \text{ m.s}^{-1}$.

METIS presents the Darcy velocity as result. In view to calculate the transit time, we need to consider the cinematic velocity (u^*) expressed by:

$$u^* = \frac{U}{\omega}$$

with ω the cinematic porosity.

Then, the time needed by the water to transit into the system from the recharge area to the springs is calculated:

$$t = \frac{L}{u^*}$$

with

u^* = the water cinematic velocity (m.s^{-1})

t = the water transit time (s)

L = the distance of the flow path (m)

The average Darcy velocity calculated by the model and the calculated water transit times are detailed in the Table 5.9.

	Aquifer 1			Aquifer2			Aquifer3		
Average Velocity u^* (m.s ⁻¹)	3.20 x 10 ⁻⁶			6.10 x 10 ⁻⁶			6.12 x 10 ⁻⁶		
Average Velocity u^* (m.y ⁻¹)	100			192			193		
	Av.	Min	Max	Av.	Min.	Max.	Av.	Min.	Max
Distance Recharge to SB1(m)	11500	8000	15000	11500	8000	15000	11500	8000	15000
Transit time(years)	113	79	148	-	-	-	-	-	-
Distance Recharge to SB2 (m)	18500	15000	22000	18500	15000	22000	18500	15000	22000
Transit time (years)	183	148	217	96	77	114	95	77	113

Table 5.9: Estimation of the water transit time for the Aquifer 1, 2 and 3 for three distances: Recharge area (1500 m asl) to SB1 (400 m asl), recharge to SB2 (200 m asl) and SB1 to SB2.

Considering the distance between the beginning of the paleo-channel and the SB2 (i.e. 15 km), the average transfer time is estimated at 183 years for the Aquifer 1, 96 years for the Aquifer 2 and 95 years for the Aquifer 3. This transit time is relatively long and justifies the absence of seasonal variation observed with the temporal monitoring of the springs. This confirms the low nitrate concentration as it will be discussed in the next chapter. As expected with the conceptual model, the model estimates a transit time within the Aquifer 2 and 3 is shorter than into the Aquifer 1 (30 years of difference).

Notice that at SB2, the water coming from the Aquifer 1 and Aquifer 2 are mixed. Thus, depending on the importance of the connection between the Aquifer 1 and Aquifer 2 at SB2, the springs will have distinct hydrodynamic and physical properties. The “connection level” between the Aquifer 1 and 2, explains the range of physico-chemical variable value that we obtain with the spring monitoring. This “connection level” depends especially of the paleo-channel dimension.

Moreover, the transit time estimations presented here do not take into account the water transfer within the unsaturated zone, which can, of course, widely increase the total transit time depending on its thickness (between 10 to 600 m according the field observation). This point has to be improved.

We saw that the tritium analysis results induce two water datation interpretations: one considered as old, before 1950 and another relatively recent, after 2005. With the modeling results, it seems that the first assumption is confirmed.

5.5 Synthesis

With a simple 2D flow, mass and heat transfer modeling approach, we were able to reproduce the measured values of flow, $\delta^{18}O$ and water temperature on the Eastern flank of Merapi volcano. The conceptual model of the internal structure built with the field observations has been verified and a quantification of the groundwater fluxes is assessed. The main recharge occurs above 800 m asl within a multilayered aquifer system. The first

aquifer is relatively shallow (less than 30 m) and is covered by the detritic fan upstream the SB1 which plays the role of recharge area to the SB1. This unconfined aquifer developed in a buried paleo-channel has a relatively good hydrodynamic properties ($K_1 = 1.0 \times 10^{-4} \text{ m s}^{-1}$).

The second aquifer system is deeper (70 m) and composed by buried paleo-channels taking their origin in high elevation (1000- 800 m asl). This system has a high permeability and a groundwater transfer time near 100 years.

The presence of a third aquifer system has been tested and it appears that the simulations are better. This result is consistent with the theory of multi-levels of buried paleo-channels and the stratigraphical log interpretation.

The simulations of the water table are consistent with the observation in the low land but in the upper part, the results have to be taken carefully. Indeed, the simulation considers a shallow aquifer whereas the temporally springs and the geological survey showed that the structure is certainly more complex with an alternation of non-connected perched aquifers separated by aquitard layers. A precise geophysics survey combine with 3D modeling approach could improve the representation of the multi-layered system in high elevations.

The heat spatial distribution and especially the “spring temperature anomaly” of SB2 have been reproduced. Considering the large amount of groundwater recharge and the high hydraulic properties of the aquifer formations, the physical heat transfer is mainly controlled by the advection instead of the conduction. Thus, for this range of depth (0-200m), the geothermal flux does not have an important impact on the groundwater temperature which is more controlled by the air gradient temperature. Same observations are done for the sensitivity test on thermal parameters.

The simulations have been done in steady state situation but the water residence time into the system has been calculated. The average transit time for the SB2 ranges near 100 years while the transit time from the recharge to SB1 appears to be near 180 years. The groundwater velocity is thus faster into the Aquifer 2 (192 m.y^{-1}). This highlights that in this kind of complex and heterogenous hydrological system of volcano-detritic environment, the groundwater can use preferential pathways which not depends of fractured lava deposits but buried paleo-river beds. Therefore, a complete assessment of the geological and geomorphological history of this environment has to be applied in complement of any hydrological and hydrogeological study.

All the results presented here arise from an average approach values. The assumption to consider the average value of all the springs for each spring belt is strong. We saw that several springs have their own behavior, hence, probably a different groundwater circulation pathway through an individual buried paleo-channel exists by spring (e.g. the Pusur and Soka springs compare to the others springs of SB1). This simplification is a

first step in the improvement of the hydrogeological pattern of a complex volcano-detritic edifice. To improve this modelling, more constrained data is required, such as: water level records of the deep aquifer in the highlands, air temperature records, precise geometry of the buried paleo-channels. Transitory state and 3D representation could be seen as perspective of this work.

6

Hydrochemical approach

Introduction

The availability of reliable and substantial water resources and the fertility of volcanic soils, have brought about since ancient times the intense settlement and agricultural exploitation of the lower flanks of the Merapi volcano. The enhanced anthropogenic pressure together with improved standards of living has substantially increased the demand for water. The consequence has been a greater exploitation of groundwater resources, which are the only available source, in this area, for drinking, agricultural and industrial purposes. Thus, the question about the groundwater quality remains.

6.1 Hydrochemical and geochemical analysis

Hydrochemical and isotopic information can be used to interpret the origin and mode of groundwater recharge, refine estimates of time scales of recharge and groundwater flow, decipher reactive processes, provide paleohydrological information, and calibrate groundwater flow models. Each groundwater system in an area is known to have a unique chemistry, which is acquired as a result of chemical alteration of the meteoric water recharging the system. Hence, hydrochemistry can be interpreted to understand the key processes that have occurred during the movement of water through aquifers and to obtain information about the recharge, the rate and direction of movement, the nature of the aquifer through which it has circulated and anthropogenic activities influencing it (Glynn & Plummer, 2005).

In the present work, an attempt is made to sample water in the Eastern flank of Merapi giving emphasis to the aquifer systems. The sampling campaigns have been performed both in dry and wet season to define the temporal variability of the groundwater hydrochemical and isotopic pattern. The samples were analyzed for their major ions, stable isotopes, tritium and emerging contaminant.

6.1.1 Major and Minor elements

Two groundwater sampling surveys were carried out between the 12th and 15th March 2012 (end of the rainy season) and 11th and 13th of November 2012 (end of the dry season, beginning of the next wet season). Thirty three samples were collected in March and 27 in November on the East flank of Merapi volcano: 1) in March, 20 springs, 4 dug wells, 3 bore wells and the rainfall water at 6 different locations, 2) in November, 26 springs and 1 bore wells.

Electrical conductivity, temperature and pH measurements as well as bicarbonate concentration determination by acidic titration (with a solution of a 0.02 M of H₂SO₄) were

performed directly after the sampling, in the field. The hydrochemical samples were filtered through a 0.45 mm cellulose membrane filter immediately after sampling. Samples destined for major cation analysis were acidified to pH 2.0 with HNO₃ (nitric acid, 65%) immediately after filtration. The samples have been stored in brown glass in a cool box until their analysis in France.

The rain water samples were taken during punctual rainfall events at different elevations. At least, 50 mL have been collected during each event. The quantity was not sufficient to make a complete hydrochemical analysis, and only the stable isotopes characterization has been made. The samples for major anion and cation analysis were conserved into plastic bottles and maintained at ambient air (25°C) during the campaign, the storage in Indonesia and the travel to France. Then at 4°C in the laboratory before the analyses. All the samples have been transported by plane in the week after the sampling campaign. Concentrations of ionic species were determined by the Laboratory of the BRGM Orléans (France) by ion chromatography with detection limits of 0.5 mg/L for potassium (K⁺), sodium (Na⁺), calcium (Ca²⁺), magnesium (Mg²⁺), sulphates (SO₄²⁻), nitrates (NO₃⁻), chloride (Cl⁻), silica (SiO₂⁻); 0.02 mg/L for iron (Fe²⁺) and 0.1 mg/L for lithium (Li²⁺) and fluoride (F⁻).

6.1.2 Emerging contaminant analysis

A diverse array of synthetic organic compounds are used by the society in vast quantities for a range of purposes including the production and preservation of food, industrial manufacturing processes, as well as for human and animal healthcare. Rapid urbanization and frequent disposal of wastewater to surface water and groundwater cause widespread contamination of freshwater supplies with synthetic chemicals as pharmaceuticals, insecticides, surfactants, endocrine disruptors, including hormones. These chemicals are collectively referred to as Emerging Organic Contaminants (EOCs) (Pal et al., 2010). The characteristic of these contaminants is that they do not need to be persistent in the environment to cause negative effects, since their high transformation and removal rates can be offset by their continuous introduction into the environment. One of the main sources of emerging contaminants are untreated urban waste waters and intensive agriculture fertilizers and pesticides. There has been a wealth of studies on the occurrence and/or fate of EOCs in surface water and groundwater, for recent reviews see Heberer (2002); Petrovic (2003); Richardson (2012); Lapworth et al. (2012); Richardson & Ternes (2014).

A water sampling survey has been done the 18th and 19th September 2012 to verify the occurrence or not of pesticides and emerging contaminants into the groundwater in view to identify a possible contamination of the deep groundwater by the surface water. Four

points have been sampled (1.5 L) for the analysis of following emerging contaminants: ace-sulfame, saccharin and sucralose, for specific informations about these EOCs see [Buerge et al. \(2009\)](#); [Scheurer et al. \(2009\)](#); [Buerge et al. \(2011\)](#). Five points have been chosen for the pesticides analysis. The analysis have been made in Danone-Evian laboratory (France) using high resolution mass spectrometry with gas chromatography and liquid chromatography.

6.2 Results

6.2.1 Groundwater hydrochemical properties

As the East flank of Merapi has high population density and the agriculture practices extensively developed, a question about the groundwater resource quality is an obvious fact.

6.2.1.1 Water quality

6.2.1.1.1 Nitrates distribution

Nitrate and nitrite are naturally occurring ions that are part of the nitrogen cycle. Nitrate is used mainly in inorganic fertilizers, and sodium nitrite is used as a food preservative, especially in cured meats. The nitrate concentration in groundwater and surface water is normally low but can reach high levels as a result of agricultural runoff or contamination with human or animal wastes. The toxicity of nitrate to humans is mainly attributable to its reduction to nitrite ([WHO, 2011](#)).

The main potential health risks from nitrate are considered to be methaemoglobinaemia ([Fan & Steinberg, 1996](#); [Greer & Shannon, 2005](#)), oesophageal and stomach cancer ([Powlson et al., 2008](#)), diabetes ([Longnecker & Daniels, 2001](#)), and thyroid hypertrophy ([Aschebrook-Kilfoy et al., 2012](#)). The World Health Organization's recommendation ([WHO, 2011](#)) is that drinking water should not contain more than $50 \text{ mg.L}^{-1} \pm 1$ of nitrate (or $10 \text{ mg NO}_3 \pm \text{-N L} \pm 1$).

On the Eastern flank of Merapi volcano, according to the analysis done in this study, the nitrate concentration are below 50 mg L^{-1} and are ranging from $0,02 \text{ mg L}^{-1}$ to $45,20 \text{ mg L}^{-1}$. The nitrate values distribution seems follow the spring zones repartition: i) in the upper part (above 600 m asl), the concentration presents all the values a maximum of $45,20 \text{ mg L}^{-1}$ at spring 20 (Fig. 6.1), ii) the SB1 shows nitrate values between 20 and 30 mg/L , iii) the SB2 have nitrates values under 10 mg L^{-1} .

The spring 20 is located downstream a village with a consequent cow farming relatively close to the outlet, who can provoke a nitrate contamination. Indeed, the other springs

in the upper part are relatively far from the villages and down into the river gullies. The high values of the SB1 can be explain by the fact that urban area are more developed around these springs. We suppose that contamination is coming from the high density of human and animals wastes in this zone. This spring belt could represent a shallow groundwater, with a recharge area located between 400 and 600 m asl, more sensible to the pollution from the surface activities. At the opposite the low values of the SB2 could show a deep groundwater system with a recharge area in high elevation (above 1000 m asl). A quantification of the fertilizers used on the East flank of the Merapi volcano, could help to confirm these hypothesis.

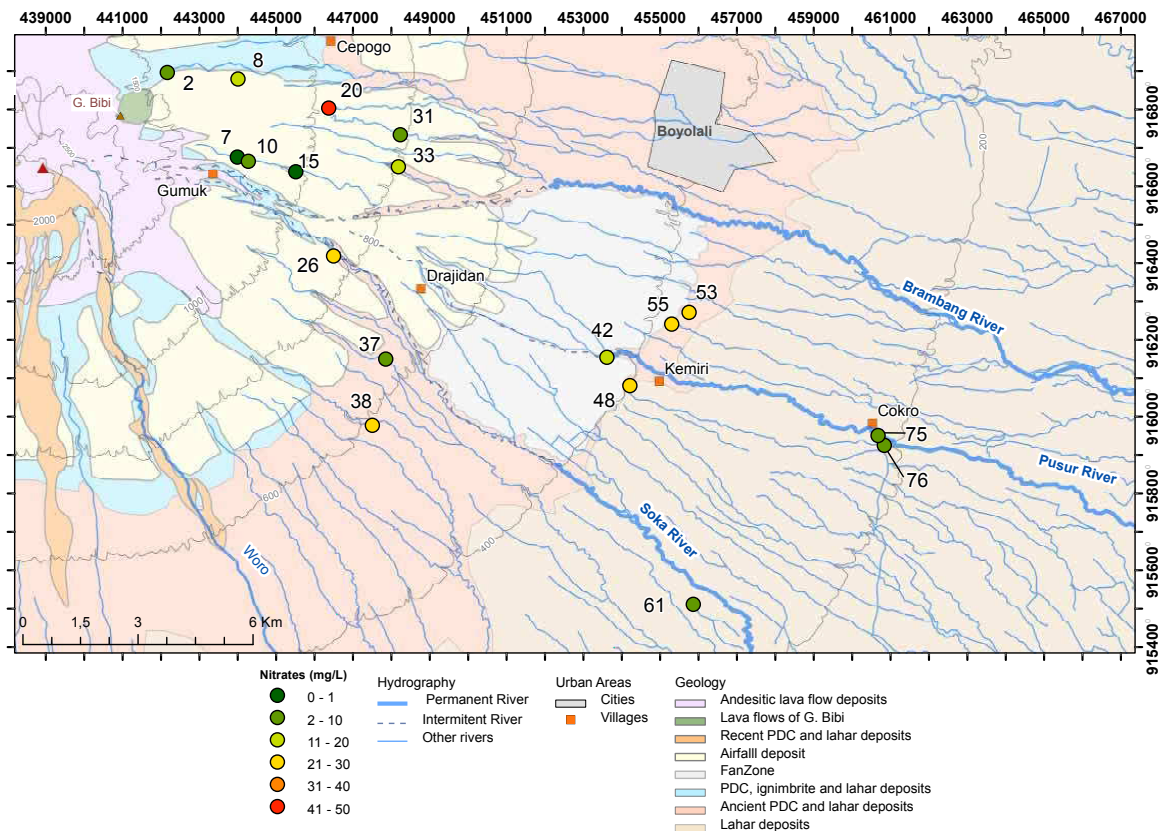


Figure 6.1: Spatial distribution of Nitrates values in springs water and dug wells (sampling survey of March 2012)

6.2.1.1.2 Emerging contaminants

The emerging contaminants analysis did not reveal any contamination. All the values are below the quantification limits. Several options can be considered. In one hand, there is no pollution coming from the chemical manufacturing products in this area, in the other

hand, it is possible that contamination exists anyway but the soil properties play the role of filter and limit the products to spread far from the pollution source. The source can also be discontinuous (pulse effect) or diffuse (dillution important) and do not represent a concentration sufficient given the significant presence of water flow. Precise soil analysis could confirm these options.

6.2.1.1.3 Bacteria contamination

We did not perform bacteria analysis but relatively recent studies about water quality in Central Java provide values range for the fecal coliform and total coliform contamination. [Budisatria et al. \(2007\)](#) show that most of the shallow wells (less than 15 m) tested had bacterial counts ranging from 0 to 2300 cfu/100 ml (cfu: Colonies Forming Units) while the acceptable limits is 0 cfu/100 ml [WHO \(2011\)](#). The depth of the water sources has an effect too, deep groundwater at depths of about 33 and 82 m containing few numbers of faecal coliform (7 colonies/100 ml) compared to the shallow ones ([Budisatria et al., 2007](#)). High concentrations of bacteria in tropical countries like Indonesia are predictable, because of the climate (high temperature and humidity). Therefore, to avoid any contamination, the people are used to boiled water to destroy bacterial pathogens before to use it as drinking water.

6.2.1.1.4 Groundwater facies

The hydrochemical analysis done in March and November 2012 are treated together in order to identify the hydrochemical facies of water at two different hydrological periods, during the wet season for March and end of the dry season for November.

The major and trace elements present in groundwater systems can have four possible origins: i) the rain as the reference signal inputs of the system, ii) water-rock interactions which provide information on the residence time of the water in the lithological formations, iii) anthropogenic inputs and iv) redox processes in anaerobic environment that occur within reducing environment (wetlands, confined aquifers with low recharge rate) ([Charlier, 2007](#)).

Major elements (wt. %)	Lava Flows, Merapi summit	Pyroclastic Series
SiO ₂	55 - 57	51 - 55
TiO ₂	0.6 - 0.8	0.7 - 0.8
Al ₂ O ₃	18.2 - 19.1	18.7 - 21.4
Fe ₂ O ₃	7.5 - 8.3	7.5 - 8.4
MnO	0.1 - 0.2	0.1 - 0.2
MgO	2.3 - 3.4	2.3 - 3.5
CaO	8.0 - 8.4	8.4 - 9.5
Na ₂ O	3.3 - 4.0	3.2 - 3.5
K ₂ O	1.6 - 1.8	1.6 - 2.4
P ₂ P ₅	0.2 - 0.3	0.2 - 0.3

Table 6.1: Chemical composition of lava and pyroclastic formation on Merapi volcano (Gertisser & Keller, 003b).

The most represented minerals in andesitic volcanic environment are plagioclase ((Na, Ca)Al₂Si₂O₈), alkaline feldspar (KAlSi₃O₈), quartz and pyroxenes ((Mg,Fe)SiO₃). These minerals are present in lava flow deposits and pyroclastic formations and can be at the origin of the major elements as Ca, Mg, K, Na, Fe and SiO₂ into the groundwater (Tab. 6.1).

It was assumed that adequate sampling, control and analytical measures were performed at the time of original sampling. However it must be acknowledged that some error may compromise the quality of the existing hydrochemical dataset. In order to reduce these, charge balance error (CBE) was calculated to identify samples that are electrically unbalanced. At a macroscopic scale all water bodies are electrically neutral, with the sum of positive ionic charges (cations) equaling the sum of the negative ionic charges (anions) (Freeze & Cherry, 1979). As a result the calculation of CBE for each site can be used as an indication of data quality.

The CBE has been calculated according to the following equation:

$$Charge\ Balance\ Error = \frac{(\sum anions - \sum cations)}{\sum(anions - cations)} \quad (6.1)$$

We consider that the results are valid if the CBE is under |10|%. Six samples do not fit this definition (maximum at |22.3|%) and they belong to the upper springs. The low water mineralization with high sensibility to the pH variation cause by the interaction with the CO₂ could explain these gaps.

The following elements take their origin from the fertilizers and laundry detergent: Cl, SO₄, and NO₃. The Tables 6.2 and 6.3 summarize the results of the hydrochemical surveys at during the wet season 2011-2012 (March 2012) and end of dry season (November 2012).

Table 6.2: Results of the hydrochemical analysis of March 2012.

Type	Site	Coord. WGS84		Elevation	Date	pH	EC	Temp.	T.A.*	K ⁺	Na ⁺	Ca ²⁺	Mg ²⁺	Fe ²⁺	Li ²⁺	SO ₄ ²⁻	NO ₃ ⁻	Cl ⁻	F ⁻	SiO ₂ ⁻	HCO ₃ ⁻	Ionic Balance	¹⁸ O	² H	³ H	Error ±		
		X (m)	Y (m)	Garmin 76x (m±3m)	(-)	(-)	µS/cm	°C	mg/L CaCO ₃	mg/l	mg/l	mg/l	mg/l	mg/l	mg/l	mg/l	mg/l	mg/l	mg/l	mg/l	mg/l	%	(± 0.15‰ / SMOW)	(± 1‰ / SMOW)	TU	TU		
Rainfall	G	442881	9166194	1436	12/03/12																							
Rainfall	G1	442881	9166194	1436	15/03/12																							
Rainfall	S	450529	9164184	629	13/03/12																							
Rainfall	B	454870	9167314	485	13/03/12																							
Rainfall	J	455866	9155109	283	14/03/12																							
Rainfall	A	460835	9159270	250	12/03/12																							
UP*	2	442167	9168961	1358	13/03/12	6.8	119	19.1	60	3.2	7.8	14.1	2.3	<LQ	1.40E-03	1.7	1.8	1.0	0.2	73.0	7.3	-5.0	-9.1	-57.8	0.7		0.17	
UP	5	443993	9166758	1241	12/03/12	7.1	116	19.6	47																			
UP	7	444008	9168792	1206	12/03/12	6.9	127	21.5	60	4.7	9.3	13.0	2.0	<LQ	1.50E-03	10.4	<LQ	5.8	0.3	83.1	7.3	-17.7	-8.0	-48.2				
UP	8	444279	9166647	1196	13/03/12	6.6	146	21.5	71	4.4	8.8	14.3	3.6	<LQ	1.98E-03	6.5	17.4	5.0	0.3	76.3	8.7	-14.1	-8.3	-52.6				
UP	10	445516	9166377	1171	12/03/12	8.4	129	21.0	50	4.4	9.4	13.3	2.4	<LQ	1.85E-03	8.3	4.0	4.7	0.4	82.9	6.1	-15.4	-7.8	-49.5	0.8		0.29	
UP	15	446373	9168033	1019	12/03/12	8.6	111	22.9	70	4.7	9.3	10.7	2.2	<LQ	1.46E-03	1.0	<LQ	1.8	0.2	90.6	8.5	-16.9	-7.5	-46.2				
UP	20	446500	9164181	986	13/03/12	6.3	264	22.7	65	7.4	11.2	28.5	6.4	<LQ	2.19E-03	14.7	45.2	16.6	0.2	86.7	7.9	-8.5	-8.2	-52.0				
UP	26	448237	9167338	875	13/03/12	8	110	22.7	62	4.8	10.1	31.3	7.7	<LQ	6.10E-04	7.2	22.5	18.3	0.2	92.3	7.6	0.6	-7.4	-46.8				
UP	27	448188	9166506	840	13/03/12	7.6	261	23.9	117	4.8	9.0	10.0	2.0	<LQ	9.60E-04	1.0	1.1	1.4	0.2	91.2	14.3	-22.3	-7.6	-47.2				
UP	35	447859	9161496	792	13/03/12	6.6	232	24.0	115	4.9	8.8	28.1	6.4	<LQ	1.54E-03	16.2	18.1	8.5	0.2	91.1	14.0	-4.2	-7.4	-45.9	1		0.30	
UP	37	447510	9159772	639	13/03/12	7.6	165	23.7	63	3.2	7.1	21.7	4.0	<LQ	1.18E-03	2.1	6.0	3.7	0.1	91.9	7.7	-3.3	-7.1	-44.1				
UP	38	453617	9161544	591	12/03/12	6.5	294	25.3	118	8.0	10.6	33.2	9.3	<LQ	1.25E-03	13.8	29.9	14.3	0.1	98.8	7.7	1.8	-7.0	-44.0				
SB01*	42	454216	9160805	446	15/03/12	6.4	247	25.8	99	6.0	11.2	27.6	6.7	<LQ	1.12E-03	9.8	18.9	7.7	0.2	93.0	12.1	1.3	-7.3	-45.9	0.6		0.35	
SB01	48	455758	9162712	417	14/03/12	6.3	302	26.1	105	6.1	14.9	32.7	8.4	<LQ	1.71E-03	13.1	24.5	16.4	0.1	99.2	12.8	1.7	-7.1	-44.4				
SB01	52	455307	9162408	394	14/03/12	6.2	331	26.4	105	7.9	15.7	36.9	10.1	<LQ	1.72E-03	14.5	25.9	13.7	0.1	98.9	12.8	8.6	-6.9	-42.2				
SB01	55	422520	9158740	389	14/03/12	6.3	288	26.3	105	6.2	13.6	35.4	9.6	0.052	2.19E-03	15.9	26.8	12.3	0.1	96.7	12.8	5.5	-6.9	-42.3				
SB01	44	455867	9155110	435	15/03/12	6.3	254	28.5	87	6.6	10.3	26.4	5.9	<LQ	4.60E-04	14.3	22.8	5.5	0.1	79.5	10.6	1.6	-7.2	-45.5	0.4		0.48	
SP02*	61	460841	9159251	283	14/03/12	6.8	211	25.4	105	4.1	13.6	20.2	8.4	<LQ	1.89E-03	8.4	4.4	5.8	0.2	86.6	12.8	6.9	-7.6	-46.7				
SP02	76	460679	9159505	225	12/03/12	6.8	207	23.9	93	3.9	13.8	19.7	8.7	<LQ	2.32E-03	5.4	4.2	6.0	0.2	84.5	11.3	9.9	-7.8	-48.0	0.6		0.41	
SP02	78	460678	9159505	221	14/03/12	6.8	244	23.3	150	4.7	15.2	20.9	11.1	<LQ	3.45E-03	4.3	6.3	8.2	0.2	83.7	18.3	12.3	-8.1	-50.2				
Dug well	DWS	448419	9167040	829	15/03/12	6.3	323	26.6	135	7.0	11.2	33.5	9.5	<LQ	2.60E-03	13.0	22.9	24.1	0.1	99.1	13.2	-1.6	-7.2	-46.0				
Dug well	DW02	448427	9167052	804	15/03/12	6.2	291	26.6	108	12.3	14.6	34.8	9.1	<LQ	2.36E-03	7.1	20.9	16.9	0.1	98.1	16.5	8.5	-6.7	-40.5				
Dug well	DW09	453368	9159009	390	15/03/12	6.2	395	26.8	126	6.4	14.0	37.7	8.6	<LQ	1.52E-03	8.6	24.1	13.1	0.2	99.5	16.8	7.2	-7.0	-44.0	0.9		0.24	
Bore well	BW01	450199	9165434	697	15/03/12	6.7	241	24.7	90	5.7	9.8	30.8	6.2	<LQ	1.18E-03	6.4	13.2	7.7	0.2	91.8	11.0	6.4	-7.2	-46.0				
Bore well	AW01	460835	9159270	206	13/03/12	6.9	212	23.5	105	6.3	12.2	25.2	7.0	<LQ	2.74E-03	5.5	13.2	9.9	0.2	97.4	14.0	0.7	-7.4	-47.2				

T.A. = Total Alkalinity; UP* = Upper springs; SB1* = Spring belt 1; SB2* = Spring belt 2

Table 6.3: Results of the hydrochemical analysis of November 2012.

Type	Site	Coord. WGS84		Elevation	Date	pH	EC	Temp.	T.A.*	K ⁺	Na ⁺	Ca ²⁺	Mg ²⁺	Fe ²⁺	Li ²⁺	SO ₄ ²⁻	NO ₃ ⁻	Cl ⁻	F ⁻	SiO ₂ ⁻	HCO ₃ ⁻	Ionic Balance	¹⁸ O	² H	³ H	Error ±
		X (m)	Y (m)																							
UP*	1	442735	9167059	1396	01/11/12	6.8	119	19.1	60	4.1	7.4	11.8	1.6	<LQ	2.50E-03	9.3	0.5	10.2	0.5	76.6	5.2	-24.6				
UP	2	442167	9168961	1358	27/10/12	7.1	116	19.6	47	2.9	7.8	14.6	2.3	<LQ	2.50E-03	5.7	<LQ	2.5	0.5	70.1	7.9	-6.8				
UP	6	443853	9168783	1210	11/11/12	6.9	127	21.5	60	4.4	9.0	15.3	3.5	<LQ	3.00E-03	9.0	17.4	5.6	0.1	71.5	8.5	-4.3				
UP	8	444008	9168792	1196	10/11/12	6.6	146	21.5	71	5.4	16.1	21.0	12.8	<LQ	5.50E-03	5.3	4.0	10.5	0.3	79.3	14.9	19.1				
UP	20	446373	9168033	986	28/10/12	8.4	129	21.0	50	7.0	11.0	29.0	6.2	<LQ	3.50E-03	25.0	<LQ	16.0	0.5	81.8	8.6	1.8				
UP	26	446500	9164181	875	12/11/12	8.6	111	22.9	70	13.9	10.4	13.1	2.8	<LQ	1.50E-03	4.0	45.2	8.8	0.5	72.6	8.1	-0.5				
UP	27	448237	9167338	840	26/10/12	6.3	264	22.7	65	5.0	10.2	33.4	7.7	<LQ	1.00E-03	7.8	26.0	21.0	0.2	87.5	13.4	-0.3				
UP	38	447510	9159772	591	14/11/12	8	110	22.7	62	7.6	10.4	32.7	8.8	<LQ	2.00E-03	13.0	27.0	12.4	0.2	92.3	15.0	2.2				
SB01*	42	453617	9161544	446	17/11/12	7.6	261	23.9	117	5.9	10.9	28.8	6.5	<LQ	2.50E-03	20.0	18.1	8.0	0.3	87.6	12.2	5.2				
SB01	44	452252	9158755	435	05/11/12	6.6	232	24.0	115	6.9	15.1	42.3	10.1	<LQ	2.50E-03	22.5	6.0	13.0	0.1	92.1	17.6	16.8				
SB01	48	454216	9160805	417	16/11/12	7.6	165	23.7	63	6.1	13.5	32.2	7.7	<LQ	3.00E-03	20.0	29.9	14.0	0.3	91.2	13.7	7.0				
SB01	49	454085	9160288	414	06/11/12	6.5	294	25.3	118	6.3	15.1	32.9	8.1	<LQ	3.00E-03	9.5	24.2	13.3	0.2	93.5	17.0	4.9				
SB01	52	455758	9162712	394	31/10/12	6.4	247	25.8	99	8.4	15.0	36.6	9.2	<LQ	3.00E-03	14.0	24.8	12.8	0.1	91.2	19.1	8.4				
SB01	53	456198	9164154	392	30/10/12	6.3	302	26.1	105	15.6	18.7	41.6	10.9	<LQ	3.50E-03	17.8	25.9	34.3	0.2	92.9	14.1	14.1				
SB01	55	455307	9162408	389	15/11/12	6.2	331	26.4	105	5.7	13.8	35.1	9.3	<LQ	4.00E-03	22.5	26.8	9.3	0.2	94.1	14.3	12.0				
SP02*	61	455867	9155110	283	03/11/12	6.3	288	26.3	105	4.1	13.2	20.4	7.9	<LQ	3.00E-03	10.7	22.8	6.0	0.4	81.7	12.7	8.0				
SP02	63	459615	9163434	279	19/11/12	6.3	254	28.5	87	6.5	16.5	26.8	20.9	<LQ	3.75E-02	6.2	4.4	12.0	0.2	79.1	20.9	29.5				
SP02	67	459853	9158381	259	08/11/12	6.8	211	25.4	105	3.9	13.5	20.0	8.0	<LQ	2.50E-03	7.2	4.5	5.8	0.3	80.2	14.9	8.0				
SP02	69	460389	9160663	250	09/11/12	6.8	207	23.9	93	3.1	16.2	23.9	14.2	<LQ	7.00E-03	6.4	6.3	10.7	0.3	79.9	20.9	19.1				
SP02	71	460046	9159531	247	02/11/12	6.8	244	23.3	150	4.2	14.0	19.6	9.2	<LQ	4.50E-03	6.6	24.1	7.5	0.4	78.3	18.2	10.5				
SP02	72	460481	9160647	244	18/11/12	6.3	323	26.6	135	6.3	16.3	24.9	14.9	<LQ	9.50E-03	4.8	10.0	11.0	0.2	80.8	21.1	18.7				
SP02	74	461292	9160751	236	07/11/12	6.2	291	26.6	108	6.6	17.1	26.9	19.7	<LQ	3.00E-02	4.7	11.8	12.8	0.2	79.7	24.9	23.4				
SP02	76	460841	9159251	225	13/11/12	6.2	395	26.8	126	3.8	13.4	19.2	8.1	<LQ	3.50E-03	7.5	22.9	6.0	0.4	78.3	13.4	10.1				
SP02	78	460678	9159505	221	29/10/12	6.7	241	24.7	90	4.5	15.0	20.0	10.0	<LQ	5.00E-03	5.0	6.7	8.3	0.3	78.0	16.4	11.8				
Bore well	MW2-S	461978	9158983	191	11/12/1	7	425	28.0	206	6.1	20.9	40.1	14.5	1.564	3.26E-03	10.8	<0.5	8.0	0.2	93.8	25.1	26.9	-7.4	-46.7	<0.7	
Bore well	MW2-D	461978	9158983	191	09/02/13	7.2	772	28.6	150	4.7	75.8	34.9	9.4	0.531	0.00534	7.2	<0.5	128.9	0.3	74.9	18.3	4.93005	-6.21	-40.96	0.8	0.2

*UP: Upper Part, SB01: Spring belt 01, SB02: Spring belt 02

The data set reveals that water mineralization is variable, ranging from 110 to 395 $\mu\text{S}/\text{cm}$. Average pH is equal to 6.9 and the average temperature is 23.9°C, ranging from 19.1°C to 28.5°C. Alkalinity titration measurements vary from 50 to 150 $\text{mg}\cdot\text{L}^{-1}$ CaCO_3 . Groundwater composition for the springs is dominated by the major ions SiO_2^- and Ca^{2+} (mean values of 33% and 25%, respectively). On the 52 samples, the sulfate, nitrate and chlorine show the wider range but all the elements concentrations are below the potability recommendation OMS (1972) (Nitrates, Magnesium: 50 $\text{mg}\cdot\text{L}^{-1}$, Sodium: 250 $\text{mg}\cdot\text{L}^{-1}$, Potassium: 12 $\text{mg}\cdot\text{L}^{-1}$, Sulfates: 250 $\text{mg}\cdot\text{L}^{-1}$, Chlorines: 200 $\text{mg}\cdot\text{L}^{-1}$).

Water chemistry identified at the end of the wet and dry season is dominated by the major ions corresponding to chloride, sulfates and calcium and magnesium-type waters (Fig. 6.2 and Fig. 6.3). Some springs of the upper part trend to calcium chloride and sodium bicarbonate-type waters. This trend can be explained by the uses of detergents in the springs by the locals notably, in the small springs of the upper parts (Springs 26 and 15 for instance).

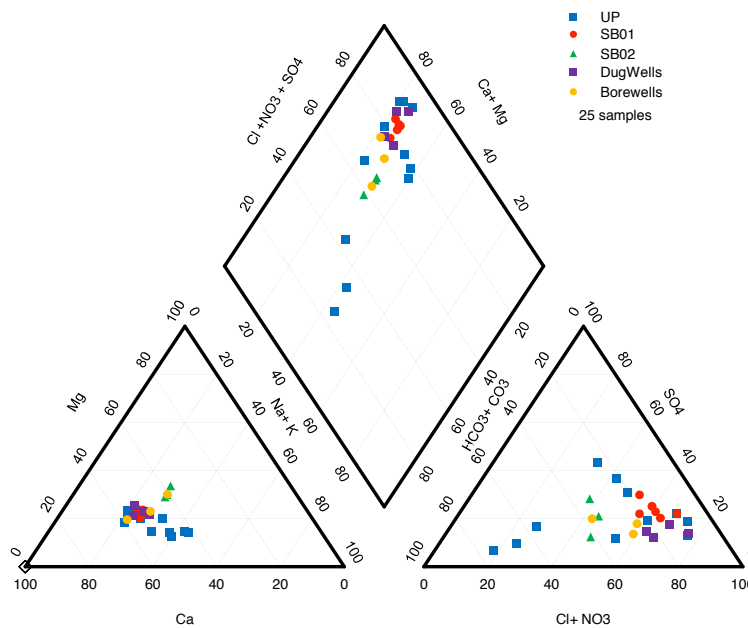


Figure 6.2: Piper plots of groundwater chemistry at the end of the wet season (campaign March 2012)

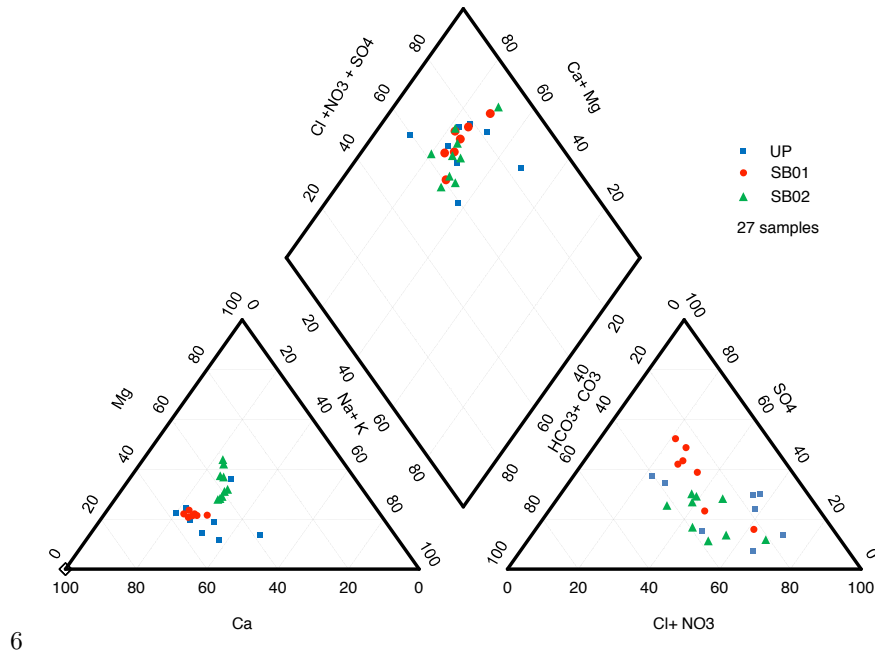


Figure 6.3: Piper plots of groundwater chemistry at the end of the dry season (campaign November 2012)

Plotting the water concentration in NO_3^- , SiO_2 , Na^+ , Cl^- , K^+ and Mg^{2+} depending on the elevation, it appears an increasing trend of the concentration with the decreasing elevation (Fig. 6.4 and Fig. 6.5). This trend is particularly visible considering the magnesium concentration or the total mineralization of the water (values ranging from 112 to 292 mg L^{-1} for April 2012 and 110 to 275 mg L^{-1}). The springs in the upper parts and the shallow wells have a large range from 112 to 225 mg.L^{-1} . The water from the SB1 are concentrated around 230 mg L^{-1} except the spring 42 and 44 which are less mineralized ($< 200 \text{ mg L}^{-1}$). This trend is consistent with the enhancement of the water mineralization by rock-water interaction through the water pathway. Nevertheless, the SB2 do not follow this trend and have low values of total mineralization (from 160 to 175 mg.L^{-1}). The production well of AQUA presents a total mineralization higher than the springs of the SB2 but still below the mineralization increasing trend.

The springs 44 and 42 appear as to have a chemical signature closer to the waters from the SB2 than one of the SB1. The hydrodynamic circulation and the interaction type water/rocks of these springs are probably relatively similar with the SB2.

The geological survey shows that the springs 44 and 42 are depression springs, located in the center of the Soka and Pusur River incisions, respectively. At the opposite of the other springs of the SB1, these springs do not show any constructions or human changes in their outlet sites. These springs present a flow rate more important than the other springs at the same elevation and are perennial.

The hydrochemical facies of the springs is relatively similar between March and November 2012 with a slight increase of total mineralization for the springs located in the upper parts. That is indicate a stability of the aquifer system drained by the SB1 and SB2 but a seasonal response of the upper part perched aquifers.

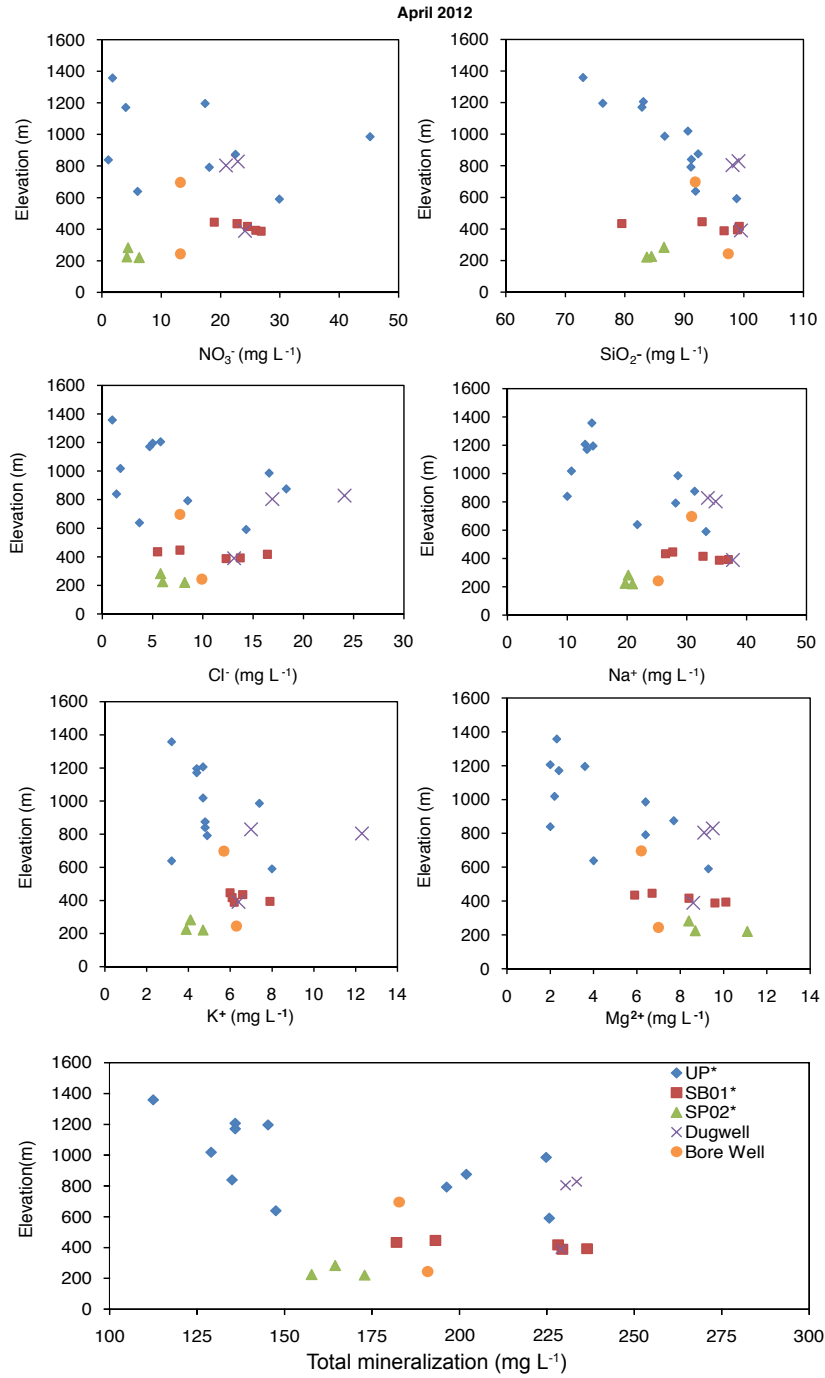


Figure 6.4: Nitrate, Silica, Chlorine, Potassium and Magnesium, Sodium concentration (mg.L⁻¹) and total mineralization (mg.L⁻¹) of spring water (*UP: upper part, SB1: Spring belt 01, SB2: Spring belt 02), dug wells and bore wells depending on the elevation for the campaign of March 2012. The increasing trend of the water mineralization with the decreasing elevation shows the enhancement of the water mineralization by rock-water interaction through the water pathway.

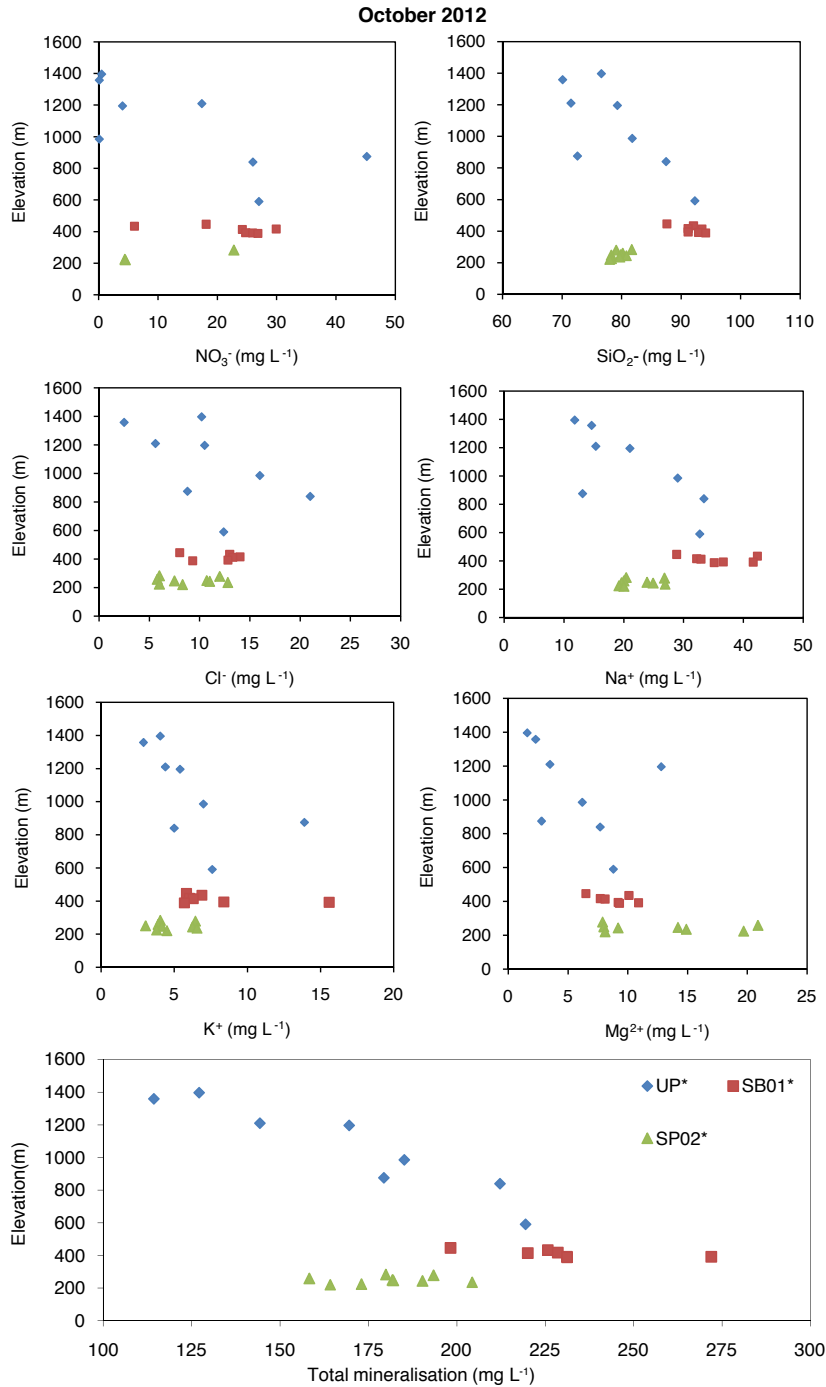


Figure 6.5: Nitrate, Silica, Chlorine, Potassium and Magnesium, Sodium concentration (mg.L^{-1}) and total mineralization (mg.L^{-1}) of spring water (*UP: upper part, SB1: Spring belt 01, SB2: Spring belt 02) depending on the elevation for the campaign of November 2012.

Join et al. (1997) used the Na/Cl molar ratio to find a relationship between the chemical characteristics of springs and the aquifer type. Thus, they differentiate superficial springs

with high ratios from those of the basal aquifer which have low ratios. Similarly, plotting Na vs. Cl along the 1:1 line (Fig. 6.6) allow us to distinguish the spring zones. Indeed, the upper springs appear with a high Na/Cl ratio while the SB2 springs have a low ratio; SB1 have intermediate values. The SB2 has greater Na proportion compare to the other springs.

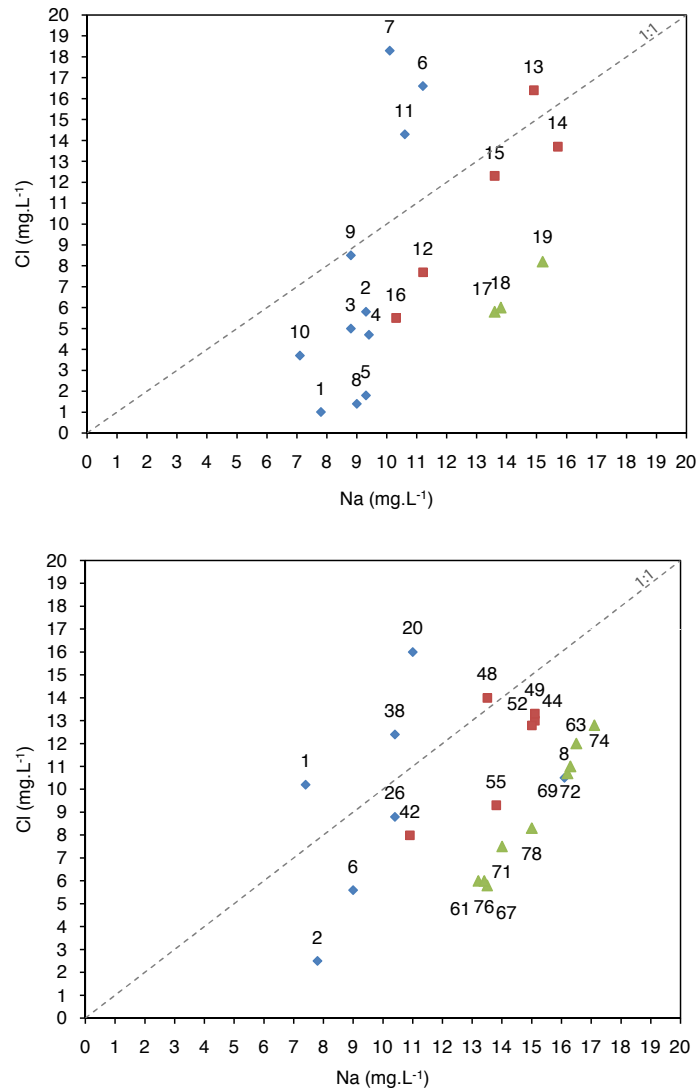


Figure 6.6: Concentration of Na as a dependent variable of Cl for the 25 sample in March 2012 (top) and the 24 sample of November 2012 (bottom).

According to the geological and geomorphological observations, we suppose that the aquifer drained by the springs of SB2 follows the paleo-channel of the buried rivers and streams. These paleo-channels are composed by a sand matrix with an accumulation of blocs and boulders of andesitic lava as the present-day rivers. These channels with a limited lateral extension would play a role of preferential flow path with a high permeability

and high porosity for the groundwater.

The springs of the upper part do not follow this scheme of hydrosystem: most of the springs in the upper part are not perennial and have a very low flow rate. These outlets drain probably some local aquifers into the ash fall deposits characterized by a very fine material. The water transit time through this system is relatively long compared to the previous described type and the mineralization will increase along the Merapi slopes due to water-rock interactions.

The springs in the SB1 zone have probably both configurations. The springs 42 and 44 of the SB1 zone for instance, are crossed by in the actual channels of two main rivers. The water coming out these springs could have the signature of the two hydrosystems types: 1) the water will pass through the ash fall deposits in the upper part and the total concentration of elements will increase with the decreasing of the elevation; 2) the paleo-channel of the Soka and Pusur will then drain the water until the springs.

Conclusion

As a main result of the hydrochemical approach, we highlight that the groundwater quality on the Eastern flank of the Merapi is generally good for drinking purposes. The main spring water type is Ca-Mg-Cl-HCO₃. The springs in the upper part show a wide range of hydrogeochemical signature while the SB1 and SB2 values are more concentrated. The results show a positive orographic gradient of the groundwater total mineralization: the mineralization increases with the decreasing of the elevation except for the SB2. The groundwater circulation within paleo-channel limitates the rock/water interactions.

The concentrations in pollutant are below the detection threshold. As we saw earlier with the hydrogeological interpretation, the groundwater transit time is relatively long (100 years) and it might be possible that a contamination occurred recently is still not visible now but could cause a severe pollution in long term. Thus, the question about the groundwater quality on the Eastern flank of Merapi volcano has to be considered on long period. Nevertheless, considering the soils properties, the long residence time and the multi-layered architecture increase the filtration intensity and reduce the pollution spreading.

Conclusion

Despite the lacks of data and literature about the hydrogeological functioning of the detritic stratovolcanoes, the water resources of this kind of environment affect more than 110 millions people living within 100 km of a stratovolcano just in South-Asia. The unequal rainfall distribution related to a seasonal climate pattern and the complex hydrogeological behavior of these volcano-sedimentary environments trigger water use conflicts between water consumers such as farmers, water public distributors and drinking water bottle companies. The tensions between the water users are intensified by the lack of knowledge about the global water cycle in this kind of context. This work contributes to the knowledge enhancement of this strato-volcano submitt to tropical conditions.

This PhD-Thesis has to be seen within the wider project involving many collaboration groups with a common objective: improve the knowledge on the water resources of an andesitic volcano-detritic catchment in tropical humid climate through the identification of the extent, the geometry and hydrodynamic properties of the aquifers in view to better manage this resource. To reach this objective, better understanding of the water cycle in its globality through a multi-disciplinary approach at watershed scale appeared as an essential method.

This multi-disciplinary study is located on the East flank of Merapi volcano located in Central Java, Indonesia. The study area is focused on the hydrological catchment of the Pusur river and includes the surrounded watersheds of the Soka and Brambang rivers. The total area of the experimental site on the Merapi's Eastern flank is 330 km² with a wide elevation range (from 200 to 1500 m above the sea level, asl). As the available historical data are scarce in this site, the study encompasses all needed disciplines for the establishment of a conceptual model:

1. the geological and geomorphological approach to characterize the internal structure and the deposits architecture on this zone of the Merapi
2. the climate characterization with the estimation of the water balance terms and the description of main hydrological processes
3. the implementation of hydrogeological, hydrochemical and geochemical monitoring to determine the relevant tracers of the groundwater circulations

4. the application of a coupled numerical model between flow circulation and heat transfer to confirm the hydrogeological conceptual model and quantify the water resource.

Geological and geomorphological approach

New geological and geomorphological surveys coupled with GIS analysis allowed to improve the knowledge about the Eastern flank of Merapi structure and the architecture of the volcano-sedimentary deposits.

The lithological facies shown distance and lateral variation with a dominant of erosion and dismantling processes of the recent eruptive products in the upper slopes leading to the intense and quick sedimentation of remobilized material on the low land. The ashes and air fall deposits cover the landscape at large scale (more than 10 km²) in contrast with the channelized deposits such as pyroclastic flows, lahar, lava blocks collapses and debris flows are centered within the river beds and can reach more than 20 km from the summit. The massive andesitic lava flows and the weathered tuff deposits have aquitard properties while pyroclastic flow and debris flow deposits are considered as aquifer layers. Thus, most of the permeable layers are concentrated into the river bed with an accumulation of coarse, blocks and remobilized material.

Despite of the important activity of the Merapi volcano, its Eastern flank has been spared by recent major eruptions. However, this flank possesses the marks of previous catastrophic events which changed the deposits arrangement. A local drainage disturbance has been identified and interpreted as the collapse of a part of the Merapi flank near 5000 years Before Present (B.P.). This event created a detritic fan that could be related to an earthquake associated to a volcanic eruption, a intense rainfall event or the combination of both phenomenon. The detritic fan has a triangular shape covering approximately 45 km² and a volume estimated from 2.2 to 3.1 km³. The Soka and Brambang rivers changed their stream paths to get around the detritic fan and create the drainage anomaly. The detritic fan filled the paleo-Pusur valley and the surrounding rivers from 1000 to 400 m asl. Therefore, when the river beds are buried by the recent eruptions or landslides, they become underground paleo-channels of coarse material surrounded by fine and welded tuff and ash formations. These structures are connected to the upper parts and reached the low lands through the volcanic edifices. These paleo-channels create preferential groundwater path ways.

Geophysics approach with geoelectric method have allowed us to estimate the geometry of these paleo-channels. The dimensions are around 10 m height and 70 m wide and they are buried between 30 to 70 m deep. The comparison with the paleo-channels incised by the present rivers show similar dimensions.

Based on these results, a 3D geological and geomorphological conceptual model has been built and highlights the channelized formations, able to reach long distance range and constituted of low consolidated porous media (i.e. aquifer behavior). The aquitard formations are constituted by welded tuff, non-fractured massive andesitic lava flows and air fall deposits.

Climate and hydrological behavior

Focus on the three main catchments, the Soka, the Pusur and the Brambang hydrological watersheds, a climatic and a hydrological monitoring network have been implemented to complete the existing one managed by governmental institutions. The measure of the climatic variables has been made over two hydrological years: October 2011 to November 2012 and October 2012 to November 2013. Each year is divided in wet (November to June) and dry season (July to October). An assessment of these years has shown that the year 2011-2012 had relatively low to median precipitation rate (1639 mm) while the year 2012-2013 had high precipitation (2337 mm) compared to the few available historical data (collected since 1989 at Cokro station, Klaten). A rainfall gradient is observed on the study area, with more rainfall on the upstream zones (900 m asl) and northern part of the catchment than the valleys and the southern zone.

The watersheds have been divided according to the three gauging stations settled at 400 m asl on the Soka, Pusur and Brambang rivers. Thus, the water balance terms have been firstly calculated on catchments of upper Pusur (10.8 km²), upper Soka (21.8 km²) and upper Brambang (30.3 km²). Based on the Penman-Montheith method, the potential evapotranspiration (PET) has been estimated in collaboration with CIRAD partners and an analytic method developed by the FAO (Allen et al., 1998). The estimations show an inverse correlation between the PET and the elevation. Moreover, like for the air temperature, the PET annual variation is relatively low (889 mm in 2011-2012 and 884 mm in 2012-2013).

Using a Thornthwaite water balance model, the real evapotranspiration (RET) has been estimated. The rainfall and the RET have been combined to calculate the effective rainfall for each watershed. The effective rainfall has a strong correlation coefficient with the rainfall data, showing that the uncertainty on the PET values have a limited impact on the water balance results.

The hydrograph data of the gauging stations at 400 m asl, have been analyzed to describe the rivers discharge pattern on each watersheds. It lead to identify two components of the discharge flow: the runoff (surface water) and the base flow (groundwater contribution). The groundwater contribution to the river discharge is predominantly for all the catchments, the mean annual average of base-flow for upper Soka represents 76.3% of the total discharge (with a minimal value of 29% during the wet season and a maximal value

of 100% during the dry season), for upper Pusur it is 86% (min.75%, max. 100%) and for upper Brambang 80% (min.31%, max. 100%).

At this watershed scale, water balance interpretation highlights an important infiltration capacity of the upper catchments (infiltration represents 33% to 45% of the effective rainfall depending on the year and the watershed). Based on the estimation of the water flow that recharges aquifers, the extrapolated volume related to the whole recharge area is estimated at approximately 145 million m³ during the hydrological year 2011-2012 and 164 million m³ in 2012-2013.

Hydrogeological functioning

A hydrogeological data base has been built with the inventory of springs, dug wells and bore wells from Klaten to Boyolali cities. Three spring zones have been defined, the upper springs from 1500 to 600 m asl, the spring belt n°1 (SB1) near 400 m asl, located at the termination of the detritic fan and the spring belt n°2 (SB2) near 200 m asl. The flow rate range of these spring zones is increasing from upper part to the low lands (mean annual flow rate is 0.012 m³.s⁻¹ for the upper springs, 0.04 m³.s⁻¹ for SB1 and 0.05 m³.s⁻¹ with mean maximal value at 1.16 m³.s⁻¹).

The SB1 is composed by depression springs aligned along the 400 m asl topographic line at the termination of the detritic fan which is covering the aquifer formations. The SB2 is constituted by fault springs near 200 m asl.

A monitoring network has been settled through monthly physico-chemical variables analysis on springs, dug wells and bore wells. To complete this relative continuous monitoring, two hydrogeochemical analysis have been performed at the end of the wet season and at the end of the dry season 2011-2012.

The spatial distribution of the spring water temperature follows the trend dominated by the air temperature orographic gradient (-0.8°C per 100 m, with less than 0.01°C inter-annual variation) except the SB2. Indeed, the majority of springs have a water temperature close to their outlet elevation, showing that most of the aquifers drained by the springs have a local recharge. In contrast, the SB2 has temperature colder than the air temperature at the outlet. Considering the temperature as conservative tracer of the recharge elevation, we have interpreted this temperature anomaly as the proof of higher elevation recharge process (i.e. regional recharge). The distribution of water stable isotopes ($\delta^{18}O$ and $\delta^{16}O$) confirm the results obtained with the spatial distribution of spring temperature. Considering the possibilities of mixing effects between the local and regional groundwater circulations, the SB2 temperature anomaly results from a mix between 47 to 51% of the water coming from high elevation (1500 m asl) while the other part is coming from the local recharge area (400 to 600 m asl).

Two monitored bore wells have been drilled and several hydraulic tests have been performed to estimate the hydrodynamic parameters of the aquifers. Two aquifers system have been identified. The water transit time has been estimated considering a vertical and horizontal component of transfer.

In the upper part, due to high river incision, most of the aquifers are perched. The first consequent aquifer system is a unconfined multi-layers system composed by an alternation of aquifer and aquitard layers. The hydraulic conductivity of this aquifer is relatively low (i.e. 1.46×10^{-5} to $4.07 \times 10^{-5} \text{m.s}^{-1}$). This aquifer system has a local recharge area and contributes to low springs flow in the upper parts and to the SB1 at 400 m asl and to the SB2 at 200 m asl. The mean water transit time in the upper part is close to the hydrological year time scale for the perched aquifers. At SB1, some springs are connected to buried paleo-channel aquifers (e.g. Pusur and Soka springs) whereas others have a similar behavior than the upper springs. Therefore, the estimated water transit time for this aquifer has range from 4 to 10 years.

The second aquifer system composed by buried blocks and coarse material organized in paleo-channels is confined and has high hydraulic conductivity ($2.70 \times 10^{-4} \text{m.s}^{-1}$). The recharge areas of this aquifer are divided between the upstream zone (i.e. 1200 to 800 m asl) of the Merapi and between 600 to 400 m asl. In both cases, the recharge occurs into the non-consolidated material of the temporally streams' river beds. A large amount of groundwater contributes to the SB2 outflow while the rest (5%) continues to the East boundary. This is a regional groundwater circulation. Based on the stratigraphic lithological log this aquifer system is composed by channelized coarse and block material formations. A majority of the SB2 are connected to these paleo-channel aquifers and have transit time slightly shorter than the other units (96 years versus 183 years).

The tritium analysis used to estimate an age of the water revealed a large range with extreme possibilities: long residence time with recharge date estimates before 1950 or after 1968. Thus, in this case, it is not possible to estimate a realistic transfer time with this method.

The hydrochemical analysis has shown that the water quality is relatively good, with only punctual bacterial contaminations in the upper parts of the catchment. The volcanic multi-layered system seems to be a efficient chemical pollutants filter and has a low total mineralization. Nevertheless, the relatively fast transfer time of the deep aquifer system and its sensitive recharge area located into the permeable river beds (i.e. convergence zone of villages wastewater) could be a risk of contamination in the future.

In term of volume, the mean annual groundwater recharge is estimated at 150 million $\text{m}^3 \cdot \text{y}^{-1}$. 5% of this recharge flow out at SB1 (almost 1 million $\text{m}^3 \cdot \text{y}^{-1}$) and 80 % flow out at SB2 (127 million $\text{m}^3 \cdot \text{y}^{-1}$). Near 15% of the groundwater recharge reach the Bengawan-Solo without going out the hydrosystem (21 million $\text{m}^3 \cdot \text{y}^{-1}$).

Combining the results of this research axe, we were able to propose a hydrogeological conceptual model of the groundwater circulations through a complex andesitic stratovolcano edifice.

Numerical modelling of the groundwater circulation

In view to confirm the conceptual model of the hydrogeological functioning, a modelling approach of coupled groundwater flow, mass transfer and heat transfer in 2D vertical cross-section has been performed. We used the code METIS (Modélisation des Ecoulements et des Transferts avec Interactions en milieu Saturé) developed at the Ecole Nationale Supérieure des Mines de Paris, Goblet (1981). This code is a physical based numerical model using the finite difference methods to discretize the differential equations.

The model boundary conditions are based on:

- i) the results of the geological and geomorphological study for the internal structure and the identification of the aquifer and aquitard formations;
- ii) the hydroclimatic observations to define the input parameters (groundwater recharge, air temperature gradient...);
- iii) the hydrogeological measurement to estimate the hydraulic parameters and the physico-chemical variables at the outlet of the hydrogeological features. The hydraulic head at SB1 and SB2 have been imposed.

Flow circulation

As a first step, the simulations were conducted in 2D vertical cross section, in steady state flow conditions. The objectives of the modeling approach were to simulate the flow rates and compare them to the observed measures. METIS allows also to obtain the hydraulic head and the water velocity in any point of the model mesh.

The SB1 flow rate simulations show a slight overestimation (mean annual value, $5.0 \times 10^{-5} \text{ m}^3 \cdot \text{s}^{-1}$ compared to $3.2 \times 10^{-5} \text{ m}^3 \cdot \text{s}^{-1}$) that can be explained by the fact that the observations represent the shallow aquifer discharge measured at the spring point whereas the shallow aquifer's flow drained by the river between the two spring belts is not took into account.

The sensivity tests performed on the geometry shown that the flow rate of the SB2 can be relatively well simulated with the presence of a third aquifer system (mean annual flow rate of $3.7 \times 10^{-4} \text{ m}^3 \cdot \text{s}^{-1}$ for the simulations is slightly higher than $3.2 \times 10^{-4} \text{ m}^3 \cdot \text{s}^{-1}$ for the observations).

It appears also that the estimation of the hydraulic conductivity of the detritic fan assimilated similar to the first aquifer system is not valid. Indeed, the highest amount of

recharge rate is located over the detritic fan zone and it was difficult to keep a realistic hydraulic head with this configuration. The sensibility test shown that a hydraulic conductivity of the recharge zone at $5 \times 10^{-4} \text{ m.s}^{-1}$ and a detritic fan at $5 \times 10^{-5} \text{ m.s}^{-1}$ allow good simulation of flow circulations.

Heat transfer

To complete the boundary condition enumerate above, the geothermal flux has been defined at the base of the mesh and has been estimated as imposed temperature calculated at 200 m below the surface according to a global geothermal gradient of $+3.3^\circ\text{C}$ per 100 m depth. Although this method shows correct results, the approach has to be improved. The use of a geothermal flux, non constant through the mesh bottom will be more realistic.

The simulations of the spring temperature are in the range of the observed ones (SB1: simulation at 25.7°C to compare at observation ranging from 25.5 to 27.0°C ; SB2: sim. 24.8°C while obs. ranging from 22.5°C to 25.0°C). That validate the hydrogeological conceptual model but improvement can still be made and will be considered as perspectives of this work.

Perspectives

Although it could be considered as classic method, it is rare that the same research project has the possibility to conduct the entire investigations from climatic to geological characterization of a catchment especially in relative short time (three years).

The results of this "pilot site" proved the relevant choice of a multi-disciplinary approach. This study provides an encouraging feature in the improvement of hydrogeological knowledge of complex hydrogeological environment in equatorial tropical region. Thus, this approach can be replicate to other sites to acquire background knowledge of the hydrogeological system that is often lacking for users/managers of water resources.

Nevertheless, it is also imperative to maintain the network of hydro-climatic measurements on Merapi site in view to confirm the interpretation through long term data chronicles and be able to anticipate the consequences of climate change on water resources. However, the monitoring protocol can appears heavy to carry on and lighter version is required. Indeed, as we saw, the system's temporal variations are scarce. Therefore, the measure can be done at key moments instead of continuously.

That is why, we propose a spring, dug wells and bore wells physico-chemical variables measure at the end of the dry season (September or October) during the wet season (January or February) and at the end of the wet season (April or May). However, the daily rainfall records together with daily temperature are needed to monitor the climate pattern and adjust the springs monitoring in case of any change or extreme event.

In order to pursue that approach, an operation manager is needed and should be the coordinator of the sampling protocol and the data collect integration. So far, these two main points still need to be improved.

A number of aspects remains to be further examined. They have been divided according to their application site:

Recharge zone

- The better characterization of the vadoze zone properties through soil analysis in the upper slopes could help to provide useful data: 1) to provide solutions to limit the erosion at the plot or micro-catchment scales, 2) to identify the threshold effect of the soil during the intense rainfall periods, 3) to define the temperature variation along the non-saturated zone and integrated the values in the coupled flow and heat transfer model.
- The implementation of deep monitoring wells (200 m deep minimal) in the high elevation to confirm the water table estimated by the modeling approach.

Discharge zone

- A large scale geophysical survey could be done 1) to confirm the paleo-channel geometry at different elevations, 2) to verify the role of the Opak river fault into the SB2 occurrence.
- The interactions between the aquifers formations and the Pusur river upstream and downstream the SB2 could be investigated by the implementation of shallow piezometers in the village on the riversides.

Total watershed scale

- An improvement of the river discharge monitoring with more gauging stations along the main rivers and implement a precise monitoring of the Bengawan-Solo river, defined as the East hydraulic boundary of the system. This improved monitoring could confirm the interactions surface water/groundwater and allow to better quantify the groundwater amount which not flows through the SB1 either SB2.
- A comparison between the Eastern flank of Merapi with others catchment on strato-volcano edifices in Java, Indonesia or in other countries with the similar context.

Numerical modeling

The simulation of flow circulation, geothermal flux instead imposed temperature, transient simulation and heat transfer in 3D with the impact of the surrounded rock thermal prop-

erties could be an improvement into the transfer time estimation and the water resource quantification.

Bibliography

- Abram, N. J., McGregor, H. V., Gagan, M. K., Hantoro, W. S., & Suwargadi, B. W. (2009). Oscillations in the southern extent of the Indo-Pacific Warm Pool during the mid-Holocene. *Quaternary Science Reviews*, 28(25-26), 2794–2803. 18
- Aldrian, E. & Dwi Susanto, R. (2003). Identification of three dominant rainfall regions within indonesia and their relationship to sea surface temperature. *International Journal of Climatology*, 23(12), 1435–1452. 18, 20, 114
- Allen, R. G., Pereira, L. S., Raes, D., & Smith, M. (1998). Crop evapotranspiration - guidelines for computing crop water requirements. *FAO Irrigation and drainage paper 56*, 56(300), 6541. 106, 287
- Anderson, M. (2005). Heat as a ground water tracer. *Ground Water*, 43(9), 951–968. 230
- Andreastuti, S. D., Alloway, B. V., & Smith, I. E. M. (2000). A detailed tephrostratigraphic framework at merapi volcano, central java, indonesia: implications for eruption predictions and hazard assessment. *Journal of Volcanology and Geothermal Research*, 100(1-4), 51–67. doi: DOI: 10.1016/S0377-0273(00)00133-5. 15, 58, 59, 62
- Andrews, J. N., Burgess, W. G., Edmunds, W. M., Kay, R. L. F., & Lee, D. J. (1982). The thermal springs of bath. *Nature*, 298(5872), 339–343. 206, 230, 233
- Anonymous (2004). Law of the republic of indonesia number 7 of 2004 concerning water resources. 36
- Asai, K., Satake, H., & Tsujimura, M. (2009). Isotopic approach to understanding the groundwater flow system within an andesitic stratovolcano in a temperate humid region: case study of ontake volcano, central japan. *Hydrological Processes*, 23, 559–571. 167
- Aschebrook-Kilfoy, B., Heltshe, S. L., Nuckols, J. R., Sabra, M. M., Shuldiner, A. R., Mitchell, B. D., Airola, M., Holford, T. R., Zhang, Y., & Ward, M. H. (2012). Modeled nitrate levels in well water supplies and prevalence of abnormal thyroid conditions among the Old Order Amish in Pennsylvania. *Environmental health : a global access science source*, 11(1), 6. 271

- Auvet, B. (2013). *L'eau des hautes terres du volcan. Hydrologie et érosion d'un petit bassin agricole sur les pentes du volcan Merapi (Java, Indonésie)*. Master thesis report, Université Pierre et Marie Curie, MinesParisTech et AgroParisTech. 126
- Aynew, T., Demlie, M., & Wohnlich, S. (2008). Hydrogeological framework and occurrence of groundwater in the ethiopian aquifers. *Journal of African Earth Sciences*, 52(3), 97–113. doi: DOI: 10.1016/j.jafrearsci.2008.06.006. 22
- Bahar, I. (1984). *Contribution à la connaissance du volcanisme indonésien: Le Merapi (Centre Java), cadre structural, pétrologie, géochimie et implications volcanologiques*. PhD thesis, Université de Montpellier, 213p. 57
- Bank, W. (2013). *Indonesia - Climate Change Development Policy Loan Project*. Technical Report Report ICR 2690, World Bank, Washington DC. 21, 30, 349
- Bautista, C. B. (1996). *The Mount Pinatubo disaster and the people of Central Luzon*. In: Newhall, C.G., Punongbayan, R.S. (Eds.), *Fire and Mud: eruptions and lahars of Mount Pinatubo, Philippines*. Phivolcs/University of Washington Press. 16
- Beauducel, F. (1998). *Structures et comportement mécanique du volcan Merapi (Java) : une approche méthodologique du champ de déformations*. PhD thesis. 13
- Beck, A., Garven, G., & Stegena, L. (1990). Hydrogeological regimes and their subsurface thermal effects. *Eos, Transactions American Geophysical Union*, 71(36), 1070–1071. 231
- Belousov, A., Belousova, M., & Voight, B. (1999). Multiple edifice failures, debris avalanches and associated eruptions in the holocene history of shiveluch volcano, kamchatka, russia. *Bulletin of Volcanology*, 61(324-342). 53
- Berthommier, P. (1990). *Étude volcanologique du Merapi (Centre Java): téphrostratigraphie et chronologie - produits éruptifs*. PhD thesis. 13, 45, 56, 57, 58, 92
- Berthommier, P., Camus, G., Condomines, M., & Vincent, P. (1990). Le merapi (centre-java): Éléments de chronologie d'un strato-volcan andésitique. *C. R. Acad. Sci.*, 311, 213–218. 55, 60, 350
- Bertrand, G. (2009). *Apport du traçage naturel (ions majeurs, isotopes) à l'étude du fonctionnement des aquifères volcaniques. (Bassin d'Argnat, Auvergne, France)*. PhD thesis, Université Blaise Pascal-Clermont-Ferrand 2. 167, 168
- Bertrand, G., Celle-Jeanton, H., Huneau, F., Loock, S., & Renac, C. (2010). Identification of different groundwater flowpaths within volcanic aquifers using natural tracers for the evaluation of the influence of lava flows morphology (argnat basin, chaîne des puys, france). *Journal of Hydrology*, 391(3-4), 223–234. doi: DOI: 10.1016/j.jhydrol.2010.07.021. 167

- Bethke, C. (1989). Modeling subsurface flow in sedimentary basins. *Geologische Rundschau*, 78(1), 129–154. 229
- Blyth, F. (1970). The nomenclature of pyroclastic deposits. *Bulletin of Volcanology*, 6(1), 145–156. 45, 47
- Bogie, I. & Mackenzie, K. (1998). The application of a volcanic facies model to an andesitic statovolcano hosted geothermal system at wayang windu, java, indonesia. In *Proceedings 20th NZ Geothermal workshop* (pp. 265–270). 54, 55, 61, 350
- Boudon, G., Camus, G., Gourgaud, A., & Lajoie, J. (1993). The 1984 nuée-ardente deposits of merapi volcano, central java, indonesia: stratigraphy, textural characteristics, and transport mechanisms. *Bulletin of Volcanology*, 55(5), 327–342. 12
- Bourgeois, R., Lopez, J.-M., Sosiawan, H., & Kartiwa, B. (2008). Boire ou manger? boire et manger. vers une gestion intégrée d'un bassin versant en indonésie. 2, 38
- Brown, R. & Calder, E. (2005). Pyroclastics. In R. C. Selley, L. R. M. Cocks, & I. R. Plimer (Eds.), *Encyclopedia of Geology* (pp. 386 – 397). Oxford: Elsevier. 47
- Budisatria, I., Udo, H., a.J. van der Zijpp, Murti, T., & Baliarti, E. (2007). Air and water qualities around small ruminant houses in Central Java - Indonesia. *Small Ruminant Research*, 67(1), 55–63. 273
- Buerge, I. J., Buser, H.-R., Kahle, M., Müller, M. D., & Poiger, T. (2009). Ubiquitous occurrence of the artificial sweetener acesulfame in the aquatic environment: an ideal chemical marker of domestic wastewater in groundwater. *Environmental science & technology*, 43(12), 4381–5. 271
- Buerge, I. J., Keller, M., Buser, H.-R., Müller, M. D., & Poiger, T. (2011). Saccharin and other artificial sweeteners in soils: estimated inputs from agriculture and households, degradation, and leaching to groundwater. *Environmental science & technology*, 45(2), 615–21. 271
- Cabrera, M. C. & Custodio, E. (2004). Groundwater flow in a volcanic–sedimentary coastal aquifer: Telde area, gran canaria, canary islands, spain. *Hydrogeology Journal*, 12(3), 305–320. 24
- Camus, G., Gourgaud, A., Mossand-Berthommier, P. C., & Vincent, P. M. (2000). Merapi (central java, indonesia): An outline of the structural and magmatological evolution, with a special emphasis to the major pyroclastic events. *Journal of Volcanology and Geothermal Research*, 100(1-4), 139–163. doi: DOI: 10.1016/S0377-0273(00)00135-9. 45, 55, 56, 57, 58, 60, 62, 67, 80, 82, 92, 350

- Capra, L., Macias, J., Scott, K. M., Abrams, M., & Garduño-Monroy, V. (2002). Debris avalanches and debris flows transformed from collapses in the trans-mexican volcanic belt, mexico - behavior, and implications for hazard assessment. *Journal of Volcanology and Geothermal Research*, 113(1-2), 81–110. 53
- Carey, Steven, N. (1991). *Transport and deposition of tephra by pyroclastic flows and surges*, volume 45. Society for sedimentary geology. 46, 47, 49
- Carlston, C., Thatcher, L., & Rhodehamel, E. C. (1961). Tritium as a hydrologic tool the wharton tract study. *USGS*, (pp. 503–512). 168
- Carvalho, M., Nunes, J. C., & Acciaioli, M. H. (2007). Trace elements in groundwater of active stratovolcanoes in s. miguel island (azores). *VI Congresso Ibérico de Geoquímica*. 22
- Castro, M. C., Patriarche, D., & Goblet, P. (2005). 2-D numerical simulations of groundwater flow, heat transfer and 4He transport — implications for the He terrestrial budget and the mantle helium–heat imbalance. *Earth and Planetary Science Letters*, 237(3-4), 893–910. 235
- Cattan, P., Ruy, S., Cabidoche, Y.-M., Findeling, a., Desbois, P., & Charlier, J. (2009). Effect on runoff of rainfall redistribution by the impluvium-shaped canopy of banana cultivated on an Andosol with a high infiltration rate. *Journal of Hydrology*, 368(1-4), 251–261. 126
- Cattoni, E., Cecconi, M., & Pane, V. (2007). Geotechnical properties of an unsaturated pyroclastic soil from roma. *Bulletin of Engineering Geology and the Environment*, 66, 403–414. 240, 241, 368
- Charbonnier, S., Germa, a., Connor, C., Gertisser, R., Preece, K., Komorowski, J.-C., Lavigne, F., Dixon, T., & Connor, L. (2013). Evaluation of the impact of the 2010 pyroclastic density currents at Merapi volcano from high-resolution satellite imagery, field investigations and numerical simulations. *Journal of Volcanology and Geothermal Research*, 261, 295–315. 2, 15
- Charbonnier, S. J. & Gertisser, R. (2011). Deposit architecture and dynamics of the 2006 block-and-ash flows of merapi volcano, java, indonesia. *Sedimentology*, (pp. 1–40). 14, 51
- Charlier, J.-B. (2007). *Fonctionnement et modélisation hydrologique d'un petit bassin versant cultivé en milieu volcanique tropical*. PhD thesis. 138, 141, 273
- Charlier, J.-B., Lachassagne, P., Ladouche, B., Cattan, P., Moussa, R., & Voltz, M. (2011). Structure and hydrogeological functioning of an insular tropical humid andesitic

- volcanic watershed: A multi-disciplinary experimental approach. *Journal of Hydrology*, 398(3-4), 155–170. doi: DOI: 10.1016/j.jhydrol.2010.10.006. 22, 25
- Cioni, R., Santacroce, R., & Sbrana, A. (1999). Pyroclastic deposits as a guide for reconstructing the multi-stage evolution of the somma-vesuvius caldera. *Bulletin of Volcanology*, 61(4), 207–222. 45
- Clark, W., E. (1967). Computing the barometric efficiency of a well computing the barometric efficiency of a well computing the barometric efficiency of a well computing the barometric efficiency of a well. *Journal of Hydraulic Engineering*, 93(4), 93–98. 167
- Clarke, A. J. (2014). El Niño physics and El Niño predictability. *Annual review of marine science*, 6, 79–99. 18, 178, 348
- Clements, B., R., H., Smyth, H., & A., C. M. (2009). Thrusting of a volcanic arc: a new structural model for java. *Petroleum Geoscience*, 15, 159–174. 8, 9, 11, 348
- Cole, P. D., Guest, J., Duncan, A. M., Chester, D., & Bianchi, R. (1992). Post-collapse volcanic history of calderas on a composite volcano: an example from roccamonfina, southern italy. *Bulletin of Volcanology*, 54, 253–266. 45
- Commer, M., Helwig, S. L., Hördt, A., Scholl, C., & Tezkan, B. (2006). New results on the resistivity structure of merapi volcano (indonesia), derived from three-dimensional restricted inversion of long-offset transient electromagnetic data. *Geophysical Journal International*, 167(3), 1172–1187. 2, 236
- Cook, P., Hatton, T., Pidsley, D., a.L. Herczeg, Held, a., O’Grady, a., & Eamus, D. (1998). Water balance of a tropical woodland ecosystem, Northern Australia: A combination of micro-meteorological, soil physical and groundwater chemical approaches. *Journal of Hydrology*, 210(1-4), 161–177. 99, 138
- Craig, H. (1961). Isotopic variations in meteoric waters. *Sciences*, 133(3465), 1702–1703. 207
- Criswell, C. W. (1987). Chronology and pyroclastic stratigraphy of the may 18, 1980, eruption of mount st. helens, washington. *Journal of Geophysical Research: Solid Earth*, 92(B10), 10237–10266. 46, 47
- Cruz, J. V. (2003). Groundwater and volcanoes: examples from the azores archipelago. *Environmental Geology*, 44(3), 343–355. 22
- Cruz, T., Cabrera, M. C., & Heredia, J. (2007). Steady-state three-dimensional flow simulation in a volcanic-sedimentary aquifer. *Groundwater and ecosystems*, (pp. 1–9). 22

- Cundari, A. & Ollier, C. D. (1970). Inverted relief due to lava flows along valleys. *Australian Geographer*, 11(3), 291–293. 57
- Custodio, E. (2004). Hydrogeology of volcanic rocks. In V. S. Kovalevsky, G. P. Kruseman, & K. R. Rushton (Eds.), *Groundwater studies: an international guide for hydrogeological investigations - IHP-VI*, volume Series on Groundwater No. 3. United Nations Educational, Scientific and Cultural Organization. 21, 24, 25, 240, 241, 368
- Custodio, E., Guerra, J. A., Jimenez, J., Medina, J., A., & Soler, C. (1983). The effects of agriculture on the volcanic aquifers of the canary islands. *Environmental Geology*, 5(4), 225–231. 21, 22
- Davis, S. N. (1999). Humboldt, arago, and the temperature of groundwater. *Hydrogeology Journal*, 7(5), 501–503. 206, 232
- De Belizal, E., Lavigne, F., & Grancher, D. (2011). Quand l'aléa devient la ressource : l'activité d'extraction des matériaux volcaniques autour du volcan merapi (indonésie) dans la compréhension des risques locaux. *Cybergeog: European Journal of Geography (en ligne), Environnement, Nature, Paysage, document 525*, (pp. 1–25). 16, 45
- de Bélizal, E., Lavigne, F., Hadmoko, D. S., Degeai, J.-P., Dipayana, G. A., Mutaqin, B. W., Marfai, M. A., Coquet, M., Mauff, B. L., Robin, A.-K., Vidal, C., Cholikh, N., & Aisyah, N. (2013). Rain-triggered lahars following the 2010 eruption of Merapi volcano, Indonesia: A major risk. *Journal of Volcanology and Geothermal Research*, 261, 330–347. 16
- de Marsily, G. (1986). *Quantitative Hydrogeology*. Academic Press. 236
- deGroot Hedlin, C. & Constable, S. (1990). Occam's inversion to generate smooth, two-dimensional models form magnetotelluric data. *Geophysics*, 55, 1613–1624. 84
- Dellino, P. & Volpe, L. L. (2000). Structures and grain size distribution in surge deposits as a tool for modelling the dynamics of dilute pyroclastic density currents at la fossa di vulcano (aeolian islands, italy). *Journal of Volcanology and Geothermal Research*, 96(1–2), 57 – 78. 48
- Deming, D. (1993). Regional permeability estimates from investigations of coupled heat and groundwater flow, north slope of alaska. *Journal of Geophysical Research: Solid Earth*, 98(B9), 16271–16286. 232
- Demlie, M., Wohnlich, S., Wisotzky, F., & Gizaw, B. (2007). Groundwater recharge, flow and hydrogeochemical evolution in a complex volcanic aquifer system, central ethiopia. *Hydrogeology Journal*, 15(6), 1169–1181. 167

- Dove, M. R. (2007). Perception of volcanic eruption as agent of change on merapi volcano. *Journal of Volcanology and Geothermal Research*, 172, 329–337. 45
- D'Ozouville, N., Auken, E., Sorensen, K., Violette, S., de Marsily, G., Deffontaines, B., & Merlen, G. (2008). Extensive perched aquifer and structural implications revealed by 3d resistivity mapping in a galapagos volcano. *Earth and Planetary Science Letters*, 269, 518–522. 22
- Dubois, N., Oppo, D., & Galy, V. (2014). Indonesian vegetation response to changes in rainfall seasonality over the past 25,000 years. *Nature . . .*, 7(June), 513–517. 80
- El-Swaify, S. A., Dangler, E. W., & Armstrong, C. L. (1982). *Soil erosion by water in the tropics*. Technical report, University of Hawaii. 46
- Elsenbeer, H. (2001). Hydrologic flowpaths in tropical rainforest soils? a review. *Hydrological Processes*, 15(10), 1751–1759. 99
- Entwisle, D., Hobbs, P., Jones, L., Gunn, D., & Raines, M. (2005). The relationships between effective porosity, uniaxial compressive strength and sonic velocity of intact borrowdale volcanic group core samples from sellafield. *Geotechnical and Geological Engineering*, 23, 793–809. 221
- Falkland, A. (1999). Tropical island hydrology and water resources current knowledge and future needs. (pp. 237–298). 21
- Fan, A. M. & Steinberg, V. E. (1996). Health implications of nitrate and nitrite in drinking water: an update on methemoglobinemia occurrence and reproductive and developmental toxicity. *Regulatory toxicology and pharmacology : RTP*, 23(1 Pt 1), 35–43. 271
- Fetter, C. (1994). *Applied Hydrogeology*. Number 691pp. Macmillan. 21, 142, 149, 357
- Fisher, R. V. (1966). Rocks composed of volcanic fragments and their classification. *Earth-Science Reviews*, 1(4), 287–298. 47
- Fisher, R. V. (1979). Models for pyroclastic surges and pyroclastic flows. *Journal of Volcanology and Geothermal Research*, 6(3–4), 305 – 318. 47, 48
- Fleitmann, D., Burns, S. J., Mangini, A., Mudelsee, M., Kramers, J., Villa, I., Neff, U., Al-Subbary, A. a., Buettner, A., Hippler, D., & Matter, A. (2007). Holocene ITCZ and Indian monsoon dynamics recorded in stalagmites from Oman and Yemen (Socotra). *Quaternary Science Reviews*, 26(1-2), 170–188. 19
- Flint, L. E. & Selker, J. S. (2003). Use of porosity to estimate hydraulic properties of volcanic tuffs. *Advances in Water Resources*, 26(5), 561–571. doi: DOI: 10.1016/S0309-1708(02)00182-3. 25, 221, 240, 241, 368

- Forster, C. & Smith, L. (1989). The influence of groundwater flow on thermal regimes in mountainous terrain: A model study. *Journal of Geophysical Research: Solid Earth*, 94(B7), 9439–9451. 231
- Foster, S. S. D., Ellis, A. T., Losilla-Penon, M., & Rodriguez-Estrada, H. V. (1985). Role of volcanic tuffs in ground water regime of valle central, costa rica. *Ground Water*, 23(6), 795–801. 25, 141
- Freeze, R., A. & Cherry, J., A. (1979). *Groundwater*. New Jersey: Prentice Hall Inc. 274
- Fujinawa, A., Ban, M., Ohba, T., Kontani, K., & Miura, K. (2008). Characterization of low-temperature pyroclastic surges that occurred in the northeastern japan arc during the late 19th century. *Journal of Volcanology and Geothermal Research*, 178(1), 113 – 130. <ce:title>Dynamics of Volcanic Explosions: Field Observations, Experimental Constraints and Integrated Modelling of Volcanic Explosions: Field Observations, Experimental Constraints and Integrated Modelling</ce:title>. 48
- Furbish, D., J. (1991). The response of water level in a well to a time series of atmospheric loading under confined conditions. *Water Resources Research*, 27(557-568). 167
- Garcia Cacho, L., Diez-Gil, J., & Arana, V. (1994). A large volcanic debris avalanche in the Pliocene Roque Nublo Stratovolcano , Gran Canaria , Canary Islands. *Journal of Volcanology and Geothermal Research*, 63, 217–229. 81, 353
- Garven, G. (1995). Continental-scale groundwater flow and geologic processes. *Annual Review of Earth and Planetary Sciences*, (pp. 89–117). 229
- Gat, J. R. (1996). Oxygen and Hydrogen Isotopes in the Hydrologic Cycle. *Annual Review of Earth and Planetary Sciences*, 24(1), 225–262. 167
- Gerstenecker, C., Läufer, G., Steineck, D., Tiede, C., & Wroberl, B. (2005). Validation of digital elevation model around the merapi volcano, java, indonesia. *Natural Hazards and Earth System Science*, 5(6), 863–876. 60, 70, 79, 238, 350, 352, 363
- Gertisser, R., Cassidy, N., Charbonnier, S., Nuzzo, L., & Preece, K. (2012a). Overbank block-and-ash flow deposits and the impact of valley-derived, unconfined flows on populated areas at merapi volcano, java, indonesia. *Natural Hazards*, 60, 623–648. 57
- Gertisser, R., Charbonner, S., Keller, J., & Quidelleur, X. (2012b). The geological evolution of merapi volcano, central java, indonesia. *Bulletin of Volcanology*, 74, 1213–1233. 2, 45, 55, 56, 58, 59, 60, 80, 350
- Gertisser, R., Charbonner, S., Troll, V., Keller, J., Preece, K., Chadwick, J., Barclay, J., & Herd, R. (2011). Merapi (java, indonesia): anatomy of a killer volcano. *Geology Today*, 27(2), 57–62. 2, 12

- Gertisser, R. & Keller, J. (2003). Temporal variations in magma composition at merapi volcano (central java, indonesia): magmatic cycles during the past 2000 years of explosive activity. *Journal of Volcanology and Geothermal Research*, 123(1-2), 1–23. doi: DOI: 10.1016/S0377-0273(03)00025-8. 57
- Gertisser, R. & Keller, J. (2003b). Trace element and sr, nd, pb and o isotope variations in medium-k and high-k volcanic rocks from merapi volcano, central java, indonesia: Evidence for the involvement of subducted sediments in sunda arc magma genesis. *Journal of Petrology*, 44(3), 457–489. 274, 369
- Giggenbach, W. F. & Soto, R. C. (1992). Isotopic and chemical composition of water and steam discharges from volcanic-magmatic-hydrothermal systems of the guanacaste geothermal province, costa rica. *Applied Geochemistry*, 7(4), 309 – 332. 22
- Glynn, P. D. & Plummer, L. N. (2005). Geochemistry and the understanding of ground-water systems. *Hydrogeology Journal*, 13(1), 263–287. 167, 269
- Goblet, P. (1981). *Modélisation des transferts de masse et d'énergie en aquifère*. PhD thesis, Ecole Nationale Supérieure des Mines de Paris. 4, 226, 229, 233, 239, 290
- Gomez, C., Janin, M., Lavigne, F., Gertisser, R., Charbonnier, S., Lahitte, P., Hadmoko, S. R., Fort, M., Wassmer, P., Degroot, V., & Murwanto, H. (2010). Borobudur, a basin under volcanic influence: 361,000 years bp to present. *Journal of Volcanology and Geothermal Research*, 196(3-4), 245–264. doi: DOI: 10.1016/j.jvolgeores.2010.08.001. 45
- Gonfiantini, R., Roche, M.-A., Olivry, J.-C., Fontes, J.-C., & Zuppi, G. M. (2001). The altitude effect on the isotopic composition of tropical rains. *Chemical Geology*, 181(1-4), 147–167. 168
- Greer, F. R. & Shannon, M. (2005). Infant methemoglobinemia: the role of dietary nitrate in food and water. *Pediatrics*, 116(3), 784–6. 271
- Griffiths, G. M., Salinger, M. J., & Leleu, I. (2003). Trends in extreme daily rainfall across the south pacific and relationship to the south pacific convergence zone. *International Journal of Climatology*, 23(8), 847–869. 114
- Griffiths, M., Drysdale, R. N., Gagan, M. K., Frisia, S., Zhao, J.-X., Ayliffe, L. K., Hantoro, W. S., Hellsrom, J. C., Fischer, M. J., Feng, Y.-X., & Suwargadi, B. W. (2010). Evidence for holocene changes in australian – indonesian monsoon rainfall from stalagmite trace element and stable isotope ratios. *Earth and Planetary Science Letters*, 292(1-2), 27–38. 80

- Grosse, P., van Wyk de Vries, B., Euillades, P. A. and Kervyn, M., & Petrinovic, I. A. (2012). Systematic morphometric characterization of volcanic edifices using digital elevation models. *Geomorphology*, 136, 114–131. 61
- Ha, K.-J., Heo, K.-Y., Lee, S.-S., Yun, K.-S., & Jhun, J.-G. (2012). Variability in the east asian monsoon: a review. *Meteorological Applications*, 19(2), 200–215. 19
- Hadi, A. & Shrestha, D. (2011). Runoff dynamics through parameterizing a hydrological model in a watershed: a case study in upper serayu basin, central java province, indonesia. *Indonesian Journal of Geography*, 42(1). 20
- Hahn, J., Lee, Y., Kim, N., Hahn, C., & Lee, S. (1997). The groundwater resources and sustainable yield of cheju volcanic island, korea. *Environmental Geology*, 33(1), 43–53.
- Hall, R. (2002a). Cenozoic geological and plate tectonic evolution of se asia and the sw pacific: computer-based reconstructions, model and animations. *Journal of Asian Earth Sciences*, 20(4), 353–431. doi: DOI: 10.1016/S1367-9120(01)00069-4. 9
- Hall, R. (2002b). SE Asian Heatflow: call for new data. *SEAPEX press*. 245
- Hall, R. (2008). Continental growth at the indonesian margins of southeast asia. *Ores and orogenesis: Circum-Pacific tectonics, geologic evolution, and ore deposits: Arizona Geological Society Digest: Arizona Geological Society Digest*, 22, 245–258. 8, 348
- Hamada, J.-I., Yamanaka, M. D., Matsumoto, J., Fukao, S., Winarso, P. A., & Srihimawati, T. (2002). Spatial and Temporal Variations of the Rainy Season over Indonesia and their Link to ENSO. *Journal of the Meteorological Society of Japan*, 80(2), 285–310. 20
- Hamilton, W. B. (1988). Plate tectonics and island arcs. *Geological Society of America Bulletin*, 100(10), 1503–1527. 8, 11
- Hansen, J. & Lacis, A. (1992). Potential climate impact of mount pinatubo eruption. *Geophysical Research . . .*, 19(2), 215–218. 19
- Happell, J. D., Ostlund, G., & Mason, A., S. (2004). A history of atmospheric tritium gas (ht) 1950-2002. *Tellus*, 56B(3), 183–193. 168
- Hayba, D. O. & Ingebritesen, S. E. (1994). The computer model hydrotherm, a three-dimensional finite-difference model to simulate ground-water flow and heat transport in the temperature range of 0 to 1,200 degrees celsius. *US Geological Survey Professional Paper*, (pp.85). 232
- Heberer, T. (2002). Occurrence, fate, and removal of pharmaceutical residues in the aquatic environment: a review of recent research data. *Toxicology letters*, 131(1-2), 5–17. 270

- Hendon, H. H. (2003). Indonesian rainfall variability: Impacts of enso and local air-sea interaction. *Journal of Climate*, 16(11), 1775–1790. 19, 118
- Herman, R. (2001). An introduction to electrical resistivity in geophysics. *American Association of Physics Teachers.*, 69(9), 943–952. 84, 353
- Hildenbrand, A., Gillot, P.-Y., & Marlin, C. (2008). Geomorphological study of long-term erosion on a tropical volcanic ocean island: Tahiti-nui (french polynesia). *Geomorphology*, 93(3-4), 460–481. 46
- Hooke, J. (2003). Coarse sediment connectivity in river channel systems: a conceptual framework and methodology. *Geomorphology*, 56(1-2), 79–94. 64
- Houpeurt, A., Delouvrier, J., & Iffly, R. (1965). Fonctionnement d'un doublet hydraulique de refroidissement. *La Houille Blanche*, 3, 239–246. 236
- Hudak, P. F. (1996). *Hydrogeology field manual*. Department of geography University of North Texas. 21
- Hurwitz, S., Kipp, K. L., Ingebritesen, S. E., & Reid, M. (2003). Groundwater flow, heat transport, and water table position within volcanic edifices: Implications for volcanic processes in the cascade range. *Journal of Geophysical Research*, 108(B12), 1–19. 21, 22, 25, 233, 240, 241, 368
- IAEA-WMO (2001). Global network of isotopes in precipitation: The gnip database. 169, 358
- Ingebritesen, S., Sherrod, D., & Mariner, R. H. (1992). Rates and patterns of groundwater flow in the Cascade Range volcanic arc, and the effect on subsurface temperatures. *Journal of Geophysical . . .*, 97(91), 4599–4627. 233
- Jacob, C., E. (1950). *Flow of groundwater; in, Rouse, H.* New York: John Wiley and Sons, Ltd. 336
- Jain, S. K. & Singh, V. P. (2005). Isohyetal method. *Water Encyclopedia*. 105
- Jalludin, M. & Razack, M. (2004). Assessment of hydraulic properties of sedimentary and volcanic aquifer systems under arid conditions in the republic of djibouti (horn of africa). *Hydrogeology Journal*, 12, 159–170. 21
- James, E., Manga, M., Rose, T., & Hudson, G. (2000). The use of temperature and the isotopes of o, h, c, and noble gases to determine the pattern and spatial extent of groundwater flow. *Journal of Hydrology*, 237(1–2), 100 – 112. 233
- Join, J., Coudray, J., & Longworth, K. (1997). Using principal components analysis and Na/Cl ratios to trace groundwater circulation in a volcanic island: the example of Reunion. *Journal of Hydrology*, 190, 1–18. 281

- Jourdain, N. C., Gupta, A. S., Taschetto, A. S., Ummenhofer, C. C., Moise, A. F., & Ashok, K. (2013). The Indo-Australian monsoon and its relationship to ENSO and IOD in reanalysis data and the CMIP3/CMIP5 simulations. *Climate Dynamics*, 41(11-12), 3073–3102. 20, 349
- Jousset, P., Pallister, J., & Suroño (2013). The 2010 eruption of merapi volcano. *Journal of Volcanology and Geothermal Research*, 261, 1–6. 59
- Julian, P. & Chervin, R. (1978). A study of the Southern Oscillation and Walker circulation. *Monthly Weather Review*. 18
- Karatson, D., Favalli, M., Tarquini, S., Fornaciai, A., & Wörner, G. (2010). The regular shape of stratovolcanoes: A dem-based morphometrical approach. *Journal of Volcanology and Geothermal Research*, 193, 171–181. 54, 61
- Karnawati, D., Pramumijoyo, S., & Hendrayana, H. (2006). Geology of yogyakarta, java: The dynamic volcanic arc city. *The 10th IAEG International Congress, Nottingham, United Kingdom, 6-10 September 2006*, Paper number 363, 1–7. 11, 12, 348
- Kartadinata, E. (2002). *Exploitation drilling wells in Pulonharjo village, Klaten, Central Java*. Technical report, PT. Tirta Investama. 34, 155, 157, 158, 357
- Kartiwa, B., Lidon, B., & Sosiawan, H. (2013). *Results of water balance assessment of Kali Pusur watershed groundwater recharge area from January 2012 to December 2012*. Working paper, CIRAD, IAHRI. 106, 107, 124, 131
- Katili, J. A. (1975). Volcanism and plate tectonics in the indonesian island arcs. *Tectonophysics*, 26(3-4), 165–188. doi: DOI: 10.1016/0040-1951(75)90088-8. 9, 21
- Kelfoun, K., Legros, F., & Gourgaud, A. (2000). A statistical study of trees damaged by the 22 november 1994 eruption of merapi volcano (java, indonesia): relationships between ash-cloud surges and block-and-ash flows. *Journal of Volcanology and Geothermal Research*, 100(1–4), 379 – 393. 47
- Kiernan, K., Wood, C., & Middleton, G. (2003). Aquifer structure and contamination risk in lava flows: insights from iceland and australia. *Environmental Geology*, 43(7), 852–865. 22
- Kirsch, R. (2006). *Groundwater geophysics*. Springer edition. 83
- Komorowski, J.-C., Jenkins, S., Baxter, P., Picquout, A., Lavigne, F., Charbonnier, S., Gertisser, R., Preece, K., Cholikh, N., Budi-Santoso, A., & Suroño (2013). Paroxysmal dome explosion during the merapi 2010 eruption: Processes and facies relationships of associated high-energy pyroclastic density currents. *Journal of Volcanology and Geothermal Research*, 261, 260–294. 15, 59

- Konecky, B. L., Russell, J. M., Rodysill, J. R., Vuille, M., Bijaksana, S., & Huang, Y. (2013). Intensification of southwestern Indonesian rainfall over the past millennium. *Geophysical Research Letters*, (pp. n/a–n/a). 19
- Kusuma, B. (2008). Globalizing Market in Indonesia: Politics of Market and the Impact toward National Social Welfare. In *2nd Asean Academic Society International Conference* (pp. 1–4). Bangkok, Thailand. 34
- Kyuma, K., Saleh, A., Subagjo, H., Masunaga, T., & Wakatsuki, T. (2006). Effect of green revolution technology from 1970 to 2003 on sawah soil properties in Java, Indonesia: I. Carbon and nitrogen distribution under different land management and soil types. *Soil Science and Plant Nutrition*, 52(5), 634–644. 29
- Langseth, M. & Herman, B. (1981). Heat transfer in the Oceanic Crust of the Brazil Basin. *Journal of Geophysical Research*, 86(1), 10805–10819. 206
- Lapworth, D. J., Baran, N., Stuart, M. E., & Ward, R. S. (2012). Emerging organic contaminants in groundwater: A review of sources, fate and occurrence. *Environmental pollution (Barking, Essex : 1987)*, 163, 287–303. 270
- Lavigne, F. & Thouret, J.-C. (2003). Sediment transportation and deposition by rain-triggered lahars at Merapi volcano, central Java, Indonesia. *Geomorphology*, 49(1-2), 45–69. doi: DOI: 10.1016/S0169-555X(02)00160-5. 16, 53
- Lavigne, F., Thouret, J. C., Voight, B., Suwa, H., & Sumaryono, A. (2000). Lahars at Merapi volcano, central Java: an overview. *Journal of Volcanology and Geothermal Research*, 100(1-4), 423–456. doi: DOI: 10.1016/S0377-0273(00)00150-5. 16, 53, 57
- Legesse, D., Vallet-Coulomb, C., & Gasse, F. (2003). Hydrological response of a catchment to climate and land use changes in Tropical Africa: case study South Central Ethiopia. *Journal of Hydrology*, 275(1-2), 67–85. 99
- Legros, F. & Marti, J. (2001). Formation of inversely graded basal layers in ignimbrite by progressive aggradation. *Journal of Volcanology and Geothermal Research*, 111, 25–33. 47
- Lidon, B. (2012). *Critical analysis of historical monthly and annual rainfall data series available in Kali Pusur watershed*. Unpublished, CIRAD. 32, 100, 108, 125, 349
- Lirer, L., Vincci, A., Alberico, I., Gifuni, T., Bellucci, F., & Petrosino, P. (2001). Occurrence of inter-eruption debris flow and hyperconcentrated flood-flow deposits on Vesuvio volcano, Italy. *Sedimentary Geology*, 139, 151–167. 46
- Lloyd, J., Pim, R., Watkins, M., & Suwara, A. (1985). The problems of groundwater assessment in the volcanic-sedimentary environment of central Java. *Quarterly Journal of Engineering Geology and Hydrogeology*, 18, 47–61. 21, 23, 24, 39, 349

- Loke, M., Acworth, I., & Dahlin, T. (2003). A comparison of smooth and blocky inversion methods in 2d electrical imaging surveys. *Exploration Geophysics*, 34, 182–187. 84
- Longnecker, M. P. & Daniels, J. L. (2001). Environmental contaminants as etiologic factors for diabetes. *Environmental health perspectives*, 109 Suppl 6(July), 871–6. 271
- Lubis, R. F., Sakura, Y., & Delinom, R. (2008). Groundwater recharge and discharge processes in the Jakarta groundwater basin, Indonesia. *Hydrogeology Journal*, 16(5), 927–938. 245
- Macdonald, G., Abbott, A., & Peterson, F. (1983). Volcanoes in the sea. the geology of hawaii. (pp. 571). 22
- MacRae, G. & Hodgkin, D. (2011). Half full or half empty? shelter after the jogjakarta earthquake. *Disasters*, 35(1), 243–267. 2
- Mandal, A. K., Zhang, J., & Asai, K. (2011). Stable isotopic and geochemical data for inferring sources of recharge and groundwater flow on the volcanic island of rishiri, japan. *Applied Geochemistry*, 26(9–10), 1741 – 1751. 167
- Manga, M. (1998). Advective heat transport by low-temperature discharge in oregon cascades. *Geology*, 26(9), 799–802. 22, 232, 233
- Manga, M. & Kirchner, J. W. (2004). Interpreting the temperature of water at cold springs and the importance of gravitational potential energy. *Water resources research*, 40(5), 1–8. 22, 206, 233, 259
- Manville, V. & Hodgson, K. (2011). Paleohydrology of volcanogenic lake break-out floods in the taupo volcanic zone, new zealand. In S. G. Evans, R. L. Hermanns, A. Strom, & G. Scarascia-Mugnozza (Eds.), *Natural and Artificial Rockslide Dams*, volume 133 of *Lecture Notes in Earth Sciences* (pp. 519–541). Springer Berlin / Heidelberg. 72
- Manville, V., Nemeth, K., & Kano, K. (2009a). Source to sink: A review of three decades of progress in the understanding of volcanoclastic processes, deposits, and hazards. *Sedimentary Geology*, 220, 136–161. 54
- Manville, V., Segschneider, B., Newton, E., White, J. D. L., Houghton, B. F., & Wilson, C. J. N. (2009b). Environmental impact of the 1.8 ka taupo eruption, new zealand: Landscape responses to a large-scale explosive rhyolite eruption. *Sedimentary Geology*, 220(3-4), 318–336. 72
- Mathisen, M. E. & McPherson, John, G. (1991). Volcanoclastic deposits: Implications for hydrocarbon exploration. *Sedimentation in Volcanic Settings*, 45. 49
- Maurer, J. (1990). Indonésie. la modernisation des traditions agrohydrauliques à java et bali. *Revue de géographie de Lyon*, 65(1), 27–37. 29

- Mazor, E. (1975). Multitracing and multisampling in hydrological studies. In IAEA (Ed.), *Interpretation of environmental isotope and hydrochemical data in groundwater hydrology* (pp. 7–36).: IAEA Vienna. 168
- McWhorter, D. B. & Sunada, D. K. (1977). *Groundwater hydrology and hydraulics*. Water Resources Publications (Fort Collins, Colo.).
- Melchior, A. (2011). Le m erapi: la "montagne de feu" au centre de l' le de java, indon sie. *LAVE, Liaison des amateurs de volcanologie europ enne*, 149, 8–14. 2, 45
- Miksic, J. (1990). *Borobudur: Golden tales of the Buddahs*. Periplus Editions. 29
- Mizutani, T. (1990). Longitudinal profiles of radial valleys on the merapi volcano in central java, indonesia. *Geogr. Rep. Tokyo Metrop. Univ.*, 25, 183–194. 21
- Moron, V., Robertson, A. W., & Boer, R. (2008). Spatial coherence and seasonal predictability of monsoon onset over indonesia. *Journal of Climate*, 22, 840–850. 20
- Mueller, S., Scheu, B., Kueppers, U., Spieler, O., Richard, D., & Dingwell, D. B. (2011). The porosity of pyroclasts as an indicator of volcanic explosivity. *Journal of Volcanology and Geothermal Research*, 203(3–4), 168 – 174. 24, 25, 221, 245, 369
- M uller, A. & Haak, V. (2004). 3-d modeling of the deep electrical conductivity of merapi volcano (central java): integrating magnetotellurics, induction vectors and the effects of steep topography. *Journal of Volcanology and Geothermal Research*, 138(3-4), 205–222. doi: DOI: 10.1016/j.jvolgeores.2004.05.023. 236
- Mulligan, B. M. (2006). *Geochemical evolution and groundwater flow in a volcanic aquifer*. PhD thesis, University of Calgary, Calgary Alberta. 167
- Murti, T. (2012). Profil Of Milk Industry In The Province Of Central Java (Study Of Milk Cooperatives Profitability). *International Seminar on Animal Industry*. 33
- Musy, A. & Higy, C. (2004). *Hydrologie: une science de la nature*, volume Vol. 21. PPUR Presses Polytechniques. 104
- Nagao, T. & Uyeda, S. (1995). Heat-flow distribution in Southeast Asia with consideration of volcanic heat. *Tectonophysics*, 251, 153–159. 233, 245
- Naylor, R., Falcon, W., Rochberg, D., & Wada, N. (2001). Using El Nino/Southern Oscillation climate data to predict rice production in Indonesia. *Climatic Change*, (pp. 255–265). 20
- Naylor, R. L., Battisti, D. S., Vimont, D. J., Falcon, W. P., & Burke, M. B. (2007). Assessing risks of climate variability and climate change for indonesian rice agriculture. *Proceedings of the National Academy of Sciences of the United States of America*, 104(19), 7752–7757. 20

- Neall, V. E. (1996). *Hydrological Disasters Associated with Volcanoes*, volume 24, chapter 12, (pp. 395–425). Water Science and Technology Library. 17
- Neuman, S. (1972). Theory of flow in unconfined aquifers considering delayed response of the water table. *Water Resources Research*, 8(4), 1031–1045. 337, 365
- Newhall, C., Bronto, G., Alloway, S., Banks, B., Bahar, N. G., del Marmol, I., Hadisantono, M. A., Holcomb, R. D., McGeehin, R. T., Miksic, J., Rubin, J. N., Sayudi, M., Sukhyar, S. D., Andreastuti, R., Tilling, S., Torley, R. I., Trimble, R., & D. Wirakusumah, A. D. (2000). 10,000 years of explosive eruptions of merapi volcano, central java: archaeological and modern implications. *Journal of Volcanology and Geothermal Research*, 100(1-4), 9–50. doi: DOI: 10.1016/S0377-0273(00)00132-3. 15, 45, 51, 55, 56, 57, 58, 60, 350
- Newhall, C. & Self, S. (1982). The volcanic explosivity index /vei/ - an estimate of explosive magnitude for historical volcanism. *Journal of Geophysical Research*, 87, 1231–1238. 15
- Norini, G., GropPELLI, G., Capra, L., & De Beni, E. (2004). Morphological analysis of nevado de toluca volcano (mexico): new insights into the structure and evolution of an andesitic to dacitic stratovolcano. *Geomorphology*, 62(1-2), 47–61. 22
- Oguchi, T., Saito, K., Kadomura, H., & Grossman, M. (2001). Fluvial geomorphology and paleohydrology in Japan. *Geomorphology*, 39(1-2), 3–19. 21
- OMS (1972). Normes internationales pour l'eau de boisson. In Genève (Ed.), *Organisation Mondiale de la Santé*, volume 3 (pp.74). 277
- Oppo, D. W., Rosenthal, Y., & Linsley, B. K. (2009). 2,000-year-long temperature and hydrology reconstructions from the Indo-Pacific warm pool. *Nature*, 460(7259), 1113–6. 19
- Pain, C. F. & Ollier, C. D. (1995). Inversion of relief - a component of landscape evolution. *Geomorphology*, 12, 151–165. 57
- Pal, A., Gin, K. Y.-H., Lin, A. Y.-C., & Reinhard, M. (2010). Impacts of emerging organic contaminants on freshwater resources: review of recent occurrences, sources, fate and effects. *The Science of the total environment*, 408(24), 6062–9. 270
- Pallister, J. S., Schneider, D. J., Griswold, J. P., Keeler, R. H., Burton, W. C., Noyles, C., Newhall, C. G., & Ratdomopurbo, A. (2013). Merapi 2010 eruption—Chronology and extrusion rates monitored with satellite radar and used in eruption forecasting. *Journal of Volcanology and Geothermal Research*, 261, 144–152. 14

- Palmer, B. A. & Neall, V. E. (1991). Contrasting lithofacies architecture in ring-plain deposits related to edifice construction and destruction, the quaternary stratford and opunake formations, egmont volcano, new zealand. *Sedimentary Geology*, 74(1-4), 71–88. 53
- Parsons, M. L. (1970). Groundwater thermal regime in a glacial complex. *Water resources research*, 6(6), 1701–1720. 231
- Person, M., Raffensperger, J., Ge, S., & Garven, G. (1996). Basin-scale hydrogeologic modelling. *Reviews of Geophysics*, (95), 61–87. 229
- Petrovic, M. (2003). Analysis and removal of emerging contaminants in wastewater and drinking water. *TrAC Trends in Analytical Chemistry*, 22(10), 685–696. 270
- Pierrehumbert, R. T. (2000). Climate change and the tropical Pacific: the sleeping dragon wakes. *Proceedings of the National Academy of Sciences of the United States of America*, 97(4), 1355–8. 18
- Poulenard, J., Podwojewski, P., Janeau, J., & Collinet, J. (2001). Runoff and soil erosion under rainfall simulation of Andisols from the Ecuadorian Páramo: effect of tillage and burning. *Catena*. 126
- Powlson, D. S., Addiscott, T. M., Benjamin, N., Cassman, K. G., de Kok, T. M., van Grinsven, H., L'Hirondel, J.-L., Avery, A. a., & van Kessel, C. (2008). When does nitrate become a risk for humans? *Journal of environmental quality*, 37(2), 291–5. 271
- Procter, J. N., Cronin, S. J., & Zernack, A. (2009). Landscape and sedimentary response to catastrophic debris avalanches, western taranaki, new zealand. *Sedimentary Geology*, 220(3-4), 271–287. 53
- Pryet, a., D'Ozouville, N., Violette, S., Deffontaines, B., & Auken, E. (2012). Hydrogeological settings of a volcanic island (San Cristóbal, Galapagos) from joint interpretation of airborne electromagnetics and geomorphological observations. *Hydrology and Earth System Sciences*, 16(12), 4571–4579. 22
- Quilty, E. G. & Roeloffs, E. A. (1991). Removal of barometric pressure response from water level data. *Journal of Geophysical Research*, 96(10), 209–218. 167
- Rasmussen, T. C. & Crawford, L. A. (1997). Identifying and removing barometric pressure effects in confined and unconfined aquifers. *Ground Water*, 35(502-511). 167
- Rasmusson, E. M. & Wallace, J. M. (1983). Meterological aspects of el nino/southern oscillation. *Science*, 222(4629), 1195–1202. 18

- Raymond, J., Therrien, R., Gosselin, R., & Lefebvre, R. (2011). Numerical analysis of thermal response tests with a groundwater flow and heat transfer model. *Renewable Energy*, 36(1), 315–324. 232
- Richardson, S. D. (2012). Environmental mass spectrometry: emerging contaminants and current issues. *Analytical chemistry*, 84(2), 747–78. 270
- Richardson, S. D. & Ternes, T. a. (2014). Water analysis: emerging contaminants and current issues. *Analytical chemistry*, 86(6), 2813–48. 270
- Riggs, N. R. & J., B.-S. C. (1991). Facies analysis of an ancient, dismembered, large caldera complex and implications for intra-arc subsidence: Middle jurassic strata of cobre ridge, southern arizona, usa. *Sedimentary Geology*, 74, 39–68. 55, 350
- Rijsdijk, A. (2005). Evaluating sediment sources and delivery in a tropical volcanic watershed. *Sediment budget 2*, (pp. 16–23). 46
- Riza, H. (2008). Resources Report on Languages of Indonesia. *IJCNLP*, (pp. 93–94). 26
- Robock, A. (2000). Climate and volcanic eruptions. *Reviews of Geophysics*, 38(1998), 191–219. 19
- Rodolfo, K. S. & Arguden, A. T. (1991). Rain-lahar generation and sediment-delivery systems at mayon volcano, philippines. *Sedimentation in Volcanic Settings*, 45, 71–87. 54, 72, 78, 80
- Rodysill, J. R., Russell, J. M., Crausbay, S. D., Bijaksana, S., Vuille, M., Edwards, R. L., & Cheng, H. (2013). A severe drought during the last millennium in east java, indonesia. *Quaternary Science Review*, 80, 102–111. 19, 20
- Roe, G. H. (2005). Orographic Precipitation. *Annual Review of Earth and Planetary Sciences*, 33(1), 645–671. 113
- Ryan, W., Carbotte, S., Coplan, J., O'Hara, S., Melkonian, A., Arko, R., Weissel, R., Ferrini, V., Goodwillie, A., Nitsche, F., Bonczkowski, J., & Zemsky, R. (2009). Global multi-resolution topography synthesis. *Geochemical, Geophysical and Geosystem*, 10. 10, 348
- Saar, M. O. (2011). Review: Geothermal heat as a tracer of large-scale groundwater flow and as a means to determine permeability fields. *Hydrogeology Journal*, 19(1), 31–52. 232, 233, 362
- Saji, N. H., Goswami, B. N., Vinayachandran, P. N., & Yamagata, T. (1999). A dipole mode in the tropical Indian Ocean. *Nature*, 401(6751), 360–3. 18

- Sass, J. H., Lachenbruch, A. H., Galanis Jr, S. P., Morgan, P., Priest, S. S., Moses Jr, T. H., & Munroe, R. J. (1994). Thermal regime of the southern basin and range province 1. heat flow data from arizona and the mojave desert of california and nevada. *Journal of Geophysical Research*, 99(b11), 22093–22119. 232
- Scheurer, M., Brauch, H.-J., & Lange, F. T. (2009). Analysis and occurrence of seven artificial sweeteners in German waste water and surface water and in soil aquifer treatment (SAT). *Analytical and bioanalytical chemistry*, 394(6), 1585–94. 271
- Scholl, M. a., Ingebritsen, S. E., Janik, C. J., & Kauahikaua, J. P. (1996). Use of Precipitation and Groundwater Isotopes to Interpret Regional Hydrology on a Tropical Volcanic Island: Kilauea Volcano Area, Hawaii. *Water Resources Research*, 32(12), 3525–3537. 167
- Schwarzkopf, L. M., Schmincke, H.-U., & Cronin, S. J. (2005). A conceptual model for block-and-ash flow basal avalanche transport and deposition, based on deposit architecture of 1998 and 1994 merapi flows. *Journal of Volcanology and Geothermal Research*, 139(1–2), 117 – 134. <ce:title>Modeling and Simulation of Geophysical Mass Flows</ce:title>. 15, 53
- Selles, A., Defontaine, B., Hendrayana, H., & Violette, S. (2012). Characterisation of the volcano-sedimentary deposits of an active strato-volcano: the merapi case example (central java, indonesia). *Proceeding of 5th AUN/SEED-Net Regional Conference on Geo-disaster mitigation in ASEAN*. 63
- Setyanto, P., Makarim, A., Fagi, A., Wassmann, R., & Buendia, L. (2000). *rop management affecting methane emissions from irrigated and rainfed rice in Central Java (Indonesia)*, volume 58. Springer Netherlands. 31
- Siebert, L. (1984). Large volcanic debris avalanches: Characteristics of source areas, deposits, and associated eruptions. *Journal of Volcanology and Geothermal Research*, 22(3-4), 163–197. 53, 59, 81, 82, 353
- Simoen, S. (2001). Sistem akuifer di lereng gunungapi merapi bagian timur dan tenggara : Studi kasus di kompleks mataair sungsang boyolali jawa tengah. *Majalah Geografi Indonesia*, 15(1). 45
- Singhal, B. B. S. & Gupta, R. P. (2010). *Hydrogeology of Volcanic Rocks*, (pp. 257–268). Springer Netherlands. 22, 221, 240, 241, 368
- Sisavath, E. (2011). *Processus de transfert des éléments volcanodétritiques dans les plaines abyssales autour de l’île de La Réunion (Océan Indien): Exemple du système turbidique de Cilaos*. PhD thesis, Université de la Réunion. 59

- Smith, Gary, A. (1988). Sedimentology of proximal to distal volcanoclastics dispersed across an active foldbelt: Ellensburg formation (late miocene), central washington. *Sedimentology*, 35(6), 953–977. 54, 55, 350
- Smith, Gary, A. (1991). Facies sequences and geometries in continental volcanoclastic sediments. *Sedimentation in Volcanic Settings*, SEPM, Special Publication 45(45), 109–122. 46, 53, 59
- Smith, Gary, A. & Lowe, Donald, R. (1991). Lahars: Volcano-hydrologic events and deposition in the debris flow-hyperconcentrated flow continuum. *Sedimentation in Volcanic Settings*, 45, 59–70. 16, 53, 59
- Smith, R. L. (1960). Zones and zonal variations in welded ash flows. *US Geological Survey Professional Paper*, 354(F). 22
- Smyth, H. H., J., H. R., & P., K. (2005). East previous termjava:next term cenozoic basins, volcanoes and ancient basement. *Indonesian Petroleum Association Thirtieth Annual Convention and Exhibition*. 9, 11
- Smyth, H. R., Hall, R., & Nichols, G. J. (2008). Cenozoic volcanic arc history of east java, indonesia: The stratigraphic record of eruptions on an active continental margin. *Geological Society of America Special Papers*, 436, 199–222. 11
- Smyth, R. C. & M., S. J. J. (2006). The hydrology of tuffs. *Geological Society of America Special Papers*, 408.
- Sparks, R. S. J. (1975). Stratigraphy and geology of the ignimbrites of vulsini volcano, central italy. *Geologische Rundschau*, 64(1), 497–523. 49
- Sparks, R. S. J. (1976). Grain size variations in ignimbrites and implications for the transport of pyroclastic flows. *Sedimentology*, 23, 147–188. 50, 349
- Sriyana, S. (2011). KAJIAN PEMANFAATAN POTENSI SUMBER DAYA AIR TERPADU (STUDI KASUS MATA AIR INGAS (COKRO), KEC. COKRO TULUNG KABUPATEN KLATEN-. *TEKNIK*, 32(1). 34
- Sruoga, P. & Rubinstein, N. (2007). Processes controlling porosity and permeability in volcanic reservoirs from the austral and neuquén basins, argentina. *AAPG Bulletin*, 91(1), 115–129. 22, 24, 99
- Stallman, R. W. (1963). Computation of Ground-Water Velocity from Temperature Data. In R. Bentall (Ed.), *Methods of Collecting and Interpreting Ground-Water Data*, volume 1544-H of *Geological Survey Water-Supply Paper* (pp. H36–H46). 232
- Statistik, B. P., Ed. (2010). *Hasil sensus penduduk 2010. Provinsi Nusa Tenggara Timur*. 31, 367

- Stinton, A. J. & Sheridan, M. F. (2008). Implications of long-term changes in valley geomorphology on the behavior of small-volume pyroclastic flows. *Journal of Volcanology and Geothermal Research*, 176(1), 134 – 140. <ce:title>Recent and active volcanism in the Ecuadorian Andes</ce:title>. 47
- Surjono, S. S. & Yufianto, A. (2011). Geo-disaster laharic flow along putih river, central java, indonesia. *Journal of Asian Earth Sciences*, 3(2), 103–110. 53, 59
- Surono, Jousset, P., Pallister, J., Boichu, M., Buongiorno, M. F., Budisantoso, A., Costa, F., Andreastuti, S., Prata, F., Schneider, D., Clarisse, L., Humaida, H., Sumarti, S., Bignami, C., Griswold, J., Carn, S., Oppenheimer, C., & Lavigne, F. (2012). The 2010 explosive eruption of Java’s Merapi volcano—A ‘100-year’ event. *Journal of Volcanology and Geothermal Research*, 241-242, 121–135. 14, 15, 348
- Tachikawa, T., Kaku, M., Iwasaki, A., Gesch, D., Oimoen, M., Zhang, Z., Danielson, J., Krieger, T., Curtis, B., Haase, J., Abrams, M., Crippen, R., & Carabajal, C. (2011). *ASTER Global Digital Elevation Model Version 2 – Summary of Validation Results*. Tech. report, NASA Land Processes Distributed Active Archive Center and the Japan-US ASTER Science Team. 70
- Takahashi, T. & Tsujimoto, H. (2000). A mechanical model for merapi-type pyroclastic flow. *Journal of Volcanology and Geothermal Research*, 98(1–4), 91 – 115. 49
- Taniguchi, M., Shimada, J., Tanaka, T., Kayane, I., Sakura, Y., Shimano, S., Dapaah-Siakwan, & Kawashima, S. (1999). Disturbances of temperature-depth profiles due to surface climate change and subsurface water flow: An effect of linear increase in surface temperature caused by global warming and urbanization in the tokyo metropolitan area, japan. *Water resources research*, 35(5), 1507–1517. 231, 362
- Theis, C., V. (1935). The relation between the lowering of the piezometric surface and the rate and duration of discharge of a well using groundwater storage. *Transactions of American Geophysical Union*, 16, 519–524. 335
- Theunissen, B., de Vos, J., Sondaar, P. Y., & Aziz, F. (1990). The establishment of a chronological framework for the hominid-bearing deposits of java; a historical survey. *Geological Society of America Special Papers*, 242, 39–54. 29
- Thornthwaite, C. W. (1948). An approach toward a rational classification of climate. *Geographical Review*, 38(1), 55–94. 104, 108, 121, 135
- Thornthwaite, C. W. & Mather, J. R. (1955). The water balance. *Publication in Climatology/Laboratory of Climatology; Drexel Institute of Technology*, 8(1). 104

- Thouret, J. C., Lavigne, F., Kelfoun, K., & Bronto, S. (2000). Toward a revised hazard assessment at merapi volcano, central java. *Journal of Volcanology and Geothermal Research*, 100(1-4), 479–502. doi: DOI: 10.1016/S0377-0273(00)00152-9. 15
- Thouret, J.-C., Lavigne, F., Suwa, H., & Sukatja, B. (2007). Volcanic hazards at Mount Semeru, East Java (Indonesia), with emphasis on lahars. *Bulletin of Volcanology*, 70(2), 221–244. 80
- Tierney, J. E., Oppo, D. W., Rosenthal, Y., Russell, J. M., & Linsley, B. K. (2010). Coordinated hydrological regimes in the Indo-Pacific region during the past two millennia. *Paleoceanography*, 25(1), PA1102. 19
- Torres, R., Mouginis-Mark, P., Self, S., Garbdeil, H., Kallianpur, K., & Quiambao, R. (2004). Monitoring the evolution of the pasig–potrero alluvial fan, pinatubo volcano, using a decade of remote sensing data. *Journal of Volcanology and Geothermal Research*, 138(3-4), 371–392. 72
- Trenberth, E. K. & Hoar, J. T. (1996). Longest on record. *Geophysical Research Letters*, 23(1), 57–60. 18
- Tuong, T. (2000). *Characterizing and understanding rainfed environments*. 31, 33
- Tuong, T. & Bouman, B. (2003). Rice production in water-scarce environments. *Water productivity in agriculture: . . .*, (pp. 53–67). 33
- Ui, T., Yanamoto, h., & Suzuki-Kamata, K. (1986). Characterization of debris avalanche deposits in japan. *Journal of Volcanology and Geothermal Research*, 29(1-4), 231–243. 81, 353
- Van Bemmelen, R. W. (1949). *The Geology of Indonesia*, volume vol. IA. The Hague, Netherlands, govt. print. off., edition. 2, 7, 8, 45, 58
- Vanhoebrouck, P. (2004). *Dukun in Yogyakarta*. PhD thesis, Cultural Anthropology Leid. 37
- Vazquez, J. A. & Ort, M. H. (2006). Facies variation of eruption units produced by the passage of single pyroclastic surge currents, hopi buttes volcanic field, usa. *Journal of Volcanology and Geothermal Research*, 154(3–4), 222 – 236. 48
- Vázquez, R., Capra, L., Caballero, L., Arámbula-Mendoza, R., & Reyes-Dávila, G. (2014). The anatomy of a lahar: Deciphering the 15th September 2012 lahar at Volcán de Colima, Mexico. *Journal of Volcanology and Geothermal Research*, 272(September 2012), 126–136. 17
- Vessel, R. D. & Davis, D. K. (1981). *Nonmarine sedimentation in an active fore arc basin.*, volume 31. ETHRIDGE, F. G. and FLORES, R. M. (eds). 54, 55, 350

- Violette, S., d'Ozouville, Noémi, D. B., Pryet, A., Fortin, J., & Adelinet, M. (2013). Hydrogeology of the galapagos archipelago: an integrated and comparative approach between islands. *Galapagos Islands: a natural laboratory for Earth Sciences*, AGU Chapman Monograph Series. 22
- Violette, S., Ledoux, E., Goblet, P., & Carbonnel, J.-P. (1997). Hydrologic and thermal modeling of an active volcano: the piton de la fournaise, reunion. *Journal of Hydrology*, 191(1-4), 37–63. doi: DOI: 10.1016/S0022-1694(96)03071-5. 22, 233, 234
- Vittecoq, B., Deparis, J., Violette, S., Jaouën, T., & Lacquement, F. (2014). Influence of successive phases of volcanic construction and erosion on Mayotte Island's hydrogeological functioning as determined from a helicopter-borne resistivity survey correlated with borehole geological and permeability data. *Journal of Hydrology*, 509, 519–538. 22
- Voight, B., Constantine, E., Siswoidjyo, S., & Torley, R. (2000). Historical eruptions of merapi volcano, central java, indonesia, 1768–1998. *Journal of Volcanology and Geothermal Research*, 100(1–4), 69 – 138. 46, 58, 60, 350
- Voight, B. & Davis, M. (2000). Emplacement temperatures of the november 22, 1994 nuée ardente deposits, merapi volcano, java. *Journal of Volcanology and Geothermal Research*, 100(1–4), 371 – 377. 59
- Wakatsuki, T., Buri, M., Bam, R., Ademiluyi, S., & Azogu, I. (2013). Sawah Ecotechnology: Farmers' personal irrigated sawah systems to realize the Green Revolution and Africa's rice potential. In *Proceedings of the 1st International Conference on Rice for Food, Market , and Development (rice - Africa) Conference on Rice for Food, Market and Development (rice-Africa)*, volume 1 (pp. 1–16). Abuja, Nigeria. 32
- Walker, G. (1971). Grain-size characteristics of pyroclastic deposits. *Journal of Geology*, 79, 696–714. 45, 49
- Walker, G., Huntingdon, A., T., Sanders, A., T., & Dinsdale, J., L. (1973). Lengths of lava flows. *Physical Sciences*, 274(1238). 51
- Walter, T. R., Wang, R., Luehr, B.-G., Wassermann, J., Behr, Y., Parolai, S., Anggraini, A., Günther, E., Sobiesiak, M., Grosser, H., Wetzell, H.-U., Milkereit, C., Sri Brotopuspito, P. J. K., Harjadi, P., & Zschau, J. (2008). The 26 may 2006 magnitude 6.4 yogyakarta earthquake south of mt. merapi volcano: Did lahar deposits amplify ground shaking and thus lead to the disaster? *Geochemistry, Geophysics, Geosystems*, 9(5), n/a–n/a. 11, 12, 14, 348
- Waples, D. W. & Waples, J. S. (2004). A review and evaluation of specific heat capacities of rocks, minerals, and subsurface fluids. part 1: Minerals and nonporous rocks. *Natural Resources Research*, 13(2), 97–122. 22

- Webster, P. J., Magaña, V. O., Palmer, T. N., Shukla, J., Tomas, R. A., Yanai, M., & Yasunari, T. (1998). Monsoons: Processes, predictability, and the prospects for prediction. *Journal of Geophysical Research: Oceans*, 103(C7), 14451–14510. 18, 19
- White, J. D. L. & Schmincke, H.-U. (1999). Phreatomagmatic eruptive and depositional processes during the 1949 eruption on la palma (canary islands). *Journal of Volcanology and Geothermal Research*, 94(1-4), 283–304. 22
- Whittier, R., Rotzoll, K., Dhal, S., El-Kadi, A., Ray, C., & Chang, D. (2009). Groundwater source assessment program for the state of hawaii, usa: methodology and example application. *Hydrogeology Journal*, 18(3), 711–723. 22
- WHO (2011). Guidelines for drinking-water quality. In *World Health Organization*, volume 1. 271, 273
- Wihardjaka, a., Kirk, G., Abdulrachman, S., & Mamaril, C. (1999). Potassium balances in rainfed lowland rice on a light-textured soil. *Field Crops Research*, 64(3), 237–247. 31
- Winarto, Y. & Stigter, K. (2013). Agrometeorological Learning Increasing Farmers' Knowledge in Coping with Climate Change and Unusual Risks. *Southeast Asian . . .* 32
- Winograd, I. J. (1971). Hydrogeology of ash flow tuff: A preliminary statement. *Water Resources Research*, 7(4), 994–1006. 221, 245, 369
- Wirakusumah, A. D., Juwana, H., & Loebis, H. (1989). Geological map of merapi volcano, central java. *Edited by Sudradjat A. and Effendi A.C.*, scale 1:50 000, Volcanological survey of Indonesia. 13, 60, 89, 144, 152, 348, 350, 356, 357
- Wohletz, K. H. & Sheridan, M. F. (1979). A model of pyroclastic surge. *Geological Society of America Special Papers*, 180, 177–194. 49
- Wood, W. W. & Fernandez, Louis, A. (1988). *Volcanic rocks*, volume O-2. Geological Society of America. 25
- Wright, J. V., Smith, A. L., & Self, S. (1980). A working terminology of pyroclastic deposits. *Journal of Volcanology and Geothermal Research*, 8(2–4), 315 – 336. 45, 47, 51, 349
- Yitbarek Baye, A. (2009). *Hydrogeological and hydrochemical framework of complex volcanic system in the Upper Awash River basin, Central Ethiopia : with special emphasis on inter-basins groundwater transfer between Blue Nile and Awash rivers*. PhD thesis. 167

- Yurstever, Y. & Gat, J. (1981). *Atmospheric waters*, (pp. 103–139). Number 210. IEA Vienna Tech. Rep. 207
- Zaim, Y., Ciochon, R. L., Polanski, J. M., Grine, F. E., Bettis, E. A., Rizal, Y., Franciscus, R. G., Larick, R. R., Heizler, M., Aswan, Eaves, K. L., & Marsh, H. E. (2011). New 1.5 million-year-old *Homo erectus* maxilla from Sangiran (Central Java, Indonesia). *Journal of human evolution*, 61(4), 363–76. 29
- Zehetner, F. & Miller, W. P. (2006). Erodibility and runoff-infiltration characteristics of volcanic ash soils along an altitudinal climosequence in the Ecuadorian Andes. *Catena*, 65(3), 201–213. 126
- Zernack, A., Procter, J. N., & Cronin, S. J. (2009). Sedimentary signatures of cyclic growth and destruction of stratovolcanoes: A case study from mt. taranaki, new zealand. *Sedimentary Geology*, 220(3-4), 288–305. 22

Appendix

A Geology and geomorphology

A.1 Pyroclastic rocks classification

Grade size limits used in pyroclastic classifications	Grade size limits used by authors relating pyroclastic and epiclastic sediments and rocks					
	Wentworth and Williams, 1932	Blyth, 1940	Panto, 1963	Fisher, 1961	Wright, 1980	Challinor, 1967
256 mm	Blocks and bombs	Blocks and bombs	Blocks and bombs	Blocks and bombs	Blocks and bombs	Blocks and bombs
64 mm						
50 mm	Lapilli	Lapilli	Lapilli	Lapilli	Lapilli	Lapilli
32 mm						
30 mm					Volcanic gravel	
25 mm						
10 mm	coarse	coarse	Dust	coarse	coarse	Sand
4 mm						
2.5 mm	Ash	Ash	Dust	coarse	coarse	Sand
2 mm						
1 mm	Fine	Fine	Dust	coarse	Ash	Sand
0.5 mm						
0.25 mm	Fine	Fine	Dust	Ash	Ash	Ash and dust
0.1 mm						
0.06 mm	Fine	Dust-ash	Dust	Fine	Ash	Ash and dust
0.05 mm						
0.015 mm						

Figure A.1: Classification of the pyroclastic rocks.

A.2 Merapi volcano evolution

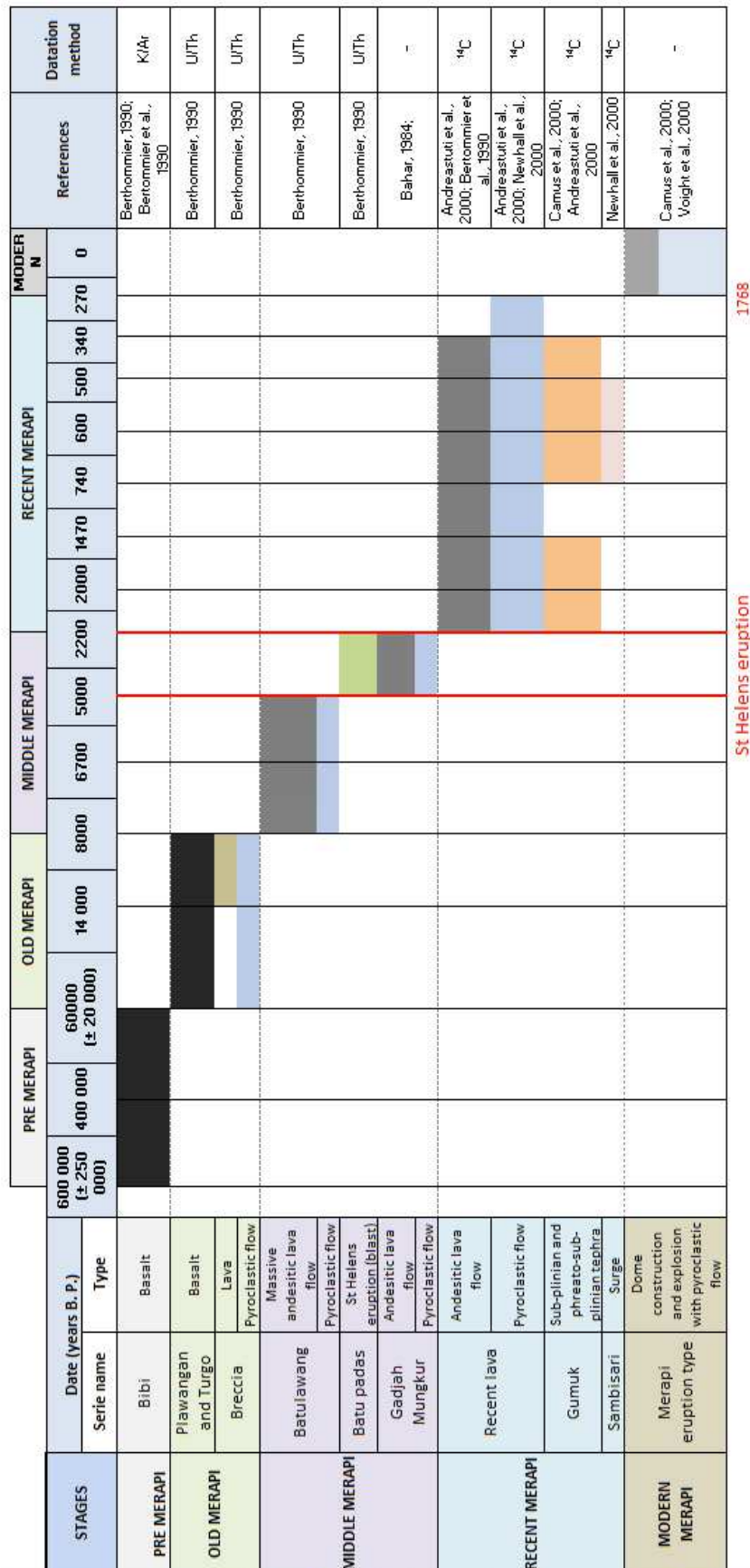


Figure A.2: Time scale of the Merapi volcano evolution and the main deposit types.

B Geophysics

B.1 Profiles

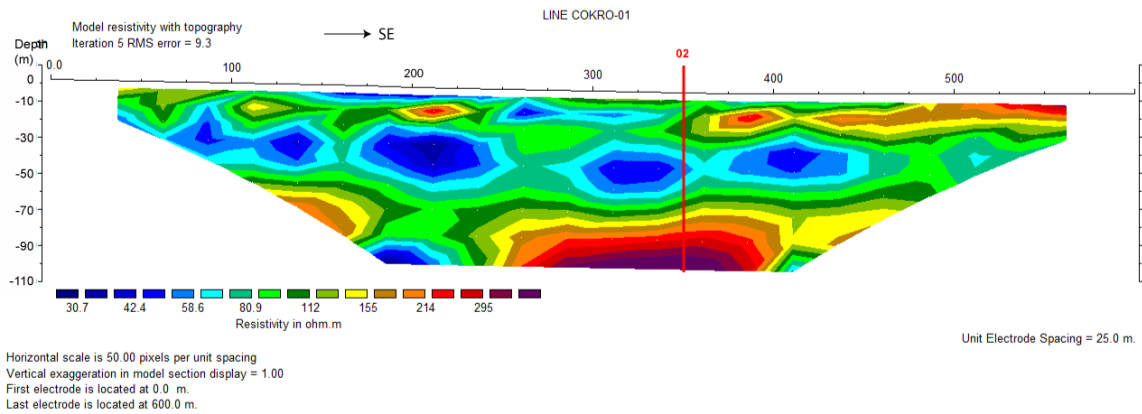


Figure B.1: Profile n°1

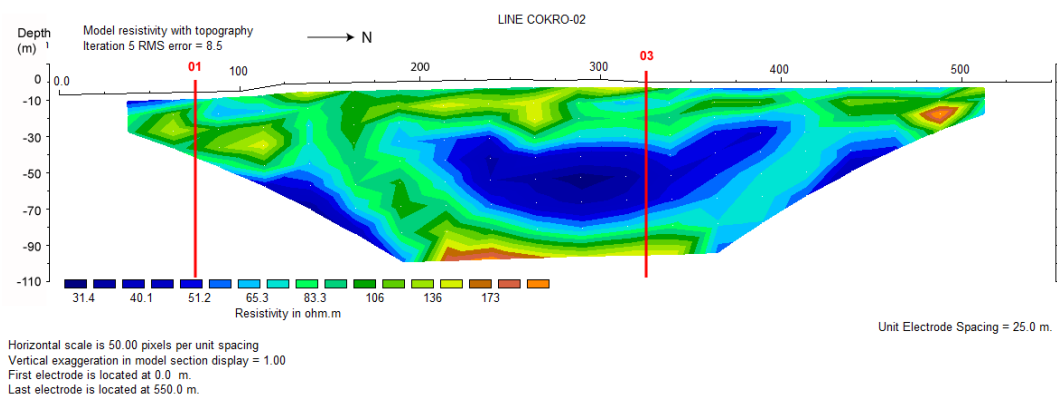


Figure B.2: Profile n°2

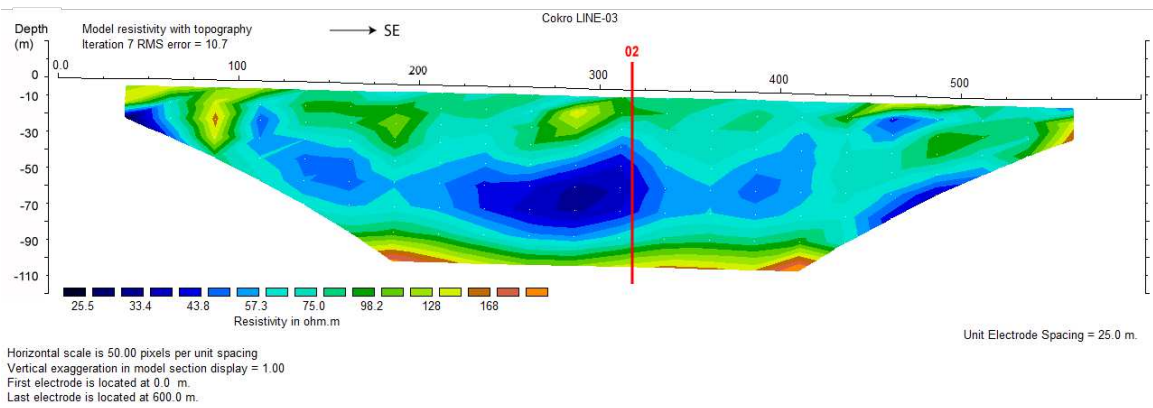


Figure B.3: Profile n°3

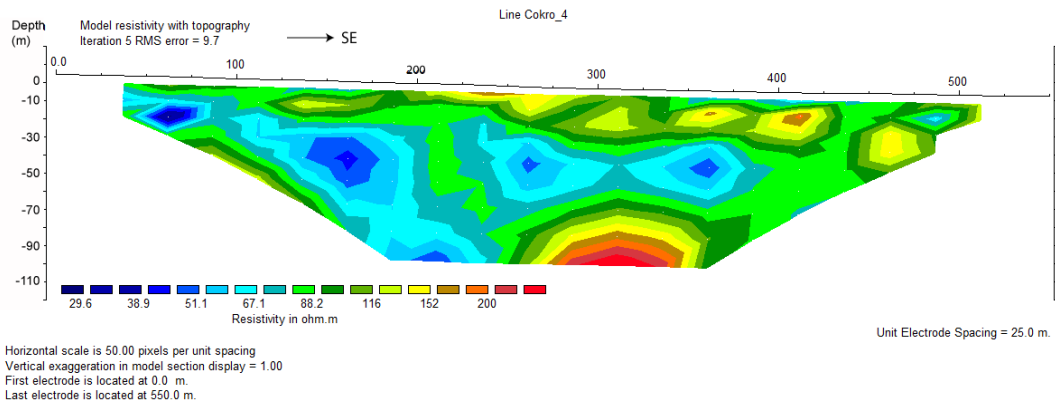


Figure B.4: Profile n°4

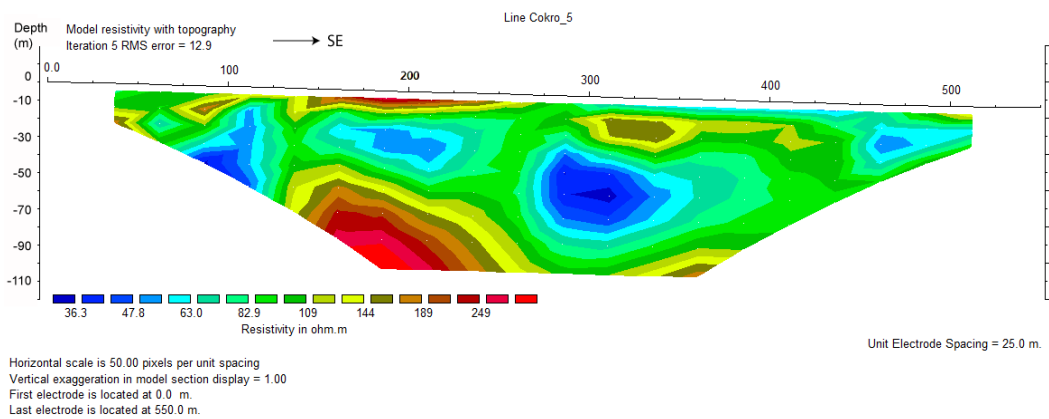


Figure B.5: Profile n°5

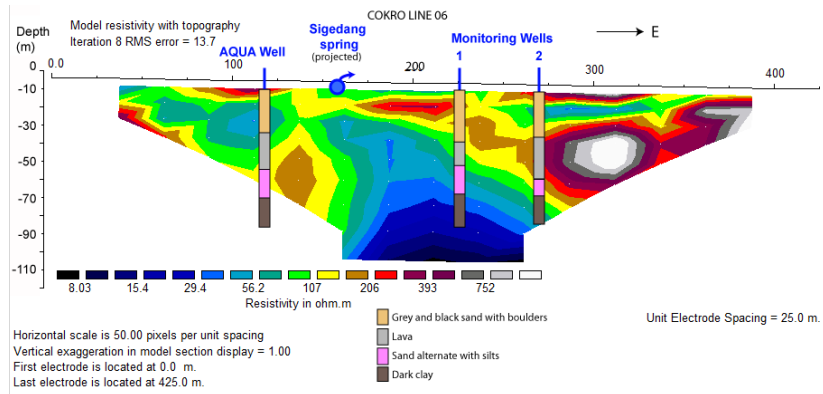


Figure B.6: Profile n°6 with AQUA wells and Sigedang spring projected on the profile (20 m and 60 m respectively).

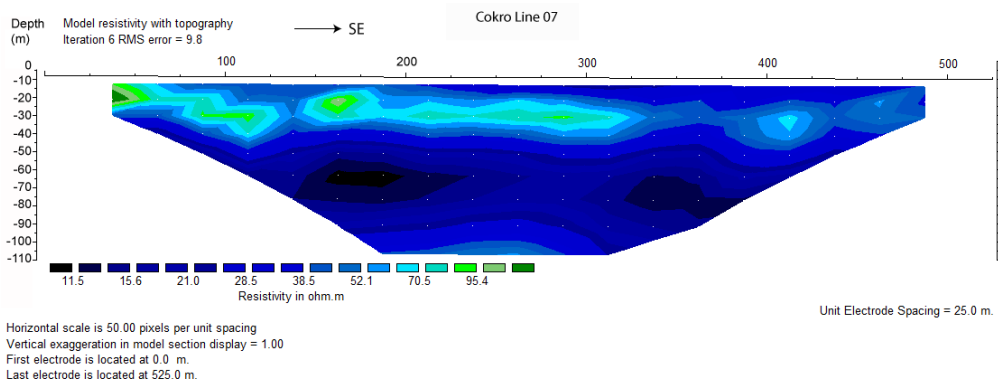


Figure B.7: Profile n°7

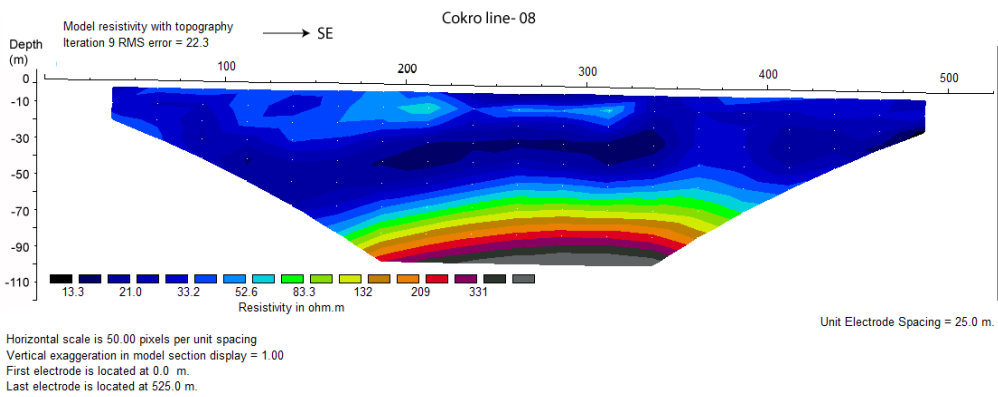


Figure B.8: Profile n°8

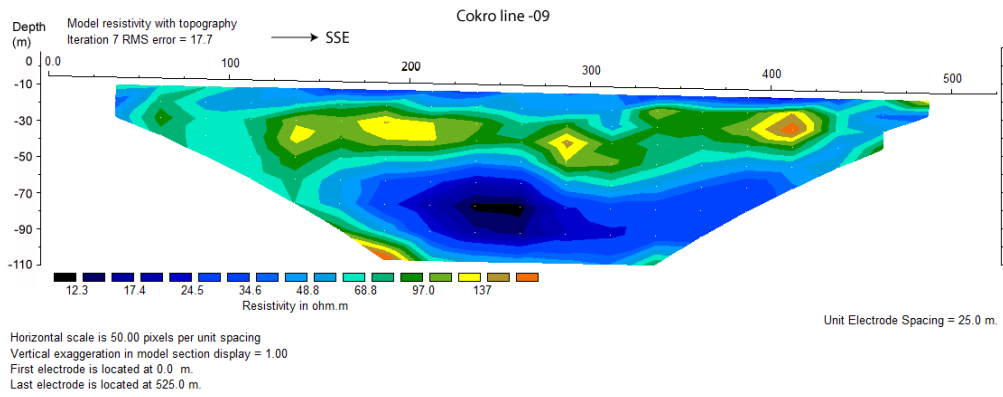


Figure B.9: Profile n°9

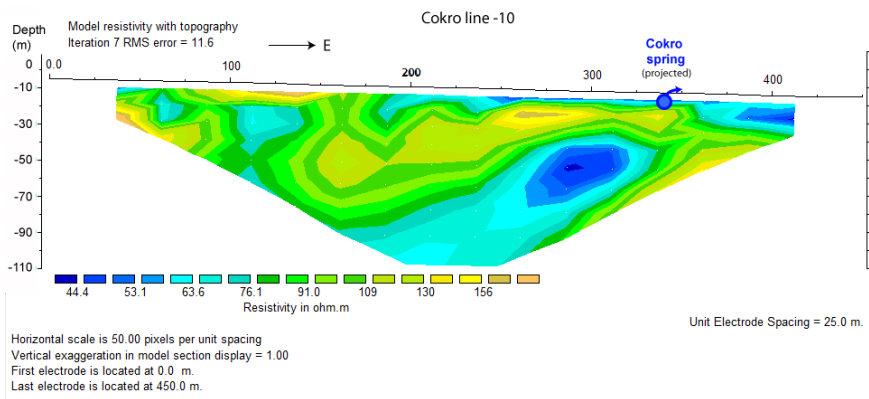
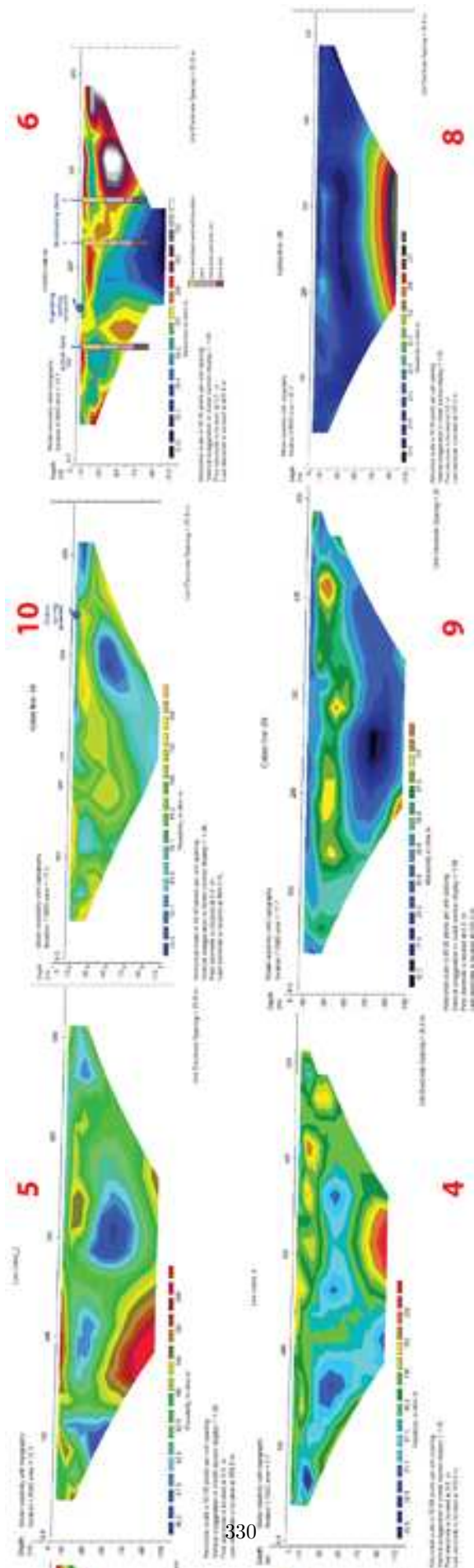


Figure B.10: Profile n°10

B.2 Lines



B.3 Soundings

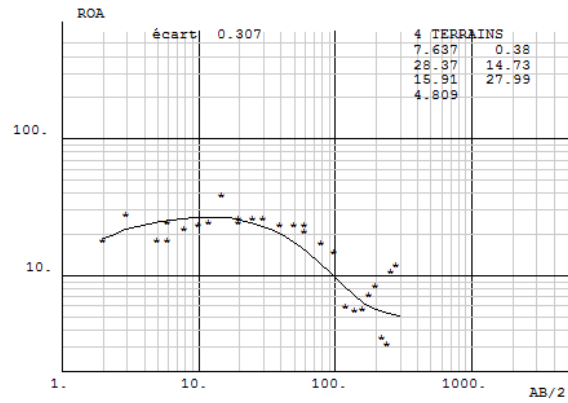


Figure B.12: Sounding point 01

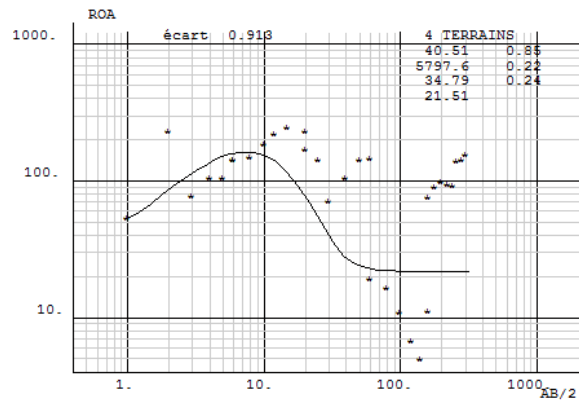


Figure B.13: Sounding point 02

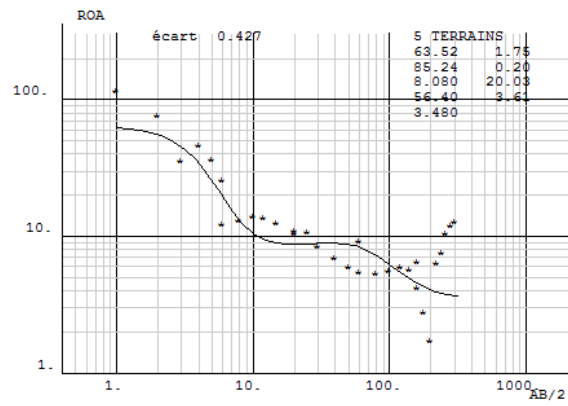


Figure B.14: Sounding point 03

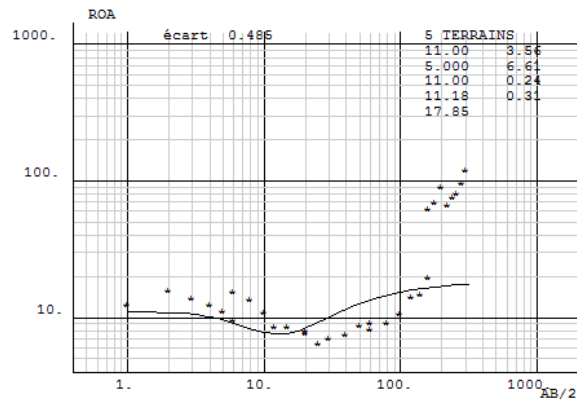


Figure B.15: Sounding point 04

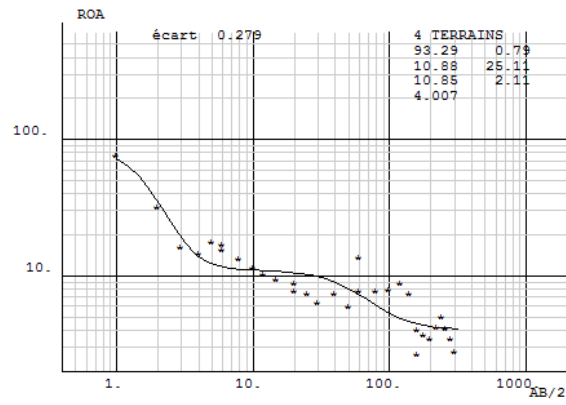


Figure B.16: Sounding point 05

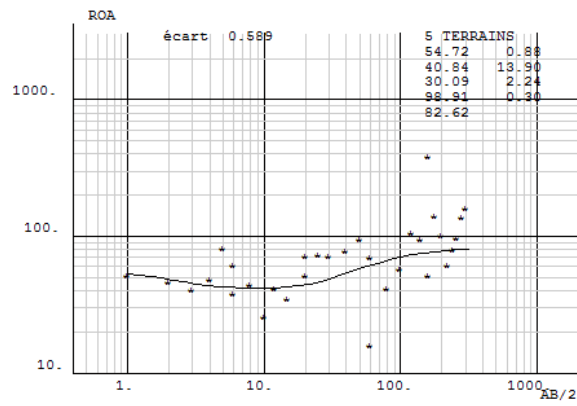


Figure B.17: Sounding point 06

C Hydrogeology

C.1 Hydraulic test protocol

There are many types of pumping tests which are available for evaluating aquifer's hydraulic parameters based on graphical method. Two commonly used methods are described here which include: (1) Theis curve and the Jacob's simplification matching for confined aquifer, (2) Dupuit equation matching for unconfined aquifer.

The assumptions to use the Theis methods ([Theis, 1935](#)) are:

- Aquifer is homogeneous, confined, isotropic, and is of infinite extent
- Well completely penetrates (and get water from) the entire aquifer formation
- The well is pumped at a constant flow rate
- Transmissivity is constant
- Water is removed from storage and discharged instantaneously
- The well diameter is considered as small so that well storage is negligible

Although all these assumptions often are not justified in the field, Theis's equation can be applied successfully:

$$s = h_0 - h = \frac{Q}{4\pi T} W(u) \quad (\text{C.1})$$

where $u = \frac{r^2 S}{4Tt}$ and $W(u) = \int_u^\infty \frac{e^{-x}}{x} dx = -0.5772 - \ln u + u - \frac{u^2}{2 \cdot 2!} + \frac{u^3}{3 \cdot 3!} - \dots$

s drawdown [m]

h_0 initial head in a well at distance r [m]

h	head at distance r at time t [m]
t	relative time since pumping begins [s]
r	distance from the pumping well (in our case equal to the radius of the pumping well) [m]
Q	pumping rate [$\text{m}^3 \cdot \text{s}^{-1}$]
b	aquifer's saturated thickness [m]
T	transmissivity [$\text{m}^2 \cdot \text{s}^{-1}$] with $T = Kb$
K	hydraulic conductivity [m s^{-1}]
S	storativity [-]

with

$$S = \frac{4Tt}{r^2\left(\frac{1}{u}\right)} \quad (\text{C.2})$$

$W(u)$ well function [-]

u auxiliary parameter [-]

As the flow rate is constant, we can defined $\log s$ from the eq. C.1 as:

$$\log s = \left[\log\left(\frac{Q}{4\pi T}\right) \right] + \log W(u)$$

and

$$\log \frac{t}{r^2} = \left[\log\left(\frac{S}{4T}\right) \right] + \log \frac{1}{u}$$

Thus, bracketed terms are constant and $\log s$ and $\log \frac{t}{r^2}$ are related in the same way as $\log W(u)$ is related to $\log \frac{1}{u}$.

Using graphical solution on the Theis-type curve, $W(u)$ and $\frac{1}{u}$ can be found, thus, S and T can be calculated.

But in our case as the aquifer is confined, we used the simplification introduced by [Jacob \(1950\)](#). Because $u = \frac{r^2 S}{4Tt}$, S and T are constants, this simplification is valid for small r , and as we measure the drawdown at the pumping well itself, here we have the minimal value of r .

When $\frac{r^2}{t}$ is small, the terms in the convergent series for $W(u)$ may be ignored after the second term.

Therefore, the Jacob's approximation of Theis's flow equation is expressed as:

$$s = \frac{2.3Q}{4\pi T} \log \Delta t \quad (\text{C.3})$$

Jacob’s method allows solution for T and S using simple graphical methods by plotting s versus $\log t$.

The equation to determine T becomes:

$$T = \frac{2.3Q}{4\pi\Delta s} \tag{C.4}$$

and to determine S:

$$S = \frac{2.25Tt_0}{r^2} \tag{C.5}$$

For the unconfined aquifers, we used the Neuman solution (Neuman, 1972), based on the following assumptions:

- The aquifer is unconfined
- The aquifer has a see mingly infinite area extent
- The aquifer is homogeneous and of uniform thickness over the area influenced by the test
- Prior to pumping, the water table is horizontal over the area that will be influenced by the test
- The aquifer is pumped at a constant discharge rate
- The well penetrates the entire aquifer and thus receives water from the entire saturated thickness of the aquifer

Time-drawdown curves on log-log plot therefore usually show a typical S-shape, from which we can recognize three distinct segments: a steep early-time segment, a flat intermediate-time segment, and a relatively steep late-time segment (Fig. C.1).

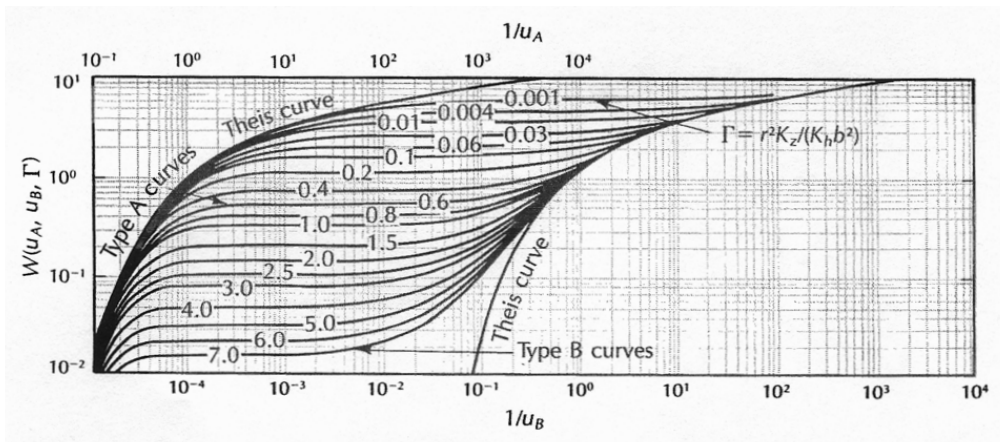


Figure C.1: Neumann’s type curves for unconfined aquifer (Neuman, 1972).

Neuman solution can be defined by the following equation:

$$s = \frac{Q}{4\pi T} w(u_A, u_B, \Gamma) \quad (\text{C.6})$$

where

$$u_A = \frac{r^2 S}{4Tt} \text{ for early time-drawdown data}$$

$$u_B = \frac{r^2 S_y}{4Tt} \text{ for later time-drawdown data}$$

$$\Gamma = \frac{r^2 K_z}{b^2 K_h}$$

with

S_y Volume of water released from storage per unit surface area per unit decline of the water table, i.e. released by dewatering of the aquifer (= specific yield)

K_z Hydraulic conductivity for vertical flow [m s^{-1}]

K_h Hydraulic conductivity for horizontal flow [m s^{-1}]; for isotropic aquifer $K_z=K_h$
and $\Gamma = \frac{r^2}{b^2}$

C.2 Spring physico-chemical variables measures

C.2.1 Spring monthly flow rate

	UP								MOY	Max	min
	1	2	6	7	20	26	30	38			
	Jelok	Bulu Kidul	Wonogang	Tutup	Candirejo	Lanjaran	Sokorejo	Kali Suden			
Elevation	1396	1358	1210	1206	986	875	830	591			
Nov-11	2.00E-03	8.35E-02	1.00E-03	1.00E-04	9.00E-04	1.00E-04		1.88E-04	1.25E-02	8.35E-02	1.00E-04
Dec-11	3.50E-03	9.00E-02	1.55E-03	8.00E-06	1.35E-03	1.35E-04	5.50E-04	2.45E-04	1.22E-02	9.00E-02	8.00E-06
Jan-12	5.00E-03	9.00E-02	1.89E-03	1.20E-05	1.33E-03	1.10E-04	5.00E-04	2.61E-04	1.24E-02	9.00E-02	1.20E-05
Feb-12	3.00E-03	1.05E-01	1.50E-03	1.75E-05	3.00E-04	1.50E-04	4.33E-04	1.25E-04	1.38E-02	1.05E-01	1.75E-05
Mar-12	3.00E-03	9.40E-02	1.64E-03	1.40E-05		1.00E-04	4.00E-04	1.20E-04	1.42E-02	9.40E-02	1.40E-05
Apr-12	3.00E-03	9.10E-02	1.10E-03	1.00E-05	1.20E-03	1.50E-04	2.50E-04	3.05E-04	1.21E-02	9.10E-02	1.00E-05
May-12	3.30E-03	9.00E-02	2.00E-03	6.00E-06	1.50E-03	1.20E-04	2.11E-05	2.00E-04	1.21E-02	9.00E-02	6.00E-06
Jun-12	2.25E-03	9.50E-02	1.78E-03	1.46E-05	1.15E-03	1.00E-04	3.60E-04	3.57E-04	1.26E-02	9.50E-02	1.46E-05
Jul-12	1.20E-03	8.40E-02	2.00E-03	1.00E-04	1.50E-03	1.00E-04	1.00E-04	1.23E-04	1.11E-02	8.40E-02	1.00E-04
Aug-12	1.00E-03	8.68E-02	1.28E-03	1.48E-05	8.13E-04	0.00E+00	4.00E-05	2.16E-04	1.13E-02	8.68E-02	0.00E+00
Sept-12	1.40E-03	9.00E-02	1.72E-03	1.00E-05	1.34E-03	1.23E-04	5.25E-04	2.53E-04	1.19E-02	9.00E-02	1.00E-05
Oct-12	1.50E-03	8.00E-02	2.00E-03	1.34E-05	1.10E-03	1.00E-04	9.00E-05	4.00E-04	1.07E-02	8.00E-02	1.34E-05
Nov-12	3.00E-03	9.95E-02	1.57E-03	1.58E-05	3.00E-04	1.25E-04	4.17E-04	1.23E-04	1.31E-02	9.95E-02	1.58E-05
Dec-12	2.30E-03	9.25E-02	1.37E-03	5.40E-05	4.00E-04	2.00E-04	1.00E-04	2.13E-04	1.21E-02	9.25E-02	5.40E-05
Jan-13	3.15E-03	9.05E-02	1.55E-03	1.00E-05	1.34E-03	1.23E-04	5.25E-04	2.53E-04	1.22E-02	9.05E-02	1.00E-05
Feb-13	3.40E-03	1.00E-01	1.82E-03	1.48E-05	9.00E-04	1.00E-04		6.00E-04	1.53E-02	1.00E-01	1.48E-05
Mar-13	1.73E-03	8.95E-02	1.89E-03	1.20E-05	1.33E-03	1.00E-04	2.30E-04	2.40E-04	1.19E-02	8.95E-02	1.20E-05
Apr-13	1.10E-03	8.54E-02	1.64E-03	5.74E-05	1.16E-03	5.00E-05	7.00E-05	5.00E-04	1.12E-02	8.54E-02	5.00E-05
May-13	1.20E-03	8.84E-02	1.50E-03	8.00E-06	1.35E-03	1.35E-04	1.36E-04	2.53E-04	1.16E-02	8.84E-02	8.00E-06
Jun-13	1.45E-03	8.50E-02	1.86E-03	1.03E-05	1.33E-03	1.10E-04	1.91E-04	2.00E-04	1.13E-02	8.50E-02	1.03E-05
Jul-13	2.25E-03	8.98E-02	1.78E-03	1.46E-05	7.00E-04	1.13E-04	2.53E-04	2.61E-04	1.19E-02	8.98E-02	1.46E-05
Aug-13	2.65E-03	9.60E-02	1.47E-03	3.49E-05	3.50E-04	1.63E-04	2.58E-04	1.68E-04	1.26E-02	9.60E-02	3.49E-05
Sept-13	2.73E-03	9.15E-02	1.46E-03	3.20E-05	8.69E-04	1.61E-04	3.13E-04	2.33E-04	1.22E-02	9.15E-02	3.20E-05
Oct-13	3.28E-03	9.53E-02	1.69E-03	1.24E-05	1.12E-03	1.11E-04	5.25E-04	4.27E-04	1.28E-02	9.53E-02	1.24E-05

Figure C.2: Monthly average upper springs flow rates over the period 2011-2013.

Elevation	SB01					MOY	max	min
	42	44	49	53	55			
	Pusur	Soka	Karangduren	Slembi	Gandol			
	446	435	414	392	389			
Nov-11	6.00E-02	7.70E-02	4.00E-02	2.00E-03	2.30E-02	4.04E-02	7.70E-02	2.00E-03
Dec-11	7.00E-02	7.15E-02	1.40E-02	2.95E-03	1.90E-02	3.55E-02	7.15E-02	2.95E-03
Jan-12	8.50E-02	6.25E-02	1.21E-02	3.40E-03	1.96E-02	3.65E-02	8.50E-02	3.40E-03
Feb-12	8.90E-02	8.70E-02	3.90E-02	2.00E-03	2.55E-02	4.85E-02	8.90E-02	2.00E-03
Mar-12	1.08E-01	8.20E-02	2.54E-02	3.00E-03	3.00E-02	4.96E-02	1.08E-01	3.00E-03
Apr-12	9.80E-02	7.65E-02	5.00E-02	1.95E-03	2.45E-02	5.02E-02	9.80E-02	1.95E-03
May-12	1.10E-01	7.70E-02	2.00E-02	4.00E-03	2.10E-02	4.64E-02	1.10E-01	4.00E-03
Jun-12	1.30E-01	7.75E-02	1.20E-02	3.57E-03	2.60E-02	4.98E-02	1.30E-01	3.57E-03
Jul-12	1.20E-01	6.00E-02	1.00E-02	5.00E-03	1.00E-02	4.10E-02	1.20E-01	5.00E-03
Aug-12	1.00E-01	5.00E-02	1.42E-02	4.45E-03	2.28E-02	3.83E-02	1.00E-01	4.45E-03
Sept-12	8.23E-02	5.50E-02	1.21E-02	4.73E-03	1.64E-02	3.41E-02	8.23E-02	4.73E-03
Oct-12	9.00E-02	9.50E-02	5.00E-02	3.00E-03	2.20E-02	5.20E-02	9.50E-02	3.00E-03
Nov-12	1.20E-01	1.00E-01	7.60E-03	2.30E-03	2.40E-02	5.08E-02	1.20E-01	2.30E-03
Dec-12	9.70E-02	1.10E-01	1.43E-02	2.40E-03	2.10E-02	4.89E-02	1.10E-01	2.40E-03
Jan-13	1.20E-01	1.20E-01	1.64E-02	6.00E-03	2.70E-02	5.79E-02	1.20E-01	6.00E-03
Feb-13	1.12E-01	1.15E-01	1.71E-02	2.76E-03	1.75E-02	5.28E-02	1.15E-01	2.76E-03
Mar-13	1.08E-01	1.18E-01	9.00E-03	4.60E-03	2.40E-02	5.27E-02	1.18E-01	4.60E-03
Apr-13	1.40E-01	1.00E-01	3.70E-02	4.00E-03	2.30E-02	6.08E-02	1.40E-01	4.00E-03
May-13	1.36E-01	1.09E-01	2.00E-02	3.20E-03	2.70E-02	5.90E-02	1.36E-01	3.20E-03
Jun-13	1.20E-01	8.25E-02	2.70E-02	2.50E-03	2.40E-02	5.12E-02	1.20E-01	2.50E-03
Jul-13	1.02E-01	9.56E-02	1.00E-02	1.20E-03	1.20E-02	4.41E-02	1.02E-01	1.20E-03
Aug-13	1.08E-01	8.91E-02	1.85E-02	1.85E-03	1.80E-02	4.70E-02	1.08E-01	1.85E-03
Sept-13	1.11E-01	9.23E-02	1.43E-02	1.53E-03	1.50E-02	4.69E-02	1.11E-01	1.53E-03
Oct-13	1.30E-01	9.07E-02	2.00E-02	4.00E-03	2.00E-02	5.29E-02	1.30E-01	4.00E-03

Figure C.3: Monthly average SBI springs flow rates over the period 2011-2013.

	SB02							
	61 Jolotundo	67 Ponggok	72 Nila	74 Pelem	75 Sigedang	76 Kapilaler	78 Cokro	
Elevation	283	259	244	236	226	225	221	
Nov-11	8.00E-02	8.00E-01	2.90E-01	3.00E-02	7.00E-02			
Dec-11	7.25E-02	8.00E-01	2.80E-01	2.20E-02	6.90E-02			
Jan-12	7.50E-02	8.00E-01	3.10E-01	4.00E-02	7.50E-02		1.15E+00	
Feb-12	8.00E-02	8.47E-01	2.90E-01	4.20E-02	6.00E-02	2.73E-01	1.18E+00	
Mar-12	5.00E-02	8.23E-01	3.40E-01	2.30E-02	7.00E-02	3.20E-01	1.17E+00	
Apr-12	5.85E-02	8.70E-01	2.85E-01	2.20E-02	6.00E-02	3.63E-01	1.19E+00	
May-12	3.60E-02	8.32E-01	2.95E-01	3.00E-02	5.90E-02	3.65E-01	1.19E+00	
Jun-12	7.63E-02	8.51E-01	3.00E-01	4.00E-02	7.80E-02	3.21E-01	1.15E+00	
Jul-12	3.20E-02	8.00E-01	3.15E-01	7.00E-03	7.50E-02	3.46E-01	1.17E+00	
Aug-12	2.40E-02	7.90E-01	3.13E-01	1.90E-02	6.00E-02	3.90E-01	1.14E+00	
Sept-12	6.50E-02	7.30E-01	2.90E-01	1.00E-01	7.00E-02	4.10E-01	1.15E+00	
Oct-12	3.00E-02	8.10E-01	3.00E-01	1.00E-02	8.60E-02	3.60E-01	1.17E+00	
Nov-12	5.00E-02	8.30E-01	3.00E-01	2.20E-02	7.00E-02	3.70E-01	1.13E+00	
Dec-12	6.00E-02	7.90E-01	3.01E-01	5.00E-02	7.50E-02	3.19E-01	1.18E+00	
Jan-13	6.50E-02	8.10E-01	3.02E-01	2.20E-02	8.00E-02	3.49E-01	1.13E+00	
Feb-13	2.80E-02	8.76E-01	3.03E-01	5.00E-02	7.00E-02	3.50E-01	1.17E+00	
Mar-13	7.00E-02	8.40E-01	3.03E-01	4.00E-02	7.00E-02	3.25E-01	1.19E+00	
Apr-13	8.00E-02	8.00E-01	2.90E-01	3.00E-02	7.10E-02	3.65E-01	1.15E+00	
May-13	4.00E-02	8.20E-01	3.00E-01	2.00E-02	7.20E-02	3.82E-01	1.16E+00	
Jun-13	4.50E-02	8.10E-01	3.10E-01	4.00E-02	7.80E-02	3.24E-01	1.13E+00	
Jul-13	3.00E-02	7.90E-01	3.00E-01	3.00E-02	7.00E-02	3.96E-01	1.12E+00	
Aug-13	4.65E-02	8.00E-01	2.90E-01	4.00E-02	7.40E-02	3.50E-01	1.15E+00	
Sept-13	4.90E-02	7.95E-01	3.20E-01	1.20E-02	6.00E-02	3.46E-01	1.15E+00	
Oct-13	5.00E-02	8.00E-01	3.40E-01	5.00E-02	5.90E-02	3.26E-01	1.13E+00	

Figure C.4: Monthly average SB2 springs flow rates over the period 2011-2013.

C.2.2 Spring monthly temperature

	UP									MOY
	1	2	6	7	20	26	30	38		
	Jelok	Bulu Kidul	Wonoganggi	Tutup	Candirejo	Lanjaran	Sokorejo	Kali Suden		
Elevation	1396	1358	1210	1206	986	875	830	591		
Nov-11	19.9	20.1	21.3	22.0	24.0	22.0	23.0	24.0		22.0
Dec-11	20.4	22.0	22.3	21.9	23.5	19.6	21.3	24.3		21.9
Jan-12	19.8	21.0	21.1	22.0	22.4	20.5	21.0	23.5		21.4
Feb-12	19.4	19.9	23.5	21.3	22.2	22.1	24.0	24.9		22.1
Mar-12	19.9	19.1	22.3	21.5	22.6	22.7	23.9	25.3		22.2
Apr-12	19.6	19.4	20.9	22.2	22.5	22.2	23.4	25.5		21.9
May-12	20.1	19.3	21.0	21.9	22.6	22.3	23.6	25.5		22.0
Jun-12	20.0	19.7	21.4	21.3	22.6	20.6	22.9	25.0		21.7
Jul-12	19.5	19.3	20.1	21.2	22.6	19.8	23.0	23.9		21.2
Aug-12	18.1	20.4	21.0	22.0	22.5	18.2	22.2	24.9		21.2
Sept-12	18.9	20.3	22.0	22.0	22.6	21.6	23.7	25.1		22.0
Oct-12	19.2	19.3	21.5	21.6	22.6	21.7	24.5	25.0		21.9
Nov-12	19.5	20.4	21.4	21.4	22.4	22.4	22.9	25.0		21.9
Dec-12	19.1	20.3	21.5	21.9	22.6	21.6	22.8	24.6		21.8
Jan-13	19.8	19.7	20.2	22.1	22.5	20.6	23.7	25.2		21.7
Feb-13	19.9	19.5	21.4	21.6	22.6	22.5	23.4	25.2		22.0
Mar-13	19.7	20.1	23.1	21.6	22.4	22.6	23.5	25.3		22.3
Apr-13	19.5	19.1	21.4	21.7	22.6	21.6	23.8	25.3		21.9
May-13	19.4	19.8	21.3	22.0	22.6	19.8	24.5	24.9		21.8
Jun-13	19.3	19.4	21.9	21.8	22.6	22.5	22.2	25.2		21.9
Jul-13	19.3	19.7	21.4	21.5	22.5	22.7	22.1	25.3		21.8
Aug-13	19.9	19.6	21.9	21.7	22.4	21.4	23	25.0		21.9
Sept-13	19.8	20.3	21.5	21.8	22.3	20.8	22.4	25.0		21.7
Oct-13	19.5	19.6	21.6	21.8	22.4			24.8		21.6

Figure C.5: Monthly average upper springs temperature over the period 2011-2013.

SB01						
	42	44	49	53	55	
	Pusur	Soka	Karangdurer	Slambi	Gandol	MOY
Elevation	446	435	414	392	389	
Nov-11	25.8	24.2	26.1	26.4	26.5	25.8
Dec-11	25.5	24.6	26.3	25.4	27.1	25.8
Jan-12	25.4	25.2	26.3	25.4	27.3	25.9
Feb-12	26.3	27.5	26.1	26.5	27.4	26.8
Mar-12	24.4	28.5	26.5	26.0	26.3	26.3
Apr-12	25.6	25.8	26.2	26.4	25.2	25.8
May-12	25.9	28.1	26.3	26.5	26.7	26.7
Jun-12	25.6	27.2	26.1	25.5	26.2	26.1
Jul-12	25.6	26.0	26.6	26.3	26.6	26.2
Aug-12	25.0	27.6	26.3	26.2	25.8	26.2
Sept-12	25.7	26.9	26.3	26.4	26.0	26.3
Oct-12	26.6	26.2	26.5	26.5	27.0	26.6
Nov-12	26.1	27.5	26.4	26.5	27.1	26.7
Dec-12	27.0	26.8	26.3	27.1	26.2	26.7
Jan-13	26.0	27.2	26.3	27.4	27.1	26.8
Feb-13	25.7	27.0	26.2	26.1	26.0	26.2
Mar-13	25.7	27.1	26.3	26.7	27.0	26.6
Apr-13	28.0	26.4	26.3	26.5	26.7	26.8
May-13	25.7	26.7	26.3	26.5	26.5	26.3
Jun-13	25.5	26.8	26.3	26.5	26.4	26.3
Jul-13	25.4	27.4	26.1	26.6	26.7	26.4
Aug-13	25.7	26.8	26.3	26.2	26.2	26.2
Sept-13	25.5	27.2	26.3	26.1	26.3	26.3
Oct-13	25.7	26.9	25.7	25.8	25.7	26.0

Figure C.6: Monthly average SBI springs temperature over the period 2011-2013.

SB02							
	61	67	72	74	75	76	78
	Jolotundo	Ponggok	Nila	Pelem	Sigedang	Kapilaler	Cokro
Elevation	283	259	244	236	226	225	221
Nov-11	8.00E-02	8.00E-01	2.90E-01	3.00E-02	7.00E-02		
Dec-11	7.25E-02	8.00E-01	2.80E-01	2.20E-02	6.90E-02		
Jan-12	7.50E-02	8.00E-01	3.10E-01	4.00E-02	7.50E-02		1.15E+00
Feb-12	8.00E-02	8.47E-01	2.90E-01	4.20E-02	6.00E-02	2.73E-01	1.18E+00
Mar-12	5.00E-02	8.23E-01	3.40E-01	2.30E-02	7.00E-02	3.20E-01	1.17E+00
Apr-12	5.85E-02	8.70E-01	2.85E-01	2.20E-02	6.00E-02	3.63E-01	1.19E+00
May-12	3.60E-02	8.32E-01	2.95E-01	3.00E-02	5.90E-02	3.65E-01	1.19E+00
Jun-12	7.63E-02	8.51E-01	3.00E-01	4.00E-02	7.80E-02	3.21E-01	1.15E+00
Jul-12	3.20E-02	8.00E-01	3.15E-01	7.00E-03	7.50E-02	3.46E-01	1.17E+00
Aug-12	2.40E-02	7.90E-01	3.13E-01	1.90E-02	6.00E-02	3.90E-01	1.14E+00
Sept-12	6.50E-02	7.30E-01	2.90E-01	1.00E-01	7.00E-02	4.10E-01	1.15E+00
Oct-12	3.00E-02	8.10E-01	3.00E-01	1.00E-02	8.60E-02	3.60E-01	1.17E+00
Nov-12	5.00E-02	8.30E-01	3.00E-01	2.20E-02	7.00E-02	3.70E-01	1.13E+00
Dec-12	6.00E-02	7.90E-01	3.01E-01	5.00E-02	7.50E-02	3.19E-01	1.18E+00
Jan-13	6.50E-02	8.10E-01	3.02E-01	2.20E-02	8.00E-02	3.49E-01	1.13E+00
Feb-13	2.80E-02	8.76E-01	3.03E-01	5.00E-02	7.00E-02	3.50E-01	1.17E+00
Mar-13	7.00E-02	8.40E-01	3.03E-01	4.00E-02	7.00E-02	3.25E-01	1.19E+00
Apr-13	8.00E-02	8.00E-01	2.90E-01	3.00E-02	7.10E-02	3.65E-01	1.15E+00
May-13	4.00E-02	8.20E-01	3.00E-01	2.00E-02	7.20E-02	3.82E-01	1.16E+00
Jun-13	4.50E-02	8.10E-01	3.10E-01	4.00E-02	7.80E-02	3.24E-01	1.13E+00
Jul-13	3.00E-02	7.90E-01	3.00E-01	3.00E-02	7.00E-02	3.96E-01	1.12E+00
Aug-13	4.65E-02	8.00E-01	2.90E-01	4.00E-02	7.40E-02	3.50E-01	1.15E+00
Sept-13	4.90E-02	7.95E-01	3.20E-01	1.20E-02	6.00E-02	3.46E-01	1.15E+00
Oct-13	5.00E-02	8.00E-01	3.40E-01	5.00E-02	5.90E-02	3.26E-01	1.13E+00

Figure C.7: Monthly average SB2 springs flow rates over the period 2011-2013.

D Pictures



Figure D.1: Termination of the massive andesitic lava flow near 1000 m asl on the Northern part of the watershed (near Cepogo village). The regressive erosion dismantles the lava in large blocks which are remobilized during the flood events. The pipe in foreground transports water from the Wonogangu spring (on the left) to Cepogo village (on the right).



Figure D.2: Few meters after the Pusur spring. The regressive erosion incises the detritic fan and the tuff deposit to reveal the top of the aquifer layer composed by coarse and boulder materials. From the Pusur spring, the Pusur river is perennial, showing that the river drains the aquifer.



Figure D.3: Pumping system to bring water from the upper spring to the villages.



Figure D.4: At Bulu Kidul spring, the famers have installed PVC pipe directly into the river bed to catch the top of the paleo-channel aquifer. The river shows a low surface flow here but 500 m downstream, the river bed is completely under water.



Figure D.5: During the dry season, several farmers are using shallow illegal wells to irrigate their rice field.



Figure D.6: Water sampling for isotope analysis at Slembi spring. As the springs are regularly used for domestic activities, the samples have been taken as close as possible of the main outlet of the spring.

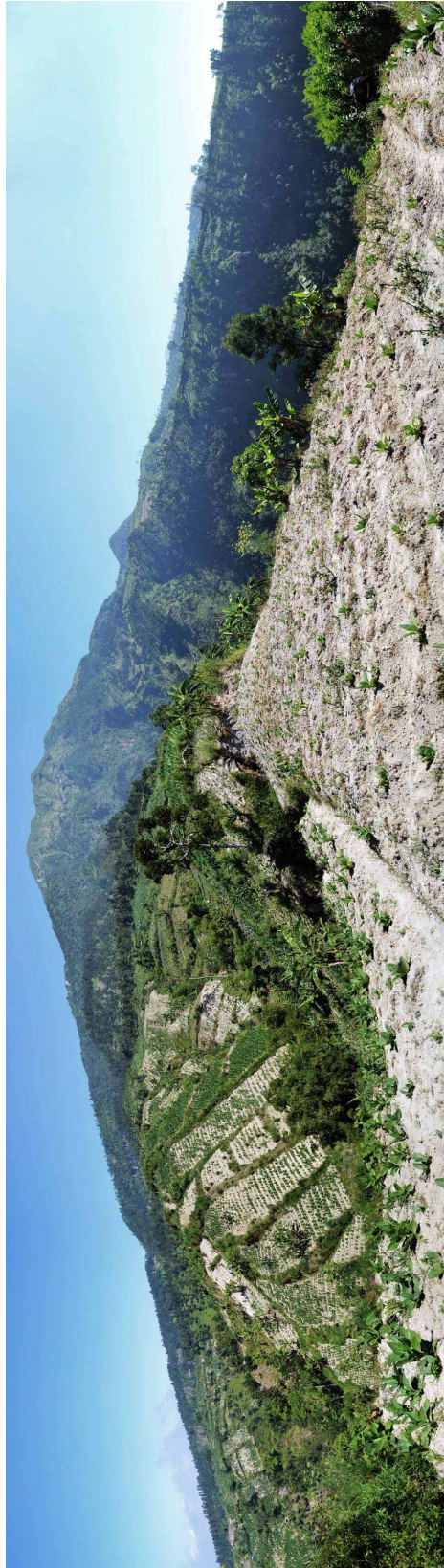


Figure D.7: View of the Pasar Bubar ridge (the Merapi Summit is just beyond) from the upper parts of the Eastern flank of the Merapi volcano (Picture taken at 1456 m asl). Notice on the left, the farmers are working on crops on slopes above than 45° . The G. Bibi is visible by the triangular relief on the right.

List of Figures

1.1	Geography of Indonesia, tectonic boundaries and volcanic activity. Indonesia is in green, and neighbouring countries are in grey. Bathymetric contours are at 200 m, 1000 m, 3000 m, 5000 m, and 6000 m. The location of the three most famous explosive eruptions known of the Indonesian volcanoes are shown in red text. Red arrows show plate convergence vectors for the Indian plate (IND-EUR) and the Philippine Sea plate (PSP-EUR) relative to Eurasia, and for the Australian plate relative to the Pacific plate (AUS-PAC). There is little thrusting at the Timor trough. The Seram trough and Flores-Wetar thrusts are the sites of active thrusting. Modified after Hall (2008)	8
1.2	Regional cross-section of Java margin (Modified after Clements et al. 2009).	8
1.3	Index map of the study area. Maps obtained by GeoMapApp (Ryan et al., 2009).	10
1.4	Geological map of Merapi and Yogyakarta basin showing the Opak River fault. Modified after Karnawati et al. (2006) ; Walter et al. (2008)	12
1.5	Simplified version of the 1:50000 geological map of Merapi volcano published in 1989 (Wirakusumah et al., 1989). UTM coordinates.	13
1.6	Sunrise on Merapi volcano, view from the Merbabu volcano (North).	14
1.7	Morphology of the summit area. Before the October–November eruption (left) and after the eruption (right). Depth of the new crater is about 200m (Surono et al., 2012).	15
1.8	Panorama of Merapi crater in March 2013. The andesitic dome is clearly visible (center).	16
1.9	Hazard map of Merapi area modified after Merapi Volcano Observatory of Yogyakarta (Balai Penyelidikan dan Pengembangan Teknologi Kegunung-ganian (BPPTK)) after the eruption of November 2010.	17
1.10	Mean sea-surface temperature (SST) in the tropical Pacific Ocean for the period January 1982-December 2012 (Clarke, 2014).	18

1.11	Observed rainfall (mm/day) on the period December to March averaged over 2001–2010, from the satellite based data TRMM-3B43. The stream lines show the surface wind from the atmospheric reanalysis ERAinterim averaged over the same period (Jourdain et al., 2013).	20
1.12	Map showing volcanoes that have been active in the last 10 000 years. Red triangles indicate the stratovolcanoes, the black points indicate the other types of volcanoes (calderas, shield volcanoes etc.). Data from the Smithsonian Institution, Global Volcanism Program.	23
1.13	Conceptual diagram of the hydrogeology of the volcanic-sedimentary sequence (Lloyd et al., 1985).	24
1.14	Study area map with the complete names of the rivers (K. means <i>Kali</i> , i.e. river in Javanese). The red line separates the Boyolali and the Klaten districts.	27
1.15	Map of the three hydrological watershed locations studied in this research project on the Eastern flank of Merapi volcano. UTM projection.	28
1.16	Main regencies and cities surrounding Mount Merapi. Numbers in brackets are estimated populations from World Bank, 2013	30
1.17	Land use map on the East flank of Merapi resulting from the field and satellite image analysis by the CIRAD and IAHRI (Lidon, 2012).	32
1.18	Sigedang spring. Its flow rate provides water to the downstream irrigated areas and is daily used by the people for laundry and cleaning activities but also for relaxing bath.	34
1.19	Danone-AQUA production and monitoring wells location map.	35
1.20	Water tank in rural area used for rain water storage during the rainy season and distribution during the dry season.	37
1.21	Offering near the Slembi spring. The offering can be made for special occasions or to invoke the “spring spirit” with request on the spring flow rate.	38
2.1	Pyroclastic fall deposits	48
2.2	Pyroclastic surge deposits incised by temporally river.	49
2.3	Schematic profile of an ignimbrite flow unit and the illustration of the wide ranges of facies of layers 1, 2 and 3. Modified after Sparks (1976)	50
2.4	Pyroclastic flow deposits with fine brown cemented matrix and coarse decimetric lava rocks included.	50
2.5	Lateral facies variation of the pyroclastic flow deposits. Modified after Wright et al. (1980)	51

2.6	Lithofacies of the volcanoclastic and reworked epiclastic deposits on the East flank of Merapi volcano and their depositional conditions into the valleys and interfluves. Note that the deposits can be cross-stratified and accumulated.	52
2.7	Volcanoclastic facies trends illustrates central-proximal-medial-distal facies variations in an andesitic system. Modified after Vessel & Davis (1981) ; Smith (1988) ; Bogie & Mackenzie (1998) ; Riggs & J. (1991)	55
2.8	Picture of Gunung Merapi and Gunung Bibi (to the right) from Klaten . .	56
2.9	East 3D views of the upstream Merapi flank and the major geological features. The geological history of Merapi volcano is detailed. Its geological history is complex and therefore controversial (Berthommier et al., 1990 ; Camus et al., 2000 ; Newhall et al., 2000 ; Voight et al., 2000 ; Gertisser et al., 2012b). In this study, we propose a combination of periods described in the literature: Proto-Merapi: >200 ka to 30 ka BP; Old Merapi: 30 ka to 4.8 ka BP; Middle Merapi: 4.8 ka to 2.2 ka BP; Recent Merapi: 2.2 ka to 0.3 ka BP and Modern Merapi: 0.3 ka BP to the present. Modified after the geological map by Wirakusumah et al. (1989) and Merapi DEM (ground resolution 15 m, courtesy of C. Gerstenecker, Technische Universität Darmstadt, Germany (Gerstenecker et al., 2005)).	60
2.10	Longitudinal profiles of the three main rivers on the eastern flank of Merapi: the Brambang (green), Pusur (red) and Soka (blue) Rivers and the interfluve topography (dot line) based on the DEM ASTER GDEM V2 data. The Soka River profile elevation is lower than the other rivers, reflecting an advanced state of erosion. The presence of the Merbabu volcano to the north could also explain a N-S orientation of Merapi deposits. In the north, Merapi deposits rest on Merbabu volcano but not in the south. Note three breaks in slope at 1000 m asl, 400 m asl and 200 m asl.	62
2.11	Conceptual model of the geometrical repartition of the volcano-clastic deposits along the eastern flank of Merapi volcano.	64
2.12	The last step to the top of Merapi. In foreground, a lava block fractured under the combined action of rain and temperature (night/day). September 2012.	65
2.13	Massive andesitic lava flow deposit incised by the river (up). These massive and thick layers (more than 20 m) consituted a long aquitard formation and the water flow over is (down).	66

2.14 Dismantling process of the lava flow deposits in the upper slopes of Merapi. The andesitic lava flow deposits are fractured and collapse by blocks or by full “lava plate”. After drawing of Benoît Deffontaines. 67

2.15 Andesitic lava block into the Brambang river bed remobilized during flood events. The stick length is one meter. 68

2.16 Conceptual block diagram of the upper Brambang and Soka Rivers (900 to 1200 m asl). All the major features have been concentrated in one portion of the river. 69

2.17 Andesitic lava block laying on welded tuff deposits on the Soka river. The blocks are accumulated in “natural dams” within the river meander, until the next flood which will remobilize most of them. 70

2.18 Map of the drainage network on Merapi volcano. A) Global view of the main rivers around the eastern flank of Merapi, B) identification of the drainage system anomaly with intercepted drainages by the Soka and Brambang Rivers, C) upstream (700 to 400 m asl) theoretical geometry of the drainage network, D) the map of the anomaly area characterized by a triangular shape and the springs occurrence at the downward limit of the anomaly. 71

2.19 Transversal topographic profiles at 9 different elevations showing the variation in river incision depths estimated from the DEM (15-m resolution) (courtesy of C. Gerstenecker, Technische Universität Darmstadt, Germany) for profiles A to G and from the DEM ASTER GDEM V2 model (30 m of ground resolution) for profiles H and I. The vertical and the horizontal scales are not the same on each profile. Note the incision difference between the two rivers, Soka and Brambang, and the Pusur River in the central position. This difference disappears below 400 m asl, highlighting the downstream end of the drainage anomaly. 73

2.20 Correlation of simplified lithostratigraphic sections of Merapi Volcano along the Brambang, Pusur and Soka rivers upstream (left) to downstream (right). The logs represent the synthesis of 4 zones depending on the elevation: zone A: from 1500 to 900 m asl, zone B: from 900 to 600 m asl, zone C: from 500 to 350 m asl and zone D: from 350 to 200 m asl. Note that the thickness of the formation is decreasing with the elevation. 75

- 2.21 *Debris avalanche deposits*: A) Large fractured megaclast of andesite, B) Basal layer with poly lithologic gravel and boulders, *Channelized debris flow deposits*: C) Channel axial profile filled by a coarse debris flow deposit, D) Longitudinal profile of channel filled by boulder and sandy matrix; *Hyperconcentrated debris flow*: E) Moderately normal graded pebble and large andesite boulder, F) Poly lithologic hyperconcentrated flow; *Fluvial deposits*: G) Sedimentary figures of bedding deposits with mature gravels; *Aeolian deposits*: H) Fine-grained cross-bedded sand. 77
- 2.22 Topographical and geological longitudinal cross-section of the detrital fan along the Pusur River axis (NW-SE) with 2 additional transversal cross-sections along the isohypses at 1000 and 500 m asl. The lithological facies have been simplified into 5 units. The local landslide formations are represented on the valley sides. Note that the paleo-Pusur River (represented by the central paleo-channel) is covered by an andesitic lava flow in the upstream parts and by the detrital fan downstream. The spring alignment at 400 m asl occurs at the termination of the detritic system where the paleo-channel outcrops. 78
- 2.23 Synthetic reconstitution of the recent superficial geomorphological history of the eastern flank of Merapi volcano. A: During the Old Merapi period, the rivers were organized radially. B: An extreme event occurred at the beginning of the Middle Merapi stage (approximately 5 ka BP). A detrital fan of debris avalanche deposits lay on the breaking slope near 500 m asl. C: After the extreme event at the end of the Middle Merapi stage (from 4 ka to 1.7 ka BP), the production of andesitic lava filled the paleo-valleys and closed the paleo-Pusur River. The high rate of erosion caused a relief inversion. D: Present day situation: the rivers flow in the paleo-interfluves, channelized by the lava flow deposits. The Brambang and Soka Rivers are divergent around the detrital fan and catch the surrounding radial rivers. The present day Pusur River incises the detrital fan by regressive erosion. At the end of the fan, an alignment of springs (spring belt) shows a change of lithology between the fan and the paleo-topography. Drawing on Merapi DEM (15-m resolution) (courtesy of C. Gerstenecker, Technische Universität Darmstadt, Germany, [Gerstenecker et al. \(2005\)](#)). 79

2.24	(A) Apparent coefficient of friction (H/L) versus volume of the deposit, and (B) relation between the maximum collapse height (H) and maximum travel distance (L) of the East flank of Merapi avalanche compared to other avalanches on stratovolcanoes. (RN=Roque Nublo (Canary Islands); EG=Egmont (New Zealand); FJ=Fuji (Japan); AS=Asama (Japan); AK=Akagi (Japan); CH=Chokai (Japan); BE=Bezymianny (Russia); SC=Schiveluch (Russia); SH=St.Helens (USA); CO=Colima (Mexico); PO=Popocatepetl (Mexico); SO=Socompa (Argentina/Chile); SA=Shasta (USA); the red shape shows the range of values for the East flank of Merapi avalanche). The data are taken from Siebert (1984) ; Ui et al. (1986) and Garcia Cacho et al. (1994) . The dashed lines in (B) represent the H/L constant ratios.	81
2.25	Some common electrode configurations for resistivity studies Herman (2001)	84
2.26	Geophysical profiles and resistivity sounding points around the Pusur River near the springs (SB2) and Danone-AQUA wells.	86
2.27	Electrical resistivity of the profile 2.	88
2.28	Electrical resistivity of the profile 7.	89
2.29	Electrical sounding n°10 with inversion model of the thickness of the layers (m).	90
2.30	Electrical sounding n°13 with inversion model of the thickness of the layers (m).	90
2.31	Electrical sounding n°1 with inversion model of the thickness of the layers (m).	90
2.32	Litho-stratigraphic logs of the AQUA monitoring wells	91
2.33	Electrical profile n°6 and the location of the AQUA wells projected 20 m to the north and Sigedang spring projected 60 m to the north.	92
2.34	Schematic conceptual model of the volcanoclastic distribution of facies associated with andesitic stratovolcanoes adapted for the eastern flank of Merapi volcano. The facies illustrate the proximal to distal variation and the lateral distribution, depending on the valley and the interfluvial dynamic.	94
3.1	Study area and the hydrological watersheds of Pusur, Soka and Brambang Rivers.	100
3.2	Deficient rain gauge at Gedaren village.	101
3.3	Manual temperature monitoring.	102

3.4	Hydroclimatic network map. Existing rain-gauges managed by the Klaten and Boyolali regencies (blue), the new rain-gauges installed in Jemowo, Sukurejo and Boyolali village (purple), weather station in gumuk village (red) and the Automatic Water Level Recorders (AWLR) settled on the main rivers.	103
3.5	Automatic Water level recorder (AWLR) on the Pusur river at Kemiri dam (400 m asl). The floating system is protected from the solid discharge by a PVC tube (in white) and fixed on the dam's wall.	103
3.6	Water balance processes illustration.	105
3.7	Map of the hydrological watershed locations on the Eastern flank of Merapi volcano. For each river, the hydrological watersheds monitored by the automatic water level recorder (AWLR) at 400 m asl is separated from the total watersheds extended from 2500 to 85m asl. In thumbnail, the elevation profile of the Eastern flank of Merapi volcano with the identification of 5 main break-in-slopes (2400m asl, 1200m asl, 800m asl, 400m asl and 220m asl). After the data from the Advanced Spaceborne Thermal Emission and Reflection Radiometer (ASTER), Global Digital Elevation Model Version 2 (GDEM V2) from the National Aeronautics and Space Administration (NASA) with 30 meters of resolution and 1 x 1 degree tiles.	109
3.8	Rice field on the low land, near Klaten city.	111
3.9	Long series of annual rainfall registered in Cokro Tulung (hydrological years Nov. 1989- Oct. 2013)	112
3.10	Monthly rainfall distribution through 24 years in Cokro-Tulung station (1989-2013). The monitored years 2011-2012 and 2012-2013 are isolated to define the trend of these years compare to the historical chronicle. The blank dots are the extreme events values, the dot line represent less than 25% of the data, the black line is the average monthly value, n=number of hydrological years.	113
3.11	Monthly rainfall at three elevations: 1436, 631 and 244 m asl, Gumuk, Musuk and AQUA respectively, for the hydrological year 2011-2012 and 2012-2013.	115
3.12	Annual rainfall for all stations of the research area sort by elevation for the period Nov. 2011 to Oct. 2012 (light blue) and Nov. 2012 to Oct. 2013 (deep blue).	116
3.13	Isohyet map for the hydrological year 2011-2012.	116
3.14	Isohyet map for the hydrological year 2012-2013.	117

3.15 Monthly average of climatic variables measured at Gumuk Weather Station (1456 m asl) over the two hydrological years 2011-2012 and 2012-2013. The blue marks demarcate the rainy season. 119

3.16 Annual potential Evapotranspiration (PET) by Thornthwaite method in millimeters for all the stations and their elevation (m asl) for the period of November 2011 to October 2013. 120

3.17 Comparison between the monthly average Potential Evapotranspiration (PET, blue bars) and the Real evapotranspiration (RET, yellow bars) at three elevations, 1436 m asl (Gumuk), 631 m asl (Musuk) and 301 m asl (Cokro-Tulung) over the period Nov.2011- Oct. 2013. The blue marks show the rainy seasons. 122

3.18 Estimation of the annual effective rainfall (mm) over the study area from November 2011 to October 2012. 123

3.19 Estimation of the annual effective rainfall (mm) over the study area from November 2012 to October 2013. 124

3.20 Monthly volumes of water registered by the AWLR on the Upper Brambang, Upper Pusur and Upper Soka rivers from December 2011 to December 2012. 127

3.21 Estimated mean daily discharge ($\text{m}^3 \cdot \text{s}^{-1}$) spilled over the dam where the AWLR (15 min recorder) is settled and derived to the intake on Upper Soka AWLR site, compare to the daily effective rainfall at Gumuk station and the monthly cumulated effective rainfall calculated over the upper Soka watershed from November 2011 to December 2012 128

3.22 Estimated mean daily discharge ($\text{m}^3 \cdot \text{s}^{-1}$) spilled over the dam and derived to the intake on Upper Pusur AWLR site (15 min recorder), compare to the daily effective rainfall at Sukorejo station and the monthly cumulated effective rainfall calculated over the upper Pusur watershed from November 2011 to December 2012 129

3.23 Estimated mean daily discharge ($\text{m}^3 \cdot \text{s}^{-1}$) spilled over the dam and derived to the intake on Upper Brambang AWLR site (15 min recorder), compare to the daily effective rainfall at Musuk station and the monthly cumulated effective rainfall calculated over the upper Brambang watershed from November 2011 to December 2012 130

3.24 Example of hydrograph analysis with the separated flows on the Brambang hydrograph. The hydrograph is decomposed in two parts: i) the direct runoff of the rainfall and ii) the flow coming from subsurface and groundwater contribution (base flow). 132

3.25 Monthly volumes of water registered by the AWLR on the upper Soka river from December 2011 to December 2012. Runoff (surface-hypodermic flow) and base flow (flow passing through an aquifer) contribution are separated. 133

3.26 Monthly volumes of water registered by the AWLR on the upper Pusur river from December 2011 to December 2012. Runoff (surface-hypodermic flow) and base flow (flow passing through an aquifer) contribution are separated. 134

3.27 Monthly volumes of water registered by the AWLR on the upper Brambang river from December 2011 to December 2012. Runoff (surface-hypodermic flow) and base flow (flow passing through an aquifer) contribution are separated. 134

4.1 Spatial distribution of the inventoried springs. On the study area including the watersheds of the Soka, Brambang and Pusur rivers, 3 springs zones have been identified depending on their elevations. 143

4.2 Spring zones defined depending on the spring elevations with the geological map modified after [Wirakusumah et al. \(1989\)](#). (A) the upper spring zone with lithological contact springs on the gully sides at the boundary between an aquifer and aquitard formation. (B) Spring belt 1, depression springs located along the topographic curve 400 m asl and covered by the detritic fan. (C) Spring belt 2, probably contact fault springs line up around 220 m asl. 144

4.3 Upper part springs. UP: River incision reveals the perched aquifer layer and spring conditions are observed. MIDDLE: Small temporary springs into tuff and lapilli deposits. BOTTOM: The “Water bearers” carry the water from the springs, mainly close to the rivers to the village located on the ridge. 145

4.4 Springs on the spring belt 1 location (SB1). Pusur and Tambak springs respectively. The Pusur river is perennial with a important flow rate while the other have high seasonal variations. Tambak spring is daily used for domestic cleaning activities. 146

4.5 Selected springs on the spring belt 2 (SB2) location. UP: Gedong spring, with an averaged flow rate of 500 L.s^{-1} , is mainly used for village water supply (pumping foreground). MIDDLE: Sunsang spring with a is mainly used as fish farming and BOTTOM: Cokro spring with averaged flow rate above 1000 L.s^{-1} is used ofr different purposes as cities drinking supply, irrigation supply and aquatic park supply. 148

4.6	Types of springs identified on Eastern flank of Merapi volcano, terminology after Fetter (1994) . (A) Lithological contact Springs occur where the erosion reveals the boundary between aquifer layers overlying less permeable rock or aquitards. (B) Depression springs are formed when the groundwater table intersects surface topography. (C) Contact fault springs lie along fault lines where the lithological formations have shifted from each other along the fault plan forming a barrier or a drain to groundwater movement.	149
4.7	Dug well near 450 m elevation (23 m deep).	152
4.8	Monitored dug well locations on geological map modified after Wirakusumah et al. (1989) .	152
4.9	Danone-AQUA production and monitoring well location map.	154
4.10	Lithological stratigraphic log of Danone-AQUA production well (PW) and the identified aquifer layers, modified after Kartadinata (2002) . The elevation of the dug wells have been measured with Differential Global Positioning System (DGPS) with an accuracy of 0.01 m. On the left, on the scale, the light blue arrow represents the water level of the first aquifer while the deep blue represents the second aquifer system.	157
4.11	Lithological stratigraphic log of Danone-AQUA monitoring wells (BH1 and BH2) and the identified aquifer layers, modified after Kartadinata (2002) . The elevation of the dug wells have been measured with Differential Global Positioning System (DGPS) with an accuracy of 0.01 m. The water level is not measured but both are artesian wells.	158
4.12	Bore wells inventoried on the Eastern flank of Merapi volcano. The color chart of the wells indicates the total depth.	159
4.13	Monitored bore wells MW01 upstream the SB2, Danone-AQUA well and MW02 downstream the SB2 near the Pusur River.	161
4.14	Schematic diagram of the monitoring wells (MW01 and MW02) configuration.	162
4.15	Lithological stratigraphic log of the monitoring well (MW01) located upstream the spring belt 2 and the identified aquifer layers. The elevation of the dug wells have been measured with Differential Global Positioning System (DGPS) with an accuracy of 0.01 m. The water level has been measured for the first aquifer system the 19/02/2013 (clear blue) and for the second one the 04/04/2013 (deep blue). As the water level of the deep aquifer is above the first one, the second aquifer system is confined.	164

4.16 Lithological stratigraphic log of the monitoring well (MW02) located downstream the spring belt 2 and the identified aquifer layers. The elevation of the dug wells have been measured with Differential Global Positioning System (DGPS) with an accuracy of 0.01 m. The water level has been measured for the first aquifer system the 05/11/2012 (clear blue) and for the second one the 06/01/2013 (deep blue). As the water level of the deep aquifer is below the first one, the second aquifer system is unconfined. . . . 165

4.17 Atmospheric Tritium concentration time evolution at Jakarta (Indonesia) between 1959 and 1997 completed by the data from Quezon city (Philippines) between 1999 and 2007 and the data extrapolation until 2012 based on the trend line equation. [IAEA-WMO \(2001\)](#) 169

4.18 Monthly average water level (bi-monthly measurement) elevation of the 15 monitored dug wells (first part) compared with the monthly rainfall at two elevations (Gumuk, 1456 m asl and Musuk, 631 m asl). The rainy season period is highlighted in blue. The error on the water level measurement is 0.1 m. Three variation trends can be observed (cf Text): dug wells with Red titles= trend 1; Green titles= trend 2; Purple titles= trend 3. 172

4.19 Monthly average water level (bi-monthly measurement) elevation of the 15 monitored dug wells (second part) compared with the monthly rainfall at two elevations (Gumuk, 1456 m asl and Musuk, 631 m asl). The rainy season period is highlighted in blue. The error on the water level measurement is 0.1 m. Three variation trends can be observed (cf Text): dug wells with Red titles= trend 1; Green titles= trend 2; Purple titles= trend 3. 173

4.20 Multi-layered configuration with alternation of pervious (grey andesitic boulders and gravels) and impervious layers (brown tuff and compacted ash) assimilated similar at the shallow aquifer (Brambang river). 174

4.21 Dry river bed composed by remobilized and unconsolidated boulder and lava block which create a preferential zone for water infiltration compared to the river edges composed by thick ash airfall and tuff deposits. 175

4.22 Piezometric map of the shallow aquifer at the end of the dry season 2011-2012 (September 2012) based on the water level monitoring of 15 dug wells. 176

4.23 Illustration of the seasonal water level variations of the upper part of the shallow multi-layered aquifer system measured into the dug wells. The shallow aquifer system (at least until 30 m below the ground surface) is composed by an alternation of aquitard (welded tuffs, air-fall deposits) and aquifer (sand, ignimbrite, decimetric lava blocks) formations. During the dry season, several disconnected perched aquifer formations provide a constant water level into the dug wells. Where the river incises the perched aquifer several perennial springs flow into the dry river bed, which is a preferential zone for the deep infiltration and groundwater recharge. During the wet season, the water level increases while the water infiltrates into the unsaturated zone and reaches the different aquifer layers. 177

4.24 Comparison of the monthly rainfall of Musuk (631 m asl) and Cokro (301 m asl) stations with the monthly average production artesian flow rate within the Danone AQUA well October 2009 to December 2013 for Musuk and AQUA well and from August 2008 to December 2013 for Cokro station. . . 179

4.25 Comparison of the monthly average artesian and production flow rate within the Danone AQUA well with the water level, temperature and Electric conductivity over the period October 2009 to December 2013 for Musuk and AQUA well and from August 2008 to December 2013 for Cokro station. The first chart shows the total volume flowing out the artesian well and the extracted volume used by Danone-AQUA for the drinking bottle production. The difference is released and considered as overflow to the Sigidang spring and then used for irrigation purpose. 180

4.26 Comparison of the daily rainfall of Gumuk, Musuk and Cokro stations with the daily average water level elevation within the monitoring well 1 (MW1) the monitoring well 2 (MW2) and with the daily flow rate at the Danone-AQUA well (PW) for the period January 2013 to March 2014. The date in blue represents the wet season. 182

4.27 Piezometric head representation between the three monitored wells, the Cokro spring (spring n°78) and the Pusur river. The elevations have been measured with a differential GPS and the hydraulic gradients of the shallow and deep aquifer system can be calculated. 184

4.28 Water level elevation corrected with atmospheric pressure during the pumping well in April 2013 at MW1 well. 185

4.29 Log/log plot of the drawdown (m) versus time (s) of the pumping test at MW1 on the shallow aquifer. $Q=0.002 \text{ m}^3 \text{ s}^{-1}$ with maximal drawdown of 1 m. 186

4.30 Drawdown and recovery (m) versus relative time (s) of the pumping test at MW2 on the shallow aquifer. $Q=0.002 \text{ m}^3 \text{ s}^{-1}$ with maximal drawdown of less than 1 m. 187

4.31 Log/log plot of the drawdown (m) versus time (s) of the pumping test at MW2 on the shallow aquifer. $Q=0.002 \text{ m}^3 \text{ s}^{-1}$ with maximal drawdown of less than 1 m. 187

4.32 Drawdown and recovery (m) versus relative time (s) of the pumping test at MW2 on the shallow aquifer. $Q=0.002 \text{ m}^3 \text{ s}^{-1}$ with maximal drawdown of 17.3 m. 188

4.33 Log/log plot of the drawdown (m) versus time (s) of the pumping test at MW2 on the deep aquifer. $Q=0.002 \text{ m}^3 \text{ s}^{-1}$ with maximal drawdown of 17.3 m. 188

4.34 Picture of small buried paleo-channel on the Soka river side. The andesitic boulders are unsorted and buried into a fine matrix of ash and tuff. 190

4.35 Monthly average values and minimal and maximal values of flow rate on the 20 monitored springs from November 2011 to October 2013. The results have been divided in 3 spring zones (upper, SB1 and SB2). The wet seasons are indicated in blue. 191

4.36 Monthly average values and minimal and maximal values of flow rate on the 20 monitored springs from November 2011 to October 2013 compared with the monthly rainfall at three elevations (Gumuk, 1456 m asl; Musuk, 631 m asl; and AQUA, 221 m asl). The results have been divided in three spring zones (upper, SB1, SB2). The wet seasons are indicated in blue. The error on each measured depends of the spring zone. For the Upper springs, the mean monthly flow rate are given with an error of $0.0005 \text{ m}^3 \cdot \text{s}^{-1}$; at SB1 the error is $0.001 \text{ m}^3 \cdot \text{s}^{-1}$ and for SB2, the error on flow rate is at $0.01 \text{ m}^3 \cdot \text{s}^{-1}$ 193

4.37 Monthly average values of electric conductivity on the 20 monitored springs from November 2011 to October 2013 compared with the monthly rainfall at three elevations (Gumuk, 1456 m asl; Musuk, 631 m asl; and AQUA, 221 m asl). The results have been divided in three spring zones (upper, SB1, SB2). The wet seasons are indicated in blue. The values are presented with an error of $10 \mu\text{S cm}^{-1}$ 195

4.38 Monthly average values of water temperature on the 20 monitored springs from November 2011 to October 2013 compared with the monthly rainfall at three elevations (Gumuk, 1456 m asl; Musuk, 631 m asl; and AQUA, 221 m asl). The results have been divided in three spring zones (upper, SB1 and SB2). The wet season are indicated in blue. 197

4.39 Average water flow rate of the monitored springs during the wet season 2012-2013 (January 213) and during the end of the dry season (August 2013). The results have been divided in three spring zones (upper, SB1, SB2). 199

4.40 Average water flow rate of the monitored springs during the wet season 2012-2013 (January 213) reported on the geological map. 200

4.41 Monthly average electrical conductivity values on the 20 monitored springs in November 2012. 201

4.42 Monthly average electrical conductivity values on the 20 monitored springs in January 2013. 202

4.43 Annual average values of water and air temperatures on the 20 monitored springs for two hydrological years Nov. 2011 - Oct. 2012 and Nov.2012 - Oct. 2013. The dashed line represents the orographic air temperature gradient. The temperature is noted with an error of 0.1°C for the springs and 0.2°C for the air. 204

4.44 Monthly average values of water temperature on the 20 monitored springs in January 2013. 205

4.45 Relationship between the $\delta^{18}\text{O}$ values from the 3 spring zones (upper, SB1 and SB2), the dug wells, bore wells (data from the isotopic survey of April 2012) and the AQUA production well (data from the UGM isotopic survey in November 2007) according to the elevation 209

4.46 Relationship between the $\delta^{18}\text{O}$ values from the three spring zones (upper, SB1 and SB2) (data from the isotopic survey of October 2012) according to the elevation 210

4.47 $\delta^{18}\text{O}$ spatial distribution into the groundwater in April 2012. 211

4.48 Spatial distribution of ^3H values in spring water (sampling survey of March 2012) 213

4.49 Spatial distribution of ^3H values in spring water (sampling survey of October 2012) 214

4.50 Distances and elevations chosen to calculate the groundwater transit time from the recharge areas to the spring zones (upper, SB1, SB2) through four pathways reported on the East flank of Merapi cross-section (from DEM ASTER GDEM V2 with 30 m ground resolution). (cf Fig. 4.51). 219

4.51 Saturated cross-sections considered to calculate the groundwater transit time associated to each spring zone: (A) upper springs, (B) spring belt 1 (SB1), and two configurations possible for the second spring belt (SB2) where (C) suggests one unique recharge area whereas (D) considers a mix between shallow and deep groundwater circulations. 220

4.52 Hydrogeological conceptual model of the Eastern flank of Merapi volcano. Identifying two groundwater circulations through a shallow aquifer system composed by an alternation of aquifers and aquitards, and with a deep aquifer system formed by preferential path flow whose are the buried paleo-rivers. 224

5.1 Schematic temperature profiles showing deviations from the geothermal gradient caused by surface warming in the surficial zone and convection in the geothermal zone. The ground water recharge results in concave upward profiles, whereas groundwater discharge results in convex upward profiles (modified after [Taniguchi et al. 1999](#)). 231

5.2 Illustration of a typical (forced-convection) groundwater flow field caused by topographic relief (at any scale) that repeats horizontally and results in the indicated boundary conditions. The bold flow lines indicate the edges of unit flow cells where boundary conditions apply. The boundary conditions are zero groundwater and constant heat flow at the base, no heat and no groundwater flow at the sides (usually due to model symmetry representing repeated ridge-valley combinations), and constant hydraulic head and mean annual surface temperature (possibly following the adiabatic lapse rate of the atmosphere) at the top, representing the water table. A fault is included as a reminder that an advective heat discharge boundary condition may be required. Numbers indicate typical steady-state geotherm profiles expected in the respective groundwater flow field regions: (1) isothermal (cold) near-surface profile in a recharge region, (2) low-temperature horizontal flow at some depth that has not completely thermally equilibrated at the given position, (3) linear profile as thermally equilibrated flow is perpendicular to the geothermal heat flow vector, and (4) elevated near-surface geothermal gradients in discharge zones ([Saar, 2011](#)). 232

5.3	From observations to modeling: A) Eastern flank of Merapi map with the experimental catchment boundaries, the spring zones and the cross-section chosen for the modeling. On the left, the precise DEM (ground resolution 15 m, courtesy of C. Gerstenecker, Gerstenecker et al. (2005)) shows the ancient caldera which culminates at 1500 m asl (red dot line) as west boundary of the watershed. On the right, the DEM ASTER GDEM V2 with 30 m ground resolution. B) Schematic illustration of the conceptual model of the groundwater circulation through the saturated zone on the Eastern flank of the Merapi. The spring belt 1 (SB1) at 400 m asl drains a shallow aquifer with local recharge area covered by detritic fan. This shallow aquifer reaches also the spring belt 2 (SB2) near 200 m asl. The remaining questions concern the water table position in the high elevations and the number of deep aquifer systems. C) hydraulic conductivity grid configuration employed in numerical simulations with the METIS model and the flow and heat boundary conditions.	238
5.4	Simplified diagram of the different zones used for the numerical model. The recharge is calculated for 3 zones (upper parts, the fan zone and the area between the two spring belts) along the model cross-section line.	242
5.5	Calculation of the mass equivalent to the $\delta^{18}O$ concentration along the model profile based on the isotope orographic gradient observed in April 2012. The concentration has been normalized to simplify the mass transfer input parameter.	244
5.6	Test 1: Flow simulation with initial configuration after the conceptual model. The simulated flow rate (Q1 and Q2) are compared to the observed ones (Q1obs: $3.25 \times 10^{-5} \text{m}^3 \cdot \text{s}^{-1}$ and Q2obs: $3.57 \times 10^{-4} \text{m}^3 \cdot \text{s}^{-1}$). Simulation in 2D cross-section calculated in steady flow with METIS.	247
5.7	Test 20: Flow simulation n°20 with best results. The simulated flow rates (Q1 and Q2) are compared to the observed ones (Q1obs: $3.25 \times 10^{-5} \text{m}^3 \cdot \text{s}^{-1}$ and Q2obs: $3.57 \times 10^{-4} \text{m}^3 \cdot \text{s}^{-1}$). Simulation in 2D cross-section calculated in steady flow with METIS.	250
5.8	Test 40: Mass concentration spatial distribution within 2D cross-section. The simulated concentrations C1 and C2 values have to be compared to the observed ones: C1obs. ranges from 2.5 to 3.5 and C2 obs. from 1.5 to 2.5. All the simulations have been calculated in steady flow with METIS.	252
5.9	Test 40: Hydraulic head along the model profile. The simulated flow rate (Q1 and Q2) are compared to the observed ones (Q1obs: $3.25 \times 10^{-5} \text{m}^3 \cdot \text{s}^{-1}$ and Q2obs: $3.57 \times 10^{-4} \text{m}^3 \cdot \text{s}^{-1}$). Simulation in 2D cross-section calculated in steady flow with METIS.	252

5.10 Water table simulation for the aquifer 1 and Aquifer 2 with the test 40. The topographic profile has been drawn after the DEM ASTER GDEM V2 with 30 m ground resolution. 253

5.11 Test 50: Calculated mass concentration spatial distribution within 2D cross-section after the model geometry sensitivity test n°50. The calculated concentrations C1 and C2 values have to be compared to the observed ones: C1obs. ranges from 2.5 to 3.5 and C2 obs. from 1.5 to 2.5. All the simulations have been calculated in steady flow with METIS. 256

5.12 Water table simulation for the aquifer 1 and Aquifer 2 with the test 50. The topographic profile has been drawn after the DEM ASTER GDEM V2 with 30 m ground resolution. 256

5.13 Impact of the variation of the imposed temperature considered as geothermal gradient on the mean annual spring temperature (T1 and T2 at SB1 and SB2 respectively). The range of observed spring temperature range is noted by reddish and green zones. 260

5.14 Calculated temperature spatial distribution for the test 56 with the bottom imposed temperature at 22°C. 261

5.15 Zoom of the SB2 zone on the calculated temperature profile for the test 56 with imposed temperature 22°C. 261

5.16 Groundwater Darcy velocity calculated by the model METIS for flow, mass and heat transfer and visualized with COMET and the distances used to calculate the water transfer time. The vector representing the velocity ranging from $2.3 \times 10^{-15} \text{m.s}^{-1}$ to $2.5 \times 10^{-5} \text{m.s}^{-1}$ 262

6.1 Spatial distribution of Nitrates values in springs water and dug wells (sampling survey of March 2012) 272

6.2 Piper plots of groundwater chemistry at the end of the wet season (campaign March 2012) 277

6.3 Piper plots of groundwater chemistry at the end of the dry season (campaign November 2012) 278

6.4 Nitrate, Silica, Chlorine, Potassium and Magnesium, Sodium concentration (mg.L^{-1}) and total mineralization (mg.L^{-1}) of spring water (*UP: upper part, SB1: Spring belt 01, SB2: Spring belt 02), dug wells and bore wells depending on the elevation for the campaign of March 2012. The increasing trend of the water mineralization with the decreasing elevation shows the enhancement of the water mineralization by rock-water interaction through the water pathway. 280

6.5	Nitrate, Silica, Chlorine, Potassium and Magnesium, Sodium concentration (mg.L ⁻¹) and total mineralization (mg.L ⁻¹) of spring water (*UP: upper part, SB1: Spring belt 01, SB2: Spring belt 02) depending on the elevation for the campaign of November 2012.	281
6.6	Concentration of Na as a dependent variable of Cl for the 25 sample in March 2012 (top) and the 24 sample of November 2012 (bottom).	282
A.1	Classification of the pyroclastic rocks.	322
A.2	Time scale of the Merapi volcano evolution and the main deposit types. . .	324
B.1	Profile n°1	325
B.2	Profile n°2	325
B.3	Profile n°3	326
B.4	Profile n°4	326
B.5	Profile n°5	326
B.6	Profile n°6 with AQUA wells and Sigedang spring projected on the profile (20 m and 60 m respectively).	327
B.7	Profile n°7	327
B.8	Profile n°8	327
B.9	Profile n°9	328
B.10	Profile n°10	328
B.11	Lateral lines of resistivity profiles near SB2.	330
B.12	Sounding point 01	332
B.13	Sounding point 02	332
B.14	Sounding point 03	332
B.15	Sounding point 04	333
B.16	Sounding point 05	333
B.17	Sounding point 06	333
C.1	Neumann's type curves for unconfined aquifer (Neuman, 1972).	337
C.2	Monthly average upper springs flow rates over the period 2011-2013.	339
C.3	Monthly average SB1 springs flow rates over the period 2011-2013.	340
C.4	Monthly average SB2 springs flow rates over the period 2011-2013.	341
C.5	Monthly average upper springs temperature over the period 2011-2013. . .	342
C.6	Monthly average SB1 springs temperature over the period 2011-2013. . . .	343
C.7	Monthly average SB2 springs flow rates over the period 2011-2013.	343

D.1 Termination of the massive andesitic lava flow near 1000 m asl on the Northern part of the watershed (near Cepogo village). The regressive erosion dismantles the lava in large blocks which are remobilized during the flood events. The pipe in foreground transports water from the Wono-ganggu spring (on the left) to Cepogo village (on the right). 344

D.2 Few meters after the Pusur spring. The regressive erosion incises the detritic fan and the tuff deposit to reveal the top of the aquifer layer composed by coarse and boulder materials. From the Pusur spring, the Pusur river is perennial, showing that the river drains the aquifer. 345

D.3 Pumping system to bring water from the upper spring to the villages. . . . 345

D.4 At Bulu Kidul spring, the famers have installed PVC pipe directly into the river bed to catch the top of the paleo-channel aquifer. The river shows a low surface flow here but 500 m downstream, the river bed is completely under water. 345

D.5 During the dry season, several farmers are using shallow illegal wells to irrigate their rice field. 346

D.6 Water sampling for isotope analysis at Slembi spring. As the springs are regularly used for domestic activities, the samples have been taken as close as possible of the main outlet of the spring. 346

D.7 View of the Pasar Bubar ridge (the Merapi Summit is just beyond) from the upper parts of the Eastern flank of the Merapi volcano (Picture taken at 1456 m asl). Notice on the left, the farmers are working on crops on slopes above than 45°. The G. Bibi is visible by the trianguar relief on the right. 347

List of Tables

1.1	Representative values of porosity, effective porosity and hydraulic conductivity for the main rock types on andesitic volcano-detritic edifices.	26
1.2	Demography evolution in Central Java from 1971 to 2010 (Statistik, 2010)	31
2.1	Litho-facies determination of the volcano-sedimentary deposits and hydrogeological type of formations of the East flank of Merapi volcano.	63
2.2	Characteristics of the volcano-sedimentary deposits environment along the East flank of Merapi volcano.	65
3.1	Location of the automatic water level recorders (AWLR) used to monitor surface water fluxes within the 3 catchments and details of the total catchments located within the experimental site. The coordinates are expressed in meters within WGS84 referential (UTM).	110
3.2	Rainfall and volume calculation at the watershed scale. The “Upper” watersheds define the catchment monitored upstream the AWLR. The “Total Watershed” is defined as the complete study area combining the 3 main watersheds (Soka, Pusur and Brambang watersheds). The volume calculations have been done by isohyets method.	117
3.3	Average annual potential evapotranspiration estimation (PET) by Thornthwaite method and its volume calculation at the watershed scale. The “Upper” watersheds define the catchment monitored upstream the AWLR. The “Total Watershed” is defined as the complete study area combining the 3 main watersheds (Soka, Pusur and Brambang watersheds).	121
3.4	The effective rainfall and its volume calculation at the watershed scale. The “Upper” watersheds define the catchment monitored upstream the AWLR. The “Total Watershed” is defined as the complete study area combining the 3 mains watersheds (Soka, Pusur and Brambang watersheds).	125

3.5	Runoff and base flow volume estimation for the hydrological year 2012-2013 deduced from the portion of the effective rainfall of the year 2011-2012. The runoff values are expressed in million of m ³ and in percentage of effective rainfall.	135
3.6	Water balance estimation on the AWLR watersheds and the total watersheds (WS) for the period from Nov.2011 to Oct. 2013. The results are expressed in millimeters (mm), millions of cube meters (10 ⁶ m ³) and percentage of rainfall.	136
4.1	Spring monitored since October 2011 until now. The altitudes have been measured with a Differential Global Positioning System (DGPS) with an accuracy of 0.01 m.	150
4.2	Dug well monitored since October 2011 until now. The elevation of the dug wells has been measured with Differential Global Positioning System (DGPS) with an accuracy of 0.01 m.	153
4.3	Hydraulic parameters of the shallow and deep multi-layered aquifer systems at MW1 and MW2 locations.	189
4.4	Water mixing ratios on six springs of SB2 zone considering recharge areas located at 1200 m asl and 400 m asl. The ratios are established based on the comparison of the annual mean spring temperature (over the period 2012-2013) and the orographic air temperature gradient (-0.8°C per 100 m elevation).	207
4.5	Mixing ratios deduced from the spring's δ ¹⁸ O concentrations , considering recharge areas at 1200 m and 400 m asl for six springs of the SB2 zone. . .	212
4.6	Calculation of the cinematic velocity and the water transit time for each spring zone after the Darcy's law based on the hydraulic parameters estimated with the pumping test.	222
5.1	Parameters used in groundwater flow, heat transfer and mass transport simulations.	235
5.2	Initial hydraulic conductivity values of the model units. The values of the shallow and deep aquifer are based on the hydraulic tests while the others are based on the literature for the corresponding lithology Hurwitz et al. (2003) ; Flint & Selker (2003) ; Custodio (2004) ; Cattoni et al. (2007) ; Singhal & Gupta (2010)	241

5.3 Recharge and discharge values calculated from the observations to the METIS model. The mean annual recharge is expressed in $m.s^{-1}$ and $m^3.y^{-1}$. The model discharge is calculated from the average annual discharge of the springs and reported on the model cross-section unit line. . . 243

5.4 Thermal transfer parameters depending on the lithological formation (Mueller et al., 2011; Winograd, 1971) 245

5.5 Hydraulic conductivity sensitivity test and results on flow rates at SB1 and SB2 (Q1 and Q2 respectively), residual flow rate (Q3) and maximal piezometric head (h) for selected flow simulations. 249

5.6 Tests on the hydraulic conductivity of the model units and the impact on the simulated mass concentration at SB1 and SB2 (C1 and C2 respectively), the simulated flow rates of SB1 and SB2 (Q1 and Q2), on the simulated residual flow rates and the simulated maximal piezometric head. 251

5.7 Sensivity tests of the geometry of the different units in calculated flow and mass simulations and their impact on the mass concentration at SB1 and SB2, the SB1 and SB2 flow rates, the calculated residual flow rate and the calculated maximal piezometric head. 255

5.8 Thermal parameter sensitivity test with the impact on the spring temperatures (T1 and T2 at SB1 and SB2 respectively) 258

5.9 Estimation of the water transit time for the Aquifer 1, 2 and 3 for three distances: Recharge area (1500 m asl) to SB1 (400 m asl), recharge to SB2 (200 m asl) and SB1 to SB2. 263

6.1 Chemical composition of lava and pyroclastic formation on Merapi volcano (Gertisser & Keller, 003b). 274

6.2 Results of the hydrochemical analysis of March 2012. 275

6.3 Results of the hydrochemical analysis of November 2012. 276

